sustainability

Special Issue Reprint

Application of Remote Sensing and Machine Learning in Sustainable Agriculture

Edited by
Mihai Valentin Herbei, Ana Cornelia Badea, Aleksandar Ristić and Paul Sestras

mdpi.com/journal/sustainability

MDPI

Application of Remote Sensing and Machine Learning in Sustainable Agriculture

Application of Remote Sensing and Machine Learning in Sustainable Agriculture

Guest Editors

Mihai Valentin Herbei
Ana Cornelia Badea
Aleksandar Ristić
Paul Sestras

MDPI

Basel • Beijing • Wuhan • Barcelona • Belgrade • Novi Sad • Cluj • Manchester

Guest Editors

Mihai Valentin Herbei
Faculty of Agriculture
University of Life Sciences
"King Mihai I" from Timisoara
Timișoara
Romania

Ana Cornelia Badea
Faculty of Geodesy
Technical University of Civil
Engineering
Bucharest
Romania

Aleksandar Ristić
Computing and Control
Department
University of Novi Sad
Novi Sad
Serbia

Paul Sestras
Faculty of Forestry and
Cadastre
University of Agricultural
Sciences and Veterinary
Medicine Cluj-Napoca
Cluj-Napoca
Romania

Editorial Office
MDPI AG
Grosspeteranlage 5
4052 Basel, Switzerland

This is a reprint of the Special Issue, published open access by the journal *Sustainability* (ISSN 2071-1050), freely accessible at: https://www.mdpi.com/journal/sustainability/special_issues/6MOA32L7F3.

For citation purposes, cite each article independently as indicated on the article page online and as indicated below:

Lastname, A.A.; Lastname, B.B. Article Title. *Journal Name* **Year**, *Volume Number*, Page Range.

ISBN 978-3-7258-9437-6 (Hbk)
ISBN 978-3-7258-9438-3 (PDF)
https://doi.org/10.3390/books978-3-7258-9438-3

© 2026 by the authors. Articles in this reprint are Open Access and distributed under the Creative Commons Attribution (CC BY) license. The reprint as a whole is distributed by MDPI under the terms and conditions of the Creative Commons Attribution-NonCommercial-NoDerivs (CC BY-NC-ND) license (https://creativecommons.org/licenses/by-nc-nd/4.0/).

Contents

Mihai Valentin Herbei, Ana Cornelia Badea, Aleksandar Ristić and Paul Sestras
Application of Remote Sensing and Machine Learning in Sustainable Agriculture
Reprinted from: *Sustainability* **2026**, *18*, 9472, https://doi.org/10.3390/su18189472 . . . . . **1**

Xingchen Dong, Shiqian Guo, Zichen Guo, Xu Jiang, Senyu Mao, Ruihong Jia and Ji Wang
Remote Sensing Inversion Model of Cultivated Land Salinity Based on Attention Mechanism and Lightweight CNN: Construction, Validation, and Multi-Model Comparative Analysis
Reprinted from: *Sustainability* **2026**, *18*, 8372, https://doi.org/10.3390/su18168372 . . . . . **9**

Rubab Shafique, Sharzil Haris Khan, Jihyoung Ryu and Seung Won Lee
Weather-Driven Predictive Models for Jassid and Thrips Infestation in Cotton Crop
Reprinted from: *Sustainability* **2025**, *17*, 2803, https://doi.org/10.3390/su17072803 . . . . . **34**

Asparuh I. Atanasov, Atanas Z. Atanasov and Boris I. Evstatiev
A Remote Sensing Approach for Biomass Assessment in Winter Wheat Using the NDVI Second Derivative in Terms of NIR
Reprinted from: *Sustainability* **2025**, *17*, 7299, https://doi.org/10.3390/su17167299 . . . . . **51**

Luminiţa L. Cojocariu, Nicolae Marinel Horablaga, Cosmin Alin Popescu, Adina Horablaga, Monica Bella-Sfîrcoci and Loredana Copăcean
Mapping Grassland Suitability Through GIS and AHP for Sustainable Management: A Case Study of Hunedoara County, Romania
Reprinted from: *Sustainability* **2026**, *18*, 1155, https://doi.org/10.3390/su18031155 . . . . . **72**

Claudiu Coman, Ecaterina Coman, Vasile Gherheș, Anna Bucs and Dana Rad
Application of Remote Sensing and Machine Learning in Sustainable Agriculture
Reprinted from: *Sustainability* **2025**, *17*, 5601, https://doi.org/10.3390/su17125601 . . . . . **105**

Dušan Jovanović, Miro Govedarica, Milan Gavrilović, Ranko Čabilovski and Tamme van der Wal
Multi-Source Data Integration for Sustainable Management Zone Delineation in Precision Agriculture
Reprinted from: *Sustainability* **2025**, *17*, 6931, https://doi.org/10.3390/su17156931 . . . . . **123**

Vasile Adrian Nan, Gheorghe Badea, Ana Cornelia Badea and Anca Patricia Grădinaru
A Systematic Review of AI-Based Classifications Used in Agricultural Monitoring in the Context of Achieving the Sustainable Development Goals
Reprinted from: *Sustainability* **2025**, *17*, 8526, https://doi.org/10.3390/su17198526 . . . . . **153**

Jalampelli Thirupathi, Nandagopal Malarvizhi and Potula Sree Brahmanandam
From Benchmark Accuracy to Field Performance: Hybrid Deep Learning-Based Plant Disease Classification with IoT-Enabled Environmental Monitoring
Reprinted from: *Sustainability* **2026**, *18*, 6867, https://doi.org/10.3390/su18136867 . . . . . **193**

Ahmed Attia, Prem Woli, Charles R. Long, Francis M. Rouquette, Jr. and Gerald R. Smith
Satellite-Guided Delineation of Crop Production Zones from Official Crop Statistics for Spatial Agricultural Decision Support
Reprinted from: *Sustainability* **2026**, *18*, 6937, https://doi.org/10.3390/su18146937 . . . . . **223**

sustainability

MDPI

Editorial

Application of Remote Sensing and Machine Learning in Sustainable Agriculture

Mihai Valentin Herbei [1,*], Ana Cornelia Badea [2], Aleksandar Ristić [3] and Paul Sestras [4]

[1] Department of Sustainable Development and Environmental Engineering, Faculty of Agriculture, University of Life Sciences "King Mihai I", 300645 Timisoara, Romania
[2] Faculty of Geodesy, Technical University of Civil Engineering of Bucharest, 020396 Bucharest, Romania; ana.badea@utcb.ro
[3] Computing and Control Department, University of Novi Sad, 21000 Novi Sad, Serbia; aristic@uns.ac.rs
[4] Department of Land Measurements and Exact Sciences, Faculty of Forestry and Cadastre, University of Agricultural Sciences and Veterinary Medicine Cluj-Napoca, 400372 Cluj-Napoca, Romania; paul.sestras@usamvcluj.ro
* Correspondence: mihaiherbei@usvt.ro

1. Introduction

Global agriculture is undergoing a period of profound transformation, driven by the need to increase food production in a context characterized by climate change, the degradation of natural resources and increasing pressure on agricultural ecosystems. In these conditions, the development of agricultural systems capable of efficiently using available resources, reducing environmental impact and ensuring food security is one of the main challenges of contemporary research [1,2].

In the last two decades, Earth observation technologies, generically known as remote sensing, have become important tools for monitoring crops and assessing the spatial and temporal variability of the agricultural environment. The availability of satellite images provided by the Landsat and Copernicus Sentinel programs; the development of unmanned aerial platforms; and the emergence of multispectral, hyperspectral and thermal sensors have allowed the collection of considerable volumes of geospatial information. These data can be used both at regional and individual farm levels [3,4].

In parallel, the rapid evolution of Machine Learning and Deep Learning algorithms has fundamentally changed the way agricultural geospatial data are analyzed and interpreted. Modern algorithms allow the identification of complex relationships between biogeophysical variables, climatic factors and agricultural processes, facilitating crop classification, production estimation, disease and pest detection, soil property assessment and the development of intelligent decision support systems [5,6].

The integration of remote sensing, Geographic Information Systems, field sensors and artificial intelligence is one of the foundations of precision agriculture and the concept of smart agriculture. These technologies contribute to optimizing the use of agricultural inputs, reducing production costs, reducing environmental impact and increasing the resilience of agricultural systems to climate change and variability in soil and climate conditions [7,8].

Starting from these premises, the Special Issue "Application of Remote Sensing and Machine Learning in Sustainable Agriculture" was launched with the aim of bringing together research that highlights how geospatial technologies and modern artificial intelligence methods can contribute to the development of a more efficient and sustainable agriculture. The eight published articles cover complementary areas, from predictive models for pest monitoring and plant disease identification to biomass estimation, delimitation

of production and management areas, land suitability assessment and systematic analysis of artificial intelligence applications in agricultural monitoring [9–16].

The aim of this editorial is to highlight the main contributions of these works, to identify the common themes that connect them and to discuss the development prospects of research at the intersection of remote sensing, artificial intelligence, geospatial analysis and sustainable agriculture.

2. The Role of Remote Sensing and Artificial Intelligence in Sustainable Agriculture

The digital transformation of agriculture is one of the most important developmental directions of recent years, supported by advances in remote sensing, Geographic Information Systems and artificial intelligence. These technologies allow the collection, integration and analysis of large volumes of geospatial data, providing essential information for crop monitoring, natural resource assessment and agricultural management decisions [3–8].

Remote sensing offers the possibility of repeated monitoring of agricultural areas using satellite images and unmanned aerial platforms. Vegetation indices, spectral information, digital terrain models, climate data and field measurements can be integrated to assess the state of vegetation, estimate biomass, identify areas affected by water or nutrient stress, and monitor crop evolution during the growing season [3,4].

Remote sensing data also offers the possibility of analyzing the spatial variability of crops and soils. This variability can be translated into thematic maps and management areas, usable for the differentiated application of fertilizers, plant protection products, irrigation water and other inputs. Thus, geospatial technologies contribute to reducing the unnecessary use of resources and limiting the negative effects on the environment.

At the same time, the development of Machine Learning and Deep Learning algorithms has allowed for more efficient use of these large volumes of data. Models based on artificial intelligence are used for crop classification, agricultural production estimation, disease and pest identification, soil properties analysis and the development of automated decision support systems [5,6]. An important advantage of these methods is the ability to identify nonlinear relationships and complex interactions between variables, difficult to highlight by conventional statistical methods.

An important trend in current research is the integration of multiple sources of information into a single analysis flow. Data from satellites, UAV platforms, ground sensors, weather stations, soil databases and official agricultural statistics are combined to obtain more accurate and robust spatial models. This multi-source approach contributes both to increasing the accuracy of the results and to extending their applicability in different geospatial and agricultural contexts [7,8,12].

The development of the concept of Explainable Artificial Intelligence is also an important direction for smart agriculture. In addition to achieving high predictive performance, modern models aim to provide explanations regarding the contribution of the variables used and the factors influencing the results. Interpretability of models can increase user confidence and facilitate the adoption of AI-based solutions in agricultural practice [9].

However, high accuracy obtained under experimental conditions does not automatically guarantee similar performance under real field conditions. Lighting differences, non-uniform backgrounds, phenological variations, variety diversity and pedoclimatic conditions can significantly influence the performance of models. For this reason, validation in real farms, the use of diverse data sets and the development of generalizable models are essential requirements for the transfer of technologies from the research environment to operational applications [16].

https://doi.org/10.3390/su18189472

In this context, the articles brought together in this Special Issue illustrate the evolution of the field towards integrated systems, in which remote sensing, GIS, sensors and artificial intelligence are no longer used separately but as complementary elements of a digital ecosystem for the monitoring and sustainable management of agriculture.

3. Special Issue Contributions

The eight articles published in this Special Issue can be grouped into four major directions:

- ➢ Using artificial intelligence to develop predictive models and classify diseases and pests;
- ➢ Using remote sensing to monitor crops and estimate biophysical parameters;
- ➢ Integrating GIS and multi-source data into analysis and decision support processes;
- ➢ Assessing current trends and development prospects of smart agriculture.

Although the studies use different methodologies and address specific problems, they converge towards the same objective: transforming geospatial, climate and biological data into useful information for the development of efficient, resilient and sustainable agriculture.

3.1. Artificial Intelligence and Predictive Models in Sustainable Agriculture

One of the main directions highlighted by the papers published in this Special Issue is the use of artificial intelligence to develop predictive models capable of supporting the decision-making process in agriculture. The evolution of Machine Learning and Deep Learning algorithms allows the analysis of large volumes of data from heterogeneous sources and the identification of complex relationships between environmental factors, crop development and the occurrence of various agricultural risks [5,6].

The study conducted by Shafique et al. [9] proposes the development of predictive models to estimate the risk of infestation with jassids (cicadas) and thrips in cotton crops, using meteorological variables and ensemble learning algorithms. The integration of temperature, relative humidity, evaporation and other meteorological parameters allows the anticipation of periods favorable for the development of pests. Such an approach can contribute to the optimization of phytosanitary interventions and the reduction in unjustified pesticide application.

An important element of the study is the use of the SHAP method for interpreting the results of the models. By highlighting the contribution of each variable to the prediction, this method allows for understanding the relationships between meteorological conditions and pest population dynamics. The study thus demonstrates that predictive performance can be combined with interpretability, representing an important step towards the development of transparent and applicable early warning systems in agricultural practice.

A complementary approach is presented by Thirupathi et al. [16], who analyze the differences between the performances obtained by Deep Learning models on standardized image sets and the results recorded in real field conditions. The authors propose a hybrid architecture based on image segmentation, convolutional neural networks and bidirectional recurrent units of the GRU type for the classification of plant diseases.

Although the model achieves high performances on reference data sets, the evaluation under real conditions highlights a reduction in accuracy, determined by lighting variations, complex backgrounds, different stages of plant development and environmental conditions. The integration of environmental monitoring through IoT sensors complements image analysis and highlights the need to develop robust and generalizable models, capable of functioning in operational crop health monitoring systems.

Taken together, the two studies highlight the evolution of artificial intelligence from simple classification models to complex systems, capable of integrating climate information, digital images and data from distributed sensors. In both cases, the focus is not exclusively

https://doi.org/10.3390/su18189472

on achieving high accuracy but also on developing interpretable, robust and applicable tools in the variable conditions specific to real agriculture [9,16].

Therefore, the contributions included in this direction demonstrate that artificial intelligence is no longer just a tool for data analysis but is becoming a central component of smart agriculture, capable of supporting phytosanitary management and the development of strategies based on prediction and prevention.

3.2. Remote Sensing and Geospatial Data Integration for Crop Monitoring

Remote sensing is one of the most dynamic areas of smart agriculture, offering the possibility of monitoring crops and agricultural environment characteristics using satellite images and unmanned aerial platforms. The evolution of multispectral, hyperspectral and thermal sensors, together with the development of vegetation indices and modern spatial analysis techniques, allows for the rapid and non-destructive assessment of crop biophysical parameters [3,4].

In this direction, the study by Atanasov et al. [11] is part of a larger study which proposes a method for assessing winter wheat biomass based on the second derivative of the relationship between NDVI and near-infrared reflectance (NIR). The method aims to identify inflection points and dynamic changes in crop development, providing additional information compared to the exclusive analysis of NDVI values.

Experimental validation was carried out on five winter wheat varieties, during two agricultural seasons. The results indicate a strong relationship between the proposed spectral indicator and the biomass determined in the field, highlighting the potential of the method for non-destructive monitoring of crops using UAV platforms. The study thus contributes to the development of complementary spectral methods for biomass estimation and monitoring of vegetation dynamics.

Another contribution is provided by the study by Attia et al. [13], which develops a geospatial workflow for the delineation of agricultural production areas starting from official statistics on production and cultivated areas. The authors integrate information from the Cropland Data Layer, multisensor NDVI products and evapotranspiration data derived from satellite observations.

Through this methodology, aggregate statistical information is transformed into detailed spatial representations of production potential. The approach demonstrates how remote sensing data can complement traditional agricultural statistics and generate useful cartographic products for agricultural planning, identification of productive areas and assessment of the sustainability of production systems.

The two studies illustrate complementary levels of remote sensing use in agriculture. The first is oriented towards the analysis of biophysical parameters of crops at the plot level, while the second aims to integrate satellite information into planning and management processes at the regional scale. Together, they demonstrate that satellite images and UAVs are essential components of modern monitoring and decision support systems.

A common aspect is the development of reproducible and potentially transferable methodologies. Access to open satellite images and modern geospatial processing platforms allows the adaptation of these methods for other crops and pedoclimatic conditions. From this perspective, remote sensing is asserting itself as one of the key technologies of smart agriculture.

3.3. Geographic Information Systems and Decision Support for Sustainable Agricultural Land Management

In addition to the development of remote sensing technologies and artificial intelligence algorithms, Geographic Information Systems have become an essential component of digital agriculture. Their ability to integrate data from multiple sources and perform

https://doi.org/10.3390/su18189472

complex spatial analyses allows for the assessment of land suitability, the identification of priority areas for intervention, and the substantiation of objective decisions regarding the use of natural resources [7,8].

A relevant contribution in this direction is made by the study by Jovanović et al. [12], which proposes the integration of data from multiple sources for the delimitation of management areas in precision agriculture. The authors combine measurements of electromagnetic conductivity, soil chemical properties, and vegetation and surface indices derived from Sentinel-2 images.

By using kriging interpolation, fuzzy k-means classification and Weighted Overlay analysis, management areas with different levels of complexity are delimited. The results show that the integration of surface and subsurface information allows the identification of spatially coherent and relatively stable areas, facilitating the differentiated application of inputs and a more efficient use of agricultural resources.

This direction is complemented by the study carried out by Cojocariu et al. [14], which proposes a geospatial framework for assessing the suitability of grasslands in Hunedoara County by integrating the Analytic Hierarchy Process method with Weighted Overlay analysis in a GIS environment. The model uses nine criteria grouped into three major categories: physical–geographic, ecological and socio-economic.

The integration of these criteria allows the estimation of the capacity of land to support agricultural uses compatible with conservation and sustainable development objectives. The results demonstrate the usefulness of multicriteria models for identifying areas with different levels of suitability and for substantiating decisions regarding grassland management.

The contribution of this study is not only the creation of a suitability map but also the development of a reproducible decision-making model, which can be adapted for other regions and land use categories. The integration of physical–geographic, ecological and socio-economic criteria demonstrates that decision-making processes in agriculture must simultaneously take into account the productive, ecological and social functions of the landscape.

The two studies highlight the role of GIS as an integrating platform. While remote sensing data and field measurements provide information on crop and soil properties, GIS allows them to be organized in a coherent spatial framework and to evaluate different management scenarios.

This evolution supports the development of Spatial Decision Support Systems capable of combining geospatial data, predictive models and multi-criteria methods in a single analysis flow. Thus, GIS is no longer just a representation and analysis tool, but an operational component of systems for sustainable agricultural land management.

3.4. Current Trends and Perspectives on the Integration of Remote Sensing and Artificial Intelligence in Sustainable Agriculture

The analysis of the articles published in this Special Issue highlights that smart agriculture is evolving towards integrated systems, based on the simultaneous use of remote sensing, artificial intelligence, Geographic Information Systems and distributed sensors. The value of these technologies increases significantly when they are integrated into a unified flow of data collection, analysis and interpretation.

The general perspective on these directions is provided by the bibliometric analysis and synthesis carried out by Coman et al. [10]. The authors examine the evolution of applications based on remote sensing and Machine Learning in sustainable agriculture, paying attention also to agriculture in controlled environments, real-time monitoring, precision agriculture and decision support processes.

The study highlights the growing interest in the integration of satellite images, UAV platforms, sensors and artificial intelligence algorithms. These technologies can contribute to

https://doi.org/10.3390/su18189472

improving crop monitoring, production estimation, optimizing resource use and developing more efficient agricultural systems. By its synthesis, the article provides a relevant conceptual framework for understanding the other contributions included in the Special Issue.

Another synthesis contribution is the systematic review by Nan et al. [15], which examines artificial intelligence-based classification techniques used in agricultural and environmental monitoring in the context of achieving the Sustainable Development Goals. The study highlights the rapid growth of research dedicated to the integration of artificial intelligence and remote sensing.

The applications identified include land use mapping and crop detection, production monitoring, vegetation and forest assessment, disease and pest identification, soil analysis and delineation of areas exposed to various environmental risks. The authors also highlight the uneven distribution of studies and the existence of insufficiently investigated areas.

A common direction of the published works is the orientation towards the development of automated decision support systems. Predictive models, image analysis methods and GIS applications are no longer used exclusively to describe phenomena but are becoming decision-making tools, capable of supporting crop management, resource use and agricultural planning.

At the same time, studies highlight the importance of integrating multiple sources of information. Sentinel and Landsat images, UAV platforms, IoT sensors, meteorological data, soil measurements and field observations are used in an integrated manner to develop more robust and transferable models. This approach reduces the limitations associated with using a single category of data and contributes to improving the performance of analysis and prediction algorithms.

Another important trend is the orientation towards reproducible, transparent and interpretable models. Explaining how variables influence results can contribute to increasing user confidence and the implementation of AI-based solutions in the work of farmers and institutions involved in agricultural management.

However, challenges remain regarding the standardization of data sets, the interoperability of platforms, the transferability of models across regions and crops, and the validation of results under real-world conditions. Overcoming these limitations will require interdisciplinary collaborations between specialists in agronomy, remote sensing, GIS, computer science, artificial intelligence, and environmental sciences. Taken together, the contributions brought together in this Special Issue confirm that the future of sustainable agriculture will be characterized by the ever-tighter integration of remote sensing, artificial intelligence and geospatial analysis. The development of digital platforms capable of combining information from multiple sources and providing recommendations in near real-time can contribute to optimizing resources, reducing environmental impacts and increasing the resilience of agricultural systems.

4. Conclusions

The Special Issue "Application of Remote Sensing and Machine Learning in Sustainable Agriculture" highlights the dynamics and diversity of research conducted at the intersection of remote sensing, artificial intelligence, geospatial analysis and sustainable agriculture. The eight published articles demonstrate that the development of digital agriculture does not depend on a single technology but on the integration of satellite and UAV imagery, Geographic Information Systems, artificial intelligence-based models and sensor data and field observations.

The contributions brought together in this Special Issue cover different stages of the decision-making process, from data collection and processing to the development of predictive models, delimitation of management areas and the creation of decision-support

https://doi.org/10.3390/su18189472

systems. The diversity of applications confirms that these technologies can contribute to crop monitoring, biomass and productivity estimation, phytosanitary management and land suitability assessment.

The articles also highlight several major directions for future research. These include the integration of multiple geospatial data sources, the development of explainable and robust artificial intelligence models, the expansion of cloud-based applications, and the strengthening of automated decision support systems for farmers and decision-makers.

Standardizing methodologies, developing representative data sets, and validating models under real-world conditions will be important steps to increase the adoption of these technologies. Special attention should be paid to the transferability of models across crops, regions and agricultural systems.

Overall, the published papers demonstrate that remote sensing and artificial intelligence are no longer just analytical tools but essential components of modern agriculture. We believe that the results presented in this Special Issue will support new interdisciplinary research and contribute to the development of innovative solutions for more efficient, resilient and sustainable agriculture.

5. Thanks

As Guest Editors, we express our sincere gratitude to all authors for their valuable scientific contributions that made this Special Issue possible. We also greatly appreciate the professionalism and time given by the reviewers, whose constructive comments significantly contributed to the quality of the published manuscripts. Last but not least, we thank the editorial team of *Sustainability* for their constant support and excellent collaboration throughout the entire editorial process.

Conflicts of Interest: The authors declare no conflicts of interest.

References

1. United Nations. *Transforming Our World: The 2030 Agenda for Sustainable Development*; United Nations: New York, NY, USA, 2015.
2. Food and Agriculture Organization of the United Nations. *The State of Food and Agriculture 2022: Leveraging Automation in Agriculture for Transforming Agrifood Systems*; FAO: Rome, Italy, 2022.
3. Zhang, C.; Kovacs, J.M. The Application of Small Unmanned Aerial Systems for Precision Agriculture: A Review. *Precis. Agric.* **2012**, *13*, 693–712. [CrossRef]
4. Xue, J.; Su, B. Significant Remote Sensing Vegetation Indices: A Review of Developments and Applications. *J. Sens.* **2017**, *2017*, 1353691. [CrossRef]
5. Liakos, K.G.; Busato, P.; Moshou, D.; Pearson, S.; Bochtis, D. Machine Learning in Agriculture: A Review. *Sensors* **2018**, *18*, 2674. [CrossRef] [PubMed]
6. Kamilaris, A.; Prenafeta-Boldú, F.X. Deep Learning in Agriculture: A Survey. *Comput. Electron. Agric.* **2018**, *147*, 70–90. [CrossRef]
7. Wolfert, S.; Ge, L.; Verdouw, C.; Bogaardt, M.-J. Big Data in Smart Farming—A Review. *Agric. Syst.* **2017**, *153*, 69–80. [CrossRef]
8. Gebbers, R.; Adamchuk, V.I. Precision Agriculture and Food Security. *Science* **2010**, *327*, 828–831. [CrossRef] [PubMed]
9. Shafique, R.; Khan, S.H.; Ryu, J.; Lee, S.W. Weather-Driven Predictive Models for Jassid and Thrips Infestation in Cotton Crop. *Sustainability* **2025**, *17*, 2803. [CrossRef]
10. Coman, C.; Coman, E.; Gherheș, V.; Bucs, A.; Rad, D. Application of Remote Sensing and Machine Learning in Sustainable Agriculture. *Sustainability* **2025**, *17*, 5601. [CrossRef]
11. Atanasov, A.I.; Atanasov, A.Z.; Evstatiev, B.I. A Remote Sensing Approach for Biomass Assessment in Winter Wheat Using the NDVI Second Derivative in Terms of NIR. *Sustainability* **2025**, *17*, 7299. [CrossRef]
12. Jovanović, D.; Govedarica, M.; Gavrilović, M.; Čabilovski, R.; van der Wal, T. Multi-Source Data Integration for Sustainable Management Zone Delineation in Precision Agriculture. *Sustainability* **2025**, *17*, 6931. [CrossRef]
13. Attia, A.; Woli, P.; Long, C.R.; Rouquette, F.M., Jr.; Smith, G.R. Satellite-Guided Delineation of Crop Production Zones from Official Crop Statistics for Spatial Agricultural Decision Support. *Sustainability* **2026**, *18*, 6937. [CrossRef]

14. Cojocariu, L.L.; Horablaga, N.M.; Popescu, C.A.; Horablaga, A.; Bella-Sfîrcoci, M.; Copăcean, L. Mapping Grassland Suitability Through GIS and AHP for Sustainable Management: A Case Study of Hunedoara County, Romania. *Sustainability* **2026**, *18*, 1155. [CrossRef]
15. Nan, V.A.; Badea, G.; Badea, A.C.; Grădinaru, A.P. A Systematic Review of AI-Based Classifications Used in Agricultural Monitoring in the Context of Achieving the Sustainable Development Goals. *Sustainability* **2025**, *17*, 8526. [CrossRef]
16. Thirupathi, J.; Malarvizhi, N.; Brahmanandam, P.S. From Benchmark Accuracy to Field Performance: Hybrid Deep Learning-Based Plant Disease Classification with IoT-Enabled Environmental Monitoring. *Sustainability* **2026**, *18*, 6867. [CrossRef]

Disclaimer/Publisher's Note: The statements, opinions and data contained in all publications are solely those of the individual author(s) and contributor(s) and not of MDPI and/or the editor(s). MDPI and/or the editor(s) disclaim responsibility for any injury to people or property resulting from any ideas, methods, instructions or products referred to in the content.

sustainability

MDPI

Article

Remote Sensing Inversion Model of Cultivated Land Salinity Based on Attention Mechanism and Lightweight CNN: Construction, Validation, and Multi-Model Comparative Analysis

Xingchen Dong [1], Shiqian Guo [1,*], Zichen Guo [2], Xu Jiang [3], Senyu Mao [4], Ruihong Jia [1] and Ji Wang [1]

[1] Gansu Provincial General Station of Cultivated Land Quality Construction and Protection, Lanzhou 730020, China; dongxc_gsgbz@126.com (X.D.); jrh_gssgbz@163.com (R.J.); wangji_gsgbz@hotmail.com (J.W.)
[2] College of Water Conservancy and Hydropower Engineering, Gansu Agricultural University, Lanzhou 730070, China; guozichen1993@lzb.ac.cn
[3] College of Geography and Environmental Science, Northwest Normal University, Lanzhou 730070, China; 202521203123@nwnu.edu.cn
[4] Agricultural Technology Extension Center of Linze County, Zhangye 734200, China; mdlmsy20131126@163.com
* Correspondence: guosq_gsgbz@126.com

Abstract

Soil salinization threatens agriculture in arid regions, and remote sensing retrieval still faces challenges of unclear mechanisms and poor generalization. Based on Sentinel-2 data, this study compares the retrieval performance of various machine learning and deep learning models for farmland soil salt content, and introduces an attention mechanism for optimization. The main conclusions are as follows: (1) Random Forest achieved the highest accuracy among classical machine learning models (R^2 = 0.334), while CNN performed better among deep learning models (R^2 = 0.70), making it suitable for modeling scenarios with a single dominant salt type, well-defined spatial structures, and samples covering major environmental gradients. (2) In the problem of multispectral salinity retrieval, the complementarity of errors among base models was poor, preventing the ensemble model from fully leveraging its advantages. (3) Specific indices derived from near-infrared, red-edge, and blue–green bands performed well for sulfate-type salinity retrieval. (4) In the seed maize production area of Gansu, approximately 75.47% of farmland is non-saline, with severely saline land accounting for 1.42%; over the past decade, 74.84% of the area experienced a decrease in salt content, among which areas with a significant decline (accounting for 9.31%) corresponded consistently with regions where continuous engineering salt removal and microbial fertilizer management had been implemented for ten years. This demonstrates that, under conditions of limited ground samples, combining Sentinel-2 spectral information with moderate local spatial context can enhance the ability to detect salinity changes in relatively uniform irrigated areas.

Keywords: remote sensing inversion; attention-based convolutional neural network; soil salinity

1. Introduction

Soil salinization, a prevalent form of land degradation in arid and semi-arid regions, poses a significant global threat to agricultural productivity and ecological stability [1,2]. It

causes soil consolidation and reduces agricultural productivity, with its potential interaction with desertification posing additional environmental risks [3]. As a persistent process that hinders natural land recovery, soil salinization imposes long-term impacts on human living environments and economic development [4]. Globally, 20% of irrigated land is affected by salinization, particularly in countries such as Australia, China, Egypt, India, Iran, Iraq, Mexico, Pakistan, and Uzbekistan [5]. China, possessing the world's third-largest extent of saline–alkali land (approximately 3.69×10^7 hm^2, or about 4.88% of its utilizable land area), is severely impacted [6]. Effectively monitoring the spatial distribution and temporal dynamics of salinization, especially in cultivated lands, is therefore fundamental for sustainable agriculture and ecological security in this vital area [7].

Traditional methods for monitoring soil salinization primarily include: field sampling followed by laboratory chemical analysis; in situ conductivity measurement using electromagnetic or resistivity probes (e.g., EM38); and process-based models driven by water and salt transport processes [8,9]. Among these, laboratory chemical analysis remains the benchmark for quantitative ion studies, offering high accuracy but being time-consuming, labor-intensive, and unable to capture large-scale spatial heterogeneity [10,11]. Probe measurements are more expedient and can be extrapolated to estimate conditions over an area through interpolation; however, their effective detection depth is dependent on field conditions. While process models possess predictive capabilities, their numerous parameters make the results sensitive to input errors [12]. Consequently, satellite remote sensing has emerged as an indispensable tool, offering synoptic, repetitive, and cost-effective observations essential for accurate assessment, dynamic monitoring, and informed decision-making for salinization control in farmland [13–15].

The exploration of remote sensing for monitoring salinization is grounded in a well-established scientific foundation, demonstrating its critical importance for efficient and large-scale assessment. Due to their relatively low acquisition cost, multispectral satellite sensors are the preferred method for mapping and monitoring soil salinity at regional scales. The most commonly used multispectral remote sensing data sources for soil salinity estimation are Landsat (TM, ETM+, and OLI) [16,17], Sentinel-2 [18,19], and MODIS [20,21]. Considering both spatial and temporal resolution, Sentinel-2—with its spatial resolution of 10–20 m and a high revisit frequency of 5 days—is more suitable as the primary data source for monitoring.

A key focus has been the relationship between spectral features and soil salinity. Studies have consistently shown that salinity information is embedded in spectral data, from identifying optimal band combinations in multispectral imagery [22] to establishing linear relationships between reflectance and surface salinity using hyperspectral data [23]. The near-infrared and shortwave infrared bands of these sensors are recognized as effective for spectrally distinguishing saline soils [24]. Furthermore, various Vegetation and Soil Salinity Indices calculated from multiple bands are also used as input variables for predictive models, though it remains unclear under which conditions they are more effective [7]. This scientific principle has been further operationalized through various modeling approaches. Researchers have successfully linked spectral parameters to salinity levels to examine soil conditions [25], constructed inversion and calibration models using field data [22], and developed models relating spectral data to salt content and other properties [26]. Furthermore, advanced analyses of texture features derived from imagery have also proven effective, showing significant correlations with soil salinity metrics [27]. This body of work collectively validates the scientific basis for using remote sensing as a reliable, non-contact method to overcome the limitations of traditional ground-based techniques, enabling the spatially extensive and temporally frequent monitoring essential for managing saline–alkali land. However, in constructing retrieval models for soil salt content in arid farmland, the

relative importance of different multispectral satellite band combinations still requires further investigation.

In recent years, the integration of satellite remote sensing and machine learning for regional soil salinity prediction has attracted increasing interest from researchers. Scholars commonly employ algorithms such as Random Forest (RF), Support Vector Machine (SVM), XGBoost, DNN, CatBoost, and CNN, while incorporating as many auxiliary datasets as possible into soil salinity inversion models, such as topography, vegetation, soil texture, moisture, and hydrological data [28]. For instance, Hassan Fathizad et al. [29] used the RF algorithm to invert soil salinity trends in the Yazd-Ardakan Plain in Iran (R^2 = 0.73), finding that groundwater parameters and derivatives of vegetation indices with digital elevation were most important in the inversion. Hong Jiang et al. [30] tested SVM and neural network algorithms in the Yanqi Basin of Xinjiang, China, and concluded that SVM achieved better accuracy (R^2 = 0.79). Yuanbo Wang et al. [31] utilized multi-source environmental predictors and a hybrid Grey Wolf Optimizer–Random Forest–XGBoost model, achieving high prediction accuracy for surface salinity (R^2 = 0.91). Qianqian Zhang et al. [32] compared the accuracy of algorithms, including DNN, RF, and SVM, using Sentinel-1 data, and developed a DNN model for inverting saline–alkaline content in northeastern China (R^2 = 0.74). Nan Wang et al. [33] tested partial least squares regression, CNN, SVM, and RF, and concluded that RF is the optimal regression model for soil salinity inversion in arid and semi-arid regions (R^2 = 0.75). Different algorithms may have their own advantages when fitting the relationship between soil sample salinity and covariates. Neural networks may excel in nonlinear fitting [34], while tree-based models like RF can prevent overfitting through the introduction of randomness [35], as also evidenced in other soil inversion problems [36]. Most studies have employed covariates such as elevation and land use as auxiliary variables in modeling. However, when the retrieval problem focuses on fitting the relationship between soil salinity and spectral data in flat agricultural areas, it becomes more necessary to concentrate research efforts on mining multispectral satellite information. It is essential to explore which algorithm is more generally applicable and why it performs better.

In summary, remote sensing retrieval of soil salt content in farmland in arid and semi-arid regions plays a crucial role in regional agricultural management. However, the performance and behavior of salt content retrieval models still require further testing. Therefore, we collected 260 saline–alkali soil samples from farmland in Linze County, Gansu Province, located in a typical arid-to-semi-arid transition zone in China. Using Sentinel-2 imagery, we evaluated the retrieval capabilities of RF, XGBoost, DNN, CatBoost, and CNN models. We further enhanced the optimal model by introducing an attention mechanism and tested the performance of ensemble models, aiming to identify an effective framework for sulfate-dominated salt content retrieval. This study will provide architectural support and procedural guidance for salinity retrieval and the retrieval of other soil properties under similar soil conditions.

2. Materials and Methods

2.1. Overview of the Study Area

Linze County, under the jurisdiction of Zhangye City in Gansu Province, is one of China's most crucial seed corn production bases. The county is situated in the central part of the Hexi Corridor. It borders Ganzhou District to the east, Gaotai County to the west, the Qilian Mountains to the south (adjoining Sunan Yugur Autonomous County), and Alxa Right Banner of the Inner Mongolia Autonomous Region to the north. The elevation within the county ranges from 1358 to 2142 m above sea level, featuring generally flat terrain dominated by gentle slopes. From south to north, the area can be divided into

https://doi.org/10.3390/su18168372

three geographical zones: the southern Qilian Mountains region, the central corridor plain formed by alluvial deposits of the Heihe River system, and the northern Heli Mountains denudation remnant hill region (Figure 1) [37].

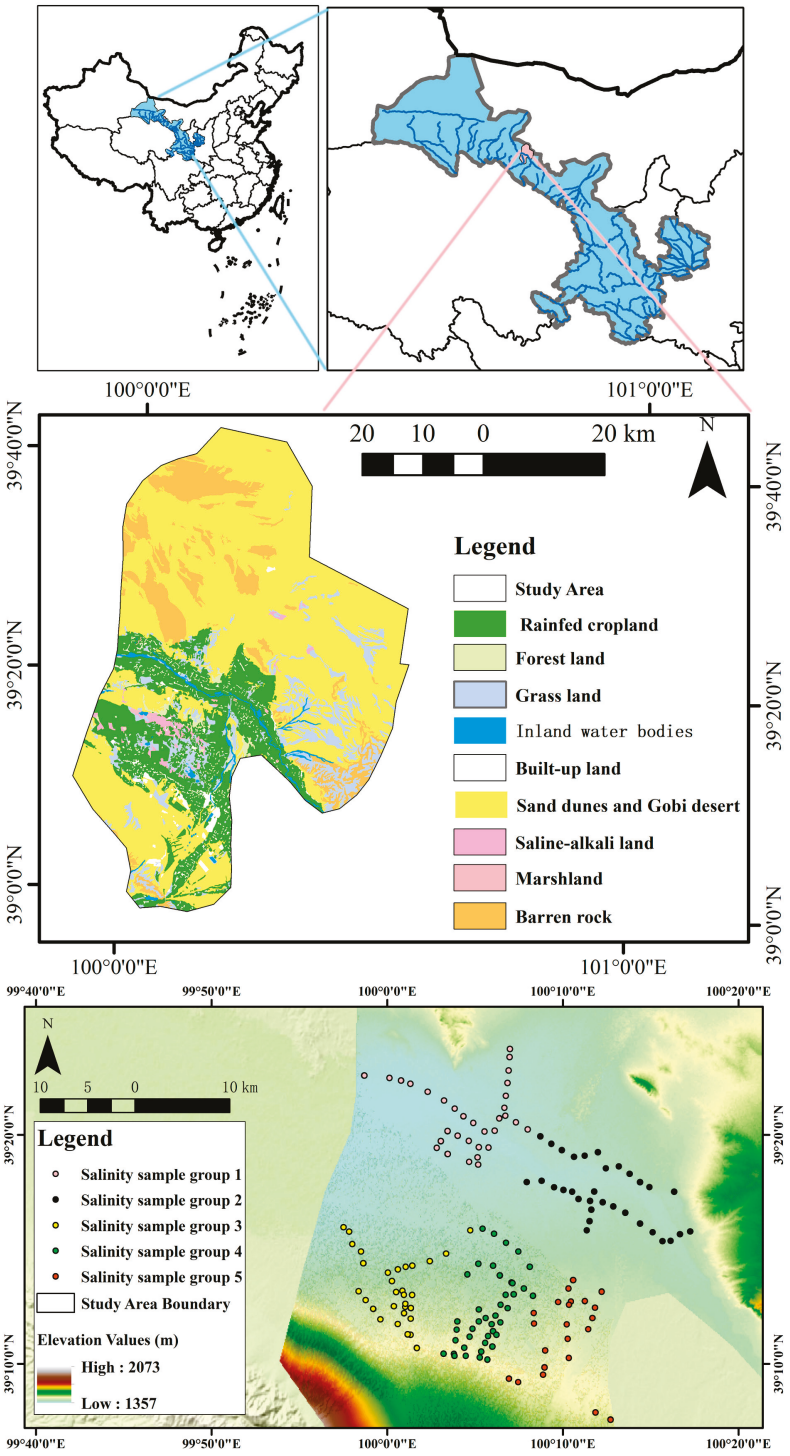

Figure 1. Map of the Study Area: Location, Land Use, and Elevation. Base map: Standard Map of China (Chinese version) from the Standard Maps Service of the Ministry of Natural Resources of the People's Republic of China (http://bzdt.ch.mnr.gov.cn), Map Approval No. GS(2022)1873 [38]; Boundary lines unmodified.

The average annual precipitation is 140 mm, while the average annual evaporation reaches 1400 mm. Evaporation far exceeds precipitation, resulting in severe water scarcity.

The total population of the county exceeds 140,000 and its total area is 2729.97 km^2. Within this, agricultural land covers 59,784.71 hectares, accounting for 21.9% of the county's total land area. Agricultural irrigation primarily relies on water from the Heihe River. The extensive distribution of saline–alkaline land in the study area is primarily attributed to minerals present in the original parent material and the influx of salts carried by external water resources, which is closely related to topographic factors. The low-lying basin area surrounded by mountains on all sides is more conducive to the accumulation of high-mineralization water. Under unfavorable geographical and soil conditions, combined with intense sunlight in the arid region, groundwater is more prone to rising through soil capillary pores when the annual evaporation exceeds 2000 mm. After water evaporates, salts remain on the soil surface, leading to salinization. Furthermore, the local scarce precipitation and freshwater resources make it difficult for salts accumulated on the soil surface to be leached away. Inadequate hydraulic infrastructure impedes drainage, while inappropriate practices such as flood irrigation and unscientific fertilizer application further exacerbate soil salinization [39].

2.2. Data Collection and Preprocessing

2.2.1. Field Collection of Cropland Salinity Data

Soil samples were collected through field sampling and laboratory analysis using a conductivity meter. Sampling was conducted around 15 March and 1 October, during which no fertilization operations were carried out in the study area. In addition, sampling strictly avoided the three days following rainfall or irrigation to minimize the influence of moisture on salinity measurements. Within each 20 m $\times$ 20 m farmland plot, five soil samples were collected from the four corners and the center at a depth of 0–20 cm. These five samples were thoroughly mixed and brought back to the laboratory. The 260 sampling points represent 260 farmland plots, with each plot having only one sampling point. After pretreatment including air-drying, grinding, and sieving, the electrical conductivity of the soil extract was measured using a conductivity meter, and the total soil salt content was subsequently calculated.

2.2.2. Remote Sensing Data Preprocessing

On the Google Earth Engine cloud platform, to ensure strict temporal synchronization between remote sensing observations and field soil sampling, we first retrieved Sentinel-2 MSI Level-2A surface reflectance images corresponding to the date of each sampling point, with a time window set to $\pm$3 days around the sampling date. For Sentinel-2 image bands with different spatial resolutions, bilinear interpolation was used to resample all bands to a uniform 10 m resolution. This strategy ensured temporal consistency between the remote sensing data and ground-truth measurements. Subsequently, the 2cloudless cloud detection algorithm was applied to perform pixel-wise masking of clouds and cloud shadows in each image, and only clear images with an overall cloud coverage below a predefined threshold (20%) were retained, thereby maximizing data quality.

Based on the preprocessed images, we constructed rectangular neighborhood windows of sizes 3 $\times$ 3, 5 $\times$ 5, 7 $\times$ 7, and 9 $\times$ 9 pixels centered on the precise geographic coordinates of each sampling point. Using the reduce neighborhood function, statistical features of the reflectance values of all valid pixels within each window were extracted for each spectral band. The remote sensing bands were combined in pairs using ratio and normalization methods. Please refer to Supplementary Tables S1 and S2 for the specific calculation formulas and index naming conventions.

For all images covering the period from 2016 to 2025 used to retrieve salinity dynamics in the study area, we uniformly selected data from October of each year. Following the

same image processing workflow used in the modeling phase, monthly composite images were first generated using the median compositing method. Then, to ensure spectral consistency across different years, relative radiometric normalization was performed on all images—using the 2025 image as the reference baseline and applying histogram matching to complete the normalization process.

2.3. Modeling Methods

To prevent the influence of spatial correlation among samples on model construction, the samples were spatially divided into five groups, each containing 50–70 points. The spatial distribution of the grouped sample points is shown in Figure 1. In all models mentioned below, five-fold cross-validation was adopted: four groups were used as the training dataset for model construction, and one group served as the out-of-bag validation set. This process was repeated five times, and the average accuracy was calculated.

2.3.1. RF Modeling Approach

The Random Forest (RF) model is an ensemble learning algorithm based on the Bagging (Bootstrap Aggregating) strategy, which achieves robust predictions by combining multiple decision trees. Its core idea lies in introducing double randomness during the construction of each decision tree, thereby reducing the correlation among individual trees and ultimately enhancing the model's generalization ability and stability through collective decision-making. Specifically, during the training phase, the four subsets are first combined into the training data, and bootstrap sampling (with replacement) is used to generate multiple training subsets of the same size as the original dataset, with each subset used to train an independent decision tree. Second, at each internal node split, instead of considering all features, a fixed-size random subset of features is selected, from which the optimal splitting variable and split point are chosen. This dual randomization mechanism of "row sampling" and "column sampling" ensures significant diversity among the trees, effectively mitigating the overfitting tendency of a single decision tree. For regression tasks, the final prediction of the random forest is the arithmetic mean of the predictions from all decision trees; for classification tasks, the majority voting principle is used to determine the class. Taking regression as an example, the prediction formula can be expressed as:

$$\hat{y}(x) = \frac{1}{T}\sum_{t=1}^{T} f_t(x)$$

where T is the total number of decision trees in the forest, and $f_t(x)$ represents the output value of the t decision tree for the input vector x. To prevent individual trees from overgrowing and causing overfitting, the model controls complexity by limiting the minimum number of samples per leaf node. In this study, each leaf node is required to contain at least two samples. This constraint forces the tree to avoid overly fine splits during partitioning, thereby achieving a better balance between bias and variance across the entire forest.

2.3.2. XGBoost Modeling Approach

XGBoost (eXtreme Gradient Boosting) is an ensemble learning model based on the gradient boosting framework, consisting of 50 decision trees generated sequentially. Its core idea is to construct new trees through stepwise iteration, with each new tree aiming to fit the residuals from the previous round of predictions, thereby continuously correcting the overall model error. To control model complexity and prevent overfitting, the maximum depth of each decision tree is limited to 9, the learning rate is set to 0.05 to reduce the contribution of each tree, and the minimum child weight (min_child_weight) is specified as 5 to ensure that each leaf node contains a sufficient weighted sum of samples. The final

https://doi.org/10.3390/su18168372

prediction result is obtained by the weighted summation of the outputs from all decision trees, and its mathematical expression is:

$$\hat{y}_i = \sum_{k=1}^{K} f_k(x_i)$$

where K = 50 is the total number of decision trees, $\eta = 0.05$ is the learning rate, and $f_k(x_i)$ denotes the predicted value of the k-th tree for the input sample x_i. Through this stepwise weighted accumulation approach, XGBoost achieves a favorable balance between bias and variance, delivering high accuracy and stable predictive performance.

2.3.3. CATBoost Modeling Approach

The CatBoost (Categorical Boosting) model is a gradient boosting framework based on oblivious decision trees, and is particularly adept at handling tabular data with categorical features. In this study, CatBoost is configured as a regression model, with its architecture sequentially building decision trees of depth 9 over 50 iterations. Each iteration uses a learning rate of 0.2 to progressively reduce the prediction error from the previous step, thereby ensuring stable convergence while retaining room for correction in subsequent trees. To control model complexity and prevent overfitting, CatBoost applies L2 regularization (ridge penalty) with a strength of 10 to leaf node weights. This regularization term appears in the objective function in the form $\frac{1}{2}\lambda\sum\omega_j^2$, where λ = 10 and ω_j is the output value of the j-th leaf node. Additionally, CatBoost employs two key innovations to handle categorical features: first, Ordered Boosting, which uses temporally ordered or randomly permuted sample sequences to generate unbiased gradient estimates and reduce prediction shift; second, Target Statistics Encoding, which transforms high-cardinality categorical features into numerical statistics via Bayesian smoothing or online learning, effectively mitigating overfitting.

The final prediction $\hat{y}$ is obtained by summing the outputs of all decision trees in the ensemble, and its mathematical expression is:

$$\hat{y}(x) = \sum_{t=1}^{T} f_t(x),\ T = 50$$

where $f_t(x)$ denotes the predicted value of the t-th symmetric decision tree for the input vector x. The characteristic of symmetric decision trees is that all nodes at the same depth use the same splitting feature and threshold, which regularizes the model structure and enables faster inference. By combining the aforementioned regularization and ordered boosting strategies, CatBoost significantly reduces variance while maintaining low bias, making it particularly suitable for soil salinity retrieval tasks involving a large number of categorical variables.

2.3.4. DNN Modeling Approach

The Deep Neural Network (DNN) adopts a sequential architecture, stacked by an input layer, four hidden layers, and an output layer. The specific structure of the model is as follows: the input layer first maps the original features into a 64-dimensional space; then, the first hidden layer contains 128 neurons, aimed at extracting higher-level complex features; next, two gradually compressed hidden layers reduce the feature dimensions to 64 and 32, respectively; finally, the output layer generates a one-dimensional predicted value (continuous target variable). Each hidden layer employs the Rectified Linear Unit (ReLU) as the activation function to introduce nonlinear expressiveness. To stabilize the training process and accelerate convergence, Batch Normalization is applied after key

https://doi.org/10.3390/su18168372

hidden layers. In addition, Dropout regularization is applied after the first three hidden layers, with dropout rates set to 0.2, 0.3, and 0.2, respectively, thereby suppressing co-adaptation among neurons and effectively preventing overfitting.

The forward propagation computation of the l-th layer can be expressed as:

$$h^{(l)} = Dropout\Big(ReLU\Big(BN\Big(W^{(L)}h^{(l-1)} + b^{(l)}\Big)\Big), p_l\Big)$$

where $h^{(l-1)}$ is the output of the previous layer; $W^{(L)}$ and $b^{(l)}$ are the weight matrix and bias vector of the current layer, respectively; $BN(\ )$ denotes the batch normalization operation; $ReLU(x) = max(0, x)$ is the activation function; and $Dropout(\ , p_l)$ indicates randomly dropping neuron outputs with probability p_l. For the output layer, batch normalization and Dropout are omitted, and the predicted value is directly obtained using a linear activation: $\hat{y} = W^{(5)}h^{(4)} + b^{(5)}$.

2.3.5. CNN Modeling Approach

This study employs a variety of convolutional neural network (CNN) architectures to explore the problem of soil salinity retrieval, covering different paradigms ranging from shallow stacked designs to deep lightweight architectures. The specific architectures tested include: a simple four-layer stacked CNN, lightweight ResNet and standard ResNet-50, lightweight DenseNet and standard DenseNet, lightweight EfficientNet and standard EfficientNet, as well as two improved models that embed channel attention modules—CBAM and SE-Final Net—into the CNN backbone. Among them, the SE-Final Net incorporates an attention module at the end of the base CNN to adaptively weight the spatial–spectral features extracted by convolution, enhancing key features related to soil salinity while suppressing background noise. The weighted features are then flattened and passed through a fully connected layer to output the predicted salt content, while all other training parameters remain consistent. The weighted features were then flattened and passed through a fully connected layer to output the predicted salt content, with all other training parameters kept consistent. For each architecture, a grid search strategy is adopted for hyperparameter optimization, systematically tuning the regularization coefficient, dropout rate, weight decay, and initial learning rate to identify the optimal configuration.

The core operation of a convolutional neural network is two-dimensional convolution, whose basic formula can be expressed as:

$$Y[i, j] = \sum_{c=1}^{C_{in}} \sum_{u=1}^{U} \sum_{v=1}^{V} K[c, u, v] \cdot X[c,\ i + u - 1, j + v - 1] + b$$

where X is the input feature map (dimensions $C_{in} \times$ H $\times$ W), K is the convolution kernel (dimensions $C_{in} \times$ U $\times$ V), b is the bias term, and Y is the value of the output feature map at position $[i, j]$. This operation achieves effective extraction of spatial features by sliding the convolution kernel over the input map and computing local weighted sums. Subsequent operations typically include batch normalization, activation functions, and pooling layers to enhance nonlinear representation and reduce parameter count. On this basis, various architectures introduce residual connections, dense connections, or channel attention mechanisms, further improving the model's ability to fit the spectral–spatial characteristics of soil salinity.

2.3.6. Ensemble Learning

This study adopts a stacking ensemble strategy to integrate multiple heterogeneous base learners, aiming to improve the accuracy and robustness of soil salinity retrieval. First, all data are loaded and subjected to unified preprocessing: for CNN-type models, the

https://doi.org/10.3390/su18168372

original features are reshaped into a two-dimensional image format (e.g., spectral matrices arranged by band); for other models (such as Random Forest, XGBoost, CatBoost, DNN, etc.), the original features or identically standardized feature vectors are used directly. Subsequently, the dataset is divided into training and test sets according to a certain proportion. Five different types of base learners (e.g., CNN, ResNet, XGBoost, CatBoost, DNN) are defined and independently trained on the training set. After training, each trained base learner is used to make predictions on the training set samples, yielding five predicted values per sample. These five predicted values are concatenated into a new five-dimensional feature vector. Next, the test set samples are sequentially fed into the five base learners to obtain their prediction vectors, which are then input into the meta-learner to produce the final prediction. The final prediction is compared against the true values to compute evaluation metrics. The final prediction formula of the stacking ensemble can be expressed as:

$$\hat{y}_{stack}(x) = w^T z(x),\ z(x) = [f_1(x), f_2(x), f_3(x), f_4(x), f_5(x)]^T$$

where $f_k(x)$ is the predicted value of the k-th base learner for input x, and w is the weight vector learned by the meta-regressor. This formula indicates that the stacking model achieves adaptive integration of the strengths of heterogeneous models through a weighted linear combination of the outputs from each base learner.

2.4. Uncertainty Analysis and Trend Analysis

The model instability evaluation in this study employs identical data partitions for five-fold cross-validation across all candidate models to ensure fair and paired comparisons. In each round of cross-validation, four subsets are used to train the model, while the remaining subset serves as the independent validation set. This process is repeated five times so that each sample serves exactly once as a validation sample, yielding a corresponding out-of-fold prediction. The mean and standard deviation of R^2, RMSE, and MAE across the five validation folds are used to evaluate model stability. A smaller standard deviation indicates lower sensitivity of the model to variations in the composition of training and validation sets, implying higher model stability. Furthermore, the out-of-fold predictions from all five validation folds are pooled together to calculate the overall R^2, RMSE, and MAE of the model. Paired bootstrap resampling is employed to assess the uncertainty of each performance metric. In each bootstrap iteration, samples are drawn with replacement from the pooled "observed–out-of-fold predicted" pairs, preserving the pairing relationship between observed and predicted values. R^2, RMSE, and MAE are recalculated based on each resampled dataset. This procedure is repeated 1000 times, and the 2.5th and 97.5th percentiles of the bootstrap distribution for each metric are taken as the lower and upper bounds of the 95% confidence interval, respectively.

The computational efficiency of the models is evaluated using parameter count, multiply–accumulate operations, model size, inference latency, and peak GPU memory usage. All models are tested on an NVIDIA RTX A4000 GPU with FP64 precision and an input shape of $1 \times 10 \times 11 \times 11$. After 50 warm-up iterations, inference is repeated 500 times, and the median inference time is computed under CUDA synchronization conditions.

The uncertainty analysis method for image prediction in this study employs Monte Carlo Dropout uncertainty estimation. The implementation approach is as follows: before the inference loop, the model is kept in training mode to maintain dropout activation. N = 20 random forward passes are performed, and the mean and variance of the outputs are computed to obtain the predicted values and their associated uncertainty. To ensure efficient retrieval and uncertainty computation, a tiling strategy is adopted to accelerate the operation. Each tile is extended by 10 pixels outward to guarantee window coverage

https://doi.org/10.3390/su18168372

at the boundaries. When merging tiles, a variance merging formula with mean difference correction is used to ensure statistical unbiasedness. The prediction formula employed is as follows:

$$\mu_{final} = \frac{1}{N}\sum_{i=1}^{N} f_\theta(x_i)$$

where f_θ is the neural network model with Dropout, and x_i is the input tile for the i-th sampling pass. After retrieving the annual farmland soil salt content in the study area from 2016 to 2025, Sen's slope was used to estimate the direction and rate of change in salt content, and the Mann–Kendall test was applied to assess the statistical significance of the change trend. Independent samples from other years were too few in number, and their sampling scales were inconsistent with the 10 m resolution used in this study, rendering them unsuitable for incorporation into model calculations. Therefore, they were not used for validation.

3. Results

3.1. Construction of Remote Sensing Inversion Models for Cropland Salinization

3.1.1. Traditional Model Construction

In this section, the performance of CatBoost, XGBoost, and RF models for inverting cropland salinization was evaluated. For RF, combinations of the number of trees and leaf node size were tested; for CatBoost and XGBoost, combinations of learning rate, tree depth, and regularization terms were examined. Under the optimal parameter sets identified, the model performance evaluated via five-fold cross-validation is shown in Figure 2.

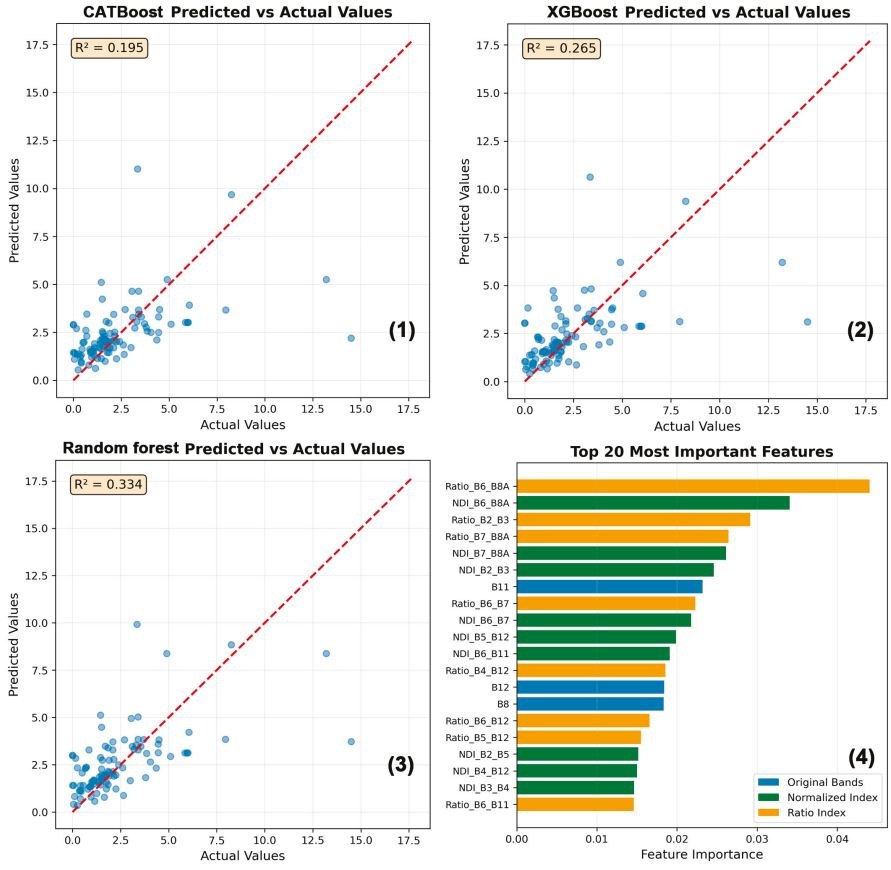

Figure 2. Accuracy Comparison of Classical Machine Learning Models: (**1**) Fitting Accuracy of the CatBoost Model; (**2**) Fitting Accuracy of the XGBoost Model; (**3**) Fitting Accuracy of the RF Model; (**4**) Feature Importance Ranking of the RF Model. Caption: Blue dots represent the scatter of measured versus predicted values, and the red line is the 1:1 line.

It can be observed from the cross-validation performance of the models (as shown in Figure 2 and Table 1) that RF > XGBoost > CatBoost, yet all R^2 values are below 0.4, while the test set accuracies are all above 0.9, indicating an overfitting state. This suggests that the data noise in the soil salinity retrieval problem is excessive—that is, the spectral heterogeneity for the same level of salinity is relatively high. Moreover, the distribution of farmland salinity itself is skewed, leading to insufficient sample learning by the models. At the same time, for the salinity retrieval problem, the multicollinearity among bands is too strong, which may hinder the performance of models with insufficient regularization strength.

Table 1. Accuracy and Confidence Interval (CI) of three classical machine learning models.

Model Name \ Evaluation Metric	R^2 (95% CI)	MAE (95% CI)	RMSE (95% CI)
RF	0.334 (−0.038–0.574)	1.212 (0.955–1.508)	1.927 (1.356–2.578)
XGBoost	0.265 (−0.099–0.504)	1.179 (0.904–1.518)	2.025 (1.328–2.760)
CatBoost	0.195 (−0.142–0.455)	1.254 (0.967–1.615)	2.120 (1.331–2.915)

In Figure 2(4), the results of RF-based feature selection for Sentinel-2 band combinations are presented. It can be observed that the top 20 selected bands primarily reflect crop status (canopy growth/water stress) that indirectly indicates soil salt content, as well as soil surface brightness/color and soil salinity/moisture. Notably, among the top ten bands, six indices (Ratio_B6_B8A, NDI_B6_B8A, Ratio_B7_B8A, NDI_B7_B8A, Ratio_B6_B7, NDI_B6_B7) are commonly used for crop canopy parameter inversion, while only four indices are related to soil color (Ratio_B2_B3, NDI_B2_B3) and salinity/moisture (B11, Ratio_B5_B12) inversion.

3.1.2. DNN Model Construction

The training and construction of the DNN model also employed a grid-based parameter search (as shown in Figure 3(4)) and an early stopping mechanism. The spectral bands used were those selected by RF in the previous section. The number of model layers tested was from 3 to 9 layers. The five-fold cross-validation accuracy, measured by R^2, ranged from −0.65 to 0.03, with the best performance achieved by a 5-layer model (R^2 = 0.079, CI: −0.482–0.443; MAE = 1.494, CI: 1.176–1.848; RMSE = 2.283, CI: 1.600–3.074). The model still exhibited overfitting, and its accuracy was even lower than that of the traditional machine learning models (as shown in Figure 3). This indicates that for cropland salinity inversion at the county scale, the DNN model still requires a substantially larger sample size. It further underscores the limitations imposed by the high collinearity among remote sensing bands on the inversion of soil parameters.

3.1.3. CNN Model Construction

The training and construction of the CNN models similarly employed a grid-based parameter search and an early stopping mechanism, using the bands selected by RF. Multiple CNN architectures were evaluated for the salinity inversion task, including: a four-layer stacked CNN, a lightweight ResNet, ResNet-50, a lightweight DenseNet, DenseNet, a lightweight EfficientNet, EfficientNet, a CNN with CBAM attention mechanism, and an SE-deep convolutional neural network. For each architecture, hyperparameter optimization was performed via grid search, including regularization parameters, dropout rates, weight decay, and learning rates. The training loss for hyperparameter optimization is shown in Figure 4(1), the RMSE loss in Figure 4(2), and the accuracy comparison under different hyperparameter combinations in Figure 4(3),(4). The accuracy for the 5 × 5 convolution-based setup is summarized in Table 2.

https://doi.org/10.3390/su18168372

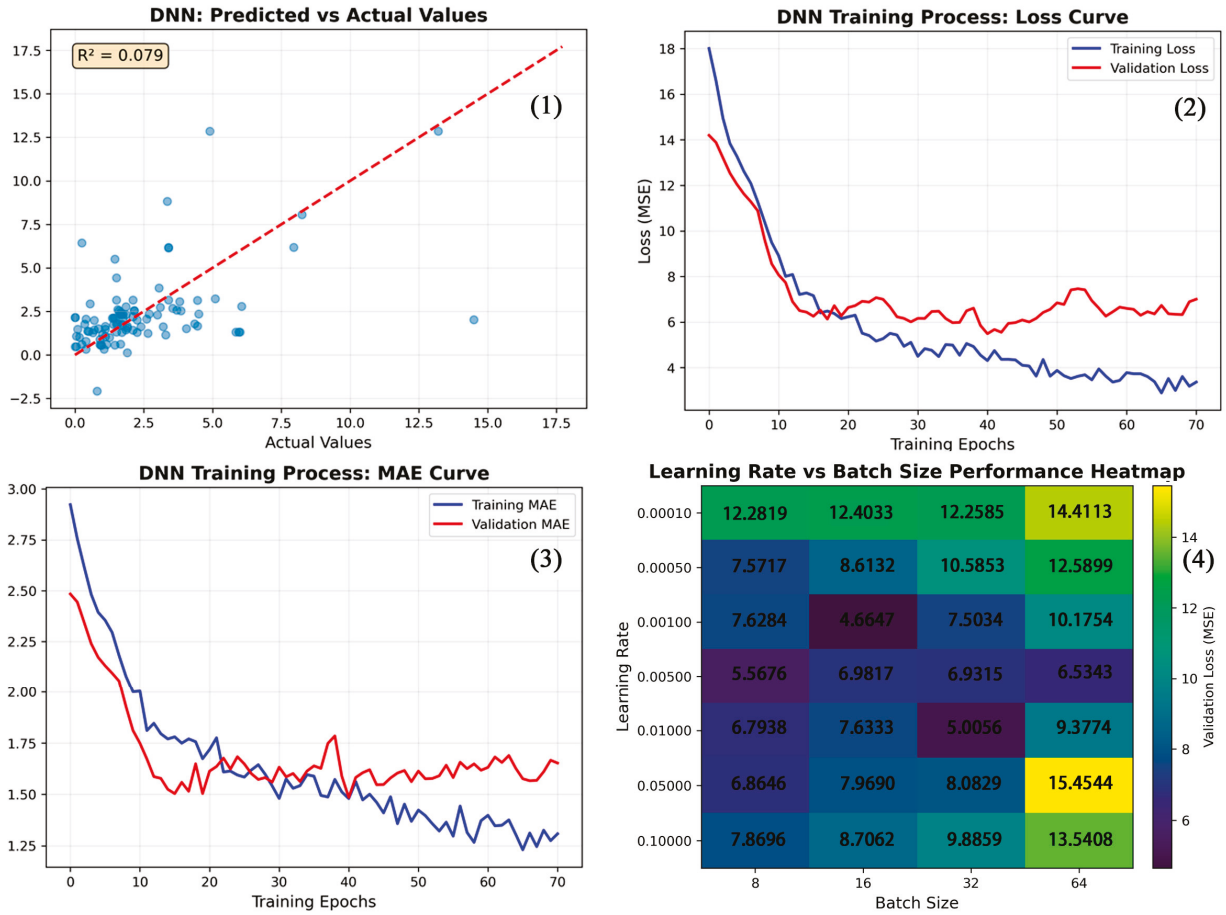

Figure 3. (**1**) DNN Inversion Model Fitting Accuracy; (**2**) DNN Training Loss of the Optimal Model; (**3**) DNN Training MAE of the Optimal Model; (**4**) DNN Comparison of Different Learning Rate and Batch Size Combinations. Caption: Blue dots represent the scatter of measured versus predicted values, and the red line is the 1:1 line.

Table 2. Generalization Performance and Error of Multiple Convolutional Neural Network Models.

Model Name \ Evaluation Metric	R^2 (95% CI)	MAE (95% CI)	RMSE (95% CI)
Stacked CNN	0.6599 (0.5586–0.7466)	0.9983 (0.8808–1.1216)	1.6893 (1.4395–1.9357)
Lightweight ResNet	0.3813 (0.2385–0.4869)	1.5124 (1.3758–1.6714)	2.2783 (2.0032–2.5849)
ResNet-50	0.7060 (0.6365–0.7922)	0.7815 (0.6731–0.9032)	1.5437 (1.2802–1.8086)
Lightweight DenseNet	0.5440 (0.4100–0.6601)	1.2114 (1.0832–1.3598)	1.9559 (1.6714–2.2784)
DenseNet	0.5442 (0.2994–0.7110)	1.0913 (0.9564–1.2527)	1.9555 (1.5534–2.3944)
Lightweight EfficientNet	0.4907 (0.3057–0.6309)	1.3082 (1.1686–1.4529)	2.0670 (1.8016–2.3507)
EfficientNet	0.6514 (0.5832–0.7153)	1.0754 (0.9612–1.2012)	1.7102 (1.4635–1.9746)
CBAM	0.5654 (0.4458–0.6677)	1.2481 (1.1367–1.3861)	1.9095 (1.6704–2.1827)
SE-Final CNN	0.6992 (0.6110–0.7822)	0.8823 (0.7714–1.0034)	1.5886 (1.3274–1.8477)

During the debugging process, we found that the CNN models with the highest accuracy were ResNet and SE-FINAL. The typical CNN architectures of DenseNet, EfficientNet, and their lightweight versions achieved lower accuracy than the stacked CNN. Moreover, adding an attention mechanism to every layer of the stacked CNN also resulted in a slight decrease in accuracy. Instead, adding the attention mechanism only at the deepest layer (SE-FINAL) yielded higher accuracy than the stacked CNN. From the model computa-

https://doi.org/10.3390/su18168372

tional efficiency table (Table 3), it can be seen that Lightweight EfficientNet has the lowest MACs and the fastest inference speed, while ResNet-50 consumes the most resources. SE-Final CNN adds only approximately 0.002 M parameters and 0.002 M MACs compared to Stacked CNN, indicating that adding the SE attention at the final layer adds almost no additional computational burden.

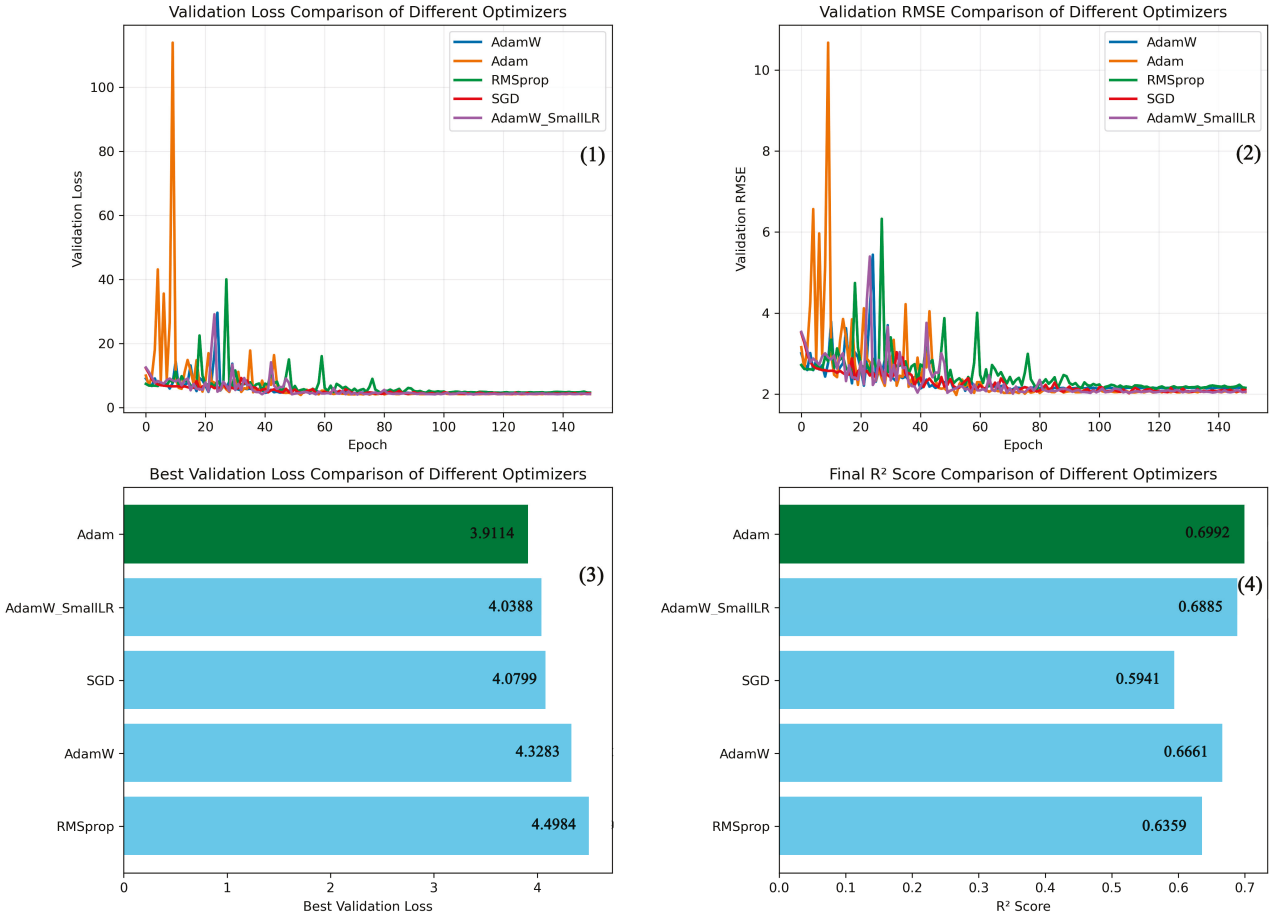

Figure 4. CNN Model Optimizer Testing: (**1**) Loss Curves of Different Optimizers; (**2**) RMSE Loss Curves of Different Optimizers; (**3**) Generalization Error of Different Optimizers; (**4**) Generalization Accuracy of Different Optimizers.

3.1.4. Construction of the Ensemble Learning Network

In this section, we use the hyperparameters of all the aforementioned optimal models to construct the stacking ensemble model. The results obtained after five-fold cross-validation are shown in Figure 5. The best accuracy is achieved when using the DNN model as the base learner (R^2 = 0.269), while the worst is when using XGBoost as the base learner (R^2 = 0.197). In terms of model stability, the DNN model as the base learner also yields the narrowest confidence intervals, whereas the CNN model exhibits wider confidence intervals. The stacking ensemble with DNN as the meta-learner demonstrates the best overall performance and is the only model with a lower bound of the 95% CI for R^2 greater than zero. However, there is noticeable overlap in confidence intervals among the different stacking models, suggesting that the differences between models may not be statistically significant. This may indicate that in the context of soil salinity retrieval, multiple models have learned erroneous data points, and the ensemble learning mechanism actually averages out the advantages currently held by the CNN models.

https://doi.org/10.3390/su18168372

Table 3. Computational efficiency of CNN models.

Model Name \ Computational Efficiency	Parameters (M)	MACs (M)	Model Size (MB)	Median Latency (ms/Sample)	Peak GPU Memory (MB)
Stacked CNN	0.295	35.472	2.269	13.710	10.811
Lightweight ResNet	0.295	35.472	2.269	13.700	10.811
ResNet-50	23.506	202.534	179.845	109.645	191.549
Lightweight DenseNet	0.140	5.991	1.157	19.235	9.501
DenseNet	0.279	6.294	2.272	30.601	10.604
Lightweight EfficientNet	0.237	1.826	1.911	4.483	10.316
EfficientNet	2.862	10.036	22.035	8.611	30.320
CBAM	0.303	35.534	2.338	14.352	10.874
SE-Final CNN	0.297	35.474	2.286	13.812	10.826

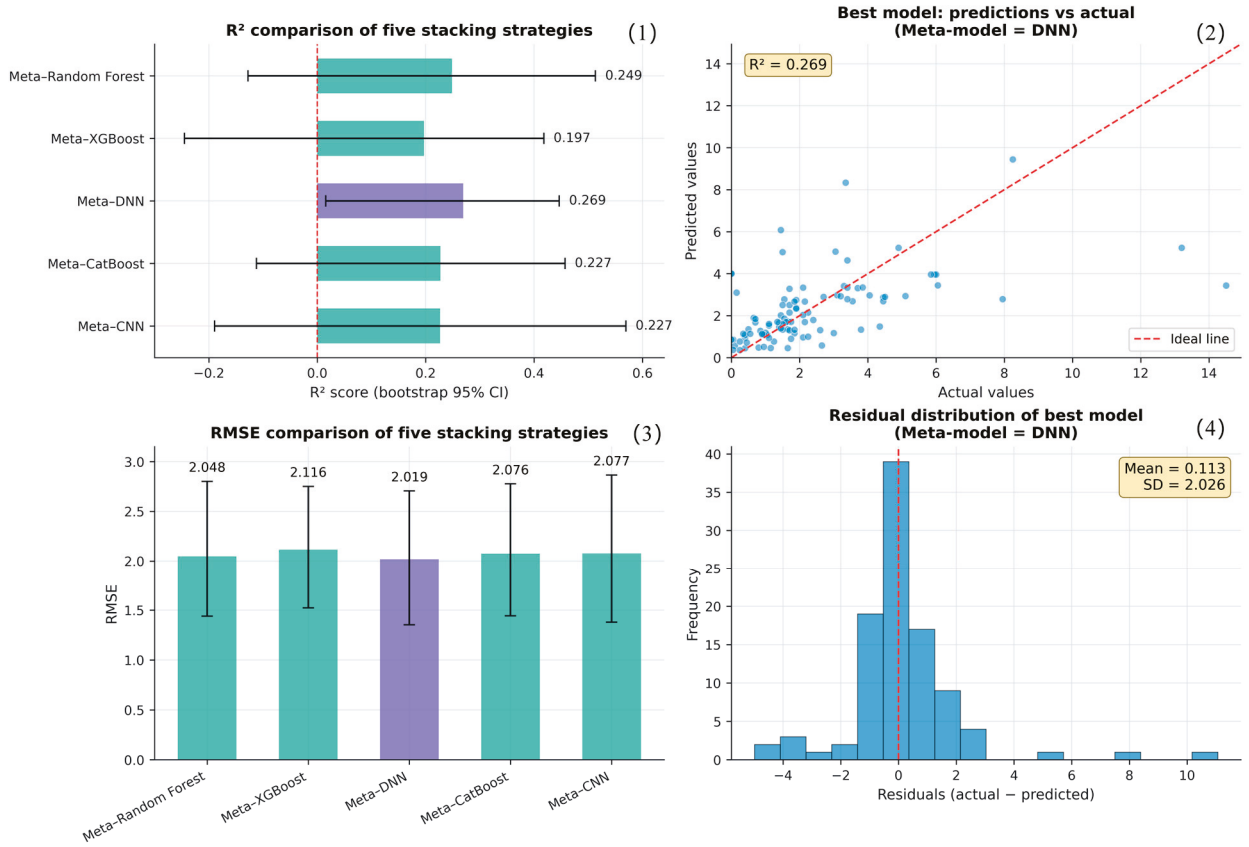

Figure 5. Stacking Model Training Accuracy: (**1**) Generalization Accuracy of Different Base Models; (**2**) Fitting Scatter Plot of the Optimal Stacking Model; (**3**) Generalization Error of Different Base Models; (**4**) Generalization Error Distribution of the Optimal Stacking Model. Caption: Blue dots represent the scatter of measured versus predicted values, and the red line is the 1:1 line.

3.2. Inversion Results of Cultivated Land Soil Salinity in the Study Area

Using the SE Final CNN network, the soil salt content of farmland in the study area after tillage in October 2025 was retrieved. The inversion results are shown in Figure 6. The vast majority of farmland in the study area is non-saline soil, with salt content below 0.3%, accounting for 75.47% of the total farmland. Mildly saline soil, with salinity below 0.5%, is widely distributed and accounts for 18.80% of the farmland area. Notably, the degree of mild salinization has increased in farmland near the Heihe River, Liusha River, and lakes.

Moderately saline soil (0.5–0.7%) is scattered sporadically within mildly salinized areas, accounting for 4.19%. Severely saline soil (>0.7%), accounting for 1.42%, is concentrated not only near water bodies but also in farmland surrounding abandoned saline–alkali wasteland. Due to the high resolution of Sentinel-2 imagery, the overall distribution pattern within individual farmland plots is also clearly discernible. As shown in Figure 6(2),(3), comparison with satellite imagery indicates that areas with higher salinity within plots are mainly located along ridges and near oilfield boundaries.

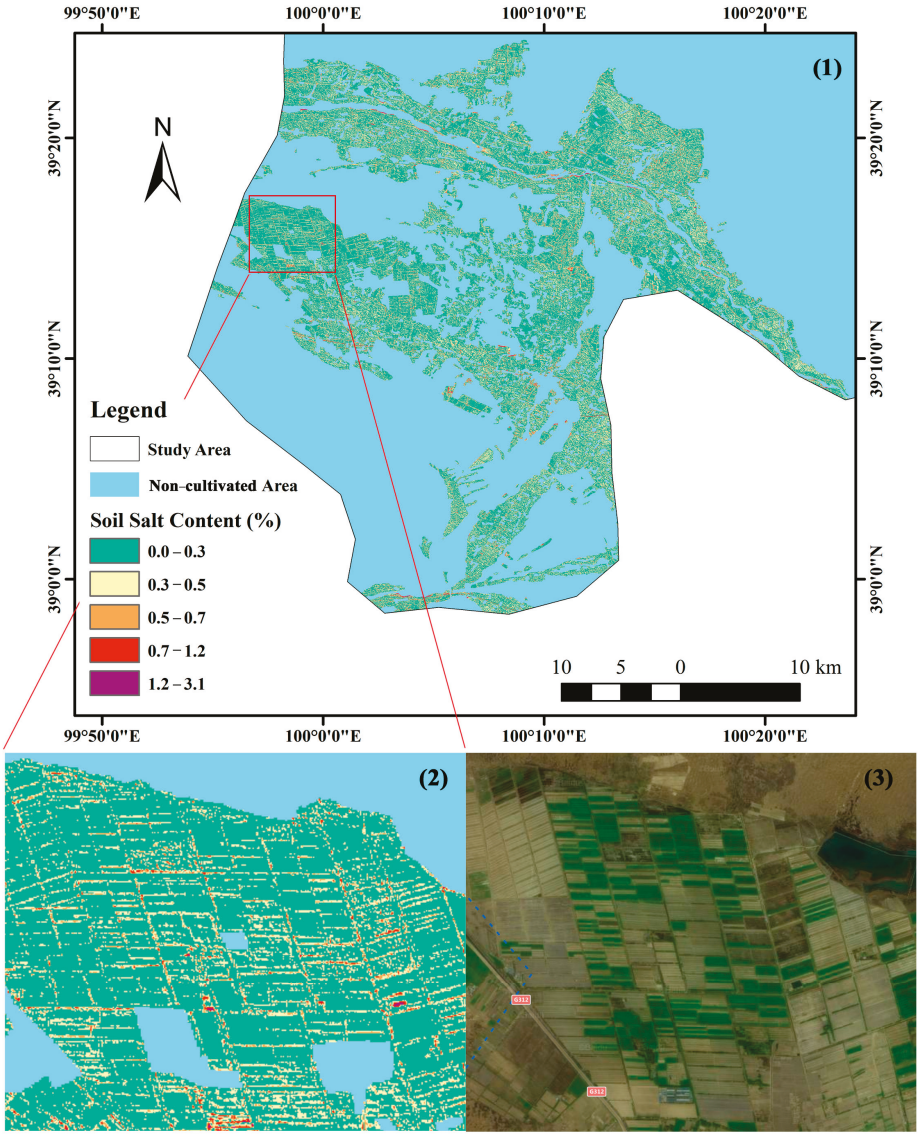

Figure 6. (**1**) Inversion Results of Cultivated Land Salinity in the Study Area after the Tillage Period in October 2025; (**2**) Enlarged detail view of the inversion map; (**3**) Satellite image corresponding to the enlarged detail view of the inversion map.

3.3. Dynamic Analysis of Cultivated Land Salinization Changes in the Study Area from 2016 to 2025

As shown in Figure 7(1), soil salinity in most cultivated areas within the study region exhibited a decreasing trend. Areas with a reduction rate exceeding 0.3 g/year are concentrated. Along the Heihe River, the decrease in soil salinity generally exceeded 0.14 g/year. In low-lying areas along the Heihe River, which originally had high background salinity and contained small wetlands, salinity showed a patchy decline, with reduction rates potentially exceeding 1.13 g/year. In contrast, a significant increase in salinity occurred

https://doi.org/10.3390/su18168372

near the southern part of the study area (Nijiaoying Village), attributable to the reduction in cultivated land area due to its proximity to the Danxia landform scenic area of Linze County.

Figure 7(2) reveals that areas with statistically significant trends almost exclusively correspond to salinity decrease, with significant reduction showing a z-score greater than 3.93. Only a few pixels showed a significant increasing trend. The predominantly non-significant trends in most pixels are mainly attributed to the low signal-to-noise ratio in the salinity time series. Interannual fluctuations driven by variations in precipitation–evaporation and soil moisture conditions often exceed the magnitude of the decadal trend, thereby limiting the statistical power of the Mann–Kendall test over the 10−year period.

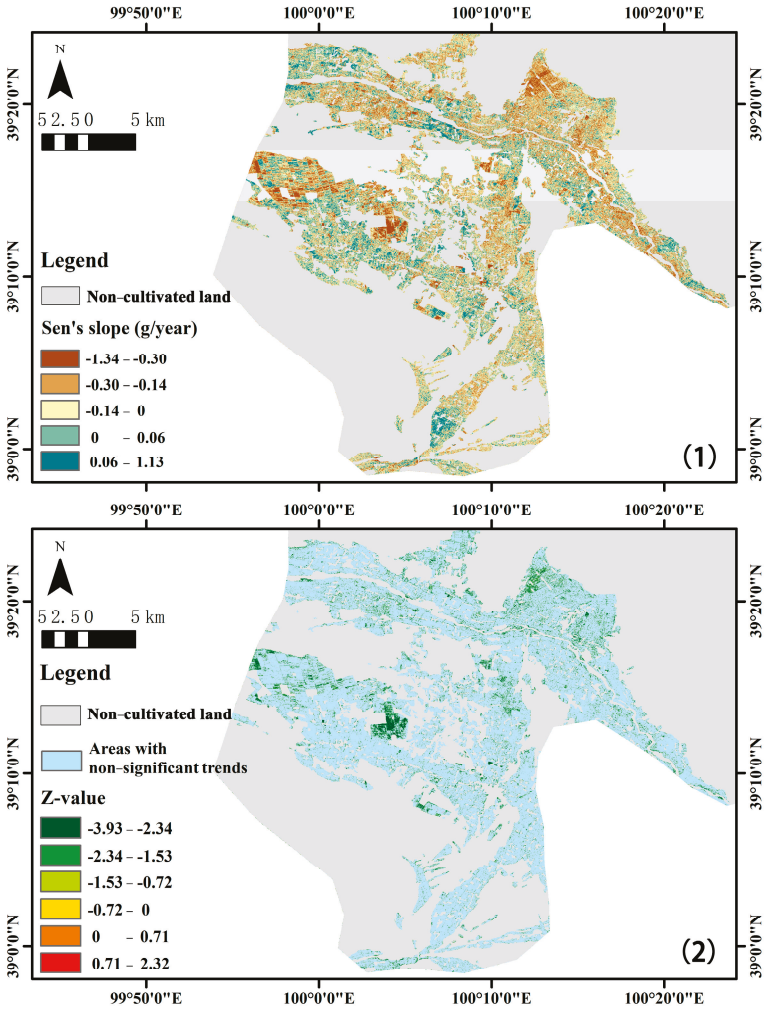

Figure 7. (**1**) Interannual Variation Trend of Soil Salinity in the Study Area (2016−2025); (**2**) Significance of Interannual Variation in Soil Salinity in the Study Area (2016−2025). Note: The interannual variation is calculated based on data from the post-tillage period (October−November).

4. Discussion

4.1. Factors Influencing the Accuracy of Remote Sensing Inversion Models for Soil Salinity

4.1.1. Model Performance Differences and Spatial Neighborhood Effects

Existing global meta-analyses have shown that RF and SVM are generally the more stable algorithms for remote sensing estimation of soil salinity. However, model accuracy is simultaneously influenced by factors such as sample size, degree of salinity variation, soil texture, sampling strategy, and the temporal match between imagery and sampling dates. There is no universally optimal algorithm applicable to all regions [7,15]. Similar results

were obtained in this study: among the traditional machine learning models, RF achieved the highest estimation accuracy (R^2 = 0.334, 95% CI: −0.038–0.574), outperforming XGBoost and CatBoost. By reducing variance through Bootstrap aggregation and random feature selection, RF can effectively handle the nonlinear relationships and collinearity among spectral indices, making it more suitable for the current data structure, characterized by a limited sample size and a relatively large number of features. However, the R^2 confidence intervals of RF, XGBoost, and CatBoost exhibited substantial overlap, indicating that the ranking of accuracy among traditional models is subject to considerable sampling uncertainty. Therefore, it is not appropriate to conclude that any single algorithm holds a universal advantage based solely on point estimates.

The estimation accuracy of CNN was significantly higher than that of RF, indicating that salinity retrieval information exists not only in the spectral response of the pixel corresponding to the sampling point but also in the spatial structure of the surrounding surface. In arid farmland, soil salinity forms spatially continuous surface signatures through bare soil patches, crop growth conditions, soil moisture, irrigation and drainage conditions, and field management practices. RF and DNN, which use the central pixel and its derived indices, cannot explicitly describe these neighborhood patterns. In contrast, CNN can simultaneously extract spectral features and local spatial textures through convolution operations, which likely accounts for its improved performance. Similar studies on Sentinel-2-based soil-type classification have also found that CNN achieves higher accuracy on homogeneous surfaces than in complex areas containing multiple soil types and interfering land cover [40]. However, those studies focused on soil classification rather than quantitative salinity retrieval, thus serving only as indirect evidence that spatial context aids CNN recognition, and do not directly prove that CNN outperforms tree-based models in all salinity retrieval tasks.

The samples were grouped according to their spatial locations, and the changes in accuracy and uncertainty during the evaluation process for convolution windows ranging from 3 × 3 to 9 × 9 pixels were tested (as shown in Figure 8(2)). The results indicated that the convolutional neural network with a 50 × 50 m window exhibited the best performance. This indicates that, under the conditions of this study area, sample design, and Sentinel-2 data, the 50 m neighborhood provides the most effective spatial context. A smaller window may not adequately capture the field-scale spatial structures related to salinity; a larger window, however, would introduce information from adjacent fields, water bodies, roads, abandoned farmland, and different management units, increasing mixed land cover and irrelevant background. Therefore, the 5 × 5 window represents a trade-off between insufficient local information and spatial mixing noise.

The performance of DNN was lower than that of RF, and increasing network depth did not yield stable improvements. This study involves a small sample size, and fully connected DNNs have a relatively large number of parameters, requiring simultaneous estimation of multi-layer weights from limited samples. Such models are prone to learning spurious correlations caused by soil moisture, surface roughness, vegetation residues, and measurement errors. Deeper networks further increase model degrees of freedom, potentially reducing rather than improving generalization ability. Research on deep learning in remote sensing has also pointed out that the advantages of deep models typically depend on sufficient and representative training data, whereas models such as SVM and RF tend to be more stable under limited training sample conditions [41]. Given the sample size and feature dimensionality of this study, the bias-variance trade-off of RF is superior to that of fully connected DNN, and the performance improvement in CNN primarily stems from spatial context rather than simply increasing network depth. Therefore, for regions with limited samples, complex salinity types, or a need for stronger interpretability, tree-

https://doi.org/10.3390/su18168372

based models such as RF can serve as robust baselines. CNN may be more advantageous when salinity-related surface features exhibit clear spatial structures, samples can cover major environmental gradients, and spatial validation demonstrates model generalization capability. This assessment still needs further verification through cross-soil-type and cross-regional experiments.

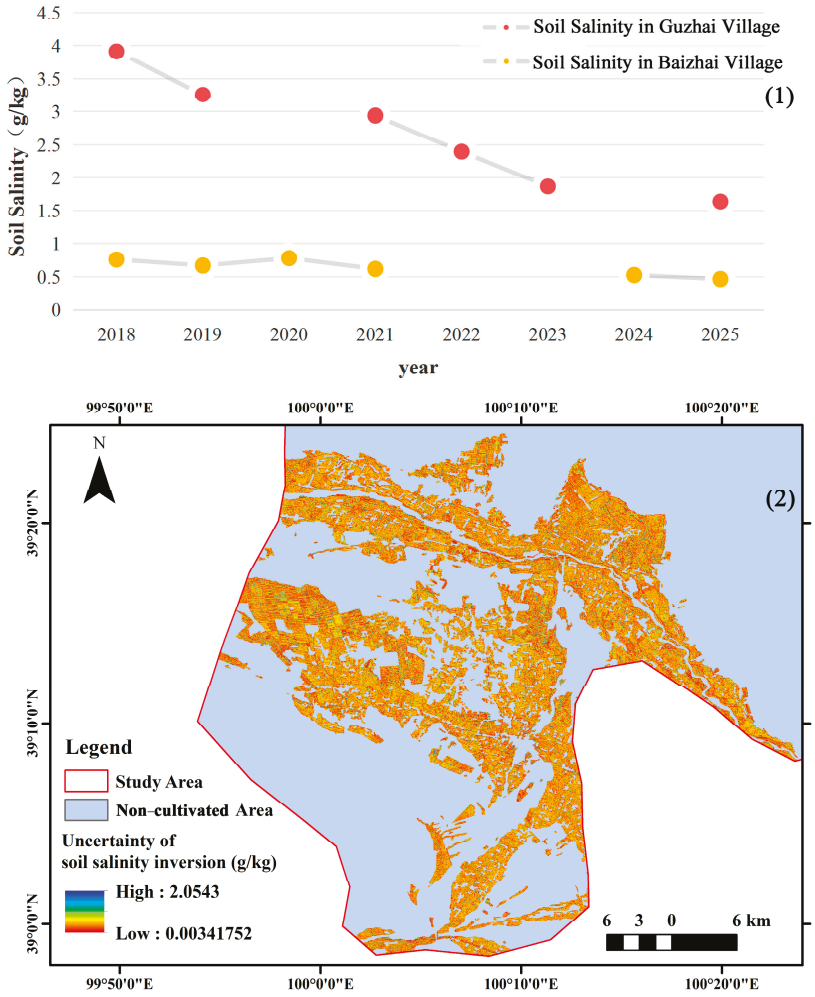

Figure 8. (**1**) Changes in Soil Salinity in the Topsoil Layer of Areas Where Salinization Control Measures Have Been Consistently Implemented in the Study Area; (**2**) Uncertainty analysis of the SE-final CNN model.

None of the five stacking strategies surpassed the best CNN. The best stacking model achieved an R^2 of approximately 0.269, while the remaining strategies ranged from about 0.197 to 0.249, indicating that simply increasing the number of models does not necessarily improve retrieval accuracy. The benefit of regression ensembles depends on the complementarity of errors among base learners. If multiple models are affected by the same input data, label errors, and surface interference, their prediction residuals will be highly correlated, making it difficult for the ensemble to achieve substantial gains through error cancellation [42]. In this study, RF, XGBoost, CatBoost, and DNN all primarily utilized the same central-pixel spectra and band combinations, and therefore may have been jointly influenced by vegetation cover, soil moisture, surface roughness, and vertical salt distribution. When a weak DNN was included as a base learner, some stacking combinations showed slight improvement, likely because the DNN provided a residual structure different from that of tree models, thereby adding a degree of model diversity [43–45].

https://doi.org/10.3390/su18168372

4.1.2. Interannual Change Monitoring and Its Application Significance

The 2016–2025 time series derived from the lightweight attention-enhanced CNN shows that soil salt content in most farmland of the study area exhibits a decreasing trend. Areas passing the Mann–Kendall significance test are predominantly concentrated in Guzhai Village, Yan'an Town, as shown in Figure 7. Since 2018, this region has successively implemented measures including organic fertilizer application combined with deep plowing, soil testing and formulated fertilization coupled with drainage and salt leaching, as well as subsurface pipe drainage, deep tillage, and organic amendment [46,47]. The multi-year variation in soil salt content is presented in Figure 8(1). Meanwhile, increased precipitation in recent years across the study area, along with region-wide implementation of deep tillage and organic fertilizer measures, corresponds to the decrease in salt content without a significant decade trend. The consistency between the remotely sensed trends and the spatiotemporal distribution of remediation measures indicates that the model is capable of identifying regional change signals aligned with sustained saline–alkali management, providing external evidence supporting the model's temporal applicability. The agreement between managed areas and significantly declining zones reinforces the environmental plausibility of the model constructed in this study. Future work could involve continuous soil sampling in both treated and untreated control areas, integrated with meteorological, irrigation, and groundwater data, employing a pre–post treatment versus control design or panel data analysis to validate the attribution of changes.

4.2. Multispectral Feature Transformation and Mapping for Soil Salinization Remote Sensing Inversion Models

4.2.1. The Role of Spectral Mixing and Feature Transformation

There is no stable and unique correspondence between soil salinity and satellite spectra. Salt composition, crystal morphology, soil moisture content, texture, organic matter, surface roughness, and vegetation cover all altered surface reflectance, causing the same salt content to exhibit different spectral characteristics, and possibly leading to similar spectral responses for different salinity levels [7,15]. Therefore, regional-scale salinity retrieval is essentially a non-unique mapping problem controlled by multiple environmental factors.

This study found that incorporating pairwise ratio indices and normalized difference indices derived from the original Sentinel-2 bands into RF improved model accuracy. This indicates that for traditional machine learning models that rely on central-pixel inputs, spectral transformation can enhance relative differences between bands while reducing the influence of overall brightness, local shadows, and certain multiplicative noise. Ratio and normalized transformations can also make explicit the band interactions that RF struggles to represent directly through limited tree depth, enabling the model to more easily identify nonlinear thresholds related to salinity. Xu et al. [48] also found in Sentinel-2 bare soil salinity mapping that green, near-infrared, and shortwave infrared bands, along with their corresponding ratio, difference, and normalized indices, enhanced salinity-related signals and improved the prediction accuracy of RF models. However, feature transformation does not generate new observational information beyond the sensor's original bands. A large number of pairwise combinations also creates highly correlated variables and increases the risk of accidentally selecting high-importance features from a small sample. Therefore, the results of this study support that carefully selected spectral transformations help RF establish mappings, rather than the notion that more combined indices are always better.

4.2.2. Response of Deep Models to Artificial Spectral Indices

Unlike RF, incorporating the same ratio and normalized difference indices into DNN and CNN did not yield consistent improvements in accuracy. One possible reason is that

https://doi.org/10.3390/su18168372

these indices are deterministic algebraic transformations of the original bands and do not add independent information. The nonlinear layers of DNN and the convolutional kernels of CNN can theoretically learn some band interactions directly from the original bands, so artificial indices may be redundant with the features learned internally by the model. Large-scale soil spectroscopy studies have shown that CNNs can directly learn features related to various soil properties from raw spectra, but this capability is typically built upon large training datasets [49].

Therefore, the finding that accuracy did not significantly improve after adding indices in this study cannot directly prove that deep models have fully exploited all salinity-related spectral information. This result may also be related to the limited sample size, the noise introduced by artificial indices, and the network architecture and regularization methods employed. In particular, the relatively low accuracy of DNN itself suggests that it failed to stably recover the salinity–spectral relationship through its deep structure. For CNN, its performance advantage is more likely to stem from both spectral interactions and spatial neighborhood information. Under the data and model configurations of this study, the artificial two-band indices did not provide stable incremental information beyond what was already captured by the original bands and spatial neighborhoods for the deep models.

4.2.3. Interpretation of Red-Edge-Related Features

In the RF importance ranking, combinations involving the red-edge, near-infrared, and shortwave infrared bands occupied high positions. The red edge is the spectral region where leaf reflectance transitions from strong absorption in the red to high reflectance in the near infrared, and is sensitive to chlorophyll content, leaf structure, senescence, and various environmental stresses. When vegetation is subjected to salt stress, chlorophyll content, cell structure, water status, and canopy coverage may change, thereby altering the red-edge slope and red-edge position. Under severe stress or senescence, the red edge may shift toward shorter wavelengths, accompanied by a decrease in near-infrared reflectance [50]. Therefore, the importance of red-edge indices may reflect the indirect impact of soil salinity on crop growth conditions, rather than being solely a direct spectral response of salt minerals themselves.

4.2.4. Blue–Green Ratio and Surface Salt Crust

The blue–green band ratio exhibited high importance in this study, which may be related to the formation of light-colored salt efflorescence or salt crusts on the surface of saline soils in the study area. Dry salt crusts generally increase overall reflectance in the visible range, while salt crust thickness, crystal grain size, soil color, and moisture content alter the relative response between blue and green bands. Consequently, the blue–green ratio may enhance the spectral contrast between saline surfaces and dark moist soil, vegetation, or soils with higher organic matter content.

Soil sample analysis in the study area indicates that the ionic composition of salt is dominated by sulfate, as shown in Figure 9, providing an environmental context for the statistical relationship between the blue–green ratio and salt content. However, the blue and green bands of Sentinel-2 are relatively broad, and light-colored salt crusts can also be formed by chlorides, carbonates, sulfates, and mixtures of these. Soil brightness is additionally influenced by texture, moisture, and organic matter. Therefore, the importance of the blue–green ratio only indicates its suitability for characterizing surface salinization differences under sulfate-dominated conditions in this study area, and it should not be regarded as a diagnostic index exclusive to sulfate.

https://doi.org/10.3390/su18168372

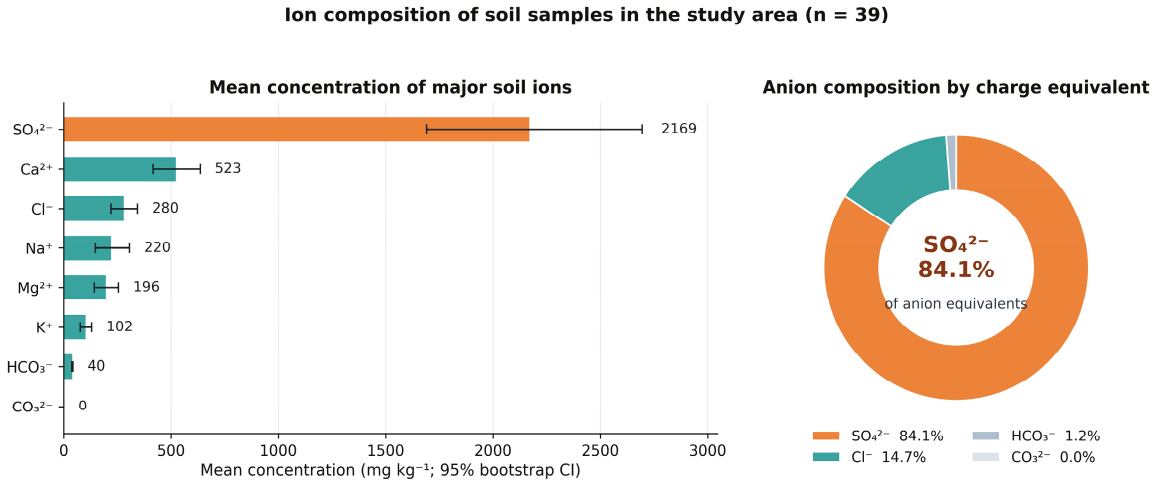

Figure 9. Statistical chart of saline–alkali ion content in 39 farmland plots within the study area.

4.3. Research Limitations and Future Directions

The salinization type involved in this study is predominantly sulfate-based, with relatively uniform soil physicochemical properties. The sample size is smaller compared to similar deep learning studies, leading to a certain degree of distributional bias in the dataset. Consequently, the generalizability of the current model to other salinization types requires further validation. Building on the discussion in the previous section, we suggest that convolutional neural networks may demonstrate better applicability in regions with minimal variation in salinization types. Future research should expand the observation scope to explore synergistic inversion mechanisms between different salinization types and soil salinity content, thereby enhancing the model's environmental adaptability and predictive stability.

Feature extraction is a critical step influencing the accuracy of remote sensing inversion and classification tasks. This study explored two approaches for feature extraction: mining associative information among multispectral bands through band combination methods, and extracting the joint representation of spectral and spatial features using convolutional operations. The methods employed are relatively conventional. Subsequent work could introduce advanced technologies, such as the Complex-Valued Optical Convolutional Accelerator, to more effectively extract the inherent physical and structural features of optical remote sensing data, thereby strengthening the model's representational and discriminative capabilities.

Furthermore, the current research is based solely on data from a single satellite source, which imposes limitations in terms of temporal coverage, spatial resolution, and data diversity. Future studies should actively pursue research on multi-source remote sensing data fusion, integrating observational information from different sensors and platforms. This approach would improve the spatiotemporal continuity, resolution, and overall accuracy of inversion results, enhancing the reliability and applicability of the methodology in complex real-world environments.

5. Conclusions

This study utilized Sentinel-2 satellite data to invert the soil salinity of cultivated land in arid and semi-arid regions. The developed inversion model demonstrates good potential for generalization and application. The main conclusions drawn from this research are as follows:

(1) Among classical machine learning models for soil salinity inversion in cultivated land, the Random Forest algorithm outperformed other models (R^2_{RF} = 0.33,

$R^2_{XGBoost}$ = 0.27, $R^2_{CATBoost}$ = 0.20). Within the deep learning models, the CNN model showed generalizable applicability, whereas the accuracy of the DNN model fell significantly short of practical application requirements (R^2_{CNN} = 0.65, R^2_{DNN} = 0.08). The CNN model is more suitable for soil salinity inversion in regions with relatively uniform soil salinization types. Building upon this foundation, this study proposes an SE-Final CNN network (R^2 = 0.70), which facilitates the efficient and accurate estimation of soil salinity.

(2) For regions with limited samples, complex salinity types, or a need for stronger interpretability, tree-based models such as RF can serve as robust baselines. CNN may be more advantageous when salinity-related surface features exhibit clear spatial structures, samples can cover major environmental gradients, and spatial validation demonstrates model generalization capability.

(3) For ensemble models combining multiple models for salinity retrieval, using the least accurate model as the base learner yielded more stable performance. However, the insufficient diversity between multispectral satellite spectra and saline–alkali sampling data led to high error correlations among sub-models within the ensemble, preventing the ensemble model from leveraging its full advantages.

(4) Compared with other bands and band combinations, the normalized difference index and ratio index of near-infrared and red-edge bands, as well as the blue–green band ratio index, are more conducive to retrieving salt content in sulfate-dominated farmland. A 50 m neighborhood provides the most effective spatial context for farmland salinity retrieval.

(5) In the main seed maize production area of Gansu, China, 75.47% of farmland is classified as non-saline, while 1.42% is severely saline, primarily distributed around water bodies and saline–alkali wasteland. Over the past decade, 74.83% of the farmland area in this region experienced a decrease in salt content, whereas 24.17% saw an increase. Areas exhibiting a significant decreasing trend (covering 9.37% of the area) correspond closely to regions where continuous engineering salt removal and organic fertilizer management have been implemented over the past ten years.

Supplementary Materials: The following supporting information can be downloaded at: https://www.mdpi.com/article/10.3390/su18168372/s1, Table S1: Sentinel-2 bands used in this study; Table S2: Complete list of pairwise Sentinel-2 indices.

Author Contributions: Conceptualization, X.D. and S.G.; methodology, X.D. and S.G.; software, X.D., S.G. and Z.G.; validation, X.D., S.G. and X.J.; formal analysis, X.D., S.G., Z.G. and X.J.; investigation, R.J. and J.W.; resources, Z.G. and S.M.; data curation, X.D., S.G. and Z.G.; writing—original draft preparation, X.D.; writing—review and editing, X.D. and S.G.; visualization, X.D., S.G. and Z.G.; supervision, S.G.; project administration, X.D. and S.G.; funding acquisition, S.G. All authors have read and agreed to the published version of the manuscript.

Funding: This research was funded by the funds program of Central Government Guides Local Science and Technology Development, grant number 24ZYQA036. The APC was funded by Xingchen Dong.

Data Availability Statement: The datasets presented in this article are not readily available because the data are part of an ongoing study. Requests to access the datasets should be directed to the corresponding author via email.

Acknowledgments: We would like to extend our sincere gratitude to the editor and the reviewers for all their assistance during the publication process of this paper.

Conflicts of Interest: The authors declare no conflicts of interest.

Abbreviations

The following abbreviations are used in this manuscript:

RF	Random Forest
XGBoost	eXtreme Gradient Boosting
DNN	Deep Neural Network
CatBoost	Categorical Boosting
CNN	Convolutional Neural Network
Lightweight ResNet	Lightweight Residual Network
ResNet-50	Residual Network with 50 layers
Lightweight DenseNet	Lightweight Densely Connected Convolutional Network
DenseNet	Densely Connected Convolutional Network
Lightweight EfficientNet	Lightweight EfficientNet
EfficientNet	Efficient Network
CBAM	Convolutional Block Attention Module
SE-Deep CNN	Deep Convolutional Neural Network with Squeeze-and-Excitation blocks
SE-Final CNN	Convolutional Neural Network with an Attention Mechanism Added in the Final Layer

References

1. Corwin, D.L. Climate change impacts on soil salinity in agricultural areas. *Eur. J. Soil Sci.* **2021**, *72*, 842–862. [CrossRef]
2. Metternicht, G.I.; Zinck, J. Remote sensing of soil salinity: Potentials and constraints. *Remote Sens. Environ.* **2003**, *81*, 1–20. [CrossRef]
3. Wu, D.; Jia, K.; Zhang, X.; Zhang, J.; Abd El-Hamid, H.T. Remote sensing inversion for simulation of soil salinization based on hyperspectral data and ground analysis in Yinchuan, China. *Nat. Resour. Res.* **2021**, *30*, 4641–4656. [CrossRef]
4. Sheng, J.; Ma, L.; Jiang, P.; Li, B.; Huang, F.; Wu, H. Digital soil mapping to enable classification of the salt-affected soils in desert agro-ecological zones. *Agric. Water Manag.* **2010**, *97*, 1944–1951. [CrossRef]
5. Ghassemi, F.; Jakeman, A.J.; Nix, H.A. *Salinisation of Land and Water Resources: Human Causes, Extent, Management and Case Studies*; CAB International: Wallingford, UK, 1995.
6. Yang, J.S.; Yao, R.J.; Wang, X.P.; Xie, W.P.; Zhang, X.; Zhu, W.; Zhang, L.; Sun, R.J. Research on Salt-affected Soils in China: History, Status Quo and Prospect. *Acta Pedol. Sin.* **2022**, *59*, 10–27.
7. Shi, H.Y.; Hellwich, O.; Luo, G.P.; Chen, C.B.; He, H.L.; Ochege, F.U.; Van de Voorde, T.; Kurban, A.; De Maeyer, P. A global meta-analysis of soil salinity prediction integrating satellite remote sensing, soil sampling, and machine learning. *IEEE Trans. Geosci. Remote Sens.* **2021**, *60*, 4505815. [CrossRef]
8. Boudibi, S.; Sakaa, B.; Benguega, Z.; Fadlaoui, H.; Othman, T.; Bouzidi, N. Spatial prediction and modeling of soil salinity using simple cokriging, artificial neural networks, and support vector machines in El Outaya plain, Biskra, southeastern Algeria. *Acta Geochim.* **2021**, *40*, 390–408. [CrossRef]
9. Seo, B.S.; Jeong, Y.J.; Baek, N.R.; Park, H.J.; Yang, H.I.; Park, S.I.; Choi, W.J. Soil texture affects the conversion factor of electrical conductivity from 1: 5 soil-water to saturated paste extracts. *Pedosphere* **2022**, *32*, 905–915. [CrossRef]
10. Periasamy, S.; Shanmugam, R.S. Multispectral and microwave remote sensing models to survey soil moisture and salinity. *Land Degrad. Dev.* **2017**, *28*, 1412–1425. [CrossRef]
11. Metternicht, G. Categorical fuzziness: A comparison between crisp and fuzzy class boundary modelling for mapping salt-affected soils using Landsat TM data and a classification based on anion ratios. *Ecol. Model.* **2003**, *168*, 371–389. [CrossRef]
12. Mulder, V.L.; de Bruin, S.; Schaepman, M.E.; Mayr, T.R. The use of remote sensing in soil and terrain mapping—A review. *Geoderma* **2011**, *162*, 1–19. [CrossRef]
13. Sahbeni, G.; Ngabire, M.; Musyimi, P.K.; Székely, B. Challenges and Opportunities in Remote Sensing for Soil Salinization Mapping and Monitoring: A Review. *Remote Sens.* **2023**, *15*, 2540. [CrossRef]
14. Corwin, D.L.; Scudiero, E. Review of soil salinity assessment for agriculture across multiple scales using proximal and/or remote sensors. *Adv. Agron.* **2019**, *158*, 1–130. [CrossRef]
15. Wang, F.; Han, L.; Liu, L.; Bai, C.; Ao, J.; Hu, H.; Li, R.; Li, X.; Guo, X.; Wei, Y. Advancements and perspective in the quantitative assessment of soil salinity utilizing remote sensing and machine learning algorithms: A review. *Remote Sens.* **2024**, *16*, 4812. [CrossRef]
16. Taghadosi, M.M.; Hasanlou, M. Trend analysis of soil salinity in different land cover types using Landsat time series data (case study Bakhtegan Salt Lake). *Int. Arch. Photogramm. Remote Sens. Spat. Inf. Sci.* **2017**, *42*, 251–257. [CrossRef]

17. Abuelgasim, A.; Ammad, R. Mapping soil salinity in arid and semi-arid regions using Landsat 8 OLI satellite data. *Remote Sens. Appl. Soc. Environ.* **2019**, *13*, 415–425. [CrossRef]
18. Taghadosi, M.M.; Hasanlou, M. Developing geographic weighted regression (GWR) technique for monitoring soil salinity using sentinel-2 multispectral imagery. *Environ. Earth Sci.* **2021**, *80*, 75. [CrossRef]
19. Zarei, A.; Hasanlou, M.; Mahdianpari, M. A comparison of machine learning models for soil salinity estimation using multi-spectral earth observation data. *ISPRS Ann. Photogramm. Remote Sens. Spat. Inf. Sci.* **2021**, *3*, 257–263. [CrossRef]
20. Lobell, D.B.; Lesch, S.M.; Corwin, D.L.; Ulmer, M.G.; Anderson, K.A.; Potts, D.J.; Doolittle, J.A.; Matos, M.R.; Baltes, M.J. Regional-scale assessment of soil salinity in the Red River Valley using multi-year MODIS EVI and NDVI. *J. Environ. Qual.* **2010**, *39*, 35–41. [CrossRef] [PubMed]
21. Zhang, T.T.; Qi, J.G.; Gao, Y.; Ouyang, Z.T.; Zeng, S.L.; Zhao, B. Detecting soil salinity with MODIS time series VI data. *Ecol. Indic.* **2015**, *52*, 480–489. [CrossRef]
22. Dwivedi, R.; Rao, B. The selection of the best possible Landsat TM band combination for delineating salt-affected soils. *Int. J. Remote Sens.* **1992**, *13*, 2051–2058. [CrossRef]
23. Farifteh, J.; Farshad, A.; George, R.J. Assessing salt-affected soils using remote sensing, solute modelling, and geophysics. *Geoderma* **2006**, *130*, 191–206. [CrossRef]
24. Allbed, A.; Kumar, L. Soil salinity mapping and monitoring in arid and semi-arid regions using remote sensing technology. *Adv. Remote Sens.* **2013**, *2*, 373–385.
25. Bouaziz, M.; Matschullat, J.; Gloaguen, R. Improved remote sensing detection of soil salinity from a semi-arid climate in Northeast Brazil. *Comptes Rendus. Géosci.* **2011**, *343*, 795–803. [CrossRef]
26. Xiao, D.; Wan, L.; Sun, X. Remote sensing retrieval of saline and alkaline land based on reflectance spectroscopy and RV-MELM in Zhenlai County. *Opt. Laser Technol.* **2021**, *139*, 106909. [CrossRef]
27. Fu, Y.H.; Wan, L.S.; Xiao, D.; Le, B.T. Remote sensing inversion of saline and alkaline land based on reflectance spectroscopy and D-TELM algorithm in Wuyuan areas. *Infrared Phys. Technol.* **2020**, *109*, 103367. [CrossRef]
28. Aldabaa, A.A.A.; Weindorf, D.C.; Chakraborty, S.; Sharma, A.; Li, B. Combination of proximal and remote sensing methods for rapid soil salinity quantification. *Geoderma* **2015**, *239*, 34–46. [CrossRef]
29. Fathizad, H.; Ardakani, M.A.H.; Sodatezadeh, H.; Kerry, R.; Taghizadeh-Mehriardi, R. Investigation of the spatial and temporal variation of soil salinity using random forests in the central desert of Iran. *Geoderma* **2020**, *365*, 114233. [CrossRef]
30. Jiang, H.; Rusuli, Y.; Amuti, T.; He, Q. Quantitative assessment of soil salinity using multi-source remote sensing data based on the support vector machine and artificial neural network. *Int. J. Remote Sens.* **2019**, *40*, 284–306. [CrossRef]
31. Wang, Y.B.; Yang, X.; Lv, X.J.; He, W.; Shao, M.; Liu, H.M.; Jia, C. Depth-Specific Prediction of Coastal Soil Salinization Using Multi-Source Environmental Data and an Optimized GWO–RF–XGBoost Ensemble Model. *Remote Sens.* **2025**, *17*, 4043. [CrossRef]
32. Zhang, Q.Q.; Li, L.; Sun, R.Z.; Zhu, D.H.; Zhang, C.; Chen, Q.Q. Retrieval of the soil salinity from Sentinel-1 Dual-Polarized SAR data based on deep neural network regression. *IEEE Geosci. Remote Sens. Lett.* **2020**, *19*, 1–5. [CrossRef]
33. Wang, N.; Xue, J.; Peng, J.; Biswas, A.; He, Y.; Shi, Z. Integrating remote sensing and landscape characteristics to estimate soil salinity using machine learning methods: A case study from Southern Xinjiang, China. *Remote Sens.* **2020**, *12*, 4118. [CrossRef]
34. Chen, S.; Billings, S.A. Neural networks for nonlinear dynamic system modelling and identification. *Int. J. Control* **1992**, *56*, 319–346. [CrossRef]
35. Liaw, A.; Wiener, M. Classification and regression by randomForest. *R News* **2002**, *2*, 18–22.
36. Guo, Z.; Li, Y.; Wang, X.; Gong, X.; Chen, Y.; Cao, W. Remote sensing of soil organic carbon at regional scale based on deep learning: A case study of agro-pastoral ecotone in northern China. *Remote Sens.* **2023**, *15*, 3846. [CrossRef]
37. Li, M. Methods and Models for Agricultural Water-Land ResourcesMulti-scale Optimal Allocation Based on Uncertainty Analysis, in College of Water Resources and Civil Engineering. Ph.D. Thesis, China Agricultural University, Beijing, China, 2017.
38. Ministry of Natural Resources of the People's Republic of China. Standard Map of China (Chinese Version); Map Approval No. GS(2022)1873. Standard Map Service. 2022. Available online: http://bzdt.ch.mnr.gov.cn (accessed on 5 August 2026).
39. Zhang, J.L.; Ji, X.B.; Chen, X.L.; Xu, S.Q.; Jiao, D.D. Regional supply-demand balance and carrying capacity of water resources for Linze Oasis in the middle of Hexi Corridor. *Arid. Land Geogr.* **2018**, *41*, 38–47.
40. Garajeh, M.K.; Feizizadeh, B.; Weng, Q.; Moghaddam, M.H.R.; Garajeh, A.K. An automated deep learning convolutional neural network algorithm applied for soil salinity distribution mapping in Lake Urmia, Iran. *Sci. Total Environ.* **2021**, *778*, 146253. [CrossRef] [PubMed]
41. Ma, L.; Liu, Y.; Zhang, X.L.; Ye, Y.X.; Yin, G.F.; Johnson, B.A. Deep learning in remote sensing applications: A meta-analysis and review. *ISPRS J. Photogramm. Remote Sens.* **2019**, *152*, 166–177. [CrossRef]
42. Brown, G.; Wyatt, J.L.; Tiňo, P. Managing diversity in regression ensembles. *J. Mach. Learn. Res.* **2005**, *6*, 1621–1650.
43. Krogh, A.; Vedelsby, J. Neural network ensembles, cross validation, and active learning. *Adv. Neural Inf. Process. Syst.* **1994**, *7*, 231–238.

44. Ho, T.K. A data complexity analysis of comparative advantages of decision forest constructors. *Pattern Anal. Appl.* **2002**, *5*, 102–112. [CrossRef]
45. Xing, H.-J.; Wang, X.-Z. Selective ensemble of SVDDs with Renyi entropy based diversity measure. *Pattern Recognit.* **2017**, *61*, 185–196. [CrossRef]
46. Linze County People's Government. Comprehensive Management of Saline-Alkali Cultivated Land in Linze County Has Achieved Remarkable Results (Chinese Version). Available online: http://www.gslz.gov.cn/dzdt/gzdb/202601/t20260129_1504345.html (accessed on 5 August 2026).
47. Yang, Z.H.; Wang, J.H.; Ji, Y.F.; Liu, H.J.; He, F.Y. Improvement Model of Saline Land in the Hexi Corridor. *Chin. Joumal Soil Sci.* **2005**, *36*, 479–482.
48. Xu, X.B.; Wang, X.G.; Yang, P.J.; Meng, Y.H.; Yu, D.Q.; Li, C.F. Strategy for mapping soil salt contents during the bare soil period through a satellite image: Optimal calibration set combined with random forest. *Catena* **2023**, *223*, 106900. [CrossRef]
49. Padarian, J.; Minasny, B.; McBratney, A.B. Using deep learning to predict soil properties from regional spectral data. *Geoderma Reg.* **2019**, *16*, e00198. [CrossRef]
50. Baranoski, G.; Rokne, J. A practical approach for estimating the red edge position of plant leaf reflectance. *Int. J. Remote Sens.* **2005**, *26*, 503–521. [CrossRef]

Disclaimer/Publisher's Note: The statements, opinions and data contained in all publications are solely those of the individual author(s) and contributor(s) and not of MDPI and/or the editor(s). MDPI and/or the editor(s) disclaim responsibility for any injury to people or property resulting from any ideas, methods, instructions or products referred to in the content.

sustainability

MDPI

Article

Weather-Driven Predictive Models for Jassid and Thrips Infestation in Cotton Crop

Rubab Shafique [1], Sharzil Haris Khan [2], Jihyoung Ryu [3] and Seung Won Lee [4,5,6,7,*]

[1] Department of Electrical Engineering, Institute of Space Technology, Islamabad 44000, Pakistan
[2] Department of Electrical and Information Engineering, Jeonbuk National University, Jeonju 54869, Republic of Korea
[3] Electronics and Telecommunications Research Institute (ETRI), Gwangju 61012, Republic of Korea
[4] Department of Precision Medicine, School of Medicine, Sungkyunkwan University, Suwon 16419, Republic of Korea
[5] Department of Artificial Intelligence, Sungkyunkwan University, Suwon 16419, Republic of Korea
[6] Department of Metabiohealth, Sungkyunkwan University, Suwon 16419, Republic of Korea
[7] Personalized Cancer Immunotherapy Research Center, School of Medicine, Sungkyunkwan University, Suwon 16419, Republic of Korea
* Correspondence: swleemd@g.skku.edu

Abstract: Agriculture is a vital contributor to global food security but faces escalating threats from environmental fluctuations and pest incursions. Among the most prevalent and destructive pests, Jassid (*Amrasca biguttula*) and Thrips (*Thrips tabaci*) frequently afflict cotton, okra, and other major crops, resulting in substantial yield losses worldwide. This paper integrates five machine learning (ML) models to predict pest incidence based on key meteorological attributes, including temperature, relative humidity, wind speed, sunshine hours, and evaporation. Two ensemble strategies, soft voting and stacking, were evaluated to enhance predictive performance. Our findings indicate that a stacking ensemble yields superior results, achieving high multi-class AUC scores (0.985). To demystify the underlying mechanisms of the best-performing ensemble, this study employed SHapley Additive exPlanations (SHAP) to quantify the contributions of individual weather parameters. The SHAP analysis revealed that Standard Meteorological Week, evaporation, and relative humidity consistently exert the strongest influence on pest forecasts. These insights align with biological studies highlighting the role of seasonality and humid conditions in fostering Jassid and Thrips proliferation. Importantly, this explainable approach bolsters the practical utility of AI-based solutions for integrated pest management (IPM), enabling stakeholders—farmers, extension agents, and policymakers—to trust and effectively operationalize data-driven recommendations. Future research will focus on integrating real-time weather data and satellite imagery to further enhance prediction accuracy, as well as incorporating adaptive learning techniques to refine model performance under varying climatic conditions.

Keywords: pest infestation; predictive modeling; agriculture; ensemble learning; SHAP analysis; explainable AI

1. Introduction

Agriculture remains a critical sector ensuring global food security, providing essential resources to sustain the growing world population. However, the sector faces multifaceted challenges arising from climate volatility, resource constraints, and pest pressures. As the world's population continues to rise, securing a stable food supply becomes increasingly complex. Shifting weather patterns, environmental disturbances, and the rise in

extreme weather events exacerbate the behavior, distribution, and population dynamics of agricultural pests. These pests, such as Jassid (*Amrasca biguttula*) and Thrips (*Thrips tabaci*), have the potential to cause substantial damage to crops like cotton, okra, and horticultural produce, leading to severe economic losses and jeopardizing food security on a global scale [1–3]. The urgency for more accurate, data-driven pest management strategies has never been greater, especially in the face of the unprecedented challenges posed by climate change [4–6].

The impacts of climate change on agriculture are far-reaching and multifactorial. Rising temperatures, altered precipitation regimes, and more frequent extreme weather events have direct and indirect effects on pest ecology [7–9]. Warmer temperatures can accelerate pest life cycles, leading to multiple generations in a single growing season, increasing the likelihood of infestations. Changes in humidity and rainfall further enhance pest survival rates and affect their distribution, complicating the task of pest control [10,11]. These climate-induced changes necessitate a proactive, dynamic approach to pest management, one that can adapt to rapidly changing conditions. Understanding weather-pest linkages and using predictive models to anticipate pest outbreaks are critical in this new climate reality, offering the potential for more precise, timely interventions and more resilient agricultural systems [12,13].

The modernization of agriculture has been facilitated by advanced sensing technologies (e.g., IoT-based sensors, remote sensing) and high-resolution climate data sets. Machine learning (ML) and artificial intelligence (AI) models, leveraging these data streams, now enable forecasting of pest occurrences, disease outbreaks, and yield fluctuations with unprecedented accuracy [14,15]. As agriculture faces increasing challenges due to climate change and pest pressures, advanced technologies are crucial for effective pest management. The integration of remote sensing and computational models is essential, as demonstrated by Ma and Liu (2020), who proposed a modified geometrical optical model for row crops, enhancing pest prediction through better light interaction analysis [16]. Additionally, genetic studies, such as those by Yang et al. (2019), highlight the potential for crop resilience through the identification of genes that can improve pest resistance [17]. The development of innovative chemical agents also plays a role in integrated pest management, with Chen et al. (2024) discovering novel anti-plant viral compounds [18], and Huang et al. (2024) investigating the use of cyclopropane-based pesticides to minimize environmental harm [19].

Moreover, the data-driven models enable early warnings and allow for targeted, site-specific interventions, reducing the need for broad pesticide application and minimizing environmental impacts. Moreover, predictive models help optimize agricultural productivity, reduce costs, and ensure the economic viability of farming [20–22].

Despite their clear advantages, the integration of predictive models into existing agricultural systems is not without its challenges. While ML and AI have shown impressive accuracy in pest prediction, their black-box nature often hinders their adoption by farmers, agronomists, and policymakers [23,24]. Without transparency, stakeholders may be hesitant to trust AI-driven recommendations, fearing unpredictability and lack of interpretability. This lack of trust can delay or prevent the widespread adoption of these technologies, limiting their potential impact on pest management. The recent advent of eXplainable AI (XAI) frameworks seeks to address these challenges by enhancing the interpretability of model predictions. By revealing the underlying drivers and providing actionable insights, XAI makes AI models more accessible to agricultural stakeholders, fostering trust and facilitating their integration into pest management practices [25,26].

This study aims to predict the presence of Jassid and Thrips based on key local weather parameters, including maximum and minimum temperature, relative humidity,

wind speed, sunshine hours, and evaporation. Using five different ML classifiers, this study seeks to identify the most accurate and reliable model for pest prediction. To enhance the interpretability of these predictions, this study applies SHAP (SHapley Additive exPlanations) values, allowing us to uncover the importance of various weather parameters in pest infestations.

The main contributions of this study are threefold:

- This study develops robust ML-based models to predict Jassid and Thrips infestation using six key meteorological predictors, demonstrating high accuracy and early warning capabilities.
- By employing SHAP to explain model outputs, this study bridges the gap between black-box ML predictions and the interpretability desired by agricultural stakeholders. This fosters trust, facilitates better decision-making, and promotes the operationalization of AI-driven solutions.
- Our explainability analysis reveals that relative humidity, minimum temperature, and maximum temperature significantly influence pest infestations. Understanding these drivers can inform climate-resilient pest management strategies and guide future research in crop protection and integrated pest management (IPM) frameworks.

2. Literature Review

This section surveys the existing literature on pest prediction models, the role of weather and climate variables in pest population dynamics, the use of AI and ML techniques in agriculture, and the emergence of explainable AI frameworks. This study emphasizes recent studies that highlight the intersection of advanced modeling techniques and the growing need for transparency, which form the basis of this research.

2.1. Pest Prediction Models and Environmental Correlation

The relationship between environmental parameters and pest dynamics is a well-established foundation in pest prediction model development. Jassids (*Amrasca biguttula biguttula*) and Thrips are prime examples of pests whose population fluctuations are closely linked to environmental conditions. Understanding these correlations is crucial for forecasting pest outbreaks and developing Integrated Pest Management (IPM) strategies. However, previous studies predominantly focus on basic meteorological parameters such as temperature and humidity, while other meteorological factors like solar radiation intensity or sudden seasonal variations have been underexplored.

In the case of Jassids, several studies highlight the influence of temperature, humidity, and other environmental factors on population growth and survivorship. For instance, ref. [27] demonstrated that Jassid populations on okra were significantly correlated with temperature and relative humidity. Their work showed that moderate temperatures combined with relatively higher humidity favor Jassid proliferation, increasing feeding damage and subsequent crop yield reduction. Similarly, ref. [28] noted that temperature and humidity levels not only affected the developmental rates and survival of Jassids but also influenced their interaction with host plants.

Thrips, on the other hand, are also closely tied to environmental variables. Researchers in [29] illustrated that Thrips species thrive under specific temperature and humidity ranges, often experiencing population surges in warm, humid conditions. Likewise, ref. [30] further supported these findings by demonstrating that specific temperature and precipitation patterns influence the seasonal flight activity of Thrips, altering their colonization dynamics and spread within crop fields. These studies collectively highlight the importance of integrating weather data—such as temperature extremes, humidity levels, and precipitation patterns—into pest prediction models. By correlating observed pest incidence with these

environmental cues, models can learn to anticipate outbreak windows, forecast potential severity, and guide timely interventions. Such predictive frameworks offer essential benefits, including reduced pesticide applications, sustainable resource allocation, and improved economic returns for farmers. As climate change continues to reshape local and regional weather patterns, refining and updating these correlation-based models with real-time meteorological data and advanced computational techniques becomes increasingly critical, ensuring that management strategies remain adaptive, effective, and ecologically sound.

The growing importance of predictive pest models in the context of food security has made it imperative to integrate accurate forecasting systems that help prevent crop losses, minimize pesticide use, and improve resource allocation in agriculture. Although statistically oriented models, such as regression and generalized linear models, have provided early insights into pest dynamics, they often fail to capture the complex non-linear interactions between multiple environmental variables, which limits their predictive power. In contrast, machine learning models can learn from data to model such interactions more accurately.

Recent research has integrated environmental and phenological data to build predictive models. For example, ref. [31] studied climate-driven population dynamics of Thrips abundance. Other works have applied regression models, generalized linear models, or statistical correlation techniques to link weather parameters (e.g., temperature, humidity, rainfall) to pest abundance and spread. One example is in [32], which uses Long Short Term Memory networks to predict Cotton pests. Although statistically oriented models provided early insights, machine learning approaches have shown the potential to improve prediction accuracy and capture non-linear interactions. While studies have primarily focused on temperature and humidity as the key drivers of pest dynamics, less emphasized factors like solar radiation intensity and sudden seasonal variations may also play significant roles in shaping pest population trends, suggesting a need for more comprehensive modeling approaches.

2.2. Machine Learning Approaches in Pest Management

Machine learning has rapidly become a cornerstone of precision agriculture. A larger number of ML algorithms, including Random Forests, SVM, Artificial Neural Networks (ANN), and gradient boosting methods, have been employed to address various agricultural challenges. In pest management, these algorithms leverage large datasets of historical weather records, pest scouting information, and agronomic practices to forecast pest outbreaks [28]. As mentioned in [33], the three approaches used for pest infestation prediction are:

- Regression Approach: Uses advanced regression algorithms to predict the number of pests in a specific area by analyzing the relationship between climatic factors and pest abundance.
- Classification Approach: Categorizes areas into “infested” or “non-infested” based on climatic variables and pest invasion patterns. This study focuses on the prediction of pest species invasions within a specific geographic region. It also employs the examination of the relationship between climatic variables and the invasion of pest species.
- Time Series Approach: Employs forecasting methods like moving averages, ARIMA, and SARIMA to predict pest numbers using past data. It provides accurate pest quantity predictions over time.

Another study [34] highlights the transformative potential of deep learning in pest management by automating tasks such as pest detection and agrochemical efficacy as-

sessment. The study emphasizes the advantages of deep learning models in processing complex data patterns. Moreover, the research mentioned in [35] reviews various ML algorithms, including random forest (RF), support vector machine (SVM), decision tree (DT), and naïve Bayes (NB), as well as DL methods like convolutional neural networks (CNNs), long short-term memory (LSTM), deep convolutional neural networks (DCNNs), and deep belief networks (DBNs), emphasizing their roles in enhancing pest detection accuracy.

2.3. Significance of Explainable AI (XAI)

Despite improved accuracy, ML-based models often function as "black boxes", making it difficult to understand why a model makes a particular prediction. In the agricultural domain, this lack of transparency can hinder trust and limit adoption among end-users who seek understandable recommendations. XAI techniques provide a systematic framework to demystify model behavior. Explainable artificial intelligence (XAI) aims to provide a suite of machine learning techniques that enable human users to understand, appropriately trust, and produce more explainable models [36]. Techniques like LIME, SHAP, and Grad-CAM have been applied to various agricultural contexts [37]. These methods quantify feature contributions to model predictions, enabling domain experts to verify that the model aligns with established scientific knowledge and does not rely on spurious correlations.

3. Dataset

For this research, an open-source dataset, as used in [32], was utilized to classify two types of pests, *Jassid* and *Thrips*, along with a *No Pest* category. The dataset, collected over several growing seasons of cotton crops, was engineered to represent these three classes: *Jassid*, *Thrips*, and *No Pest*.

The data were sourced from field observations, with environmental parameters measured at various points during the growing seasons and organized according to the Standard Meteorological Week (SMW). These observations were recorded at multiple sites to capture regional variability in environmental conditions. However, potential sources of error include inconsistencies in measurements due to instrument calibration issues or data entry errors, as well as variations in local environmental conditions across different regions. To minimize these errors, all recorded data underwent a comprehensive cleaning process that involved removing or correcting inconsistent readings, conducting outlier detection, and verifying data consistency against known environmental patterns.

A total of six meteorological factors were chosen for this study based on their well-established relevance to pest activity in prior research. These features include temperature (MaxT, MinT), humidity (RH1, RH2), wind speed (WS), sunshine hours (SSH), evaporation (EVP), and rainfall (RF). These factors have been identified in numerous studies as key drivers of pest behavior, influencing aspects such as pest reproduction, movement, and feeding habits [38,39]. For instance, temperature and humidity directly affect pest metabolism, while rainfall and wind speed impact pest dispersal. The inclusion of these six features allows the model to account for both local and seasonal environmental influences on pest populations, providing a comprehensive understanding of the ecological conditions that drive pest presence.

A summary of the features recorded in the dataset is provided in Table 1. These parameters were used to predict the presence or absence of pests, categorized into three classes: *Jassid*, *Thrips*, and *No Pest*.

Table 1. Features of the Dataset

Feature	Description
Observation Year	The years from 2005 to 2009
SMW	Standard Meteorological Week, representing the week number
MaxT	Maximum Temperature in degrees Celsius
MinT	Minimum Temperature in degrees Celsius
RH1	Relative Humidity in the Morning (%)
RH2	Relative Humidity in the Evening (%)
WS	Wind Speed in kilometers per hour
SSH	Sunshine Hours per day (h)
EVP	Evaporation in millimeters
RF	Rainfall in millimeters

Before the model training, the dataset underwent a rigorous data cleaning process, which involved eliminating missing or inconsistent readings, along with outlier detection and correction. To ensure the data's consistency and comparability, all features were standardized using either normalization or min-max scaling, depending on the feature's distribution. This was done to prevent variables with larger numeric ranges from dominating the analysis.

Feature engineering was deliberately kept minimal to preserve the ecological validity of the dataset, ensuring that the features remained aligned with the real-world environmental conditions. Finally, the dataset was split into training and testing sets using a stratified 80:20 ratio. This stratified approach ensured that each class, *Jassid*, *Thrips*, and *No Pest*, was proportionally represented in both the training and testing sets, enhancing the generalizability and reliability of the resulting models. To further analyze the distribution of these features across different pest classes, Figure 1 presents box plots for each pest category, illustrating the variations in environmental parameters excluding time-based features. These plots provide insights into the differences in feature distributions among the three classes, highlighting potential patterns and trends that contribute to pest classification.

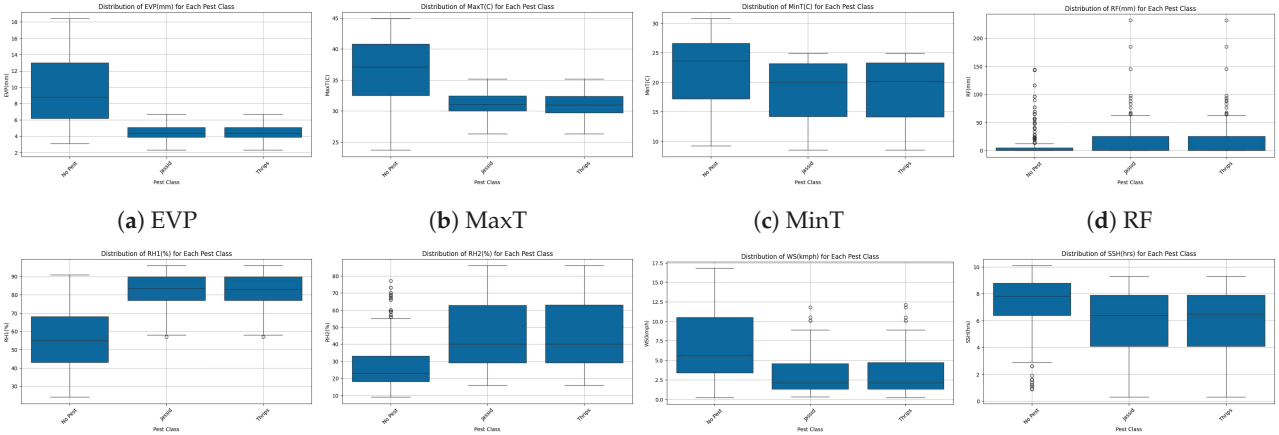

(**a**) EVP (**b**) MaxT (**c**) MinT (**d**) RF

(**e**) RH1 (**f**) RH2 (**g**) WS (**h**) SSH

Figure 1. Box plots for each Pest class across each feature excluding time-based features.

4. Methodology

This study proposes a weather-driven predictive modeling approach for forecasting Jassid and Thrips infestations in cotton crops. The methodology consists of data preprocessing, feature engineering, model training, evaluation, and ensemble learning strategies, as illustrated in Figure 2.

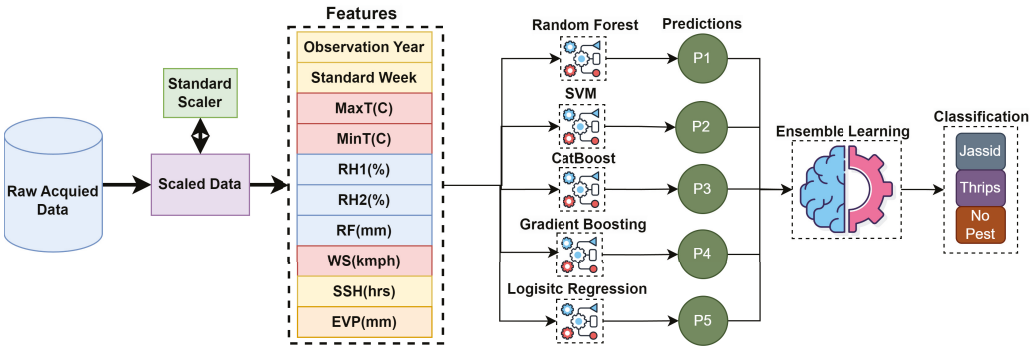

Figure 2. Flow diagram of the proposed methodology.

4.1. Pre-Processing

Data preprocessing is a critical step to ensure the dataset is clean, well-structured, and suitable for machine learning algorithms. The following preprocessing steps were performed:

4.1.1. Handling Missing Values

Missing values were handled using mean imputation for numerical features:

$$X_i^{(j)} = \frac{1}{N} \sum_{k=1}^{N} X_k^{(j)} \tag{1}$$

where $X_i^{(j)}$ represents the missing value for feature j and N is the total number of available (non-missing) samples.

4.1.2. Feature Scaling

Since different weather features have varying scales, StandardScaler was applied to standardize feature distributions:

$$X' = \frac{X - \mu}{\sigma} \tag{2}$$

where μ is the mean and σ is the standard deviation of each feature.

4.2. Classifiers Used in the Study

To classify pest infestations, multiple machine learning classifiers were employed, each leveraging different algorithmic strengths to enhance prediction accuracy. The selection of these classifiers was guided by their suitability for handling diverse types of environmental data and their ability to provide interpretable results, which is crucial for the transparency of pest management systems.

4.2.1. Random Forest (RF)

Random Forest is an ensemble learning method that builds multiple decision trees and aggregates their results. It enhances generalization and reduces overfitting. The classification output is determined by majority voting:

$$\hat{y} = \arg\max \sum_{i=1}^{n} p_i(x) \tag{3}$$

where $p_i(x)$ represents the predicted probability from tree i for input x. Random Forest is effective at handling large datasets with complex feature interactions and works well with both continuous and categorical data. However, its reliance on multiple decision trees can lead to high computational costs, especially with large datasets. Additionally,

Random Forest models are prone to overfitting if not tuned carefully, especially in the case of noisy data.

4.2.2. Support Vector Machine (SVM)

SVM is a kernel-based classification model that finds the optimal hyperplane separating different classes. The decision function is given by:

$$\hat{y} = \text{sign}(w^T x + b) \tag{4}$$

where w is the weight vector, x is the input feature vector, and b is the bias term. SVM with a radial basis function (RBF) kernel is often used to handle non-linear classification tasks. While SVMs perform well on smaller datasets, they require high-quality data for optimal performance. Furthermore, SVMs are sensitive to the choice of hyperparameters, such as the kernel and regularization terms, and can be computationally expensive when dealing with large-scale datasets.

4.2.3. Logistic Regression (LR)

Logistic regression models the probability of a class using the sigmoid function:

$$P(y = 1|X) = \frac{1}{1 + e^{-(w^T X + b)}} \tag{5}$$

where w is the weight vector, b is the bias term, and X is the input feature vector. LR is particularly effective when the relationship between features and classes is linear. However, it struggles with non-linear dependencies, which can limit its performance in more complex datasets. Additionally, it is prone to underfitting if the data is not linearly separable, and may also suffer from bias if the data is imbalanced.

4.2.4. CatBoost (CB)

CatBoost is a gradient boosting algorithm optimized for categorical data. The boosting process updates weak learners sequentially to minimize classification errors:

$$F_m(x) = F_{m-1}(x) + \gamma h_m(x) \tag{6}$$

where $F_m(x)$ is the updated model after the m-th iteration, $h_m(x)$ is the weak learner (decision tree), and γ is the learning rate. CatBoost is known for its performance on datasets with a large number of categorical variables and its ability to handle overfitting. However, like other gradient boosting methods, CatBoost can be computationally expensive, and its performance heavily relies on the quality of the input data. It is also sensitive to parameter tuning, which can affect model robustness.

4.2.5. Gradient Boosting (GB)

Gradient Boosting improves classification accuracy by sequentially training models to correct the errors of previous iterations. The loss function is minimized iteratively:

$$F_m(x) = F_{m-1}(x) - \gamma \sum_{i=1}^{N} \frac{\partial L}{\partial F_{m-1}(x_i)} \tag{7}$$

where L is the loss function, and γ is the step size. Gradient Boosting improves predictive accuracy by focusing on the hardest-to-predict instances in each iteration, which makes it well-suited for complex, non-linear datasets like pest prediction. However, similar to CatBoost, it can be prone to overfitting without proper regularization and hyperparameter tuning. Moreover, it is computationally intensive, particularly when applied to large-scale problems.

4.3. Effectiveness and Constraints of ML Algorithms

The effectiveness of each of these models depends heavily on the quality of the input data, including the accuracy and completeness of the environmental variables used for predictions. For instance, Random Forest and CatBoost generally perform well with large, heterogeneous datasets, while models like Logistic Regression and SVM can struggle if the relationships between features are non-linear. A major limitation of many of these models is their requirement for high-quality, labeled data. The risk of overfitting is especially pronounced in complex models like CatBoost and Gradient Boosting, where regularization techniques such as early stopping or pruning are necessary to prevent the model from becoming too finely tuned to the training data.

4.4. Ensemble Learning

To enhance predictive performance, two ensemble learning strategies were implemented:

- **Voting Classifier**: A soft-voting approach combining the predictions of multiple classifiers.
- **Stacking Classifier**: A meta-learner-based approach where base classifiers feed into a final logistic regression classifier.

The final prediction in soft voting is computed as:

$$\hat{y} = \arg\max \sum_{i=1}^{n} p_i(x) \tag{8}$$

where $p_i(x)$ represents the predicted probability from classifier i.

The Stacking Classifier makes use of base model outputs as input features:

$$\hat{y} = f(\hat{y}_1, \hat{y}_2, \ldots, \hat{y}_n) \tag{9}$$

where f represents the final logistic regression model.

5. Results and Analysis

5.1. Evaluation Metrics

To assess the performance of different classifiers in pest prediction, this study utilized key evaluation metrics, including Accuracy, Precision, Recall, F1 Score, and Area Under the Curve (AUC). These metrics provide a comprehensive evaluation, addressing concerns like class imbalance and predictive reliability.

5.1.1. Accuracy

Accuracy measures the proportion of correctly classified instances and is defined as:

$$Accuracy = \frac{TP + TN}{TP + TN + FP + FN} \tag{10}$$

where TP (True Positives) and TN (True Negatives) represent correctly classified pest and non-pest cases, while FP (False Positives) and FN (False Negatives) indicate misclassifications. Despite being a fundamental measure, accuracy can be misleading in imbalanced datasets, as it does not distinguish between false positives and false negatives.

5.1.2. Precision

Precision evaluates the proportion of correctly predicted pest occurrences among all predicted pest cases:

$$Precision = \frac{TP}{TP + FP} \tag{11}$$

A high precision value indicates fewer false alarms, which is crucial in pest management to avoid unnecessary interventions.

5.1.3. Recall

Recall (also called Sensitivity) quantifies the model's ability to correctly identify actual pest occurrences:

$$Recall = \frac{TP}{TP + FN} \tag{12}$$

In pest detection, high recall is essential to ensure that potential outbreaks are not missed, as false negatives could lead to severe agricultural damage.

5.1.4. F1 Score

The F1 Score is the harmonic mean of Precision and Recall, balancing both metrics:

$$F1Score = 2 \times \frac{Precision \times Recall}{Precision + Recall} \tag{13}$$

This metric is particularly useful in handling imbalanced datasets, where an optimal trade-off between precision and recall is required.

5.1.5. Area Under the Curve (AUC)

AUC provides an aggregated measure of classifier performance across all classification thresholds, representing the probability that a randomly chosen positive instance is ranked higher than a randomly chosen negative instance. A higher AUC indicates better discriminative power.

Among the classifiers evaluated, the stacking-based ensemble model achieved the highest overall performance, as shown in Table 2. The comparison highlights the superiority of ensemble methods, particularly in leveraging multiple models to enhance decision-making. The findings reinforce that selecting robust classifiers is crucial in pest prediction, ensuring reliable forecasting for timely interventions.

Table 2. Performance metrics for individual classifiers: Voting, and Stacking models.

Classifier	Accuracy	F1 Score	Precision	Recall	AUC
Stacking	90.38	0.90	0.91	0.90	0.98
SVM	68.27	0.65	0.65	0.68	0.90
Logistic Regression	72.12	0.70	0.71	0.72	0.88
Gradient Boosting	72.12	0.70	0.71	0.72	0.88
Voting	56.73	0.56	0.54	0.57	0.81
CatBoost	55.77	0.56	0.56	0.56	0.80
Random Forest	55.77	0.55	0.55	0.56	0.79

To evaluate the efficacy of different machine learning classifiers in predicting pest incidence, this study analyzed their performance using confusion matrices. The confusion matrices for these models, illustrated in Figure 3, provide insight into their classification capabilities across three classes which are Jassid, No Pest, and Thrips.

The classifiers demonstrate varying degrees of accuracy in distinguishing between the three classes. All models achieve high accuracy in identifying the "No Pest" class, with minimal misclassification. However, disparities emerge when classifying Jassid and Thrips, as detailed below:

- **Gradient Boosting and SVM** exhibit superior classification performance, particularly in differentiating between Jassid and Thrips. These models maintain a balanced distribution of predictions with fewer misclassifications.

- **CatBoost and Random Forest** tend to misclassify Thrips as Jassid more frequently. This suggests that these models struggle with distinguishing between these two pest types.
- **Logistic Regression** demonstrates competitive performance, though it lacks the robustness of ensemble-based techniques such as Gradient Boosting and SVM.

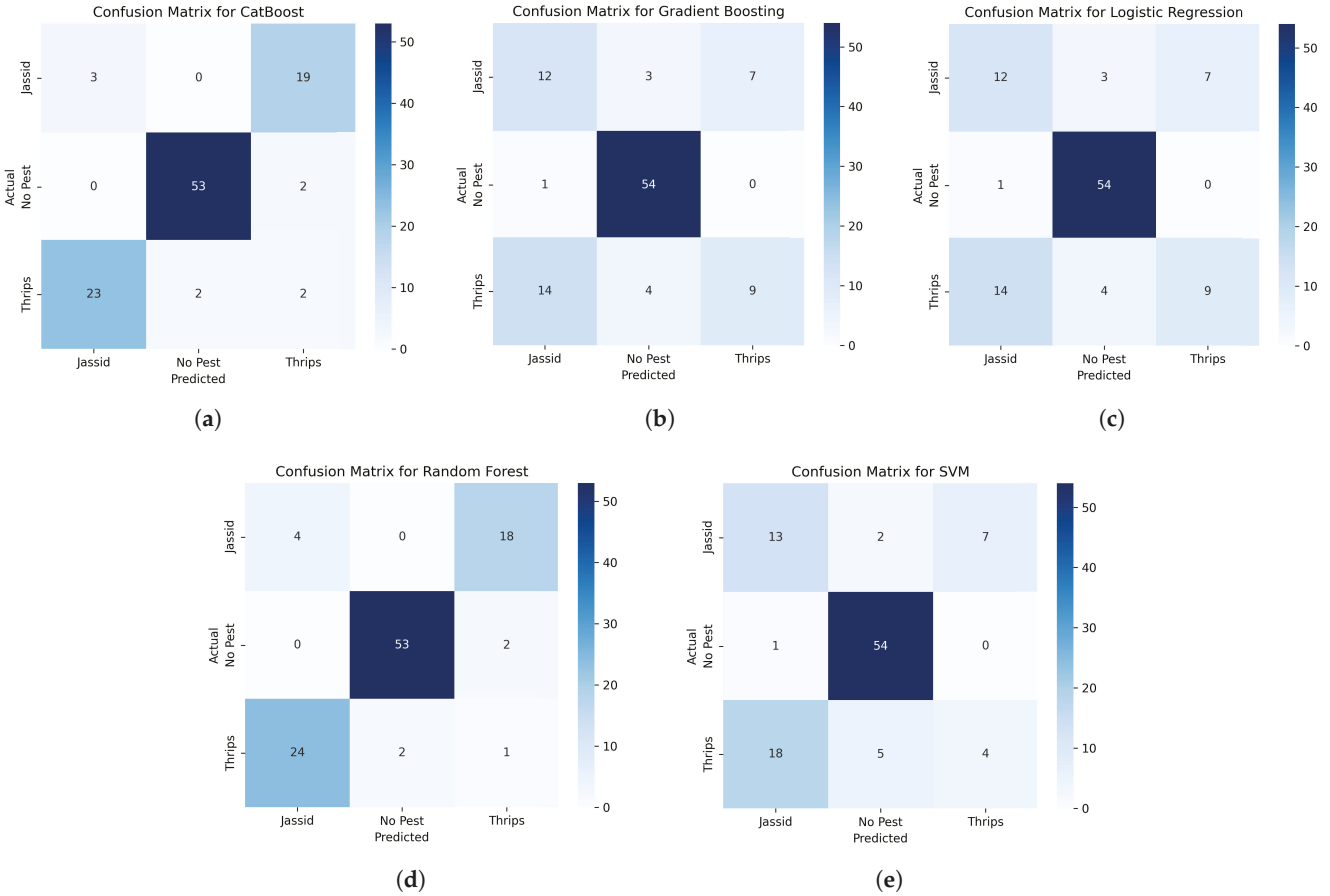

Figure 3. Confusion matrix for different classifiers.

Misclassification trends indicate that the models may benefit from alternative training strategies to enhance their discriminatory power. The results suggest that ensemble methods, particularly stacking, can further refine classification accuracy. Ensemble learning leverages the strengths of multiple classifiers by combining their predictions, thereby mitigating individual model weaknesses. This approach enhances overall model stability and generalization, leading to improved pest classification. In subsequent analyses, this study explores ensemble strategies to optimize model performance and demonstrate how stacking outperforms individual classifiers in this context.

5.2. Comparison with Ensemble Learning

Table 2 presents the comparative performance of various machine learning classifiers, including ensemble techniques such as Voting and Stacking. The Stacking model demonstrates superior classification capabilities with the highest accuracy (90.38%), F1 score (0.90), and precision (0.91), indicating its robustness in handling complex decision boundaries. Stacking leverages multiple base models and learns an optimal combination of their predictions through a meta-learner, allowing it to generalize better compared to individual classifiers. In contrast, traditional models like Support Vector Machine (SVM) and Logistic Regression, which rely on fixed decision boundaries, exhibit lower performance due to their inherent limitations in capturing intricate patterns in high-dimensional feature

spaces. Gradient Boosting, a sequential ensemble learning method, achieves similar results to Logistic Regression but benefits from boosting weak learners iteratively to improve prediction accuracy. The Voting ensemble, which aggregates predictions through majority voting, performs notably worse, suggesting that simple aggregation of classifiers may not be sufficient for complex datasets. CatBoost and Random Forest, though widely used for structured data, struggle to achieve competitive performance, highlighting the importance of selecting an appropriate ensemble strategy. The results emphasize that intelligently combining classifiers through Stacking can significantly enhance prediction accuracy by capturing diverse decision patterns from multiple models.

Figure 4 illustrates the confusion matrices for the Stacking and Voting ensemble methods, highlighting their classification performance in distinguishing Jassid, Thrips, and no-pest conditions. The Stacking ensemble demonstrates superior predictive accuracy, correctly identifying 20 instances of Jassid, 21 instances of Thrips, and 53 cases with no pest presence, with minimal misclassifications. In contrast, the Voting ensemble exhibits notable weaknesses in distinguishing Jassid and Thrips, frequently confusing Jassid with Thrips, as indicated by the 19 misclassified Jassid instances. Moreover, the Voting ensemble incorrectly predicts Jassid in 21 cases where Thrips was the actual label, underscoring its limitations in differentiating between the two pest categories. Both models perform well in predicting the absence of pests, with the Stacking model misclassifying only two cases and the Voting model making a single error in this category. These results reinforce the advantage of Stacking, which not only achieves higher overall accuracy but also maintains better balance in correctly identifying different pest types, making it a more reliable choice for pest incidence forecasting.

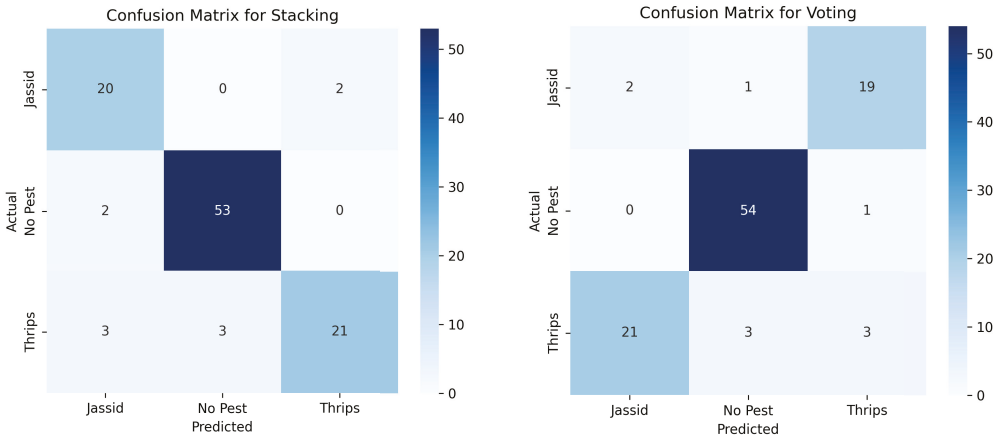

Figure 4. Confusion matrix for Stacking- and Voting-based ensemble learning

Figure 5 presents the AUC curves comparing the performance of various machine learning classifiers and ensemble learning strategies in predicting pest incidence. The Stacking ensemble method demonstrates the highest discriminative ability, achieving an AUC of 0.98, as evidenced by its near-perfect ROC curve, which closely follows the upper-left boundary of the plot. SVM also performs well with an AUC of 0.90, followed by Logistic Regression and Gradient Boosting, both achieving an AUC of 0.88. In contrast, Random Forest and CatBoost exhibit relatively lower AUC values of 0.79 and 0.80, respectively, indicating moderate classification performance. The Voting ensemble method, though improving upon some individual models, attains an AUC of 0.81, which remains significantly lower than that of Stacking. The sharp incline of the Stacking curve at low false-positive rates highlights its superior ability to minimize misclassification while maximizing true positive predictions. These results visually reinforce the advantage of ensemble learning, particularly Stacking, in enhancing predictive performance for pest incidence forecasting.

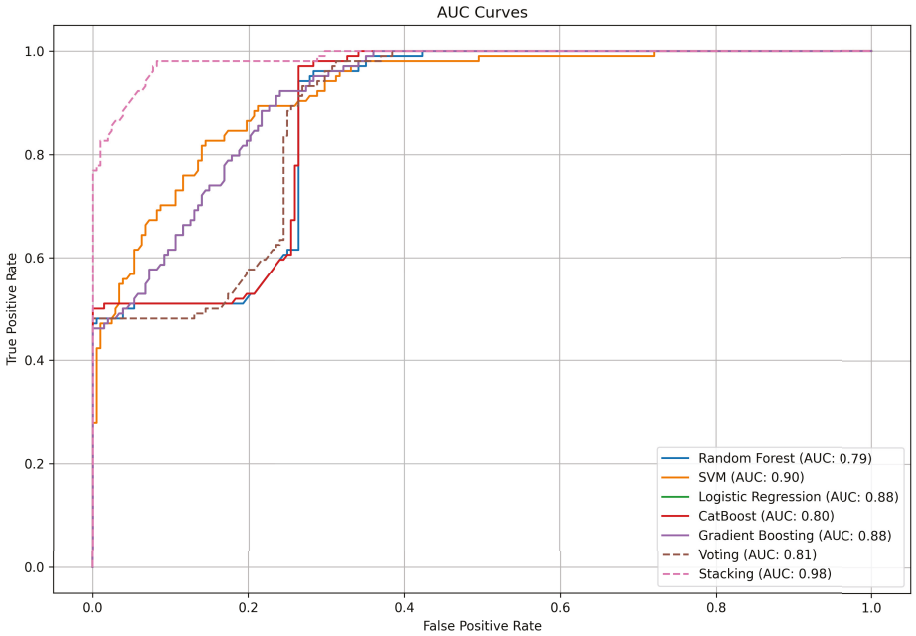

Figure 5. AUC cuves comparison between different techniques.

5.3. SHAP-Based Explainability

SHAP (SHapley Additive exPlanations) analysis has been effectively utilized in different studies to interpret complex, non-linear relationships within large datasets, enabling more transparent and interpretable models. This approach has been particularly valuable in identifying key features that influence system behavior, providing deeper insights into complex processes [40,41]. To gain deeper insights into the contribution of individual features to pest predictions, this study used SHAP to generate summary plots for three classifiers: Random Forest, Logistic Regression, and CatBoost, as illustrated in Figure 6. SHAP is a model-agnostic approach that provides a transparent understanding of how each feature influences a model's predictions by assigning importance scores to each feature, based on the individual contributions to the overall model output.

Among all three models, SMW emerged as the most influential variable in predicting pest infestations. This finding emphasizes the strong seasonal dependency of pest dynamics. Biological processes, such as pest life cycles and population peaks, are strongly regulated by environmental cues tied to specific times in the growing season. Previous research [15,18,42] corroborates these findings, demonstrating that pest outbreaks, including those of Jassid and Thrips, typically occur during distinct weeks of the growing season, reinforcing the need for timely, targeted interventions during these high-risk periods. These seasonal patterns highlight the importance of understanding the temporal variation of pest behavior and its direct correlation with seasonal climatic changes.

In addition to SMW, several meteorological factors such as evaporation (EVP), morning relative humidity (RH1), wind speed (WS), maximum temperature (MaxT), and minimum temperature (MinT) exhibited strong influence on the model's predictions. These factors are biologically relevant, as they directly impact pest behavior, survival, and proliferation. For example, evaporation and relative humidity affect the moisture levels in the environment, which are critical for the survival of pests such as Thrips, which thrive in humid conditions [43]. Similarly, temperature influences pest development rates, with warmer temperatures accelerating pest life cycles [44]. Notably, CatBoost and Random Forest models displayed distinct clustering ofSMW, evaporation, and relative humidity at higher SHAP values, indicating that increased values of these features consistently heightened the likelihood of pest presence. This suggests that these models are capturing complex,

non-linear interactions between environmental variables, which are likely indicative of underlying biological relationships.



(**a**) SHAP Analysis for Logistic Regression

(**b**) SHAP Analysis for Random Forest

(**c**) SHAP Analysis for CatBoost

Figure 6. SHAP Summary Plots for Logistic Regression, Random Forest, and CatBoost showing feature importance in pest prediction.

In contrast, Logistic Regression, due to its linear nature, exhibited a more dispersed influence across the features, with SMW, wind speed, and evaporation remaining prominent but showing a more uniform distribution in terms of their impact on predictions. This contrast emphasizes the inherent limitations of linear models in capturing non-linear dependencies, which are often present in ecological and biological systems. The ability of ensemble methods (such as CatBoost and Random Forest) and gradient boosting techniques to account for complex interactions between features underscores their effectiveness in predicting pest outbreaks, as they better capture the intricacies of pest-environment interactions. These advanced machine learning techniques, unlike traditional linear models, enable the incorporation of critical environmental factors into pest prediction systems with greater accuracy and precision.

Thus, the SHAP-based analysis reveals the advantages of leveraging advanced machine learning techniques for pest prediction, offering a transparent, interpretable framework that aligns well with biological and ecological theories. By incorporating seasonal patterns and environmental variables that influence pest life cycles, these models contribute significantly to more accurate, timely pest management strategies, particularly for high-risk periods in the growing season. Moreover, this approach promotes the integration of critical environmental factors into decision-making frameworks, supporting the development of more sustainable and data-driven pest management solutions.

6. Limitations and Future Work

This study provides valuable insights into pest prediction, but several limitations must be acknowledged. The dataset used in this research is limited to cotton crops collected over four growing seasons from 2005 to 2009. While this period covers various seasonal and climatic conditions, the data may not fully account for the impacts of climate change or evolving agricultural practices, which could influence pest dynamics over time. Additionally, the dataset is specific to a single geographical region, which limits the generalizability of the findings to other regions with different climatic conditions or agricultural practices.

Looking ahead, future work will aim to address these limitations by expanding the dataset to include additional crops and regions, allowing for broader generalization of the models. Furthermore, the potential impact of climate change will be explored in more depth, with the goal of developing models that can adapt to shifting environmental conditions. Additionally, the application of transfer learning and continuous model updates will help ensure the model's robustness and applicability in diverse agricultural contexts.

7. Conclusions

This study demonstrates the significant potential of machine learning-based models for predicting pest infestations, specifically Jassid and Thrips, using key meteorological parameters. By leveraging six essential weather features which are maximum and minimum temperature, relative humidity, wind speed, sunshine hours, and evaporation—this research successfully identified the most relevant factors influencing pest dynamics. Through rigorous evaluation of multiple classifiers, this study found that the Stacking ensemble model outperformed individual models, achieving an accuracy of 90.38%. This highlights the robustness and reliability of the proposed framework in pest prediction. Importantly, the incorporation of SHAP (SHapley Additive exPlanations) values enhances the transparency of the model, providing valuable insights into the importance of various weather parameters. The results indicate that relative humidity, temperature, and evaporation significantly affect the presence and behavior of pests, aligning with existing biological research on pest ecology. These findings underscore the critical role of explainability in fostering trust and facilitating the adoption of AI-driven pest management solutions among stakeholders such as farmers, agronomists, and policymakers.

While this study provides a strong foundation for data-driven pest management, it also highlights the limitations inherent in using a dataset from only one crop (cotton) and a single geographic region. Future research could expand this framework to other pest species and crops, and apply the model across different regions with varying climatic conditions. Moreover, integrating real-time weather data, satellite imagery, and adaptive learning techniques could further enhance the model's predictive accuracy, enabling it to better cope with the uncertainties associated with climate change and dynamic agricultural practices. Ultimately, the proposed AI framework represents a valuable building block towards a more sustainable, precision-based pest management approach, offering promising support for integrated pest management (IPM) strategies.

Author Contributions: Conceptualization, R.S.; Methodology, R.S. and S.H.K.; Software, J.R.; Validation, S.H.K. and J.R.; Formal analysis, R.S., S.H.K. and J.R.; Writing—original draft, R.S. and S.H.K.; Writing—review & editing, J.R. and S.W.L.; Supervision, S.W.L.; Project administration, S.W.L.; Funding acquisition, S.W.L. All authors have read and agreed to the published version of the manuscript.

Funding: This research was supported by the SungKyunKwan University and the BK21 FOUR (Graduate School Innovation) funded by the Ministry of Education (MOE, Korea) and National Research Foundation of Korea (NRF). This work was also supported by National Research Foun-

dation (NRF) grants funded by the Ministry of Science and ICT (MSIT) and Ministry of Education (MOE), Republic of Korea (NRF[2021-R1-I1A2(059735)]; RS[2024-0040(5650)]; RS[2024-0044(0881)]; RS[2019- II19(0421)]).

Institutional Review Board Statement: Not applicable.

Informed Consent Statement: Not applicable.

Data Availability Statement: Data are contained within the article.

Conflicts of Interest: The authors declare no conflicts of interest.

References

1. Gupta, S.K.; Yadav, A.K.; Maheshwari, S.; Maurya, P.K.; Kumar, P. Population dynamics of major insect pests of okra in relation to weather parameters. *Plant Arch.* **2024**, *24*, 304–308.
2. Syed, T.; Abro, G.; Khuhro, R.; Dhauroo, M. Relative resistance of cotton varieties against sucking pests. *Pak. J. Biol. Sci* **2003**, *6*, 1232–1233. [CrossRef]
3. Zhou, Y.; Zhou, H.; Chen, Y. An automated phenotyping method for Chinese Cymbidium seedlings based on 3D point cloud. *Plant Methods* **2024**, *20*, 151. [CrossRef] [PubMed]
4. Subedi, B.; Poudel, A.; Aryal, S. The impact of climate change on insect pest biology and ecology: Implications for pest management strategies, crop production, and food security. *J. Agric. Food Res.* **2023**, *14*, 100733.
5. Kaushal, M.; Atieno, M.; Odjo, S.; Baijukya, F.; Gebrehawaryat, Y.; Fadda, C. Nature-Positive Agriculture—A Way Forward Towards Resilient Agrifood Systems. *Sustainability* **2025**, *17*, 1151. [CrossRef]
6. Han, H.; Sha, R.; Dai, J.; Wang, Z.; Mao, J.; Cai, M. Garlic origin traceability and identification based on fusion of multi-source heterogeneous spectral information. *Foods* **2024**, *13*, 1016. [CrossRef]
7. Bale, J.S.; Masters, G.J.; Hodkinson, I.D.; Awmack, C.; Bezemer, T.M.; Brown, V.K.; Butterfield, J.; Buse, A.; Coulson, J.C.; Farrar, J.; et al. Herbivory in global climate change research: Direct effects of rising temperature on insect herbivores. *Glob. Chang. Biol.* **2002**, *8*, 1–16.
8. Kirui, E.C.; Kidoido, M.M.; Akutse, K.S.; Wanyama, R.; Boni, S.B.; Dubois, T.; Dinssa, F.F.; Mutyambai, D.M. Factors Influencing the Adoption of Agroecological Vegetable Cropping Systems by Smallholder Farmers in Tanzania. *Sustainability* **2025**, *17*, 1148. [CrossRef]
9. He, L.; Shan, Y.q.; Liu, C.; Cao, H.; Liu, X.n.; Guo, Y. Prediction of bedload transport inside vegetation canopies with natural morphology. *J. Hydrodyn.* **2024**, *36*, 556–569.
10. Wolfert, S.; Ge, L.; Verdouw, C.; Bogaardt, M.J. Big data in smart farming—A review. *Agric. Syst.* **2017**, *153*, 69–80.
11. Zhuo, T.; He, L.; Chai, B.; Zhou, S.; Wan, Q.; Lei, X.; Zhou, Z.; Chen, B. Micro-pressure promotes endogenous phosphorus release in a deep reservoir by favouring microbial phosphate mineralisation and solubilisation coupled with sulphate reduction. *Water Res.* **2023**, *245*, 120647. [PubMed]
12. Yu, K.; Chai, B.; Zhuo, T.; Tang, Q.; Gao, X.; Wang, J.; He, L.; Lei, X.; Chen, B. Hydrostatic pressure drives microbe-mediated biodegradation of microplastics in surface sediments of deep reservoirs: Novel findings from hydrostatic pressure simulation experiments. *Water Res.* **2023**, *242*, 120185. [PubMed]
13. Lu, S.; Xiao, X. Neuromorphic computing for smart agriculture. *Agriculture* **2024**, *14*, 1977. [CrossRef]
14. Sharma, A.; Tripathi, P. Artificial Intelligence in Agriculture: A Literature Survey. *Int. J. All Res. Educ. Sci. Methods* **2021**, *9*, 510–513.
15. Zhang, D.; Wang, Y.; Gu, Q.; Liu, L.; Wang, Z.; Zhang, J.; Meng, C.; Yang, J.; Zhang, Z.; Ma, Z.; et al. Cotton RLP6 Interacts with NDR1/HIN6 to Enhance Verticillium Wilt Resistance via Altering ROS and SA. *Mol. Plant Pathol.* **2025**, *26*, e70052.
16. Ma, X.; Liu, Y. A Modified Geometrical Optical Model of Row Crops Considering Multiple Scattering Frame. *Remote Sens.* **2020**, *12*, 3600.
17. Yang, X.; Xia, X.; Zhang, Z.; Nong, B.; Zeng, Y.; Wu, Y.; Xiong, F.; Zhang, Y.; Liang, H.; Pan, Y.; et al. Identification of anthocyanin biosynthesis genes in rice pericarp using PCAMP. *Plant Biotechnol. J.* **2019**, *17*, 1700.
18. Chen, S.; Yang, Z.; Sun, W.; Tian, K.; Sun, P.; Wu, J. TMV-CP based rational design and discovery of α-Amide phosphate derivatives as anti plant viral agents. *Bioorg. Chem.* **2024**, *147*, 107415.
19. Huang, X.; Tang, X.; Liao, A.; Sun, W.; Lei, L.; Wu, J. Application of cyclopropane with triangular stable structure in pesticides. *J. Mol. Struct.* **2024**, *1326*, 141171.
20. Demirel, M.; Kumral, N.A. Artificial intelligence in integrated pest management. In *Artificial Intelligence and IoT-Based Technologies for Sustainable Farming and Smart Agriculture*; IGI Global: Hershey, PA, USA, 2021; pp. 289–313.
21. Rehman, M.U.; Eesaar, H.; Abbas, Z.; Seneviratne, L.; Hussain, I.; Chong, K.T. Advanced drone-based weed detection using feature-enriched deep learning approach. *Knowl.-Based Syst.* **2024**, *305*, 112655. [CrossRef]

22. Jiang, C.; Wang, Y.; Yang, Z.; Zhao, Y. Do adaptive policy adjustments deliver ecosystem-agriculture-economy co-benefits in land degradation neutrality efforts? Evidence from southeast coast of China. *Environ. Monit. Assess.* **2023**, *195*, 1215. [PubMed]
23. Liakos, K.G.; Busato, P.; Moshou, D.; Pearson, S.; Bochtis, D. Machine learning in agriculture: A review. *Sensors* **2018**, *18*, 2674. [CrossRef]
24. Luo, J.; Zhao, C.; Chen, Q.; Li, G. Using deep belief network to construct the agricultural information system based on Internet of Things. *J. Supercomput.* **2022**, *78*, 379–405.
25. Linardatos, P.; Papastefanopoulos, V.; Kotsiantis, S. Explainable ai: A review of machine learning interpretability methods. *Entropy* **2020**, *23*, 18. [CrossRef] [PubMed]
26. Wang, M.; Lin, H.; Lin, H.; Du, P.; Zhang, S. From species to varieties: How modern sequencing technologies are shaping Medicinal Plant Identification. *Genes* **2024**, *16*, 16. [CrossRef]
27. Asif, M.U.; Muhammad, R.; Khan, M.H.; Sohail, M. Seasonal population dynamics of cotton jassid (*Amrasca devastans*) in different cotton varieties under field conditions. *J. Entomol. Res.* **2019**, *43*, 315–318. [CrossRef]
28. Durgabai, R.; Bhargavi, P. Pest management using machine learning algorithms: A review. *Int. J. Comput. Sci. Eng. Inf. Technol. Res. IJCSEITR* **2018**, *8*, 13–22.
29. Asif, M.U.; Muhammad, R.; Khan, M.H.; Sohail, M.; Awais, M. Incidence and population dynamics of thrips (*Thrips tabaci*) on different cotton varieties in Tandojam, Sindh, Pakistan. *Int. J. Biol. Biotech* **2020**, *17*, 783–788.
30. Morsello, S.C.; Groves, R.L.; Nault, B.A.; Kennedy, G.G. Temperature and precipitation affect seasonal patterns of dispersing tobacco thrips, Frankliniella fusca, and onion thrips, *Thrips tabaci* (Thysanoptera: Thripidae) caught on sticky traps. *Environ. Entomol.* **2014**, *37*, 79–86. [CrossRef]
31. Patil, J.; Mytri, V. A prediction model for population dynamics of cotton pest (*Thrips tabaci* Linde) using multilayer-perceptron neural network. *Int. J. Comput. Appl.* **2013**, *67*, 4.
32. Xiao, Q.; Li, W.; Kai, Y.; Chen, P.; Zhang, J.; Wang, B. Occurrence prediction of pests and diseases in cotton on the basis of weather factors by long short term memory network. *BMC Bioinform.* **2019**, *20*, 688.
33. Mittal, M.; Gupta, V.; Aamash, M.; Upadhyay, T. Machine learning for pest detection and infestation prediction: A comprehensive review. *Wiley Interdiscip. Rev. Data Min. Knowl. Discov.* **2024**, *14*, e1551.
34. Clark, R.D. Putting deep learning in perspective for pest management scientists. *Pest Manag. Sci.* **2020**, *76*, 2267–2275. [PubMed]
35. Chithambarathanu, M.; Jeyakumar, M. Survey on crop pest detection using deep learning and machine learning approaches. *Multimed. Tools Appl.* **2023**, *82*, 42277–42310.
36. Dwivedi, R.; Dave, D.; Naik, H.; Singhal, S.; Omer, R.; Patel, P.; Qian, B.; Wen, Z.; Shah, T.; Morgan, G.; et al. Explainable AI (XAI): Core ideas, techniques, and solutions. *ACM Comput. Surv.* **2023**, *55*, 1–33.
37. Razak, S.F.A.; Yogarayan, S.; Sayeed, M.S.; Derafi, M.I.F.M. Agriculture 5.0 and Explainable AI for Smart Agriculture: A Scoping Review. *Emerg. Sci. J.* **2024**, *8*, 744–760.
38. Devi, R.S.; Mahadevappa, S. Effect of weather parameters on the incidence of thrips, *Thrips tabaci* Lindeman on *Bt* cotton. *Int. J. Environ. Clim. Chang.* **2021**, *11*, 107–112.
39. Soni, R.; Dhakad, N. Seasonal incidence of cotton jassid, *Amrasca biguttula biguttula* (Ishida) on trasgenic BT cotton and their correlation with weather parameters. *Int. J. Agric. Innov. Res.* **2016**, *4*, 2319–1473.
40. Abbas, Z.; ur Rehman, M.; Tayara, H.; Zou, Q.; Chong, K.T. XGBoost framework with feature selection for the prediction of RNA N5-methylcytosine sites. *Mol. Ther.* **2023**, *31*, 2543–2551.
41. Mir, B.A.; Rehman, M.U.; Tayara, H.; Chong, K.T. Improving enhancer identification with a multi-classifier stacked ensemble model. *J. Mol. Biol.* **2023**, *435*, 168314.
42. Taylor, R.A.; Ryan, S.J.; Lippi, C.A.; Hall, D.G.; Narouei-Khandan, H.A.; Rohr, J.R.; Johnson, L.R. Predicting the fundamental thermal niche of crop pests and diseases in a changing world: A case study on citrus greening. *J. Appl. Ecol.* **2019**, *56*, 2057–2068. [PubMed]
43. Yadav, S.; Korat, J.; Yadav, S.; Mondal, K.; Kumar, A.; Kumar, H.; Kumar, S. Impacts of climate change on fruit crops: A comprehensive review of physiological, phenological, and pest-related responses. *Int. J. Environ. Clim. Chang.* **2023**, *13*, 363–371.
44. Tonnang, H.E.; Sokame, B.M.; Abdel-Rahman, E.M.; Dubois, T. Measuring and modelling crop yield losses due to invasive insect pests under climate change. *Curr. Opin. Insect Sci.* **2022**, *50*, 100873. [PubMed]

Disclaimer/Publisher's Note: The statements, opinions and data contained in all publications are solely those of the individual author(s) and contributor(s) and not of MDPI and/or the editor(s). MDPI and/or the editor(s) disclaim responsibility for any injury to people or property resulting from any ideas, methods, instructions or products referred to in the content.

sustainability

MDPI

Article

A Remote Sensing Approach for Biomass Assessment in Winter Wheat Using the NDVI Second Derivative in Terms of NIR

Asparuh I. Atanasov [1,*], Atanas Z. Atanasov [2,*] and Boris I. Evstatiev [3]

[1] Department of Mechanics and Elements of Machines, Technical University of Varna, 9010 Varna, Bulgaria
[2] Department of Agricultural Machinery, Agrarian and Industrial Faculty, University of Ruse "Angel Kanchev", 7004 Ruse, Bulgaria
[3] Department of Automatics and Electronics, Faculty of Electrical Engineering, Electronics and Automation, University of Ruse "Angel Kanchev", 7004 Ruse, Bulgaria; bevstatiev@uni-ruse.bg
* Correspondence: asparuh.atanasov@tu-varna.bg (A.I.A.); aatanasov@uni-ruse.bg (A.Z.A.)

Abstract

Traditional NDVI-based biomass estimation methods often suffer from saturation at high vegetation density and limited sensitivity during early crop growth, which reduces their effectiveness for precise monitoring. This study addresses these limitations by introducing the use of the second derivative of NDVI with respect to near-infrared (NIR) reflectance as a novel indicator of inflection points and dynamic changes in crop development. The proposed method is mathematically derived, and a corresponding index is calculated. Field trials were conducted on five winter wheat varieties over two growing seasons (2021–2023). The results demonstrated a strong correlation between the derived index and actual biomass measurements. To validate the findings, linear regression analysis between the second derivative of NDVI and biomass scores yielded R and R^2 values equal to 1. These findings confirm the high predictive power and reliability of the method for non-destructive UAV-based biomass monitoring in precision agriculture.

Keywords: winter wheat; precision agriculture; remote sensing; UAV; second derivative of NDVI in terms of NIR

1. Introduction

One of the key parameters of precision agriculture is the ability to estimate the amount of biomass. Remote sensing significantly accelerates this process, allowing for the assessment of plant mass accumulation throughout the vegetation period. This, in turn, supports effective planning of agrotechnical measures and improves yield forecasting. Traditionally, biomass assessment is based on representative field samples, which provide discrete data rather than a comprehensive spatial overview. Standard measurements of plant mass are often obtained at harvest using farmer-reported data, which are typically imprecise and collected after the completion of vegetation processes.

The importance of determining crop phenology for yield prediction has been discussed in [1,2], while the impact of climate change on crop development has been explored in [3]. The complexity of biomass assessment increases when dealing with multiple crops or cultivars [4]. Different studies have proposed and investigated methodologies for yield estimation [5], temporal–spatial modeling [6], spatial determination for various crops [7], and real-time monitoring applications [8], among others. Variations in temperature and their impact on biomass depending on location and timing were addressed in [9,10].

Remote sensing plays a crucial role in collecting data directly from the field [11], and numerous studies have explored satellite-based acquisition of reflective vegetation indices (VI) [12–14]. Some of these works have demonstrated their potential for identifying phenological stages and estimating biomass [15–17]. The analysis of these data is often performed using regression analysis [18,19], although this method may not fully capture the variability in crop development. To overcome these limitations, machine learning approaches have been introduced [20], enabling the use of multiple dependent and independent variables for yield prediction [21]. In recent years, many studies have proposed biomass assessment solutions based on deep learning and UAV-obtained hyperspectral [22] or visual spectrum imaging [23]. While deep learning has shown very promising results, it has its limitations, such as higher requirements for the volume and quality of training data, the hardware and software for data analysis, etc. [24]. Furthermore, its results could be difficult to understand by farmers who do not have the appropriate expertise.

Among vegetation indices, the normalized difference vegetation index (NDVI) is one of the most widely used [25], particularly for simulation-based data analysis [26]. This popularity stems from the integration of multispectral cameras on unmanned aerial vehicles (UAVs), which record near-infrared (NIR) wavelengths [27–30]. This way, a fast and efficient means of acquiring NDVI is provided, enabling repeated observations over the same area for in-depth analysis. NDVI has been successfully applied to estimate biomass, track phenological trends, and differentiate crop varieties, thus contributing to more accurate yield prediction [31,32]. Biomass estimation in wheat [33] and maize [34] using correlation analysis or mathematical modeling has also been used.

An alternative approach involves analyzing the first and second derivatives of different VI time series, such as NDVI and EVI, to assess phenological development, especially during early growth and rapid development stages [35,36]. It is capable of capturing the acceleration or deceleration of changes in the VI and enables early diagnosis of stress factors or disease before visible symptoms occur, including the detection of drought impacts and sudden vegetation changes.

In Ref. [37], the changes in the NDVI time series curve were explored to determine planting and harvesting dates for crops like corn and soybeans. Additionally, Ref. [38] investigates the use of the second derivative of the NDVI time series as an indicator of biomass, derived from data acquired via a multispectral camera mounted on an unmanned aerial system (UAS). Both studies estimate the second derivative of NDVI over time, denoted as NDVI(t). In Ref. [39], the first NDVI derivatives over time were used as an indicator for the most active tillering stage of rice growth, and the second derivative as an indicator for estimating the maturity stage. In another study [40], NDVI's first derivative was used to form a criterion for the identification of degradation and disturbance in wooded areas, which relies on annual maximal pixel-level NDVI values. Other studies have used NDVI and its derivatives for biomass estimation and phenological monitoring [41–43].

Despite recent advances in the use of vegetation indices for remote biomass estimation, significant gaps remain. Standard NDVI-based approaches face limitations such as signal saturation in dense canopies and low sensitivity during early crop development. These issues restrict their effectiveness in capturing subtle but agronomically important changes in biomass accumulation. This problem is partially taken care of by the application of derivatives of NDVI time series; however, existing research has primarily focused on NDVI's use in phenological differentiation, stress detection, or as a time-series indicator for crop monitoring. Furthermore, the application of other derivatives of NDVI for spatial biomass mapping, such as those with respect to near-infrared reflectance, remains practically unexplored.

To address these gaps, we want to explore the application of the second derivative of NDVI with respect to NIR reflectance and its ability to enhance responsiveness to structural and physiological variations in vegetation, which is the main contribution of this study. Our specific goal is to assess the potential of using the second derivative of NDVI with respect to NIR, derived from UAV-acquired multispectral imagery, as a quantitative indicator for biomass estimation in winter wheat. The main objectives are (1) to compute the NDVI second derivative in terms of NIR from UAV imagery collected over fields sown with multiple winter wheat varieties, (2) to obtain in-field biomass measurements through physical sampling, and (3) to analyze the statistical relationship between the computed NDVI derivative and the measured biomass data.

2. Materials and Methods

The study was conducted using remote sensing of different winter wheat varieties over two full growing seasons, corresponding to the 2021–2022 and 2022–2023 agricultural years. Agricultural fields were monitored throughout the entire wheat development period. To validate the remote sensing data, a visual assessment of the crops was performed in the field. Additionally, the results were compared with quantitative measurements of canopy coverage obtained from vertically captured UAV imagery, and biomass above the soil surface was estimated accordingly.

2.1. Study Area

The studied fields are located on the territory of the city of Dobrich, Republic of Bulgaria, and their coordinates are 43.553083N, 27.832161E and 43.548491N, 27.757799E. The locations of the experimental fields are shown in Figure 1. The fields were sown with common winter wheat (*Triticum aestivum* L.) during the studied periods.

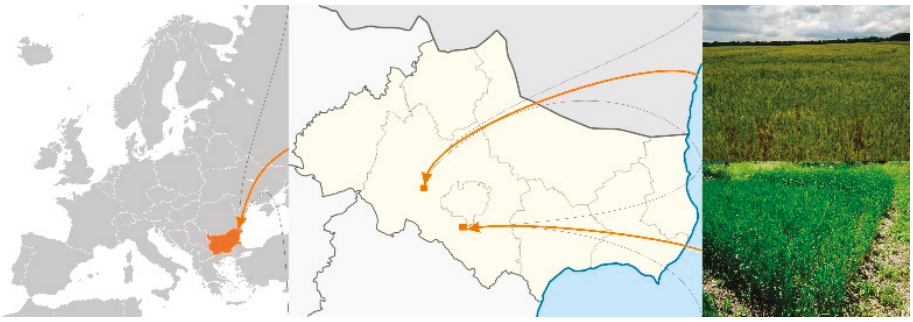

Figure 1. Geographical locations of the experimental fields.

2.2. UAV Flight Planning and Data Collection

The study was carried out using the DJI Mavic 2 Pro UAV [44], which has a take-off weight of 907 g and a maximum flight speed of 72 km/h. For data collection, the UAV was operated in "P" mode, limiting the flight speed to 10 m/s to ensure image stability. Mission planning was performed using the Pix4Dcapture software [45]. Flights were conducted at an altitude of 100 m above ground level, with an overlap of 80% both longitudinally and laterally to ensure optimal coverage for photogrammetric processing.

The UAV is equipped with an integrated RGB camera, capturing images in the red, green, and blue spectral bands. However, to calculate NDVI, NIR data are required. For this purpose, a multispectral Mapir Survey3W RGN camera [46] was mounted on the UAV. This camera captures data in the red (R), green (G), and NIR bands using a modified Sony Exmor R IMX117 12 MP sensor (Bayer RGB type). The lens features an 87° horizontal field of view (HFOV), 19 mm focal length, f/2.8 aperture, and −1% extreme low distortion non-fisheye optics.

The Survey3W operates autonomously and is not directly connected to the UAV's flight controller. It was configured in automatic mode to capture images at 1 s intervals. Each image was georeferenced using a u-blox UBX-G7020-KT GPS module [47]. Figure 2 illustrates the planned flight path used to capture the study area. The meandering trajectory was calculated based on the sensor size, flight altitude, and image overlap parameters.

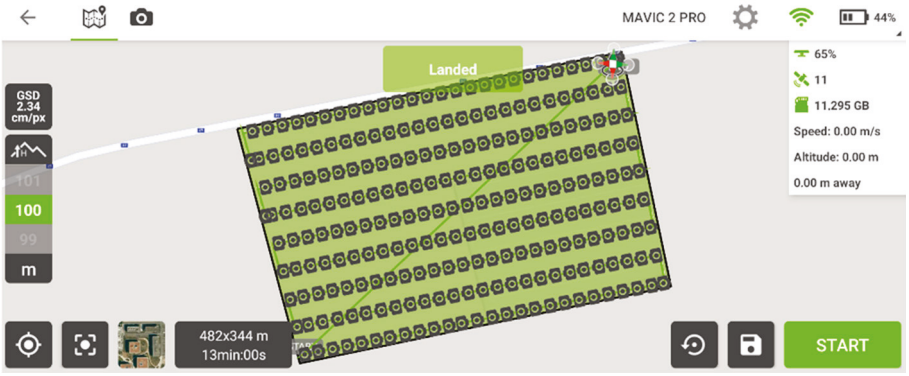

Figure 2. The flight plan used for aerial image acquisition over the experimental field, with the positions and orientations of individual images overlaid on the field map included.

During a single mission over the test field, the built-in Mavic 2 Pro camera captured 132 images, while the Survey3W camera produced 337 images. The planned ground sampling distance (GSD) for the 20 MP built-in RGB camera was 2.34 cm/pixel, with a final processed resolution of 2.39 cm/pixel. For the Survey3W camera, the processed resolution was 3.71 cm/pixel. Both resolutions provided sufficient spatial detail to allow assessment of individual leaves and biomass distribution within the crop canopy.

2.3. Crop Evaluation

To verify the remote sensing results, field measurements were conducted during vegetation stages. These included plant height, crop volume estimation, plant density, and quantitative field coverage. A visual scoring system was used to assess biomass density and canopy coverage. A score of 10 was assigned to plots exhibiting dense, uniform vegetation with well-developed wheat, while a score of 1 represented areas with no visible crop cover.

The actual volumetric weight of the biomass was not measured as the evaluation was based solely on remote sensing data. This presents an inherent limitation of the method: it allows for the estimation of crop density and relative biomass distribution but not the precise biomass quantity. Nonetheless, theoretical biomass values can be derived through mathematical models incorporating plant height, density, and species-specific characteristics.

2.4. Data Analysis

The normalized difference vegetation index is used to quantify vegetation and estimate biomass changes of the vegetation processes in crops. Chlorophyll in vegetation reflects more NIR and green light compared to other wavelengths. It absorbs more red and blue light. It is calculated as the ratio between the red (R) and NIR values according to the formula [25]:

$$NDVI = \frac{NIR - R}{NIR + R}, \quad (1)$$

where NIR is the reflectance in the near-infrared spectrum (850 nm) and R is the reflectance in the red spectrum (660 nm). NDVI values range from –1 to + 1, where higher values indicate more vigorous and dense vegetation.

The second derivative of NDVI is commonly denoted as NDVI (t) when based on a time series. It is interpreted as a measure of variation over time and is used to identify

inflection points in the NDVI curve. These inflection points correspond to transitions in crop development and can signal abrupt changes in growth dynamics.

In this study, however, the second derivative is not derived in terms of time but is estimated instead in terms of the NIR reflectance. The second derivative in terms of NIR NDVI″ is calculated from the NDVI surface as a numerical approximation of curvature, allowing for the detection of local accelerations or decelerations in the NIR component of NDVI, which reflect underlying crop structure and biomass distribution. The specific formula used for this calculation is:

$$NDVI'' = \frac{\partial^2}{\partial NIR^2}\left(\frac{NIR - R}{NIR + R}\right) \quad (2)$$

The mathematical solution to Equation (2) is:

$$NDVI'' = \frac{\partial}{\partial NIR}\left(\frac{\partial}{\partial NIR}\left(\frac{NIR - R}{NIR + R}\right)\right) = \frac{2(NIR - R)}{(NIR + R)^3} - \frac{2}{(NIR + R)^2} \quad (3)$$

and it could be further simplified mathematically to:

$$NDVI'' = -\frac{4R}{(NIR + R)^3} \quad (4)$$

The result of this equation is then used to compute the mathematical value of the second derivative of the NDVI in terms of NIR, which provides insights into changes in vegetation growth dynamics. For simplicity, from now on in this study, when we say the second derivative of NDVI, it is assumed to be in terms of NIR, unless explicitly stated otherwise.

Additionally, the method applied for the remote estimation of soil water content is based on the reflectance vegetation index, normalized difference water index (NDWI), as proposed by [48].

$$NDWI = \frac{(G - NIR)}{(G + NIR)}, \quad (5)$$

where NIR is the reflectance in the near − infrared spectrum(850 nm), and G denotes the reflectance in the green spectrum (550 nm).

NDWI is used to assess the surface water content and vegetation moisture. According to the findings reported by [48], NDWI values greater than 0.5 typically correspond to water bodies, while vegetated surfaces generally return lower index values, ranging between 0 and 0.2.

The second derivative of NDVI with respect to NIR was chosen for its ability to capture curvature and inflection points in the NDVI response curve. Unlike the standard NDVI, which may saturate or mask subtle variations, NDVI″ amplifies local changes in vegetation reflectance. This makes it particularly suitable for detecting early growth dynamics and differentiating biomass levels that would otherwise appear similar in NDVI values.

Uncertainty and Comparative Advantages of Vegetation Indices

Equations (1)–(4) rely on reflectance values obtained from multispectral imaging. Therefore, the accuracy of NDVI, NDVI″, and NDWI is subject to various uncertainties, including the following:

Sensor calibration and noise: Slight misalignments or inconsistencies in camera sensitivity across the NIR, red, or green bands can introduce bias into calculated indices.

Atmospheric conditions: Variability in lighting, cloud cover, and humidity at the time of UAV flights can affect reflectance values, especially in shorter wavelengths.

Viewing geometry and canopy structure: Shadows, leaf angle distribution, and flight altitude can affect reflectance measurements.

Georeferencing errors: Spatial mismatch between bands or overlapping images can distort index values at field boundaries.

NDVI, being a ratio-based index, partially mitigates some of these effects, but it saturates at high canopy densities and becomes less sensitive in mature crops. In contrast, NDVI″, as a second-order derivative, enhances sensitivity to small changes in reflectance, especially during early or transitional growth phases. This makes it particularly valuable for detecting growth acceleration/deceleration, even when NDVI remains stable or saturated.

NDWI, on the other hand, complements both indices by being responsive to vegetation water content. It is particularly effective in identifying water stress or evaluating surface moisture in early development stages or during dry periods—aspects that NDVI alone cannot resolve.

While NDVI provides a robust baseline for biomass estimation, NDVI″ improves responsiveness to physiological changes, and NDWI adds environmental context, particularly in water-limited scenarios. The use of NDVI″ and NDWI thus enhances the precision and diagnostic power of remote sensing-based crop monitoring.

2.5. Processing of Results

The software product Pix4Dfields, developed by Pix4D S.A. (Prilly, Switzerland) [49], was used to process the obtained results. A working window with superimposed positions of the photos from the RGN camera obtained during a flight over the field is shown in Figure 3. This camera takes pictures continuously from take-off to landing at an interval of 1 s; therefore, the photos from takeoff until the desired starting position and from the final position to the landing point were excluded from the analysis. This way, it is ensured that the different shooting heights do not impact the interpretation of the photos during the creation of an orthomosaic.



Figure 3. A working window of the Pix4Dfields software with the positions of the photos from the RGN camera.

Set for the source data maximum ground sampling distance (GSD) = 0 sm/pix, maximum total megapixels = 50 MP.

The software product used for image processing generates a digital surface model (DSM) and a zoning map rapidly, owing to the use of cloud-based computational infrastructure. Based on these outputs, various reflectance indices, including NDVI and NDWI, are calculated. The software also allows for implementing custom index formulas as needed.

2.6. Mathematical Modeling

A regression analysis was performed using Microsoft Excel to examine the relationship between the dependent variable Y (biomass score) and the independent variable X (second derivative of NDVI in terms of NIR, denoted as NDVI″). This method was selected to provide a mathematical description of the correlation between the two variables and to estimate the regression coefficients b_0 and b_1 of a simple linear regression model, expressed as follows [50]:

$$Y_i = b_0 + b_1 * X_i \quad (6)$$

The analysis aimed to determine the strength and direction of the linear relationship by estimating the correlation coefficient R and the coefficient of determination R^2.

3. Results and Discussion

3.1. Results Obtained from Field Research

During the surveys, meteorological data from the observed field were also recorded to support the interpretation of the remote sensing results. For the 2021–2022 season, measurements were collected at field location 43.553083N, 27.832161E, including air temperature (Figure 4a), atmospheric humidity (Figure 4b), and cloud cover (Figure 4c).

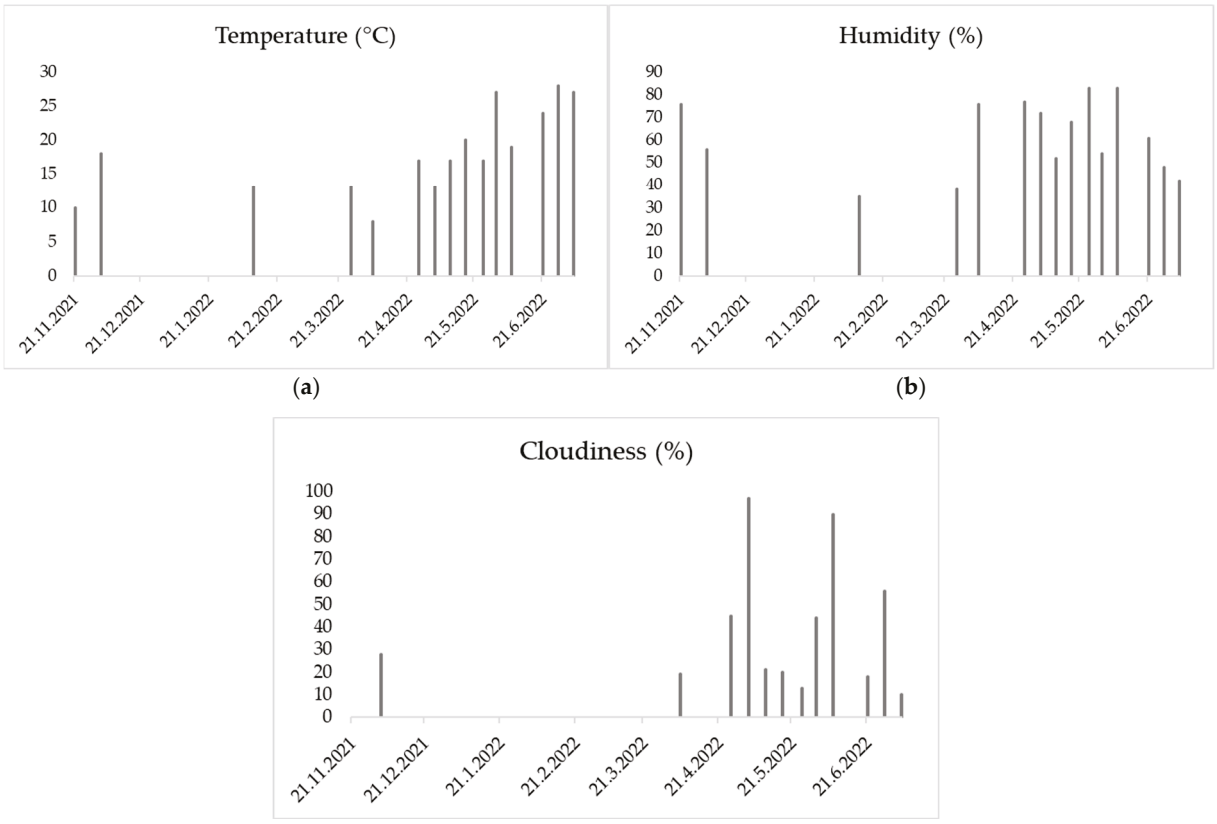

Figure 4. Meteorological features for the 2021–2022 season for the field at 43.553083N, 27.832161E: Air temperature (**a**), Humidity (**b**) and Cloudiness (**c**).

These environmental parameters are not only relevant to the growth and development of winter wheat but also have a direct influence on the quality and reliability of the reflectance indices, such as NDVI and NDWI, derived from UAV imagery.

Wheat measurements related to physical parameters, collected on the days of filming, are presented in Table 1. The table includes measured values for stem diameter, density

within a 30 cm segment, and a scoring value. The scoring system was developed to reflect the overall density of the plant biomass, which varies with an increasing number of leaves and their desiccation. The total stem volume, plant height, and inter-row spacing at the time of formation were also considered.

Table 1. Measured values from a field experiment with the winter wheat variety Falado during the 2021–2022 season.

Data	21 Nov 2021	3 Dec 2021	10 Feb 2022	26 Mar 2022	5 Apr 2022	26 Apr 2022	3 May 2022	10 May 2022	17 May 2022	25 May 2022	31 May 2022	7 Jun 2022	21 Jun 2022	28 Jun 2022	5 Jul 2022
Average stem diameter [mm]	1	1.3	1.7	2	2.6	2.7	2.9	2.9	2.9	2.9	2.9	2.9	2.9	2.9	2.9
Layer Density of 300 [mm]	12.2	24.4	36.6	48.8	61	85.4	122	122	122	122	122	85.4	85.4	85.4	73.2
biomass scoring	1	2	3	4	5	7	10	10	10	10	10	7	7	7	6

Although actual biomass was not directly measured through destructive sampling in this study, physical parameters were recorded in Table 1. These parameters are commonly used in biomass estimation models and can serve as proxies for evaluating crop structure and relative biomass development.

The decision to rely on remote sensing data and indirect field observations was based on the study's objective to evaluate non-destructive, scalable monitoring techniques. Direct measurement of biomass (e.g., via oven-drying methods) was not feasible for this particular campaign due to time and labor constraints.

In future work, destructive sampling will be incorporated to validate and improve the remote estimates generated through spectral indices.

During the 2021–2022 growing season, the field was sown with the common winter wheat variety Falado. The results for the vegetation index NDVI and its second derivative NDVI″ obtained throughout the season are presented in Figure 5a. Representative photographs of the crop at various vegetation stages are shown in Figure 5b.

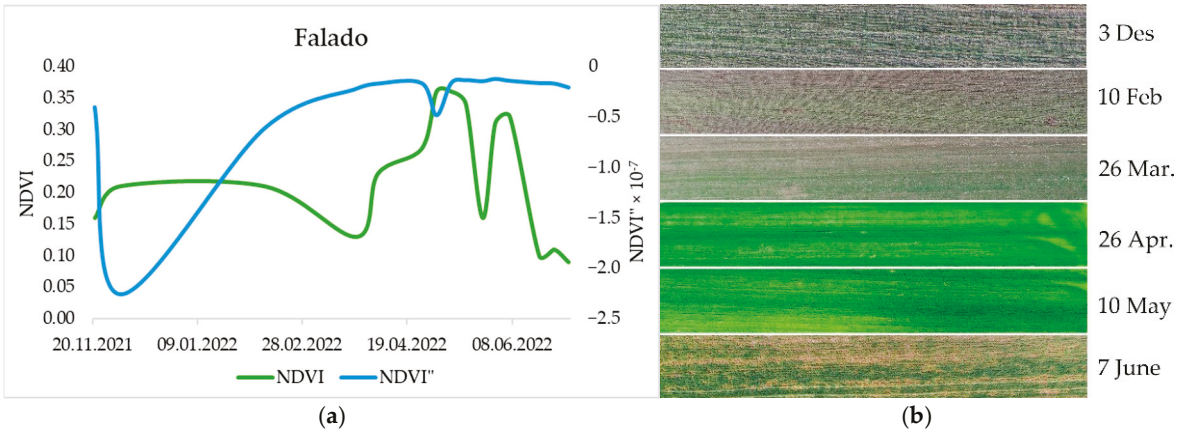

Figure 5. Changes in the NDVI and second derivative NDVI″ indices for a wheat field during the 2021–2022 growing season (**a**); aerial photographs of the field taken from 100 m altitude (**b**).

The measurements showed that after the tillering stage, due to unusually high seasonal temperatures, the vegetation did not enter dormancy but continued to develop. By mid-December, UAV imagery revealed that the wheat canopy covered 100% of the field. Biomass

accumulation continued to increase until the heading stage and began to decline with the onset of maturity, characterized by foliage wilting. This pattern is also reflected in the graph of NDVI″, where values approach zero during the period following the spring revival of the wheat. Subsequent fluctuations are attributed to climatic variations such as temperature and precipitation, which influence the presence or absence of stress.

The NDWI index for the field during the 2021–2022 season is shown in Figure 6. The lowest NDWI value was recorded at the end of April. At the same time, a decrease in NDVI″ was observed, corresponding to the highest NDVI value during this period. This coincides with the wheat transition from the tillering phase to the spindle phase.

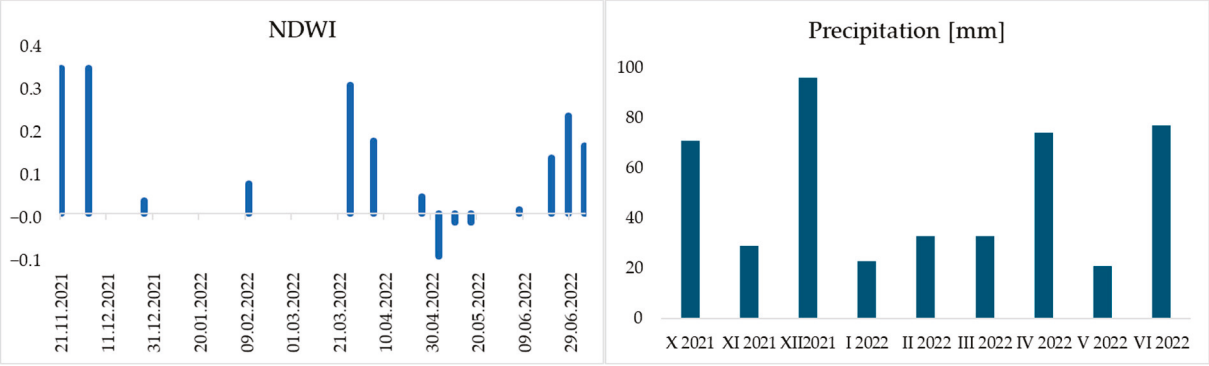

(**a**) (**b**)

Figure 6. Changes in the NDWI index during the 2021–2022 season (**a**) and precipitation levels for the same season (**b**).

Meteorological parameters recorded for the field at coordinates 43.548491N, 27.757799E during the 2022–2023 season are presented in Figure 7, including air temperature (a), illumination (b), wind speed (c), humidity (d), and precipitation amount (e).

During the 2022–2023 season, four winter wheat varieties—Marilyn, Enola, Annapurna, and Avenue—were studied in the experimental field at coordinates 43.548491N, E27.757799 (Figures 8, 10, 12 and 14). The results of NDVI and NDVI″ for the Marilyn variety are presented in Figure 8a,b show UAV photographs of the crop at various vegetation stages from 100 m altitude.

The warm autumn contributes to the rapid development of the crop and the increase in NDVI after tillering. Wheat covers a large part of the soil (when photographed by a UAV), and with the accumulation of biomass, the NDVI″ increases sharply, which continues without interruption until mid-December. Spring frosts in early February lower the NDVI, which also lowers the NDVI″. The subsequent development of wheat has an intense change in NDVI due to climatic features (temperature and amount of precipitation). We have an increase in the index at the end of February with the accumulation of biomass and a subsequent drop due to climatic features. An increase was also registered during tillering in mid-April, followed by a sharp drop. We have the highest value at tillering in early May, followed by a decrease. This dynamic is directly related to the climatic features during the period (Figure 7), but this only changes the reflection in the NIR region, which diagnoses the presence of stress and does not change the amount of biomass, and the NDVI″ remains at high values. Field studies conducted in the field did not detect any visual change in the wheat because NIR is invisible to the human eye. The amount of biomass is maintained until maturity.

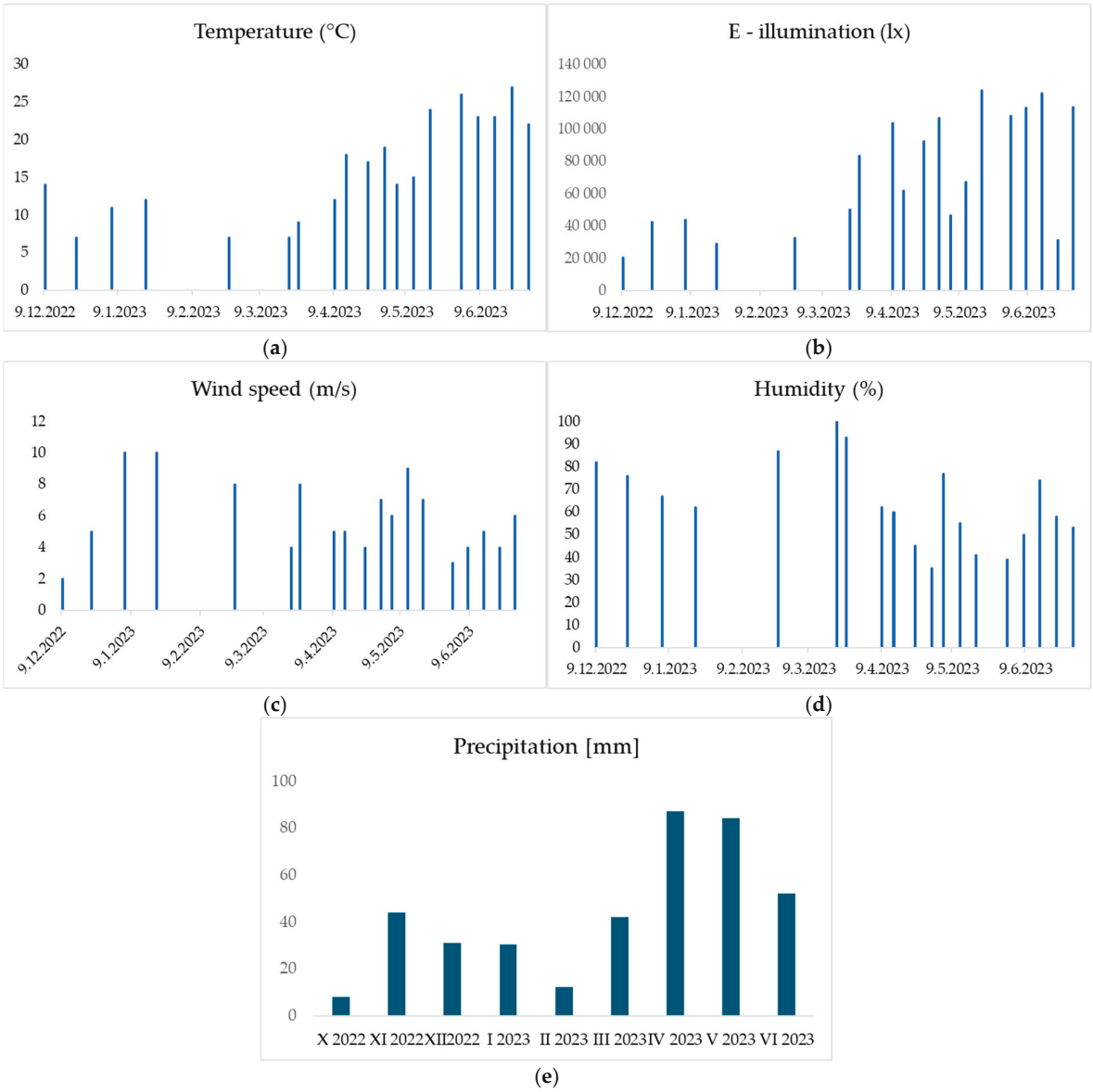

Figure 7. Meteorological parameters for the field at coordinates N43.548491, E27.757799 during the 2022–2023 season: air temperature (**a**), illumination (**b**), wind speed (**c**), humidity (**d**), and precipitation amount (**e**).

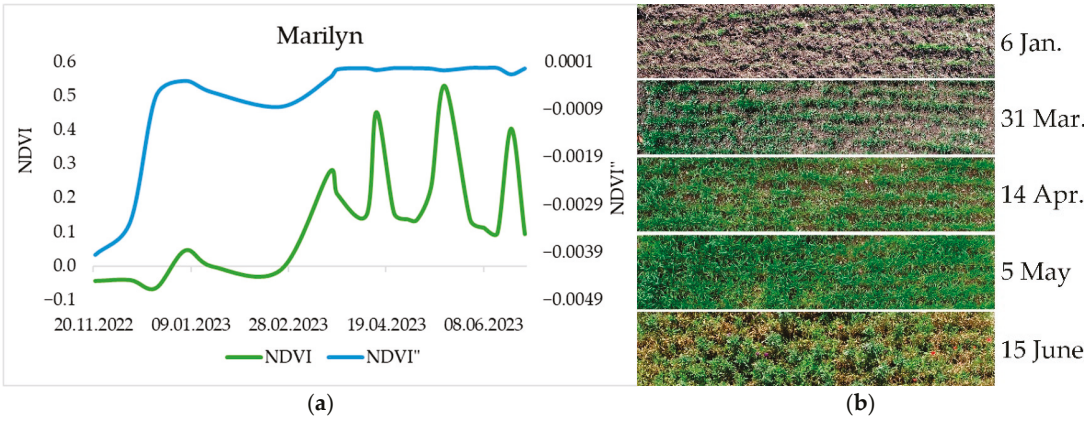

Figure 8. Variations in NDVI and NDVI″ indices for a field with winter wheat variety Marilyn during the 2022–2023 season (**a**); aerial photographs of the field from 100 m altitude taken during different vegetation stages (**b**).

Figure 9 illustrates the variation in the NDWI index for the field sown with the Marilyn variety during the 2022–2023 season. The observed trend closely follows the patterns of precipitation (Figure 7d) and humidity (Figure 7e) and shows strong temperature dependence (Figure 7a), as remote sensing primarily captures surface moisture content, which is significantly influenced by air temperature and wind speed.

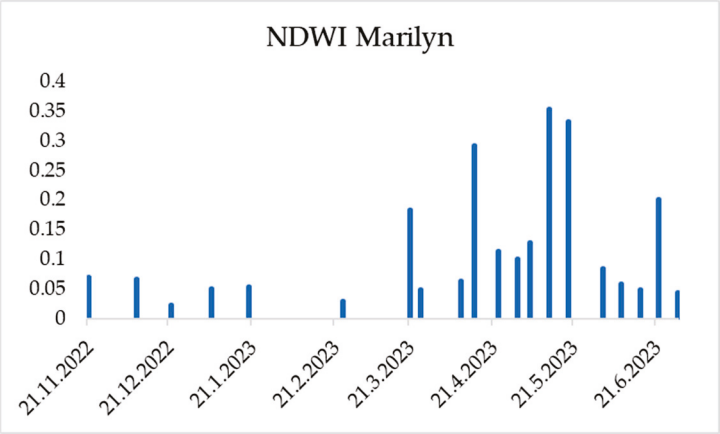

Figure 9. Variations in the NDWI index in the field sown with the Marilyn variety during the 2022–2023 season.

For the Enola variety, after the onset of tillering (observed around 3 December 2021), a period of dormancy began due to decreasing temperatures and adverse meteorological conditions. This phase led to a gradual decline in NDVI values. In mid-February 2022, with the rise in temperatures, active vegetation resumed, and NDVI increased again. However, a temporary drop in the index was recorded in mid-March, likely due to late spring frosts.

During April, continued biomass accumulation contributed to a new rise in NDVI, although minor fluctuations occurred in response to variable weather conditions. The highest NDVI value was recorded in early March, coinciding with the peak of vegetative growth.

NDVI″, the second derivative of NDVI, showed a sharp increase immediately following tillering, reflecting rapid biomass accumulation confirmed through field measurements. During dormancy, the NDVI″ index declined slightly. Upon resumption of growth in February, it increased again and remained relatively stable at a high level, despite NDVI fluctuations. The NDVI″ index effectively corresponds to the percentage of soil surface covered by wheat vegetation (Figure 10).

The variation in the NDWI index for the Enola variety during the 2022–2023 season is presented in Figure 11. The increase in index values during the spring months correlates with increased precipitation (Figure 7e), elevated humidity, and relatively moderate temperatures.

The Annapurna variety exhibited similar trends in both NDVI and NDVI″ indices to those observed in Enola (Figure 12). Field observations confirmed full soil coverage by the wheat crop, which was achieved by the end of the tillering stage. At the same time, a sharp increase in NDVI″ was recorded, with subsequent fluctuations remaining close to zero. Despite variations in NDVI, the NDVI″ values remained relatively stable. This consistency corresponds to the accumulated biomass, as also evident from the UAV-acquired images (Figure 12b).

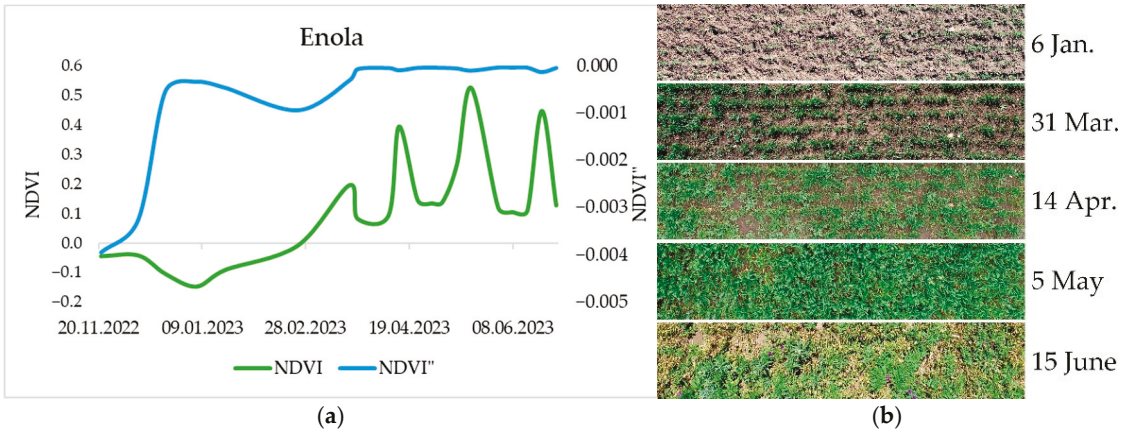

Figure 10. Variations in NDVI and NDVI″ indices for the field sown with wheat variety Enola during the 2022–2023 crop year (**a**); aerial photographs of the field taken from 100 m altitude at different vegetation stages (**b**).

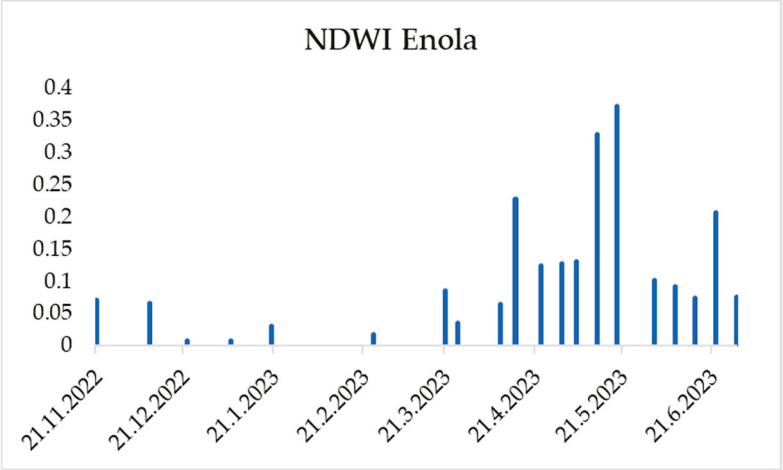

Figure 11. Variations of the NDWI index in the field planted with winter wheat variety Enola during the 2022–2023 season.

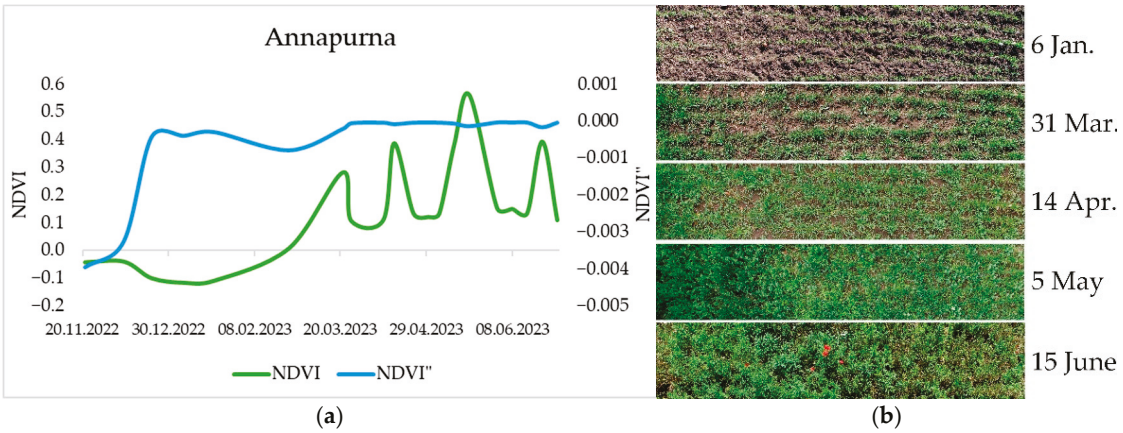

Figure 12. Variations in NDVI and NDVI″ indices for the field planted with winter wheat variety Annapurna during the 2022–2023 crop year (**a**); UAV-acquired images of the field at 100 m altitude during vegetation stages (**b**).

The change in the NDWI index in the Avenue variety field during the 2022–2023 season follows similar trends to those observed in the other studied varieties (Figure 13). This consistency is attributed to the experiment being conducted on a single field with

uniform characteristics across its area. Figure 14 illustrates the changes in the NDVI and NDVI″ indices for the Avenue variety throughout the 2022–2023 season. The NDVI″ trend reaches its peak following the tillering stage, followed by a decline as the crop enters dormancy. After late February, with the resumption of active growth, the NDVI″ values stabilize near zero, exhibiting only slight fluctuations. These observations are supported by field assessments and UAV photographs shown in Figure 14b.

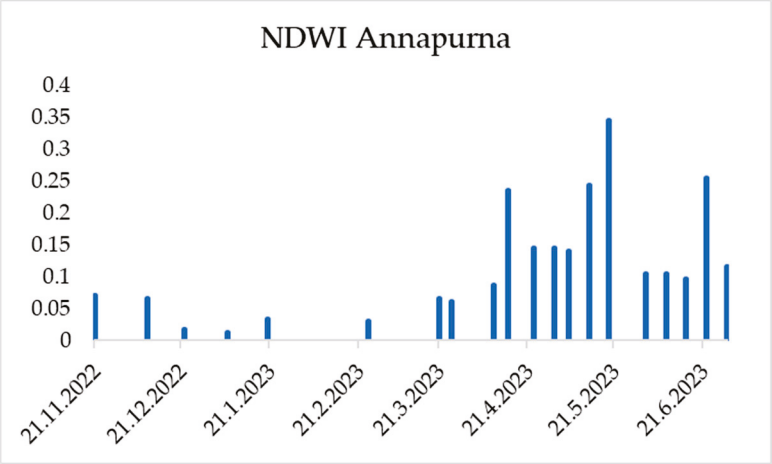

Figure 13. Variations in the NDWI index in the field planted with winter wheat variety Avenue during the 2022–2023 season.

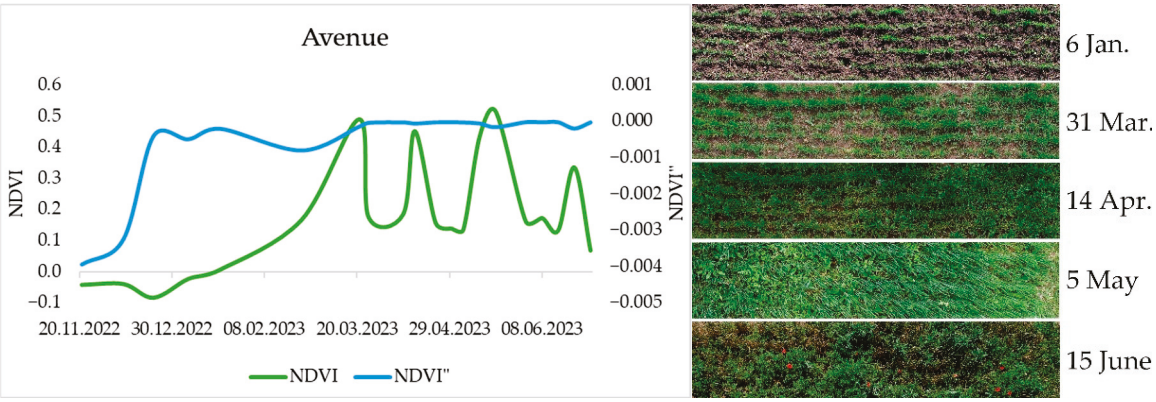

Figure 14. Variations in NDVI and NDVI″ indices for the field planted with winter wheat variety Avenue during the 2022–2023 crop year (**a**); UAV-acquired images of the field at 100 m altitude during vegetation stages (**b**).

Figure 14 presents the change in the NDVI and NDVI″ index for the Avenue variety in the 2022–2023 season. Wheat is dormant until mid-January, which determines the low NDVI values. From the beginning of February, after coming out of dormancy, we have a smooth increase in NDVI due to tillering until reaching 0.5 on March 21, followed by a decrease due to spring frosts. When tillering in early April, we also have an increase, which is followed by a decrease in late April. On May 20, when grading, the highest index value was obtained. In early June, temperatures exceed 30 °C (Figure 7), as a result of which we have a decrease in the index. The resulting trend in NDVI″ changes reaches a maximum after the tillering period in early December. After this period, there is a decrease when entering dormancy. After the end of February, with the onset of active vegetation, the value remains stable around zero with slight fluctuations. This has been confirmed by field research and photographs taken by UAV Figure 14b.

The change in the NDWI index in the Avenue variety field for the 2022–2023 season, shown in Figure 15, follows the same features with high values in the spring, which corresponds to the amount of precipitation and high humidity.

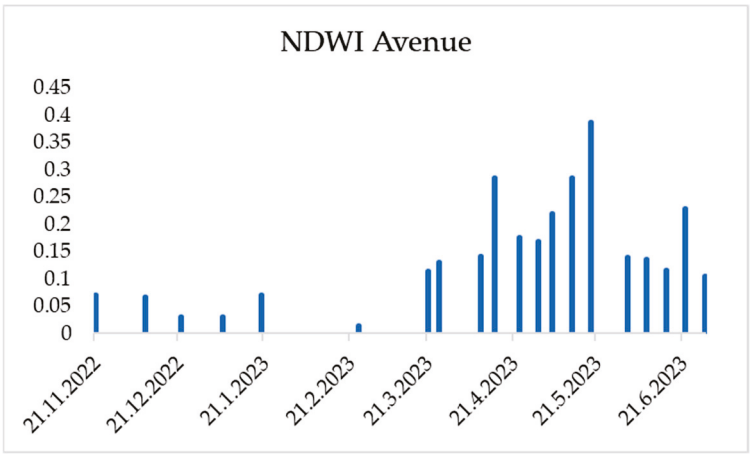

Figure 15. Variations in the NDWI index in the Avenue variety field for the 2022–2023 season.

The general trend shows a sharp increase in the value of NDVI″ after the complete coverage of the field by wheat. The changes in the NDVI index are caused by the registered stress. The second derivative can be used to estimate the quantitative coverage of the soil by wheat, but to estimate the biomass, it is necessary to know the height of the crop at the time of shooting.

A generated map of the NDVI index is shown in Figure 16a, and of the NDVI″ in Figure 16b. The selected field for visualization is sown with wheat and is presented in Figure 5. In this case, we have an alternation of areas with higher and lower NDVI due to different seeding densities. This is even more pronounced in NDVI″, which visualizes areas with low biomass density. In the lower part of Figure 16b, more green can be observed in contrast to the NDVI map; this is due to the corn crop that has accumulated a large amount of biomass. In the right part of both figures, there is a field buffer zone: in Figure 16a, almost solid green is visible, while in NDVI″ can be distinguished the crown of individual trees and the space between them, which have a lower index value.

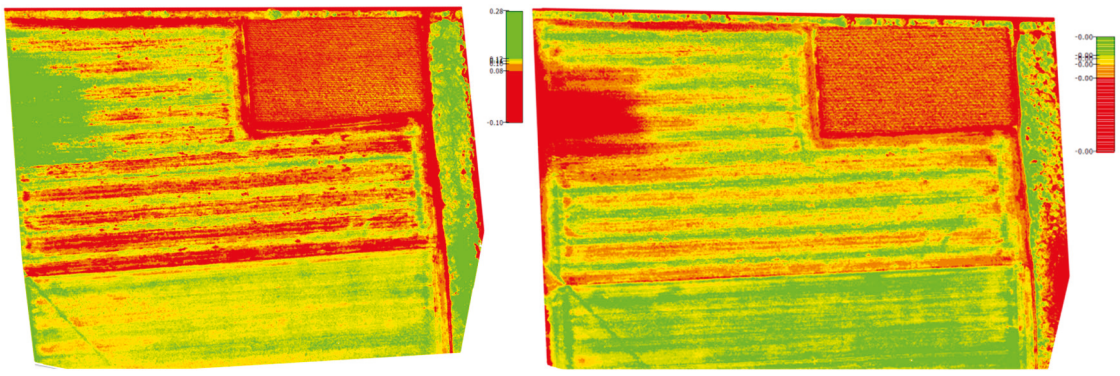

(**a**) (**b**)

Figure 16. Maps of the NDVI index (**a**) and NDVI″ (**b**) for 31 May 2022.

In Figure 17a, a map of the NDWI index for 31 May 2022 is shown, and in Figure 17b, an RGN orthomosaic composed of 334 individual images is shown. A comparison with the NDVI index map reveals that areas with high crop density—indicative of substantial biomass—exhibit low moisture values. This phenomenon is attributed to the inability to

observe the soil beneath dense vegetation cover, resulting in the recorded moisture values reflecting the water content within the wheat plants themselves.

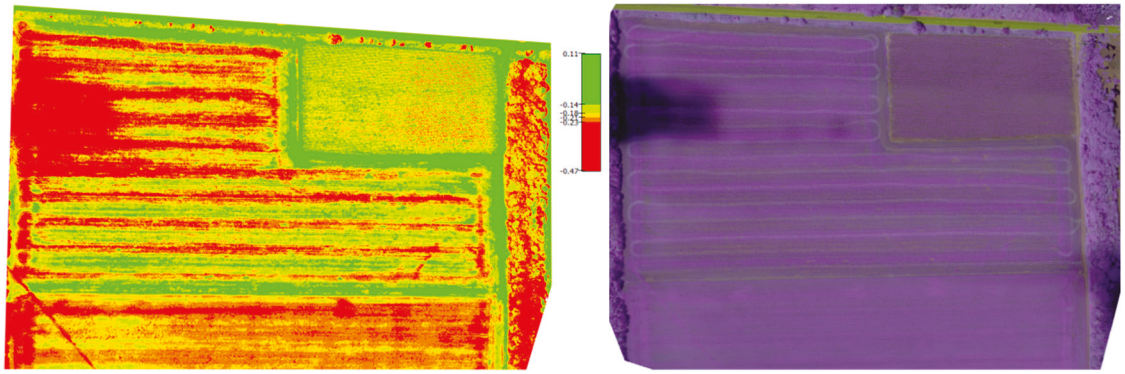

(**a**) (**b**)

Figure 17. NDWI index map (**a**) and RGN orthomosaic (**b**).

3.2. Analysis of the Data Obtained

To analyze the data obtained from the respective field, both the stage of wheat development and the amount of accumulated biomass at the time of measurement were examined. Based on these parameters, a scoring system was established to represent the biomass level at each observation point, where the highest biomass was assigned a score of 10 and the lowest a score of 1. The maximum score was recorded in May, corresponding to the peak of the vegetative stage. As the crop entered the maturity phase, leaf senescence occurred, leading to a gradual decline in biomass score toward a value of 1.

The analysis was conducted using Microsoft 365 Excel, Version 2503 (Build 18,623.20208) [51]. Linear regression was performed via the Data Analysis tool pack using the Regression function. The analysis examined the relationship between NDVI values and the biomass score derived from field observations. A total of $n = 28$ observations (from multiple dates and each wheat varieties studied across two growing seasons) were used in the regression. The resulting regression statistics are summarized in Table 2.

Table 2. Regression statistics between the NDVI″ and biomass score.

Multiple R	**1**
R-Squared	1
Adjusted R-Squared	−1.0769231
Standard Error	1.1899×10^{-15}
Observations	1

It can be observed that the values for multiple R and R-squared are both equal to 1, indicating a perfect linear correlation (100% dependency) between the variables. The obtained standard error is 1.2×10^{-15}, representing the average deviation of the observed values from the fitted regression line. Such a strong correlation underscores the potential of using the NDVI″ derived from remote sensing data as an efficient and non-destructive proxy for estimating crop biomass. This capability enables enhanced monitoring of crop growth dynamics and supports timely decision-making in precision agriculture, including optimized fertilization, irrigation, and yield forecasting.

Table 3 presents the ANOVA results for the linear regression model. For the results to be considered statistically significant, the value of the significance F criterion must be less than 0.05, indicating that the model is adequate and effectively describes the relationship

between the dependent and independent variables. In this case, the obtained value is F = 1.84 × 10^{-29}, which confirms the validity and statistical significance of the model. The residuals show a deviation from the predicted regression line of 2.6 × 10^{-15}, indicating a minimal error in the model's predictions.

Table 3. Analysis of variance (ANOVA) results for the linear regression model examining the relationship between the NDVI″ and biomass score.

	df	**SS**	**MS**	**F**
Regression	14	180.7728	12.91234	1.28 × 10^{32}
Residual	13	1.84 × 10^{-29}	1.42 × 10^{-30}	
Total	27	180.7728		

These results are received for *p*-value = 7.71709976187206 × 10^{-203}, which is much less than 0.05 and is considered statistically significant and indicates that there is strong evidence against the null hypothesis. The derived NDVI″ index does not directly capture the temporal dynamics of vegetation growth but is instead correlated with the accumulated biomass. The analysis reveals that following wheat germination, NDVI″ increases sharply. However, in subsequent stages, its values fluctuate around zero and do not align with the progression pattern typically observed in standard NDVI trends.

A key requirement for accurate biomass estimation using this approach is prior knowledge of the crop type and average plant height. These parameters are essential for calibrating the mathematical model and ensuring the reliability of the derived biomass estimates. Nonetheless, the proposed methodology allows for rapid, non-destructive assessment of crop condition using UAV-mounted multispectral imaging systems. The resulting NDVI″ maps offer a high-resolution spatial representation of field variability, enabling precise identification of zones with differing biomass levels.

The proposed approach has significant practical value for precision agriculture by supporting informed decision-making related to irrigation, fertilization, and yield forecasting. It also provides a cost-effective and scalable alternative to labor-intensive field surveys. However, some limitations of the study should be noted. The approach relies on high-quality multispectral data and accurate temporal sampling to capture key phenological stages. Variability in sensor calibration, atmospheric conditions, and canopy structure may affect the precision of NDVI″ calculations. Furthermore, the model was tested on winter wheat varieties under specific climatic and soil conditions; thus, its applicability to other crops or regions requires further validation.

However, the proposed NDVI″ calculation method is not crop-specific and relies solely on Red and NIR reflectance data. Therefore, it can be adapted for other crop types and UAV platforms, provided that calibrated multispectral imagery is available. The formula is software-independent and may be implemented in any environment that supports raster operations or index calculation, including open-source tools such as Python, QGIS, or commercial platforms like ENVI and Pix4DFields.

A linear regression analysis (presented in Table 4) was performed to examine the relationship between the NDWI index and the amount of precipitation (Figure 6a,b). The field was sown with common winter wheat, variety Falado, during the 2021–2022 season. The regression statistics show that the multiple R is 0.5, indicating a 50% correlation, while the R-squared value is 0.25, corresponding to a 25% degree of explained variance.

Table 4. Regression statistics between the NDWI and the amount of rainfall.

Multiple R	**0.503136403**
R-Squared	0.25314624
Adjusted R-Squared	−1.142857143
Standard Error	0.170729714
Observations	1

This result is expected, as precipitation increases soil moisture in the deeper layers. However, the NDWI index reflects moisture content only in the upper soil layer. The moisture of this surface layer cannot be directly determined by precipitation alone; it is also influenced by air temperature, cloud cover, wind speed, and wind strength. These factors have a direct impact on the surface soil moisture content.

Table 5 shows the analysis of variance (ANOVA) between the NDWI and rainfall.

Table 5. Analysis of variance (ANOVA) results for the linear regression model examining the relationship between the NDWI and rainfall.

	df	**SS**	**MS**	**F**
Regression	8	0.069159553	0.008644944	2.372651487
Residual	7	0.204040447	0.029148635	-
Total	15	0.2732	-	-

These results are received for p-value = 0.00172, which is much less than 0.05 and is considered statistically significant and indicates that there is strong evidence against the null hypothesis.

An analysis of the relationship between NDWI and precipitation was conducted for the period before the wheat canopy covered more than 50% of the field surface (as seen from above). The results show a perfect linear correlation, with multiple R = 1, R-squared = 1, and standard error = 0.

These results indicate that the NDWI can provide reliable data before the field is more than 50% covered by vegetation. Monitoring the index during this early stage may offer valuable information during the sowing period, when wheat seeds are typically placed at a depth of 3 to 5 cm.

3.3. Comparative Analysis of Vegetation Indices

In the context of this study, the NDVI, its second derivative (NDVI″), and NDWI were used as key indicators for assessing vegetation status, biomass accumulation, and surface moisture dynamics. While their mathematical definitions are provided earlier in the manuscript, this section summarizes their practical use cases, advantages, and limitations.

The NDVI is a well-established vegetation index that reflects the overall greenness and vigor of crops. It is most effective during the mid to late vegetative stages when canopy closure is sufficient. The NDVI is widely used due to its simplicity and strong correlation with leaf area and biomass. However, in dense vegetation, it tends to saturate, making it less sensitive to further increases in biomass.

The NDVI″, the second derivative of the NDVI with respect to NIR reflectance, provides an additional insight into the dynamics of crop development. It is particularly sensitive to structural and physiological changes, making it useful in detecting early growth trends or stress responses before visible symptoms appear. Compared to the NDVI, NDVI″ is less prone to saturation and better reflects variations in canopy structure. How-

ever, its computation requires high-quality spectral data and may amplify noise if not carefully processed.

The NDWI serves as an indicator of water content in vegetation and soil. It complements NDVI-based analysis by identifying areas experiencing moisture stress or excessive wetness. While not directly linked to biomass, the NDWI helps interpret drops or fluctuations in NDVI/NDVI″ values in relation to environmental conditions such as drought, rainfall, or irrigation. Its effectiveness is highest when the vegetation cover is not too dense, as dense canopies may obscure soil moisture signals.

These three indices function best when used in combination. NDVI establishes the general vegetation condition, NDVI″ enhances sensitivity to developmental changes, and NDWI provides environmental context, especially regarding water availability. Together, they enable a more comprehensive understanding of crop status and improve the reliability of remote biomass estimation.

In this study, the application of the second derivative of the NDVI (NDVI″) is introduced as a novel approach. To the best of the authors' knowledge, no prior research has investigated this specific variant of the index. The ongoing analysis aims to further evaluate its potential capabilities and limitations. These limitations may include factors such as the spatial resolution of the input data or vertical heterogeneity in canopy density within the studied crop.

4. Conclusions

This study demonstrated that the second derivative of the NDVI with respect to NIR (NDVI″) is a reliable indicator for estimating aboveground biomass in winter wheat using UAV-acquired multispectral data. Field trials conducted over two seasons and across five wheat varieties showed a strong correlation between NDVI″ values and biomass scores derived from physical measurements and visual assessments.

Regression analysis revealed an almost perfect linear relationship ($R \approx 0.99999999$), indicating the model's strong predictive power under the tested conditions. While direct biomass sampling was not performed, the field-derived parameters provide a practical basis for relative biomass estimation.

The proposed method is non-destructive, scalable, and suitable for application in precision agriculture.

Future work will focus on including destructive biomass sampling to calibrate and validate the NDVI″ model with absolute biomass values. Testing the method across different crop types and environmental conditions helps assess its generalizability. Additional vegetation indices and machine learning techniques are integrated to improve accuracy and automation. These advancements would contribute to the development of robust, adaptive tools for monitoring biomass dynamics across a wider range of crops and agroecological conditions.

Author Contributions: Conceptualization, A.I.A. and A.Z.A.; methodology, A.I.A.; software, A.I.A.; validation, A.I.A., A.Z.A. and B.I.E.; formal analysis, A.I.A. and A.Z.A.; investigation, A.I.A.; resources, A.I.A.; data curation, A.I.A.; writing—original draft preparation, A.I.A. and A.Z.A.; writing—review and editing, A.Z.A. and B.I.E.; visualization, A.I.A.; supervision, A.Z.A.; project administration, A.Z.A.; funding acquisition, A.Z.A. All authors have read and agreed to the published version of the manuscript.

Funding: This study is financed by the European Union—NextGenerationEU, through the National Recovery and Resilience Plan of the Republic of Bulgaria, project No. BG-RRP-2.013-0001.

Institutional Review Board Statement: Not applicable.

Data Availability Statement: The data presented in this study are available upon request from the corresponding authors.

Acknowledgments: The authors are very grateful to the anonymous reviewers whose valuable comments and suggestions improved the quality of the paper.

Conflicts of Interest: The authors declare no conflicts of interest.

Abbreviations

The following abbreviations are used in this manuscript:

NDVI	Normalized difference vegetation index
NDVI″	Second derivative of NDVI in terms of NIR
NDWI	Normalized difference water index
NIR	Near-infrared
RGN	Red + Green + Near Infrared
RGB	Red + Green + Blue
HFOV	Horizontal field of view

References

1. Yang, L.; He, X.; Shen, F.; Zhou, C.; Zhu, A.X.; Gao, B.; Chen, Z.; Li, M. Improving prediction of soil organic carbon content in croplands using phenological parameters extracted from NDVI time series data. *Soil Tillage Res.* **2020**, *196*, 104465. [CrossRef]
2. Wang, H.; Magagi, R.; Goïta, K.; Trudel, M.; McNairn, H.; Powers, J. Crop phenology retrieval via polarimetric SAR decomposition and Random Forest algorithm. *Remote Sens. Environ.* **2019**, *231*, 111234. [CrossRef]
3. Anwar, M.R.; Liu, D.L.; Farquharson, R.; Macadam, I.; Abadi, A.; Finlayson, J.; Wang, B.; Ramilan, T. Climate change impacts on phenology and yields of five broadacre crops at four climatologically distinct locations in Australia. *Agric. Syst.* **2015**, *132*, 133–144. [CrossRef]
4. *FAO Handbook on Crop Statistics: Improving Methods for Measuring Crop Area, Production and Yield*; Pasetto, L., Ed.; FAO Statistics Division (ESS): Rome, Italy, 2018.
5. Biazin, B.; Wondatir, S.; Tilahun, G.; Asaro, N.; Amede, T. Using AquaCrop as a Decision-Support Tool for Small-Scale Irrigation Systems Was Dictated by the Institutional and Market Incentives in Ethiopia. *Front. Water* **2021**, *3*, 96. [CrossRef]
6. Lorite, I.J.; García-Vila, M.; Santos, C.; Ruiz-Ramos, M.; Fereres, E. AquaData and AquaGIS: Two Computer Utilities for Temporal and Spatial Simulations of Water-Limited Yield with AquaCrop. *Comput. Electron. Agric.* **2013**, *96*, 227–237. [CrossRef]
7. Han, C.; Zhang, B.; Chen, H.; Wei, Z.; Liu, Y. Spatially Distributed Crop Model Based on Remote Sensing. *Agric. Water Manag.* **2019**, *218*, 165–173. [CrossRef]
8. Liu, L.; Zhang, X.; Yu, Y.; Gao, F.; Yang, Z. Real-Time Monitoring of Crop Phenology in the Midwestern United States Using VIIRS Observations. *Remote Sens.* **2018**, *10*, 1540. [CrossRef]
9. Tian, H.; Ren, W.; Tao, B.; Sun, G.; Chappelka, A.; Wang, X.; Pan, S.; Yang, J.; Liu, J.S.; Felzer, B.M.; et al. Climate extremes and ozone pollution: A growing threat to China's food security. *Ecosyst. Health Sustain.* **2016**, *2*, e01203. [CrossRef]
10. Cho, S.J.; McCarl, B.A. Climate change influences on crop mix shifts in the United States. *Sci. Rep.* **2017**, *7*, 40845. [CrossRef]
11. Ortiz-Monasterio, J.I.; Lobell, D.B. Remote sensing assessment of regional yield losses due to sub-optimal planting dates and fallow period weed management. *Field Crops Res.* **2007**, *101*, 80–87. [CrossRef]
12. De Castro, A.; Six, J.; Plant, R.; Peña, J. Mapping Crop Calendar Events and Phenology-Related Metrics at the Parcel Level by Object-Based Image Analysis (OBIA) of MODIS-NDVI Time-Series: A Case Study in Central California. *Remote Sens.* **2018**, *10*, 1745. [CrossRef]
13. Kotsuki, S.; Tanaka, K. SACRA-A method for the estimation of global high-resolution crop calendars from a satellite-sensed NDVI. *Hydrol. Earth Syst. Sci.* **2015**, *19*, 4441–4461. [CrossRef]
14. Pan, Y.; Nie, Y.; Watene, C.; Zhu, J.; Liu, F. Phenological Observations on Classical Prehistoric Sites in the Middle and Lower Reaches of the Yellow River Based on Landsat NDVI Time Series. *Remote Sens.* **2017**, *9*, 374. [CrossRef]
15. Boschetti, M.; Stroppiana, D.; Brivio, P.A.; Bocchi, S. Multi-year monitoring of rice crop phenology through time series analysis of MODIS images. *Int. J. Remote Sens.* **2009**, *30*, 4643–4662. [CrossRef]
16. Huang, X.; Liu, J.; Zhu, W.; Atzberger, C.; Liu, Q. The Optimal Threshold and Vegetation Index Time Series for Retrieving Crop Phenology Based on a Modified Dynamic Threshold Method. *Remote Sens.* **2019**, *11*, 2725. [CrossRef]
17. Sakamoto, T.; Wardlow, B.D.; Gitelson, A.A.; Verma, S.B.; Suyker, A.E.; Arkebauer, T.J. A two-step filtering approach for detecting maize and soybean phenology with time-series MODIS data. *Remote Sens. Environ.* **2010**, *114*, 2146–2159. [CrossRef]

18. Shammi, S.A.; Meng, Q. Use Time Series NDVI and EVI to Develop Dynamic Crop Growth Metrics for Yield Modeling. *Ecol. Indic.* **2021**, *121*, 107124. [CrossRef]
19. Johnson, D.M.; Rosales, A.; Mueller, R.; Reynolds, C.; Frantz, R.; Anyamba, A.; Pak, E.; Tucker, C. USA Crop Yield Estim. MODIS NDVI: Are Remote. Sensed Models Better Than Simple Trend Anal. *Remote Sens.* **2021**, *13*, 4227. [CrossRef]
20. Lischeid, G.; Webber, H.; Sommer, M.; Nendel, C.; Ewert, F. Machine Learning in Crop Yield Modelling: A Powerful Tool, but No Surrogate for Science. *Agric. For. Meteorol.* **2022**, *312*, 108698. [CrossRef]
21. van Klompenburg, T.; Kassahun, A.; Catal, C. Crop Yield Prediction Using Machine Learning: A Systematic Literature Review. *Comput. Electron. Agric.* **2020**, *177*, 105709. [CrossRef]
22. Hu, H.; Zhou, H.; Cao, K.; Lou, W.; Zhang, G.; Gu, Q.; Wang, J. Biomass Estimation of Milk Vetch Using UAV Hyperspectral Imagery and Machine Learning. *Remote Sens.* **2024**, *16*, 2183. [CrossRef]
23. Vahidi, M.; Shafian, S.; Thomas, S.; Maguire, R. Pasture Biomass Estimation Using Ultra-High-Resolution RGB UAVs Images and Deep Learning. *Remote Sens.* **2023**, *15*, 5714. [CrossRef]
24. Yang, Z.-Y.; Xia, W.-K.; Chu, H.-Q.; Su, W.-H.; Wang, R.-F.; Wang, H. A Comprehensive Review of Deep Learning Applications in Cotton Industry: From Field Monitoring to Smart Processing. *Plants* **2025**, *14*, 1481. [CrossRef] [PubMed]
25. Rouse, J.W.; Haas, R.H.; Shell, J.A.; Deering, D.W.; Harlan, J.C. *Monitoring the Vernal Advancement and Retrogradation (Green Wave Effect) of Natural Vegetation*; Texas A & M University, Remote Sensing Center: College Station, TX, USA, 1974.
26. Atanasov, A.I.; Atanasov, A.Z.; Evstatiev, B.I. Application of NDVI for Early Detection of Yellow Rust (*Puccinia striiformis*). *AgriEngineering* **2025**, *7*, 160. [CrossRef]
27. Kyratzis, A.; Skarlatos, D.; Fotopoulos, V.; Vamvakousis, V.; Katsiotis, A. Investigating Correlation among NDVI Index Derived by Unmanned Aerial Vehicle Photography and Grain Yield under Late Drought Stress Conditions. *Procedia Environ. Sci.* **2015**, *29*, 225–226. [CrossRef]
28. Duan, B.; Fang, S.; Zhu, R.; Wu, X.; Wang, S.; Gong, Y.; Peng, Y. Remote Estimation of Rice Yield with Unmanned Aerial Vehicle (Uav) Data and Spectral Mixture Analysis. *Front. Plant Sci.* **2019**, *10*, 204. [CrossRef]
29. Atanasov, A.I.; Mihova, G.M.; Atanasov, A.Z.; Vlăduț, V. Long-Term Assessment of NDVI Dynamics in Winter Wheat (Triticum aestivum) Using a Small Unmanned Aerial Vehicle. *Agriculture* **2025**, *15*, 394. [CrossRef]
30. Hassan, M.A.; Yang, M.; Rasheed, A.; Yang, G.; Reynolds, M.; Xia, X.; Xiao, Y.; He, Z. A Rapid Monitoring of NDVI across the Wheat Growth Cycle for Grain Yield Prediction Using a Multi-Spectral UAV Platform. *Plant Sci.* **2019**, *282*, 95–103. [CrossRef]
31. White, M.A.; Nemani, R.R. Real-Time Monitoring and Short-Term Forecasting of Land Surface Phenology. *Remote Sens. Environ.* **2006**, *104*, 43–49. [CrossRef]
32. Atkinson, P.M.; Jeganathan, C.; Dash, J.; Atzberger, C. Inter-Comparison of Four Models for Smoothing Satellite Sensor Time-Series Data to Estimate Vegetation Phenology. *Remote Sens. Environ.* **2012**, *123*, 400–417. [CrossRef]
33. Marti, J.; Bort, J.; Slafer, G.A.; Araus, J.L. Can Wheat Yield Be Assessed by Early Measurements of Normalized Difference Vegetation Index? *Ann. Appl. Biol.* **2007**, *150*, 253–257. [CrossRef]
34. Seo, B.; Lee, J.; Lee, K.D.; Hong, S.; Kang, S. Improving Remotely-Sensed Crop Monitoring by NDVI-Based Crop Phenology Estimators for Corn and Soybeans in Iowa and Illinois, USA. *Field Crops Res.* **2019**, *238*, 113–128. [CrossRef]
35. Misra, G.; Buras, A.; Menzel, A. Effects of Different Methods on the Comparison between Land Surface and Ground Phenology—A Methodological Case Study from South-Western Germany. *Remote Sens.* **2016**, *8*, 753. [CrossRef]
36. Tan, B.; Morisette, J.T.; Wolfe, R.E.; Gao, F.; Ederer, G.A.; Nightingale, J.; Pedelty, J.A. An Enhanced TIMESAT Algorithm for Estimating Vegetation Phenology Metrics from MODIS Data. *Remote Sens.* **2011**, *4*, 361–371. [CrossRef]
37. Yang, Y.; Tao, B.; Liang, L.; Huang, Y.; Matocha, C.; Lee, C.D.; Sama, M.; Masri, B.E.; Ren, W. Detecting Recent Crop Phenology Dynamics in Corn and Soybean Cropping Systems of Kentucky. *Remote Sens.* **2021**, *13*, 1615. [CrossRef]
38. Sánchez, N.; Plaza, J.; Criado, M.; Pérez-Sánchez, R.; Gómez-Sánchez, M.Á.; Morales-Corts, M.R.; Palacios, C. The Second Derivative of the NDVI Time Series as an Estimator of Fresh Biomass: A Case Study of Eight Forage Associations Monitored via UAS. *Drones* **2023**, *7*, 347. [CrossRef]
39. Liu, T.; Liu, X.; Liu, M.; Wu, L. Evaluating Heavy Metal Stress Levels in Rice Based on Remote Sensing Phenology. *Sensors* **2018**, *18*, 860. [CrossRef]
40. Ghilardi, F.; De Petris, S.; Torti, V.; Giacoma, C.; Borgogno-Mondino, E. A possible role of NDVI time series from Landsat Mission to characterize lemurs habitats degradation in Madagascar. *Sci. Total Environ.* **2025**, *974*, 179243. [CrossRef]
41. Lumbierres, M.; Méndez, P.F.; Bustamante, J.; Soriguer, R.; Santamaría, L. Modeling Biomass Production in Seasonal Wetlands Using MODIS NDVI Land Surface Phenology. *Remote Sens.* **2017**, *9*, 392. [CrossRef]
42. Schucknecht, A.; Meroni, M.; Kayitakire, F.; Boureima, A. Phenology-Based Biomass Estimation to Support Rangeland Management in Semi-Arid Environments. *Remote Sens.* **2017**, *9*, 463. [CrossRef]
43. Perry, E.; Sheffield, K.; Crawford, D.; Akpa, S.; Clancy, A.; Clark, R. Spatial and Temporal Biomass and Growth for Grain Crops Using NDVI Time Series. *Remote Sens.* **2022**, *14*, 3071. [CrossRef]
44. DJI. 2025. Available online: https://www.dji.com/bg/mavic-2/info (accessed on 25 June 2025).

45. Pix4Dcapture. 2025. Available online: https://www.pix4d.com/product/pix4dcapture/ (accessed on 25 June 2025).
46. Mapir. 2025. Available online: https://www.mapir.camera/collections/survey3/products/survey3w-camera-red-green-nir-rgn-ndvi (accessed on 25 June 2025).
47. Mapir. 2025. Available online: https://www.mapir.camera/en-gb/products/survey3-gps-receiver?srsltid=AfmBOoqfvv5La7_44iDyEXSN6rLrOeX0T_pT29XgFU01rYAn8PdA-Ikp (accessed on 25 June 2025).
48. McFEETERS, S.K. The Use of the Normalized Difference Water Index (NDWI) in the Delineation of Open Water Features. *Int. J. Remote Sens.* **1996**, *17*, 1425–1432. [CrossRef]
49. Pix4Dfields. 2025. Available online: https://www.pix4d.com/product/pix4dfields/ (accessed on 25 June 2025).
50. Dimitrov, S.D. Example application of a simple linear regression and correlation in transportation studies using MS Excel. *Mech. Transp. Commun.* **2010**, *2*, BG-3.9–BG-3.16. (In Bulgarian)
51. Microsoft, 2025. Available online: https://www.microsoft.com/en-us/microsoft-365 (accessed on 25 June 2025).

Disclaimer/Publisher's Note: The statements, opinions and data contained in all publications are solely those of the individual author(s) and contributor(s) and not of MDPI and/or the editor(s). MDPI and/or the editor(s) disclaim responsibility for any injury to people or property resulting from any ideas, methods, instructions or products referred to in the content.

sustainability

MDPI

Article

Mapping Grassland Suitability Through GIS and AHP for Sustainable Management: A Case Study of Hunedoara County, Romania

Luminiţa L. Cojocariu [1,2], Nicolae Marinel Horablaga [1,2,*], Cosmin Alin Popescu [3], Adina Horablaga [3], Monica Bella-Sfîrcoci [4] and Loredana Copăcean [3,*]

[1] Department of Agricultural Technologies, Faculty of Agriculture, University of Life Sciences "King Mihai I" from Timisoara, 300645 Timisoara, Romania; luminita_cojocariu@usvt.ro
[2] Laboratory for Pratology and Forage Crop Improvement, Agricultural Research and Development Station Lovrin, 307250 Lovrin, Romania
[3] Department of Sustainable Development and Environmental Engineering, Faculty of Agriculture, University of Life Sciences "King Mihai I" from Timisoara, 300645 Timisoara, Romania; cosmin_popescu@usvt.ro (C.A.P.); adinahorablaga@usvt.ro (A.H.)
[4] Romanian Grassland Society, 400372 Cluj-Napoca, Romania; monicasfircoci@gmail.com
* Correspondence: marinel_horablaga@usvt.ro (N.M.H.); loredanacopacean@usvt.ro (L.C.)

Abstract

Grasslands represent an essential resource for rural economies and for the provision of ecosystem services, yet they are increasingly affected by anthropogenic pressures, functional land-use changes, and institutional constraints. This study develops a geospatial decision-support framework for assessing grassland suitability in Hunedoara County, Romania, by integrating the Analytic Hierarchy Process (AHP) and Weighted Overlay Analysis (WOA) within a GIS environment. The assessment is based on nine criteria thematically grouped into three dimensions: (A) physical-geographical, including topographic suitability, climatic pressure, and hydrological risk exposure; (B) ecological and conservation-related, reflected by ecological conservation value, ecological carrying capacity, and the anthropic pressure index; and (C) socio-economic and functional, represented by spatial accessibility, recreational value, and policy support mechanisms. Suitability is defined as the integrated capacity of grasslands to sustain productive and multifunctional uses compatible with ecological conservation and the existing policy framework. Results indicate that 0.43% of the grassland area exhibits very high suitability (Class 1), 44.51% high suitability (Class 2), and 54.75% moderate suitability (Class 3), while unfavorable areas account for only 0.31% of the total (Class 4). The proposed methodology is reproducible and transferable, providing support for prioritizing management interventions, agri-environmental payments, and rural planning in mountainous and hilly regions.

Keywords: grasslands; GIS; spatial decision support system; Analytic Hierarchy Process; Weighted Overlay Analysis; ecosystem services

1. Introduction

In the rural landscapes of Europe, natural and semi-natural grasslands hold an essential role both in terms of agricultural production and ecosystem services [1,2]. These areas provide fodder resources for livestock, serve as habitats for rare wildlife species, and contribute to biodiversity conservation and hydrological regulation, carbon storage, and

also offer cultural and recreational value (provisioning, regulating, supporting, and cultural services) [2–6]. Moreover, grasslands are vital to the economic structure of extensive pastoral farms and to the resilience of rural territories, especially in mountainous and hilly regions [7–9], a context highly relevant for the study area.

However, in recent decades many grasslands have been subjected to increasing pressures: abandonment of traditional agriculture, overgrazing, land fragmentation, changes in land use, along with environmental and climatic drivers [10]. These trends threaten the ecosystem services provided by grasslands and the stability of agro-pastoral systems [11–13]. In response, agricultural policies, including agri-environmental payments and subsidies under national and European frameworks, have increasingly aimed to support the conservation and sustainable management of grasslands [14–16].

In Central, Eastern, and Southern Europe, the abandonment of traditional agriculture is often driven by structural socio-demographic processes, such as rural depopulation and ageing, labor migration, and the low economic attractiveness of agricultural activities in marginal or mountainous areas [10,17–19]. These dynamics contribute to the underutilization or abandonment of grasslands and highlight the need for spatial tools capable of distinguishing between areas with high functional potential and those requiring differentiated support and management measures, including in Hunedoara County [20].

In this context, land-use sustainability can no longer be addressed solely as a normative principle or a general policy objective, but requires an operational translation capable of capturing spatial differences in functional land potential. In the scientific literature, such operationalization is achieved through the integration of biophysical, anthropogenic, and institutional criteria within spatial analytical frameworks, enabling differentiated assessments of land-use suitability and compatibility, including in mountainous regions [21–23]. In this study, sustainability is approached from a spatial perspective through measurable criteria relevant to grassland use, reflecting biophysical constraints, anthropogenic pressures, accessibility, and institutional compatibility, thereby providing the basis for spatial evaluation and decision-support tools [24].

Although agriculture is often broadly associated with environmental pressures, its impacts vary depending on intensity, management practices, and spatial context. In many cases, unsustainable land use reflects a mismatch between land use and its underlying biophysical and socio-institutional characteristics, thereby justifying the need for models capable of differentiating levels of land-use favorability and suitability.

To address current challenges in land-use planning and environmental protection, numerous studies have combined Multi-Criteria Decision Analysis (MCDA) with Geographic Information Systems (GIS), particularly through GIS-AHP (Analytic Hierarchy Process) integration, as a reliable support framework for assessing land suitability for agricultural purposes or conservation objectives [25–27]. This integration is driven by the need to manage increasingly complex decision-making contexts, where land-use patterns are influenced simultaneously by biogeographical, ecological, socio-economic and institutional factors that are difficult to evaluate through traditional approaches [21,28,29].

MCDA provides a systematic framework based on multiple criteria, enabling the integration of quantitative and qualitative information to support complex decision-making processes [30–34]. Among MCDA techniques, the AHP method is widely used due to its ability to structure decision problems and to estimate the relative importance of criteria, making it suitable for territorial assessments involving heterogeneous factors [35,36].

At the applied level, the integration of GIS-MCDA enables the generation of spatial favorability or suitability maps that support territorial planning, sustainable resource management, and public policy formulation [37–40]. Beyond spatial analysis per se, these models function as decision-support tools by facilitating the comparison of alternatives

https://doi.org/10.3390/su18031155

and the prioritization of interventions in contexts characterized by multiple constraints and dynamic pressures [37,41,42].

Within the field of grassland studies, GIS-MCDA/AHP methodologies have been applied to favorability zoning for biodiversity conservation as well as for identifying sustainable agricultural approaches such as controlled grazing or the maintenance of ecosystem services [41,43–45]. These applications highlight the importance of integrating both environmental factors (soil, climate, topography) and socio-economic dimensions (accessibility, local practices, agricultural policies) within decision-making processes to ensure the long-term sustainability of grassland resources [37–39,46].

Recent literature also points to a shift from static suitability models toward Spatial Decision Support Systems (SDSS) capable of integrating policies, costs and management scenarios. Applications range from agricultural and conservation planning to future land-use forecasting and rural development strategy formulation [39,47,48]. In this context, the use of MCDA and geospatial sciences is expanding beyond mere spatial mapping, becoming an integral part of planning and policy-making processes, including within the context of Common Agricultural Policy (CAP) implementation.

Nevertheless, in Romania, GIS-based suitability assessments remain largely focused on general agricultural land/crop potential, rather than treating grasslands as a distinct functional land-use category and linking results to management and policy instruments. For instance, national-scale digital suitability mapping has been developed for major crops, but without an explicit grassland-oriented and policy-targeting SDSS framing [26]. At the same time, although grasslands are widely acknowledged as key targets for agri-environmental and biodiversity-related measures under CAP-type schemes [15,46], few studies operationalise this policy dimension through integrated spatial decision-support outputs for grassland prioritisation. This gap is particularly pronounced in mountainous and hilly counties, where grasslands represent a central component of rural identity and local economies. Beyond the geographical dimension, this gap also reflects conceptual and methodological limitations in the existing literature, related to the fragmented integration of analytical criteria and the lack of explicit links to decision-making processes and public policies. In this respect, the contribution of the present study lies not only in its application to an underexplored regional context, but also in the proposal of an integrated analytical framework explicitly oriented toward functional grassland prioritization and decision support for land management and rural planning.

Based on these considerations, the central research question of this study is whether and how a GIS-AHP-based geospatial model can support spatially explicit decision-making processes related to grassland management and rural planning. Specifically, the model is designed to inform land-use zoning decisions, the prioritisation of agri-environmental and compensatory payments, the identification of areas requiring grazing intensity regulation or ecological restoration interventions, as well as the targeting of rural development measures. In this context, the working hypothesis is that the integration of biophysical, ecological, socio-economic, and institutional criteria within a GIS-AHP multicriteria framework, followed by weighted aggregation and spatial classification of the results, generates differentiated spatial patterns of grassland favourability. These patterns reflect distinct combinations of environmental constraints, anthropogenic pressures, and the policy-institutional context, thereby enabling the identification of priority areas for agricultural management, ecological conservation, and rural development interventions.

In line with this hypothesis, the aim of the study is to develop a geospatial decision-support tool for the evaluation and prioritization of grassland favorability, intended to support grassland resource management and rural planning processes at the level of Hunedoara County, Romania. To achieve this aim, the research pursues the following

https://doi.org/10.3390/su18031155

objectives: (1) to select and operationalize relevant biophysical, ecological, and socio-economic criteria for grassland favorability assessment; (2) to integrate these criteria into a GIS-based AHP multicriteria model in order to estimate the spatial favorability of grassland resources; (3) to classify and map grassland favorability and identify priority areas for management interventions; and (4) to analyze the distribution of priority areas in relation to administrative units and to derive applicable intervention directions for rural planning and sustainable grassland management.

The originality of this study lies in the integration, within a unified GIS-AHP framework, of biophysical, ecological, socio-economic, and institutional factors influencing the functionality and patterns of grassland use in a mountainous and hilly county of Romania. The proposed methodology is replicable, relies on open-source geospatial data, and enables the integrated spatial representation of the analyzed factors in the form of comprehensive or site-specific favorability maps, providing cartographic outputs relevant for prioritizing management measures and agricultural support.

2. Materials and Methods

The adopted methodology is based on a conceptual model for the spatial assessment of grassland favorability, in which sustainability is interpreted as the result of interactions between physico-geographical constraints, anthropogenic pressures, and the institutional framework. The sequence of methodological steps represents not merely a technical GIS processing workflow, but an analytical logic intended to translate these dimensions into a coherent multicriteria framework capable of revealing spatial patterns relevant to land management and territorial planning.

2.1. Study Area

The study area (Figure 1) is located in the central-western part of Romania and corresponds to the administrative territory of Hunedoara County. The county lies approximately between 45°30′ N and 46°20′ N latitude and 22°20′ E and 23°40′ E longitude, occupying a transitional position between the Apuseni Mountains of the Western Carpathians and the Southern Carpathians of Romania [49]. Hunedoara County covers a total area of 706,034 ha and is characterized by predominantly mountainous and hilly relief, with elevations ranging from 151 m in river floodplains and depressions to 2494 m along high mountain ridges, resulting in a wide diversity of environmental conditions.

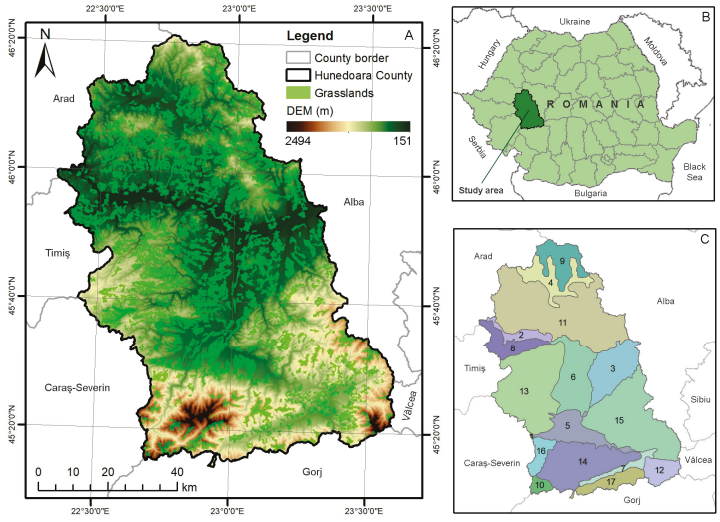

Figure 1. Geographical context of the study area-Hunedoara County. (**A**)-Digital Elevation Model and distribution of grassland areas; (**B**)-Location of Hunedoara County within Romania; (**C**)-Main

relief units of Hunedoara County: 1-Bistra Corridor; 2-Mureș Corridor; 3-Orăștie Corridor; 4-Brad-Hălmagiu Depression; 5-Hațeg Depression; 6-Hunedoara Depression; 7-Petroșani Depression; 8-Bega Hills; 9-Bihor Mountains; 10-Godeanu Mountains; 11-Metaliferi Mountains; 12-Parâng Mountains; 13-Poiana Ruscă Mountains; 14-Retezat Mountains; 15-Șureanu Mountains; 16-Țarcu Mountains; 17-Vâlcan Mountains (processed after [49–52]).

The climate of Hunedoara County is classified as moderately temperate-continental, with a multiannual average air temperature of approximately 9.8 °C and mean annual precipitation of about 1048 mm. Rainfall is distributed throughout the year, with maximum values occurring in early summer (June) [53]. Variability in precipitation and temperature contributes to the development of diverse soil conditions, including Cambisols, Luvisols, and Regosols, which influence grassland productivity and use [54]. According to demographic data from the National Institute of Statistics [55], Hunedoara County has a population of 361,657 inhabitants, with a declining trend over recent decades, reflecting socio-demographic changes that also affect land-use dynamics.

Hunedoara County was selected as the study area due to its high representativeness for the Romanian Carpathian region in terms of relief diversity, grassland distribution, and agro-pastoral land-use systems. The county occupies a transitional position between the Western and Southern Carpathians and encompasses a wide altitudinal range, multiple relief units, and heterogeneous climatic and ecological conditions [49]. This complexity generates a broad spectrum of grassland types [7,12], management intensities, and institutional contexts, typical for mountainous and hilly Carpathian regions [11,46,56]. Consequently, Hunedoara County provides an appropriate case study for testing the applicability of GIS-AHP-based spatial decision-support models, with results that can be transferred to other Carpathian areas facing similar environmental and socio-economic conditions.

Within the study area, 873 grassland entities were identified, with a total cumulative area of 129,118 ha [51]. The smallest grassland patch covers 0.12 ha, while the largest reaches 3344 ha, with an average area of 147.90 ha. Grassland distribution is characterized by a predominance of small-sized patches, most of them being under 500 ha. Grasslands in Hunedoara County are distributed across all major relief units (Figure 1), and this extensive spatial coverage, combined with the diversity of altitudinal, climatic, and pedological conditions, confers a complex and heterogeneous character to grassland ecosystems in the region.

2.2. Geospatial Data and Preprocessing

The study relied exclusively on free (open-source) geospatial datasets obtained from official european and national sources, used to characterize grassland resources in Hunedoara County. All datasets were harmonized within a common projection system (Stereographic 1970) and processed to enable integration into the multicriteria modelling framework.

1. Grassland delineation and characterization. Grasslands were extracted from the Corine Land Cover dataset [51], then validated through cross-referencing with Sentinel-2 satellite imagery [57], orthophotos, and cadastral information provided by the National Agency for Cadastre and Land Registration (NACLR) [58]. The final polygon geometries served as the spatial basis for all derived thematic analyses.

In this study, “grasslands” are defined as a land-use/land-cover category derived from Corine Land Cover (CLC 2018) [51], corresponding to permanent grassland classes (231 and 321 code). The analysis therefore treats grasslands as a functional spatial category for territorial assessment and decision support, rather than as a detailed typology of habitat or vegetation communities. We acknowledge that this category may include heterogeneous ecological and floristic conditions; however, the aim of the study is to capture county-scale spatial favourability patterns based on comparable, reproducible open datasets.

https://doi.org/10.3390/su18031155

2. Physical-geographical data. Topographic conditions were obtained from a Digital Elevation Model (25 m spatial resolution) [50], from which slope and aspect were derived. The climatic variable was expressed through the Lang index, calculated for each meteorological station based on multiannual mean temperature and precipitation data for the period 2014–2023, recorded at 17 stations [53]. The point-based Lang index values were subsequently interpolated using inverse distance weighting (IDW) to generate a continuous raster surface, which was resampled to the common spatial resolution of 25 m used in the GIS-AHP analysis. To estimate hydrological risk affecting grasslands, a planar (2D) Euclidean distance raster to the hydrographic network [52] was generated in a GIS environment. This proximity-based indicator was used as a proxy to identify areas potentially exposed to flooding, water stagnation, or excess moisture in the vicinity of watercourses, without explicitly modelling hydrological flow or runoff processes.

3. Ecological data. The ecological value of grasslands was determined by intersecting grassland polygons with protected area polygons [59], in order to identify grassland surfaces located within protected perimeters. This approach allows the identification of grasslands subject to conservation-related constraints and associated with higher ecological value due to their inclusion in protected areas. while grazing capacity was evaluated based on livestock density (Livestock Units-LU/ha) reported at administrative-territorial unit level [52,55,60].

4. Socio-economic and functional data. Anthropogenic pressure was calculated using the Grassland Anthropic Impact Index (GAII) [10]-the ratio between grassland areas and human population [55]. Territorial accessibility was derived from the Euclidean distance from the road network, initially provided in vector format [52]. Recreational potential was estimated using spatial data on catalogued tourist sites [61], and institutional support for grasslands was mapped based on eligibility zones corresponding to National Programme of Rural Development (NPRD) measures M10 (Agri-environment and climate) and M13 (Mountain zone) [62,63]. All indicators used in the analysis were operationalised as raster layers at a spatial resolution of 25 m.

5. GIS preprocessing. All geospatial datasets were resampled, standardized, and converted to raster format at a common spatial resolution of 25 m using ArcGIS Desktop 10.8 (Esri, Redlands, CA, USA) [64]. The resulting thematic raster layers formed the basis for subsequent multicriteria spatial integration. Climatic and socio-economic datasets, originally available at coarser spatial resolutions or administrative-unit levels, were adapted using standard GIS interpolation and rasterization procedures, assuming spatial homogeneity within the original reporting units. This harmonization to a common resolution enabled consistent cell-by-cell integration in the weighted overlay analysis while preserving the relative spatial patterns of each factor at the county scale.

The use of a uniform spatial resolution aimed to ensure analytical consistency for multicriteria integration at a regional scale, being suitable for capturing general grassland favourability patterns while acknowledging the limitations related to spatial generalization and loss of local variability.

2.3. Criteria Selection and Hierarchical Structuring

For the multidimensional assessment of grassland potential, nine relevant factors were selected, reflecting the complex interaction between natural conditions, anthropogenic pressures, and socio-economic opportunities. These factors were grouped into three main dimensions (A-C): physical-geographical, ecological, and socio-economic (Table 1), with this structuring serving a thematic and interpretative purpose only. Factor selection was based on a review of the relevant literature, data availability, and the practical applicability of each criterion in the context of sustainable grassland management. Within the AHP

framework, all nine factors are evaluated at the same decision level, without a formal multi-level hierarchical structure.

Table 1. Multidimensional criteria used for grassland suitability assessment.

Dimension (Thematic Grouping)	Dimension	Factor Identifier	Factor	Indicator Type
A	Physical-geographical	A1-TS	Topographic Suitability	Natural
		A2-CP	Climatic Pressure	Natural
		A3-HRE	Hydrological Risk Exposure	Natural
B	Ecological and conservation	B1-ECV	Ecological Conservation Value	Ecological
		B2-ECC	Ecological Carrying Capacity	Ecological
		B3-API	Anthropic Pressure Index	Socio-ecological
C	Socio-economic and functional	C1-SA	Spatial Accessibility	Infrastructural
		C2-RV	Recreational Value	Economic
		C3-PSM	Policy Support Mechanism	Political-institutional

The selection of variables was guided by their ecological and functional relevance to grassland use, their ability to capture meaningful spatial variation at the regional scale, and their alignment with agricultural policy and territorial planning instruments. Variable choice was informed by the relevant literature, the institutional framework, and the availability of official, comparable, and reproducible geospatial data. It is acknowledged that some datasets entail inherent limitations, such as spatial resolution or temporal lag; however, these do not affect the main objective of the analysis, which focuses on identifying territorial patterns of grassland favorability.

Within the proposed model, criteria were selected and interpreted according to their analytical role, distinguishing between suitability factors (enhancing functional potential), constraint criteria (limiting use), and indicators of anthropogenic pressure or institutional context. This conceptual distinction enables a coherent integration of criteria within the AHP hierarchy and reduces ambiguity between suitability and restriction. Potential thematic overlaps among criteria were assessed at a conceptual level, and the hierarchical structure was defined to ensure that each criterion contributes distinctly to the spatial favourability assessment.

Each factor was operationalised as a raster layer at a spatial resolution of 25 m, derived from the processing of the corresponding raw datasets (DEM, hydrographic network, protected areas, statistical and institutional data) in accordance with the GIS procedures described above. The resulting values were subsequently standardised to a common scale in order to enable coherent integration of the criteria within the multicriteria analysis.

A. The physical-geographical dimension reflects the natural constraints and vulnerabilities that influence the usability and ecological stability of grasslands:

A.1. Topographic suitability (A1-TS) was assessed through slope and aspect; it influences accessibility, slope processes, and vegetation type;

A.2. Climatic vulnerability (A2-CP), quantified using the Lang index (precipitation/temperature ratio), indicates the climatic favorability for grassland vegetation. The index was used due to its ability to synthetically express the relationship between water availability and thermal conditions, which is relevant for regional-scale spatial analyses;

A.3. Hydrological Risk Exposure (A3-HRE) expresses the flood risk that may compromise grassland functionality;

https://doi.org/10.3390/su18031155

B. The ecological and conservation dimension includes factors describing ecological value, ecosystem resilience, and anthropogenic pressures:

B.1. Ecological Conservation Value (B1-ECV) reflects the degree to which grasslands overlap protected natural areas (High Nature Value-HNV grasslands);

B.2. Ecological Carrying Capacity (B2-ECC) was expressed through livestock density (LU/ha), influencing ecological balance and the risk of under-or overgrazing;

B.3. Anthropic Pressure Index (B3-API) was calculated as the grassland area/population ratio, indicating the intensity of human use;

C. The socio-economic and functional dimension targets accessibility, economic use, and institutional-policy support provided for grassland areas:

C.1. Spatial Accessibility (C1-SA) was represented through distance from the road network, influencing the logistics of pastoral activities;

C.2. Recreational Valuation (C2-RV) was expressed through proximity to tourist attractions, highlighting opportunities for diversifying grassland-based economic functions;

C.3. Policy Support Mechanism (C3-PSM) was defined through eligibility for support measures (M10, M13 under NPRD), emphasizing the policy context that enables sustainable use.

2.4. Analytic Hierarchy Process (AHP) Analysis for Determining Factor Weights

The application of the AHP method allows the quantification of relative importance relationships among the selected criteria, reflecting the differentiated roles of environmental factors, accessibility, and the institutional context in shaping grassland favorability. The spatial integration of the derived weights aims to highlight territorial patterns resulting from this interaction, providing the analytical basis for evaluating the research hypothesis.

To determine the relative importance of the nine factors, the AHP method was applied [30], enabling pairwise comparison of criteria and the calculation of their weights within a hierarchical model, where the pairwise comparison matrix (Table 2) reflects the prioritization of factors according to their relevance for sustainable grassland evaluation, and the consistency check, performed through the consistency index (CI = 0.0206) and the consistency ratio (CR = 0.0142), both below the acceptability threshold (CR < 0.10), which confirms the consistency of the evaluations reached by consensus within the author team.

Table 2. Analytic Hierarchy Process (AHP) pairwise comparison matrix and derived factor weight coefficients for grassland potential evaluation.

Matrix	A1-TS	A2-CP	A3-HRE	B1-ECV	B2-ECC	B3-API	C1-SA	C2-RV	C3-PSM	Weight (%)
A1-TS	1	3/2	2	2	2	3	2	2	1	18
A2-CP	2/3	1	2	2	2	3	3	3	1	18
A3-HRE	1/3	1/3	1	0.8	1	1.2	1.2	1.2	0.8	8
B1-ECV	1/2	1/2	1.25	1	3/2	2	2	2	1	12
B2-ECC	1/2	1/2	1	2/3	1	3/2	3/2	3/2	1	10
B3-API	1/3	1/3	0.8	1/2	2/3	1	3/2	3/2	1	8
C1-SA	1/2	1/3	0.8	1/2	2/3	2/3	1	3/2	1	8
C2-RV	1/2	1/3	0.8	1/2	2/3	2/3	2/3	1	1	7
C3-PSM	1	1	1.25	1	1	1	1	1	1	11

In this study, the term "expert judgement" refers to the structured evaluation performed by the author team, based on their domain expertise in grassland management, GIS-based spatial analysis, and rural policy, and implemented following the standard AHP procedure. The subjectivity inherent to pairwise comparisons is controlled through the

formal consistency assessment (CI and CR), which ensures the internal coherence and traceability of the weighting process.

The factor weights were applied in the Weighted Overlay Analysis (WOA) to integrate the nine factors into the final grassland potential map.

2.5. Spatial Modelling and GIS-Based Multicriteria Analysis

The nine factors selected for assessing grassland potential were integrated into a multicriteria analysis within a GIS environment [38], structured as a SDSS. For each factor, standardized thematic raster layers were generated, in which values were reclassified on an ordinal scale from 1 to 5, corresponding to the level of potential impact on the agro-pastoral use of grasslands (Table 3).

Table 3. Criteria, thresholds and scores used in the GIS-AHP multicriteria analysis.

Factor/Score -Impact Level	A1-TS		A2-CP [1]	A3-HRE	B1-ECV	B2-ECC [2]	B3-API [3]	C1-SA	C2-RV	C3-PSM [4]
	Slope (40%)	Aspect (60%)								
Unit	degrees	-	-	km	-	LU/ha	ha/ inhabitant	km	km	-
1-None or very low	0–5	E-SE	100–160	2.6–3.7	Presence of prot. areas	0.71–1.00	0.71–1.00	0–5	0–5	a
2-Low	5.1–10	S-SV	>160	1.1–2.5		0.41–0.70	1.01–4.00	5.1–10	5.1–10	b
3-Moderate	10.1–20	V	60–100	0.51–1.0		1.10–2.00	0.51–0.70	10.1–15	10.1–15	c
4-High	20.1–35	NV-NE	40–60	0.11–0.5		0.10–0.40	0.10–0.50	15.1–20	15.1–20	d
5-Very high	35.1–58	N	20–40	0–0.1	Absence of prot. areas	2.10–3.00	4.10–8.00	20.1–25	20.1–25	e
Legend										
1	A2-CP, expressed through the Lang Index (R = P/T), where P = mean annual precipitation (mm) and T = mean annual temperature (°C). Climate classes: 20–40 = steppe, 40–60 = semi-arid, 60–100 = warm temperate, 100–160 = humid temperate, >160 = wet [65].				3	B3-API, calculated as GAII = grassland surface area/inhabitants (ha/inhabitant) [10].				
2	B2-ECC, expressed as LU/grassland surface area (ha), where LU = number of animals × livestock conversion coefficient: 1 for cattle, 0.14 for goats and sheep [66].				4	C3-PSM, based on differentiated subsidy eligibility categories *: a-M10-P1, P2.1, P2.2, M13-MZ; b-M10-P1, P2.1, P2.2, M13-SNC; c-M10-P1, P2.1, P2.2; d-M10-P11.2.1, P11.2.2, P11.2.3, P3.2.1, P3.2.2, M13-SNC; e-grasslands without M10 subsidy				

* Package 1 (P1)-HNV grasslands; Package 2 (P2)-Traditional agricultural practices-variant 2.1/2.2: manual operations/light machinery on permanent grasslands used as hay meadows; Package 3 (P3)-Grasslands of high importance for bird species-variant 3.2.1/3.2.2: manual operations/light machinery on grasslands important for *Lanius minor* and *Falco vespertinus*; Sub-package 11.2-Grasslands important for the Great Bustard (*Otis tarda*)-variant 11.2.1/11.2.2/11.2.3: manual operations/light machinery/heavy machinery on grasslands of critical relevance for *Otis tarda*; M13 MZ-Compensatory payments in mountain zones; M13 SNC-Compensatory payments for areas facing Significant Natural Constraints (SNC) [62,63].

In this study, the ordinal scale (1–5) expresses the degree to which a given factor constrains or conditions the sustainable use and management of grasslands, rather than implying direct metric equivalence between heterogeneous variables. Higher scores indicate stronger limiting effects or higher functional risk, depending on the nature of the factor. For physical and ecological variables, higher scores reflect increased environmental constraints, whereas for socio-demographic indicators such as GAII, higher scores are interpreted as signals of functional vulnerability related to depopulation, labour shortages, and the risk of underuse or abandonment.

In this study, reclassification thresholds were either directly adopted from the literature and existing normative standards or adjusted based on local data distributions and the functional context of the analysed grasslands.

The reclassification thresholds presented in Table 3 were established using two complementary approaches, depending on the nature of each indicator. For continuous variables with a well-defined statistical distribution, reclassification was performed using the Nat-

https://doi.org/10.3390/su18031155

ural Breaks (Jenks) [64]. method in order to identify dominant internal thresholds. For indicators with functional or normative relevance, such as spatial accessibility, carrying capacity, or institutional support, manual classifications were applied, adapted to local conditions and the objectives of the analysis. For example, for factor C1-SA, distances were calculated from the national road network, and increasing distance was interpreted as a progressively stronger limiting constraint.

It is acknowledged that discretizing continuous variables into classes may introduce uncertainty and generalization effects; however, this step is necessary for multicriteria integration and consistent interpretation at the analysis scale.

The internal classification of values was based on processed raw geospatial data, field observations, the methodological expertise of the author team, and thresholds validated in the scientific literature [46,56,67,68]. The weights assigned to the nine factors were calculated using the AHP, and the decision consistency was verified through the Consistency Index (CI) and Consistency Ratio (CR), the latter remaining below the acceptable threshold of 0.10 (Table 2), confirming the methodological robustness of the pairwise comparisons and the stability of the weighting structure adopted for the model.

In the spatial integration stage, the weighted thematic raster layers corresponding to each criterion were combined by means of the WOA tool in ArcGIS, resulting in a composite suitability score for every grassland polygon. The integration process, illustrated conceptually in Figure 2, shows how the three main decision dimensions, physical-geographical (A), ecological and conservation (B), and socio-economic and functional (C), converge into a unified model that synthesizes spatial variability and assigns differentiated suitability levels to each grassland unit. The final composite values were classified using the Natural Breaks (Jenks) method into four potential categories: very high, high, moderate and unfavourable, allowing a clear hierarchical separation of grassland suitability across the entire study area.

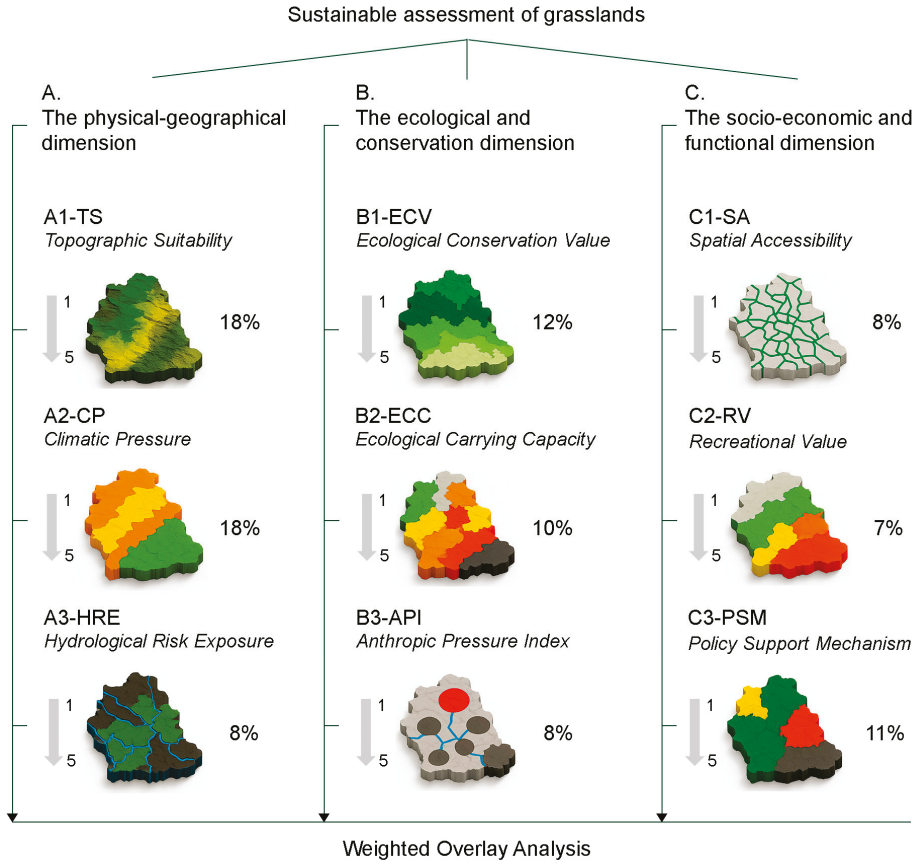

Figure 2. Conceptual structure of the multicriteria evaluation framework for grasslands.

To evaluate the robustness of the model, Pearson correlation analyses were performed between the included factors, alongside internal comparisons of factor values across the four suitability classes. The results confirmed the distinct internal composition of the classes, reinforcing the internal validity of the spatial decision structure and suggesting that the combination of natural, ecological and socio-economic variables performs reliably in discriminating areas with contrasting management potential.

The resulting model provides a coherent spatial distribution of grassland favorability, enabling the identification of overused, underutilized, or vulnerable sectors and offering decision support for sustainable management and the targeting of interventions within the CAP. In this sense, the model not only maps existing conditions but also highlights strategic areas where conservation measures, grazing regulation or agri-environmental payments may yield the greatest long-term benefit.

3. Results

The spatial distribution of grasslands in Hunedoara County was analysed using statistical and geospatial indicators employed as exploratory tests of spatial structure, with the aim of assessing whether the observed patterns are driven by spatial proximity or by the local combination of criteria integrated within the GIS-AHP analysis. In this context, the global spatial autocorrelation analysis (Moran's I) applied to grassland areas in Hunedoara County yielded an index value of 0.0191, a z-score of 1.37, and a *p*-value of 0.1699. These results indicate a slightly clustered spatial distribution that is not statistically significant ($p > 0.05$), suggesting the absence of a clear global tendency toward significant clustering or dispersion of grassland areas.

3.1. Results of the Influencing Factor Assessment

3.1.1. Physico-Geographical Constraints and Conditioning Factors

Topographic Suitability (A1-TS)

The spatial analysis applied to the study area (Figure 3) shows that 14,176 ha of grasslands, representing 11% of the total, fall within very favourable zones, where topographic impact is negligible or very low, with slopes between 0–5° and an east-southeast aspect. These areas provide excellent conditions for mowing and grazing, without exploitation constraints or risks of physical degradation.

A total of 36% of the grasslands, equivalent to 45,135 ha, are slightly affected by topographic conditions (impact class 2), corresponding to slopes of 5.1–10° and S-SW aspects, yet generally remaining favourable for pastoral use. Approximately 43,236 ha, representing 34%, are moderately affected by the A1-TS factor (class 3), located on slopes of 10.1–20° with western exposure, where local difficulties may arise in the application of mechanized maintenance work, along with risks of reduced soil fertility and vegetation productivity. Meanwhile, 22,068 ha of grasslands (18%) are strongly constrained by the same factor (class 4), situated on slopes of 20.1–35° and NW-NE aspects, where erosion vulnerability is high and requires special management interventions. Finally, 973 ha (1%) fall within highly unfavourable areas, strongly influenced by A1-TS (class 5), characterized by slopes exceeding 35.1° and northern exposure, representing the most limited and ecologically fragile terrains regarding use and stability.

Overall, 47% of the grasslands (59,310 ha) lie in favourable or relatively favourable topographic conditions, highlighting a valuable potential for pastoral utilisation. In contrast, grasslands significantly affected by this factor (impact classes 4 and 5) sum up to 23,041 ha (19%), representing areas where adaptive management interventions and institutional support are required.

https://doi.org/10.3390/su18031155

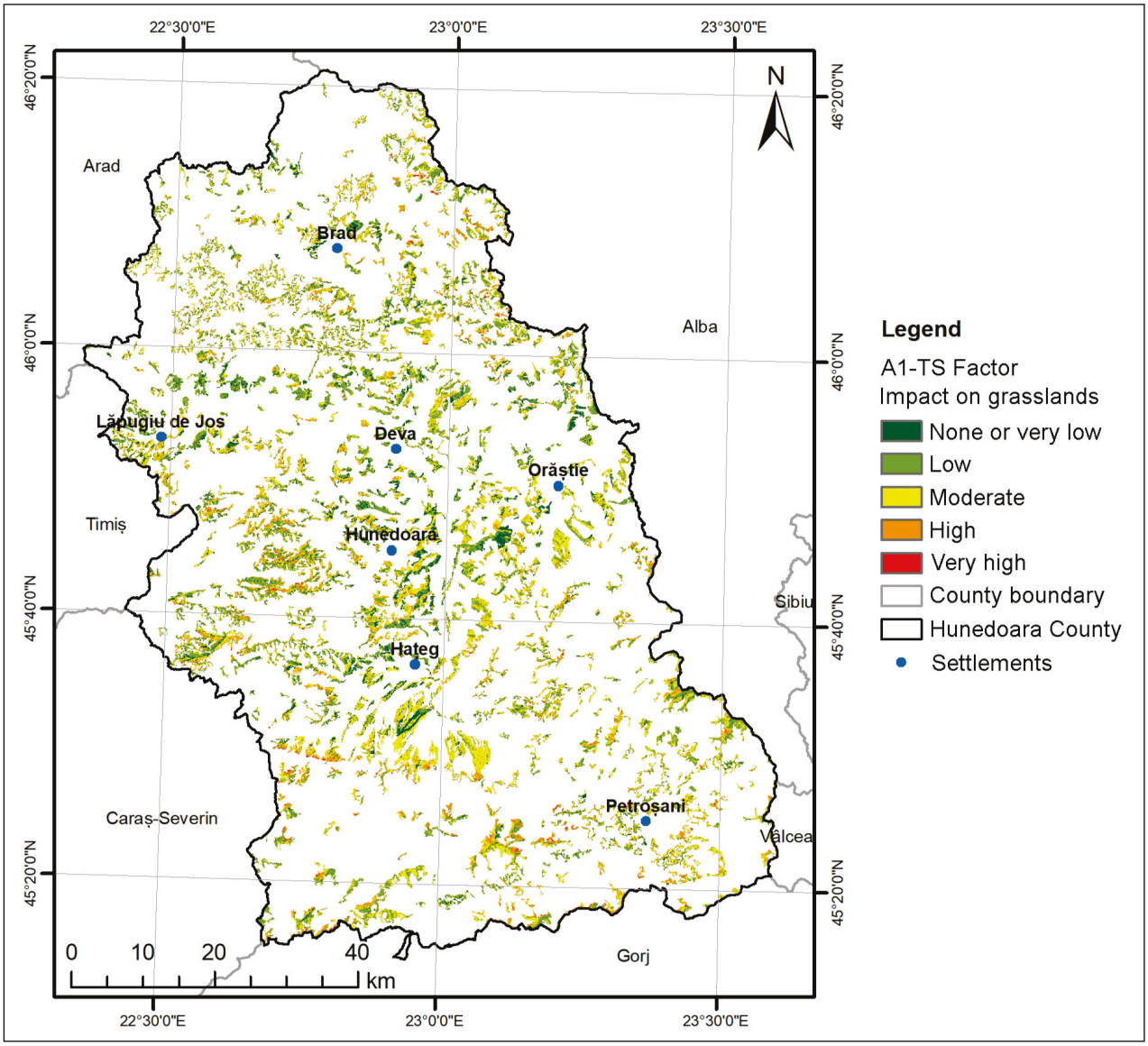

Figure 3. Spatial distribution of grasslands according to the A1-TS factor.

Spatially, grasslands belonging to the favourable and relatively favourable A1-TS classes are predominantly concentrated in the Mureș, Orăștie and Bistra corridors, as well as in the Hunedoara and Hațeg depressions, where gentler relief supports pastoral use. In contrast, strongly and very strongly constrained classes are mainly located in the Retezat, Parâng, Țarcu and Vâlcan mountain ranges, where steep slopes and unfavourable exposure limit accessibility and management intensity.

Climatic Pressure (A2-CP)

Based on Lang Index values and therefore on climatic impact, grasslands were grouped into four classes, distributed as shown in Figure 4.

Results indicate that 81,781 ha of grasslands, representing 63% of the total area, occur under favourable climatic conditions, being very weakly or weakly affected by climatic pressure. Of these, 40,053 ha (31%) fall within class 1, defined by temperate-humid climatic conditions with no major climatic constraints, while 41,728 ha (32%) belong to class 2, specific to a humid climate, slightly more sensitive to seasonal variations yet still favourable for vegetation development (Figure 4).

https://doi.org/10.3390/su18031155

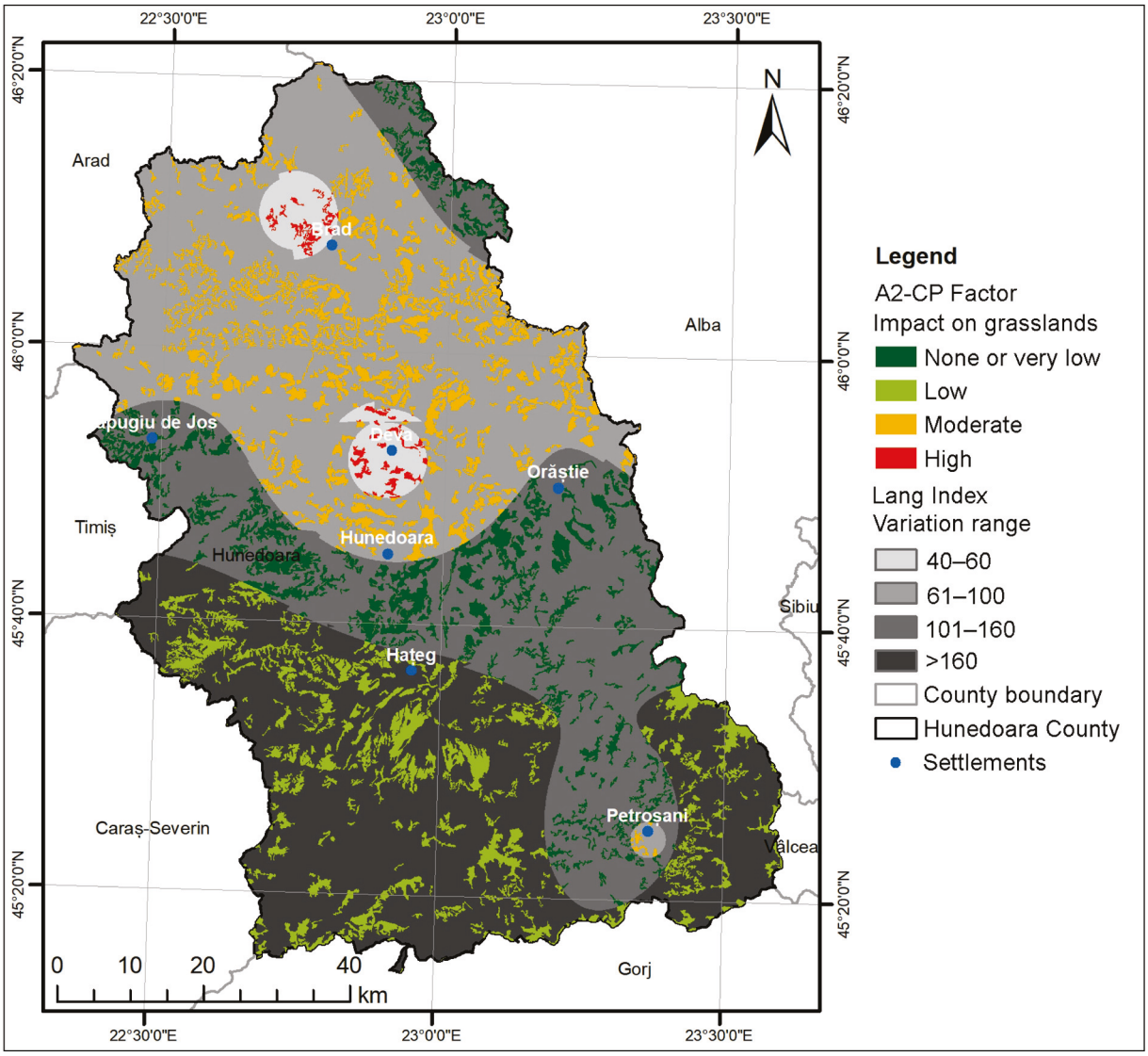

Figure 4. Spatial distribution of grasslands according to the A2-CP factor.

Additionally, 34% of the grasslands (44,542 ha) are moderately affected by climatic conditions (class 3. warm temperate climate), where episodes of thermal or hydric stress may become relevant during certain seasons, particularly in lowland and hilly areas.

The area under high climatic pressure (class 4) is very limited, totalling only 3161 ha (≈2%). These grasslands are located in semi-arid zones (R = 40–60), where reduced water availability and elevated temperatures can restrict vegetation development and lower production capacity, requiring monitoring and adaptive management measures.

Overall, the spatial distribution of grasslands according to the A2-CP factor indicates a clear predominance of favourable climatic conditions for sustainable grassland development and use. Thus, 98% of grassland surfaces occur in areas with null/low or moderate climatic pressure, supporting the stability of these ecosystems and their agricultural potential within the socio-economic context of rural communities.

The spatial distribution of climatic vulnerability classes highlights a concentration of favourable conditions within intramontane depressions and low-altitude corridors (Hunedoara, Hațeg, Mureș), while higher climatic pressure classes are associated with high mountain areas of the Retezat, Parâng and Șureanu ranges, where altitude and exposure intensify thermal and hydric stress.

Hydrological Risk Exposure (A3-HRE)

https://doi.org/10.3390/su18031155

From the perspective of the A3-HRE factor, grasslands in the study area were classified into five impact classes based on their distance from rivers, as illustrated in Figure 5.

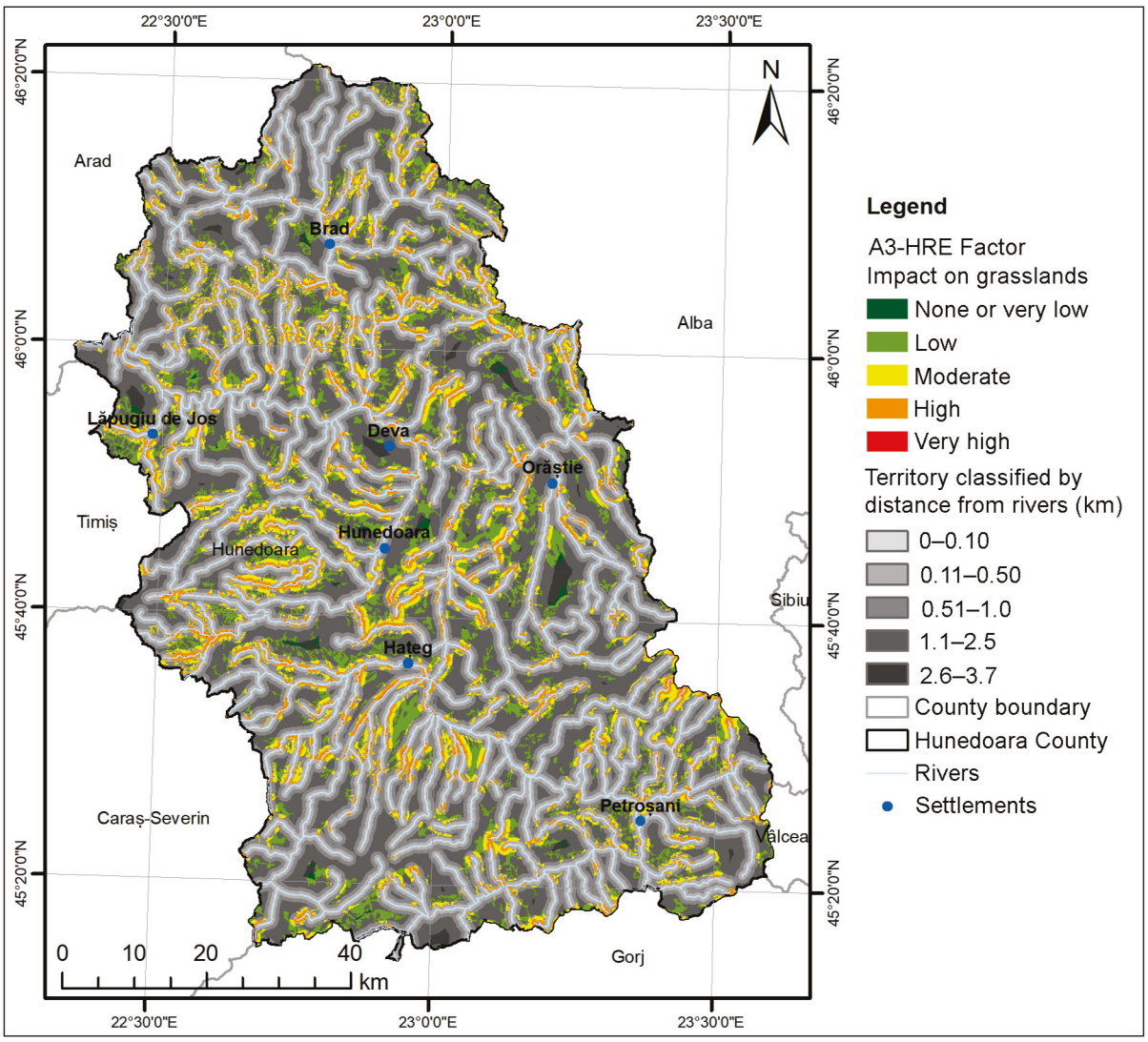

Figure 5. Spatial distribution of grasslands according to the A3-HRE factor.

In this context, A3-HRE should be interpreted as a proximity-based indicator reflecting relative exposure to moisture-related constraints in the vicinity of watercourses, rather than as a direct representation of flood hazard or hydrological processes. The spatial pattern therefore highlights areas potentially affected by excess soil moisture or management limitations associated with river proximity, without implying detailed differentiation of floodplain morphology or hydrodynamic behaviour.

Spatial analysis results show that most of the grasslands included in the study are located at safe distances from watercourses, and are therefore less exposed to flood risk. Only 1% of the total surface (1176 ha) falls within class 1, characterised by null or very low hydrological impact, located more than 2.6 km from the hydrographic network. A proportion of 35% of grasslands, totalling 45,604 ha, falls within class 2, where hydrological impact is low and distances from rivers range between 1.1 and 2.5 km. Additionally, 42,744 ha (33% of the total) correspond to the moderate-risk class, situated 0.51–1.0 km from the river network.

Grasslands belonging to these three categories amount to 69% of the total (89,524 ha) and define the most favourable areas in terms of hydrological exposure (Figure 5).

https://doi.org/10.3390/su18031155

Conversely, 5% of the grassland area (6611 ha) lies within less than 100 m from watercourses (class 5), representing highly vulnerable zones where flood events may significantly impact vegetation; meanwhile, 26% of grasslands (33,350 ha) are located 101–500 m from rivers, exhibiting a high level of exposure and requiring continuous monitoring and, in some cases, protection and mitigation measures.

Spatially, grasslands with low A3-HRE exposure are mainly located on interfluves and mountain slopes, whereas higher exposure classes are concentrated along major river corridors, particularly within the Mureș corridor and the Hunedoara and Hațeg depressions, where proximity to watercourses imposes additional management constraints.

3.1.2. Ecological Values and Conservation

Ecological Conservation Value (B1-ECV)

Overlay analysis results indicate that 42,041 ha of grasslands (32%) fall within protected areas (Figure 6), zones in which human activities are strictly regulated and ecological processes enjoy formal protection. These areas are considered highly favourable in terms of ecological value, playing a key role in maintaining ecosystem integrity.

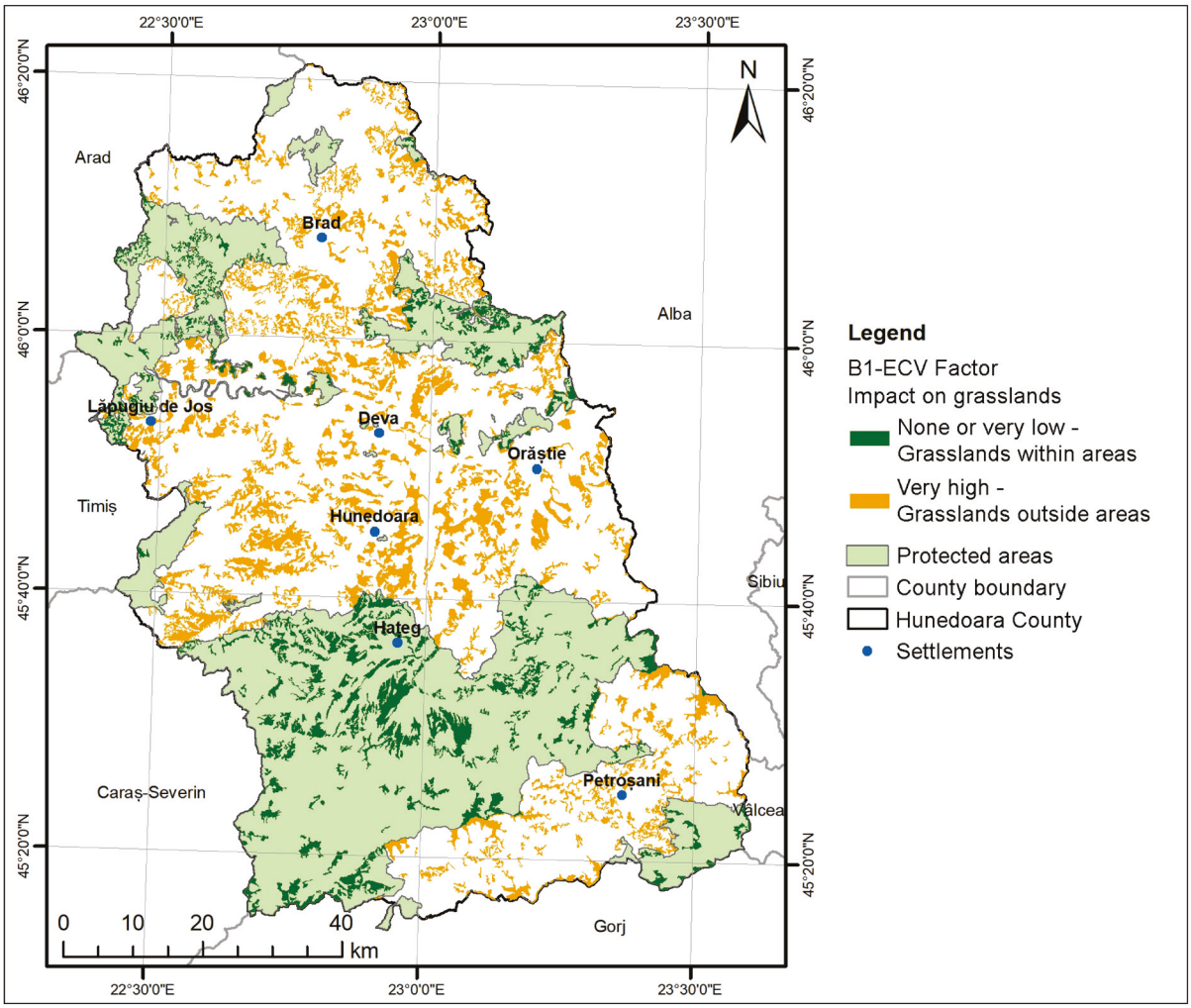

Figure 6. Spatial distribution of grasslands according to the B1-ECV factor.

Of the total grassland area analysed, 68% (87,481 ha) lies outside protected natural areas, which makes these surfaces more vulnerable to conversion, degradation or intensification in the absence of clear ecological protection measures.

https://doi.org/10.3390/su18031155

The spatial distribution of grasslands according to the B1-ECV factor illustrates a contrasting reality: although a significant proportion of grasslands is included within protected areas, the majority of the surface (over two thirds) does not benefit from an institutional conservation framework. In this sense, the B1-ECV factor enables the identification of ecologically favourable grasslands while simultaneously signalling the need for additional sustainable management measures for those located outside the protected area network.

Grasslands overlapping protected areas are mainly concentrated within the Retezat, Țarcu, Parâng and Vâlcan mountain ranges, reflecting the spatial coincidence between high ecological value grasslands and major conservation units. In contrast, grasslands outside protected areas dominate corridors and depressions, where land-use pressures are generally higher.

Ecological Carrying Capacity (B2-ECC)

The results of the B2-ECC-based assessment (Figure 7) show that the most favourable grasslands, from the perspective of zoopastoral balance, are those with optimal utilisation or low-pressure regimes. Thus, 37,540 ha, representing 29% of the total surface, fall into the category of optimal use, approaching the natural support capacity, while 51,541 ha (40%) lie within the low-impact class, characterised by low but sustainable grazing pressure, allowing efficient vegetation regeneration.

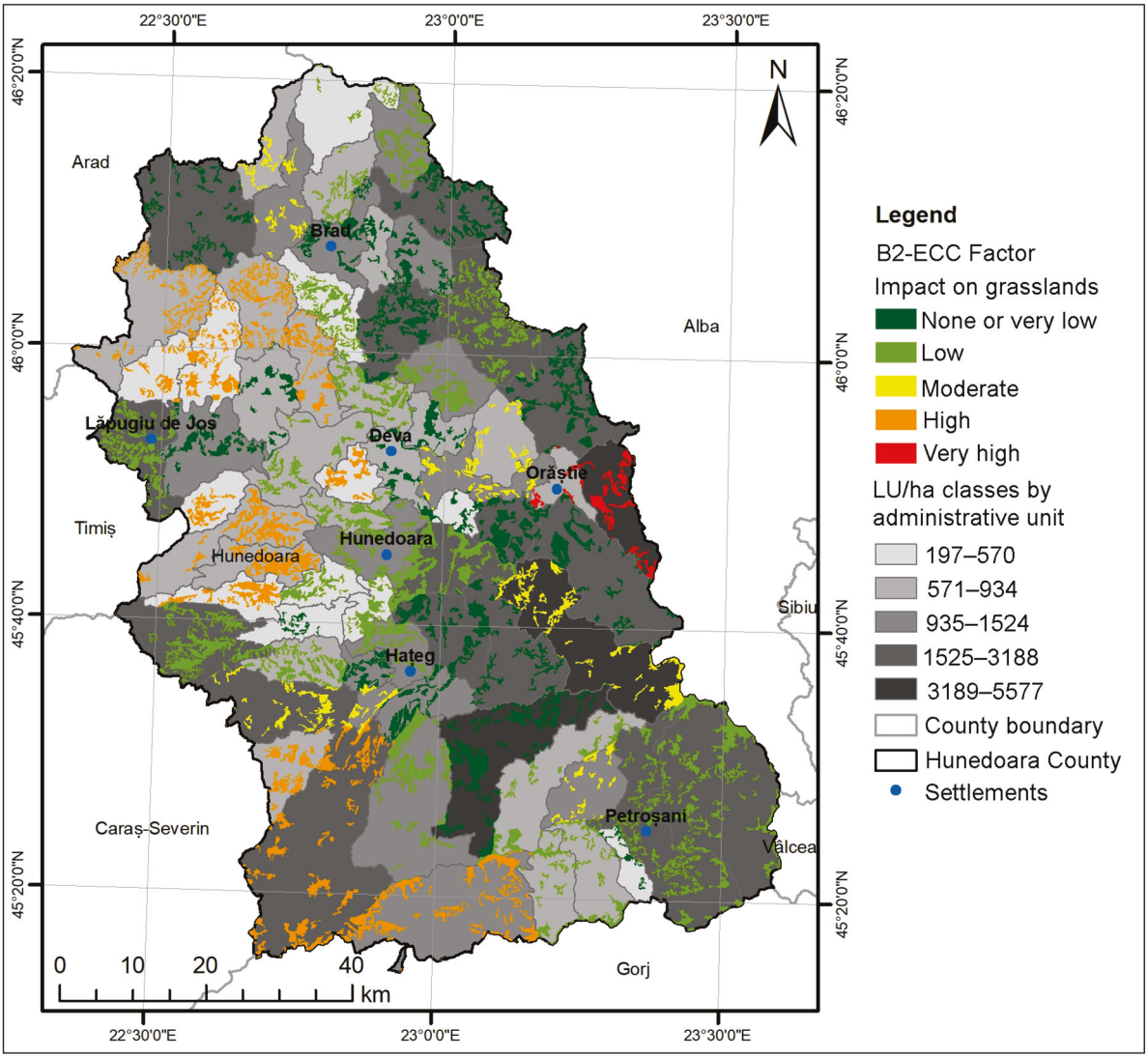

Figure 7. Spatial distribution of grasslands according to the B2-ECC factor.

https://doi.org/10.3390/su18031155

Together, these two categories account for approximately 70% of the grasslands, indicating a general trend of moderate and balanced use across the study area.

However, clear dysfunctions are also present. A total of 9563 ha (7%) fall into the class of grasslands moderately affected by the B2-ECC factor, where livestock load ranges between 1.10 and 2.00 LU/ha and the risk of overgrazing becomes significant. Additionally, 28,536 ha (22%) were classified in the high-impact class due to underutilisation, defined by less than 0.40 LU/ha, reflecting sectors where pastoral resources are insufficiently exploited. Furthermore, 2335 ha (2% of the total) belong to class 5, where livestock pressure exceeds 2.10 LU/ha, indicating excessive grazing impact with degrading effects on vegetation cover and soil stability.

The spatial pattern of B2-ECC reflects the administrative aggregation of livestock density data and therefore highlights differences in grazing pressure and management intensity between territorial units rather than fine-scale ecological gradients. The resulting geometry is an inherent characteristic of the underlying statistical data and should be interpreted as an indicator of management-related pressure on grasslands, complementing the physically continuous variables included in the model.

The spatial pattern of the B2-ECC indicator shows more balanced grassland use in mountain and submontane areas, particularly in the Poiana Ruscă, Șureanu and Metaliferi units, while underuse is more frequent in peripheral and poorly accessible areas, and overgrazing occurs locally in depressions and corridors with high livestock density.

Anthropic Pressure Index (B3-API)

The distribution of grasslands according to the B3-API factor (Figure 8) highlights major differences in the anthropogenic pressure exerted on pastoral resources. Thus, 13,813 ha (11% of the total) fall into the class where B3-API impact is null or very low, corresponding to GAII values between 0.71–1.0 ha/inhabitant, reflecting an optimal ratio between available resources and the potential user population. On 44,947 ha (35%), pressure is low, indicated by GAII values between 1.1 and 4.0 ha/inhabitant, which favours the maintenance of a balance between use and conservation. A proportion of 15% (20,036 ha) lies within the moderate-impact class (GAII 0.51–0.70 ha/inhabitant), where anthropogenic pressure becomes visible and may gradually reduce the vegetation's regenerative capacity.

Furthermore, 35,539 ha (27%) fall into the high-impact category, with GAII values between 0.10–0.50 ha/inhabitant; these grasslands are located in densely populated areas or in regions with insufficient pastoral resources, indicating overexploitation and increased degradation risk. Finally, 15,179 ha (12%) exhibit very high B3-API impact (GAII 4.1–7.7 ha/inhabitant), representing areas where grassland availability is high but risks of underuse, abandonment or establishment of low-value forage vegetation are significant.

The results show a large variation in anthropogenic pressure depending on the local socio-demographic context. Nearly 40% of grasslands (classes 3 and 4) occur in areas where the ratio between population and pastoral resource is unbalanced and requires protective measures.

Spatially, grasslands characterised by null or low B3-API impact are mainly concentrated in mountain and submontane areas, particularly within the Retezat, Țarcu, Godeanu and Vâlcan ranges, where population density is low and pastoral use is extensive or seasonal. In contrast, high and very high impact classes are predominantly located in the Hunedoara and Hațeg depressions, as well as in the Mureș and Orăștie corridors, where population concentration and land fragmentation generate increased socio-ecological pressure on grassland resources.

https://doi.org/10.3390/su18031155

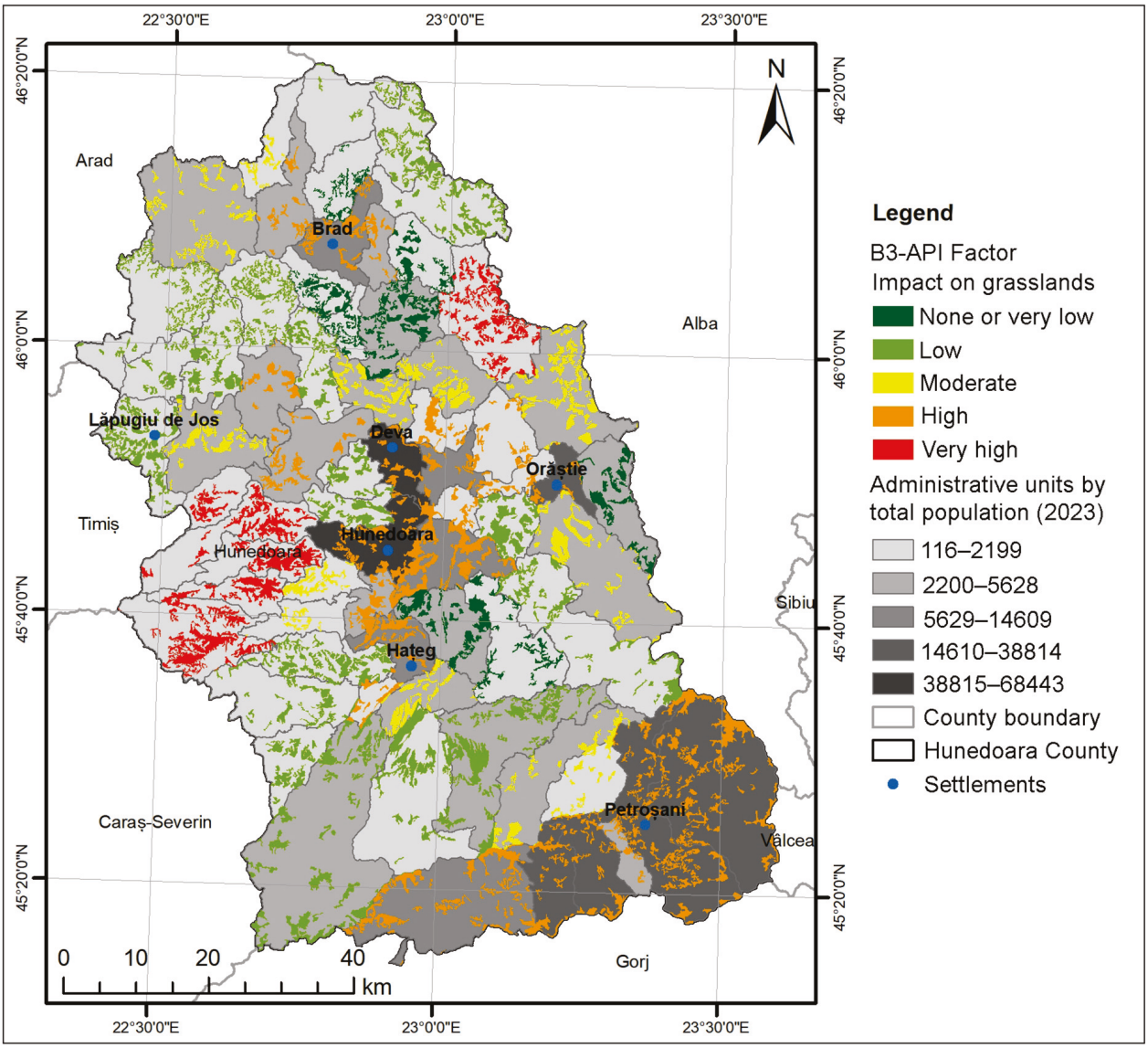

Figure 8. Spatial distribution of grasslands according to the B3-API factor.

3.1.3. Accessibility, Functionality and Institutional Support

Spatial Accessibility (C1-SA)

Spatial analysis results show that most grasslands included in the study benefit from good connectivity to the road network. A total of 65,426 ha (51% of the surface) lie within less than 5 km of road infrastructure, the most favourable category, where rapid access facilitates efficient and economically viable exploitation. Additionally, 39,497 ha (31%) are located 5.1–10 km from road networks, which indicates generally good accessibility but with slightly increased logistical constraints (Figure 9).

Together, the two categories previously mentioned account for more than 80% of the total grassland area (104,923 ha), confirming the generally favourable role of the road network in supporting the utilisation of these resources.

Regarding less accessible areas, 24,128 ha of grasslands (18%) are located 10.1–20 km from roads, often situated in mountainous or marginal zones where pastoral activities may be more costly or seasonally restricted. Only 434 ha (<1%) lie more than 20 km from the road network, representing isolated grasslands with limited accessibility and low agricultural potential according to this indicator-unless infrastructural improvements are implemented.

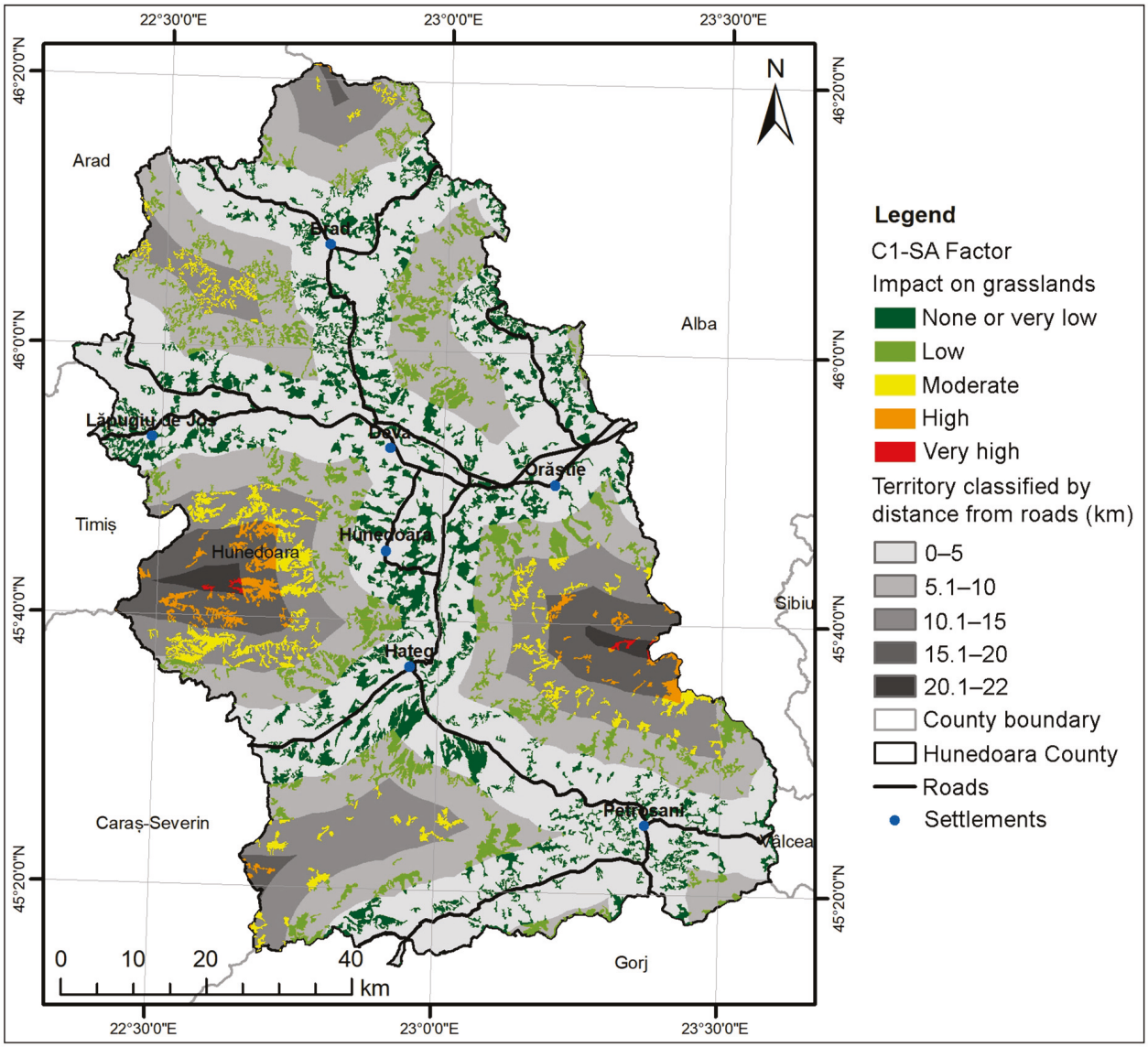

Figure 9. Spatial distribution of grasslands according to the C1-SA factor.

Spatially, grasslands with high accessibility are concentrated in the Mureș, Orăștie and Hunedoara corridors, where road network density facilitates regular use. In contrast, grasslands with low accessibility are mainly located in the Retezat, Godeanu, Țarcu and Parâng mountain ranges, where infrastructure is limited and use is often seasonal or extensive.

Recreational Valuation (C2-RV)

Following geospatial layer interpretation, results show that 57,495 ha of grasslands (45%) are located less than 10 km from areas of tourist interest (Figure 10).

Grasslands located at medium to long distances from tourist attractions show a gradual decrease in recreational potential: 15,601 ha (12%) lie 15.1–20 km away, while 37,572 ha (29%) are situated more than 20 km from tourism sites, in areas with minimal tourist influence, where integration into visitation circuits or rural tourism projects would require additional investment. This distribution highlights that a substantial proportion of grasslands (more than one third) benefit from good or very good recreational accessibility, opening opportunities for economic diversification in rural communities, reducing pressure from exclusive agricultural use, and enhancing their social value.

https://doi.org/10.3390/su18031155

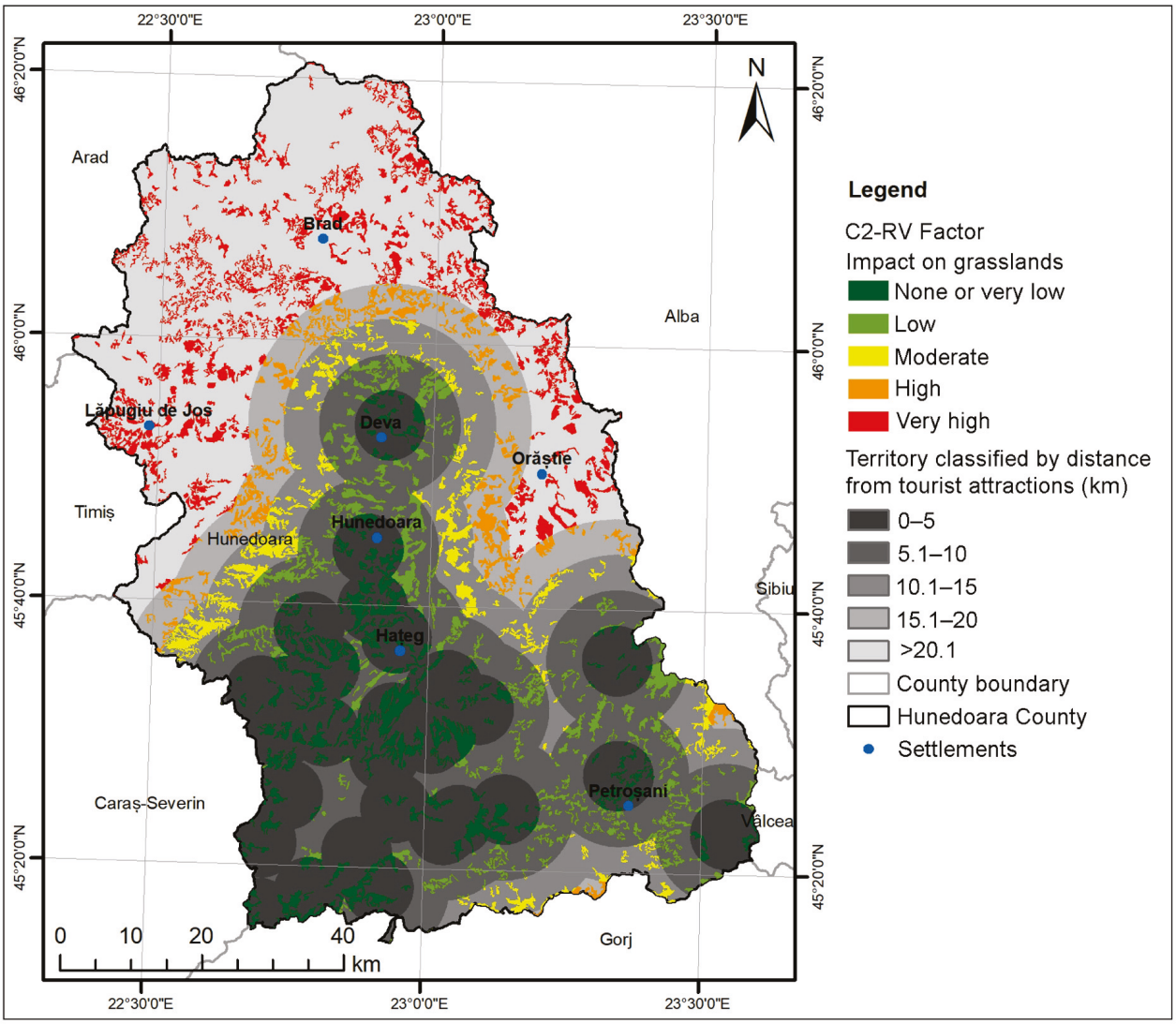

Figure 10. Spatial distribution of grasslands according to the C2-RV factor.

Grasslands with high recreational potential are predominantly located near the Retezat, Parâng and Șureanu mountain ranges, as well as within the Hunedoara and Hațeg depressions, where major tourist attractions and related infrastructure are concentrated. In contrast, grasslands situated in peripheral or weakly connected areas, particularly in the southern and south-western parts of the county, exhibit low recreational potential.

Policy Support Mechanism (C3-PSM)

The results show that a large proportion of the grassland surface benefits from effective support schemes (Figure 11). A total of 92,181 ha, representing 71% of the total, fall under cumulative support through M10 and M13-MZ measures, contributing significantly to maintaining ecological quality and productivity, particularly in mountain regions or areas with high natural value. Additionally, 28,027 ha of grasslands (22%) benefit exclusively from M10-P1 and P2 support, which provides partial but still effective assistance for preserving agro-ecological functions.

Areas where support is more specific or limited occupy comparatively reduced surfaces. A total of 6257 ha (5%) fall under M10-P3.2 measures aimed at bird habitat conservation, with moderate influence on direct grassland use. Moreover, 3049 ha (2%) benefit from support targeted especially toward areas severely affected by natural constraints (M13-SNC), in combination with M10.

https://doi.org/10.3390/su18031155

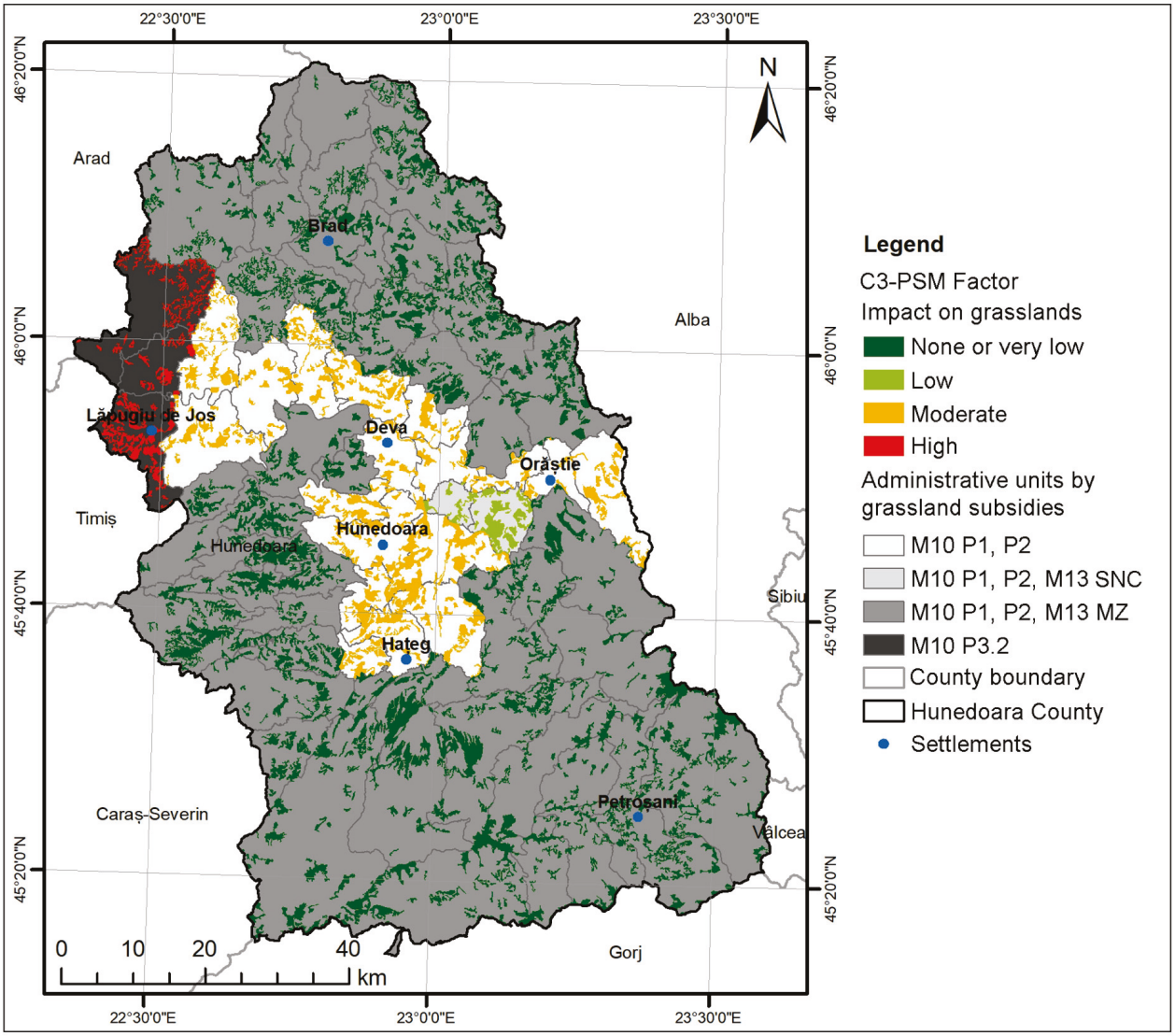

Figure 11. Spatial distribution of grasslands according to the C3-PSM factor.

The spatial distribution of institutional support shows a concentration of cumulative measures (M10 and M13) in mountain and submontane areas, particularly within the Retezat, Țarcu, Parâng and Vâlcan ranges, where natural constraints justify stronger support. In contrast, partial or limited support schemes are more frequent in lowland corridors and depressions, where socio-economic pressures are higher and eligibility for compensatory measures is more restricted.

Before integrating the nine factors into the multicriteria evaluation through the WOA method, a correlation analysis was performed to avoid possible informational overlaps that might affect the validity of the weights established through AHP. Thus, a Pearson correlation matrix was generated based on reclassified values extracted from a random sample of 500 points distributed across the study area and visualised as a heatmap (Figure 12).

The results indicate a low correlation between most factor pairs ($r < 0.3$), suggesting distinct spatial variability and a low degree of redundancy.

The analysis of relative factor contributions indicates that the resulting suitability is not driven by a single dominant factor, but rather by interactions and trade-offs between biogeophysical constraints, anthropogenic pressures, and the institutional framework. In some cases, favorable natural conditions are partially offset by accessibility or institutional limitations, leading to differentiated positioning within the suitability classes.

https://doi.org/10.3390/su18031155

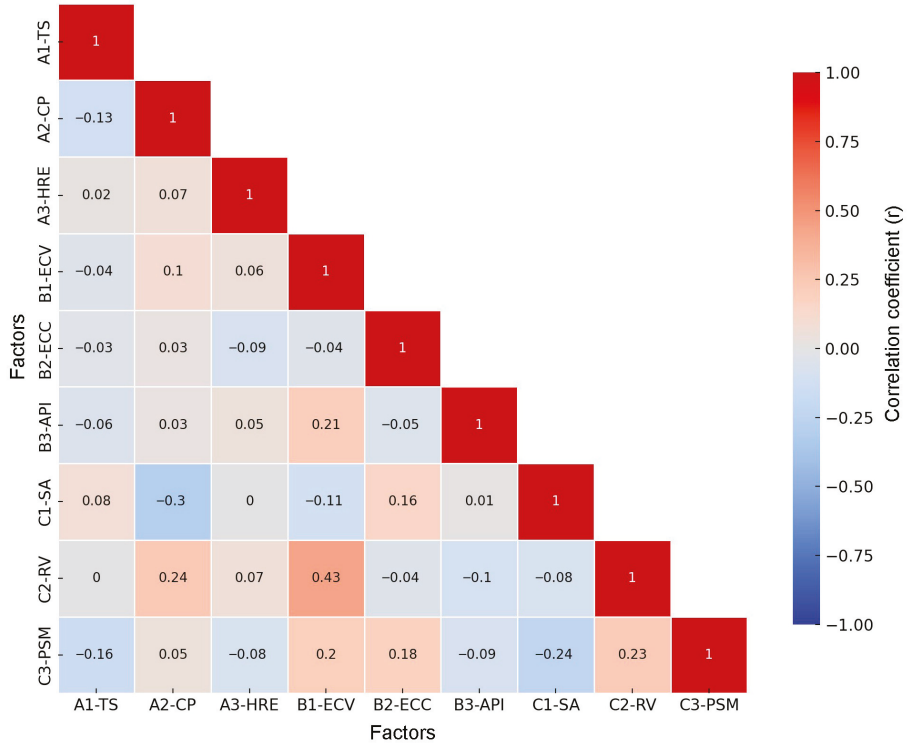

Figure 12. Heatmap of correlation coefficients between the assessment factors (lower-triangle values displayed).

3.2. Composite Grassland Potential Score

Following the WOA multicriteria analysis, the total grassland surface was classified into four favourability (potential) classes (Figure 13).

1. Class 1-grasslands with very high potential; this class includes 498 grassland entities, covering a total area of 503 ha (0.43% of the total). The average size of these units is 1.01 ha, with a maximum of 252.39 ha and a standard deviation of 11.34 ha.

Grasslands in this category are characterised by a low level of overall limitations resulting from the integration of factors, driven primarily by favourable physical-geographical conditions and the presence of a conservation-related institutional framework. The very high potential reflects low anthropogenic pressure and a regulatory regime rather than conditions of socio-economic intensification.

2. Class 2-grasslands with high potential; this is the most extensive class, comprising 6842 grassland entities and a total area of 52,221 ha (44.51%). The average area is 7.63 ha, with moderate variability (standard deviation of 46.40 ha).

These grasslands correspond to areas with a relatively low combined influence of limiting factors within the integrated index. The classification reflects the outcome of weighted multicriteria integration of the analysed factors, rather than the process-based accumulation of individual constraints, indicating generally favourable conditions with moderate limitations arising from different groups of factors.

3. Class 3-Moderate-potential grasslands: includes 5717 units, totalling 64,229 ha (54.75% of the analysed surface). The mean area is 11.23 ha and the standard deviation is 65.34 ha, indicating a more heterogeneous distribution. Grasslands in this class are subject to moderate limitations and require targeted interventions to improve suitability.

4. Class 4-Unfavourable grasslands: the least represented category, with only 459 grassland units covering 362 ha (0.31%). The mean surface is 0.79 ha, with a standard deviation of 1.76 ha, showing a predominance of small, scattered plots. Unfavourable

https://doi.org/10.3390/su18031155

grasslands are characterised by high cumulative impact and require restoration, rehabilitation or potential land-use reconversion.

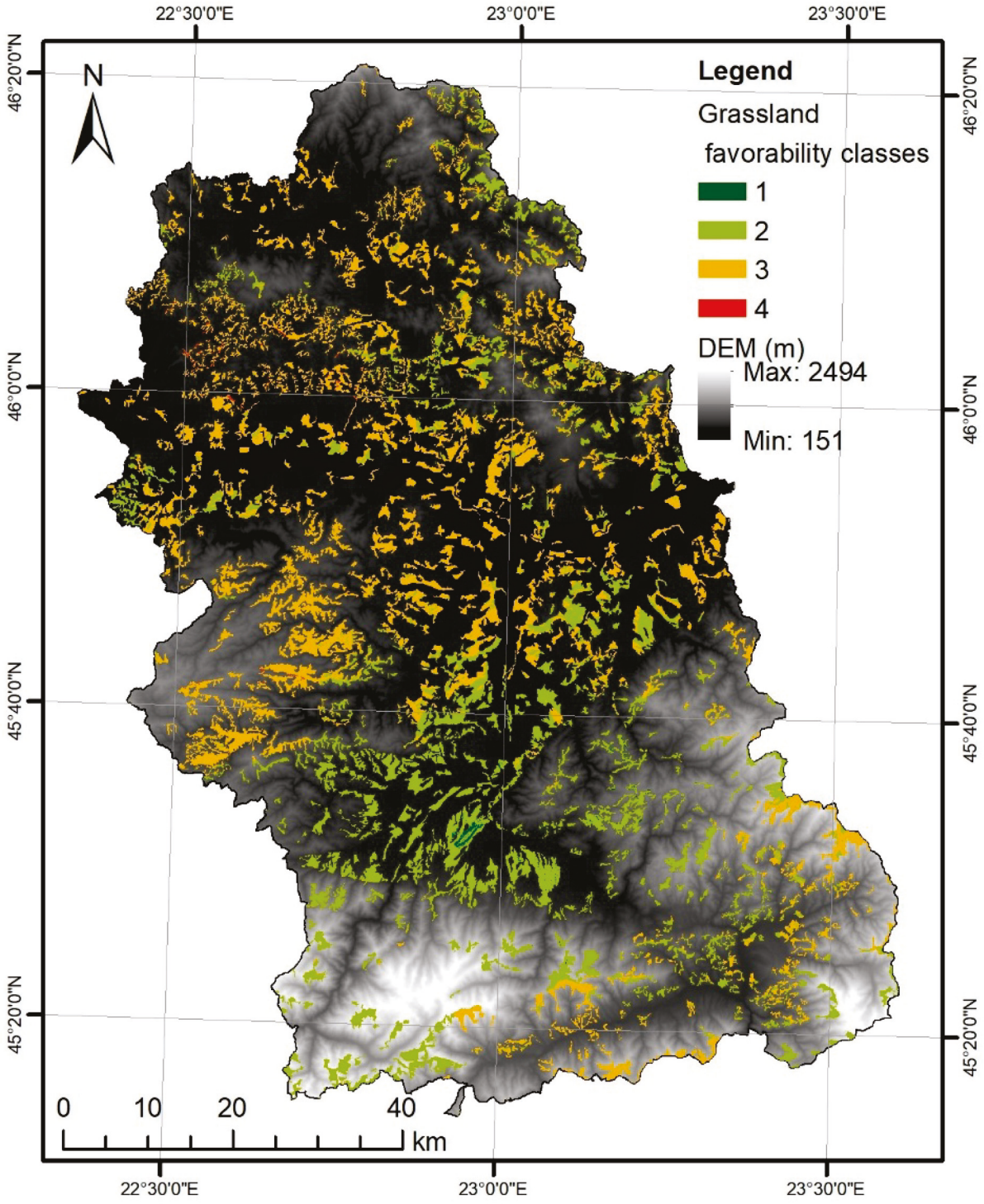

Figure 13. Grassland favorability map in Hunedoara County (WOA results).

From a spatial perspective, grasslands with very high and high potential are predominantly concentrated in lowland corridors and intramontane depressions (Mureș, Orăștie, Hunedoara, Hațeg), as well as in submontane areas of the Poiana Ruscă, Metaliferi and Șureanu ranges, where favourable physical conditions coincide with good accessibility and institutional support. In contrast, grasslands with moderate potential dominate extensive mountain areas, reflecting trade-offs between topographic constraints, ecological pressures,

https://doi.org/10.3390/su18031155

and accessibility limitations. Unfavourable classes are scarce and spatially fragmented, mainly associated with peripheral, poorly accessible or strongly constrained areas, where the cumulative effect of limiting factors significantly reduces pastoral functionality.

Although the results are presented as discrete suitability classes, these classes aggregate continuous multicriteria scores, implying a notable degree of internal heterogeneity. In particular, areas located at the boundaries between moderate and high suitability reflect gradual transitions in environmental conditions, accessibility, and institutional support rather than sharp spatial thresholds.

The integrated analysis of the absolute values and relative proportions associated with the nine factors included in the WOA model revealed notable variations among the four grassland suitability classes.

The mean favourability score, computed as a weighted sum of the reclassified factor values (via WOA), ranges from 1.43 in Class 1 (very high-potential grasslands) to 3.55 in Class 4 (unfavourable grasslands). This gradient reflects a gradual deterioration of ecological and territorial conditions, expressed through the cumulative influence of limiting factors (Figure 14).

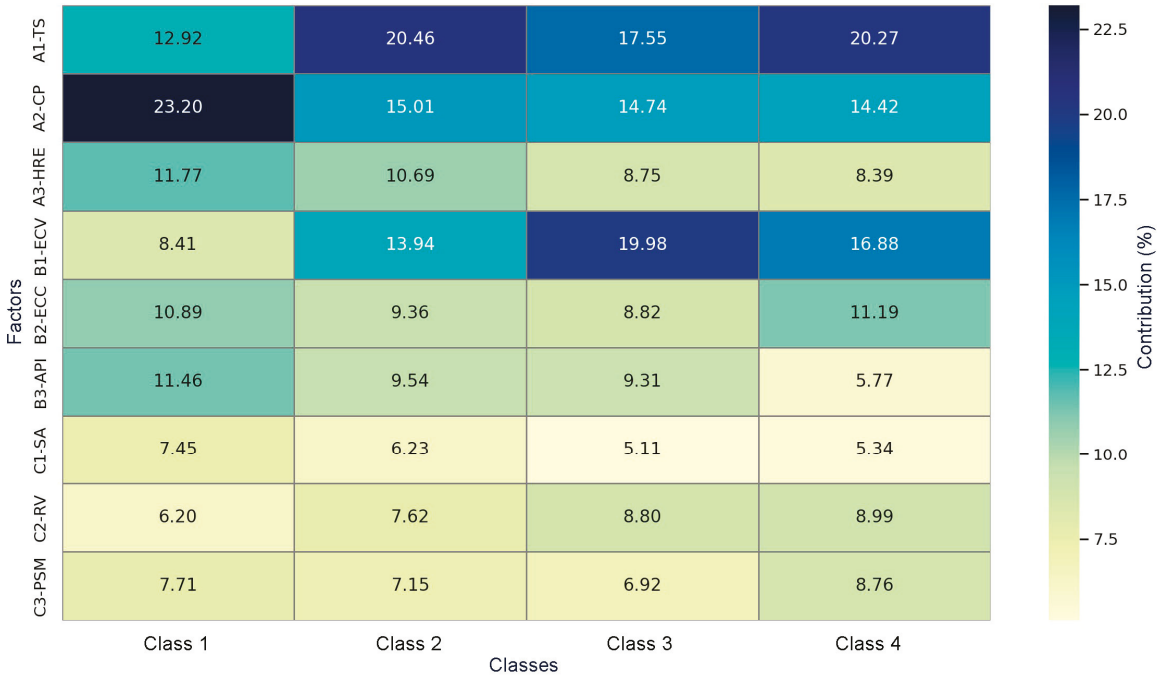

Figure 14. Factors contribution to grassland favorability classes.

Regarding the relative contribution of each factor to the total score per class (Figure 14), several distinctive patterns can be observed.

In Class 1, representing grasslands with very high potential, factor A2-CP shows the highest contribution (23.20%), followed by topographic conditioning A1-TS (12.92%) and hydrological exposure A3-HRE (11.77%). This configuration indicates that the most favourable grasslands occur in areas with optimal physico-geographical conditions and low anthropogenic pressure.

In Class 2, corresponding to high-potential grasslands, the influence of A1-TS increases substantially (20.46%), while the weight of B1-ECV doubles compared to Class 1 (13.94%), suggesting a shift towards areas with slightly more restrictive physical geography but with stronger ecological protection due to the presence of natural protected areas.

In Class 3, which includes grasslands with moderate potential, B1-ECV becomes dominant (19.98%), signalling increased ecological pressure. At the same time, the contribution

of socio-economic factors (C2-RV and C3-PSM) rises slightly, indicating that anthropogenic influences become more apparent.

In Class 4, which comprises unfavourable grasslands, the influence of topographic factors reaches its maximum (20.27%), while the role of institutional and tourism-related factors continues to increase. This trend is generally associated with the peripheral location of these grasslands and insufficient infrastructure in the most disadvantaged areas.

Overall, the combined interpretation of absolute values and relative weights shows that A1-TS, A2-CP and B1-ECV are the primary determinants of grassland favourability. By contrast, socio-ecological variables, C1-SA, C2-RV and C3-PSM, exert a lower influence across the overall study area, yet become increasingly relevant in marginal zones where grasslands are less functional and involve greater limitations for productive use.

The results should be interpreted in light of the inherent limitations of multicriteria aggregation, which involves the generalization of complex spatial processes and the discretization of continuous variables. In this context, the suitability map represents a synthetic decision-support tool, while a more detailed interpretation of spatial patterns, marginal areas, and policy implications is developed in the Section 4.

4. Discussion

4.1. Grassland Suitability as a Result of the Interaction Between Natural Constraints, Ecological Pressures, and the Socio-Institutional Context

The suitability map obtained through the integration of WOA analysis with AHP weights highlights a distribution dominated by intermediate suitability classes, reflecting the heterogeneous territorial conditions of Hunedoara County. More than 99% of the analyzed grassland area falls within the moderate, high, and very high suitability classes, while areas classified as unsuitable have a limited spatial extent. This distribution is consistent with findings reported in other GIS-MCDA applications conducted in mountainous or hilly regions, where the integration of biogeophysical, ecological, and socio-economic criteria commonly results in a concentration of scores in the mid-range rather than in extreme polarizations [32,36,39,44,46,69–72].

The interpretation of these results requires methodological caution. Within the MCDA framework, factor weights and contributions indicate their relative importance in differentiating suitability classes rather than the direct intensity of pressures or the absolute degree of constraint. Accordingly, factors such as topographic conditioning (A1-TS) and climatic pressure (A2-CP), which have high weights (18% each), primarily act as structural factors, explaining the spatial variation in suitability without necessarily implying degradation or severe limitations. For instance, although 19% of grasslands are located on slopes steeper than 20° (A1-TS classes 4 and 5), these areas are not inherently excluded from use but rather require adapted management practices and differentiated access, as also reported in other GIS-AHP applications carried out in complex relief settings [39,44].

The distribution of physical-geographical factors confirms the existence of clear territorial thresholds. From a climatic perspective, approximately 98% of grasslands fall into classes characterized by null, low, or moderate climatic pressure (Lang index > 60), indicating a generally favorable framework for vegetation development and for grazing and mowing use. Areas with high climatic pressure (≈2% of the total area) are spatially limited and do not significantly influence the overall suitability structure at the county scale, a situation comparable to that reported in similar studies conducted in European mountainous regions [32,73].

The ecological dimension introduces important functional differentiations. Approximately 32% of grasslands are located within protected natural areas, conferring high ecological value but also additional constraints on use. At the same time, carrying-capacity

https://doi.org/10.3390/su18031155

analysis shows that about 70% of grasslands operate under optimal or low-pressure use regimes (≤1 LU/ha), while nearly 24% are characterized by underutilization (<0.40 LU/ha), and around 9% indicate values associated with overgrazing risk (>1.10 LU/ha). Such functional imbalances are frequently reported in the literature on mountainous grasslands and highlight the need to link suitability assessments with conservation objectives and adaptive management strategies [32,41,44].

Socio-economic and institutional factors further refine the interpretation of suitability. More than 80% of grasslands are located within 10 km of the road network, indicating good accessibility; however, the distribution of socio-demographic pressure is highly contrasting. Approximately 39% of grasslands fall within classes of high and very high socio-ecological pressure, reflecting either resource overexploitation in densely populated areas or underutilization in areas affected by depopulation. In this context, institutional support (weighted at 11%) plays a key role in the functional differentiation of grasslands, particularly in mountainous and peripheral areas [62], where eligibility for measures M10 and M13 can offset accessibility constraints and demographic pressures, in line with European approaches to High Nature Value farmland and the compensation of natural constraints [74–77].

Recent studies emphasize the usefulness of integrating GIS and multicriteria analyses into territorial planning processes and the design of agricultural policy instruments, especially in vulnerable rural or mountainous contexts, where natural and socio-economic constraints require spatially differentiated, decision-oriented approaches [24,78–82].

Therefore, the suitability derived from the model should not be interpreted as a simple hierarchy of grassland "quality", but rather as an expression of territorial compatibility among environmental conditions, use intensity, and the support framework. Similar to other GIS-AHP applications functioning as spatial decision-support systems, the results enable the identification of distinct patterns: areas with high suitability but vulnerable to underutilization; areas with moderate suitability where adaptive management is critical; and areas where cumulative constraints suggest prioritizing conservation or restoration interventions [37,39,80,83].

This integrated interpretation provides the suitability map with operational value for rural planning and sustainable grassland management and is aligned with recent trends in the development of Spatial Decision Support Systems for agricultural and territorial policies [38,48,84–88].

4.2. Contribution of Factors and the Decision-Support Value of the GIS-AHP-WOA Model

The analysis of the weights derived from the application of the Analytic Hierarchy Process (AHP) highlights the differentiated role of the selected factors in structuring the composite suitability score and, implicitly, the model's capacity to spatially discriminate between distinct grassland types.

In this context, it is essential to emphasize that these weights do not express the direct intensity of environmental or socio-economic pressures. Instead, they reflect the relative importance of each factor within the multicriteria process used to differentiate alternatives, in accordance with MCDA logic [28,30,37].

Physical-geographical factors, particularly topographic conditioning (A1-TS) and climatic pressure (A2-CP), which recorded the highest weights (18% each), act as structural elements of the model, controlling the baseline spatial variation of suitability. This observation is consistent with the results of other GIS-MCDA applications conducted in mountainous and hilly regions, where topography and climate are recognized as dominant factors in delineating land functional potential through their cumulative influence on accessibility, ecological stability, and use-related costs [21,35,36,39]. However, their high

weight within the model does not imply a direct causal relationship with degradation or use limitation, but rather reflects their capacity to spatially differentiate suitability classes within a territory characterized by complex relief.

Ecological factors (B1-ECV and B2-ECC), weighted at 12% and 10%, respectively, introduce an essential qualitative dimension into the interpretation of results, related to conservation value and the balance of livestock use relative to grassland carrying capacity. The integration of these criteria makes it possible to identify situations in which suitability derived from natural conditions is moderate or high but is accompanied by institutional constraints or functional risks associated with underutilization or overuse. This approach is consistent with studies emphasizing the need to link suitability assessments with conservation objectives and the maintenance of ecosystem services, particularly in mountainous grasslands [41,43–45,89–91].

Socio-economic and institutional factors (C1-SA, C2-RV, and C3-PSM), although characterized by lower individual weights (between 7% and 11%), play an important role in refining the interpretation of suitability and in transforming the resulting map into a decision-support tool. In particular, institutional support (C3-PSM), with a weight of 11%, highlights how policy frameworks can modulate the feasibility of grassland use, especially in areas characterized by physical-geographical constraints or limited accessibility. This finding is consistent with literature emphasizing the role of agricultural and rural development policies in maintaining the functional use of grasslands and reducing the risk of abandonment in marginal areas [15,38,40,92–95].

From a decision-making perspective, the main value of the GIS-AHP-WOA model does not lie in the simple ranking of grasslands into suitability classes, but in its ability to highlight distinct combinations of factors that lead to similar or contrasting outcomes. Thus, grasslands assigned to the same suitability class may exhibit different functional profiles: some are predominantly constrained by natural conditions, while others are limited by socio-demographic pressures or institutional constraints. This differentiation is essential for using the model as a Spatial Decision Support System (SDSS), enabling the adaptation of management interventions, support measures, and planning objectives to local contexts [37,40–42,93,95].

In this respect, the proposed model aligns with contemporary approaches in the GIS-MCDA literature that go beyond static suitability mapping and aim to support decision-making processes in contexts characterized by multiple constraints and potentially conflicting objectives [29,41,96]. By coherently integrating physical-geographical, ecological, and socio-institutional criteria, the GIS-AHP-WOA framework provides a transparent analytical basis for prioritizing interventions and facilitating dialogue between land-use, conservation, and rural development objectives, without assuming simplified causal relationships between factors and outcomes.

4.3. Uncertainties, Limitations, and Directions for Future Research

As with any spatial multicriteria analysis, the proposed GIS-AHP-WOA model is subject to a set of uncertainties and limitations that must be considered when interpreting the results and using them for decision support. A first source of uncertainty is related to the quality and spatial resolution of the input data. The exclusive use of open-source datasets ensured the reproducibility and transferability of the methodology, but it also imposed spatial generalizations, particularly for variables available at the administrative level (e.g., livestock density and socio-demographic pressure). These generalizations may mask fine-scale local variations and should therefore be interpreted as contextual indicators rather than as detailed representations of parcel-level processes [37,86,96].

https://doi.org/10.3390/su18031155

A second limitation arises from the process of criteria selection and weighting using the AHP method. Although the evaluations were conducted by consensus and validated through consistency indicators (CR < 0.10), the assignment of weights remains inherently dependent on expert judgment [30,93,96]. Consequently, the results should not be interpreted as absolute values, but rather as the outcome of a coherent analytical framework designed to highlight relative spatial differentiation. The sensitivity of the model to moderate variations in weights was not explored exhaustively, representing an important direction for future research.

The discretization of continuous variables into ordinal classes and their aggregation through Weighted Overlay Analysis constitute another potential source of uncertainty. Although the reclassification thresholds were established based on the literature and local data distributions, this step involves an inherent loss of information and may influence the boundaries between suitability classes [37,39]. Accordingly, transitions between classes should be interpreted as zones of functional continuity rather than as abrupt breaks in grassland quality or usability.

In addition, the model adopts a static approach based on multiannual average conditions and relatively stable territorial structures. As a result, it does not capture the temporal dynamics of grassland use, rapid changes in socio-economic pressures, or the short-term effects of extreme climatic events. The integration of dynamic components or prospective scenarios could improve the explanatory and decision-support capacity of the model.

Despite these limitations, the GIS-AHP-WOA framework provides a coherent and transparent representation of relative grassland suitability at the county scale. Explicitly acknowledging uncertainties does not diminish the value of the results; rather, it clarifies their domain of applicability and emphasizes that the suitability map should be used as a strategic, decision-support and guidance tool, complementary to detailed analyses and field-based assessments.

In this context, future research may focus on testing the sensitivity of the model to variations in weights and reclassification thresholds, integrating higher-resolution or temporally explicit data (e.g., multiannual time series derived from remote sensing), and exploring alternative land-use and institutional support scenarios, with the aim of strengthening the role of the model as an adaptive decision-support tool for rural planning and sustainable grassland management.

5. Conclusions

This study demonstrates the applicability of integrating the Analytic Hierarchy Process (AHP) within a GIS framework, combined with Weighted Overlay analysis, for the spatial assessment of grassland suitability and for supporting sustainable management decisions at the regional scale. The application of the GIS-AHP-WOA model in Hunedoara County highlights differentiated territorial patterns resulting from the interaction between physical-geographical constraints, ecological values, and the socio-institutional context.

The results indicate that more than 99% of the grassland area falls within moderate, high, and very high suitability classes, suggesting a generally favorable potential for use. However, the integrated analysis of factors reveals significant functional imbalances: approximately 24% of grasslands are characterized by underutilization (<0.40 LU/ha), while about 9% show risks associated with overgrazing (>1.10 LU/ha), underscoring the need for differentiated management interventions.

Topographic conditioning and climatic pressure, which recorded the highest weights in the model (18% each), act as structural drivers of spatial suitability, while ecological and socio-institutional factors further refine use feasibility at the local level. In this context, institutional support (11%) plays a key role in maintaining the functional use of grass-

https://doi.org/10.3390/su18031155

lands, particularly in mountainous and peripheral areas, where natural constraints and demographic pressures are more pronounced.

The main contribution of the study lies in treating grasslands as functional decision units and in positioning the GIS-AHP-WOA model as a spatial decision-support system capable of supporting the prioritization of management, conservation, and rural planning interventions. The methodology is reproducible, based on open-source geospatial data, and transferable to other regions characterized by complex relief and multiple constraints.

The explicit acknowledgment of methodological limitations and uncertainties emphasizes that the results should be used as a strategic guidance tool, complementary to detailed analyses. Future research may focus on testing the sensitivity of the model to variations in weights and on integrating dynamic components, with the aim of strengthening its role in supporting sustainable grassland management.

Author Contributions: Conceptualization, L.L.C., N.M.H. and L.C.; methodology, L.L.C. and L.C.; software, C.A.P., N.M.H., A.H. and L.C.; validation, L.L.C., N.M.H., C.A.P., A.H., M.B.-S. and L.C.; formal analysis, N.M.H., C.A.P., A.H. and M.B.-S.; investigation, L.L.C., A.H., M.B.-S. and L.C.; resources, N.M.H., C.A.P. and A.H.; data curation, N.M.H. and M.B.-S.; writing-original draft preparation, L.L.C., N.M.H., M.B.-S. and L.C.; writing-review and editing, L.L.C. and L.C.; visualization, L.L.C., N.M.H., C.A.P., A.H., M.B.-S. and L.C.; supervision, L.L.C., C.A.P. and A.H.; project administration, L.L.C., N.M.H. and L.C.; funding acquisition, N.M.H., C.A.P. and A.H. All authors have read and agreed to the published version of the manuscript.

Funding: The publication of the present paper was supported by the University of Life Sciences "King Mihai I" from Timisoara, Romania.

Institutional Review Board Statement: Not applicable.

Informed Consent Statement: Not applicable.

Data Availability Statement: The raw data supporting the conclusions of this article will be made available by the authors on request.

Acknowledgments: The authors thank the GEOMATICS Research Laboratory, University of Life Sciences "King Mihai I" from Timişoara, for the facility of software used for this study.

Conflicts of Interest: The authors declare no conflicts of interest.

References

1. Török, P.; Janišová, M.; Kuzemko, A.; Rūsiņa, S.; Dajić Stevanović, Z. Grasslands, Their Threats and Management in Eastern Europe. In *Grasslands of the World: Diversity, Management and Conservation*; Squires, V.R., Dengler, J., Hua, L., Feng, H., Eds.; CRC Press: Boca Raton, FL, USA, 2018; pp. 64–88. [CrossRef]
2. Păcurar, F.S.; Rotar, I.; Vaida, I.; Gaga, I.; Costantea, D. Ecological and Agronomical Value of *Agrostis capillaris-Festuca rupicola* Grasslands. *Rom. J. Grassl. Forage Crops* **2020**, *22*, 55–62.
3. Bengtsson, J.; Bullock, J.M.; Egoh, B.; Everson, C.; Everson, T.; O'Connor, T.; O'Farrell, P.J.; Smith, H.G.; Lindborg, R. Grasslands-More Important for Ecosystem Services than You Might Think. *Ecosphere* **2019**, *10*, e02582. [CrossRef]
4. Pergola, M.; De Falco, E.; Cerrato, M. Grassland Ecosystem Services: Their Economic Evaluation Through a Systematic Review. *Land* **2024**, *13*, 1143. [CrossRef]
5. Stanciu, A. Sustainable Forage Yield Improvement Through Perennial Grass-Legume Intercropping in Degraded Grasslands. *Turk. J. Agric. For.* **2025**, *49*, 215–241. [CrossRef]
6. Canișag, E.; Samuil, C.; Sîrbu, C.; Nazare, A.-I.; Grigoraş, B.-I.; Vîntu, V. The Effect of Fertilization on Floristic Composition and Biodiversity of Montane Grasslands (HNV) in the Eastern Carpathians. *Plants* **2026**, *15*, 80. [CrossRef]
7. Samuil, C.; Stavarache, M.; Sîrbu, C.; Vîntu, V. Influence of Sustainable Fertilization on Yield and Quality Food of Mountain Grassland. *Not. Bot. Horti Agrobot. Cluj-Napoca* **2018**, *46*, 410–417. [CrossRef]
8. Ghețe, I.; Rotar, I.; Pleșa, A.; Ghețe, A.; Șerban, C.; Stoian, V. Effect of Mineral Fertilization on Vegetation of HNV Pastures in the Apuseni Mountains (Romania). *Plants* **2025**, *14*, 3564. [CrossRef]
9. Janišová, M.; Škodová, I.; Magnes, M.; Iuga, A.; Biro, A.-S.; Ivașcu, C.M.; Ďuricová, V.; Buzhdygan, O.Y. Role of Livestock and Traditional Management Practices in Maintaining High Nature Value Grasslands. *Biol. Conserv.* **2025**, *309*, 111301. [CrossRef]

10. Cojocariu, L.L.; Copăcean, L.; Ursu, A.; Sărățeanu, V.; Popescu, C.A.; Horablaga, M.N.; Bordean, D.-M.; Horablaga, A.; Bostan, C. Assessment of the Impact of Population Reduction on Grasslands with a New "Tool": A Case Study on the "Mountainous Banat" Area of Romania. *Land* **2024**, *13*, 134. [CrossRef]
11. Călușeru, A.L.; Cojocariu, L.; Horablaga, M.N.; Bordean, D.M.; Horablaga, A.; Cojocariu, A.; Borozan, A.B.; Iancu, T. Romanian national strategy for the conservation of biodiversity 2013–2020: Integration of European environmental policies. In Proceedings of the SGEM 2013 Conference Proceedings, Albena, Bulgaria, 16–22 June 2013; Volume 2, pp. 723–728. Available online: https://www.proquest.com/docview/1462397524?pq-origsite=gscholar&fromopenview=true&sourcetype=Conference%20Papers%20&%20Proceedings (accessed on 24 November 2015).
12. Vaida, I.; Păcurar, F.; Rotar, I.; Tomoș, L.; Stoian, V. Changes in Diversity Due to Long-Term Management in a High Natural Value Grassland. *Plants* **2021**, *10*, 739. [CrossRef]
13. Dey, R.; Sharma, S.B.; Thakkar, M.G. Maximising Ecological Value and Assessing Land Suitability for Sustainable Grassland Management in Asia's Largest Tropical Grassland, Western India. *Sci. Rep.* **2024**, *14*, 13658. [CrossRef]
14. Călușeru, L.A.; Cojocariu, L.; Borlea, F.; Bordean, D.M.; Horablaga, A. Rural development of mountain areas in Romania: Challenges and targets for the year 2020. In Proceedings of the SGEM 2015 Conference Proceedings, Albena, Bulgaria, 18–24 June 2015; Volume 5, pp. 791–798.
15. Ravetto Enri, S.; Nucera, E.; Lonati, M.; Alberto, P.F.; Probo, M. The Biodiversity Promotion Areas: Effectiveness of Agricultural Direct Payments on Plant Diversity Conservation in the Semi-Natural Grasslands of the Southern Swiss Alps. *Biodivers. Conserv.* **2020**, *29*, 4155–4172. [CrossRef]
16. Morán-Alonso, N.; Viedma-Guiard, A.; Simón-Rojo, M.; Córdoba-Hernández, R. Agricultural Land Suitability Analysis for Land Use Planning: The Case of the Madrid Region. *Land* **2025**, *14*, 134. [CrossRef]
17. Navarro, L.M.; Pereira, H.M. Rewilding Abandoned Landscapes in Europe. *Ecosystems* **2012**, *15*, 900–912. [CrossRef]
18. van der Zanden, E.H.; Verburg, P.H.; Schulp, C.J.E.; Verkerk, P.J. Trade-Offs of European Agricultural Abandonment. *Land Use Policy* **2017**, *62*, 290–301. [CrossRef]
19. Pawlewicz, A.; Pawlewicz, K. The Risk of Agricultural Land Abandonment as a Socioeconomic Challenge for the Development of Agriculture in the European Union. *Sustainability* **2023**, *15*, 3233. [CrossRef]
20. Dolton-Thornton, N. Viewpoint: How Should Policy Respond to Land Abandonment in Europe? *Land Use Policy* **2021**, *102*, 105269. [CrossRef]
21. Bozdağ, A.; Yavuz, F.; Dönertaş, A. AHP and GIS-Based Land Suitability Analysis for Cihanbeyli (Turkey) County. *Environ. Earth Sci.* **2016**, *75*, 555. [CrossRef]
22. D'Adamo, I.; Gastaldi, M. Sustainable Development Goals: A Regional Overview Based on Multi-Criteria Decision Analysis. *Sustainability* **2022**, *14*, 9779. [CrossRef]
23. Gherdan, A.E.M.; Bacter, R.V.; Maerescu, C.M.; Iancu, T.; Ciolac, R.; Ungureanu, A. Sustainable Tourism Development in Mountain Regions: A Case Study of Peștera Village, Brasov County, Applying the Analytic Hierarchy Process. *Sustainability* **2025**, *17*, 1452. [CrossRef]
24. Heydari, R.; Fathololoumi, S.; Soltanbeygi, M.; Firozjaei, M.K. A Sustainability-Oriented Spatial Multi-Criteria Decision Analysis Framework for Optimizing Recreational Ecological Park Development. *Sustainability* **2025**, *17*, 731. [CrossRef]
25. Chandio, I.A.; Matori, A.N.B.; Wan Yusof, K.B.; Talpur, M.A.H.; Balogun, A.L.; Lawal, D.U. GIS-Based Analytic Hierarchy Process as a Multicriteria Decision Analysis Instrument: A Review. *Arab. J. Geosci.* **2013**, *6*, 3059–3066. [CrossRef]
26. Patriche, C.V.; Roșca, B.; Pîrnău, R.G.; Vasiliniuc, I.; Irimia, L.M. Digital Mapping of Land Suitability for Main Agricultural Crops in Romania. *Agronomy* **2024**, *14*, 2828. [CrossRef]
27. Yegizbayeva, A.; Aitekeyeva, N.; Konstantinova, K.; Bekmukhamedov, N.; Zhumabay, N.; Balgabayev, N. Geospatial Technology Utilization for Evaluating Land Suitability for Irrigation. *Sustainability* **2025**, *17*, 10131. [CrossRef]
28. Tudes, S.; Yigiter, N.D. Preparation of Land Use Planning Model Using GIS Based on AHP: Case Study Adana-Turkey. *Bull. Eng. Geol. Environ.* **2010**, *69*, 235–245. [CrossRef]
29. AbdelRahman, M.A.E.; Yossif, T.M.H.; Metwaly, M.M. Enhancing land suitability assessment through integration of AHP and GIS-based for efficient agricultural planning in arid regions. *Sci. Rep.* **2025**, *15*, 31370. [CrossRef] [PubMed]
30. Saaty, T.L.; Tran, L.T. On the Invalidity of Fuzzifying Numerical Judgments in the Analytic Hierarchy Process. *Math. Comput. Model.* **2007**, *46*, 962–975. [CrossRef]
31. Gbanie, S.P.; Tengbe, P.B.; Momoh, J.S.; Medo, J.; Kabba, V.T.S. Modelling Landfill Location Using Geographic Information Systems (GIS) and Multi-Criteria Decision Analysis (MCDA): Case Study Bo, Southern Sierra Leone. *Appl. Geogr.* **2013**, *36*, 3–12. [CrossRef]
32. Souissi, D.; Zouhri, L.; Hammami, S.; Msaddek, M.H.; Zghibi, A.; Dlala, M. GIS-Based MCDM-AHP Modeling for Flood Susceptibility Mapping of Arid Areas, Southeastern Tunisia. *Geocarto Int.* **2019**, *35*, 991–1017. [CrossRef]

33. Abdullah, M.F.; Siraj, S.; Hodgett, R.E. An Overview of Multi-Criteria Decision Analysis (MCDA) Application in Managing Water-Related Disaster Events: Analyzing 20 Years of Literature for Flood and Drought Events. *Water* **2021**, *13*, 1358. [CrossRef]
34. Hammami, S.; Zouhri, L.; Souissi, D.; Souei, A.; Zghibi, A.; Marzougui, A.; Dlala, M. Application of the GIS-Based Multi-Criteria Decision Analysis and Analytical Hierarchy Process (AHP) in Flood Susceptibility Mapping (Tunisia). *Arab. J. Geosci.* **2019**, *12*, 653. [CrossRef]
35. Vegad, U.; Pokhrel, Y.; Mishra, V.; Ghosh, A.; Kar, S.K. Application of Analytical Hierarchy Process (AHP) for Flood Risk Assessment: A Case Study in Malda District of West Bengal, India. *Nat. Hazards* **2018**, *94*, 349–368. [CrossRef]
36. Kumar, R.; Kumar, M.; Tiwari, A.; Majid, S.I.; Bhadwal, S.; Sahu, N.; Avtar, R. Assessment and Mapping of Riverine Flood Susceptibility (RFS) in India through Coupled Multicriteria Decision Making Models and Geospatial Techniques. *Water* **2023**, *15*, 3918. [CrossRef]
37. Geneletti, D. An Approach Based on Spatial Multi-Criteria Analysis to Map the Nature Conservation Value of Agricultural Land. *J. Environ. Manag.* **2007**, *83*, 228–235. [CrossRef] [PubMed]
38. Nguyen, T.; Verdoodt, A.; Tran, Y.; Delbecque, N.; Tran, T.; Van Ranst, E. Design of a GIS and Multi-Criteria Based Land Evaluation Procedure for Sustainable Land-Use Planning at the Regional Level. *Agric. Ecosyst. Environ.* **2014**, *200*, 1–11. [CrossRef]
39. Yalew, S.G.; van Griensven, A.; Mul, M.L.; van der Zaag, P. Land Suitability Analysis for Agriculture in the Abbay Basin Using Remote Sensing, GIS and AHP Techniques. *Model. Earth Syst. Environ.* **2016**, *2*, 101. [CrossRef]
40. Kazemi, H.; Akinci, H. A Land Use Suitability Model for Rainfed Farming by Multi-Criteria Decision-Making Analysis (MCDA) and Geographic Information System (GIS). *Ecol. Eng.* **2018**, *116*, 1–6. [CrossRef]
41. Ennaji, W.; Barakat, A.; El Baghdadi, M.; Oumenskou, H.; Aadraoui, M.; Karroum, L.A.; Hilali, A. GIS-Based Multi-Criteria Land Suitability Analysis for Sustainable Agriculture in the Northeast Area of Tadla Plain (Morocco). *J. Earth Syst. Sci.* **2018**, *127*, 79. [CrossRef]
42. Xu, J.; Jiao, C.; Zheng, D.; Li, L. Agricultural Land Suitability Assessment at the County Scale in Taiyuan, China. *Agriculture* **2024**, *14*, 16. [CrossRef]
43. Memarbashi, E.; Azadi, H.; Barati, A.A.; Mohajeri, F.; Passel, S.V.; Witlox, F. Land-Use Suitability in Northeast Iran: Application of AHP-GIS Hybrid Model. *ISPRS Int. J. Geo-Inf.* **2017**, *6*, 396. [CrossRef]
44. Vázquez-Quintero, G.; Prieto-Amparán, J.A.; Pinedo-Alvarez, A.; Valles-Aragón, M.C.; Morales-Nieto, C.R.; Villarreal-Guerrero, F. GIS-Based Multicriteria Evaluation of Land Suitability for Grasslands Conservation in Chihuahua, Mexico. *Sustainability* **2020**, *12*, 185. [CrossRef]
45. Ozsahin, E.; Ozdes, M. Agricultural Land Suitability Assessment for Agricultural Productivity Based on GIS Modeling and Multi-Criteria Decision Analysis: The Case of Tekirdağ Province. *Environ. Monit. Assess.* **2022**, *194*, 41. [CrossRef] [PubMed]
46. Cojocariu, L.; Hoancea, L.; Horablaga, N.M.; Copăcean, L.; Bordean, D.M. Assessment of the Physical and Socio-Economic Potential of the Grasslands in Banat, Romania in a Holistic Approach. *Sci. Pap. Ser. Manag. Econ. Eng. Agric. Rural Dev.* **2024**, *24*, 329–339.
47. Nyeko, M. GIS and Multi-Criteria Decision Analysis for Land Use Resource Planning. *J. Geogr. Inf. Syst.* **2012**, *4*, 341–348. [CrossRef]
48. Kouriati, A.; Tafidou, A.; Lialia, E.; Prentzas, A.; Moulogianni, C.; Dimitriadou, E.; Bournaris, T. A Multicriteria Decision Analysis Model for Optimal Land Uses: Guiding Farmers under the New European Union's Common Agricultural Policy (2023-2027). *Land* **2024**, *13*, 788. [CrossRef]
49. Posea, G.; Badea, I. *România. Unitățile de Relief (Regionarea Geomorfologică) (Relief Units-Geomorphological Region)*; Editura Științifică și Enciclopedică: București, Romania, 1984.
50. European Environment Agency. EU-DEM-European Environment Agency Dataset. 2015. Available online: https://www.eea.europa.eu/en/datahub/datahubitem-view/d08852bc-7b5f-4835-a776-08362e2fbf4b (accessed on 10 December 2015).
51. Copernicus Land Monitoring Service. Corine Land Cover (CLC). 2025. Available online: https://land.copernicus.eu/pan-european/corine-land-cover (accessed on 15 March 2025).
52. Geospatial. *România: Seturi de Date Vectoriale Generale*; Geospatial: Bucharest, Romania, 2021. Available online: http://geospatial.org/vechi/download/romania-seturi-vectoriale (accessed on 12 December 2021).
53. Climatic Databases. 2025. Available online: https://rp5.ru/Weather_in_Romania (accessed on 25 March 2025).
54. Bunea, A.; Mălinaș, A.; Ilieș, D.C.; Baias, Ș.; Herman, G.V. Emphasizing the Main Soil Classes and Types Located in Bradului Depression, Romania. *Environ. Eng. Manag. J.* **2020**, *19*, 409–417. [CrossRef]
55. Institutul Național de Statistică (INS). Tempo Online. 2023. Available online: http://statistici.insse.ro:8077/tempo-online/#/pages/tables/insse-table (accessed on 20 March 2025).

56. Sfîrcoci, M. Multidimensional Study of Grasslands in Hunedoara County Through Integrated Approaches and Analyses. Ph.D. Thesis, University of Life Sciences "King Michael I", Timișoara, Romania, 2024. Available online: https://www.usab-tm.ro/utilizatori/universitate/file/doctorat/sustinere_td/2024/sfircoci%20monica/Rezumatul%20tezei.pdf (accessed on 15 March 2025).
57. Copernicus Data Space Ecosystem. *Sentinel-2 Level-2A Data*; European Commission, European Space Agency (ESA): Darmstadt, Germany, 2023. Available online: https://dataspace.copernicus.eu (accessed on 30 November 2025).
58. Agenția Națională de Cadastru și Publicitate Imobiliară (ANCPI). Geoportal ANCPI. Available online: https://geoportal.ancpi.ro/portal/home/ (accessed on 15 December 2024).
59. Ministerul Mediului; Apelor și Pădurilor. Arii Naturale Protejate de Interes Național și Internațional. Available online: https://mmediu.ro/portal-gis/date-spatiale/arii-naturale-protejate-de-interes-national-si-international/ (accessed on 14 September 2025).
60. Romania's Government. Data Sets. 2023. Available online: https://data.gov.ro/ (accessed on 22 March 2022).
61. Evropski Pokret U Banatu. Developing Cultural Tourism in Banat Region—A Cross-Border Challenge. Available online: https://www.epuszr.org.rs/b23.html (accessed on 2 February 2024).
62. Ministry of Agriculture and Rural Development. National Programme of Rural Development (NPRD) 2014-2020, Version December 2018. Available online: https://madr.ro/docs/dezvoltare-rurala/2018/PNDR-2014-2020-versiunea-VIII-aprobata-10-decembrie-2018.pdf (accessed on 11 February 2023).
63. Payment and Intervention Agency for Agriculture (APIA). Maps for the Distribution of the Eligible Zones at the County and Local Center Level. Available online: https://apia.org.ro/materiale-de-informare/materiale-de-informare-anul-2019/ (accessed on 20 April 2022).
64. Esri. ArcGIS Desktop Documentation: ArcMap (Including ArcCatalog, ArcScene, ArcGlobe). Available online: https://desktop.arcgis.com/en/documentation/ (accessed on 15 June 2025).
65. Satmări, A. *Lucrări Practice de Biogeografie*; Editura Eurobit: Timișoara, Romania, 2010; p. 85. Available online: https://www.academia.edu/9909429/05_indici_ecometrici (accessed on 10 March 2020).
66. Iacob, T.; Vîntu, V.; Samuil, C.; Dumitrescu, N. *Pajiștea. Caracterizare-Îmbunătățire-Folosire*; Ion Ionescu de la Brad: Iași, România, 2015.
67. Copăcean, L.; Man, E.T.; Herban, S.; Popescu, C.A.; Cojocariu, L. Estimating Flood Susceptibility Based on GIS and Remote Sensing. Case Study: Hydrographic Basin of Crișul Alb River. *Present Environ. Sustain. Dev.* **2024**, *18*, 121–140. [CrossRef]
68. Dias, A.A.V.; Gunathilake, A.A.J. Analytical Hierarchical Process (AHP) Prioritization of Landslide-Causing Factors. In *Progress in Landslide Research and Technology*; Abolmasov, B., Alcántara-Ayala, I., Arbanas, Ž., Huntley, D., Konagai, K., Arbanas, S.M., Mikoš, M., Ramesh, M.V., Sassa, K., Sassa, S., et al., Eds.; Springer: Cham, Switzerland, 2025; Volume 3. [CrossRef]
69. Cengiz, T.; Akbulak, C. Application of Analytical Hierarchy Process and Geographic Information Systems in Land-Use Suitability Evaluation: A Case Study of Dümrek Village (Çanakkale, Turkey). *Int. J. Sustain. Dev. World Ecol.* **2009**, *16*, 286–294. [CrossRef]
70. Mendas, A.; Delali, A. Integration of MultiCriteria Decision Analysis in GIS to develop land suitability for agriculture: Application to durum wheat cultivation in the region of Mleta in Algeria. *Comput. Electron. Agric.* **2012**, *83*, 117–126. [CrossRef]
71. Torrieri, F.; Batà, A. Spatial Multi-Criteria Decision Support System and Strategic Environmental Assessment: A Case Study. *Buildings* **2017**, *7*, 96. [CrossRef]
72. Aldababseh, A.; Temimi, M.; Maghelal, P.; Branch, O.; Wulfmeyer, V. Multi-Criteria Evaluation of Irrigated Agriculture Suitability to Achieve Food Security in an Arid Environment. *Sustainability* **2018**, *10*, 803. [CrossRef]
73. Wang, Z.; Ma, Y.; Zhang, Y.; Shang, J. Review of Remote Sensing Applications in Grassland Monitoring. *Remote Sens.* **2022**, *14*, 2903. [CrossRef]
74. Wiśniewski, P.; Rudnicki, R.; Kistowski, M.; Wiśniewski, Ł.; Chodkowska-Miszczuk, J.; Niecikowski, K. Mapping of EU Support for High Nature Value Farmlands, from the Perspective of Natural and Landscape Regions. *Agriculture* **2021**, *11*, 864. [CrossRef]
75. Sarvia, F.; De Petris, S.; Borgogno-Mondino, E. Mapping Ecological Focus Areas within the EU CAP Controls Framework by Copernicus Sentinel-2 Data. *Agronomy* **2022**, *12*, 406. [CrossRef]
76. Zhang, X.; Zhu, W.; Yan, N.; Wei, P.; Zhao, Y.; Zhao, H.; Zhu, L. Research on Service Value and Adaptability Zoning of Grassland Ecosystem in Ethiopia. *Remote Sens.* **2022**, *14*, 2722. [CrossRef]
77. Zieliński, M.; Gołębiewska, B.; Jadczyszyn, J.; Adamski, M.; Tyburski, J. Importance of Environmental Measures Under the CAP 2023-2027 on High Nature Value Farmlands: Evidence from Poland. *Sustainability* **2025**, *17*, 7763. [CrossRef]
78. Ursu, A.; Jitariu, V.; Ciutea, A. Estimating the Impact of Human Activities on the Environment in Moldova Region (HI Index). *Present Environ. Sustain. Dev.* **2017**, *11*, 129–140. [CrossRef]
79. Abd El Karim, A.; Alogayell, H.M.; Alkadi, I.I.; Youssef, I. Mapping of GIS-Land Use Suitability in the Rural-Urban Continuum between Ar Riyadh and Al Kharj Cities, KSA Based on the Integrating GIS Multi Criteria Decision Analysis and Analytic Hierarchy Process. *Environments* **2020**, *7*, 75. [CrossRef]

80. Yuan, Z.; Wen, B.; He, C.; Zhou, J.; Zhou, Z.; Xu, F. Application of Multi-Criteria Decision-Making Analysis to Rural Spatial Sustainability Evaluation: A Systematic Review. *Int. J. Environ. Res. Public Health* **2022**, *19*, 6572. [CrossRef]
81. Măgureanu, M.; Sfîrcoci, M.; Copăcean, L.; Cojocariu, L. Monitoring the vegetation coverage of grasslands in the Poiana Ruscă Mountains using different remote sensing indices. *Present Environ. Sustain. Dev.* **2023**, *17*, 189–199. [CrossRef]
82. Niyogakiza, A.; Liu, Q. GIS-Driven Multi-Criteria Assessment of Rural Settlement Patterns and Attributes in Rwanda's Western Highlands (Central Africa). *Sustainability* **2025**, *17*, 6406. [CrossRef]
83. Oncia, S.; Herbei, M.; Popescu, C. Study of Territorial and Infrastructure Development in the Petrosani City, the Hunedoara County, Using GIS Elements. *J. Environ. Prot. Ecol.* **2013**, *14*, 225–231.
84. Wang, X.; Yu, S.; Huang, G.H. Land Allocation Based on Integrated GIS-Optimization Modeling at a Watershed Level. *Landsc. Urban Plan.* **2004**, *66*, 61–74. [CrossRef]
85. Terribile, F.; Agrillo, A.; Bonfante, A.; Buscemi, G.; Colandrea, M.; D'Antonio, A.; De Mascellis, R.; De Michele, C.; Langella, G.; Manna, P.; et al. A Web-Based Spatial Decision Supporting System for Land Management and Soil Conservation. *Solid Earth* **2015**, *6*, 903–928. [CrossRef]
86. Schillaci, C.; Panagos, P.; Marechal, A.; Montanarella, L.; Birli, B.; Munafò, M.; di Leginio, M.; Pump, J.; Stankovics, P.; Zugfil-Maletics, V.; et al. *LANDSUPPORT Decision Support Systems: Performance at EU, Country, Regional and Local Scale*; Publications Office of the European Union: Luxembourg, 2022.
87. Manna, P.; Agrillo, A.; Bancheri, M.; Di Leginio, M.; Ferraro, G.; Langella, G.; Mileti, F.A.; Riitano, N.; Munafò, M. A Geospatial Decision Support System for Supporting the Assessment of Land Degradation in Europe. *Land* **2024**, *13*, 89. [CrossRef]
88. LANDSUPPORT Consortium. LANDSUPPORT: Web-Based Integrated Geospatial Decision Support System for Sustainable Land Management. Available online: https://www.landsupport.eu (accessed on 1 September 2025).
89. Paul, M.; Negahban-Azar, M.; Shirmohammadi, A.; Montas, H. Assessment of Agricultural Land Suitability for Irrigation with Reclaimed Water Using Geospatial Multi-Criteria Decision Analysis. *Agric. Water Manag.* **2020**, *231*, 105987. [CrossRef]
90. Everest, T.; Sungur, A.; Özcan, H. Determination of Agricultural Land Suitability with a Multiple-Criteria Decision-Making Method in Northwestern Turkey. *Int. J. Environ. Sci. Technol.* **2021**, *18*, 1073. [CrossRef]
91. Sathiyamurthi, S.; Saravanan, S.; Karuppannan, S.; Balakumbahan, R.; Sivasakthi, M.; Praveen Kumar, S.; Ramya, M.; Hussain, S.; Tariq, A. Agricultural Land Suitability of Manimutha Nadhi Watershed Using AHP and GIS Techniques. *Discov. Sustain.* **2024**, *5*, 270. [CrossRef]
92. Yalew, S.G.; van Griensven, A.; van der Zaag, P. AgriSuit: A Web-Based GIS-MCDA Framework for Agricultural Land Suitability Assessment. *Comput. Electron. Agric.* **2016**, *128*, 1–8. [CrossRef]
93. Demesouka, O.E.; Anagnostopoulos, K.P.; Siskos, E. Spatial Multicriteria Decision Support for Robust Land-Use Suitability: The Case of Landfill Site Selection in Northeastern Greece. *Eur. J. Oper. Res.* **2019**, *272*, 574–586. [CrossRef]
94. Lazoglou, M.; Angelides, D. Development of a Spatial Decision Support System for Land-Use Suitability Assessment: The Case of Complex Tourism Accommodation in Greece. *Res. Glob.* **2020**, *2*, 100022. [CrossRef]
95. Krügel, F.; Mäs, S.; Hindorf, P.; Buthmann, E. An Online Multicriteria-Spatial Decision Support System for Public Services Planning. *Appl. Sci.* **2024**, *14*, 1526. [CrossRef]
96. Malczewski, J. GIS-Based Multicriteria Decision Analysis: A Survey of the Literature. *Int. J. Geogr. Inf. Sci.* **2006**, *20*, 703–726. [CrossRef]

Disclaimer/Publisher's Note: The statements, opinions and data contained in all publications are solely those of the individual author(s) and contributor(s) and not of MDPI and/or the editor(s). MDPI and/or the editor(s) disclaim responsibility for any injury to people or property resulting from any ideas, methods, instructions or products referred to in the content.

sustainability

MDPI

Review

Application of Remote Sensing and Machine Learning in Sustainable Agriculture

Claudiu Coman [1,2,*], Ecaterina Coman [3], Vasile Gherheș [4], Anna Bucs [5] and Dana Rad [6]

[1] Department of Social Sciences and Communication, Faculty of Sociology and Communication, Transilvania University of Brasov, 500036 Brasov, Romania
[2] The Academy of Romanian Scientists, 050044 Bucharest, Romania
[3] Department of Management and Economic Informatics, Faculty of Economic Sciences and Business Administration, Transilvania University of Brasov, 500036 Brasov, Romania; ecaterina.coman@unitbv.ro
[4] Department of Communication and Foreign Languages, Interdisciplinary Research Center for Communication and Sustainability, Politehnica University of Timisoara, 300006 Timisoara, Romania; vasile.gherhes@upt.ro
[5] Doctoral School of Social Sciences and Humanities, University of Craiova, 200585 Craiova, Romania; anna.bucs@gmail.com
[6] Center of Research Development and Innovation in Psychology, Faculty of Educational Sciences Psychology and Social Work, Aurel Vlaicu University of Arad, 310045 Arad, Romania; dana@xhouse.ro
* Correspondence: claudiu.coman@unitbv.ro

Abstract: The growing demand for sustainable food production has driven significant advancements in modern agriculture, including increasing interest in Controlled Environment Agriculture (CEA), a high-tech solution designed to provide fresh, local, and organic products. Although the integration of various technologies in agriculture continues to expand, many opportunities remain to improve environmental performance and operational efficiency. Recent advancements in Remote Sensing (RS) and Machine Learning (ML) offer promising tools for enhancing resource efficiency, improving sustainability, and optimizing processes across various agricultural settings. This study presents a bibliometric analysis of the application of Remote Sensing and Machine Learning in agriculture, highlighting publication trends, influential research contributions, and emerging themes in this interdisciplinary field. While the majority of the analyzed literature addresses general agricultural modernization, the growing relevance of RS and ML in artificial climate facilities and controlled environments has been evident in more recent research. Furthermore, we explore how RS and ML technologies contribute to real-time monitoring, precision agriculture, and decision-making in agriculture.

Keywords: controlled environment agriculture; remote sensing; machine learning; sustainable food production; bibliometric analysis

1. Introduction

Climate change has become one of the most pressing global challenges, particularly in agriculture, as it significantly impacts food production and security worldwide. Temperature changes, rainfall patterns, pests, and the frequency of extreme weather events all negatively influence the long-term productivity and sustainability of agriculture. It accelerates growth and expands the range of crop diseases and pests, which can further reduce yields and necessitate the increased use of agrochemicals, contributing to environmental pollution [1,2].

In this context, Controlled Environment Agriculture (CEA) has emerged as an interesting solution, offering efficient systems capable of producing fresh, local, and often organic

food. It can be defined as a highly efficient agricultural method that grows plants in completely controlled indoor spaces, such as vertical farms, minimizing the use of land, water, and nutrients compared with traditional agriculture [3]. As one of the pioneers in this field, Despommier [4] outlined several advantages of vertical farming, including year-round crop production, elimination of weather-related losses and agricultural runoff, significant water savings, and opportunities for urban revitalization and ecosystem restoration. Despite these benefits, CEA's sustainability is often overlooked, and a more detailed understanding of its potential is crucial for promoting its application and cultivating consumer acceptance [5]. While CEA has the potential to provide sustainable, organic, and tasty local food, public understanding and credibility must be deepened to overcome environmental concerns about unnatural aspects [6]. Furthermore, CEA's limited focus and intense capital and energy needs limit its valuable contributions to the urban food system [7].

Recent advancements in Remote Sensing (RS) and Machine Learning (ML) present opportunities to address these challenges. Improved satellite systems and sensor networks now allow researchers to collect and analyze vast amounts of agricultural data with high precision [8,9]. Machine learning algorithms, such as Random Forests, neural networks, and long short-term memory (LSTM) models, are already being applied across the agricultural field for tasks like crop and disease recognition, growth prediction, and yield optimization [10,11]. Together, they form the foundation of smart farming systems that can make CEA more precise, efficient, and sustainable.

Instead of relying on a reactive approach, farmers can adopt a predictive strategy enabled by the insights provided by RS and ML on environmental trends, thus supporting better planning and decision-making [12,13]. Object-based classification methods, spectral analysis, and airborne laser scanning are used to identify everything from habitat trees to plantation age, although challenges remain, particularly when it comes to extracting social and functional information from commercial remote sensing data [14–16]. Moreover, ML-driven technologies provide valuable information for processing remote sensing data to enhance the quality and quantity of agricultural output [17]. Hyperspectral, multispectral, and aerial images offer comprehensive insights into the health and dynamics of agricultural systems [18].

Recent scholarly work emphasizes the role of sensor networks, big data, and the Internet of Things (IoT) in processing and analyzing agricultural data to support sustainable practices [9]. Additionally, machine learning algorithms are widely used technologies in this field. However, not all challenges are technological. Research on land use and land cover change in the context of environmental issues has become an increasingly important topic [12,19]. For example, the growing concern over microplastics in soil highlights knowledge gaps regarding their long-term effects on crop productivity and food safety, an area where improved monitoring and data analysis could also play a key role [20].

Researchers have focused on the development and optimization of machine learning models for processing, analyzing, and interpreting data retrieved from remote sensing, particularly for land cover/use classification processes and the presentation of bioscope parameter estimation [21]. Furthermore, scholars are exploring the use of neural networks for automated crop and pest/disease recognition, long short-term memory (LSTM) networks for predicting crop growth, and various tools to support farmers in the decision-making process [11,22]. The literature also suggests that improved satellite systems have created a need for new models that can help analyze spectral time series [8]. In this context, machine learning techniques, such as the Random Forest algorithm, have been widely applied in agricultural and land cover research [10].

Although the intersection of ML and RS has been extensively studied in open-field agriculture, their integration within CEA remains underexplored. Only a handful of biblio-

metric analyses exist in this field. Dsouza et al. [3] conducted a thematic analysis (n = 610) of the research landscape of controlled environment agriculture (CEA), identifying four research areas: technical, biological, environmental, and socio-economic. They found that CEA has several benefits over traditional agriculture, including a reduced environmental impact due to its proximity to urban centers, which minimizes the need for transportation. Additionally, CEA supports urban economies by creating skilled jobs and promoting sustainability. Similarly, Abdollahi et al. [23] carried out a bibliometric analysis of the potential of wireless sensor networks (WSN) in agriculture. They analyzed 2444 documents from the Scopus database and found that WSN applications in precision agriculture can modernize data collection, contributing to the automation of farming systems.

In contrast, Bertoglio et al. [24] explored the Digital Agricultural Revolution (DAR) through a bibliometric analysis of 4995 articles (2012–2019), highlighting its role in enhancing sustainable farming practices to address climate change and food security. However, they identified several barriers to the widespread adoption of ML in agriculture, including the high cost of technology, lack of technical expertise among farmers, data privacy concerns, and difficulty in deploying ML models in resource-constrained rural environments. The authors argue that addressing these socio-economic and infrastructural challenges is as important as making technical advancements.

Recent research has highlighted the growing role of machine learning (ML) and deep learning (DL) in advancing precision agriculture. Rejeb et al. [25] discuss the evolution from traditional ML algorithms (e.g., Random Forest, Support Vector Machines) to advanced deep learning methods (e.g., Convolutional Neural Networks, Recurrent Neural Networks), which have significantly improved accuracy in image-based agricultural applications. While traditional algorithms remain popular due to their interpretability and lower computational cost, deep learning (DL) models have demonstrated superior performance in image-based tasks, such as disease identification and weed classification. Ojo et al. [22] note in their review that the majority of DL applications (82%) focus on greenhouses, with the main tasks being yield estimation (31%) and growth monitoring (21%). Other significant applications include disease detection, microclimate prediction, nutrient estimation, small insect detection, and robotic harvesting. Indoor farms and vertical farming systems also utilize DL for stress-level monitoring, growth monitoring, and yield estimation, although to a lesser extent. However, as Kabir et al. [26] pointed out, the widespread adoption of these technologies faces barriers such as high costs and the need for specialized expertise, particularly in resource-limited regions.

Together, these findings describe a new approach to agricultural research and practice that combines data, technology, and environmental awareness to support more sustainable systems [27]. However, the available literature is often too general or narrowly focused on specific technologies. To address this gap, the present study aims to explore the integration of Remote Sensing (RS) and Machine Learning (ML) into Controlled Environment Agriculture (CEA) through a structured, comprehensive approach. Through bibliometric and content analyses, this paper highlights the progress and key contributions of the field and identifies emerging research directions. Based on this objective, the following research questions were formulated:

RQ1: What are the key publication trends, influential articles, and the most productive authors and countries in the field of Machine Learning and Remote Sensing applied to Controlled Environment Agriculture (CEA)?

RQ2: What are the research directions for the use of Machine Learning and Remote Sensing in sustainable agriculture?

RQ3: How are Machine Learning and Remote Sensing technologies applied within CEA systems to enhance sustainability, resource management, and operational efficiency?

2. Materials and Methods

This study was conducted in two main phases. In the first phase, we performed a bibliometric analysis of 70 papers selected according to the selection criteria presented in Figure 1 (PRISMA—Preferred Reporting Items for Systematic Reviews and Meta-Analyses–diagram). The filters applied to the topic of the papers ensured that the selected studies remained focused on systems relevant to Controlled Environment Agriculture (CEA) (e.g., greenhouses, vertical farms, and indoor farming). At the same time, the emphasis on sustainability connects the dataset to broader environmental goals. By integrating concepts related to both machine learning and remote sensing, the search strategy captures a relevant body of literature that addresses the operational and strategic dimensions of sustainability within CEA systems. No filter was applied to the publication years, allowing for a comprehensive analysis of the temporal evolution of the research field. The selection of documents from the Web of Science (WoS) database was conducted on 15 April 2025. The analysis identified publication trends, the most influential articles, and the most productive authors and countries in this field.

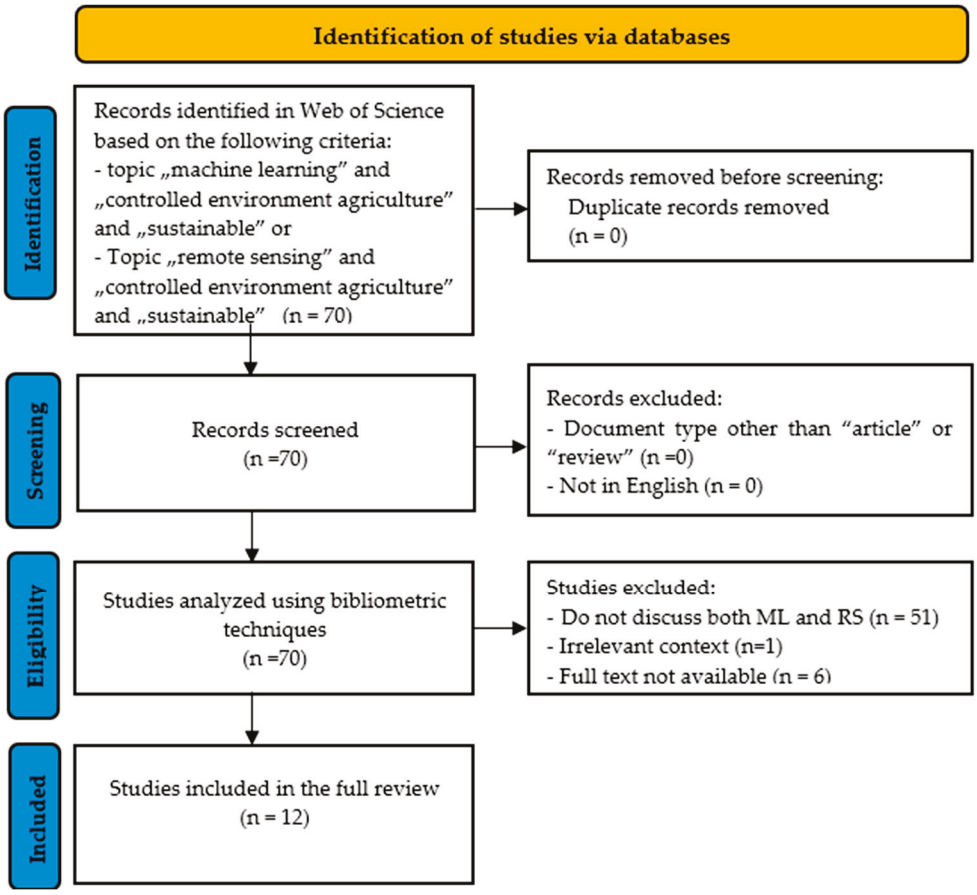

Figure 1. PRISMA flow diagram for the selection of studies on the use of remote sensing and machine learning in agriculture.

The raw data of 70 documents were downloaded from the Web of Science (WoS) database in "plain text files" format. Subsequently, the co-occurrence technique was applied, as it allows the examination of relationships between topics within a research field [28,29] and the identification of influential topics and emerging trends [30]. VOSviewer version 1.6.18 was employed for this purpose as it offers distinctive functionalities for the visualization and analysis of bibliometric data [31]. To ensure the relevance and clarity of the network visualization map, a threshold of at least two occurrences was set for the

inclusion of a term. The clustering process was normalized using the 'association strength' method, and a minimum cluster size of 10 terms was established. Clusters were then analyzed to identify key research directions and trends.

In the second phase of our study, we sought to gain a deeper understanding of the application of Machine Learning (ML) and Remote Sensing (RS) in Controlled Environment Agriculture (CEA). Therefore, we conducted an in-depth content analysis of studies that explicitly addressed the integration of both ML and RS technologies in CEA systems and for which full-text access was available. As a result, 12 articles were selected for inclusion in this phase of the analysis.

3. Results

To address the three interrelated research questions, we first present the results of the bibliometric analysis, focusing on publication trends, influential articles, and key contributors (RQ1). Subsequently, the identification of research directions, derived from keyword co-occurrence mapping, is presented (RQ2) and integrated with qualitative content analysis to explore how Machine Learning and Remote Sensing are applied in CEA systems to support sustainability and operational efficiency (RQ3).

As shown in Figure 2, the first article on this topic was published in 2001, and academic activity in this area remained minimal until 2019. The number of publications began to rise as technology advanced. Starting in 2019, the number of articles continued to increase, reaching 13 papers in 2024. The upward trend is evident, especially since we are only at the beginning of 2025, and already seven articles have been published. Considering the importance of the topic, we estimate that the number of publications will exceed 20 by the end of the year. A notable observation is that, despite the clear growth in research output over the years, the overall number of publications in this field remains relatively low. This suggests that while interest and activity are increasing, the field is still in a developing stage, with plenty of room for further exploration and contribution.

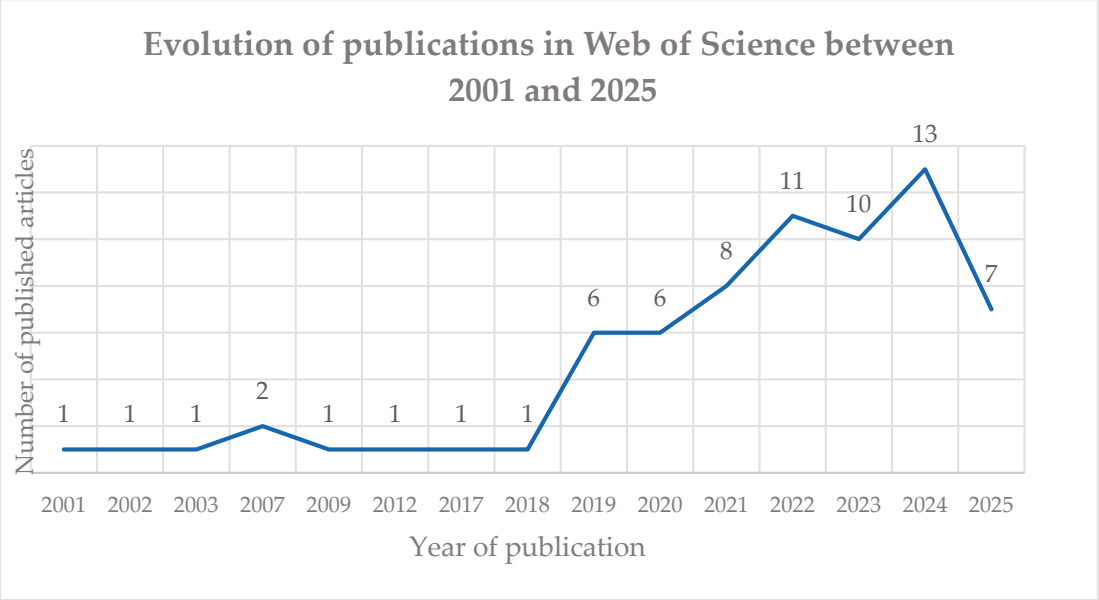

Figure 2. Evolution of published articles on RS and ML in agriculture between 2001 and 2025.

As shown in Figure 3, an analysis of the distribution of scientific production by country reveals a clear imbalance, with a few nations contributing a substantial share of publications. India leads with 12 publications, closely followed by the United States with 11 and the People's Republic of China with 9. These three countries dominate the dataset, and this

concentration reflects not only technological infrastructure but also institutional investment in agritech research. This distribution underscores the research output in a few highly active countries while also highlighting more limited participation from a wider range of countries.

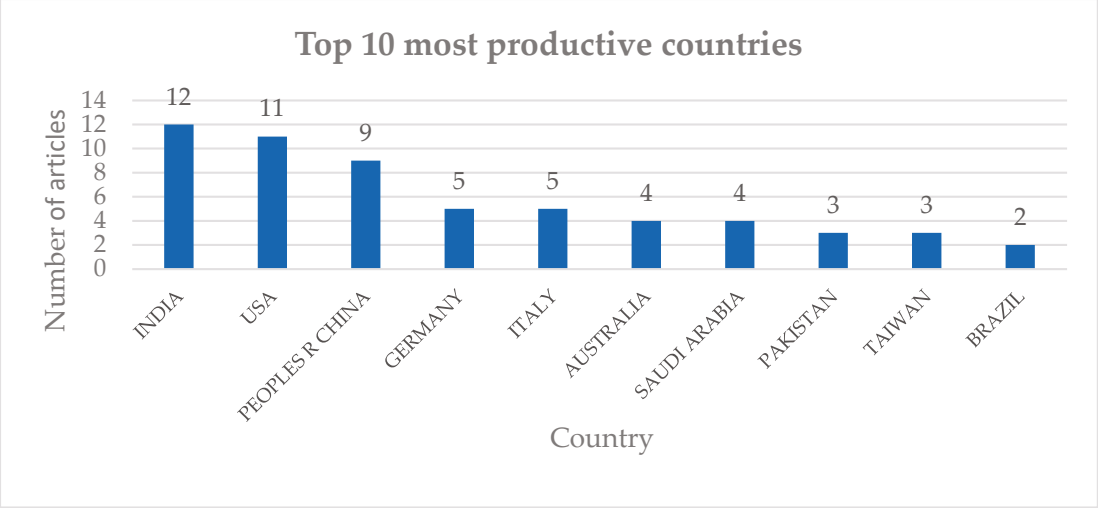

Figure 3. Country-level distribution of research output on remote sensing and machine learning in agriculture (2001–2025).

In examining the most influential documents within our dataset (Table 1), it is evident that the most cited articles reflect a broader, interdisciplinary approach. Some highly cited works emphasize the importance of soil health [32], water management for irrigation [33], and sustainable land management practices, especially in addressing the growing global issue of soil salinization, which poses a significant threat to long-term agricultural productivity [34]. At the same time, several articles are directly aligned with the core theme, particularly those related to machine learning, object detection (YOLOWeeds), autonomous navigation using deep learning, and sensor/drone technologies for sustainable crop management, with citation counts ranging from 110 to 120 [35–39]. The similar citation levels of these studies highlight the active research interest in using advanced technologies, such as object detection algorithms and remote sensing, for sustainable weed control and land consolidation policies. These contributions highlight how machine learning is becoming a key enabler of automation, precision, and efficiency in controlled environments.

The article "Renewable energy-powered semi-closed greenhouse for sustainable crop production using model predictive control and machine learning for energy management" [40] represents a direct integration of machine learning within a CEA framework, showcasing sustainable innovations that align closely with the core theme of this research. Notably, one of the high-impact articles highlights the importance of developing sustainable grazing systems to enhance both land quality and the overall health and welfare of animals [41]. Overall, the development of this field is largely based on established work in environmental management, precision agriculture, and artificial intelligence-based solutions, laying the foundation for future innovations in sustainable CEA systems.

Table 1. Top 10 most influential papers.

Authors	Article Title	Citations	Year
Barrios, E [32]	Soil biota, ecosystem services, and land productivity	611	2007
Singh, A [34]	Soil salinization management for sustainable development: A review	275	2021
Dang, FY et al. [35]	YOLOWeeds: A novel benchmark of YOLO object detectors for multi-class weed detection in cotton production systems	120	2023
Esposito, M et al. [36]	Drone and sensor technology for sustainable weed management: A review	119	2021
Yurui, L. et al. [37]	Impacts of land consolidation on the rural human-environment system in typical watershed of the Loess Plateau and implications for rural development policy	113	2019
Vilialba, JJ and Provenza, FD [41]	Seff-medication and homeostatic behaviour in herbivores: Learning about the benefits of nature's pharmacy	91	2007
Hu, G and You, F [38]	Land-Use/Land-Cover Changes and Its Contribution to Urban Heat Island: A Case Study of Islamabad, Pakistan	75	2020
Schultz, B and De Wrachien, D [33]	Irrigation and drainage systems research and development in the 21st century	48	2002
Hu, G and You, F [40]	Renewable energy-powered semi-closed greenhouse for sustainable crop production using model predictive control and machine learning for energy management	47	2022
Aghi, D et al. [39]	Local Motion Planner for Autonomous Navigation in Vineyards with a RGB-D Camera-Based Algorithm and Deep Learning Synergy	47	2020

In addition, our analysis shows that five authors, Chang EJ, Chauhan BS, Deng KZ, Kava C, and Sharma A, stand out as the top contributors to the research field. Each contributed two records, comprising approximately 2.86% of the dataset. The highest number of publications appeared in the journal "Sustainability" (seven articles), followed by "Computers and Electronics in Agriculture", "IEEE Access", and "Sensors", each with three articles.

In order to identify the most important research areas and themes in the field of innovative approaches to CEA, we carried out a keyword co-occurrence analysis. This allows us to track the main interests of researchers, stemming from the keywords we found in titles, abstracts, and keywords identified by the authors. Out of the 609 keywords, 79 met the threshold of appearing at least twice. A network visualization of keyword co-occurrences is presented in Figure 4, showing 464 links and four clusters, with a Total Link Strength (TLS) of 553. In the following section, we examine these clusters individually, describing each research direction along with the related findings from the 12 fully reviewed articles.

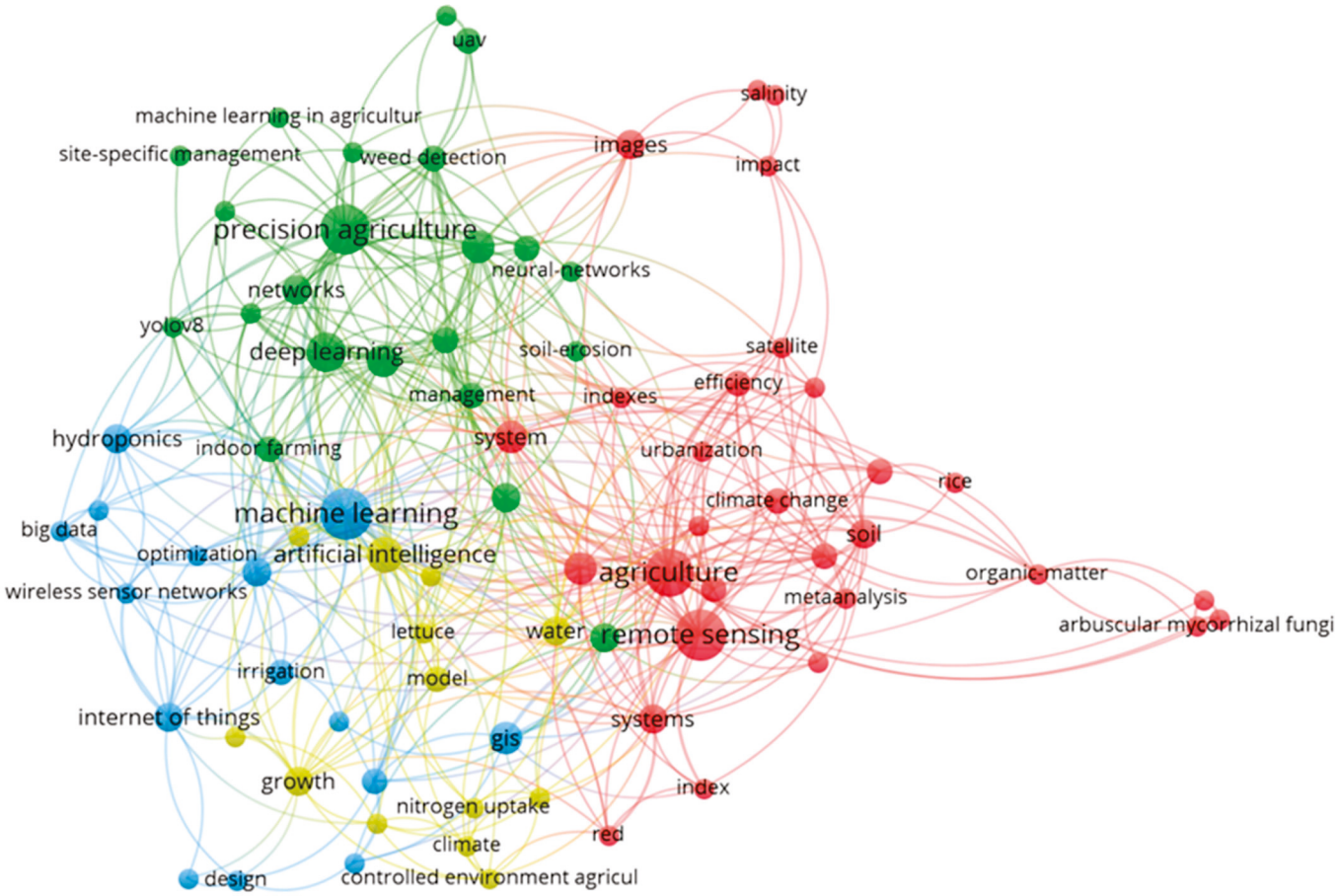

Figure 4. Network visualization of keyword co-occurrences in publications on the use of remote sensing and machine learning in agriculture (2001–2025).

3.1. Cluster 1 (Red): Climate-Responsive Agriculture and Soil Management via Remote Sensing

The first cluster (red) had 29 items and 43 links, with a total link strength (TLS) of 56. This cluster contains research that clearly centers on the challenges and innovations in agriculture under negative environmental effects, particularly climate change and soil degradation. The integration of remote sensing and data-driven approaches with traditional agricultural knowledge stands out.

Many keywords from the first cluster point toward issues of soil salinization, organic matter, and conservation agriculture, which suggests that researchers are focused on maintaining or improving soil health in changing environments. It is about productivity and long-term sustainability. This cluster shows how researchers keep soils viable as climate and land use change do.

The appearance of "arbuscular mycorrhizal fungi" and "biological control" adds an interesting nuance, as it shows that there is attention on biological and microbial solutions in addition to technological ones. Therefore, while remote sensing and machine learning methods like "random forest" are being used to monitor or predict outcomes, there is also a recognition that working with natural systems (like fungal networks or beneficial soil organisms) is part of the solution. Specifically, researchers employ a random forest (RF) machine learning model as the base classifier for the RUSBoost ensemble technique to predict the spatial distribution of land suitability classes for sugar beet, a key crop in specific regions [14]. Others employed the Random Forests algorithm, a widely used machine learning classifier, to map 12 land cover classes, including different peatland types, based on multi-sensor remote sensing data [42].

There is a strong emphasis on climate here, too, but what is interesting is how that plays into food security and efficiency. This is not just about managing crops; it is about feeding populations, especially as urbanization continues and usable agricultural land becomes more limited. It makes sense that crops like "rice" show up here, tied to food systems in climate-vulnerable regions like "China", which is also mentioned as a keyword, pointing to the geographic location of case studies.

Our qualitative analysis reveals that the potential of machine learning models, like MaxEnt, is applied in agricultural applications in Thailand, particularly for modeling crop suitability. MaxEnt, a presence-only modeling approach, has been shown to be effective in identifying suitable areas for both upland and lowland crops, including rice varieties [43]. However, the model's performance was sensitive to the geographic and environmental distribution of observed crop data. This highlights the importance of data quality and distribution in the training datasets, which directly impact model reliability.

Researchers have highlighted the rapid increase in the use of plastic greenhouses (PGs) all across the planet, especially in Asia, and underscored their negative effects on the local environment. These effects include a major change in the soil's physical and chemical makeup, disruption of the water cycle, and a decrease in biodiversity [44]. Medium-resolution Landsat Operational Land Imager (OLI) remote-sensing data are the primary data source for PG identification. Others in China utilize images captured from remote sensing equipment (like drones or fixed cameras) to continuously monitor the greenhouse environment. These images provide detailed data on various environmental parameters, such as temperature, humidity, light intensity, and plant health [14].

The presence of "indexes", "images" and "satellites" suggests that remote sensing tools are central to this research domain. They are being used not just for mapping but also for making decisions: identifying areas of risk, monitoring soil quality over time, and assessing the impacts of different farming systems. The use of remote sensing and cloud-based processing techniques allows for near-real-time monitoring of forest cover changes, enhancing transparency and providing timely information to local authorities and stakeholders. Landsat 7 satellite imagery and the Google Earth Engine (GEE) platform were used for processing and analyzing the remote sensing data. The authors demonstrated the effectiveness of this approach in quantifying forest cover changes at the regional scale, overcoming the challenges of traditional desktop-based GIS software [45].

In essence, this cluster is where agriculture intersects with remote sensing. It is framed by the need to adapt to climate pressure and preserve food systems. Technology, ecology, and sustainability have also been discussed. Various systems have been developed that integrate autonomous Unmanned Aerial Vehicles (UAVs) with machine learning (ML) frameworks to support sustainable agriculture and environmental monitoring, aligning with broader environmental conservation goals [46]. The potential of using UAVs for various remote sensing applications, such as tree health assessment, tree population estimation, and water resource identification, is crucial for sustainable environmental monitoring. The first brain employs deep reinforcement learning (DRL) principles to enable UAV navigation in complex agricultural terrain. In contrast, the second brain utilizes the Faster R-CNN algorithm to achieve 98% accuracy in tasks like tree counting, water detection, and plant health analysis [46].

3.2. Cluster 2 (Green): AI-Powered Vision Systems for Precision Agriculture

The second cluster (green) contained 22 items, 28 links, and a total link strength of 36. This cluster focuses on including artificial intelligence and computer vision tools in agriculture, emphasizing how these technologies are used to monitor crops and support precision management. The presence of items like "computer vision", "deep learning",

"neural networks", "image processing", "classification", "YOLOv8", "machine vision", and "networks" indicates the use of techniques rooted in machine learning and AI-based visual analysis. The mention of "machine learning in agriculture" and "prediction" indicates that this cluster is about more than just image recognition. Rather, it is about building intelligent systems that can analyze and interpret agricultural data in real-time to support decision-making. These systems are being trained to detect and classify different crop types, identify weeds, and even assess conditions like "soil erosion", all based on visual input from drones or ground-based sensors.

Deep learning techniques, including convolutional neural networks (CNNs), region-based CNNs, and YOLO models, have been used for various agricultural applications, such as fruit and flower detection, crop yield estimation, and plant disease identification [37]. This cluster highlights several emerging trends in machine vision and deep learning applications for agriculture, such as the use of hybrid techniques, integration of multiple sensor modalities, and the development of real-time automated systems for tasks like robot harvesting [47].

One of the more interesting aspects of this cluster is how it links advanced AI methods—Like those found in "YOLOv8" and other object detection architectures with very practical, field-level applications such as "weed detection", "crop identification" and "site-specific management". These are not abstract models, and they are being applied to solve real problems on farms, especially in the context of "precision agriculture". "Indoor farming" also appears, which suggests that some of these technologies are being tested or deployed in controlled environments where lighting, plant spacing, and background conditions can be optimized for vision-based systems. This may also facilitate the generation of large datasets for training neural networks.

This cluster addresses the challenge of accurately identifying *Chilo suppressalis pest*, a major threat to rice crops in the temperate and subtropical regions of Asia. The proposed approach, which integrates smartphone-captured images with a deep learning-based classification model, represents a significant methodological innovation in the field of precision agriculture and intelligent pest management. Researchers have focused on developing a user-friendly, smartphone-based system that can provide rapid and accurate pest identification for farmers, which is a relevant and impactful contribution [48]. A deep learning-based approach, specifically utilizing a 400-unit artificial neural network, is justified and grounded in the existing literature on machine learning applications in agriculture.

Most of these papers aim to improve the accuracy and efficiency of agricultural monitoring, either through the early detection of crop stress or more targeted use of inputs. Therefore, terms like "management", "prediction", "site-specific management", and "sustainable agriculture" appear together. This cluster links technical solutions with overall agricultural goals, especially regarding sustainability and resource optimization.

It is also worth mentioning that the keyword "UAV" suggests a strong role for drone-based imaging in this space. UAVs provide a flexible and scalable platform for collecting high-resolution visual data, which is essential for training and deploying many of the AI models mentioned in this cluster. The proposed system architecture and POMDP-based motion planner aim to improve the reliability and robustness of UAV operations in the face of environmental uncertainty and imprecise object detection, contributing to the more sustainable and efficient use of these technologies [49].

Other studies have utilized a multi-sensor approach combining optical (Sentinel-2), C-band SAR (Sentinel-1), and L-band SAR (ALOS PALSAR) data, along with topographic information, to accurately map peatlands and distinguish between undisturbed and disturbed (pasture) peatland classes [42]. Overall, this cluster highlights a growing area of research at the intersection of agriculture, AI, and imaging technologies. The focus is

on practical applications, but it's grounded in cutting-edge developments in "machine learning", "computer vision" and neural network architecture. These tools are used to make agriculture smarter, more precise, and better adapted to future challenges.

3.3. Cluster 3 (Blue): Digital Technologies and System Optimization in Sustainable Farming

Cluster 3 (blue) has 15 items, and 32 links, with a total link strength (TLS) of 42. This cluster contains research centered on the digital background of modern agriculture and how farms are being equipped with connected technologies to become smarter, more efficient, and more sustainable. The most prominent terms, such as "internet of things", "wireless sensor networks", "big data" and "GIS" show a clear focus on connectivity, real-time monitoring, and data integration at the field level. The integration of remote sensing data with GIS and geostatistical techniques has demonstrated the effectiveness of these technologies in characterizing the spatial variability of soil properties and land suitability [50]. The collaboration between Ain Shams University (Cairo, Egypt), the National Authority for Remote Sensing and Space Sciences (Cairo, Egypt), and the Institute of Olive Tree, Subtropical Crops, and Viticulture (Crete, Greece) suggests a strong connection between academic research and practical applications in the field of sustainable agriculture.

Additionally, "smart agriculture" and "smart farming" are prevalent. Papers in this cluster typically deal with infrastructure and system designs that allow farms to function more intelligently. Sensors placed in soil or on plants, connected via wireless networks, feed data back into systems that optimize decisions regarding "irrigation", "fertilization", and environmental control.

Smart farming can provide farmers with data on topography, climate, soil parameters, and other factors to optimize the use of fertilizers, pesticides, and other inputs, thereby improving sustainability [47]. Precision agriculture and automation in the agricultural industry have the potential to moderate resource usage and increase food quality in the post-pandemic world.

"Machine learning" is also a key part of this cluster, particularly when it comes to analyzing sensor data or performing tasks like "object-based classification" of spatial imagery. The mention of "accuracy" and "optimization" suggests that much of the research here is not just about building these systems but refining them, ensuring that automation is precise, reliable, and scalable. When comparing machine learning algorithms—Cart, SVM, and RDF— in extracting PG distribution from remote sensing data, the results stipulate that the SVM classifier has the highest accuracy in identifying PGs, outperforming the other two methods in terms of recall, precision, and F-measure [34].

Another interesting component is the appearance of "hydroponics". In these systems, digital tools can monitor every aspect of plant growth, including light, nutrients, and temperature, and optimize them using feedback mechanisms. This connects to the overall goal of "sustainable development", which is also a core keyword in the cluster. The presence of "design" and "state-of-the-art" implies that many of the papers here are not just applied studies but also proposals for new architectures or system frameworks. Essentially, it lays out how digital agriculture should be built from a technical standpoint.

What separates this cluster from the previous one (which focused more on AI and vision systems) is that the emphasis here is on the systemic. It involves infrastructure, data flow, optimization algorithms, and the integration of hardware and software components. It is less about individual tasks (like detecting weeds) and more about making the entire farming system run more efficiently and sustainably through technology. Overall, this cluster includes the current push toward digitally connected agriculture that is data-driven, emphasizing IoT-based systems, sensor networks, and intelligent infrastructure designed for sustainability and resource optimization.

3.4. Cluster 4 (Yellow): Intelligent Systems for Monitoring and Enhancing CEA Performance

Cluster 4 (yellow) has 13 items, and 11 links with a total link strength (TLS) of 11. This cluster revolves around the use of artificial intelligence and data modeling to improve the growth of crops in controlled environments in spaces likeas greenhouses, vertical farms, and hydroponic systems, where environmental variables can be more manageable. The central theme here is the optimization of resources, plant growth, and efficiency. In this cluster, the efficiency of high-resolution Sentinel-2 satellite imagery and machine learning models is highlighted in enabling real-time, spatially explicit monitoring of pasture biomass parameters within small-scale controlled environments [51]. Articles from our qualitative analysis showcase how these remote sensing technologies can support precision agriculture and data-driven decision-making in CEA by providing timely and accurate information to optimize production processes. In contrast, proximal sensing, which involves sensors placed in close contact with plants or soils (e.g., chlorophyll meters, hyperspectral cameras, or root zone sensors), provides high-resolution, real-time data under artificial lighting and controlled conditions, making it critical for precision monitoring in greenhouses or vertical farms. Although the term does not explicitly appear in our dataset, the technologies described in Cluster 4 conceptually align with proximal sensing methods.

Terms like "controlled environment agriculture", "artificial intelligence", "sensors" and "model" refer to research that relies on data collection and algorithmic control. These systems use real-time feedback from environmental sensors to regulate important variables such as "temperature", "climate", "water" and "nitrogen uptake." The goal is clear: to fine-tune the growing conditions to maximize yield and reduce waste.

Notably, researchers seem to be interested in using artificial intelligence-driven techniques to use auxiliary data sources to improve the accuracy and cost reduction of geochemical mapping. A wide range of high-resolution auxiliary data sources, including airborne geophysical surveys, aerial elevation data, land gravity surveys, and satellite imagery, have been mentioned [52]. Savants discussed the use of quantile regression forests, an advanced machine learning technique, to model and predict soil geochemical properties based on these auxiliary datasets.

The presence of "principal component analysis" suggests a strong data analytics component. Papers in this cluster use statistical modeling and dimensionality reduction to better understand the complex relationships between growing conditions and plant responses. These insights are then fed into predictive or control models powered by AI.

An innovative approach has emerged in which researchers have developed a soft robotic gripper with integrated proprioceptive sensing that can be applied in a wide range of robotic applications, including manufacturing, logistics, and assistive technologies. The authors demonstrated the effectiveness of the soft gripper design and its ability to adapt to various object shapes and sizes, highlighting its potential for improving the performance and versatility of robotic systems [53]. This can contribute to the development of more sustainable and energy-efficient robotic systems for various applications.

During our qualitative analysis, we identified another proposed smartphone-based system that aligns with the principles of precision agriculture. This system would enable efficient and targeted pest management practices to reduce crop damage and minimize the environmental impact of pesticide use [48].

The term "Supply chain" points to a broader view in some studies, linking production inside controlled environments to logistics and distribution. This suggests that some studies are not only looking at plant science or engineering but also considering how CEA fits into sustainable food systems. Overall, this cluster is about intelligent systems that make growing food in controlled environments more efficient, responsive, and smart. It is where AI, sensor technology, and plant physiology come together, pushing forward the

kind of agriculture that is less dependent on external climate and more integrated with digital infrastructure.

3.5. Research Trends

The overlay visualization of the keyword co-occurrence analysis, presented in Figure 5, highlights a noticeable shift in the research focus over recent years toward the integration of artificial intelligence, specifically machine learning and deep learning, into agriculture. More recent keywords (represented in yellow tones), such as YOLOv8, weed detection, and machine learning in agriculture, indicate increased attention to computer vision and real-time data applications for tasks like crop monitoring and automated decision-making. Central themes such as precision agriculture, remote sensing, and climate change remain central, connecting both technological and environmental concerns.

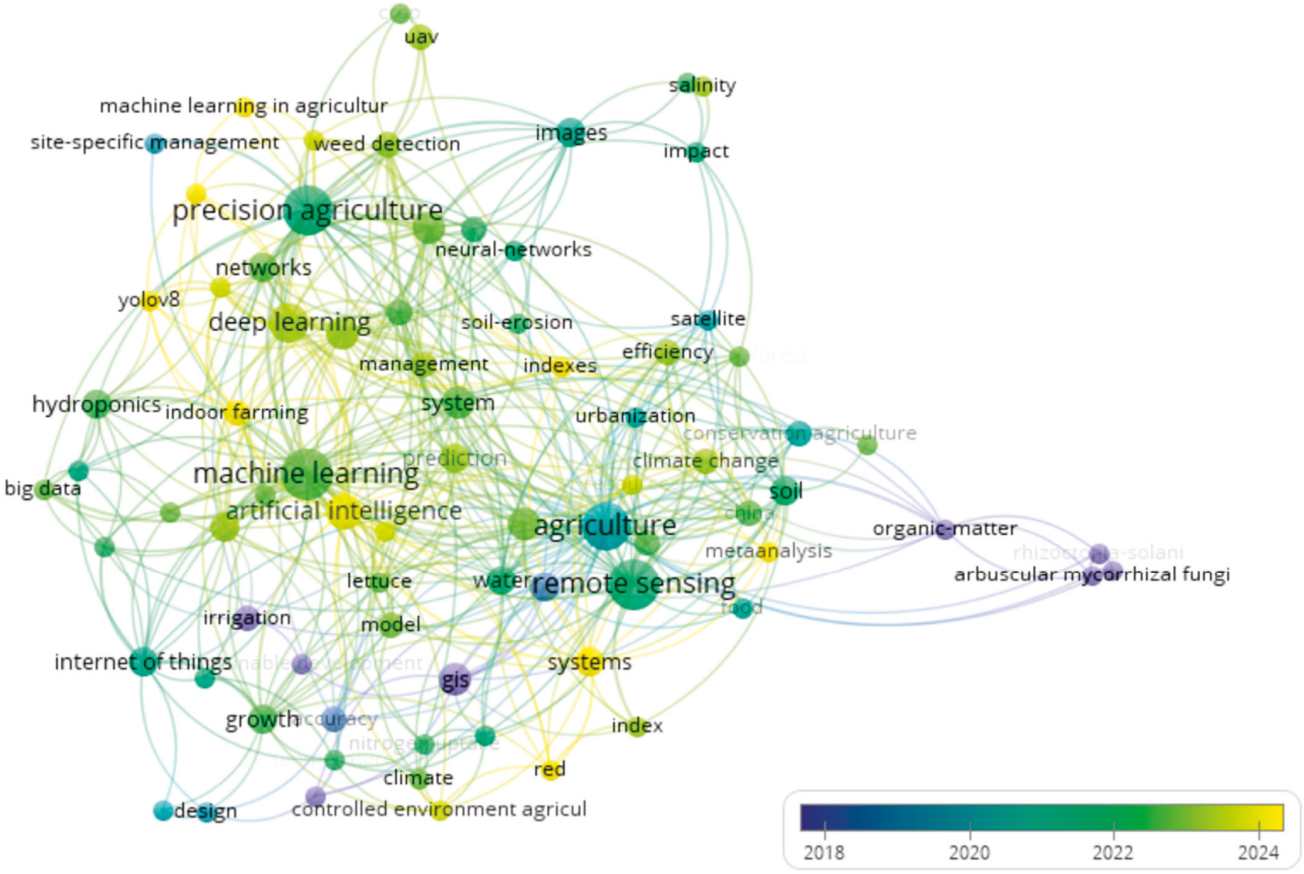

Figure 5. Overlay visualization of emerging topics on the use of remote sensing and machine learning in agriculture based on keyword co-occurrences.

In contrast, earlier research (2018–2020, shown in blue tones) was more concentrated on traditional agronomic topics like organic matter, arbuscular mycorrhizal fungi, nitrogen uptake, and irrigation. In recent years, there has been a growing emphasis on indoor farming, hydroponics, and wireless sensor networks, pointing to an extended agricultural setting and the emerging role of Internet of Things (IoT) solutions. The presence of terms such as optimization, big data, and networks further underscores the data-driven nature of this field.

4. Discussion

This study provides a comprehensive overview of the literature on the integration of Machine Learning (ML) and Remote Sensing (RS) technologies into Controlled

Environment Agriculture (CEA), with a focus on their contributions to sustainability, resource optimization, and system efficiency. Through bibliometric and content analyses, we answered our two core research questions by identifying the key contributors, emerging trends, and practical applications of RS and ML in the context of sustainable CEA systems.

Our bibliometric analysis revealed a clear upward trend in publications related to ML and RS in CEA systems. Meaningful academic engagement on this topic began after 2019, when technological advances, particularly in AI, sensor networks, and automation, enabled the development of more sophisticated applications. Despite this positive trend, the overall volume of research remains modest, indicating that this field is still in its developmental phase. This early stage presents substantial opportunities for future exploration, especially in areas where ML and RS intersect with climate resilience and sustainable farming technologies.

Our findings indicate a clear evolution from traditional agricultural research toward technology-driven approaches, particularly those grounded in artificial intelligence (AI), machine learning (ML), and data-centric strategies. The bibliometric analysis identified four dominant research clusters that align closely with the transition to smart agriculture and climate-resilient practices, thereby addressing RQ1 and RQ2 regarding major trends and influential works in the field.

Each cluster has distinct advantages and challenges. Cluster 1 integrates remote sensing and ecological approaches to enhance climate adaptation and soil management, although it may face data quality sensitivities and environmental concerns related to certain technologies like plastic greenhouses. Cluster 2 focuses on AI-powered vision for precise crop and pest monitoring, showing high accuracy with deep learning models but requiring large datasets and advanced technical capacity. Cluster 3 centers on IoT and big data for smart farming, improving resource use through sensor networks, yet faces integration complexity and adoption barriers due to the cost and skills required. Cluster 4 focuses on intelligent systems in controlled environments, offering real-time optimization and innovative automation, though substantial investment and model generalizability remain challenges. Evaluations across clusters highlight that while each approach advances sustainable agriculture, its performance and scalability depend strongly on data quality, technical capacity, and contextual factors.

A significant number of recent publications emphasize precision agriculture, computer vision, and real-time data monitoring, underlining the growing importance of AI technologies in achieving more efficient and adaptive agricultural systems. Tools like YOLOv8, which are used for object detection and real-time image analysis, are at the forefront of efforts to automate processes such as weed and pest identification, directly supporting decision-making in both open fields and indoor farming contexts.

Aligned with RQ3, our content analysis reveals that ML and RS are increasingly applied to enhance resource efficiency and environmental sustainability in CEA settings. In greenhouses, vertical farms, and hydroponic systems, sensor networks and feedback loops enable real-time adjustments to temperature, humidity, and nutrient levels. These innovations facilitate higher productivity while minimizing the use of water, fertilizer, and pesticides. Moreover, the shift toward IoT-based systems and big data analytics reflects a broader trend toward interconnected farming environments. These technologies offer opportunities to optimize irrigation and fertilization while enabling predictive models for yield estimation, plant stress detection, and crop growth forecasting. The presence of terms such as optimization, networks, and automation in the literature indicates a strong emphasis on sustainability through data-driven control.

Our review also highlights the diversification of agricultural environments, moving beyond traditional soil-based farming to include indoor farming, aquaponics, and modular

vertical agriculture. These systems are particularly promising in urban areas or regions facing climate stress where conventional agriculture is not feasible. However, their implementation still faces practical constraints, including high energy demands and economic barriers, especially in resource-limited regions.

Despite substantial technological progress, the literature has limited attention to socio-economic dimensions, including farmer readiness, labor market transitions, and policy support. This gap hinders the widespread adoption of CEA and should be prioritized in future research. A more holistic research agenda that incorporates economic viability, training programs, and community engagement is essential for scaling these innovations in a sustainable and inclusive manner.

From a theoretical perspective, this study provides a structured overview of RS and ML applications in CEA. From a practical standpoint, this study provides actionable insights for policymakers and stakeholders seeking to scale smart agricultural solutions. Recognizing the need to balance innovation with accessibility, especially in emerging economies, we recommend that future research adopts a more holistic lens that incorporates economic feasibility, training, and community-level engagement. There is also a growing need to bridge the gap between theoretical development and field deployment, particularly in low-resource settings where CEA could offer significant benefits for food security. Moreover, we consider it important to investigate the long-term impacts on biodiversity, labor markets, and urban infrastructure.

While our study provides a timely synthesis of the literature, it has some limitations. The dataset is limited to 70 documents from the Web of Science (WoS), which, while rigorous, may not fully capture the breadth of research on this topic. One limitation of our approach is that the topic-based search strategy while ensuring relevance and focus, may have excluded relevant studies that do not explicitly mention "controlled environment agriculture" in their indexed fields. Therefore, some relevant technologies and terms related to RS and ML may not have been included as prominent keywords in our bibliometric analysis. Furthermore, this analysis reflects the state of research as of 15 April 2025 and may not capture the latest developments in rapidly evolving fields such as deep learning or spectral analysis in agriculture. Nevertheless, this study successfully achieved its stated objectives by providing a structured synthesis of existing research and identifying key trends, contributors, and technological directions in the use of Machine Learning and Remote Sensing for sustainable Controlled Environment Agriculture.

Author Contributions: Conceptualization, C.C. and E.C.; methodology, E.C.; software, E.C. and A.B.; validation, C.C., E.C., V.G. and A.B.; formal analysis, A.B. and E.C.; investigation, V.G., A.B. and D.R.; data curation, E.C. and A.B.; writing—original draft preparation, A.B. and D.R.; writing—review and editing, C.C., E.C., V.G., A.B. and D.R.; visualization, E.C.; supervision, E.C.; project administration, C.C.; All authors have read and agreed to the published version of the manuscript.

Funding: This research received no external funding.

Data Availability Statement: The original contributions presented in this study are included in this article. Further inquiries should be directed to the corresponding author.

Conflicts of Interest: The authors declare no conflict of interest.

References

1. Yang, Y.; Tilman, D.; Jin, Z.; Smith, P.; Barrett, C.B.; Zhu, Y.-G.; Burney, J.; D'Odorico, P.; Fantke, P.; Fargione, J.; et al. Climate Change Exacerbates the Environmental Impacts of Agriculture. *Science* **2024**, *385*, eadn3747. [CrossRef]
2. Raza, A.; Razzaq, A.; Mehmood, S.S.; Zou, X.; Zhang, X.; Lv, Y.; Xu, J. Impact of Climate Change on Crops Adaptation and Strategies to Tackle Its Outcome: A Review. *Plants* **2019**, *8*, 34. [CrossRef] [PubMed]

3. Dsouza, A.; Newman, L.; Graham, T.; Fraser, E.D.G. Exploring the Landscape of Controlled Environment Agriculture Research: A Systematic Scoping Review of Trends and Topics. *Agric. Syst.* **2023**, *209*, 103673. [CrossRef]
4. Despommier, D. Advantages of the vertical farm. In *Sustainable Environmental Design in Architecture: Impacts on Health*; Rassia, S.T., Pardalos, P.M., Eds.; Springer: New York, NY, USA, 2012; Volume 56, pp. 259–275.
5. Gan, C.I.; Soukoutou, R.; Conroy, D.M. Sustainability Framing of Controlled Environment Agriculture and Consumer Perceptions: A Review. *Sustainability* **2022**, *15*, 304. [CrossRef]
6. Broad, G.M.; Marschall, W.; Ezzeddine, M. Perceptions of High-Tech Controlled Environment Agriculture among Local Food Consumers: Using Interviews to Explore Sense-Making and Connections to Good Food. *Agric. Hum. Values* **2022**, *39*, 417–433. [CrossRef]
7. Goodman, W.; Minner, J. Will the Urban Agricultural Revolution Be Vertical and Soilless? A Case Study of Controlled Environment Agriculture in New York City. *Land Use Policy* **2019**, *83*, 160–173. [CrossRef]
8. Papadopoulou, E.; Mallinis, G.; Siachalou, S.; Koutsias, N.; Thanopoulos, A.C.; Tsaklidis, G. Agricultural Land Cover Mapping through Two Deep Learning Models in the Framework of EU's CAP Activities Using Sentinel-2 Multitemporal Imagery. *Remote Sens.* **2023**, *15*, 4657. [CrossRef]
9. Zhang, J.; Liu, J.; Chen, Y.; Feng, X.; Sun, Z. Knowledge Mapping of Machine Learning Approaches Applied in Agricultural Management—A Scientometric Review with Citespace. *Sustainability* **2021**, *13*, 7662. [CrossRef]
10. Phalke, A.R.; Özdoğan, M.; Thenkabail, P.S.; Erickson, T.; Gorelick, N.; Yadav, K.; Congalton, R.G. Mapping Croplands of Europe, Middle East, Russia, and Central Asia Using Landsat, Random Forest, and Google Earth Engine. *ISPRS J. Photogramm. Remote Sens.* **2020**, *167*, 104–122. [CrossRef]
11. Shamsuzzoha, M.; Shaw, R.; Ahamed, T. Machine Learning System to Assess Rice Crop Change Detection from Satellite-Derived RGVI Due to Tropical Cyclones Using Remote Sensing Dataset. *Remote Sens. Appl. Soc. Environ.* **2024**, *35*, 101201. [CrossRef]
12. Nunez, S.; Verboom, J.; Alkemade, R. Assessing Land-Based Mitigation Implications for Biodiversity. *Environ. Sci. Policy* **2020**, *106*, 68–76. [CrossRef]
13. Waleed, M.; Sajjad, M.; Acheampong, A.O.; Alam, M.T. Towards Sustainable and Livable Cities: Leveraging Remote Sensing, Machine Learning, and Geo-Information Modelling to Explore and Predict Thermal Field Variance in Response to Urban Growth. *Sustainability* **2023**, *15*, 1416. [CrossRef]
14. Lin, F.; Weng, Y.; Chen, H.; Zhuang, P. Intelligent Greenhouse System Based on Remote Sensing Images and Machine Learning Promotes the Efficiency of Agricultural Economic Growth. *Environ. Technol. Innov.* **2021**, *24*, 101758. [CrossRef]
15. Santopuoli, G.; Di Febbraro, M.; Maesano, M.; Balsi, M.; Marchetti, M.; Lasserre, B. Machine Learning Algorithms to Predict Tree-Related Microhabitats Using Airborne Laser Scanning. *Remote Sens.* **2020**, *12*, 2142. [CrossRef]
16. Escasio, J.C.L.; Santillan, J.R.; Makinano-Santillan, M. Using Machine Learning Classifiers and Regression Models for Estimating the Stand Ages of Falcata Plantations from Sentinel Data. *Int. Arch. Photogramm. Remote Sens. Spat. Inf. Sci.* **2023**, *48*, 465–472. [CrossRef]
17. Akhter, R.; Sofi, S.A. Precision Agriculture Using IoT Data Analytics and Machine Learning. *J. King Saud Univ.-Comput. Inf. Sci.* **2022**, *34*, 5602–5618. [CrossRef]
18. Sathiyamurthi, S.; Subbarayan, S.; Ramya, M.; Sivasakthi, M.; Gobi, R.; Qaysi, S.; Praveen Kumar, S.; Lee, J.; Alarifi, N.; Wahba, M. Advancing Agricultural Land Suitability in Urbanized Semi-Arid Environments: Insights from Geospatial and Machine Learning Approaches. *ISPRS Int. J. Geo-Inf.* **2024**, *13*, 436. [CrossRef]
19. Hussain, K.; Mehmood, K.; Yujun, S.; Badshah, T.; Anees, S.A.; Shahzad, F.; Nooruddin; Ali, J.; Bilal, M. Analysing LULC Transformations Using Remote Sensing Data: Insights from a Multilayer Perceptron Neural Network Approach. *Ann. GIS* **2024**, 1–28. [CrossRef]
20. Paz-Kagan, T.; Alexandroff, V.; Ungar, E.D. Detection of Goat Herding Impact on Vegetation Cover Change Using Multi-Season, Multi-Herd Tracking and Satellite Imagery. *Sci. Total Environ.* **2023**, *895*, 164830. [CrossRef]
21. Liakos, K.G.; Busato, P.; Moshou, D.; Pearson, S.; Bochtis, D. Machine Learning in Agriculture: A Review. *Sensors* **2018**, *18*, 2674. [CrossRef]
22. Ojo, M.O.; Zahid, A. Deep Learning in Controlled Environment Agriculture: A Review of Recent Advancements, Challenges and Prospects. *Sensors* **2022**, *22*, 7965. [CrossRef]
23. Abdollahi, A.; Rejeb, K.; Rejeb, A.; Mostafa, M.M.; Zailani, S. Wireless Sensor Networks in Agriculture: Insights from Bibliometric Analysis. *Sustainability* **2021**, *13*, 12011. [CrossRef]
24. Bertoglio, R.; Corbo, C.; Renga, F.M.; Matteucci, M. The Digital Agricultural Revolution: A Bibliometric Analysis Literature Review. *IEEE Access* **2021**, *9*, 134762–134782. [CrossRef]
25. Rejeb, A.; Rejeb, K.; Abdollahi, A.; Al-Turjman, F.; Treiblmaier, H. The Interplay between the Internet of Things and Agriculture: A Bibliometric Analysis and Research Agenda. *Internet Things* **2022**, *19*, 100580. [CrossRef]
26. Kabir, M.; Mahedi, M.; Pervez, A.K.M.; Alam, J.; Shaili, S.J. Bibliometric Analysis of "precision Agriculture" in the Scopus Database. *World J. Adv. Res. Rev.* **2025**, *25*, 1087–1098. [CrossRef]

27. Gómez, C.; Currey, C.J.; Dickson, R.W.; Kim, H.-J.; Hernández, R.; Sabeh, N.C.; Raudales, R.E.; Brumfield, R.G.; Laury-Shaw, A.; Wilke, A.K. Controlled Environment Food Production for Urban Agriculture. *HortScience* **2019**, *54*, 1448–1458. [CrossRef]
28. Klarin, A. How to Conduct a Bibliometric Content Analysis: Guidelines and Contributions of Content Co-occurrence or Co-word Literature Reviews. *Int. J. Consum. Stud.* **2024**, *48*, e13031. [CrossRef]
29. Zupic, I.; Čater, T. Bibliometric Methods in Management and Organization. *Organ. Res. Methods* **2015**, *18*, 429–472. [CrossRef]
30. Leung, X.Y.; Sun, J.; Bai, B. Bibliometrics of Social Media Research: A Co-Citation and Co-Word Analysis. *Int. J. Hosp. Manag.* **2017**, *66*, 35–45. [CrossRef]
31. Chen, G.; Hong, S.; Du, C.; Wang, P.; Yang, Z.; Xiao, L. Comparing Semantic Representation Methods for Keyword Analysis in Bibliometric Research. *J. Informetr.* **2024**, *18*, 101529. [CrossRef]
32. Barrios, E. Soil biota, ecosystem services and land productivity. *Ecol. Econ.* **2007**, *64*, 269–285. [CrossRef]
33. Schultz, B.; De Wrachien, D. Irrigation and Drainage Systems Research and Development in the 21st Century. *Irrig. Drain.* **2002**, *51*, 311–327. [CrossRef]
34. Singh, A. Soil Salinization Management for Sustainable Development: A Review. *J. Environ. Manag.* **2021**, *277*, 111383. [CrossRef] [PubMed]
35. Dang, F.; Chen, D.; Lu, Y.; Li, Z. YOLOWeeds: A Novel Benchmark of YOLO Object Detectors for Multi-Class Weed Detection in Cotton Production Systems. *Comput. Electron. Agric.* **2023**, *205*, 107655. [CrossRef]
36. Esposito, M.; Crimaldi, M.; Cirillo, V.; Sarghini, F.; Maggio, A. Drone and sensor technology for sustainable weed management: A review. *Chem. Biol. Technol. Agric.* **2021**, *8*, 18. [CrossRef]
37. Yurui, L.; Yi, L.; Pengcan, F.; Hualou, L. Impacts of Land Consolidation on Rural Human–Environment System in Typical Watershed of the Loess Plateau and Implications for Rural Development Policy. *Land Use Policy* **2019**, *86*, 339–350. [CrossRef]
38. Sadiq Khan, M.; Ullah, S.; Sun, T.; Rehman, A.U.; Chen, L. Land-use/land-cover changes and its contribution to urban heat Island: A case study of Islamabad, Pakistan. *Sustainability* **2020**, *12*, 3861. [CrossRef]
39. Aghi, D.; Mazzia, V.; Chiaberge, M. Local Motion Planner for Autonomous Navigation in Vineyards with a RGB-D Camera-Based Algorithm and Deep Learning Synergy. *Machines* **2020**, *8*, 27. [CrossRef]
40. Hu, G.; You, F. Renewable Energy-Powered Semi-Closed Greenhouse for Sustainable Crop Production Using Model Predictive Control and Machine Learning for Energy Management. *Renew. Sustain. Energy Rev.* **2022**, *168*, 112790. [CrossRef]
41. Villalba, J.J.; Provenza, F.D. Self-Medication and Homeostatic Behaviour in Herbivores: Learning about the Benefits of Nature's Pharmacy. *Animal* **2007**, *1*, 1360–1370. [CrossRef]
42. Battaglia, M.J.; Lafuente, A.; Benavides, J.C.; Lilleskov, E.A.; Chimner, R.A.; Bourgeau-Chavez, L.L.; Skillings-Neira, P.N. Using Remote Sensing to Map Degraded Mountain Peatlands with High Climate Mitigation Potential in Colombia's Central Cordillera. *Front. Clim.* **2024**, *6*, 1334159. [CrossRef]
43. Heumann, B.W.; Walsh, S.J.; McDaniel, P.M. Assessing the Application of a Geographic Presence-Only Model for Land Suitability Mapping. *Ecol. Inform.* **2011**, *6*, 257–269. [CrossRef] [PubMed]
44. Zhang, Y.; Wei, L.; Lu, Q.; Zhong, Y.; Yuan, Z.; Wang, Z.; Li, Z.; Yang, Y. Mapping Soil Available Copper Content in the Mine Tailings Pond with Combined Simulated Annealing Deep Neural Network and UAV Hyperspectral Images. *Environ. Pollut.* **2023**, *320*, 120962. [CrossRef]
45. Uhl, A.; Melnyk, O.; Melnyk, Y.; Manko, P.; Brunn, A.; Fesyuk, V. Remote Sensing Monitoring of Changes in Forest Cover in the Volyn Region: A Cross Section for the First Two Decades of the 21st Century. *Visnyk V.N. Karazin Kharkiv Natl. Univ. Ser. Geol. Geogr. Ecol.* **2024**, *60*, 272–283. [CrossRef]
46. Almalki, F.A.; Salem, S.M.; Fawzi, W.M.; Alfeteis, N.S.; Esaifan, S.A.; Alharthi, A.S.; Alnefaiey, R.Z.; Naith, Q.H. Coupling an Autonomous UAV With a ML Framework for Sustainable Environmental Monitoring and Remote Sensing. *Int. J. Aerosp. Eng.* **2024**, *2024*, 4285475. [CrossRef]
47. Darwin, B.; Dharmaraj, P.; Prince, S.; Popescu, D.E.; Hemanth, D.J. Recognition of Bloom/Yield in Crop Images Using Deep Learning Models for Smart Agriculture: A Review. *Agronomy* **2021**, *11*, 646. [CrossRef]
48. Fallah, M.; Ghanbari Parmehr, E. Detection of Chilo Suppressalis Using Smartphone Images and Deep Learning. *J. Agric. Mach.* **2023**, *13*, 195–211. [CrossRef]
49. Sandino, J.; Maire, F.; Caccetta, P.; Sanderson, C.; Gonzalez, F. Drone-Based Autonomous Motion Planning System for Outdoor Environments under Object Detection Uncertainty. *Remote Sens.* **2021**, *13*, 4481. [CrossRef]
50. Zakarya, Y.M.; Metwaly, M.M.; AbdelRahman, M.A.E.; Metwalli, M.R.; Koubouris, G. Optimized Land Use through Integrated Land Suitability and GIS Approach in West El-Minia Governorate, Upper Egypt. *Sustainability* **2021**, *13*, 12236. [CrossRef]
51. Ogungbuyi, M.G.; Guerschman, J.P.; Fischer, A.M.; Crabbe, R.A.; Mohammed, C.; Scarth, P.; Tickle, P.; Whitehead, J.; Harrison, M.T. Enabling Regenerative Agriculture Using Remote Sensing and Machine Learning. *Land* **2023**, *12*, 1142. [CrossRef]

52. Kirkwood, C.; Cave, M.; Beamish, D.; Grebby, S.; Ferreira, A. A Machine Learning Approach to Geochemical Mapping. *J. Geochem. Explor.* **2016**, *167*, 49–61. [CrossRef]
53. Yu, Y.; Li, J.; Solomon, S.A.; Min, J.; Tu, J.; Guo, W.; Xu, C.; Song, Y.; Gao, W. All-Printed Soft Human-Machine Interface for Robotic Physicochemical Sensing. *Sci. Robot.* **2022**, *7*, eabn0495. [CrossRef] [PubMed]

Disclaimer/Publisher's Note: The statements, opinions and data contained in all publications are solely those of the individual author(s) and contributor(s) and not of MDPI and/or the editor(s). MDPI and/or the editor(s) disclaim responsibility for any injury to people or property resulting from any ideas, methods, instructions or products referred to in the content.

sustainability

MDPI

Article

Multi-Source Data Integration for Sustainable Management Zone Delineation in Precision Agriculture

Dušan Jovanović [1,*], Miro Govedarica [1], Milan Gavrilović [1], Ranko Čabilovski [2] and Tamme van der Wal [3]

[1] Faculty of Technical Sciences, University of Novi Sad, Trg Dositeja Obradovića 6, 21000 Novi Sad, Serbia; miro@uns.ac.rs (M.G.); milangavrilovic@uns.ac.rs (M.G.)
[2] Faculty of Agriculture, University of Novi Sad, Trg Dositeja Obradovića 8, 21000 Novi Sad, Serbia; ranko.cabilovski@polj.uns.ac.rs
[3] AeroVision, Stadsring 47, 3811 HN Amersfoort, The Netherlands; tamme.vanderwal@aerovision.nl
* Correspondence: dusanbuk@uns.ac.rs; Tel.: +381-63-103-8664

Abstract

Accurate delineation of within-field management zones (MZs) is essential for implementing precision agriculture, particularly in spatially heterogeneous environments. This study evaluates the spatiotemporal consistency and practical value of MZs derived from three complementary data sources: electromagnetic conductivity (EM38-MK2), basic soil chemical properties (pH, humus, P_2O_5, K_2O, nitrogen), and vegetation/surface indices (NDVI, SAVI, LCI, BSI) derived from Sentinel-2 imagery. Using kriging, fuzzy k-means clustering, percentile-based classification, and Weighted Overlay Analysis (WOA), MZs were generated for a five-year period (2018–2022), with 2–8 zone classes. Stability and agreement were assessed using the Cohen Kappa, Jaccard, and Dice coefficients on systematic grid samples. Results showed that EM38-MK2 and humus-weighted BSP data produced the most consistent zones (Kappa > 0.90). Sentinel-2 indices demonstrated strong alignment with subsurface data ($r > 0.85$), offering a low-cost alternative in data-scarce settings. Optimal zoning was achieved with 3–4 classes, balancing spatial coherence and interpretability. These findings underscore the importance of multi-source data integration for robust and scalable MZ delineation and offer actionable guidelines for both data-rich and resource-limited farming systems. This approach promotes sustainable agriculture by improving input efficiency and allowing for targeted, site-specific field management.

Keywords: precision agriculture; sustainable agriculture; management zones; EM38-MK2; basic soil properties; Sentinel-2 indices; fuzzy clustering; weighted overlay; data integration; spatiotemporal stability

1. Introduction

Precision agriculture (PA) in Europe and Serbia faces several agronomic, economic, and demographic challenges. Small to medium-sized farms dominate Central and Eastern Europe, limiting economies of scale and raising production costs per hectare [1]. Serbia reflects this trend, with an average farm size of 5.4 ha and pronounced land fragmentation [2]. Concurrently, rural depopulation, population aging, and youth migration contribute to a shortage of agricultural labor [3]. As a result, PA offers a promising strategy to boost productivity and cut input costs, even for small and fragmented farms. Technologies like automated soil sampling, satellite- and UAV-based remote sensing, proximal sensing, and advanced analytics are becoming essential for modern, sustainable agriculture [4].

Moreover, the concept of digital twins and the fusion of real-time field and satellite data have gained prominence for zone delineation and input optimization [5].

While several pilot programs have introduced PA technologies to larger farms—particularly in parts of Western Serbia—broader adoption remains limited among smallholders. Reported yield increases of 12%, and even up to 100% for specific high-value crops, suggest the agronomic potential of these technologies; however, uptake is often constrained by high initial costs, insufficient advisory support, and limited technical capacity [6]. In regions like Vojvodina, where digital infrastructure is somewhat more developed, empirical studies still highlight that PA tools such as drones, online platforms, and remote sensing are underutilized due to financial and educational barriers [7]. While the EU promotes PA through the Common Agricultural Policy (CAP), Serbia is gradually embracing it through pilot initiatives and national rural development strategies [8]. Even so, further investment in digital infrastructure, broadband connectivity, and targeted education is needed to enable wider adoption, particularly on fragmented and resource-limited farms [9]. The integration of digital and geospatial technologies is thus becoming a critical driver of sustainable agricultural production, offering a pathway to address structural limitations and reduce the rural–urban digital divide.

PA is a modern farming approach that combines various technologies to improve yields while conserving natural resources [10]. Recent studies emphasize that the integration of site-specific data sources, even on smallholder farms, is increasingly supported by open access remote sensing and low-cost proximal sensors, enabling broader PA adoption across Europe and transitional regions [5,11,12]. It is grounded in the acquisition and analysis of spatial data on soil and crop variability, facilitating the delineation of site-specific management zones (MZs). This zonation supports targeted application of fertilizers, water, and other inputs based on localized needs [13]. The effectiveness of this approach depends on the combined use of complementary data sources, including proximal sensors, laboratory soil analyses, and satellite imagery, which together provide a comprehensive understanding of field heterogeneity [14,15].

Methods relying on apparent soil electrical conductivity (EC), particularly those using the EM38-MK2 sensor, have become increasingly important for detecting spatial variability in key soil physico-chemical properties in a fast and cost-effective manner [16]. The EM38-MK2 performs continuous, non-invasive measurements at depths of 0–0.5 m and 0–1.5 m, using horizontal and vertical dipoles to generate four data channels per point [17,18]. These readings indirectly reflect soil texture, compaction, moisture, salinity, and, in some cases, organic matter content [17,19], thereby supporting efficient management zone (MZ) delineation and potentially lowering input costs [20]. The approach offers high sampling density, broad coverage, and rapid data acquisition without direct soil contact. However, accuracy may be reduced in excessively moist conditions, where EC is dominated by water content [21], and interference from nearby metallic structures or rocks can require additional data correction.

Satellite-based data, particularly from the Sentinel-2 platform, are increasingly utilized in precision agriculture due to their ability to deliver frequent and wide-area observations of vegetation and soil conditions [22,23]. Vegetation indices (VIs) such as NDVI, SAVI, and LCI provide estimates of biomass and photosynthetic activity, while the Bare Soil Index (BSI) helps detect exposed soil and monitor land degradation [24,25]. These indicators reflect phenological development and support informed decisions throughout the growing season—from sowing to harvest [26,27]. Key advantages include large spatial coverage, high revisit frequency, and access to multi-year time series at up to 10 m resolution. However, satellite data are affected by atmospheric conditions and mixed pixels, and VIs may be influenced by factors unrelated to soil status, such as disease or mechanical damage [25,28].

When combined with field and laboratory data, these indices enhance the robustness of multi-source models for delineating stable and agronomically relevant management zones [28].

Basic soil property (BSP) analysis is a critical element of precision agriculture, offering direct insight into soil fertility through measurements of nitrogen, phosphorus (P_2O_5), potassium (K_2O), pH, and humus content. These parameters are essential for planning fertilization, selecting suitable crops, and assessing productive potential. BSP is valued for its analytical precision and agronomic relevance, yet it remains constrained by the localized nature of sampling, higher per-sample costs, and laboratory processing time. Consequently, BSP data are often integrated with other sources to support spatial interpolation and produce continuous soil property maps that better reflect within-field variability.

The past few years have witnessed a methodological shift from single-source to multi-layer zonation strategies, where EM38-derived soil structure, Sentinel-2-based vegetation dynamics, and laboratory-measured fertility indicators are combined to form robust models [12,29]. These approaches are increasingly favored for their capacity to capture the full spectrum of soil–plant interactions and improve zone stability across different seasons and crop types.

Although previous research highlights the importance of evaluating management zone (MZ) delineation methods—particularly regarding temporal stability and the potential to replace costly field analyses with remote sensing—few studies have jointly examined EM38-MK2, basic soil properties (BSPs), and satellite-derived indices [30]. Moreover, limited attention has been given to how classification techniques such as kriging, fuzzy k-means, or percentile-based methods influence spatial reliability. Integrating these three data sources offers a more comprehensive representation of field variability: EM38-MK2 captures physical soil traits, BSP reflects chemical composition, and satellite indices characterize vegetation dynamics and biological activity.

This study employed kriging as the principal interpolation method for mapping the spatial distribution of soil properties. As a geostatistical approach, kriging leverages spatial autocorrelation to produce continuous prediction surfaces and is commonly used in delineating management zones in precision agriculture. However, its accuracy is sensitive to sampling density and spatial configuration [31], with errors increasing when sampling falls below 0.5 points per hectare or when field conditions are heterogeneous [14]. The method also assumes normally distributed data with stable variance—assumptions often unmet in practice—and relies on robust variogram estimation, which becomes challenging with limited data [32]. In such cases, kriging may yield overly smoothed outputs that obscure within-field variability. Integrating finer-resolution datasets, such as vegetation indices or apparent electrical conductivity (EC) maps, has been shown to enhance the spatial precision of interpolated zones [15].

Recent research highlights the value of multi-year satellite data—particularly NDVI during peak vegetation periods—for assessing the temporal consistency of field performance. Excluding outlier years that deviate from typical agroecological patterns improves management zone reliability [33]. Simplified zoning methods based on a few seasonal observations are gaining traction, especially for small or resource-limited farms [11]. Integrating proximal data (e.g., EM38-MK2) with Sentinel-2 imagery and applying kriging can reduce sampling demands without sacrificing spatial resolution [5]. Clustering algorithms like fuzzy c-means and k-means, using vegetation (VI) and bare soil indices (BSIs), have proven effective with high-resolution time series. NDVI correlates well with soil properties such as organic matter, texture, and pH [12], and its combination with EC data in unsupervised classification has shown promise, although further agronomic validation is needed [30]. Multivariate geostatistical models that integrate dense and sparse data—such

as Vis–NIR, EC, and NDVI—are increasingly employed to delineate zones capturing the full spectrum of soil variability [34].

This study aims to evaluate various methods for delineating agricultural management zones using data from EM38-MK2 measurements, basic soil properties (BSPs), and satellite-derived indices (VI/BSI), with a focus on assessing their spatiotemporal stability over a five-year period (2018–2022). It further seeks to determine the optimal number of zones and the minimal yet effective set of input parameters for practical application in precision agriculture.

The paper is structured as follows: Section 2 details the data sources and methodology; Section 3 presents the comparative results and stability assessments; Section 4 discusses key findings and their practical implications; and Section 5 concludes with recommendations for future research and operational deployment.

2. Materials and Methods

This study investigates soil spatial variability in the context of precision agriculture by integrating proximal sensing data, satellite-derived indices, and laboratory-based soil analyses to delineate stable and agronomically relevant management zones. The methodology combines several classification approaches—such as quantile-based partitioning and weighted overlay—with spatial validation metrics including the Cohen Kappa, Jaccard, and Dice coefficients.

This section outlines the applied methodology (Figure 1), focusing on multi-source data integration, selection of informative input layers, and determination of the optimal number of management zones. Fuzzy k-means clustering was the primary classification method. Its quality was evaluated using the Fuzzy Performance Index (FPI) and Normalized Classification Entropy (NCE). These tools supported informed decision-making in defining functionally relevant management zones.

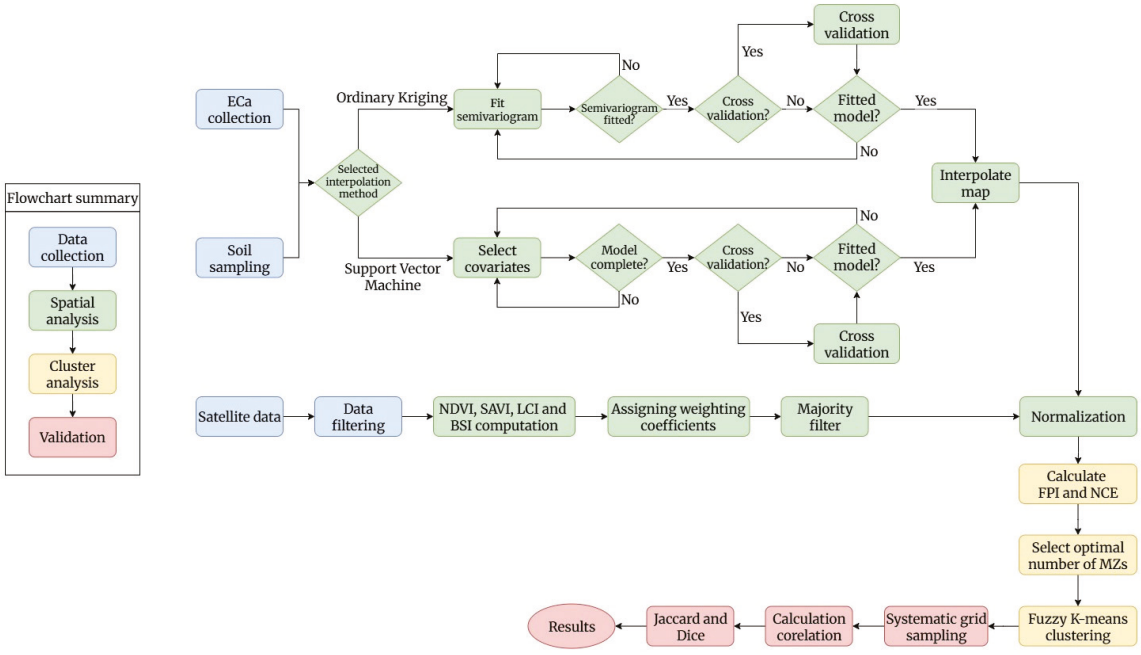

Figure 1. Graphical representation of the integrated workflow for management zone delineation.

2.1. Study Area

The study was conducted in the Komareva Humka cadastral municipality, located in southeastern Vojvodina, Serbia. As part of the Belgrade agricultural basin—formerly managed by PKB and now operated by Al Dahra Serbia [35,36]—the area is characterized

by flat, fertile terrain dominated by alluvial and chernozem soils. This landscape supports intensive field crop production, including cereals, industrial, and forage crops. Long-standing agricultural practices and well-developed irrigation and drainage infrastructure make the region one of Serbia's key arable zones.

The experimental study covered 10 agricultural parcels in Vojvodina, Serbia, ranging from 16 to 92 hectares in size, with a total area of 378 ha (44°56′ N, 20°29′ E) and elevations between 64 and 80 m a.s.l. (Figure 2). Field data were collected in July 2022—on the 11th, 15th, and 19th—shortly after wheat and barley harvests. All parcels were under intensive crop production, primarily focused on field crops.

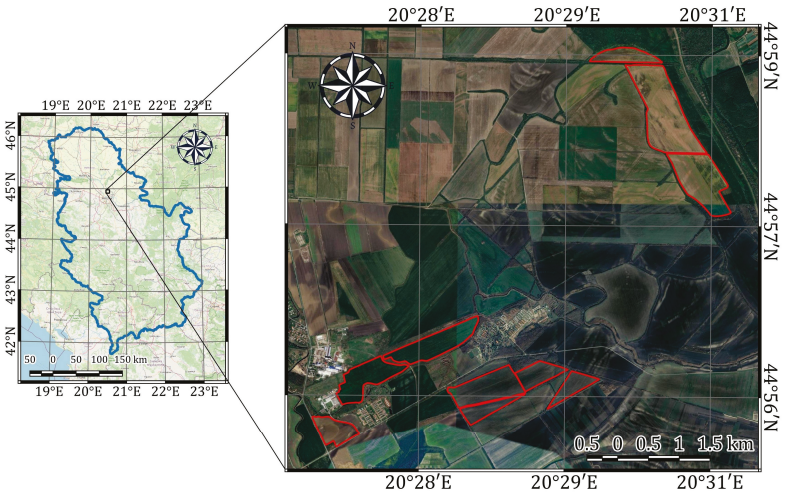

Figure 2. Map of the researched area (Serbia, Vojvodina) with 10 agricultural parcels.

The parcels were chosen based on the availability of synchronized multi-source data, which is rarely accessible under typical field conditions. Specifically, both soil chemical properties (BSPs) and EM38-MK2 electromagnetic measurements were collected on the same day, at nearly the same time, across all fields (Figure 3). This level of spatial and temporal alignment ensured consistency in data integration and allowed for reliable comparative analysis. Although the parcels included in the study range from 16 to 92 ha, the applied methods—including BSP, EM38-MK2 scanning, interpolation, fuzzy clustering, and weighted overlay—are scalable and applicable to much smaller agricultural plots. Based on practical experience with this workflow, the approach can be reliably applied to plots as small as 0.5 ha. However, due to the 10-m spatial resolution of Sentinel-2 imagery, we recommend using this workflow for parcels above that threshold to avoid degradation of classification accuracy.

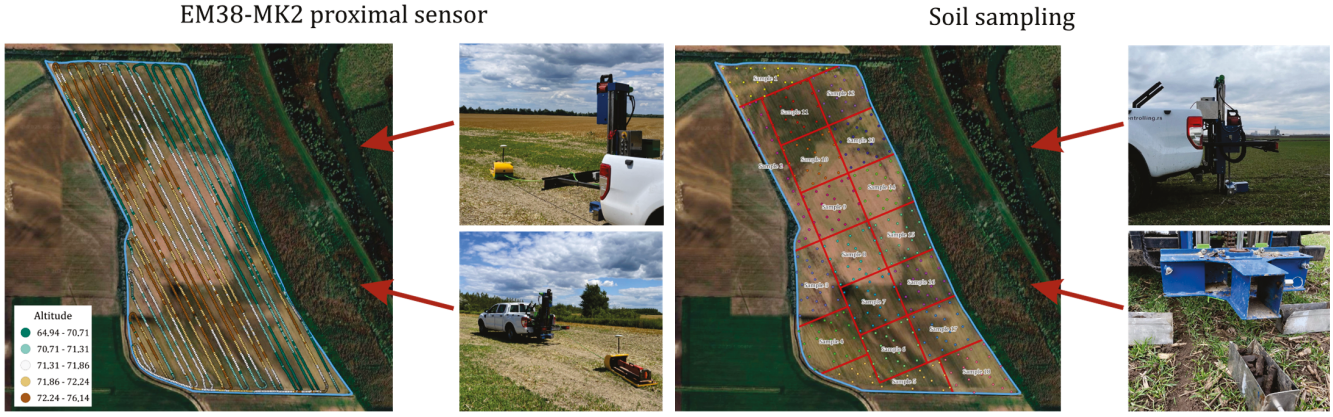

Figure 3. Measurement of soil apparent electrical conductivity (EC) and soil sampling.

2.2. Data Collection

2.2.1. EM38-MK2 Data

Soil apparent electrical conductivity (EC) was measured using the EM38-MK2 sensor (Geonics Ltd., Mississauga, ON, Canada) at four configurations (C1, C0.5, L1, L0.5), corresponding to two depths and dipole modes. The sensor records both conductivity and magnetic susceptibility components, enabling assessment of soil texture, moisture, salinity, and, under certain conditions, organic matter and nutrient distribution [17]. Thanks to its dual-coil design and enhanced sensitivity, EM38-MK2 offers improved accuracy over earlier models [37], and it has proven effective in capturing spatial variability and delineating management zones in agricultural fields [38].

The EM38-MK2 sensor was mounted on a custom sled towed by a vehicle moving at 20 km/h, with transect spacing ranging from 30 to 40 m, depending on parcel shape. This configuration yielded an average point spacing of 8.5 m. On the smallest plot (16 ha), approximately 8000 measurements were recorded, while the largest (90 ha) generated around 27,000 readings (Figure 3). Although not fully optimized [38], the sampling ensured consistent and reliable data acquisition across all parcels.

2.2.2. Sampling and Analysis of Basic Soil Properties

Soil sampling followed standardized protocols defined by ISO 18400-102:2017, which recommends systematic or stratified approaches based on field heterogeneity, typically at one composite sample per 1–5 ha [39]. International practices such as the LUCAS survey [40], FAO guidelines [41], and national protocols in Germany [42] and the U.S. [43] emphasize spatial representativeness. In Serbia, similar recommendations apply, with 3–5 ha per sample being standard in Vojvodina.

We collected soil samples at a depth of 0–30 cm using automated probes (Duoprob 60-UP and Multiprob 120, Soil Probetechnik Peters GmbH, Quakenbrück, Germany). Each ~5 ha section contained 15–25 evenly distributed points, forming one composite sample. For example, a 16 ha parcel yielded 3 samples, while a 90 ha parcel resulted in 18 composite samples (Figure 3). Laboratory analysis included pH (KCl), humus (%), total nitrogen (%), available phosphorus (P_2O_5 mg/kg), and potassium (K_2O mg/kg), in line with accredited procedures. Sampling was performed post-harvest, ensuring timely results for fertilizer planning. The methodology aligns with both national recommendations and regional agronomic practice [44,45].

2.2.3. Sentinel-2 Satellite Imagery and Indices

In addition to soil sampling and measurements of apparent electrical conductivity, satellite data from the Sentinel-2 platform were collected for all parcels included in this study. To complement field measurements, Sentinel-2 imagery from 2018 to 2022 was used to derive vegetation indices—NDVI, SAVI, LCI—and the Bare Soil Index (BSI) for all studied parcels [46–48]. For each season, NDVI time series were interpolated to identify phenologically relevant dates, resulting in five temporal configurations: one (NDVI peak), two (before + peak), three (before, peak, after), four (two before, peak, after), and five dates per year (Figure 4).

BSI was calculated using three configurations: pre-sowing (minimum NDVI), post-harvest (minimum NDVI), and a combination of both (Figure 5). These temporally stratified layers supported further zonation and stability analysis.

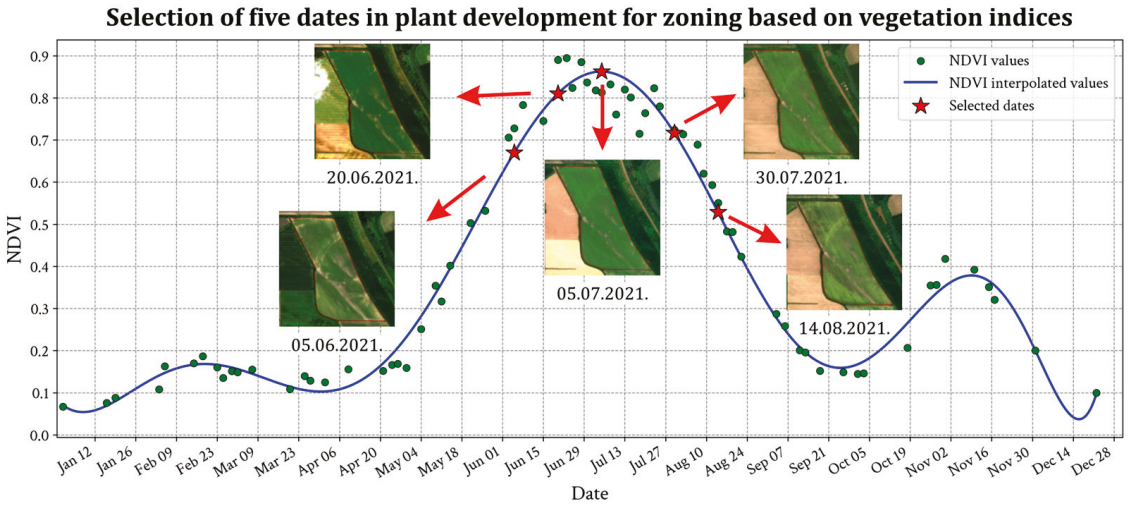

Figure 4. Schematic illustration of vegetation index (VI) date selection.

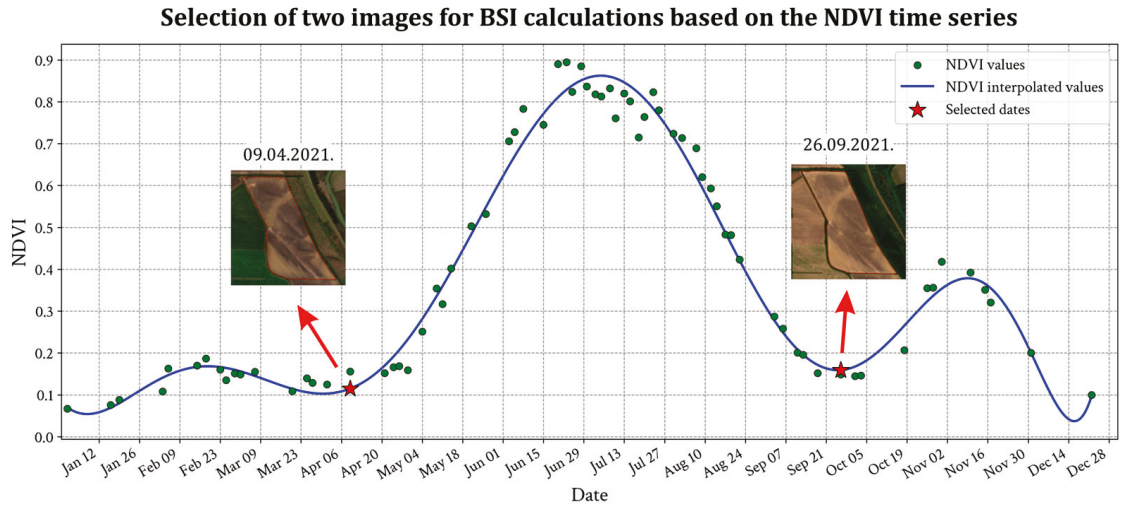

Figure 5. Schematic illustration of BSI date selection.

To address the well-documented issue of NDVI saturation under dense vegetation, we included two additional indices—SAVI and LCI—that mitigate this limitation. SAVI incorporates a soil brightness correction factor to reduce background noise in medium-density vegetation, while LCI leverages Sentinel-2 red-edge bands, which are less prone to saturation and more sensitive to chlorophyll variation. This complementary index selection was intended to enhance the robustness of zonation across different canopy densities.

2.3. Spatial Analysis

Following data acquisition from EM38-MK2 and laboratory soil analysis, spatial interpolation was performed using Ordinary Kriging or Support Vector Machines (SVMs). We applied kriging using five isotropic semivariogram models—linear, linear with threshold, exponential, spherical, and Gaussian—with the optimal model selected via cross-validation [49]. All raster outputs were normalized to a 0–1 scale and resampled to 10 m spatial resolution to ensure compatibility with Sentinel-2-based VI and BSI layers.

Figure 6 includes a total of twenty-five interpolated and normalized raster layers, grouped into five categories: four EM38-MK2 layers (C0.5, C1, L0.5, L1), five basic soil property layers (humus, pH, P_2O_5, K_2O, nitrogen), one BSI index layer, and five layers each for NDVI, SAVI, and LCI derived from different seasonal dates. All layers were resampled to 10 m spatial resolution and normalized to a 0–1 scale to enable consistent comparison.

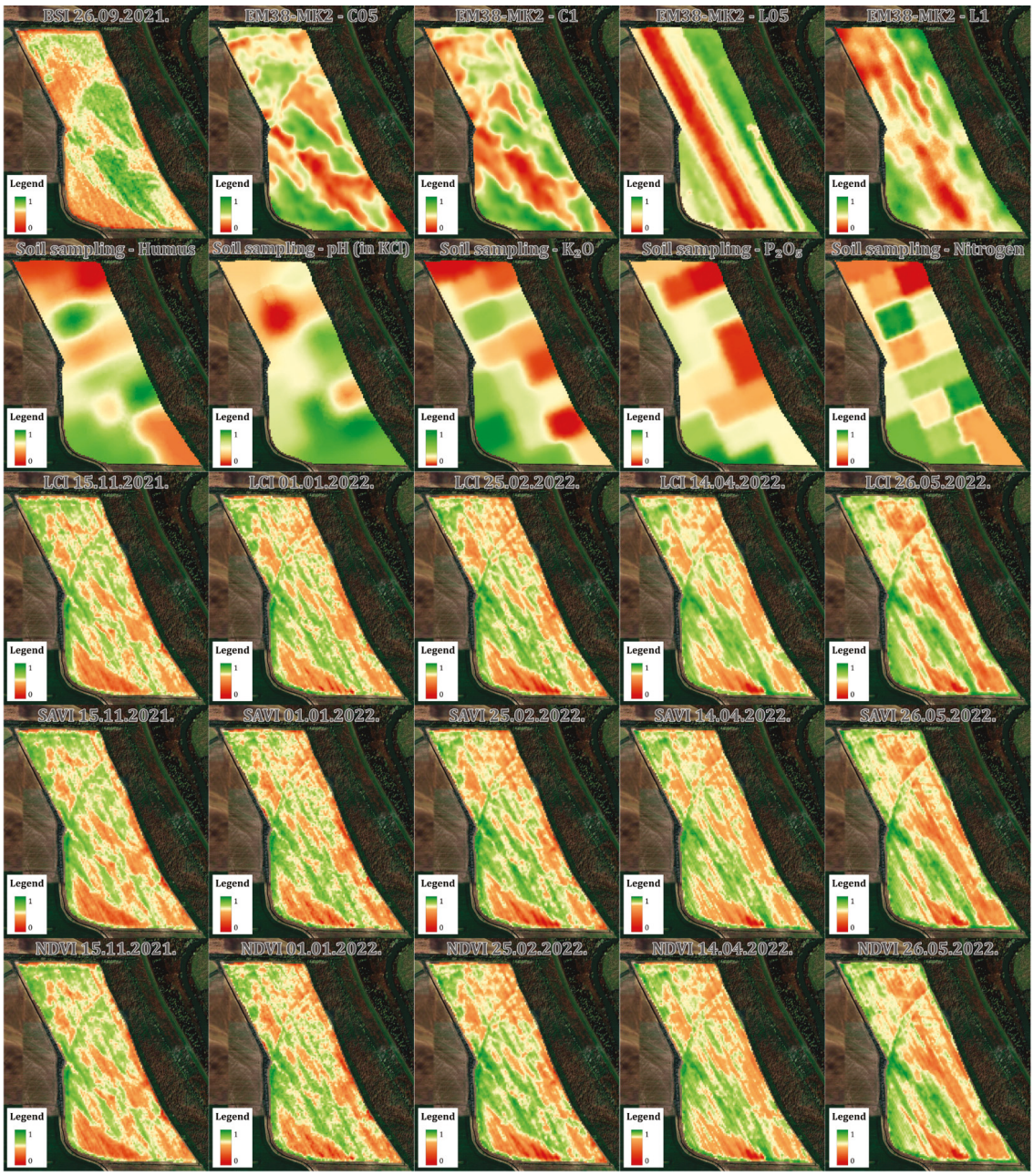

Figure 6. Set of 25 raster layers generated by interpolation and normalization. Layers include four EM38-MK2 depths, five basic soil properties, one BSI index, and five multi-date layers for each of NDVI, SAVI, and LCI.

Following cloud filtering and date selection, satellite data processing included the generation of temporally integrated vegetation and bare soil index (BSI) layers. For each of the five selected dates, NDVI, SAVI, and LCI were computed and averaged into a composite raster:

$$Mean\ Composite_{date} = \frac{NDVI + SAVI + LCI}{3} \quad (1)$$

Each raster was assigned a temporal weight, depending on the number of available dates—for example, [0.3, 0.4, 0.3] for three dates (VI) or [0.6, 0.4] for BSI (pre- and post-season). Final composites were calculated using the following:

$$Final\ Composite = \sum_{i=1}^{n} w_i \times R_i \quad (2)$$

where w_i is the weight and R_i the date-specific raster.

Post-processing included a majority filter to reduce noise and normalization to the [0, 1] scale. The resulting temporally balanced rasters served as inputs for subsequent classification and management zone delineation.

2.4. Cluster Analysis

Beyond interpolation, we classified all datasets into management zones (MZs) using fuzzy k-means clustering. To determine the optimal number of classes, Fuzzy Performance Index (FPI) and Normalized Classification Entropy (NCE) were calculated, following established recommendations [50–52]. Clustering was performed with a maximum of 100 iterations and a fuzzy exponent of 1.25. Across parcels and data types (BSP and EC), the optimal number of classes typically ranged from 2 to 8, with occasional suggestions up to 10. Consequently, classifications were conducted using 2–8 classes per dataset to analyze spatial variability and identify viable management strategies. Figure 7 illustrates an example of how the same dataset is classified using an increasing number of management zones. The figure includes 14 sub-images, which display clustering results for the EM38-MK2 C0.5 layer and a BSI layer corresponding to a selected date. Each example shows zonation maps derived using 2 to 8 classes, allowing for a visual comparison of how classification complexity affects the spatial delineation of management zones.

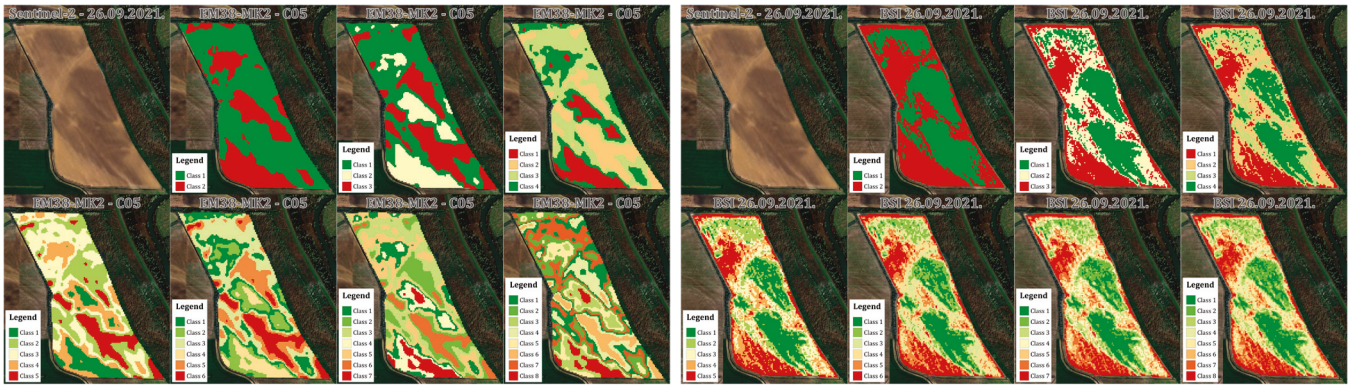

Figure 7. Example of classifications using 2 to 8 classes for one parcel and for EC C0.5 and BSI data.

Three classification approaches were applied across all 10 parcels: fuzzy k-means clustering, Weighted Overlay Analysis (WOA), and percentile-based classification. For each data combination, raster layers were generated using 2 to 8 classes, resulting in eight classified rasters per configuration.

For BSP data, two sets of fuzzy classifications were produced: (a) using all chemical properties and (b) humus only. For EM38-MK2, fuzzy classification included all individual depths (C1, C0.5, L1, L0.5), selected combinations (e.g., C1+C0.5), and each parameter separately.

The weighting coefficients used in WOA were based on agronomic relevance and adapted to the specific combination of parameters. For BSP-only configurations, two weighting schemes were used: the first assigned humus, phosphorus (P_2O_5), and potassium (K_2O) a ratio of 0.65:0.23:0.12; the second incorporated pH with adjusted weights (humus 0.63, P_2O_5 0.21, K_2O 0.11, pH 0.05).

In configurations combining BSP with EM38-MK2 ECa layers (C1 and C0.5), a portion of the total weight was allocated to ECa inputs (typically 0.2 each), while the remainder was proportionally distributed across BSP parameters. These included humus, P_2O_5, K_2O, pH, and in some schemes, total nitrogen, depending on the configuration.

This flexible approach ensured that agronomically important variables remained well represented, while incorporating physical soil structure data into the zonation models.

Percentile-based classification was applied to VI and BSI layers across five growing seasons (2018–2022), using one to five selected dates per year. For BSI in 2018, three configurations were analyzed: pre-sowing, post-harvest, and their combination. Each configuration generated 8 classified rasters (2–8 classes) per parcel (Figure 7).

2.5. Zonation Stability Analysis

To assess the reliability of spatial classifications and delineated management zones (MZ), we conducted a multi-metric stability analysis. Given the importance of spatial consistency in precision agriculture, three complementary methods were applied: (1) systematic grid sampling to examine the effect of sampling resolution [53–56]; (2) Cohen's Kappa coefficient to measure agreement between classified layers while correcting for chance [55]; and (3) the Jaccard and Dice coefficients to quantify spatial overlap in binary zonations [57,58]. This framework enables a comprehensive evaluation of zone robustness, capturing both internal consistency across methods and sensitivity to input configurations and class number. A concise overview of the underlying geostatistical and clustering methods used in this study (e.g., fuzzy k-means, kriging, and agreement indices) can be found in [50,51,55], which offer accessible introductions for readers less familiar with these techniques.

2.5.1. Systematic Grid Sampling

Zone stability was evaluated using systematic grid sampling at intervals of 100 m, 50 m, 20 m, and 10 m across all fields. On the largest parcel (90 ha), this corresponded to 88, 354, 2216, and 8857 sampling points, respectively. Values were extracted from all classified raster layers—including EC, BSP, VI, BSI, and their composites—at each grid point. This approach allowed for consistent comparison of classification outputs across methods and resolutions, minimizing random sampling effects. The extracted data served as input for computing agreement metrics such as the Cohen Kappa, Jaccard, and Dice coefficients [55,57,58].

2.5.2. Kappa Coefficient

We employed Cohen's Kappa coefficient (κ) as the primary metric to assess agreement between classified raster layers, accounting for chance-level concordance. The Kappa coefficient (κ) is defined as follows:

$$\kappa = \frac{p_o - p_e}{1 - p_e} \tag{3}$$

where p_o is the observed agreement and p_e the expected agreement under random classification. Values range from -1 (total disagreement) to 1 (perfect agreement), with values near 0 indicating randomness. The Kappa value was calculated across all raster group combinations (EC, BSP, VI/BSI, and their weighted variants), with stratification by class number (2–8) to evaluate the impact of classification granularity on consistency.

2.5.3. Jaccard and Dice

To complement the Kappa analysis and assess spatial similarity of binarized management zones, the Jaccard and Dice coefficients were applied. The Jaccard index (J) quantifies overlap as the ratio of intersection to union:

$$\mathrm{J} = \frac{|A \bigcap B|}{|A \bigcup B|} \tag{4}$$

The Dice coefficient (D) gives more weight to shared areas and is defined as follows:

$$D = \frac{2 \times |A \bigcap B|}{|A| + |B|} \quad (5)$$

These metrics were used to evaluate spatial agreement between zones produced by different methods and data combinations (e.g., EC vs. BSP, BSP & WOA vs. VI & BSI), offering additional insight into zone consistency and robustness.

3. Results

3.1. Evaluation of EM38-MK2 Data

To assess the internal consistency, classification agreement, and zonation stability of soil electrical conductivity (EC) data from the EM38-MK2 sensor, we conducted a detailed analysis. Pearson's correlation, Cohen's Kappa, and spatial similarity indices (the Jaccard and Dice coefficients) were used on original, normalized, and classified rasters interpolated at four spatial resolutions (10, 20, 50, and 100 m).

3.1.1. Correlation Analysis of Raster Layers for Zonation Stability

Correlation analysis confirmed high consistency across EC raster layers at different spatial resolutions. Normalization preserved the internal ranking of values, with Pearson's correlation coefficients equal to 1 between original and normalized rasters at all grid sizes (10–100 m). Interpolated and normalized layers exhibited strong mutual correlations, while classified rasters showed the highest agreement when the number of classes matched, regardless of EM38-MK2 channel or combination (Figure 8). Coarser grids (e.g., 100 m) resulted in higher mean correlations (≈0.615), indicating reduced local variability and enhanced zonation clarity. These findings support the use of normalized and interpolated layers for stable management zone delineation.

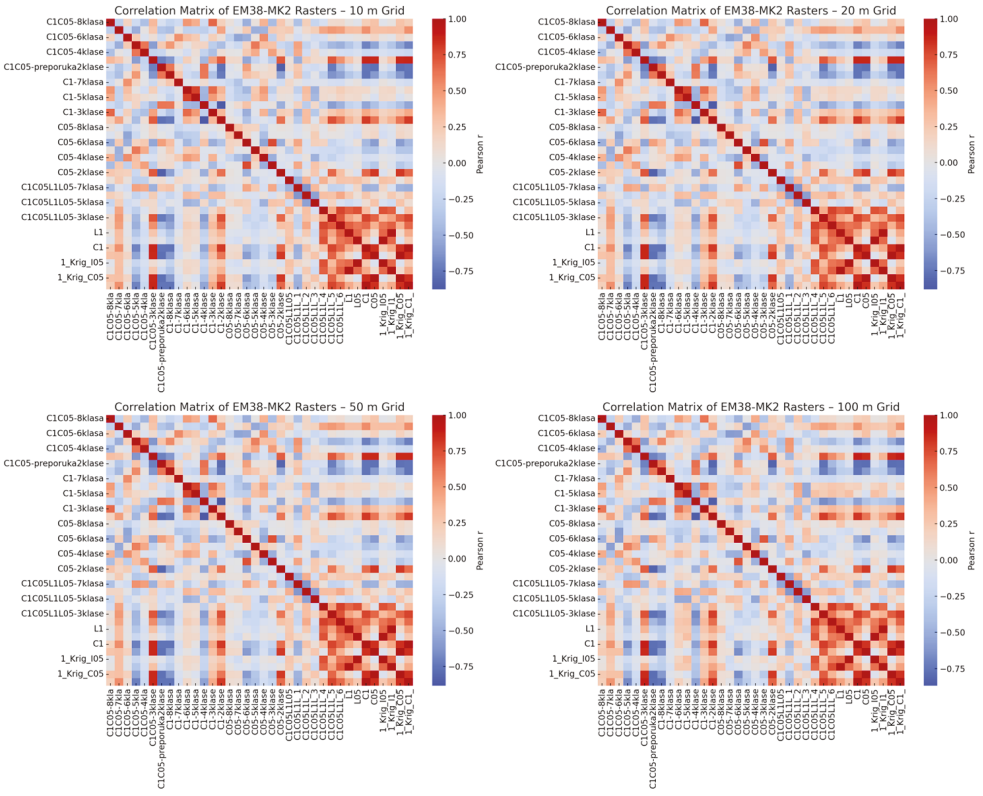

Figure 8. Correlation matrix of EM38-MK2 rasters (original, normalized, and classified) for grid resolutions 10 m to 100 m.

3.1.2. Zonation Consistency Assessment Based on the Kappa Coefficient

Cohen's Kappa coefficient was applied to evaluate zonation consistency derived from EM38-MK2 data, accounting for variations in class number and channel configuration. The highest average agreement was observed for two-class schemes (mean Kappa = 0.6436, max = 0.9541), though with substantial variability (SD = 0.2848), indicating sensitivity to localized variation. Three-class zonation offered a more balanced outcome (mean = 0.4910, max = 0.8812, SD = 0.1560), while four- and five-class configurations maintained moderate stability (mean ≈ 0.46, SD ≈ 0.1). Beyond five classes, both the mean and maximum Kappa values declined, though variability remained low (SD = 0.0505–0.0772), reflecting weaker but stable agreement.

Analysis of channel combinations (Figure 9) showed the best average agreement between C1 and the full composite (C1C05L1L05) with the mean Kappa = 0.4935. Combinations involving C05 and C1+C05 performed similarly well (mean ≈ 0.474–0.478), while inclusion of lateral channels (L1, L05) reduced consistency, likely due to added spatial noise. The highest pairwise Kappa (0.9541) was recorded for C1 vs. C1+C05 with two classes, yet this pairing also showed the lowest value in some cases (Kappa = 0.2227), illustrating strong spatial heterogeneity. The lowest average agreement was found for C05 vs. C1C05L1L05 (mean = 0.4533; range = 0.2805–0.8754), while C1+C05 vs. full composite yielded a slightly better mean of 0.4689. Conversely, C05 vs. C1+C05 produced 0.4788, and C1 vs. full set maintained the highest average (0.4935), indicating that C1 alone can be considered a reliable indicator.

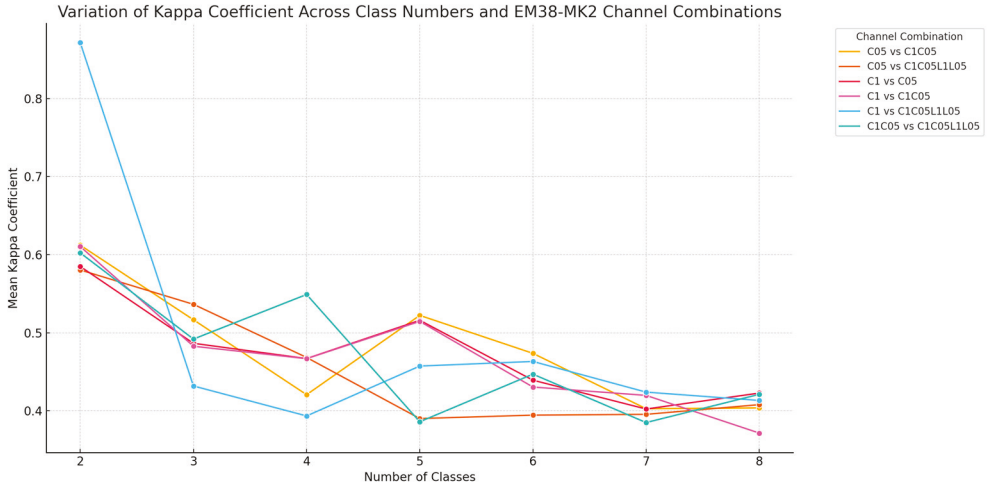

Figure 9. Mean Kappa values for EM38-MK2 channel combinations across class numbers (2–8). Vertical channel pairings (e.g., C1 vs. C1C05) showed higher consistency than combinations involving lateral channels (L1, L05), particularly in schemes with 2–4 classes.

In summary, two-class zonations achieve the strongest agreement but with high variability, whereas three-class configurations provide a good compromise. Class ranges from 3 to 5 and depth-oriented configurations—especially those based on C1—offer the most stable and reliable delineation of soil management zones.

3.1.3. Multi-Class Zonation Similarity Analysis Using the Jaccard and Dice Metrics

The Jaccard and Dice coefficients were used to assess spatial consistency of EM38-MK2-based zonation maps classified into 2–8 classes, across four configurations: C1, C05, C1C05, and C1C05L1L05. As shown in Table 1, single-depth configurations achieved the highest mean similarity: C1 (Jaccard = 0.0857, Dice = 0.1244) and C05 (Jaccard = 0.0771, Dice = 0.1147). Multi-channel setups showed slightly lower values. Despite low means, all groups included raster pairs with the Dice value > 0.9, indicating strong localized overlap.

While overall similarity values were low, configurations based on single-depth inputs (C1 and C05) showed more consistent spatial overlap, with several raster pairs achieving a Dice coefficient above 0.9. This indicates that simpler EM38-MK2 setups can capture stable spatial structures, especially when additional channels introduce noise.

Table 1. Group-wise quantitative similarity analysis based on the Jaccard and Dice coefficients.

Group	Jaccard (Mean ± SD)	Jaccard Max	Dice (Mean ± SD)	Dice Max
C1	0.0857 ± 0.1657	0.8922	0.1244 ± 0.2214	0.943
C05	0.0771 ± 0.1517	0.9428	0.1147 ± 0.2045	0.9706
C1C05	0.0710 ± 0.1396	0.8179	0.1072 ± 0.1967	0.8998
C1C05L1L05	0.0750 ± 0.1853	0.8459	0.1010 ± 0.2277	0.9165

Class number significantly influenced similarity (Table 2). Two-class schemes yielded the highest mean values (Jaccard = 0.1427, Dice = 0.2100), followed by three-class zonations. From four classes onward, both metrics declined, with the lowest overlap at eight classes (Jaccard = 0.0041, Dice = 0.0059), reflecting increased spatial fragmentation. A clear trend was observed with class number: zonations with two or three classes showed stronger spatial agreement, while higher class counts resulted in fragmentation and lower overlap. This confirms the trade-off between detail and spatial coherence.

Table 2. Similarity trends by number of classes based on the Jaccard and Dice coefficients.

Number of Classes	Jaccard Mean	Jaccard Max	Dice Mean	Dice Max
2	0.1427	0.8179	0.21	0.8998
3	0.0966	0.8194	0.1402	0.9008
4	0.0642	0.8318	0.0979	0.9082
5	0.0318	0.6204	0.05	0.7657
6	0.031	0.9428	0.0438	0.9706
7	0.0098	0.5719	0.0143	0.7276
8	0.0041	0.4039	0.0059	0.5754

Overall, zonations with 2–4 classes and single-depth inputs—especially C1 and C05—achieve the best trade-off between spatial coherence and interpretability. These configurations are suitable for standalone use or integration with additional data sources, such as vegetation indices, in precision agriculture workflows.

3.2. Evaluation of BSP Data

The effectiveness of zonation based on basic soil properties (BSPs) was evaluated using the correlation, Kappa, Jaccard, and Dice metrics.

3.2.1. Correlation Analysis of Raster Layers for Zonation Stability

Raster layers derived from humus, P_2O_5, nitrogen, pH, and K_2O showed consistently high mutual correlations across all grid resolutions (10–100 m), with mean absolute Pearson's coefficients ranging from 0.622 to 0.623. Strong ($|r| > 0.6$) and very strong ($|r| > 0.8$) relationships were stable across the dataset. Normalized and classified layers in particular demonstrated reliable internal structure, suitable even without interpolation. Highest correlations were observed between classified layers of the same variable and among composite overlays including humus, P_2O_5, and K_2O. These results confirm the robustness of BSP-based zonation across spatial scales, especially in data-constrained scenarios.

3.2.2. Zonation Consistency Assessment Based on the Kappa Coefficient

Agreement between BSP- and humus-based zonation maps and Weighted Overlay Analysis (WOA) outputs was evaluated using Cohen's Kappa. Values ranged from −0.4592 to 0.3822, with a low overall mean of 0.013, indicating generally weak consistency. Out of 294 comparisons, 159 yielded positive values and 135 yielded negative values, highlighting WOA's sensitivity to input composition and weight allocation. The highest agreement (Kappa = 0.3822) was found between a two-class BSP zonation and a WOA layer weighted by humus (65%), P_2O_5 (23%), and K_2O (12%). In general, humus-only maps aligned more closely with WOA outputs than full BSP combinations, suggesting humus as the dominant factor in spatial differentiation.

3.2.3. Multi-Class Zonation Similarity Analysis Using the Jaccard and Dice Metrics

Similarity between WOA and BSP/humus-based zonation was overall low (mean Jaccard = 0.096; Dice = 0.139). However, individual cases reached high values (Jaccard = 0.8735; Dice = 0.9325), consistently associated with humus-dominant overlays. These findings mirror the Kappa results and underscore the role of humus weighting in achieving spatial coherence.

3.3. Evaluation of VI and BSI Data

3.3.1. Correlation Analysis of Raster Layers for Zonation Stability

Classified raster layers derived from vegetation indices (VIs) and bare soil index (BSI) showed stable spatial patterns across all grid sizes, with the mean Pearson correlation values ranging from 0.32 to 0.34. Resolution had minimal impact, though 100 m grids recorded the highest number of strong correlations ($|r| > 0.8$), indicating enhanced zonation stability at coarser scales (Table 3; Figure 10). This suggests that coarser grids may enhance zonation clarity by reducing local noise, while preserving key spatial trends in VI and BSI patterns. Full correlation matrices with raster layer names for all four grid resolutions (10 m, 20 m, 50 m, and 100 m) are provided in Supplementary Table S1.

Table 3. Summary of the Pearson correlations for VI and BSI classified rasters by resolution.

Grid Resolution	Mean Mean ± Std. Dev.	Min	Max	$\|r\| > 0.6$	$\|r\| > 0.8$
10 m	0.3375 ± 0.3231	−0.2140	0.9994	360	248
20 m	0.3393 ± 0.3230	−0.2167	0.9994	360	250
50 m	0.3194 ± 0.3366	−0.2631	0.9995	356	244
100 m	0.3373 ± 0.3511	−0.3534	0.9996	382	272

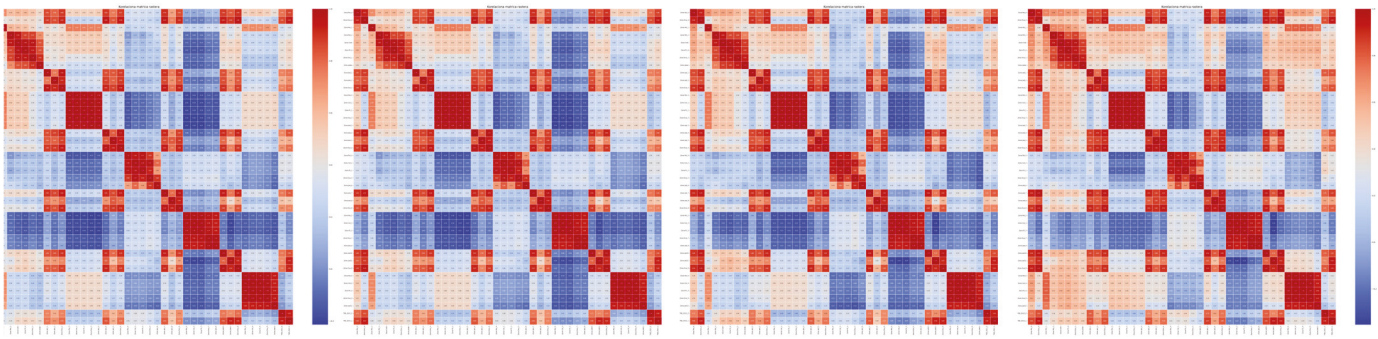

Figure 10. Correlation matrix of VI and BSI classified rasters across different resolutions. Full correlation matrices with complete raster names are available in Supplementary Table S1.

Multi-year zonations integrating VI and BSI layers exhibited strong mutual correlations, suggesting a shared spatial structure. BSI layers based on just two dates (typically pre-sowing and post-harvest) aligned closely with multi-date VI zonations, making them effective in data-constrained scenarios. The highest inter-annual correlation (r = 0.995) was observed between a two-date BSI zonation from 16 April 2020 and 5 December 2020 and a four-date VI zonation from 2021. Other high correlations (r > 0.94) were noted between the following:

- two-date BSI and multi-date VI composites;
- annual and multi-annual zonations (e.g., 2021 vs. 2018–2022);
- spring–autumn combinations across different years.

These findings underscore that both limited-date BSI and multi-date VI layers can reliably capture temporally stable spatial variability, offering practical value for zonation in varying data environments.

3.3.2. Zonation Consistency Assessment Based on the Kappa Coefficient

Cohen's Kappa analysis showed a declining trend in mean agreement with increasing class count (Table 4). Two-class zonations yielded the highest mean Kappa (0.2794), but also the highest variability (SD = 0.2841). Conversely, seven- and eight-class schemes had lower average values (0.1255 and 0.1153), but greater internal consistency (SD = 0.1758 and 0.1665, respectively). These results indicate that simpler (2–3 class) configurations offer higher agreement but greater variability, while higher class counts provide more stable yet divergent outcomes.

Table 4. Summary of the Kappa metrics across class counts (2–8).

Number of Classes	Mean Kappa	Max	Min	Std. Dev.
2	0.2794	0.9761	−0.244	0.2841
3	0.2155	0.9614	−0.1423	0.2422
4	0.1798	0.955	−0.1112	0.2179
5	0.1554	0.9435	−0.082	0.2001
6	0.1389	0.9303	−0.0695	0.1865
7	0.1255	0.9306	−0.0603	0.1758
8	0.1153	0.9162	−0.0566	0.1665

The highest observed Kappa (0.9761) was between four- and five-date VI zonations from 2019, underscoring the stabilizing impact of intra-annual data richness. The lowest value (−0.2440) occurred between two-date BSI zonations from 2019 and 2020, reflecting greater instability in sparse BSI inputs.

Zonations using 3–5 seasonal dates within the same year and based on a single index produced the most reliable results. While two-class configurations offered the strongest mean agreement, they were also the most variable. Three-class schemes provided a better balance (mean = 0.2155; SD = 0.2422), maintaining coherence with moderate spatial granularity. Increasing class count beyond four led to further decline in agreement, but with reduced variability—indicating more consistent yet less similar outcomes.

These findings confirm that both class number and temporal depth influence zonation consistency. Two- and three-class schemes with multi-date imagery offer an optimal trade-off between spatial clarity and stability.

3.3.3. Multi-Class Zonation Similarity Analysis Using the Jaccard and Dice Coefficients

Spatial similarity among VI- and BSI-based zonations was evaluated using the Jaccard and Dice coefficients across index types and acquisition date combinations (Table 5). The highest similarity was recorded for BSI prior to sowing (Jaccard = 0.2412 ± 0.2343; Dice = 0.3641 ± 0.2932), followed by post-harvest BSI and five-date VI zonations (Dice = 0.2651 ± 0.2583). All BSI configurations outperformed VI-based layers in internal coherence. Within VI groups, similarity increased with the number of acquisition dates, while single-date layers showed the lowest agreement (Dice < 0.20). This highlights the advantage of BSI layers—particularly pre-sowing—when bare soil is exposed, offering greater spatial consistency than vegetation-based metrics.

Table 5. Group-based similarity metrics (mean ± standard deviation) and maximum values for VI and BSI zonation groups.

Group	Jaccard (Mean ± SD)	Jaccard Max	Dice (Mean ± SD)	Dice Max
BSI prior to sowing	0.2412 ± 0.2343	0.8571	0.3641 ± 0.2932	0.9231
BSI after harvest	0.1902 ± 0.2179	0.8493	0.2991 ± 0.2780	0.9189
BSI both dates	0.1293 ± 0.1803	0.7023	0.1962 ± 0.2261	0.8252
VI 1 date	0.1036 ± 0.1600	0.7514	0.1561 ± 0.2064	0.8571
VI 2 dates	0.1247 ± 0.1770	0.7775	0.1861 ± 0.2236	0.8824
VI 3 dates	0.1424 ± 0.1896	0.7811	0.2144 ± 0.2369	0.892
VI 4 dates	0.1486 ± 0.1794	0.8066	0.2227 ± 0.2295	0.8922
VI 5 dates	0.1807 ± 0.2067	0.8264	0.2651 ± 0.2583	0.9052

Overall, BSI-based zonations demonstrated superior consistency, especially where bare soil is visible, whereas multi-date VI layers serve as a viable alternative when soil exposure is limited.

Analysis across class counts (Table 6) confirmed that two-class zonations yielded the highest similarity (Jaccard = 0.359; Dice = 0.496), with a gradual decline in both metrics beyond four classes. Three- and four-class schemes provided a favorable trade-off between spatial resolution and internal agreement, while higher class counts led to reduced coherence and increased variability. These findings confirm that moderate complexity in class structure ensures better overlap without excessive fragmentation, especially in high-resolution satellite data.

Table 6. Similarity metrics across class counts (2–8).

Number of Classes	Jaccard (Mean ± SD)	Jaccard Max	Dice (Mean ± SD)	Dice Max
2	0.359 ± 0.206	0.977	0.496 ± 0.214	0.988
3	0.241 ± 0.182	0.977	0.360 ± 0.201	0.988
4	0.184 ± 0.166	0.976	0.285 ± 0.190	0.988
5	0.150 ± 0.153	0.983	0.237 ± 0.180	0.992
6	0.128 ± 0.144	0.976	0.205 ± 0.171	0.988
7	0.111 ± 0.136	0.979	0.181 ± 0.164	0.989
8	0.099 ± 0.129	0.976	0.162 ± 0.157	0.988

These findings suggest that zonation schemes with 2–4 classes, based on temporally aggregated inputs—particularly BSI prior to sowing and multi-date VI layers—offer optimal stability and interpretability for defining management zones in precision agriculture (Figure 11).

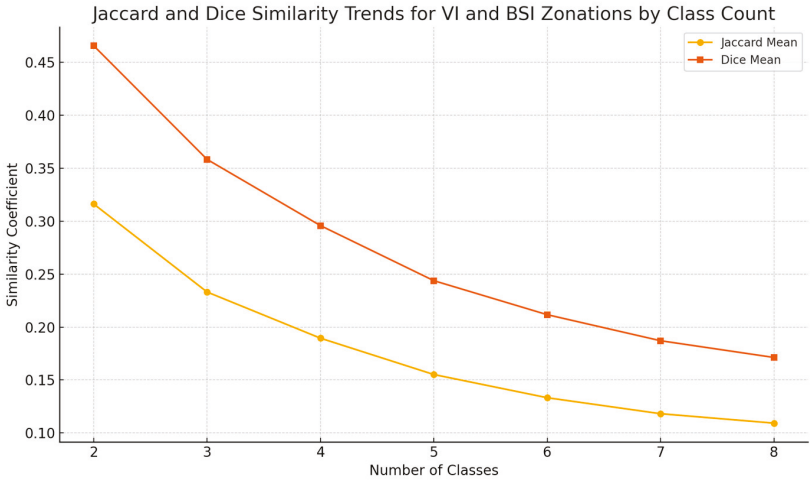

Figure 11. The Jaccard and Dice similarity trends for VI and BSI zonations by class count.

3.4. Evaluation of EM38-MK2 and VI-BSI Data

3.4.1. Correlation Analysis of Raster Layers for Zonation Stability

This analysis explores spatial correspondence between EM38-MK2-derived zonation maps and those generated from satellite-based vegetation (VI) and bare soil indices (BSIs), aiming to evaluate alignment between subsurface conductivity and surface reflectance patterns.

Strong correlations were observed across all resolutions (10–100 m), with the highest values at 50 m and 100 m where smoothing reduced noise. At these scales, Pearson's r often exceeded 0.80, especially for C05 (4-class), C1 (3-class), and L05 (5-class) configurations, with R^2 values up to 0.70. Even at 10 m resolution, correlations remained substantial (r = 0.55–0.70), particularly when using multi-date or multi-year composites.

While correlation strength decreased slightly at finer resolutions (10 m), values remained meaningful (r = 0.55–0.70), especially when VI/BSI layers were based on multi-date or multi-year composites. Zonations using 4–6 classes demonstrated greater stability and spatial alignment with VI/BSI, while 2-class models lacked sufficient granularity, and schemes with over 6 classes often introduced fragmentation.

Among all comparisons, the five-date VI layer from 2019 yielded the highest overall agreement with EM38 zones (mean r = 0.84; max r = 0.96). High correlations were also found for C1 and C05 zones at 100 m with VI 2021 and BSI 2020 (r > 0.90). Notably, even the 20th-best correlated layer exceeded r = 0.75. Figure 12 presents the top 20 Pearson correlations between EM38-MK2-based zonation layers (C1 and C0.5) and corresponding VI/BSI classifications at a 100 m grid resolution. All input layers used to generate this figure are documented in Supplementary Table S2, which provides full names and metadata for traceability.

These results confirm the strong spatial coherence between temporally aggregated VI/BSI layers and EM38-derived zones, supporting their integration for constructing robust and scalable data-driven management zones in precision agriculture.

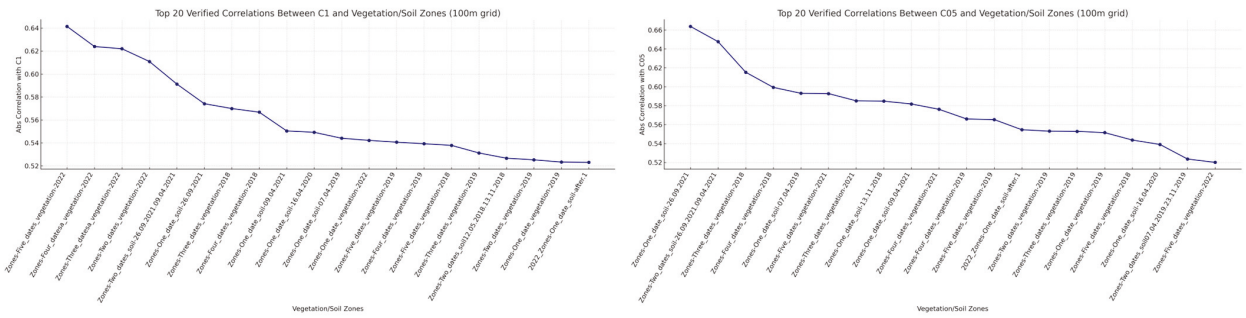

Figure 12. Top 20 correlations between C1 and C05 with VI/BSI zones for grid of 100 m resolutions.

3.4.2. Zonation Consistency Assessment Based on Kappa Coefficient

Zonation consistency between EM38-MK2 conductivity maps and VI/BSI indices was assessed using Cohen's Kappa coefficient. On average, agreement was low, with mean values across class counts (2–8) near or below zero (Table 7). Slightly higher averages appeared in 5–8 class configurations (e.g., mean Kappa = 0.02 for 5 classes), while 2–4 class schemes showed greater variability and a higher frequency of negative values, indicating divergence in spatial structure. However, selected two-class combinations—especially C1C05 vs. multi-date VI/BSI—achieved localized alignment, suggesting targeted integration may be effective in specific scenarios.

Table 7. Summary of the Kappa metrics for EM38-MK2 vs. VI/BSI zonation pairs across class counts (2–8).

Number of Classes	Mean Kappa	Max Kappa	Min Kappa	Std. Dev.
2	−0.06	0.3672	−0.3548	0.078
3	−0.031	0.1736	−0.1857	0.0506
4	−0.024	0.15	−0.1275	0.0318
5	0.02	0.0913	−0.09	0.0238
6	−0.02	0.0731	−0.0613	0.019
7	0.001	0.0611	−0.0503	0.016
8	−0.001	0.0504	−0.0629	0.0136

Despite overall low agreement, analysis of the top 100 highest Kappa values revealed specific patterns. The C1C05 EM38 configuration dominated (39% of top matches), followed by C1C05L1L05 (25%) and C1 alone (24%). Additionally, 78 of the top 100 values were based on 2-class zonations, confirming their potential for strong alignment under optimal conditions.

BSI layers appeared in 70% of top-ranked matches, particularly those from 2018 and 2019 (together 64%), highlighting their spatial stability. Though VI had a slightly higher average Kappa, BSI proved more prominent among the best-scoring combinations. Notably, all top 10 individual pairings involved 2-class C1C05 EM38 zonations combined with multi-date VI or BSI layers (Table 8).

These results indicate that, while general agreement remains weak, specific configurations—especially 2-class C1C05 zones aligned with temporally rich VI/BSI layers—can achieve meaningful spatial consistency. This emphasizes the value of targeted data combinations and temporal aggregation for robust zone delineation in precision agriculture.

Table 8. The 10 representative high-performing pairings of EM38-MK2 and VI/BSI zonation layers.

EM38-MK2 Channel Combination	VI/BSI Combination	Max Kappa
C1C05	3 dates VI 2018	0.3672
C1C05	4 dates VI 2019	0.3231
C1C05	5 dates VI 2019	0.3262
C1C05	4 dates VI 2018	0.3093
C1C05	1 date VI 2019	0.3183
C1C05	3 dates VI 2019	0.3196
C1C05	2 dates VI 2019	0.3174
C1C05	5 dates VI 2018	0.2485
C1C05	2 dates BSI 2021	0.2677
C1C05	2 dates VI 2018	0.286

3.4.3. Multi-Class Zonation Similarity Analysis Using the Jaccard and Dice Coefficients

Spatial similarity between zonation layers derived from EM38-MK2 conductivity and remote sensing indices (VI, BSI) was evaluated using the Jaccard and Dice coefficients across all agricultural sites, with class counts ranging from 2 to 8. A clear inverse relationship was observed: similarity decreased with increasing class number (Figure 13).

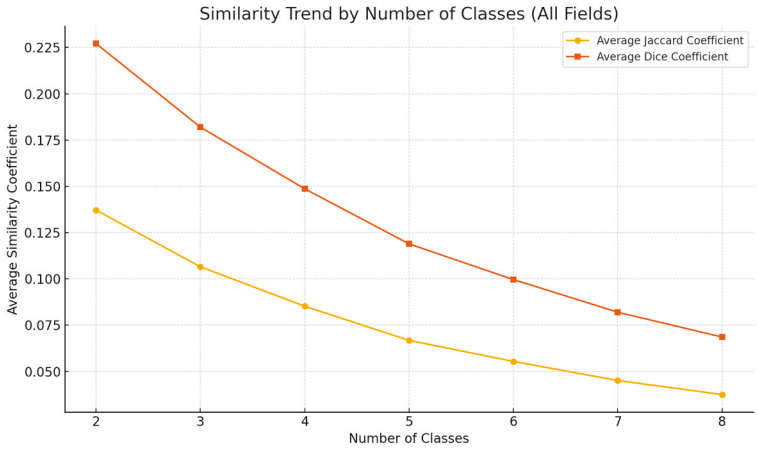

Figure 13. Similarity trends of the Jaccard and Dice coefficients by class count between EM38-MK2 and VI/BSI zonations across all fields.

Two-class zonations based on C1C05 profiles exhibited the strongest agreement with surface indices. When compared to multi-date VI from 2018 or two-date BSI from 2021, the Jaccard values exceeded 0.62 and the Dice values reached 0.77, indicating that binary conductivity zones effectively reflect dominant surface patterns. Three-class schemes also performed well, with a Dice value up to 0.71 and a Jaccard value around 0.55, particularly when paired with early-season or aggregated VI/BSI layers.

Although similarity declined in four-class schemes, selected combinations—such as C1C05 with 3-date VI 2018 or 2-date BSI 2021—still produced moderate agreement (Dice $\approx$ 0.67; Jaccard $\approx$ 0.51). For class counts above five, both metrics dropped significantly, reflecting increased fragmentation and reduced coherence.

Across all scenarios, the Dice coefficients consistently exceeded the Jaccard coefficient due to higher sensitivity to shared class members, though both followed the same trends. Overall, simpler zonations with 2–4 classes—especially those based on C1C05 conductivity—showed the highest compatibility with VI/BSI-derived zones. While overall agreement was moderate (typically Dice = 0.1–0.4), results underscore the complementary nature of subsurface and surface data for spatial soil variability assessment.

3.5. Evaluation of EM38-MK2, BSP, VI and BSI Data

3.5.1. Correlation Analysis of Raster Layers for Zonation Stability

Pearson's correlation analysis was conducted to evaluate spatial agreement among zonation layers derived from EM38-MK2, BSP, VI, and BSI datasets at 10, 20, 50, and 100 m resolutions. As presented in Table 9, mean absolute correlation values remained consistently above 0.57 across all grids, with minimal variation, and over 530 raster pairs exceeded $|r| > 0.6$ at each resolution. The 100 m grid yielded the highest number of very strong correlations (210 with $|r| > 0.8$), suggesting enhanced large-scale coherence due to reduced local noise.

Notably, hybrid layers combining EM38 and BSP data—especially humus, P_2O_5, K_2O, and pH—correlated strongly with multi-date VI and BSI layers, often surpassing $r = 0.85$ ($R^2 > 0.70$). The most stable alignments were observed in classified rasters with 3 to 5 classes and in composites integrating multi-source and seasonal data. Kriging-interpolated rasters were excluded to avoid correlation bias.

Table 9. Summary statistics of Pearson's correlations for combined EM38-MK2, BSP, VI, and BSI raster layers.

Grid Resolution	|r| > 0.4	|r| > 0.6	|r| > 0.8	Mean	Median
10 m	1379	486	187	0.583	0.517
20 m	1373	482	188	0.584	0.519
50 m	1477	496	188	0.579	0.522
100 m	1660	534	210	0.576	0.521

Although average correlation across all combinations remained modest (mean ~0.03–0.036), a large number of pairings exhibited strong alignment. At 100 m resolution, 619 raster pairs exceeded $|r| > 0.8$, compared to 571 at 10 m, highlighting the advantage of spatial aggregation (Figure 14). Full raster names corresponding to the 100 m correlation matrix in Figure 14 are available in Supplementary Table S2.

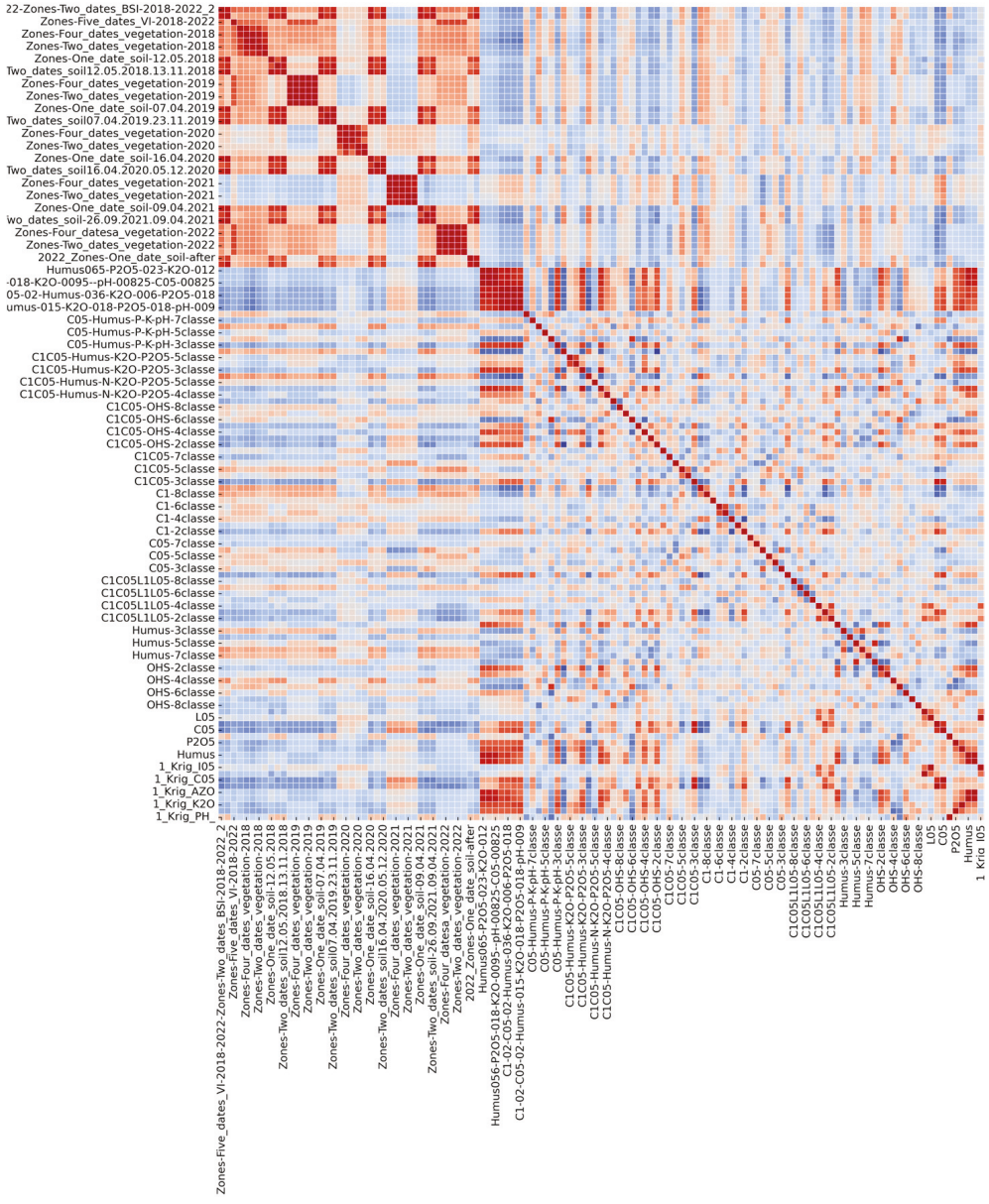

Figure 14. Correlation matrix heatmaps illustrating significant spatial correlations among EM38-MK2, BSP, VI, and BSI raster layers across for 100 m grid resolutions. Full correlation matrix with complete raster names are available in Supplementary Table S2.

These results confirm that moderate-to-coarse resolutions, combined with weighted integration of EM38-MK2, BSP, and VI/BSI data, provide a solid foundation for generating consistent and scalable management zones in precision agriculture.

3.5.2. Zonation Consistency Assessment Based on the Kappa Coefficient

Zonation agreement among different data sources was assessed using Cohen's Kappa coefficient across raster layers derived from EM38-MK2 (EM38_KL), weighted overlays with BSP (EM38_KNT), standalone BSP (BSP_KL, BSP_KNT), and VI/BSI indices (VI/BSI_KNT), covering class counts from 2 to 8. Each group included 10,000–31,000 comparisons depending on parcel size.

As shown in Table 10, the highest internal agreement was observed within BSP_KNT (mean Kappa = 0.948), followed by EM38_KNT (0.808), and their mutual comparison (0.738), confirming the reliability of WOA-based zonations. VI/BSI_KNT layers showed moderate consistency (mean = 0.552), while quantile-classified layers (EM38_KL and BSP_KL) yielded much lower values (mean < 0.36), indicating weaker internal robustness.

Table 10. Summary of the Kappa statistics comparing different data groups.

Group Combination	Mean Kappa	Std. Dev.	Min Kappa	Max Kappa
BSP_KNT vs. BSP_KNT	0.948	0.033	0.858	0.997
EM38_KNT vs. EM38_KNT	0.808	0.117	0.483	0.985
EM38_KNT vs. BSP_KNT	0.738	0.124	0.488	0.990
VI/BSI_KNT vs. VI/BSI_KNT	0.552	0.131	0.368	0.995
BSP_KNT vs. VI/BSI_KNT	0.427	0.071	0.304	0.653
EM38_KL vs. BSP_KL	0.353	0.160	−0.037	0.852

Class count strongly influenced agreement (Figure 15). The best results were consistently observed with 2-class schemes—mean Kappa up to 0.99—especially for EM38_KNT, BSP_KNT, and VI/BSI_KNT. However, consistency decreased with increasing class number; for instance, Kappa for EM38_KNT vs. VI/BSI_KNT dropped from 0.516 (2 classes) to 0.373 (8 classes).

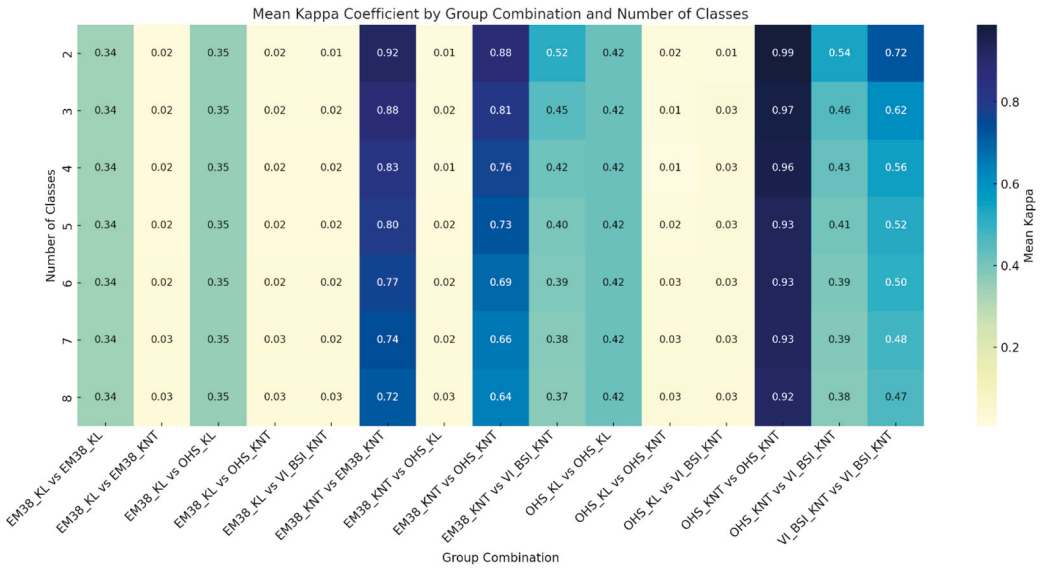

Figure 15. Influence of the number of classes on agreement.

Key findings include the following:

- EM38_KNT vs. BSP_KNT had the strongest cross-source alignment (mean = 0.738), supporting integrated geophysical–chemical zonation.
- Simple classifications (EM38_KL vs. BSP_KL) had much lower agreement (mean = 0.353), underscoring the limitations of univariate approaches.
- VI/BSI_KNT comparisons with other groups were only moderately consistent and mostly in 2–3 class schemes.

These results highlight the benefits of multi-variable weighted models for producing stable, interpretable zonations. Careful calibration of input diversity and class complexity is essential for effective spatial decision-making in precision agriculture.

3.5.3. Multi-Class Zonation Similarity Analysis Using Jaccard and Dice

Spatial similarity between zonation layers from five data sources—EM38, BSP, VI-BSI, BSP weighted, and composite EM38+BSP overlays—was assessed using the Jaccard and Dice coefficients. As presented in Table 11, the EM38+BSP group achieved the highest internal consistency (mean Dice = 0.6844; Jaccard = 0.5629), indicating that integrated geophysical and chemical data via weighted overlays yield the most coherent spatial outputs. Moderate similarity was also observed within VI-BSI and BSP groups (Dice means of 0.2339 and 0.1660, respectively).

Table 11. Summary of the Jaccard and Dice similarity coefficients across raster group comparisons.

Group Comparison	Jaccard Mean	Jaccard Max	Jaccard Std	Dice Mean	Dice Max	Dice Std
EM38 vs. EM38	0.0959	0.9775	0.1692	0.1409	0.9886	0.2238
EM38 vs. BSP	0.0831	0.6054	0.0976	0.14	0.7542	0.1501
EM38 vs. BSP weighted	0.0863	0.7343	0.105	0.1436	0.8468	0.1594
EM38 vs. Other	0.0827	0.6081	0.0893	0.1414	0.7563	0.1396
EM38 vs. VI/BSI	0.0626	0.6254	0.0693	0.1106	0.7696	0.1125
EM38+BSP vs. EM38	0.085	0.7452	0.1066	0.1411	0.854	0.1599
EM38+BSP vs. EM38+BSP	0.5629	1	0.2507	0.6844	1	0.227
EM38+BSP vs. BSP	0.0871	0.924	0.1473	0.1335	0.9605	0.2
EM38+BSP vs. BSP-weighted	0.0888	0.9445	0.1458	0.1369	0.9715	0.1986
EM38+BSP vs. Other	0.4476	0.9978	0.2606	0.5738	0.9989	0.2509
EM38+BSP vs. VI-BSI	0.0738	0.4732	0.0622	0.1317	0.6424	0.0994
BSP vs. BSP	0.1008	1	0.2187	0.1315	1	0.2635
BSP vs. BSP-weighted	0.1136	0.98	0.2025	0.1582	0.9899	0.2553
BSP vs. VI-BSI	0.0664	0.5591	0.0723	0.1166	0.7172	0.1175
BSP-weighted vs. BSP-weighted	0.1316	0.9984	0.2589	0.166	0.9992	0.2961
BSP-weighted vs. VI-BSI	0.064	0.5953	0.0716	0.1125	0.7463	0.1165
Other vs. BSP	0.0943	0.9538	0.1839	0.1331	0.9764	0.2361
Other vs. BSP-weighted	0.0932	0.9445	0.1712	0.136	0.9715	0.2238
Other vs. Other	0.844	1	0.1202	0.9104	1	0.0772
Other vs. VI-BSI	0.078	0.3935	0.0641	0.1387	0.5648	0.1019
VI-BSI vs. VI-BSI	0.1504	1	0.1648	0.2339	1	0.1958

Cross-group agreement was substantially lower. EM38 vs. VI-BSI comparisons showed the weakest spatial alignment (mean Dice $\approx$ 0.11; Jaccard < 0.07), reflecting fundamental differences between surface reflectance and subsurface conductivity. However, EM38+BSP composites aligned better with OHS-weighted rasters (Dice = 0.5738), suggesting improved compatibility through multi-source integration.

The maximum Dice and Jaccard values approached 1.0 in several within-group and hybrid configurations, especially in the "Other vs. Other" group (Dice = 0.9104), indicating near-identical zones when classification structures are well-calibrated (Figure 16). Key findings include the following:

- EM38+BSP overlays deliver the highest internal similarity.
- VI-BSI zones are consistent internally but poorly aligned with geophysical and chemical layers.
- Cross-domain similarities remain limited, underscoring the unique contributions of each data type.
- High similarity is achievable through optimized weighting and classification design.

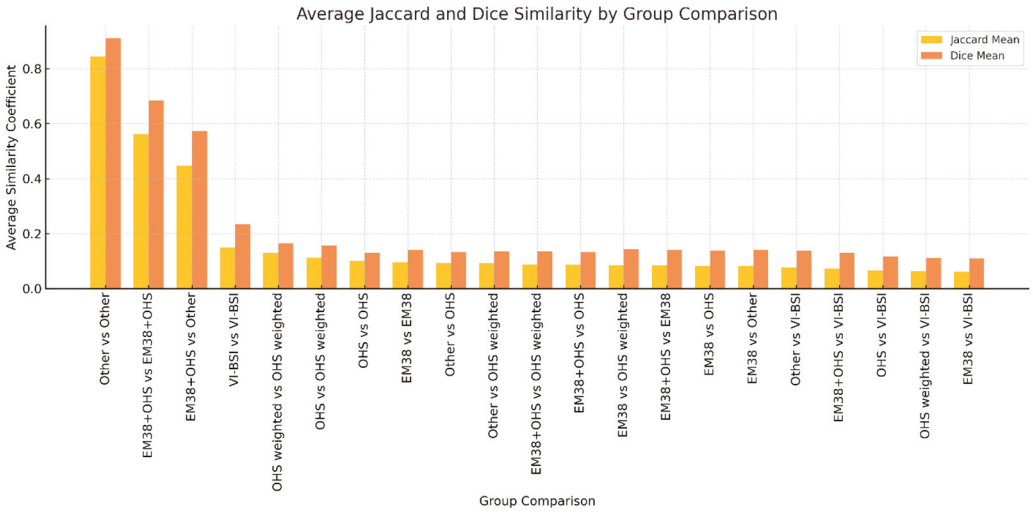

Figure 16. The mean Jaccard and Dice similarity coefficients across raster group comparisons.

These results underscore the importance of multi-source fusion for robust zonation and suggest that optimal models balance internal coherence with inter-source compatibility, tailored to specific agro-environmental contexts.

4. Discussion

4.1. Interpretation of Results in the Context of Existing Literature and Practice

The obtained results clearly demonstrate that different data sources and zonation approaches yield distinct patterns of stability, consistency, and spatial uniformity. Consistent with previous studies [15,17,32], classifications using a smaller number of zones (ranging from two to four) provide a higher degree of spatial similarity and lower inter-annual and inter-method variability. This is particularly important for practical implementation in precision agriculture.

The high stability observed in zones derived from the integration of multiple data sources (EC and BSP) through Weighted Overlay Analysis reinforces earlier findings on the effectiveness of multi-criteria approaches in soil zonation [17]. The results also show that giving more weight to humus leads to better alignment with reference zones, supporting earlier findings [19] that highlight the importance of soil organic matter.

Vegetation indices derived from Sentinel-2 data demonstrated good consistency, particularly in multi-year zonation analyses. This suggests that, with careful selection of acquisition dates and the combination of multiple indices, Sentinel-2 data can serve as a valid alternative for assessing the spatial structure of agricultural land—an observation also supported by previous studies [11,15,18].

Additionally, similar approaches to multi-year zonation evaluation have been applied by Heidari and Samavati [33], who introduced the Zoning Dissimilarity Metric (ZDM) to identify years that significantly disrupt the temporal consistency of zones derived from Sentinel-2 NDVI time series. Their analysis shows that excluding so-called "abnormal years," identified through statistical deviations in their impact on zonation, can substantially enhance the accuracy and robustness of resulting management zones. This underscores the importance of careful date selection and temporal window definition when using satellite-derived indices for zonation purposes.

Although this study primarily employed the Kappa, Jaccard, and Dice coefficients to assess zone stability, future research could incorporate metrics such as ZDM to provide a more quantitative measure of the impact individual years have on zonation patterns.

4.2. Advantages and Limitations of Different Zonation Methods

The use of interpolation methods such as kriging enables the generation of smooth, continuous surfaces suitable for spatial analysis, but their performance is highly sensitive to the distribution and density of sampling points. In contrast, percentile-based classification provides a straightforward categorization of values but does not account for spatial context.

Fuzzy k-means proved to be flexible, letting each pixel belong partly to more than one class while still preserving spatial continuity. Its key advantage lies in its ability to express gradual class membership, though it requires longer processing times and careful parameter tuning.

Weighted Overlay Analysis (WOA) offers a high degree of adaptability and the capacity to integrate multiple data sources. However, the resulting zones are highly sensitive to the selection of weight coefficients, which, if not properly calibrated, can lead to significant variation in the final outputs. For this reason, cautious application and, where possible, validation using reference laboratory data or field measurements are recommended.

Vegetation and bare soil indices (BSIs) enable rapid and cost-effective zonation but are subject to seasonal and interannual variability, as well as the influence of cloud cover and atmospheric conditions. Therefore, their use is best complemented with additional data sources to enhance reliability.

4.3. Recommendations for the Optimal Selection of Data Sources and Methods

Based on the conducted analysis, the following recommendations can be made:

- For practical implementation in precision agriculture, an optimal number of management zones lies between three and four, as this provides a balanced trade-off between spatial informativeness and zone stability.
- The use of EM38-MK2 data—particularly channel C1 or the combination of C1 and C0.5—proved to be the most effective in detecting soil variability.
- BSP data, especially when all analyzed parameters are integrated, yield reliable results and can serve as a reference for calibrating other methods.
- VI and BSI derived from Sentinel-2 imagery are useful as complementary inputs, particularly when generated from multiple acquisition dates and weighted appropriately.
- The Weighted Overlay Analysis (WOA) method demonstrated high flexibility and produced the most robust results when humus played a dominant role in the weighting scheme.
- Raster normalization and the use of spatial resolutions between 20 and 50 meters provide an optimal balance between spatial detail and zone stability.

These recommendations offer concrete guidelines for selecting appropriate methodologies based on specific objectives, data availability, and budget constraints in the context of precision soil management.

4.4. Added Value of Multi-Source Correlation Analysis

The correlation matrices between raster layers—particularly those integrating EM38, BSP, and VI/BSI data—revealed important synergies and limitations in the spatial structure captured by each source. While normalized and interpolated EM38 layers consistently showed strong internal coherence, their correlation with satellite-derived indices was the highest when both data types were aggregated over multiple temporal images. Although time series data require more processing, they help identify stable biophysical patterns beyond just seasonal effects.

A critical observation was that correlation matrices can inform not only zonation stability, but also highlight complementary data sources, as low cross-correlations may reflect distinct underlying spatial processes. Careful matrix interpretation is thus essential to avoid over-integration or misrepresentation of spatial coherence.

4.5. Toward More Interoperable and Transferable Zonation Models

An open question arising from this study is the transferability of the delineation approach across geographies and farming systems. Given the strong internal agreement in weighted overlays (especially humus-dominant schemes), there is an opportunity to adapt this methodology to other regions, such as Dutch polder landscapes, where organic matter and moisture gradients also play a key agronomic role.

To support future replication, the methodological pipeline presented here—combining proximal sensing, remote sensing, and fuzzy clustering—could be adapted into a decision-support module.

4.6. Broader Implications for Decision-Making in Data-Rich and Data-Poor Contexts

This study reinforces the emerging understanding that precision agriculture requires context-specific approaches rather than universal models. In data-rich environments, fully integrated models using all three sources (EC, BSP, VI/BSI) can generate nuanced and robust zones. Conversely, in data-scarce settings, carefully selected VI/BSI composites or single-depth EC readings (e.g., C1) can still yield sufficiently stable zonation maps, enabling broader adoption in smallholder or transitional farming systems.

4.7. Limitations of the Study

While the results presented here demonstrate consistent and interpretable management zone delineation across multiple data sources, several limitations must be acknowledged. First, Sentinel-2-based indices are sensitive to atmospheric interference, cloud cover, and vegetation phenology, which can introduce variability in inter-annual comparisons. Although multi-date compositing helps reduce these effects, some residual noise may persist. Second, interpolation of BSP data is constrained by the spatial density and distribution of samples. In areas with heterogeneous soil structure or sparse sampling (e.g., >5 ha per sample), kriging may oversmooth the data or misrepresent local variability. Finally, classification results depend on selected parameters (e.g., number of classes, weights in WOA), which may limit transferability to other contexts unless locally calibrated. Future work should further explore uncertainty quantification and sensitivity analysis in zonation models.

4.8. Overcoming Operational and Methodological Constraints

This study addressed several key operational and methodological challenges commonly encountered in precision agriculture. By combining data from EM38-MK2 sensors, basic soil properties (BSPs), and Sentinel-2-derived indices, we demonstrated that stable and interpretable management zones can be delineated without the need for high-

density sampling or complex ground campaigns. The use of optimized weighting schemes, fuzzy clustering, and temporal composites further enhanced the reproducibility and cost-efficiency of the zonation process.

Moreover, this study identified that a zonation scheme using three to four classes represents an optimal trade-off between spatial detail and operational feasibility. This level of complexity aligns with field-level management capacity, ensuring that resulting maps are both agronomically informative and practically implementable. These findings support the development of practical, scalable methods for soil and crop management that can be adapted to different production settings.

5. Conclusions

This study evaluated multiple approaches for delineating within-field management zones by integrating geophysical (EM38-MK2), chemical (basic soil properties), and spectral (VI/BSI from Sentinel-2) data. Through a multi-step analytical framework—encompassing interpolation, classification, and validation using the Kappa, Jaccard, Dice, and correlation metrics—we demonstrated that the most stable and internally consistent zonations were achieved using weighted combinations, particularly those dominated by humus content. Two- and three-class configurations generally provided the best trade-off between spatial coherence and agronomic interpretability.

A critical observation was that correlation matrices can inform not only zonation stability but also highlight complementary data sources, as low cross-correlations may reflect distinct underlying spatial processes. Careful matrix interpretation is thus essential to avoid over-integration or misrepresentation of spatial coherence.

The findings also reinforce the evolving perspective that precision agriculture must be tailored to specific agronomic and data contexts. In data-rich environments, robust multi-source models are feasible and desirable, allowing for complex, high-resolution zonation. In contrast, in data-scarce scenarios—such as smallholder or transitional farming systems—simpler inputs like two-date BSI composites or single-depth EC readings (e.g., C1) still offer viable pathways toward spatial differentiation and site-specific management.

Additionally, the strong internal agreement within humus-weighted overlays suggests potential for adapting this framework beyond the current study area. The approach may be transferable to other regions with similar soil-climate conditions, such as lowland agricultural regions characterized by high groundwater tables, organic-rich soils, and structured drainage systems common in parts of Northwestern Europe. To support future replication, the presented methodology—based on proximal sensing, remote sensing, and fuzzy clustering—can be modularized into open-source decision-support tools, enabling calibration across sites and farming systems.

Overall, this research highlights the value of integrating heterogeneous data sources and applying scalable analytical workflows for generating actionable management zones. Continued development of flexible, context-aware zonation models remains essential for advancing precision agriculture across diverse landscapes.

Supplementary Materials: The following supporting information can be downloaded at https://www.mdpi.com/article/10.3390/su17156931/s1, Table S1: Correlation matrix between classified VI and BSI raster layers at four grid resolutions (10 m, 20 m, 50 m, and 100 m), used to generate Figure 10. Table S2: Correlation matrix between EM38-MK2, basic soil properties (BSP), and VI/BSI-based zonation rasters for the 100 m grid resolution, used to generate Figure 14.

Author Contributions: Conceptualization, D.J., M.G. (Miro Govedarica) and R.Č.; methodology, D.J. and M.G. (Milan Gavrilović); software, D.J. and M.G. (Milan Gavrilović); validation, D.J. and R.Č.; formal analysis, D.J.; investigation, D.J.; resources, D.J.; data curation, D.J. and M.G. (Milan

Gavrilović); writing—original draft preparation, D.J.; writing—review and editing, D.J., M.G. (Milan Gavrilović), M.G. (Miro Govedarica), R.Č. and T.v.d.W.; visualization, D.J. and M.G. (Milan Gavrilović); supervision, M.G. (Miro Govedarica) and T.v.d.W.; project administration, D.J. and M.G. (Miro Govedarica); funding acquisition, D.J. All authors have read and agreed to the published version of the manuscript.

Funding: This research was funded under the Horizon Europe project (grant number 101129644): Soil Quality Analysis Tool (SQAT).

Institutional Review Board Statement: Not applicable.

Informed Consent Statement: Not applicable.

Data Availability Statement: Restrictions apply to the availability of these data. Data were obtained from [TerraControlling TMD] and are available [from the author Dušan Jovanović] with the permission of [TerraControlling TMD].

Acknowledgments: This research has been supported by the Ministry of Science, Technological Development and Innovation (Contract No. 451-03-137/2025-03/200156) and the Faculty of Technical Sciences, University of Novi Sad through project "Scientific and Artistic Research Work of Researchers in Teaching and Associate Positions at the Faculty of Technical Sciences, University of Novi Sad 2025" (No. 01-50/295).

Conflicts of Interest: Author Tamme van der Wal was employed by the company AeroVision. The remaining authors declare that the research was conducted in the absence of any commercial or financial relationships that could be construed as a potential conflict of interest.

Abbreviations

The following abbreviations are used in this manuscript:

EC	Electrical Conductivity
EM38-MK2	Electromagnetic Induction Sensor MK2
BSP	Basic Soil Properties
VI	Vegetation Index
BSI	Bare Soil Index
WOA	Weighted Overlay Analysis
SVM	Support Vector Machine
NDVI	Normalized Difference Vegetation Index
SAVI	Soil-Adjusted Vegetation Index
LCI	Leaf Chlorophyll Index
FPI	Fuzzy Performance Index
NCE	Normalized Classification Entropy
KNT	Weighted Overlay (Layer)
KL	Classified (Layer)
MZ	Management Zones

References

1. Fountas, S.; Carli, G.; Sørensen, C.G.; Tsiropoulos, Z.; Cavalaris, C.; Vatsanidou, A.; Liakos, B.; Canavari, M.; Wiebensohn, J.; Tisserye, B. Farm Management Information Systems: Current Situation and Future Perspectives. *Comput. Electron. Agric.* **2015**, *115*, 40–50. [CrossRef]
2. Republički Zavod Za Statistiku. *Poljoprivreda u Republici Srbiji–Strukturni Pokazatelji*; RZS: Beograd, Srbija, 2021. Available online: https://www.stat.gov.rs/ (accessed on 26 June 2025).
3. Papic, R.; Bogdanov, N. Rural Development Policy—A Perspective of Local Actors In Serbia. *Econ. Agric.* **2015**, *62*, 1079–1093. [CrossRef]
4. Zhang, C.; Kovacs, J.M. The Application of Small Unmanned Aerial Systems for Precision Agriculture: A Review. *Precis. Agric.* **2012**, *13*, 693–712. [CrossRef]

5. Rodrigues, H.; Ceddia, M.B.; Tassinari, W.; Vasques, G.M.; Brandão, Z.N.; Morais, J.P.S.; Oliveira, R.P.; Neves, M.L.; Tavares, S.R.L. Remote and Proximal Sensors Data Fusion: Digital Twins in Irrigation Management Zoning. *Sensors* **2024**, *24*, 5742. [CrossRef] [PubMed]
6. ACDI/VOCA. Making Agriculture Smarter in Serbia through Precision Farming. ACDI/VOCA. 2024. Available online: https://www.acdivoca.org/2024/02/making-agriculture-smarter-in-serbia-through-precision-farming/ (accessed on 21 July 2025).
7. Kovljenić, M.; Škorić, J.; Galetin, M.; Škorić, S. Digital Technology in Agriculture: Evidence from Farms on the Territory of AP Vojvodina. *Ekon. Poljopr.* **2023**, *70*, 583–598. [CrossRef]
8. European Commission. *Digital Technologies in Agriculture and Rural Areas—Briefing Paper*; European Union: Brussels, Belgium, 2020; Available online: https://ec.europa.eu/info/sites/default/files/food-farming-fisheries/farming/documents/report-digital-tech-agriculture_en.pdf (accessed on 26 June 2025).
9. Bešić, C.; Ćoćkalo, D.; Bakator, M.; Vidas-Bubanja, M.; Stanisavljev, S. Agriculture 5.0 Potential and the Application of Advanced Technologies in Serbia. *Ekon. Poljopr.* **2025**, *72*, 599–614. [CrossRef]
10. Mulla, D.J. Twenty Five Years of Remote Sensing in Precision Agriculture: Key Advances and Remaining Knowledge Gaps. *Biosyst. Eng.* **2013**, *114*, 358–371. [CrossRef]
11. Rokhafrouz, M.; Latifi, H.; Abkar, A.A.; Wojciechowski, T.; Czechlowski, M.; Naieni, A.S.; Maghsoudi, Y.; Niedbała, G. Simplified and Hybrid Remote Sensing-Based Delineation of Management Zones for Nitrogen Variable Rate Application in Wheat. *Agriculture* **2021**, *11*, 1104. [CrossRef]
12. Kaya, F.; Ferhatoglu, C.; Başayiğit, L. Multi-Temporal Normalized Difference Vegetation Index Based on High Spatial Resolution Satellite Images Reveals Insight-Driven Edaphic Management Zones. *AgriEngineering* **2025**, *7*, 92. [CrossRef]
13. Peralta, N.R.; Costa, J.L. Delineation of Management Zones with Soil Apparent Electrical Conductivity to Improve Nutrient Management. *Comput. Electron. Agric.* **2013**, *99*, 218–226. [CrossRef]
14. Moral, F.J.; Terrón, J.M.; Silva, J.R.M.D. Delineation of Management Zones Using Mobile Measurements of Soil Apparent Electrical Conductivity and Multivariate Geostatistical Techniques. *Soil. Tillage Res.* **2010**, *106*, 335–343. [CrossRef]
15. Taylor, J.A.; McBratney, A.B.; Whelan, B.M. Establishing Management Classes for Broadacre Agricultural Production. *Agron. J.* **2007**, *99*, 1366–1376. [CrossRef]
16. Doolittle, J.A.; Brevik, E.C. The Use of Electromagnetic Induction Techniques in Soils Studies. *Geoderma* **2014**, *223–225*, 33–45. [CrossRef]
17. Corwin, D.L.; Lesch, S.M. Apparent Soil Electrical Conductivity Measurements in Agriculture. *Comput. Electron. Agric.* **2005**, *46*, 11–43. [CrossRef]
18. Cockx, L.; Van Meirvenne, M.; Vitharana, U.W.A.; Verbeke, L.P.C.; Simpson, D.; Saey, T.; Van Coillie, F.M.B. Extracting Topsoil Information from EM38DD Sensor Data Using a Neural Network Approach. *Soil. Sci. Soc. Am. J.* **2009**, *73*, 2051–2058. [CrossRef]
19. Sudduth, K.A.; Kitchen, N.R.; Bollero, G.A.; Bullock, D.G.; Wiebold, W.J. Comparison of Electromagnetic Induction and Direct Sensing of Soil Electrical Conductivity. *Agron. J.* **2003**, *95*, 472–482. [CrossRef]
20. Kitchen, N.R.; Drummond, S.T.; Lund, E.D.; Sudduth, K.A.; Buchleiter, G.W. Soil Electrical Conductivity and Topography Related to Yield for Three Contrasting Soil–Crop Systems. *Agron. J.* **2003**, *95*, 483–495. [CrossRef]
21. Saey, T.; Simpson, D.; Vermeersch, H.; Cockx, L.; Van Meirvenne, M. Comparing the EM38DD and DUALEM-21S Sensors for Depth-to-Clay Mapping. *Soil. Sci. Soc. Am. J.* **2009**, *73*, 7–12. [CrossRef]
22. Delegido, J.; Verrelst, J.; Alonso, L.; Moreno, J. Evaluation of Sentinel-2 Red-Edge Bands for Empirical Estimation of Green LAI and Chlorophyll Content. *Sensors* **2011**, *11*, 7063–7081. [CrossRef]
23. Wang, L.; Zhou, X.; Zhu, X.; Dong, Z.; Guo, W. Estimation of Biomass in Wheat Using Random Forest Regression Algorithm and Remote Sensing Data. *Crop J.* **2016**, *4*, 212–219. [CrossRef]
24. Drusch, M.; Del Bello, U.; Carlier, S.; Colin, O.; Fernandez, V.; Gascon, F.; Hoersch, B.; Isola, C.; Laberinti, P.; Martimort, P.; et al. Sentinel-2: ESA's Optical High-Resolution Mission for GMES Operational Services. *Remote Sens. Environ.* **2012**, *120*, 25–36. [CrossRef]
25. Mzid, N.; Pignatti, S.; Huang, W.; Casa, R. An Analysis of Bare Soil Occurrence in Arable Croplands for Remote Sensing Topsoil Applications. *Remote Sens.* **2021**, *13*, 474. [CrossRef]
26. Wu, J.; Wang, D.; Bauer, M.E. Assessing Broadband Vegetation Indices and QuickBird Data in Estimating Leaf Area Index of Corn and Potato Canopies. *Field Crops Res.* **2007**, *102*, 33–42. [CrossRef]
27. Liang, L.; Qin, Z.; Zhao, S.; Di, L.; Zhang, C.; Deng, M.; Lin, H.; Zhang, L.; Wang, L.; Liu, Z. Estimating Crop Chlorophyll Content with Hyperspectral Vegetation Indices and the Hybrid Inversion Method. *Int. J. Remote Sens.* **2016**, *37*, 2923–2949. [CrossRef]
28. Zhu, Q.; Lin, H.S. Comparing Ordinary Kriging and Regression Kriging for Soil Properties in Contrasting Landscapes. *Pedosphere* **2010**, *20*, 594–606. [CrossRef]

29. Chaali, N.; Ramírez-Gómez, C.M.; Jaramillo-Barrios, C.I.; Garré, S.; Barrero, O.; Ouazaa, S.; Calderon Carvajal, J.E. Enhancing Irrigation Management: Unsupervised Machine Learning Coupled with Geophysical and Multispectral Data for Informed Decision-Making in Rice Production. *Smart Agric. Technol.* **2024**, *9*, 100635. [CrossRef]
30. Córdoba, M.A.; Bruno, C.I.; Costa, J.L.; Peralta, N.R.; Balzarini, M.G. Protocol for Multivariate Homogeneous Zone Delineation in Precision Agriculture. *Biosyst. Eng.* **2016**, *143*, 95–107. [CrossRef]
31. Radočaj, D.; Jug, I.; Vukadinović, V.; Jurišić, M.; Gašparović, M. The Effect of Soil Sampling Density and Spatial Autocorrelation on Interpolation Accuracy of Chemical Soil Properties in Arable Cropland. *Agronomy* **2021**, *11*, 2430. [CrossRef]
32. Webster, R.; Oliver, M.A. *Geostatistics for Environmental Scientists*, 2nd ed.; Wiley: Chichester, UK, 2007; pp. 119–153.
33. Heidari, R.; Samavati, F.F. A New Dissimilarity Metric for Anomaly Detection in Management Zones Delineation Constructed from Time-Varying Satellite Images. *Agriculture* **2024**, *14*, 688. [CrossRef]
34. Shaddad, S.M.; Madrau, S.; Castrignanò, A.; Mouazen, A.M. Data Fusion Techniques for Delineation of Site-Specific Management Zones in a Field in UK. *Precis. Agric.* **2016**, *17*, 200–217. [CrossRef]
35. Al Dahra. Al Dahra Acquires Assets of PKB Korporacija in Serbia for Euro 150 million. Available online: https://aldahra.com/al-dahra-acquires-assets-of-pkb-korporacija-in-serbia-for-euro-150-million/ (accessed on 26 May 2025).
36. Zakić, Z.; Rikalović, G. *Osnove Svojinske Transformacije u Agrokompleksu*; Sindikat Radnika Poljoprivrede, Prehrambene Industrije, Duvanske Industrije i Vodoprivrede Srbije: Beograd, Srbija, 1996.
37. Heil, K.; Schmidhalter, U. Comparison of the EM38 and EM38-MK2 Electromagnetic Induction-Based Sensors for Spatial Soil Analysis at Field Scale. *Comput. Electron. Agric.* **2015**, *110*, 267–280. [CrossRef]
38. Rodrigues, H.M.; Vasques, G.M.; Oliveira, R.P.; Tavares, S.R.L.; Ceddia, M.B.; Hernani, L.C. Finding Suitable Transect Spacing and Sampling Designs for Accurate Soil ECa Mapping from EM38-MK2. *Soil. Syst.* **2020**, *4*, 56. [CrossRef]
39. *ISO 18400-102:2017*; Soil Quality—Sampling—Part 102: Selection and Application of Sampling Techniques. International Organization for Standardization: Geneva, Switzerland, 2017. Available online: https://www.iso.org/standard/62843.html (accessed on 26 June 2025).
40. Eurostat. LUCAS 2018 Technical Reference Document: Land Use and Land Cover Survey. Eurostat, European Commission. Available online: https://ec.europa.eu/eurostat/web/lucas (accessed on 26 June 2025).
41. Jahn, R.; Blume, H.P.; Asio, V.; Spaargaren, O.; Schád, P. *FAO Guidelines for Soil Description*, 5th ed.; Food and Agriculture Organization of the United Nations: Rome, Italy, 2006.
42. German Federal Soil Protection and Contaminated Sites Ordinance (BBodSchV). Ordinance on the Protection of Soil and on Old Contaminated Sites. 1999. Available online: https://www.umweltbundesamt.de/en/topics/soil-land/soil-protection/soil-protection-law (accessed on 26 July 2025).
43. Soil Survey Manual. USDA Handbook No. 18, U.S. Department of Agriculture, Natural Resources Conservation Service. Available online: https://www.nrcs.usda.gov/resources/guides-and-instructions/soil-survey-manual (accessed on 26 June 2025).
44. Belić, M.; Nešić, L.; Ćirić, V. *Praktikum Iz Pedologije*; Poljoprivredni Fakultet: Novi Sad, Serbia, 2014.
45. Government of the Republic of Serbia. *Regulation on Systematic Monitoring of the Condition and Quality of Soil*; No. 88/2020; Official Gazette of the Republic of Serbia: Belgrade, Serbia, 2020.
46. Huete, A.R. A Soil-Adjusted Vegetation Index (SAVI). *Remote Sens. Environ.* **1988**, *25*, 295–309. [CrossRef]
47. Vélez, S.; Martínez-Peña, R.; Castrillo, D. Beyond Vegetation: A Review Unveiling Additional Insights into Agriculture and Forestry through the Application of Vegetation Indices. *J* **2023**, *6*, 421–436. [CrossRef]
48. Sentinel Hub. Sentinel-2 RS Indices. Available online: https://custom-scripts.sentinel-hub.com/custom-scripts/sentinel-2/indexdb/ (accessed on 26 June 2025).
49. Pereira, G.W.; Valente, D.S.M.; Queiroz, D.M.D.; Coelho, A.L.D.F.; Costa, M.M.; Grift, T. Smart-Map: An Open-Source QGIS Plugin for Digital Mapping Using Machine Learning Techniques and Ordinary Kriging. *Agronomy* **2022**, *12*, 1350. [CrossRef]
50. Li, Y.; Shi, Z.; Li, F.; Li, H.-Y. Delineation of Site-Specific Management Zones Using Fuzzy Clustering Analysis in a Coastal Saline Land. *Comput. Electron. Agric.* **2007**, *56*, 174–186. [CrossRef]
51. Moharana, P.C.; Jena, R.K.; Pradhan, U.K.; Nogiya, M.; Tailor, B.L.; Singh, R.S.; Singh, S.K. Geostatistical and Fuzzy Clustering Approach for Delineation of Site-Specific Management Zones and Yield-Limiting Factors in Irrigated Hot Arid Environment of India. *Precis. Agric.* **2020**, *21*, 426–448. [CrossRef]
52. Arno, J.; Martinez-Casasnovas, J.A.; Ribes-Dasi, M.; Rosell, J.R. Clustering of Grape Yield Maps to Delineate Site-Specific Management Zones. *Span. J. Agric. Res.* **2011**, *9*, 721. [CrossRef]
53. Valente, D.S.M.; Pereira, G.W.; De Queiroz, D.M.; Zandonadi, R.S.; Amaral, L.R.D.; Bottega, E.L.; Costa, M.M.; De Freitas Coelho, A.L.; Grift, T. Accuracy of Various Sampling Techniques for Precision Agriculture: A Case Study in Brazil. *Agriculture* **2024**, *14*, 2198. [CrossRef]

54. Scherber, C.; Beduschi, T.; Tscharntke, T. A Grid-Based Sampling Approach to Insect Biodiversity Monitoring in Agricultural Landscapes. In *Exploring and Optimizing Agricultural Landscapes*; Mueller, L., Sychev, V.G., Dronin, N.M., Eulenstein, F., Eds.; Springer International Publishing: Cham, Switzerland, 2021; pp. 415–424, ISBN 978-3-030-67448-9.
55. Stehman, S.V. Comparison of Systematic and Random Sampling for Estimating the Kappa Coefficient of Agreement. *Photogramm. Eng. Remote Sens.* **1992**, *58*, 1343–1350.
56. Laboski, N.C.; Wolkowski, R.P. Grid Soil Sampling for Precision and Profit. In Proceedings of the North Central Extension-Industry Soil Fertility Conference, Des Moines, IA, USA, 15–16 November 2007; Volume 23, pp. 33–39.
57. Maćków, W.; Bondarewicz, M.; Łysko, A.; Terefenko, P. Orthophoto-Based Vegetation Patch Analyses—A New Approach to Assess Segmentation Quality. *Remote Sens.* **2024**, *16*, 3344. [CrossRef]
58. Bell, J.; Dee, H.M. The Subset-Matched Jaccard Index for Evaluation of Segmentation for Plant Images. *arXiv* **2016**, arXiv:1611.06880.

Disclaimer/Publisher's Note: The statements, opinions and data contained in all publications are solely those of the individual author(s) and contributor(s) and not of MDPI and/or the editor(s). MDPI and/or the editor(s) disclaim responsibility for any injury to people or property resulting from any ideas, methods, instructions or products referred to in the content.

sustainability

MDPI

Systematic Review

A Systematic Review of AI-Based Classifications Used in Agricultural Monitoring in the Context of Achieving the Sustainable Development Goals

Vasile Adrian Nan, Gheorghe Badea *, Ana Cornelia Badea and Anca Patricia Grădinaru

Faculty of Geodesy, Technical University of Civil Engineering, 020396 Bucharest, Romania;
vasile-adrian.nan@phd.utcb.ro (V.A.N.); ana.badea@utcb.ro (A.C.B.); anca-patricia.gradinaru@utcb.ro (A.P.G.)
* Correspondence: gheorghe.badea@utcb.ro

Abstract

The integration of Artificial Intelligence (AI) into remote sensing data classification has revolutionized agriculture and environmental monitoring. AI is one of the main technologies used in smart farming that enhances and optimizes the sustainability of agricultural production. The use of AI in agriculture can involve land use mapping and crop detection, crop yield monitoring, flood-prone area detection, pest disease monitoring, droughts prediction, soil content analysis and soil production capacity detection, and for monitoring the evolution of forests and vegetation. This review examines recent advancements in AI-driven classification techniques for various applications regarding agriculture and environmental monitoring to answer the following research questions: (1) What are the main problems that can be solved through incorporating AI-driven classification techniques into the field of smart agriculture and environmental monitoring? (2) What are the main methods and strategies used in this technology? (3) What type of data can be used in this regard? For this study, a systematic literature review approach was adopted, analyzing publications from Scopus and WoS (Web of Science) between 1 January 2020 and 31 December 2024. By synthesizing recent developments, this review provides valuable insights for researchers, highlighting the current trends, challenges and future research directions, in the context of achieving the Sustainable Development Goals.

Keywords: agriculture; artificial intelligence; remote sensing; sustainable development goals

1. Introduction

Data-driven smart farming involves the use of recent technology developments, such as the Internet of Things (IoT) and Artificial Intelligence (AI) [1], and consists of a multidisciplinary effort to address the achievement of the Sustainable Development Goals (SDGs) [2]. These technologies include algorithm- and model-based tools [3] that require accurate geospatial data.

Agriculture 4.0 is characterized by the integration of advanced digital technologies to create a more efficient and sustainable farming sector. This implies big data analyses and the use of AI, the IoT and robotics to enhance the digitalization and automation of agricultural practices, improving productivity and resource management [4].

Various agricultural policies, such as the Common Agricultural Policy of the EU [5], promote the use of remote sensing as an appropriate control system for agriculture. Satellite images and aerial photographs, in combination with advanced algorithms and machine

learning (ML) techniques, are used to assess if farmers are fulfilling the obligations outlined in the strategic plans [6].

Agriculture and vegetation are strongly interconnected, each influencing the other in ecological and economical aspects. Plant biodiversity can enhance ecosystem functions that benefit agriculture, while intensive farming can reduce vegetation diversity [7].

In addition to satellite and UAV (Unmanned Aerial Vehicle) images, LiDAR (Light Detection and Ranging) point clouds acquired through airborne laser scanning can contribute to the mapping and analysis of vegetation, as laser signals can penetrate through forest canopies [8].

The sustainable management of land has been a valid concern for a long time, being an issue especially relevant in the context of climate change [9]. In this regards, recent technological advancements have made the use of higher-resolution remote sensing data both feasible and cost-effective, significantly increasing their practical value [10].

Inefficient use of natural resources, such as soil and water, has been proven to cause economic losses and lead to environmental damage [11]. Remote sensing technologies can be valuable tools to support precision agriculture throughout different phases of crop production. Recent progress in sensor technologies, data processing and analytics has increased the accessibility of remote sensing in agriculture [12].

The accuracy of the methods applied in agriculture depends on multiple factors, including the image resolution and analysis technique [11].

Artificial Intelligence is increasingly being integrated into remote sensing applications for agriculture, providing efficient analysis techniques of large-scale satellite and UAV data. AI techniques, such as ML and DL (deep learning), are used for a wide range of tasks in remote sensing for agriculture, promoting agricultural reform [13]. The integration of big data into predictive models and decision-support tools allows stakeholders to mitigate the impact of climate change and other environmental threats [14]. Therefore, the use of AI in remote sensing for agriculture is transforming how data is analyzed, leading to more efficient, adaptive and cost-effective strategies applied across the entire agricultural field, while contributing to the achievement of the SDGs.

Based on the current pace of progress since their adoption in 2015, none of the 17 Sustainable Development Goals are expected to be fully achieved by 2030. Globally, SDG 2 (Zero Hunger) has been stagnating and faces major challenges (Figure 1) [15].



Figure 1. World SDGs (Sustainable Development Goals) dashboard 2025 [15].

The SDGs are deeply interconnected [16,17], and the use of AI in remote sensing for agriculture offers a powerful tool to address multiple goals simultaneously. In Figure 2, the connections between SDG 6—Clean Water and Sanitations (a), SDG 9—Industry, Innovation

and Infrastructure (b), SDG 12—Responsible Production and Consumption (c) and SDG 13—Climate Action (d) and the other 16 SDGs are highlighted. Access to clean water (SDG 6) is essential for achieving Zero Hunger (SDG 2), as agriculture depends heavily on water availability. AI models trained on satellite and UAV data can improve water resource monitoring and support precision irrigation, minimizing waste and increasing crop productivity. The link between SDG 2 and SDG 13 (Climate Action) is also relevant, as enhanced resilience to climate change can support more sustainable agriculture. AI-enhanced remote sensing enables the monitoring of climate variables—such as rising temperatures, changing precipitation patterns and the intensity and frequency of extreme weather events that profoundly affect agricultural fields. Furthermore, SDG 2 connects with SDG 12 (Responsible Consumption and Production), as the efficient use of natural resources supports efforts to increase agricultural productivity. AI-driven analytics can optimize resource use, reducing environmental impacts while improving crop yields. SDG 9 (Industry, Innovation and Infrastructure) plays an important role in enabling the technological innovation behind AI applications in agriculture. These innovations enable farmers to make data-driven decisions that contribute to food security.

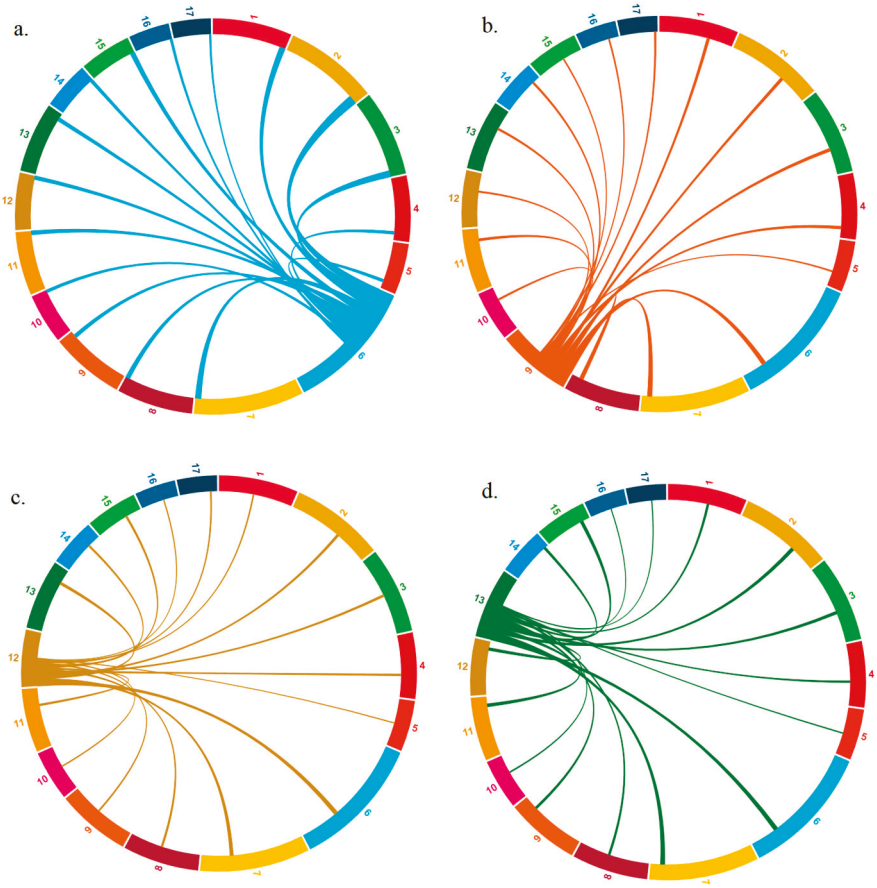

Figure 2. SDGs (Sustainable Development Goals) interlinkages [16]. (**a**) The connection between SDG 6—Clean Water and Sanitations and the other SDGs; (**b**) The connection between SDG 9—Industry, Innovation and Infrastructure and the other SDGs; (**c**) The connection between SDG 12—Responsible Production and Consumption and the other SDGs; (**d**) The connection between SDG 13—Climate Action and the other SDGs.

Therefore, it is important to have a deeper understanding of how AI can transform agricultural monitoring, in order to achieve sustainable and resilient food systems. This systematic literature review (SLR) aims to synthesize the current research on AI-based

classifications in agriculture and identify the knowledge gaps and opportunities for further research.

2. Materials and Methods

2.1. Selection Criteria

For this study, the papers that fulfilled the following criteria were selected:

- Addressed the topics of the research questions;
- Were published in peer-reviewed journals;
- Were published between 2020 and 2024;
- Were open access;
- Were written in English.

2.2. Information Sources

The methodology applied involved searching in the Scopus and Web of Science databases (Table 1), as these met the peer-reviewed journals, use of English language and open-access criteria.

Table 1. Information sources.

Data Source	Type	URL
Scopus	Digital Library	https://www.scopus.com (accessed on 18 March 2025)
Web of Science	Digital Library	https://clarivate.com/academia-government/scientific-and-academic-research/research-discovery-and-referencing/web-of-science/ (accessed on 18 March 2025)

2.3. Search Strategy

The methodology used involved searching for three keyword groups (Table 2). The first group of keywords included the types of algorithms that the research focused on, the second group focused on the domains of application for these algorithms and the third group reflected the specific focus of the studies that were analyzed.

Table 2. Groups of keywords.

Group	Keywords
Group 1	"Artificial Intelligence", "Deep Learning", "Machine Learning"
Group 2	"Remote Sensing", "Image Classification", "Point Cloud Classification", "Agriculture"
Group 3	"Environmental Monitoring", "Land Use Mapping", "Flood-Prone Area Detection", "Forest Monitoring", "Pest Disease Monitoring", "Droughts Prediction", "Soil Content Analysis", "Soil Production Capacity Detection", "Vegetation Monitoring", "Crop Detection", "Crop Yield Monitoring"

Filters for the publication date (between 1 January 2020 and 31 December 2024), language (English) and access type (open-access papers) were also applied.

The expected results were papers that used AI, DL or ML techniques applied to remote sensing, image classification, point cloud classification or agriculture in general,

that were used for agricultural and environmental monitoring-related tasks, such as land use mapping, flood-prone area detection, forest monitoring, pest disease monitoring, droughts prediction, soil content analysis and production capacity detection, vegetation monitoring, crop detection or crop yield monitoring.

For each search, certain search queries were applied (Table 3). The search results showed 472 papers on Scopus and 309 papers on WoS.

Table 3. Search queries.

Digital Library	Search Algorithm
Scopus	(TITLE-ABS-KEY("Artificial Intelligence" OR "Deep Learning" OR "Machine Learning")) AND (TITLE-ABS-KEY("Remote Sensing" OR "Image Classification" OR "Point Cloud Classification" OR "Agriculture")) AND (TITLE-ABS-KEY("Environmental Monitoring" OR "Land Use Mapping" OR "Flood-Prone Area Detection" OR "Forest Monitoring" OR "Pest Disease Monitoring" OR "Droughts Prediction" OR "Soil Content Analysis" OR "Soil Production Capacity Detection" OR "Vegetation Monitoring" OR "Crop Detection" OR "Crop Yield Monitoring"))
WoS	TS = ("Artificial Intelligence" OR "Deep Learning" OR "Machine Learning") AND TS = ("Remote Sensing" OR "Image Classification" OR "Point Cloud Classification" OR "Agriculture") AND TS = ("Environmental Monitoring" OR "Land Use Mapping" OR "Flood-Prone Area Detection" OR "Forest Monitoring" OR "Pest Disease Monitoring" OR "Droughts Prediction" OR "Soil Content Analysis" OR "Soil Production Capacity Detection" OR "Vegetation Monitoring" OR "Crop Detection" OR "Crop Yield Monitoring")

2.4. Selection Process

The selection process (Figure 3) first involved removing the papers that were found in both databases. A total of 201 duplicates were identified and excluded. An initial screening was then conducted for the 580 remaining papers. The screening involved analyzing whether the papers were relevant to this research or not by reviewing their abstracts. During this step, 426 papers were excluded. The papers that were excluded fell outside the primary scope of the research, addressing topics such as wildfires which, while related, belong to different areas of study. The next stage involved full-text assessment of the remaining 154 papers. This included sorting the papers into categories and analyzing the data, methodology and algorithms that were used for each study. Following this in-depth evaluation, 46 additional papers were removed that were not relevant to this research. Although AI and remote sensing were mentioned in these papers, they were not applied to data classification or analysis, with some studies relying on soil samples instead of remote sensing data. Finally, 108 papers were included in this review. PRISMA Checklist is available in Supplementary Materials.

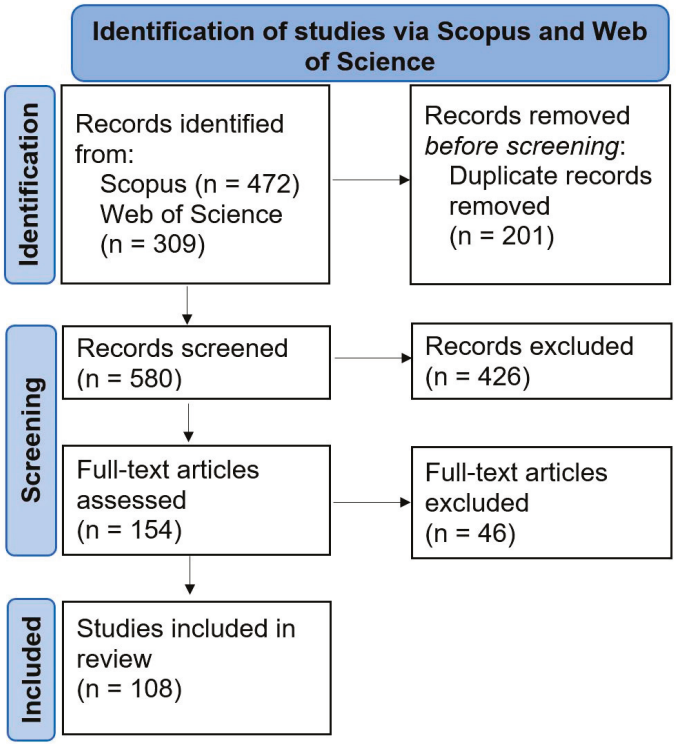

Figure 3. Prisma flow diagram.

During the selection process, an increased interest in the research topic (Figure 4) was noticed; the number of papers published by year increased by 537.5%, from 8 papers in 2020 to 51 papers in 2024.

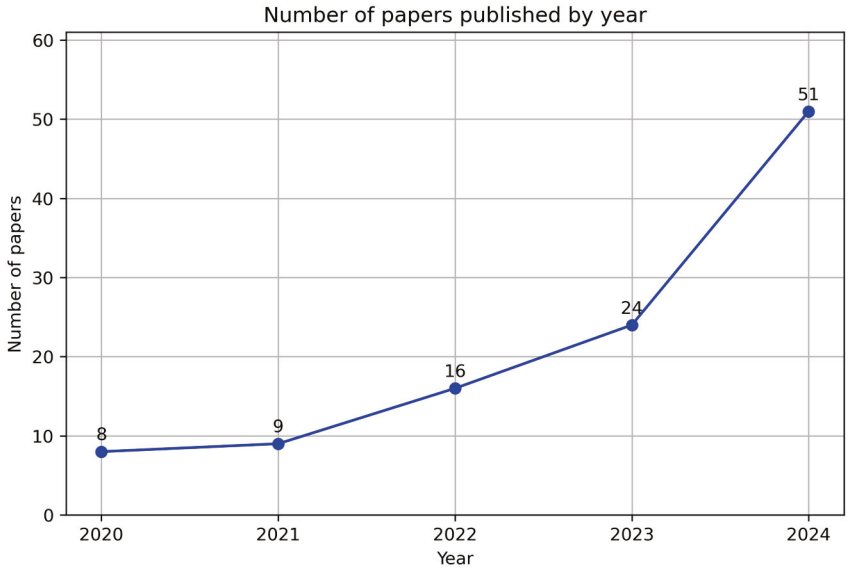

Figure 4. Number of papers published by year.

The geographic distribution of the study areas (Figure 5) showed a significantly higher number of case studies conducted in China, followed by a considerable number of papers where the study area was not specified. Countries such as Brazil, USA, Germany, France and Finland showed a moderate level of research activity in this domain. In particular, the map in Figure 6 highlights a clear lack of studies in Eastern Europe. This finding is especially relevant as Eastern Europe is renowned for its strong agricultural sector, particularly in countries like Ukraine, Romania, Hungary and Bulgaria, as they possess extensive arable

lands and have a long-standing tradition of farming, contributing significantly to both regional and global food production. In 2023, the main cereals-producing member states of the European Union, alongside countries like Poland, Germany and France, were Romania, Bulgaria and Hungary [18]. Despite the importance of agriculture in these countries, there appears to be a gap in the research focused on the integration of advanced technologies into the agricultural sector.

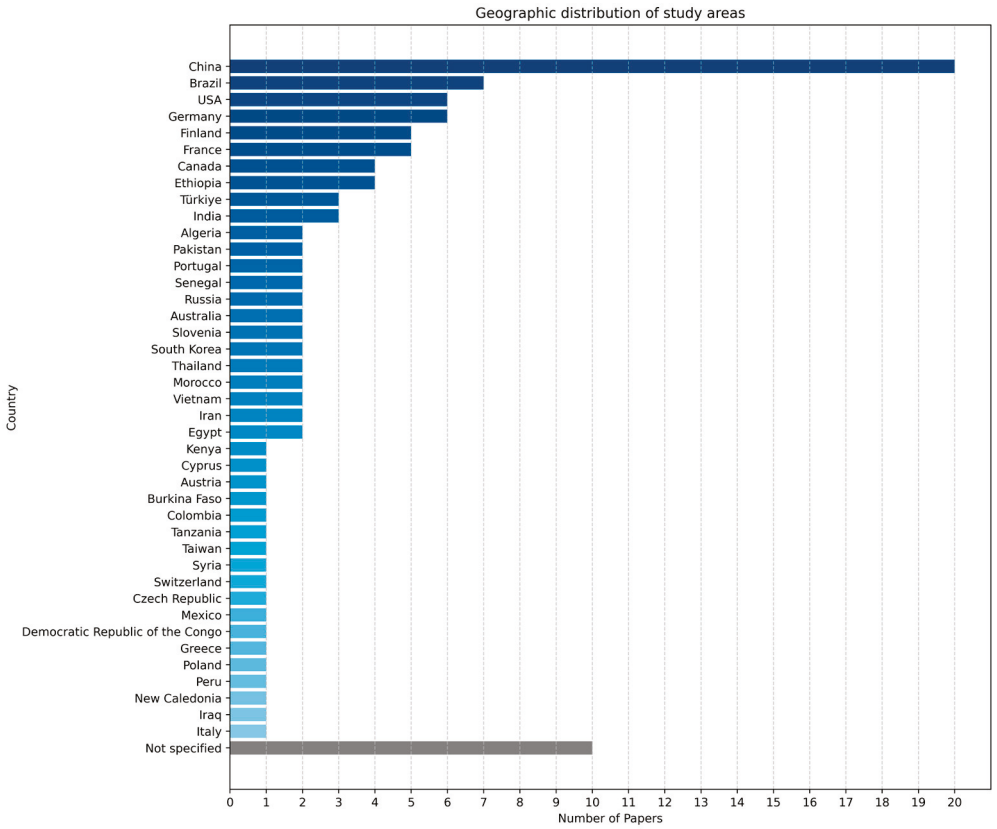

Figure 5. Geographic distribution of study areas.

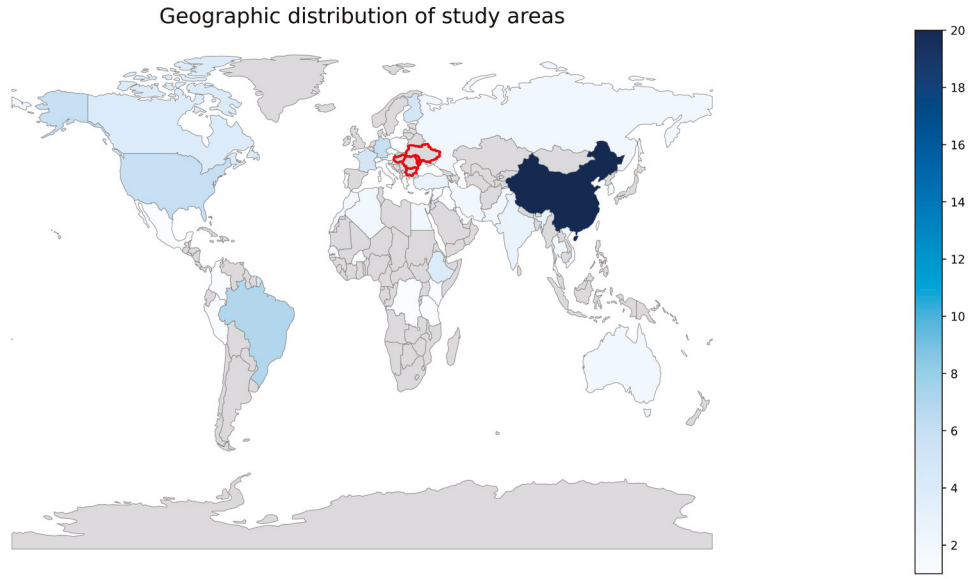

Figure 6. Map with geographic distribution of study areas.

3. Related Work

While existing studies have addressed individual challenges in agriculture and smart farming (Table 4), focusing on IoT technology [1,3], on the models and algorithms used, remote sensing for water resource management and smart irrigation [19,20], nutrient testing and scientific fertilization, disease and pest monitoring and ecosystem balance, crop-type classification and weed control, development stage monitoring and yield prediction, ref. [20] and evaluation of remote sensing platforms and sensors [10], none of these studies have integrated all the relevant aspects related to agriculture and vegetation, such as the data types used, types of AI algorithms for data processing and the sources of data, which defines its spatial resolution. This study fills this gap by offering a comprehensive review that takes into consideration all these relevant aspects.

Table 4. Related work.

Main Topic	Focuses on Problems Related to Agriculture	Focuses on Problems Related to Vegetation and Forests	Focuses on Types of AI Algorithms for Data Extraction	Focuses on Available Data Types	Focuses on Data Sources	Reference
Applications of IoT in smart farming	✓	x	x	x	x	https://www.sciencedirect.com/science/article/pii/S1364032123007165 (accessed on 9th July 2025) [1]
Applications of IoT in agricultural sector	✓	x	x	x	x	https://www.sciencedirect.com/science/article/pii/S0301479721015504 (accessed on 9th July 2025) [3]
The use of remote sensing in agriculture	✓	x	✓	x	✓	https://www.sciencedirect.com/science/article/pii/S0167739X24006551 (accessed on 9th July 2025) [20]
The use of remote sensing in agriculture	✓	x	x	✓	x	https://www.sciencedirect.com/science/article/pii/S0034425719304213 (accessed on 9th July 2025) [10]
Water resources use and management in agriculture	✓	x	x	x	x	https://www.sciencedirect.com/science/article/pii/S0378377425000617 (accessed on 9th July 2025) [19]
The use of remote sensing and machine learning in agriculture	✓	x	✓	x	x	https://www.mdpi.com/2073-4395/14/9/1975 (accessed on 9th July 2025) [13]

Other reviews fail to comprehensively address issues regarding the use of AI and remote sensing in agricultural monitoring, as they are generally application-specific and do not compare how different domains—such as land use mapping and crop detection,

crop yield monitoring, flood-prone area detection, forest and vegetation monitoring, pest disease monitoring, droughts prediction and soil content analysis and soil production capacity—overlap or diverge in terms of methods and resources. Furthermore, existing work rarely examines in an integrated way the data types employed (satellite imagery, UAV data), the AI algorithms used for data processing, the software products implemented and the data sources. By contrast, our review systematically considers all these aspects side by side across the main categories of agricultural and vegetation studies, allowing us to highlight common trends and methodological preferences.

4. Results

4.1. Answer to the First Research Question ("What Are the Main Problems That Can Be Solved Through Incorporating AI-Driven Classification Techniques in the Field of Smart Agriculture and Environmental Monitoring?")

Technologies like ML, DL, Data Science and the IoT help select the optimal crops for specific regions by identifying threats, such as pests and diseases, and can be applied across several agricultural phases, such as soil preparation, land management and environmental factors monitoring, water monitoring, pesticide recommendation and crop damage assessment, to enhance the overall productivity of crops and reduce costs and resource waste [21].

Therefore, for this study, the papers were divided into the following categories (Figure 7):

- Land use mapping and crop detection;
- Crop yield monitoring;
- Flood-prone area detection;
- Forest and vegetation monitoring;
- Pest disease monitoring;
- Droughts prediction;
- Soil content analysis and soil production capacity detection.

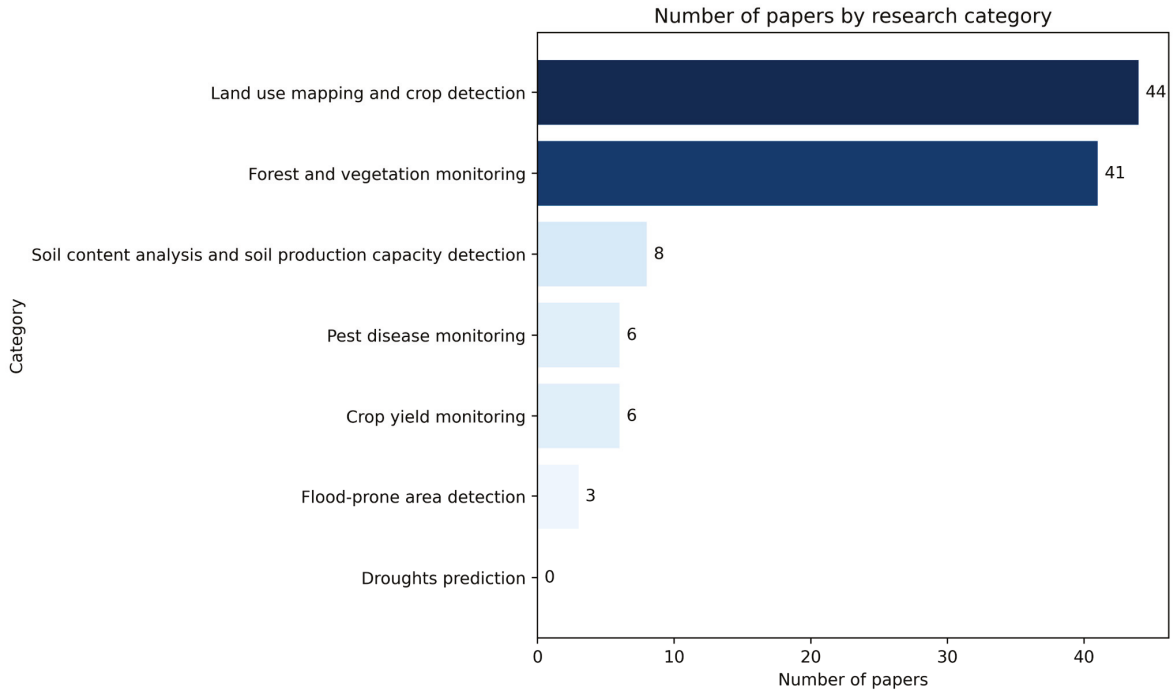

Figure 7. Number of papers by research category.

4.1.1. Land Use Mapping and Crop Detection

According to Food and Agriculture Organization of the United Nations (FAO) [22], in 2021, agricultural land occupied about a third of the world's total land area. In an effort to achieve the SDGs proposed by the United Nations [23], specifically Goal 2—Zero Hunger, some of the targets that were set were to double agricultural productivity by 2030 and maintain the genetic diversity of seeds and cultivated plants [24]. In order to achieve these goals, it is necessary to have an efficient monitoring system for land use and crops, through the use of remote sensing and Artificial Intelligence. Numerous studies have been published that assess the efficacy of involving AI and IoT in agricultural practices.

4.1.2. Crop Yield Monitoring

Crop yield monitoring is an essential part of precision agriculture. It helps farmers take immediate action according to the crops' needs, to increase productivity, reduce waste and make further data-driven decisions, contributing to the achievement of SDG 12 (Responsible Consumption and Production). Moreover, AI models can be used to predict crop yield, enabling better resource use planning and early detection of potential issues [25].

4.1.3. Flood-Prone Area Detection

Agriculture is highly vulnerable to the impact of climate change and the hydrological disasters associated with it. Rapid flood impact assessments can lead to better emergency response actions [26]. Periodic flood mapping can help develop flood control measures and enhance flood management, contributing as well to agricultural yield estimation [27]. Moreover, in dryland areas, farming systems can rely on supplementary water derived from floods [28].

4.1.4. Forest and Vegetation Monitoring

In a study by Chavarria et al. [29], it was proven that forests have a positive impact on the performance of neighboring farms and their productivity. There is evidence that forest management practices favor the preservation of species in agricultural lands [30]. Sustainably managed forests contribute to reducing soil erosion and minimizing the risk of landslides, ensuring a balanced water cycle, which is essential for agricultural development and food security [31]. Therefore, forests play an essential role in preserving the natural environment's biodiversity and ecosystem.

4.1.5. Pest Disease Monitoring

Pests are the main biological threat to agricultural and forestry production [32] and identifying areas of insect damage from remote sensing data through AI models is an important part of forest and crops health monitoring [33]. Pest and disease monitoring is a fundamental practice in smart agriculture, aimed at protecting crops and ensuring food security. It involves the detection, identification and tracking of harmful organisms that can reduce crop yield or quality.

4.1.6. Droughts Prediction

In regions characterized by water shortages and frequent drought conditions, a forecasting system for water irrigation demand needs to be developed. Such a system integrates remote sensing techniques and a soil water balance model to serve as a monitoring tool and support water resources management [34]. Comprehensive studies examining the impacts of changing water use patterns resulting from agricultural expansion, particularly increased irrigation, are still limited [35].

4.1.7. Soil Content Analysis and Soil Production Capacity Detection

Accurate soil moisture estimation plays an important role in enhancing agricultural productivity and supporting effective environmental management [36]. Assessment of soil macronutrients [37] and soil organic carbon stocks [38] can also provide a comprehensive understanding of soil health, leading to more informed decisions in smart agriculture and environmental management.

4.2. Answer to the Second Research Question ("What Are the Main Methods and Strategies Used in This Technology?")

After analyzing the AI algorithms used in the selected papers, they were split into the categories shown in Figure 8. Decision trees-based (DTs) models were the most frequent algorithms found in this SLR, with Random Forest (RF) and other derived algorithms, such as XGBoost, CART (Classification and Regression Tree), GTB (Gradient Tree Boost), Cubist or IF (Isolation Forest), found in 55 papers. A DT-based model is a supervised ML method used for classification and regression tasks. It builds a tree-like model of decision, guiding the algorithm to classify the data or predict a value by splitting the data into smaller subsets until the predefined criteria is met [39]. Deep Neural Networks (DNNs) are supervised algorithms that use labeled data and are structured in three steps. The input layer takes in a file as the data, the hidden layers pass the information from one layer to the next and the output layer produces the final result. Convolutional Neural Networks (CNNs) are a type of DNN that specialize on data with a grid-like structure, particularly images [40], and were the most used type of DNN found in this SLR. CNNs, such as DenseNet, ResNet, TempCNN, ATCNN, SLMFNet, Deeplab V3+, SegNet, U-Net, U-Net++, AlexNet, DABNet, PSPNet and other DNNs were found in 49 papers. Support Vector Machine (SVM) is a supervised ML algorithm used for classification and regression tasks. It tries to find the best boundary, known as the hyperplane, that separates the different classes in the data, with the main goal of finding the optimal boundaries between classes [41]. SVM was found in 19 papers. A significant number of papers in which hybrid models were used were also found. These models, found in 13 papers, combined different AI techniques to overcome the limitations of using a single AI method. Statistical models, such as Auto-ARIMA, GLM (Generalized Linear Model), GNB (Gaussian Naïve Bayes), LASSO (Least Absolute Shrinkage and Selection Operator), LR (Linear Regression) and NB (Normal Bayes), were found in nine papers. Among other classic supervised learning models, kNN (k-Nearest Neighbor) was the most used algorithm. It finds the closest training examples to a new, unclassified case and assigns it the most common class among those neighbors [42]. Recurrent Neural Networks (RNNs) were found in seven papers. They are DL algorithms designed for processing sequential data like time series, text or speech [43]. Transformers- and attention-based models can prioritize the center of attention and focus on the key features according to their degree of importance in complex scenarios [44]. Algorithms such as BETAM (Border-Enhanced Triple Attention Mechanism) were found in five papers in this SLR. The Fully Connected Neural Network (FCNN) MLP (Multilayer Perceptron), a type of ANN (Artificial Neural Network) with multiple layers of interconnected neurons [45], was found in four papers. Clustering algorithms, such as K-means, are unsupervised algorithms used to group similar data points into clusters by identifying the patterns and structures within the data [46], and were found in two papers. Optimization algorithms that update the parameters throughout the learning process, such as OG-WOA (Optimal Guidance-Whale Optimization Algorithm), which is applied to increase the exploitation during the search process and select the relevant features for classification [47], and QHPO (Quantum Hippopotamus Optimization algorithm), which selects the best features for the final classification using NN (Nearest Neighbor)

classifiers [48], were found in two papers. Lastly, Generative Adversarial Networks (GANs), with the potential for reconstructing high-resolution images from low-quality data through a process known as super resolution [49], were found in two papers.

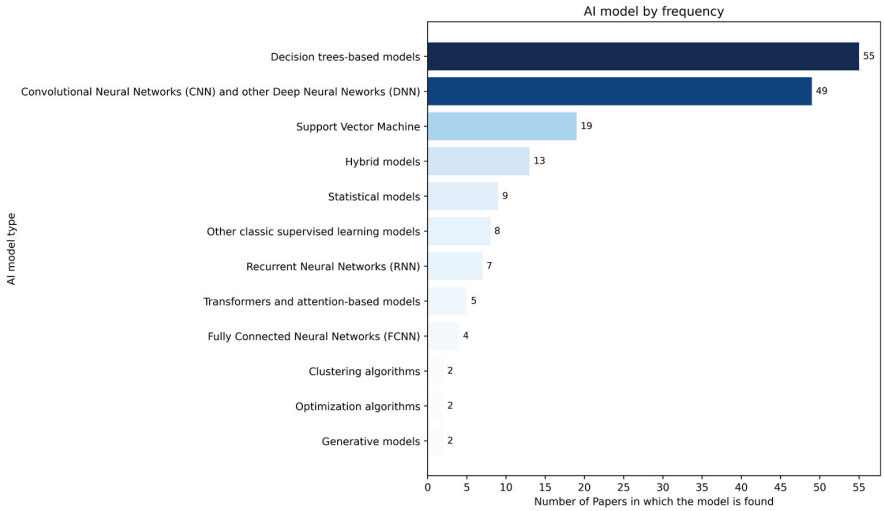

Figure 8. Algorithms used in different studies by frequency.

The implementation tools used for algorithm development and data processing were also analyzed, as illustrated in Figure 9. Python programming emerged as the most commonly used tool, appearing in 45 papers, either for training the models or for processing the data. Notably, the PyTorch open-source deep learning framework [50] was found in the majority of these papers. Google Earth Engine (GEE) was the second most frequently used platform, mentioned in 23 papers, followed by ArcGIS (Pro or Online) in 21 papers. Other notable software products included Agisoft, QGIS and SNAP (Sentinel Application Platform), each found in 10 papers. R programming was used in eight papers, Pix4D in five papers, ENVI and Matlab computing in four papers, Google Earth Pro in three papers and OTB (Orfeo Toolbox) in two papers. Other software/frameworks found in only one paper each were DrakNet Framework, C++ programming, Go programming, Grass GIS, Iota2, MODIS Reprojection Tool, SAS, Minitab 18, Sen2Cor, OpenStack, CentOS Linux programming, GDAL, ArcMap and SCP (Semi-automated Classification Plugin).

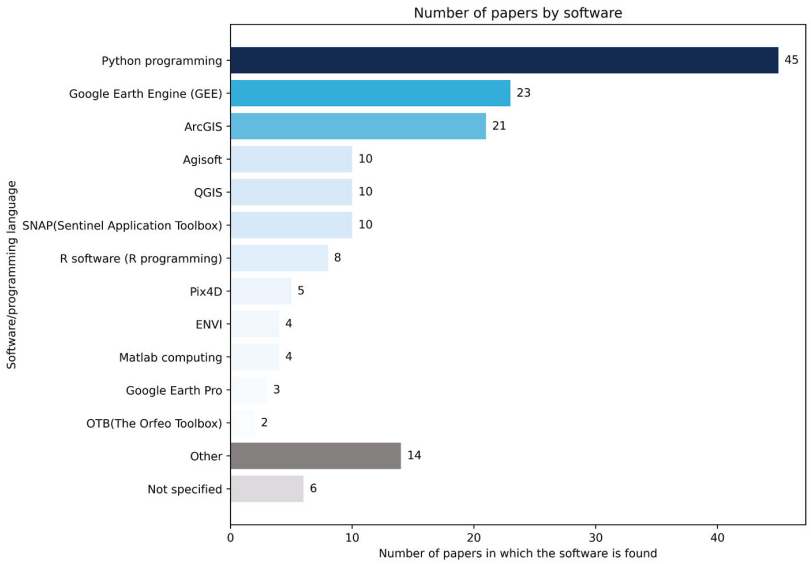

Figure 9. Software products used in different studies by frequency.

4.2.1. Land Use Mapping and Crop Detection

Out of the 44 papers in this category, only 7 were dedicated to crop detection, the other 37 being related to land use and land cover mapping. Most of them implemented DT-based algorithms. Hamidi et al. [51] proposed a method that uses an Optic-SAR (Synthetic Aperture Radar) fusion for crop mapping based on remote sensing imagery, using RF, SVM, SAE (Sparse Auto-Encoder) and GFSAE (Guided Filtered Sparse Auto-Encoder) AI algorithms and methods, to classify crops such as corn, pea, canola, soybean, oat and wheat. In a study by Snevajs et al. [52], RF was also used for crop classification based on remote sensing imagery. Gackstetter et al. [53] used RF, RNN and a transformer model for crop-type mapping based on satellite imagery. In a study by Di Tommaso et al. [54], RF was used for mapping tall and short crops based on satellite images and LiDAR data. Zhang et al. [55] used DSSGT (Dilated Spectral–Spatial Gaussian Transformer Net) to map corn, cotton, sesame, broad-leaf soybean, narrow-leaf soybean, rice and water crops. In a study by Yue & Tian [56], crops and soil were evaluated with a DT-based algorithm, RF. A specialized RF model—CRRF (Crop-Residue Random Forest)—was also proposed by Yue & Tian [56] for classifications in vegetation–soil ecosystems for crop monitoring. Alotaibi et al. [57] proposed a DTODCNN-CC (Dipper-Throated Optimization with Deep Convolutional Neural Networks-based Crop Classification) approach, applied to satellite imagery, to accurately classify crops into the following classes: maize, banana, legume and other.

Most studies in this category focused on land use and land cover classifications. For this challenge, DT-based models were preferred, with RF being the most used algorithm [58–69]. Other algorithms based on decision trees were XGBoost [70,71], CART and GTB [72].

CNNs and DNNs were the second most preferred. Rajesh et al. [73] used a CNN for land cover/land use classification from satellite imagery. In other studies, multiple types of CNNs and DNNs were used, such as MSFA-Net [74], Inception-V3 and DenseNet121 [75], ResNet and ResNet50 [47,48,76,77], TempCNN and ATCNN [70], SLMFNet [78], Deeplab V3+ [44,79], FCN and SegNet [80], UNet and UNet++ [79,81], AlexNet [71], PSPNet and DABNet [79], CMFNet [82] and other CNNs and DNNs [42,83–87].

In a study by Lemenkova [88], an SVM algorithm was used to map the land cover dynamics.

Hybrid models that combine different types of algorithms were also found in the literature. Zhang et al. adopted an approach based on an SACA (Semantic-Aware Contrastive Adaptation) framework for land cover classification [89]. Dantas et al. [70] proposed the use of an REFeD deep learning framework (data Reuse with Effective Feature Disentanglement) for land cover mapping, which incorporates an effective supervision scheme, reinforcing feature disentanglement through multiple levels of supervision. A KD-KNN algorithm was used by Mourtadha et al. [59] to perform land cover and land use classification on satellite imagery. Another hybrid model was Swin-UNet, a semantic segmentation network model, based on the Swin-Transformer block, used by Hao et al. [80] to classify land use based on remote sensing imagery. MCSGNet is a network that solves the issues of low precision and poor generalization ability, proposed by Hu et al. [76] for classifying land cover types from remote sense imagery. Vinaykumar et al. [47] proposed the OG-WOA-Bi-LSTM (Bi-directional Long Short-Term Memory) technique, an advanced satellite image classification approach that combines deep feature extraction, optimization algorithms and sequence-based classification to effectively reduce overfitting in land use and land cover classification.

Other classic supervised learning models, such as kNN, were also found in the literature. In a study by Souza and Rodrigues [61], kNN was used to classify satellite imagery

into different land use and land cover classes. The MD (minimum distance) model is another classical classification model found in the literature [72].

RNNs, which are DL models designed for sequential data and are able to maintain a memory of previous inputs, are suitable for analyses where the order and context of data are very important [90]. In a study by Nigar et al. [83], a comparison of RF, CNN and RNN models was performed for land use and land cover classification. The results showed that the RNN model provides an accuracy similar to that of the CNN model.

Optimization algorithms were also found in the literature. A study by Albarakati et al. [48] proposed the use of QHPO optimization to select the best features for final classification of land use and land cover.

Transformer algorithms and attention-based models, such as BETAM, are also used for land cover classifications based on remote sensing images. BETAM consists of a combination of three forms of attention and was used by Wang et al. [44] to perform semantic segmentation for land cover classification.

In a study by Aljebreen et al. [85], the statistical model NB was applied to the training dataset, along other algorithms (SVM, RF, DT and ANN) to perform land use and land cover classification using PlanetScope multispectral imagery.

Clustering algorithms, such as K-means and the supervised classification model LVQ (Learning Vector Quantization), were used by Ouchra et al. [91] with Google Earth Engine for land cover classification.

The overall results of this analysis are found in Figure 10.

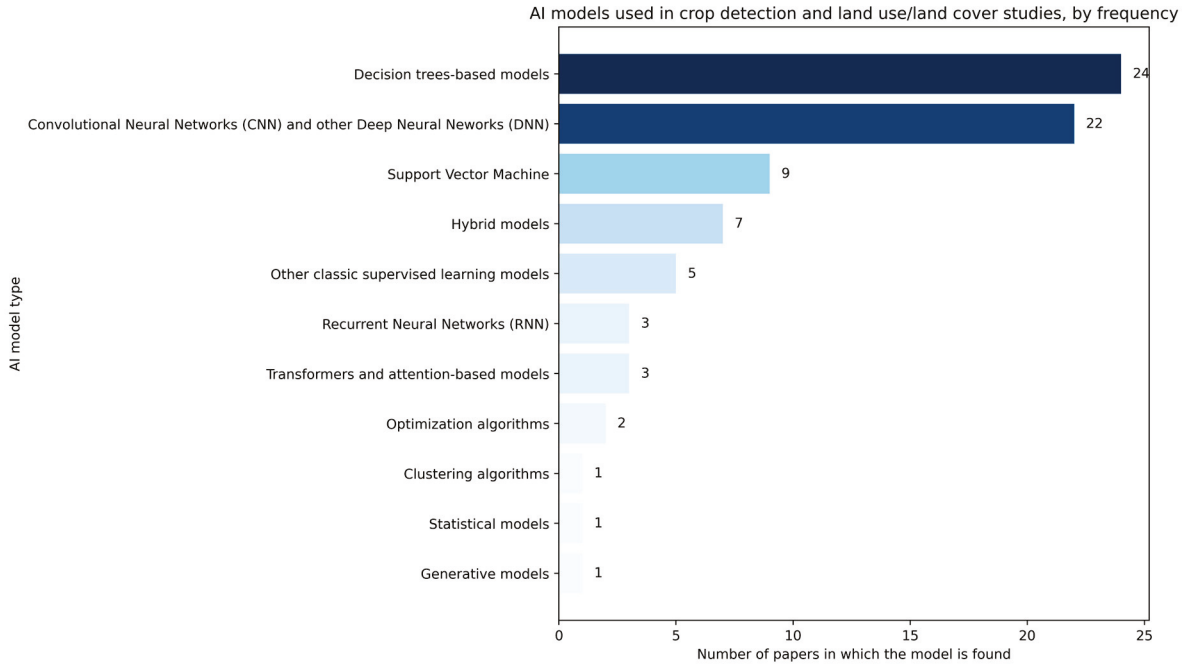

Figure 10. Artificial Intelligence models used for land use mapping and crop detection.

For land use mapping and crop detection, Python programming was the most commonly found environment for algorithm development and implementation (Figure 11). ArcGIS was also preferred, found in nine papers, while GEE software, dedicated to land surface monitoring, was found in eight papers. SNAP software was used in six papers and QGIS was chosen in five cases. Matlab Computing and R Software (programming) were each mentioned in three papers. As for the less frequent trends, Google Earth Pro and OTB were used in two papers and Agisoft and ENVI were mentioned only once each. Seven papers used other software products, while in two cases no processing software was specified.

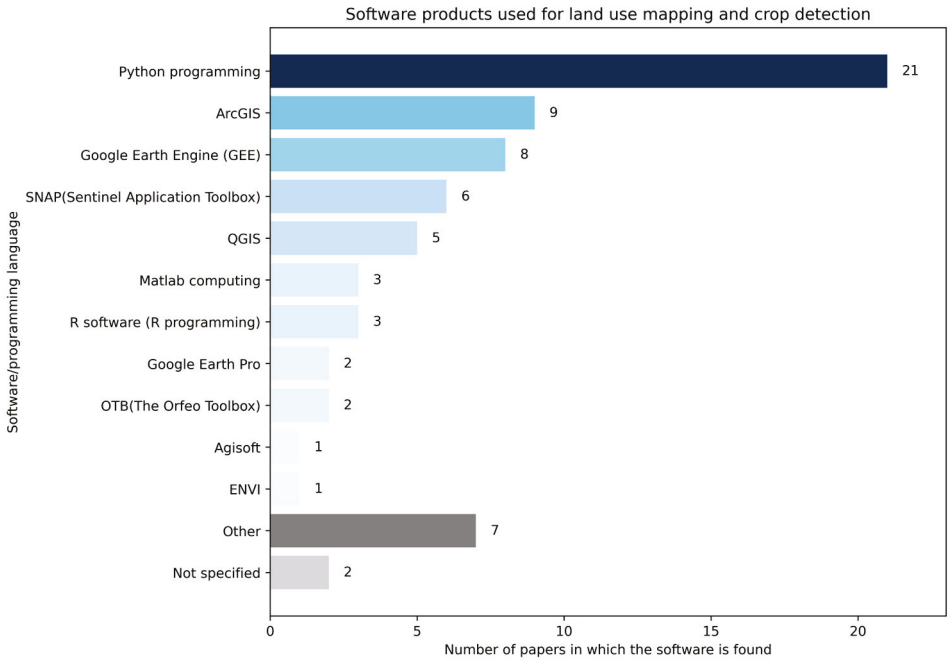

Figure 11. Software products used for land use mapping and crop detection.

4.2.2. Crop Yield Monitoring

DT-based algorithms were the most used for crop yield monitoring (Figure 12). Algorithms like RF were used to estimate millet FCover [92], to perform image preselection to eliminate unsuitable images for crop monitoring [93] and to predict the yields of corn, rice and soybean [94].

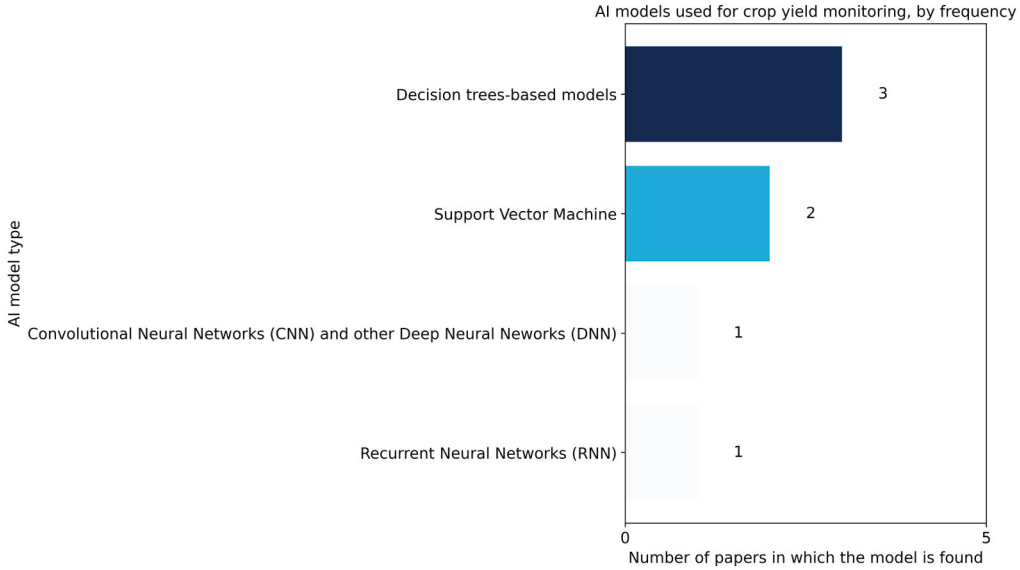

Figure 12. Artificial Intelligence models used for crop yield monitoring.

A CNN was used in a study by Sabo et al. [95] to forecast crop yield for barley, durum and soft wheat crops. ConvLSTM, an RNN, alongside a 3D-CNN, a fully convolutional architecture, were used by Nevavuori et al. [25] for crop yield monitoring and prediction. SVM algorithm was used by Lv et al. [96] in a study related to winter wheat fAPAR (fraction of Absorbed Photosynthetically Active Radiation) modeling.

For crop yield monitoring, five software applications/environments were found in this SLR (Figure 13). Among these, the programming language Python was used in four

articles. Interestingly, Pix4D was mentioned in two papers, while Agisoft, QGIS and R software (programming) were each used in one paper.

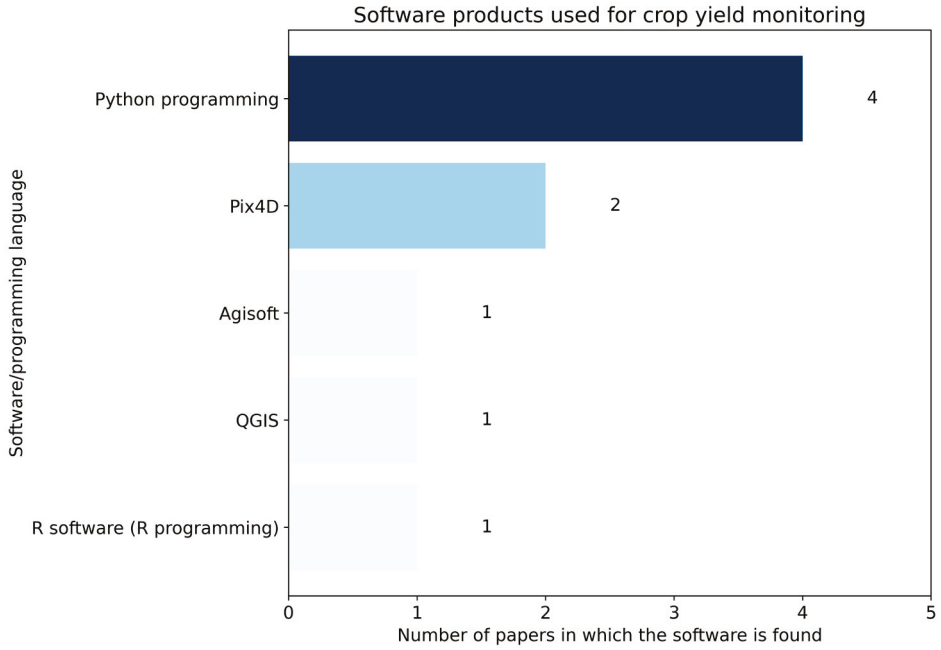

Figure 13. Software products used for crop yield monitoring.

4.2.3. Flood-Prone Area Detection

Few studies were found related to flood-prone area detection. CNNs and other DNNs, transformers- and attention-based models, decision trees-based models and Support Vector Machine models were found in one paper each. In a study by Wu et al. [97], floodwater extraction based on UAV imagery was performed using a transformer model. Pech-May et al. [98] classified flooded areas using satellite images and a U-Net neural network. Atchyuth et al. [27] used RF, CART and SVM models to map flood inundations.

For flood-prone area detection, three software products were found. ArcGIS was the most preferred, found in two articles, while Python programming and GEE were found in one study each.

4.2.4. Forest and Vegetation Monitoring

In most of the papers regarding forest and vegetation monitoring, CNNs and other DNNs were the most used algorithms (Figure 14). Xiang et al. used U-Net, ResUNet and TeranusNet to monitor forest changes using UAV data [99], and Ecke et al. used EfficientNet CNN architecture to monitor forest health based on UAV data [100]. A TempCNN model was used by Perbet et al. in a study regarding boreal forest disturbances monitoring [101]. A mask R-CNN (Mask Region-based Convolutional Neural Network) model with a ResNet-50 backbone was used by Lucas et al. to detect individual trees from aerial imagery [102]. SegForest was proposed as a segmentation model for remote sensing images by Wang et al. to estimate forest area from satellite imagery [103]. Slagter et al. used a standard CNN model to monitor tropical forest disturbance from satellite data [104]. Retallack et al. used various CNNs to detect an indicator arid shrub in UAV imagery [105], Guo et al. used an SNN (Siamese Neural Network) for forest cover change extraction from satellite images [106] and Lahssini et al. [8] used a CNN, along with other algorithms, to estimate the basal area and wood volume in forests based on LiDAR and satellite data. In a study by Mäyrä et al., a workflow for tree species classification from LiDAR data was presented, and it showed that CNN models outperform other algorithms, such as RF, GBM and SVM [107].

He et al. proposed an OUDN (Object-based U-Net-DenseNet-coupled) network for intelligent mapping of urban forests from remote sensing imagery [108]. Li et al. proposed an MSCIN (Multifeature Synthesis Perception Convolutional Network) for vegetation extraction from multisource remote sensing images [109]. The results were compared with results from other models, such as the CNN HRNet, the hybrid model OCBDL (Off-Center Bayesian Deep Learning) and RFC (Random Forest Classifier); MSCIN achieved robust vegetation extraction, having the ability to overcome internal fragmentation and unclear boundaries.

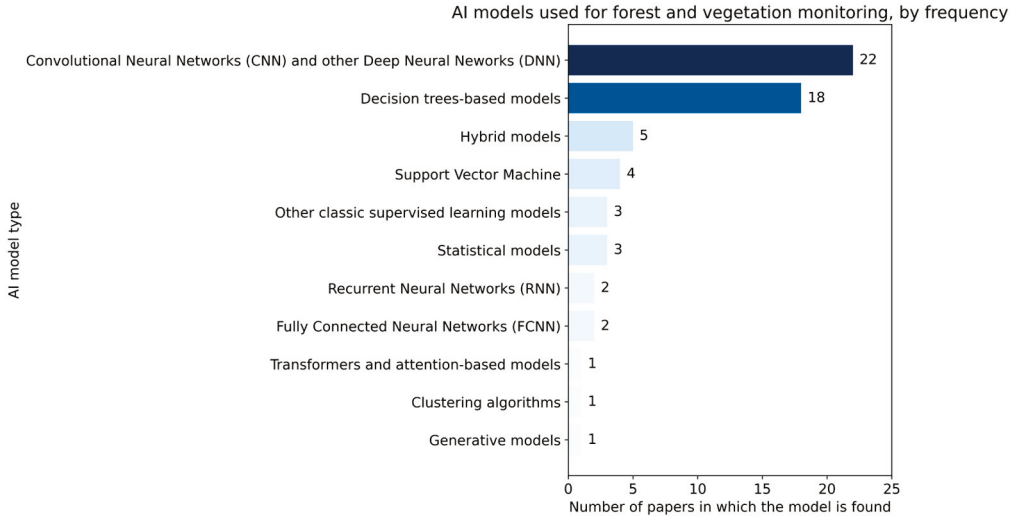

Figure 14. Artificial Intelligence models used for forest and vegetation monitoring.

The U-Net CNN was found in multiple studies for identification of certain species of trees [110], for multi-temporal forest monitoring [111], for NDVI (Normalized Difference Vegetation Index) estimation [112], for coastal forest cover change detection [113] and for deforestation detection [114], along with other CNNs, such as DeepLabv3+, SegNet, Res-UNet and FC-DenseNet.

The CNN DeepLabv3+ was used by Andrade et al. to detect deforestation from satellite imagery [115]. Other DNNs and CNNs were found in various studies for classifying deforestation patterns [116], for NDVI reconstruction and vegetation cover study [117] and for assessing changes in boreal vegetation [118].

RNNs were found in two studies for vegetation behavior forecasting based on satellite imagery [119] and for generating dense NDVI time series and covering the gaps resulting from cloud cover [120].

DT algorithms were the second most found type of algorithm during the literature review. RF was used for forest cover change detection from satellite imagery [121], to monitor changes in boreal peatland vegetation from satellite imagery [122], to map forest habitat [123] or forest canopy height [124] with satellite imagery as the base, for a forest cover dynamics assessment from satellite imagery [125], to map landscape-scale dynamics of the plant area index from radar data [126], to monitor oak dieback from satellite imagery [127], for vegetation monitoring of mountainous regions from satellite imagery [128], to map coastal mangrove forests from satellite big data [129], for forest/nonforest segmentation based on satellite data [130], for vegetation species detection from remote sensing imagery [131] and to map vegetation cover based on UAV imagery for guided species conservation [132]. Other DT algorithms used in the literature were XGBoost [124,133], GBM [129], SS-RF (Stochastic Spatial Random Forest) [134], CART [131] and IF [116].

SVM algorithm was used for forest cover change detection [121] and for vegetation cover mapping [132], and other similar algorithms, such as SVR (Support Vector Regres-

sor) [124] and OC-SVM (One-Class Support Vector Machine) [116], were also found in the literature.

Statistical models, such as ARIMA [119], QDA (Quadratic Discriminant Analysis) and GNB [130] and LR [132], were also found in the literature.

The classic supervised learning model kNN was used for forest canopy height mapping from satellite imagery [124], detection of different vegetation species from remote sensing images [131] and a basal area and wood volume estimation based on satellite images and LiDAR data [8].

A Fully Connected Neural Network MLP was found in two papers for deforestation patterns classification [116] and for basal area and wood volume estimation [8].

Perbet et al. [101] used a transformer-based model to detect and classify boreal forest disturbances from satellite imagery. Kong et al. used a generative AI model—a dual RSS-GAN network (Remote-Sensing Super-Resolution Generative Adversarial Network)—for long-term vegetation monitoring [49]. Liu et al. used the clustering model K-Means++ for tree species classification [135].

Other papers implemented the use of hybrid models, such as SiamHRnet-OCR [136] and ChangeFormer [137], for deforestation detection from satellite imagery. Zheng et al. used the Near Pseudo model for vegetation species detection from remote sensing imagery [131], Li et al. used the OCBDL model for remote sensing image vegetation extraction [109] and Liu et al. used the YOLOv7 (You Only Look Once) model for tree species classification from UAV data [135].

For forest and vegetation monitoring, after Python programming, which was found in 15 papers; GEE was the most used software product, found in 12 papers; followed by ArcGIS, used in 5 papers (Figure 15). Agisoft and QGIS were found in three papers each, while ENVI, Pix4D and R programming were found in two papers each. Google Earth Pro and SNAP were used in only one paper each.

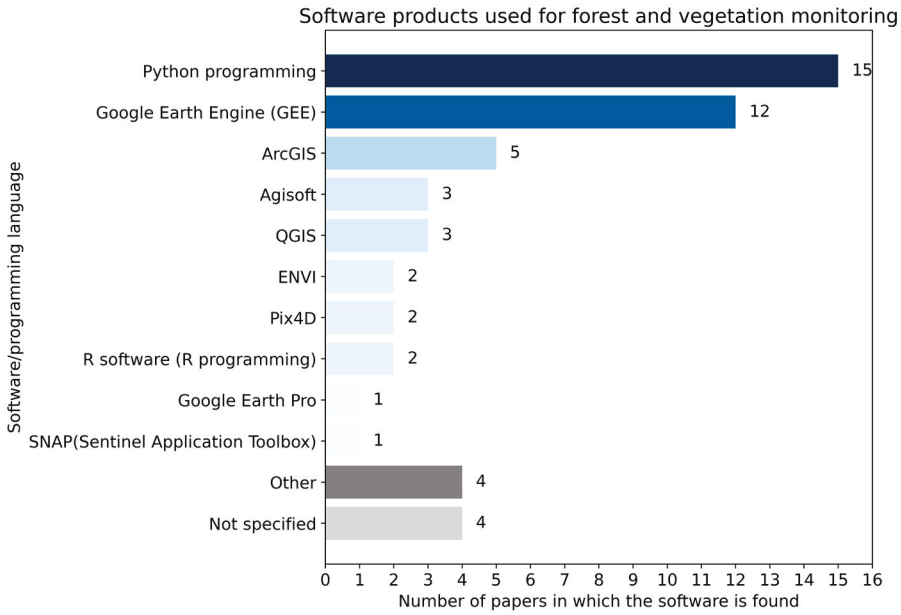

Figure 15. Software products used for forest and vegetation monitoring.

4.2.5. Pest Disease Monitoring

For pest disease monitoring, CNNs or other DNNs, found in three papers, were the most used models; decision trees-based models were found in two papers and statistical models were found in one paper. In a study by Turkulainen et al. [138], bark beetle-induced spruce damage from UASs (Unoccupied Aircraft Systems) images was determined

using DNNs. Zhang et al. [32] used Unet++ with a ResNeSt model as feature extraction backbone for pest-infested forest damage detection. Kislov et al. [139] used a DCNN (Deep Convolutional Neural Network) to detect forest disturbance based on satellite images.

RF was also found in the literature. Junttila et al. [140] used an RF to map spruce tree decline due to bark beetle infestation from multispectral imagery and Iordache et al. [141] used an ML approach based on RF to detect pine wilt disease from airborne spectral imagery.

A statistical model—ARIMA (Autoregressive Integrated Moving Average)—was used by Alkan & Aydin [33] to predict insect damage spread.

For pest disease monitoring, Agisoft was the most used software, found in three papers, followed by ArcGIS, used in two papers. In this case, Python programming and SNAP were found in one paper each, while one paper involved the use of other software products.

4.2.6. Droughts Prediction

Two studies on droughts prediction were found during the search, and neither of them implemented AI algorithms. Villani et al. [34] presented the iCOLT climate service, used for seasonal predictions of irrigation. It is a probabilistic approach, based on soil water balance modeling. Laipelt et al. [35] used the geeSEBAL model, an open-source implementation of the Surface Energy Balance Algorithm for Land (SEBAL) using Google Earth Engine [142], to assess changes in evapotranspiration resulting from cropland expansion.

4.2.7. Soil Content Analysis and Soil Production Capacity Detection

For soil analyses, DT-based models were found to be the most used in the literature (Figure 16). RF was used to estimate the soil moisture content based on UAV images [143] or on satellite data [36], to estimate the soil organic carbon based on satellite data [144,145], to assess the soil macronutrients status based on satellite imagery [37] and to map soil pollution using drone image recognition on an arsenic-contaminated agricultural field [146]. Other decision trees-based models, such as GBDT (gradient descent-boosted regression tree), which was used to estimate soil organic carbon stocks based on satellite imagery [38], Cubist [37] and ERF (Extreme Random Forest) [146], were found in the literature.

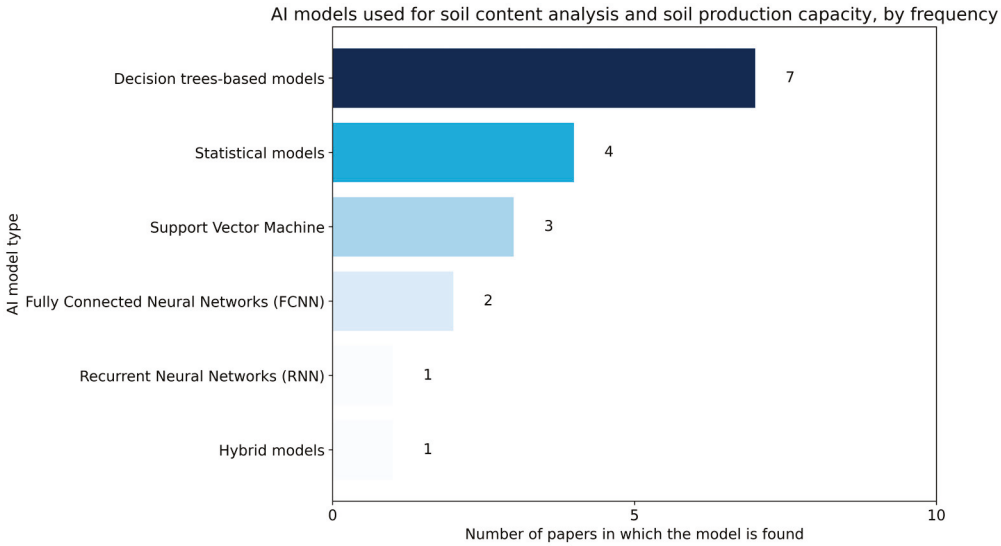

Figure 16. Artificial Intelligence models used for soil content analysis and soil production capacity.

SVM was also used to estimate the soil moisture content based on satellite data [36] and to map soil pollution using drone image recognition on an arsenic-contaminated agricultural field [146]. Another similar algorithm, SVR-RBF (Support Vector Regression with Radial Basis Function) was found in a study on organic carbon estimation in soil [144].

The statistical model GLM was used to assess soil macronutrients status based on satellite imagery [37] and to assess atrazine metabolite effects from soil contamination based on UAV images [147]. Another statistical model—LASSO—was found in the literature, implemented in a soil organic carbon estimation study [144].

Other algorithms included FCNNs [38,146], the RNN LSTM [36] and the hybrid model GA-RF (Genetic Algorithm-Optimized Random Forest) [143].

For soil content analysis and soil production capacity, Python programming and ArcGIS were preferred (Figure 17), found in three papers each. Agisoft, SNAP, GEE and R programming were used in two papers each, while QGIS, Matlab, Envi and Pix4D were found in one paper each.

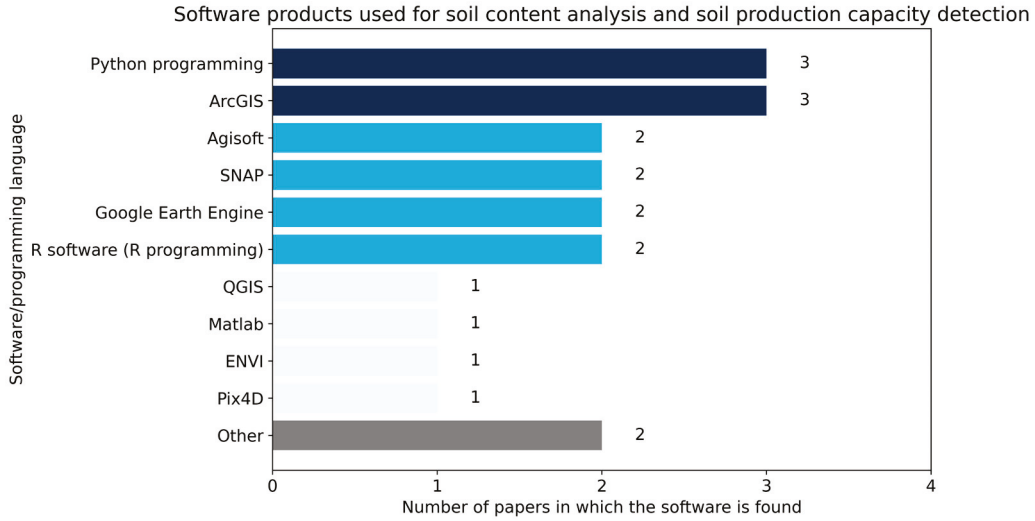

Figure 17. Software products used for soil content analysis and soil production capacity.

4.3. Answer to the Third Research Question ("What Type of Data Can Be Used in This Regards?")

The data sources were classified into the categories found in Figure 18. Satellite imagery was by far the most used data source, found in 78 papers. Next, UAV imagery was found in 18 papers and Radar data in 14 papers. Five studies used unspecified remote sensing imagery, while LiDAR data was found in four papers. In a single study, a stereo camera system placed at the study location was used.

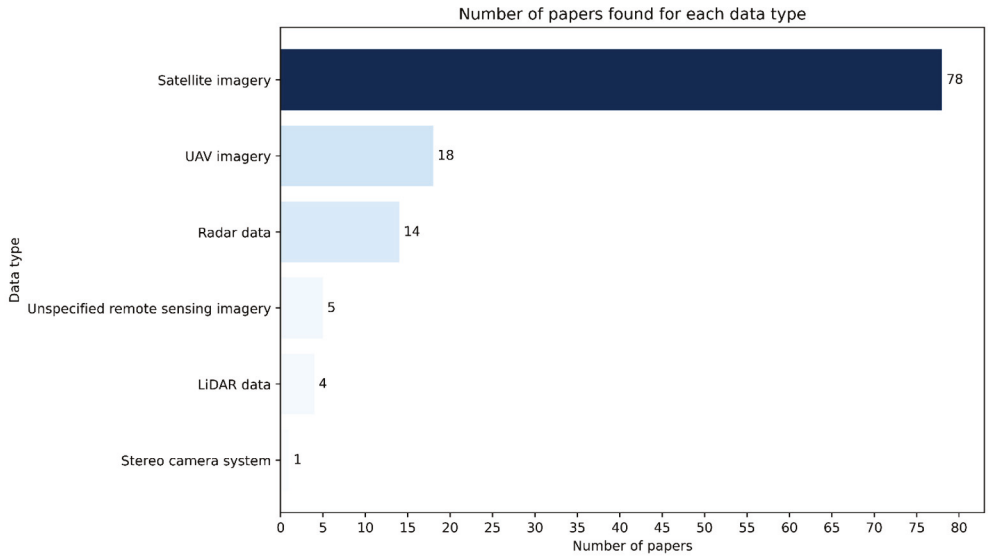

Figure 18. Papers by data type used in the studies.

The sources of data used in the selected papers were also investigated (Figure 19). Among the many available open-access satellite datasets, Sentinel data was the most commonly used, found in 43 studies. The Sentinel-1 mission, part of the Copernicus Initiative by the European Commission (EC) and the European Space Agency (ESA), comprises a constellation of two sun-synchronous polar-orbiting satellites, flying in the same orbital plane but phased 180° apart, equipped with C-band SAR systems, enabling all-weather, day-and-night Earth observations. Sentinel-1 operates in four distinct imaging modes, offering spatial resolutions down to 5 m and swath widths up to 400 km [148]. The Sentinel-2 mission is a European initiative focused on wide-swath, high-resolution, multispectral Earth observations. It consists of a pair of satellites achieving global coverage every 5 days at the Equator. Each satellite is equipped with a single payload: the Multispectral Instrument (MSI) is capable of capturing imagery across 13 spectral bands. These include the following: four bands at a 10 m resolution, six bands at a 20- m resolution and three bands at a 60 m resolution, with a swath width of 290 km [149].

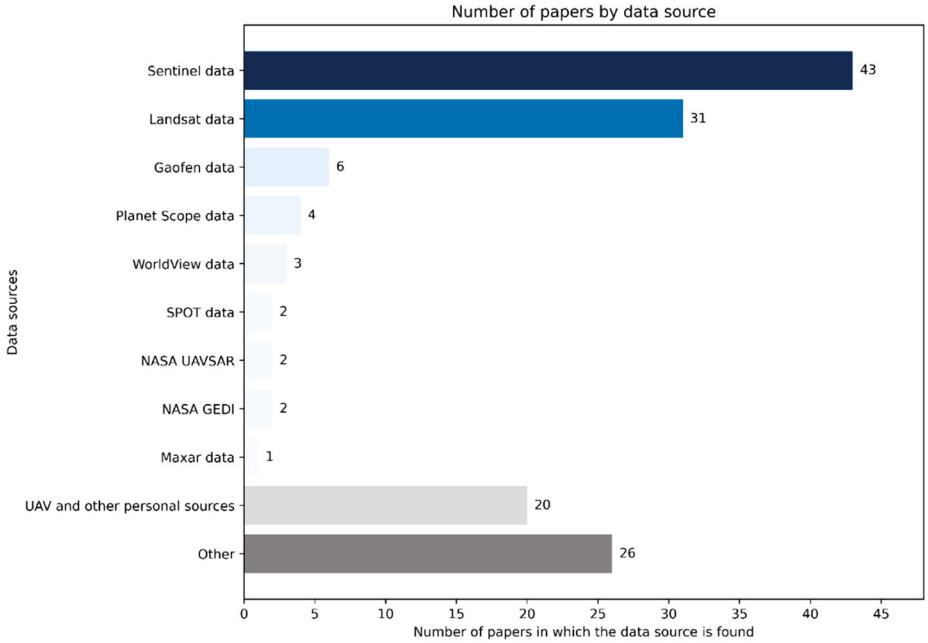

Figure 19. Papers by data source used in the studies.

Landsat data was found in 31 papers. Landsat-8, launched by NASA in 2013, is equipped with the Operational Land Imager (OLI), which captures Earth imagery across the visible, near-infrared (NIR) and shortwave infrared (SWIR) spectrum. The satellite system features two additional spectral bands: Band 1 is deep blue and optimized for coastal zone observation and Band 9 is optimized for cirrus cloud detection in the NIR. Landsat-8 can ensure a 15 m resolution for panchromatic images and 30 m for multispectral ones [150]. Landsat 4, built and launched by NASA–NOAA, is equipped with the Landsat 4 Thematic Mapper (TM) sensor which features seven spectral bands, capturing data across the blue, green, red, NIR, mid-infrared (two bands) and thermal infrared (TIR) regions of the electromagnetic spectrum [151].

Gaofen (GF) is a series of Chinese high-resolution Earth imaging satellites, launched as part of the China High-Resolution Earth Observation System (CHEOS), and GF data was found in six papers, including images from the Gaofen-1 (GF-1) mission, Gaofen-2 (GF-2) mission and Gaofen-6 (GF-6) mission. GF-1 is equipped with two main imaging systems: a panchromatic and multispectral camera (PMC) and a wide-field imager (WFI). The PMC is a high-resolution pushbroom imager featuring Time Delay Integration (TDI),

consisting of two cameras that provide a swath width of 69 km at nadir. It captures imagery in one NIR and three visible bands—blue, green and red—with a spatial resolution of 8 m. Additionally, it provides 2 m resolution panchromatic images in the visible range. It makes observations in three visible bands and one NIR band, offering 16 m spatial resolution [152]. A GF-2 satellite is equipped with two PAN/MS (panchromatic/multispectral) cameras. It is capable of capturing high-resolution imagery with a Ground Sampling Distance (GSD) of 0.81 m in the panchromatic band and 3.24 m in the multispectral bands across a 45 km-wide swath [153]. A GF-6 satellite is equipped with a panchromatic/hyperspectral camera offering resolutions of 2 m and 8 m, respectively, with an image swath exceeding 90 km. Additionally, it carries a wide-angle camera with a resolution of 16 m and an expansive swath of 800 km. Both cameras employ three-mirror anastigmatic telescopes and are capable of imaging from the visible to the NIR spectrum, covering wavelengths of approximately 450–900 nm [154].

Planet Scope data was found in four papers. The Planet Scope satellite camera operates in eight spectral bands—Coastal Blue, Blue, Green I, Green, Yellow, Red, RedEdge and NIR—with a GSD (at nadir) between 3 m and 4.1 m [155].

WorldView data was found in three papers, including WorldView-2, WorldView-3 and WorldView-4. WorldView-2 is capable of capturing high-resolution imagery with a GSD of 0.46 m in the panchromatic and 1.8 m in the eight multispectral bands [156]. WorldView-3 captures imagery at 0.31 m resolution in the panchromatic, 1.24 m in the eight VNIR (visible-to-near-infrared) bands, 3.7 m in the eight SWIR bands and 30 m in the CAVIS (Clouds, Aerosols, Vapors, Ice and Snow) bands [157]. WorldView-4 was designed to expand European Space Imaging's offerings with ultra-high-resolution Earth observation capabilities, and it captures imagery at 31 cm resolution in panchromatic mode and 1.23 m resolution in multispectral mode [158].

SPOT (Satellite pour l'Observation de la Terre) data was used in two papers found in this SLR. Initiated by the French National Centre for Space Studies (CNES), five satellites were deployed between 1986 and 2015. These missions offered detailed views of the Earth's surface, enabling significant advances in areas such as cartography, vegetation monitoring, land use and land cover analysis and disaster impact assessments. All satellites in the series feature both panchromatic and multispectral imaging capabilities, covering a swath width of 60 km. SPOT-6 and SPOT-7 cover a GSD of 1.5 m at nadir in panchromatic mode and 6 m at nadir in multispectral mode [159].

NASA's UAVSTAR (Uninhabited Arial Vehicle Synthetic Aperture Radar) was found as the data source in two papers. It uses airborne radar and operates by transmitting and receiving radio waves to gather information about the Earth's surface features. UAVSAR has collected data since 2007 in the following fields of study: vegetation, ice and glaciers, soil moisture, oceanography, earthquakes, volcanoes and other [160].

The Global Ecosystem Dynamics Investigation (GEDI) is a LiDAR instrument mounted on the International Space Station, designed to deliver high-resolution observations of Earth's three-dimensional forest structure and was used in two papers in this study. It captures data at a spatial resolution of approximately 30 m per footprint, with samples spaced every 60 m along its orbital path. Additionally, it offers a spectral resolution of 1 m [161].

It is worth noting that MAXAR satellite imagery was found in one paper. Although it offers a spatial resolution ranging from 30 cm to 1.2 m and supports spectral analysis across the visible, NIR and RedEdge bands [162], the high cost of the images can be a limiting factor for broader use.

In 20 papers, UAVs and other personal data sources were used. The spatial resolution of UAV imagery is typically very high, often better than satellite imagery, depending on

the flight altitude, sensor quality and camera settings, with some of the most advanced cameras ensuring a GSD up to 3 cm [163].

Other sources, each found in only one paper, include ESA's RapidEye data, SRTM DTM mission, PolSAR data, UC Merced Land Use Dataset, ICESat-2, ISPRS Potsdam Benchmark dataset, DeepGlobe dataset, ZY-3 dataset, Fuyang remote sensing image dataset, NASA SMAP mission data, NWPU-RESISC dataset, Bing Maps aerial imagery, NASA MODIS data, Planet Fusion CubeSat imagery, NICFI satellite data, Pleiades imagery, VHR satellite imagery, LISS IV images, NASA EO-1 Hyperion sensor, NCALM sensor, QuickBird satellite imagery, IKONOS satellite imagery, ESA's RADARSAT data, Xiongan dataset and SWISSIMAGE HIST 1946 data.

4.3.1. Land Use Mapping and Crop Detection

For land use mapping and crop detection, satellite imagery was by far the most preferred data type (Figure 20). Sentinel and Landsat data were the most used (Figure 21) due to their wide availability. Other satellite data sources were Gaofen, SPOT and WorldView, found in two papers each. Other types of data found in the SLR included radar data, UAV imagery, unspecified remote sensing imagery and LiDAR data. The sources of this data were either NASA UAVSTAR, NASA GEDI, UAVs and other personal sources or other sources less frequently found in this study.

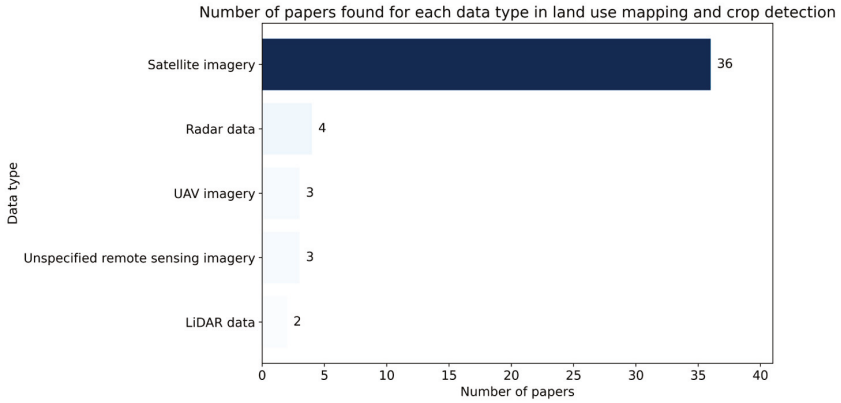

Figure 20. Data type used in land use mapping and crop detection.

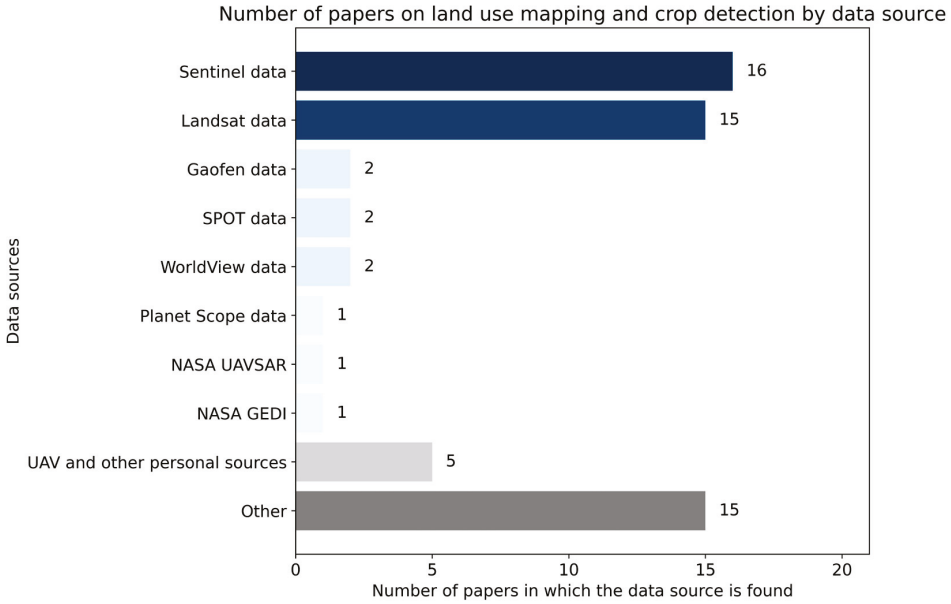

Figure 21. Data sources used in land use mapping and crop detection.

4.3.2. Crop Yield Monitoring

For crop yield monitoring, satellite imagery and UAV imagery were equally preferred (Figure 22), found in three papers each, while radar data was used in only one paper and in one study a stereo camera system was used. In this case, Sentinel data was also the most used (Figure 23) due to its availability and high resolution. Landsat, Planet Scope data and NASA UAVSTAR data were found in one paper each, while three studies used UAVs or other personal sources.

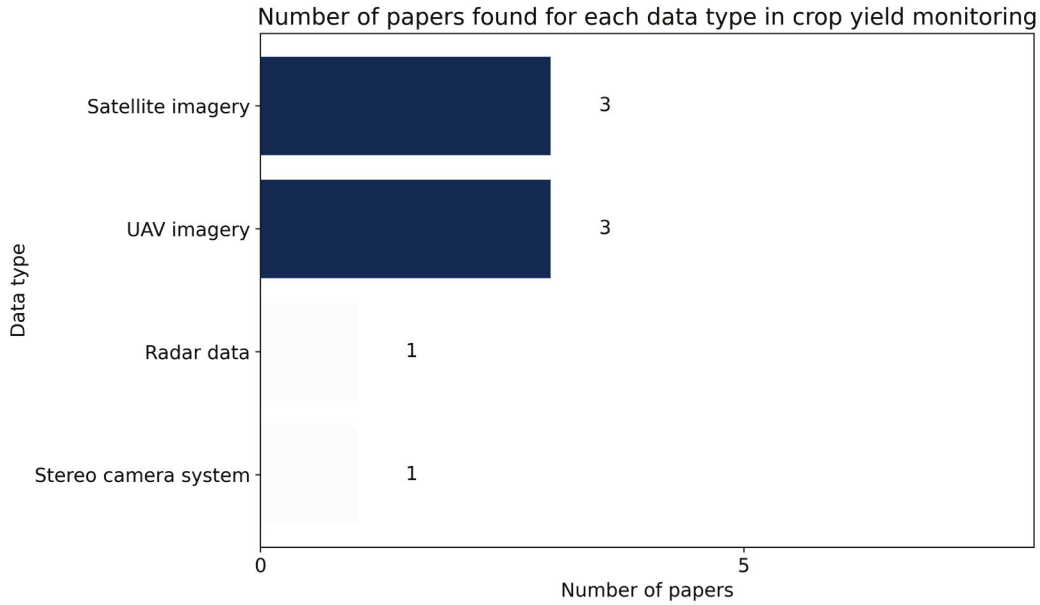

Figure 22. Data type used in crop yield monitoring.

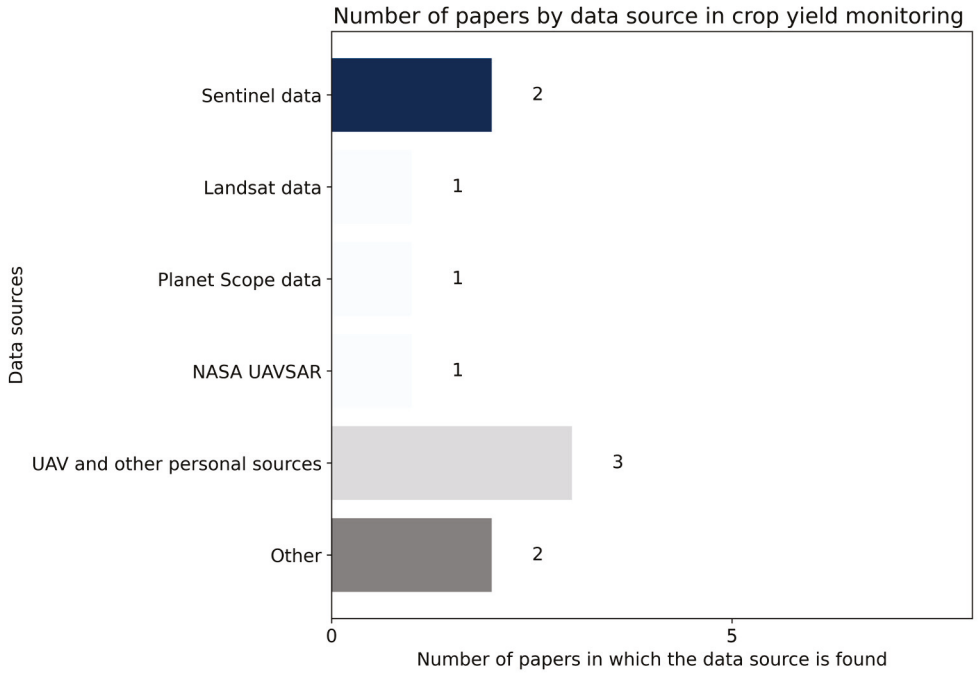

Figure 23. Data sources used in crop yield monitoring.

4.3.3. Flood-Prone Area Detection

For flood-prone area detection, radar data was preferred and used in two studies, while satellite and UAV imagery were found in one study each. For the data sources,

Sentinel data was used in two studies, while Gaofen and UAV imagery were used in one study each.

4.3.4. Forest and Vegetation Monitoring

Satellite imagery was widely used for forest and vegetation monitoring and was found in 31 papers included in this SLR (Figure 24). UAV imagery was used in five papers, radar data in three papers and LiDAR data in two papers. In two studies, unspecified remote sensing images were used. Regarding the data sources (Figure 25), Sentinel and Landsat data were the most used, being found in 17 and 14 papers, respectively. Other satellite data sources included Gaofen, PlanetScope, WorldView and Maxar, which was used in only one paper. NASA GEDI data was used in one paper, while five other studies included UAV and other personal data sources.

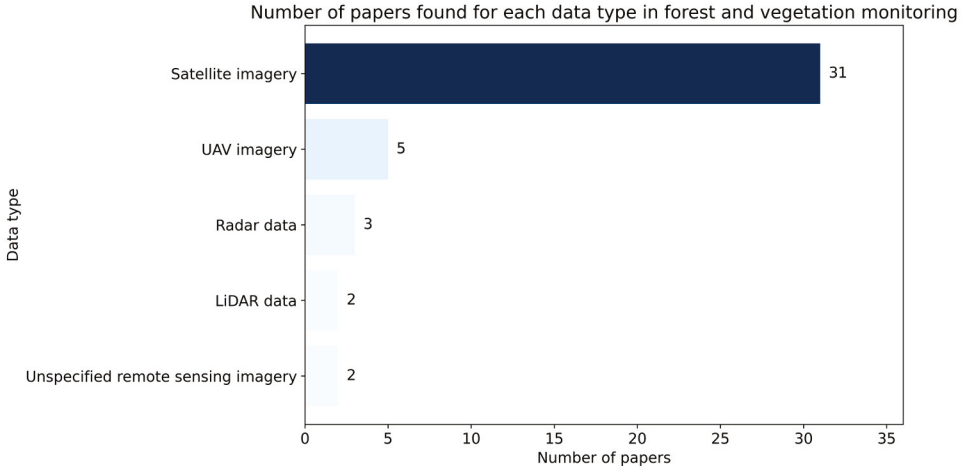

Figure 24. Data type used in forest and vegetation monitoring.

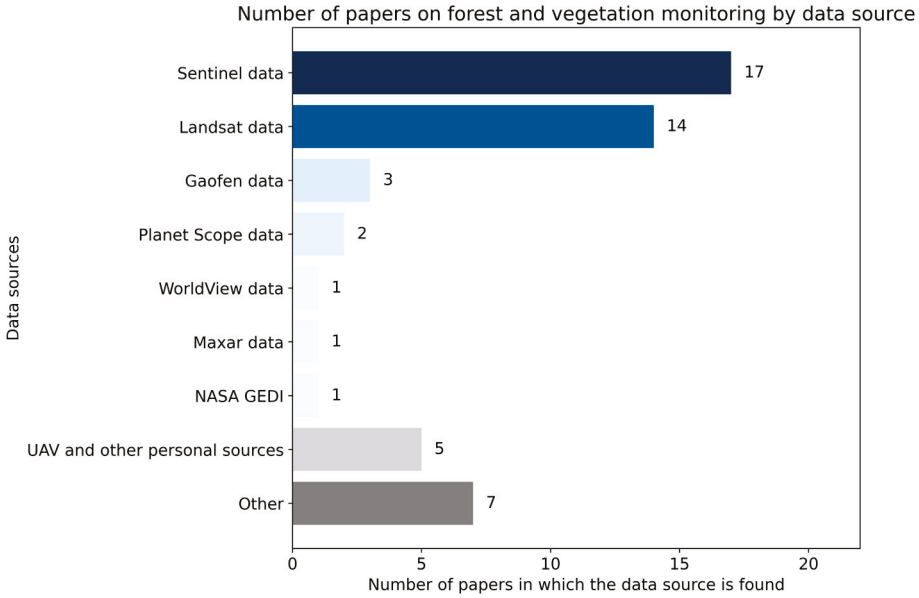

Figure 25. Data sources used in forest and vegetation monitoring.

4.3.5. Pest Disease Monitoring

For pest disease monitoring, satellite imagery was found in four papers, with Sentinel being the main data source, while UAV imagery was used in three papers and one study involved the use of other data source.

4.3.6. Droughts Prediction

While performing the initial analysis of the selected papers for this SLR, two papers regarding draughts prediction were found, which were excluded as they did not include the use of AI. In both papers, satellite imagery data sources Sentinel and Landsat were used.

4.3.7. Soil Content Analysis and Soil Production Capacity Detection

For soil content analysis and soil production capacity, satellite and UAV imagery were the most used data types (Figure 26), with Sentinel data found in three papers and Landsat data in one paper (Figure 27). Two papers included the use of radar data.

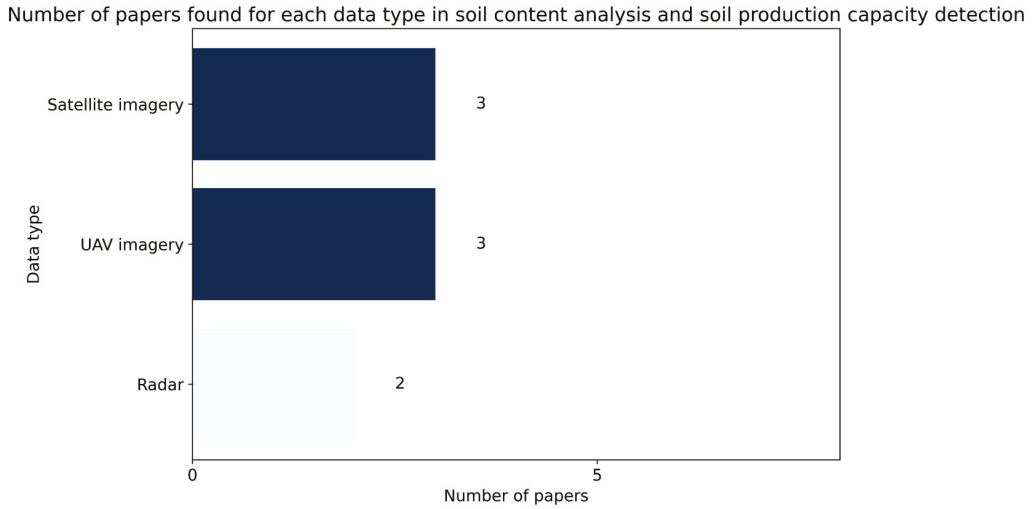

Figure 26. Data type used in soil content analysis and soil production capacity detection.

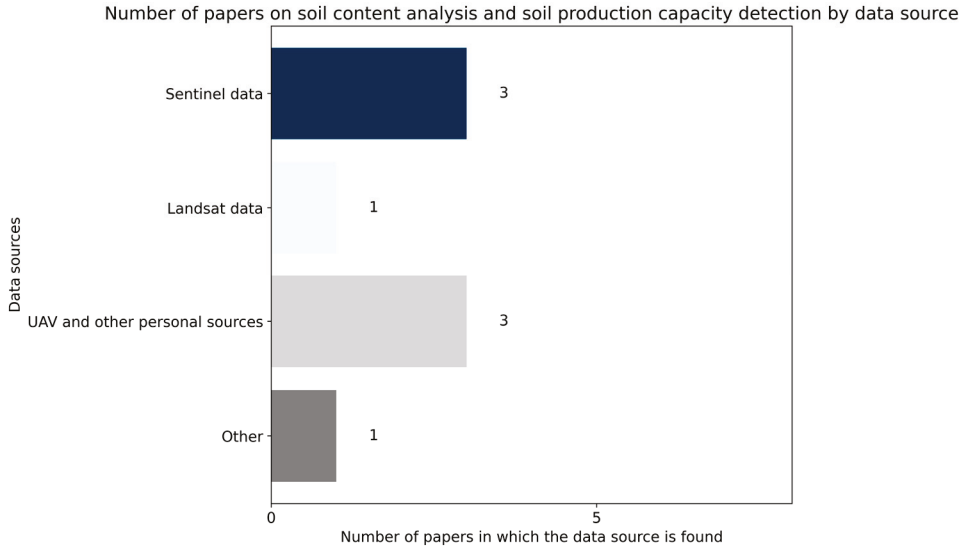

Figure 27. Data sources used in soil content analysis and soil production capacity detection.

5. Discussion

During this systematic literature review, 472 papers from Scopus and 309 papers from Web of Science were identified. After removing 201 duplicates, an initial screening of titles and abstracts was conducted on the remaining records, leading to the exclusion of 426 papers. A full-text assessment was then performed on the remaining articles, resulting in the exclusion of an additional 46 papers. Ultimately, 108 studies met the inclusion criteria and were retained for the final review.

The first significant finding of the systematic literature review is the growing interest in the application of AI in remote sensing for agricultural research, with the number of relevant publications increasing from 8 in 2020 to 51 in 2024. In terms of geographical distribution, China stands out as the country with the highest number of studies. In contrast, regions such as Eastern Europe remain underrepresented in research on the use of AI and remote sensing in agriculture. This gap is particularly noteworthy given that countries like Romania, Ukraine and Bulgaria are recognized for their extensive arable lands and significant agricultural sectors.

Based on the search queries, to answer the first research question—"What are the main problems that can be solved through incorporating AI-driven classification techniques in the field of smart agriculture and environmental monitoring?" (Figure 28)—the papers were divided into the following categories: land use mapping and crop detection, crop yield monitoring, flood-prone area detection, forest and vegetation monitoring, pest disease monitoring, droughts prediction and soil content analysis and soil production capacity detection. The categories with the highest research interest were land use mapping and crop detection (44 papers) and forest and vegetation monitoring (41 papers). In contrast, fewer studies addressed soil content analysis and soil production capacity detection (eight papers), pest disease monitoring (six papers), crop yield monitoring (six papers) and flood-prone area detection (three papers). Notably, no studies meeting the inclusion criteria were found in the category of droughts prediction. This absence highlights a significant research gap and underscores the need for further studies in this area, especially considering the increasing impact of climate change on agricultural productivity. Furthermore, other categories, such as flood-prone area detection, pest disease monitoring, crop yield monitoring and soil content analysis and soil production capacity detection were also underrepresented. These findings highlight the need for more research in these areas to support sustainable and data-driven agricultural practices.

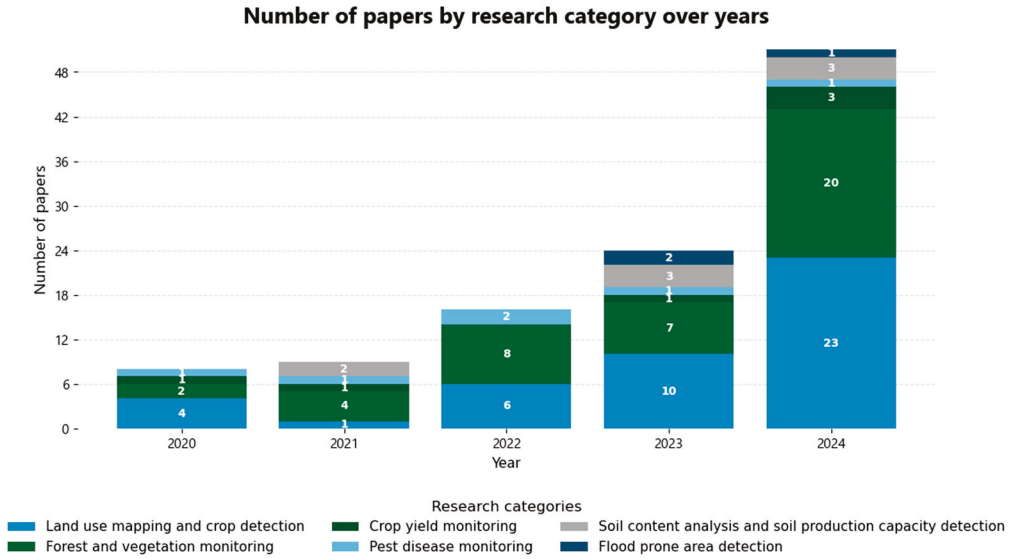

Figure 28. Answer to the first research question ("What are the main problems that can be solved through incorporating AI-driven classification techniques in the field of smart agriculture and environmental monitoring?").

To answer the second research question—"What are the main methods and strategies used in this technology?" (Figure 29)—the AI algorithms found in this SLR were divided into the following categories: decision trees-based models, Convolutional Neural Networks and other Deep Neural Networks, Support Vector Machine, hybrid models, statistical models, other classic supervised learning models, Recurrent Neural Networks, transformers

and attention-based models, Fully Connected Neural Networks, clustering algorithms, optimization algorithms and generative models. Among these, decision trees-based models (found in 55 papers) and Convolutional Neural Networks and other Deep Neural Networks (found in 49 papers) were the most commonly employed, highlighting their large-scale applicability. The widespread use of CNNs, in particular, can be attributed to their ability to effectively process grid-like data structures, such as imagery. Hybrid models are especially interesting (found in 13 papers), as they combine different AI techniques to overcome the limitations of using a single AI method. Regarding the implementation tools used for algorithm development and data processing, Python was the most commonly used programming language, mentioned in 45 papers. Its popularity is likely due to its open-source nature, extensive libraries for machine learning and remote sensing and overall versatility in handling large-scale data. Google Earth Engine was found in 23 papers in total, reflecting its relevance as a cloud-based, free for non-commercial use platform, for processing and analyzing large volumes of remote sensing data. Interestingly, ArcGIS was used in 21 papers, despite its high costs, highlighting its robust geospatial analysis capabilities and user-friendly interface, which, in addition to the available geoprocessing tools that simplify the overall classification workflows, allows for Python scripts integration for advanced algorithm development. The main methods used in each category were further studied. Decision trees-based models were the most preferred for land use mapping and crop detection, crop yield monitoring and soil content analysis and soil production capacity detection, while for the forest and vegetation monitoring and pest disease monitoring categories Convolutional Neural Networks and other Deep Neural Networks were the most used. In the three papers on flood-prone area detection, one algorithm from each of the following four categories was found: CNNs and other DNNs, transformer and attention-based models, decision-trees-based models and SVM. Python programming was the most used environment for land use mapping and crop detection, crop yield monitoring, forest and vegetation monitoring and soil content analysis and soil production capacity detection; for flood-prone area detection, ArcGIS software was the most used; and for pest disease monitoring, Agisoft was the most frequently found.

To answer the third research question—"What type of data can be used in this regards?" (Figure 30)—the data sources were classified into the following categories: satellite imagery, being by far the most frequently found type of data (78 papers); UAV imagery (found in 18 papers); radar data (found in 14 papers); unspecified remote sensing imagery (used in 5 papers); LiDAR data (found in 4 papers) and a stereo camera system (found in 1 paper). The widespread use of satellite imagery highlights its accessibility, broad spatial coverage and the availability of free and high-resolution datasets, making it a preferred choice for large-scale agricultural monitoring, while UAV data is preferred for local, more accurate observations. Overall, the open-source Sentinel data was the most used, found in 43 papers, due to its wide availability and high-spatial and -temporal resolutions, followed by the Landsat data, used in 31 papers, with a slightly lower spatial resolution. This type of data can support multi-temporal analyses, benefitting from a long historical archive. Other high-resolution data sources, such as QuickBird, were used in some studies, but their applicability is often limited by their high acquisition costs and restricted temporal coverage. In contrast, Sentinel and Landsat provide free, openly accessible data with global coverage, making them more practical for large-scale and multi-temporal studies, which explains their prevalence in the literature. Satellite imagery was the preferred data source for land use mapping and crop detection, forest and vegetation monitoring and pest disease monitoring. For crop yield monitoring and soil content analysis and soil production capacity detection, satellite and UAV imagery were equally preferred, while for flood-prone area detection, radar data was the most frequently used, due to its capacity to penetrate clouds and operate in all kinds of

weather conditions. In all categories, Sentinel data was the most used data source, due to its availability, lack of costs, high resolution and versatility.

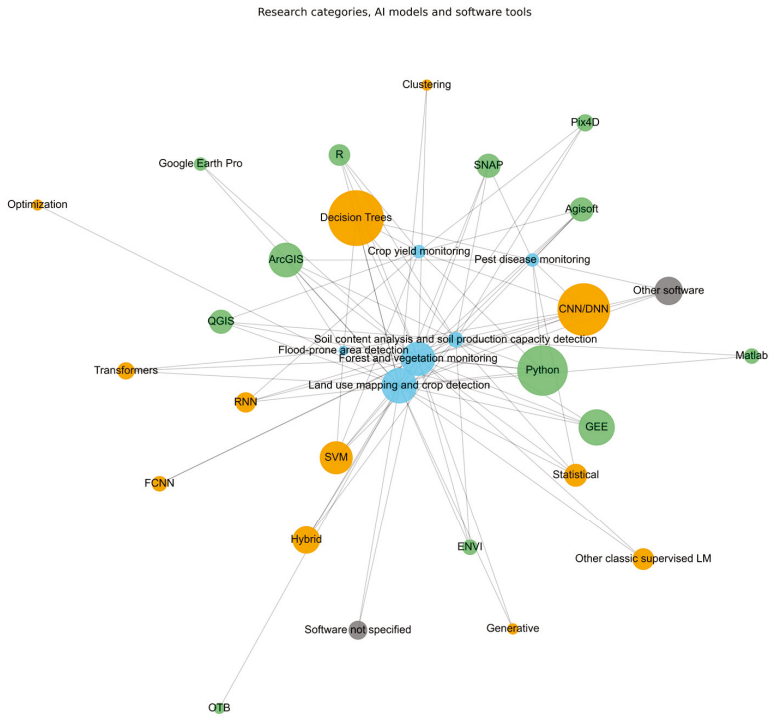

Figure 29. Answer to the second research question—"What are the main methods and strategies used in this technology?" (CNNs—Convolutional Neural Networks; DNNs—Deep Neural Networks; RNNs—Recurrent Neural Networks; FCNNs—Fully Connected Neural Networks; SVM—Support Vector Machine; GEE—Google Earth Engine; OTB—Orfeo Toolbox).

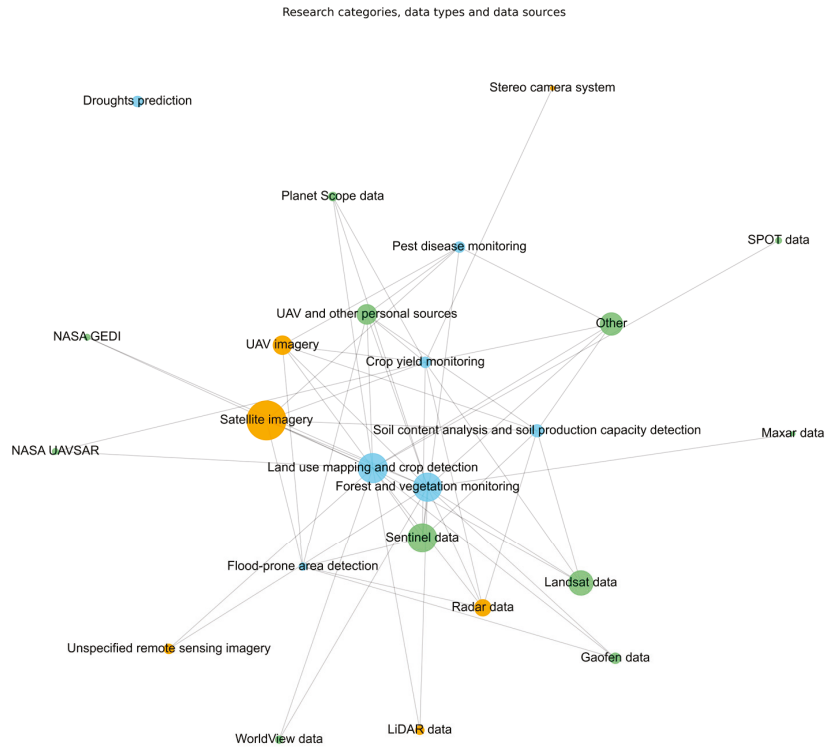

Figure 30. Answer to the third research question—"What type of data can be used in this regards?" (GEDI—Global Ecosystem Dynamics Investigation; UAVSAR—Uninhabited Arial Vehicle Synthetic Aperture Radar; SPOT—Satellite pour l'Observation de la Terre; LiDAR—Light Detection and Ranging).

6. Conclusions

This systematic literature review highlights the growing interest in research on the integration of AI and remote sensing techniques into agriculture from 2020 to 2024. The increase in publications reflects a rising global interest in developing tools to address agricultural and environmental challenges. This review revealed that the most studied topics were land use mapping and crop detection and forest and vegetation monitoring, where AI and remote sensing proved to be highly effective. However, notable research gaps were identified, particularly in droughts prediction, gaps that are especially relevant given the context of climate change and food security.

CNNs and DT-based models emerged as the most frequently used AI techniques in the analyzed studies. Their popularity is likely due to their ability to handle the complex and large datasets commonly used in remote sensing applications. Satellite imagery—particularly from open-access platforms such as Sentinel and Landsat—played an important role in these analyses, offering high-spatial, -spectral and -temporal resolutions. The accessibility and continuity of satellite data make it especially relevant for monitoring agricultural dynamics, providing up-to-date insights into land use changes and crop health.

In Table 5, the most used algorithms, software products, data type and data source for each category are highlighted, indicating the current trends in land use mapping and crop detection, crop yield monitoring, flood-prone area detection, forest and vegetation monitoring, pest disease monitoring, droughts prediction and soil content analysis and soil production capacity detection.

Table 5. Most used algorithms, software products, data type and data source for each category.

Category	Most Used Algorithm Type	Most Used Software Product	Most Used Data Type	Most Used Data Source
Land use mapping and crop detection	DT-based models	Python programming	Satellite imagery	Sentinel data
Crop yield monitoring	DT-based models	Python programming	Satellite imagery	Sentinel data
Flood-prone area detection	CNNs and other DNNs	ArcGIS	Radar data	Sentinel data
Forest and vegetation monitoring	CNNs and other DNNs	Python programming	Satellite imagery	Sentinel data
Pest disease monitoring	CNNs and other DNNs	Agisoft	Satellite imagery	Sentinel data
Droughts prediction	-	-	-	-
Soil content analysis and soil production capacity detection	DT-based models	Python programming	Satellite imagery	Sentinel data

By facilitating smarter, more efficient and data-driven agricultural practices, the integration of AI and remote sensing contributes directly to the achievement of several SDGs, including SDG 2 (Zero Hunger), SDG 9 (Industry, Innovation and Infrastructure), SDG 12 (Responsible Consumption and Production) and SDG 13 (Climate Action). The findings are relevant for SDG 6 (Clean Water and Sanitation), as remote sensing and AI techniques applied to flood-prone area detection and droughts prediction can improve water resource management and reduce the risks associated with water scarcity or excess. They also contribute to SDG 9 (Industry, Innovation and Infrastructure), as digital

technologies, AI-driven analyses and open-source satellite platforms such as Sentinel and Landsat can foster innovation in agricultural monitoring and support the development of resilient digital infrastructures for sustainable farming. Furthermore, the subject aligns with SDG 12 (Responsible Consumption and Production), since AI-based tools for soil content analysis, crop yield monitoring and pest and disease monitoring provide insights that encourage efficient resource use, minimize waste and support sustainable production systems. Finally, the study is closely linked to SDG 13 (Climate Action), as AI and remote sensing are essential for monitoring climate-related issues, such as droughts and floods.

Possible limitations of this SLR include the exclusive use of Scopus and Web of Science databases for the literature retrieval, which may have resulted in the omission of relevant studies indexed elsewhere. Additionally, only papers written in English were considered, potentially excluding relevant research published in other languages. This review focused solely on publications from 2020 onwards, and therefore may not have captured earlier foundational work in this field. During the selection process, some topics—such as mapping wildfires with AI—were excluded for being outside the scope of the SLR. Other subjects, such as the influence of wildlife on agricultural activities, were not considered in our search strategy. While agricultural activities can indeed be influenced by wildlife from surrounding forests, and AI algorithms are increasingly being applied for wildlife detection [164,165], this line of research does not necessarily rely on remote sensing data.

Finally, we observed an uneven geographic representation of the studies, with certain regions—particularly Eastern Europe—remaining underrepresented. While this could be partly due to our study's limitation to using only Scopus and WoS, it could also be the result of differences in policy support, research funding and national priorities, and variations in data availability and openness, as open-access satellite imagery and AI-ready datasets are more widely used in regions with established digital infrastructure and strong governmental support for smart agriculture initiatives.

To support the wider adoption of AI and remote sensing for sustainable agriculture, particularly in developing countries, several policy measures can be considered. Governments and institutions can promote the use of free, open-access satellite data such as Sentinel and Landsat, which provide high-quality imagery without significant financial investment. Policies that encourage data sharing, collaboration between research institutions and public–private partnerships can further enhance access to necessary infrastructure and expertise. By adopting such measures, developing countries can implement low-cost remote sensing and AI technologies to improve agricultural and vegetation monitoring, optimize resource use and increase resilience to climate-related risks.

We propose that future activities focus on filling the research gaps and continuing to promote the use of open-source data and tools, particularly in underrepresented regions, to ensure more efficient and sustainable agriculture.

Supplementary Materials: The following supporting information can be downloaded at: https://www.mdpi.com/article/10.3390/su17198526/s1, PRISMA 2020 Checklist. Reference [166] is cited in the Supplementary Materials.

Author Contributions: Conceptualization, V.A.N., G.B., A.C.B. and A.P.G.; methodology, V.A.N. and A.P.G.; validation, G.B. and A.C.B.; formal analysis, V.A.N., G.B., A.C.B. and A.P.G.; investigation, V.A.N. and A.P.G.; resources, V.A.N.; data curation, V.A.N.; writing—original draft preparation, V.A.N.; writing—review and editing, V.A.N., G.B., A.C.B. and A.P.G.; visualization, V.A.N., G.B., A.C.B. and A.P.G.; supervision, G.B. and A.C.B. All authors have read and agreed to the published version of the manuscript.

Funding: This research received no external funding.

Institutional Review Board Statement: Not applicable.

Informed Consent Statement: Not applicable.

Data Availability Statement: The original contributions presented in this study are included in the article. Further inquiries can be directed to the corresponding author.

Acknowledgments: This study was conducted within the Geodetic Engineering Measurements and Spatial Data Infrastructures Research Centre, Faculty of Geodesy, Technical University of Civil Engineering Bucharest.

Conflicts of Interest: The authors declare no conflicts of interest.

Abbreviations

The following abbreviations are used in this manuscript:

AI	Artificial Intelligence
ANN	Artificial Neural Network
ARIMA	Autoregressive Integrated Moving Average
BETAM	Border-Enhanced Triple Attention Mechanism
CART	Classification and Regression Tree
CHEOS	China High-Resolution Earth Observation System
CNN	Convolutional Neural Network
CRRF	Crop-Residue Random Forest
DL	Deep Learning
DNN	Deep Neural Network
DT	Decision Tree
EC	European Commission
ERF	Extreme Random Forest
ESA	European Space Agency
FAO	Food and Agriculture Organization
FCNN	Fully Connected Neural Network
GAN	Generative Adversarial Network
GA-RF	Genetic Algorithm-Optimized Random Forest
GEDI	Global Ecosystem Dynamics Investigation
GEE	Google Earth Engine
GF	Gaofen
GLM	Generalized Linear Model
GNB	Gaussian Naïve Bayes
GSD	Ground Sampling Distance
GTB	Gradient Tree Boost
IF	Isolation Forest
IoT	Internet of Things
kNN	k-Nearest Neighbor
LASSO	Least Absolute Shrinkage and Selection Operator
LiDAR	Light Detection and Ranging
LR	Linear Regression
LSTM	Long Short-Term Memory
LVQ	Learning Vector Quantization
ML	Machine Learning
MLP	Multilayer Perceptron
MSI	Multispectral Instrument
NB	Normal Bayes
NDVI	Normalized Difference Vegetation Index
NIR	Near Infrared
NN	Nearest Neighbor

OC-SVM	One-Class Support Vector Machine
OG-WOA	Optimal Guidance-Whale Optimization Algorithm
OLI	Operational Land Imager
OTB	Orfeo Toolbox
OUDN	Object-Based U-Net-DenseNet
PMC	Panchromatic and Multispectral Camera
QDA	Quadratic Discriminant Analysis
QHPO	Quantum Hippopotamus Optimization
RF	Random Forest
RNN	Recurrent Neural Network
RSS-GAN	Remote Sensing Super-Resolution Generative Adversarial Network
SAR	Synthetic Aperture Radar
SCP	Semi-Automated Classification Plugin
SDG	Sustainable Development Goal
SEBAL	Surface Energy Balance Algorithm for Land
SLR	Systematic Literature Review
SNAP	Sentinel Application Platform
SPOT	Satellite pour l'Observation de la Terre
SS-RF	Stochastic Spatial Random Forest
SVM	Support Vector Machine
SWIR	Shortwave Infrared
TIR	Thermal Infrared
UAV	Unmanned Aerial Vehicle
UAVSTAR	Uninhabited Arial Vehicle Synthetic Aperture Radar

References

1. Huo, D.; Malik, A.W.; Ravana, S.D.; Rahman, A.U.; Ahmedy, I. Mapping Smart Farming: Addressing Agricultural Challenges in Data-Driven Era. *Renew. Sustain. Energy Rev.* **2024**, *189*, 113858. [CrossRef]
2. THE 17 GOALS | Sustainable Development. Available online: https://sdgs.un.org/goals (accessed on 9 July 2025).
3. Maroli, A.; Narwane, V.S.; Gardas, B.B. Applications of IoT for Achieving Sustainability in Agricultural Sector: A Comprehensive Review. *J. Environ. Manag.* **2021**, *298*, 113488. [CrossRef]
4. Javaid, M.; Haleem, A.; Singh, R.P.; Suman, R. Enhancing Smart Farming through the Applications of Agriculture 4.0 Technologies. *Int. J. Intell. Netw.* **2022**, *3*, 150–164. [CrossRef]
5. CAP at a Glance—European Commission. Available online: https://agriculture.ec.europa.eu/common-agricultural-policy/cap-overview/cap-glance_en (accessed on 9 July 2025).
6. van der Velden, D.; Klerkx, L.; Dessein, J.; Debruyne, L. Governance by Satellite: Remote Sensing, Bureaucrats and Agency in the Common Agricultural Policy of the European Union. *J. Rural. Stud.* **2025**, *114*, 103558. [CrossRef]
7. Cappelli, S.L.; Domeignoz-Horta, L.A.; Loaiza, V.; Laine, A.-L. Plant Biodiversity Promotes Sustainable Agriculture Directly and via Belowground Effects. *Trends Plant Sci.* **2022**, *27*, 674–687. [CrossRef] [PubMed]
8. Lahssini, K.; Teste, F.; Dayal, K.R.; Durrieu, S.; Ienco, D.; Monnet, J.-M. Combining LiDAR Metrics and Sentinel-2 Imagery to Estimate Basal Area and Wood Volume in Complex Forest Environment via Neural Networks. *IEEE J. Sel. Top. Appl. Earth Obs. Remote Sens.* **2022**, *15*, 4337–4348. [CrossRef]
9. Pereira, P.; Brevik, E.C.; Muñoz-Rojas, M.; Miller, B.A.; Smetanova, A.; Depellegrin, D.; Misiune, I.; Novara, A.; Cerdà, A. Chapter 2—Soil Mapping and Processes Modeling for Sustainable Land Management. In *Soil Mapping and Process Modeling for Sustainable Land Use Management*; Pereira, P., Brevik, E.C., Muñoz-Rojas, M., Miller, B.A., Eds.; Elsevier: Amsterdam, The Netherlands, 2017; pp. 29–60, ISBN 978-0-12-805200-6.
10. Weiss, M.; Jacob, F.; Duveiller, G. Remote Sensing for Agricultural Applications: A Meta-Review. *Remote Sens. Environ.* **2020**, *236*, 111402. [CrossRef]
11. Sishodia, R.P.; Ray, R.L.; Singh, S.K. Applications of Remote Sensing in Precision Agriculture: A Review. *Remote Sens.* **2020**, *12*, 3136. [CrossRef]
12. Verma, Y.; Verma, A.; Chatterjee, S.; Sagar, P. Remote Sensing Applications in Agriculture. In *Recent Trends in Agriculture*; Integrated Publications: New Delhi, India, 2024; pp. 159–180, ISBN 978-93-5834-170-6.
13. Wang, J.; Wang, Y.; Li, G.; Qi, Z. Integration of Remote Sensing and Machine Learning for Precision Agriculture: A Comprehensive Perspective on Applications. *Agronomy* **2024**, *14*, 1975. [CrossRef]

14. Jung, J.; Maeda, M.; Chang, A.; Bhandari, M.; Ashapure, A.; Landivar-Bowles, J. The Potential of Remote Sensing and Artificial Intelligence as Tools to Improve the Resilience of Agriculture Production Systems. *Curr. Opin. Biotechnol.* **2021**, *70*, 15–22. [CrossRef]
15. Sustainable Development Report 2025. Available online: https://dashboards.sdgindex.org/ (accessed on 9 July 2025).
16. Interlinkages—Goals | KnowSDGs. Available online: https://knowsdgs.jrc.ec.europa.eu/interlinkages/goals (accessed on 9 July 2025).
17. Badea, A.C. Overview of the Sustainable Development Goals in Action and on the Involvement of UTCB in Sustainability Projects. EU-CONEXUS Seminar, 2025. Available online: https://www.eu-conexus.eu/en/joint-research-institutes-seminars/overview-of-the-sustainable-development-goals-in-action-and-on-the-involvement-of-utcb-in-sustainability-projects/ (accessed on 16 June 2025).
18. Agricultural Production—Crops. Available online: https://ec.europa.eu/eurostat/statistics-explained/index.php?title=Agricultural_production_-_crops (accessed on 9 July 2025).
19. Parra-López, C.; Ben Abdallah, S.; Garcia-Garcia, G.; Hassoun, A.; Trollman, H.; Jagtap, S.; Gupta, S.; Aït-Kaddour, A.; Makmuang, S.; Carmona-Torres, C. Digital Technologies for Water Use and Management in Agriculture: Recent Applications and Future Outlook. *Agric. Water Manag.* **2025**, *309*, 109347. [CrossRef]
20. Wang, X.; Zeng, H.; Yang, X.; Shu, J.; Wu, Q.; Que, Y.; Yang, X.; Yi, X.; Khalil, I.; Zomaya, A.Y. Remote Sensing Revolutionizing Agriculture: Toward a New Frontier. *Future Gener. Comput. Syst.* **2025**, *166*, 107691. [CrossRef]
21. Bilal, A.; Liu, X.; Long, H.; Shafiq, M.; Waqar, M. Increasing Crop Quality and Yield with a Machine Learning-Based Crop Monitoring System. *Comput. Mater. Contin.* **2023**, *76*, 2401–2426. [CrossRef]
22. LavagnedOrtigue, O. (ESS) Land Statistics and Indicators 2000–2021. Available online: https://openknowledge.fao.org/server/api/core/bitstreams/5c8b2707-1bcf-4c29-90e2-3487e583f71e/content (accessed on 9 July 2025).
23. Sustainable Development. Available online: https://sdgs.un.org/ (accessed on 9 July 2025).
24. Goal 2 | Department of Economic and Social Affairs. Available online: https://sdgs.un.org/goals/goal2#targets_and_indicators (accessed on 9 July 2025).
25. Nevavuori, P.; Narra, N.; Linna, P.; Lipping, T. Crop Yield Prediction Using Multitemporal UAV Data and Spatio-Temporal Deep Learning Models. *Remote Sens.* **2020**, *12*, 4000. [CrossRef]
26. Assessing Flood Impact on Agricultural Production. Available online: https://openknowledge.fao.org/server/api/core/bitstreams/89ae84da-5b93-464a-87b4-4d99c3083528/content (accessed on 9 July 2025).
27. Atchyuth, B.A.S.; Swain, R.; Das, P. Near Real-Time Flood Inundation and Hazard Mapping of Baitarani River Basin Using Google Earth Engine and SAR Imagery. *Environ. Monit. Assess.* **2023**, *195*, 1331. [CrossRef]
28. Liman Harou, I.; Whitney, C.; Kung'u, J.; Luedeling, E. Mapping Flood-Based Farming Systems with Bayesian Networks. *Land* **2020**, *9*, 369. [CrossRef]
29. Duriaux Chavarría, J.-Y.; Baudron, F.; Sunderland, T. Retaining Forests within Agricultural Landscapes as a Pathway to Sustainable Intensification: Evidence from Southern Ethiopia. *Agric. Ecosyst. Environ.* **2018**, *263*, 41–52. [CrossRef]
30. Fragoso-Medina, M.d.C.; Navarrete-Segueda, A.; Ceccon, E.; Martínez-Ramos, M. Effects of the Forests-Agriculture Conversion on the Availability and Diversity of Forest Products in a Neotropical Rainforest Region. *Trees For. People* **2024**, *15*, 100481. [CrossRef]
31. FAO Forests and Forest Soils: An Essential Contribution to Agricultural Production and Global Food Security. Available online: http://www.fao.org/soils-portal (accessed on 9 July 2025).
32. Zhang, J.; Cong, S.; Zhang, G.; Ma, Y.; Zhang, Y.; Huang, J. Detecting Pest-Infested Forest Damage through Multispectral Satellite Imagery and Improved UNet++. *Sensors* **2022**, *22*, 7440. [CrossRef]
33. Alkan, E.; Aydin, A. Machine Learning-Based Prediction of Insect Damage Spread Using Auto-ARIMA Model. *Croat. J. For. Eng. J. Theory Appl. For. Eng.* **2024**, *45*, 351–364. [CrossRef]
34. Villani, G.; Tomei, F.; Pavan, V.; Pirola, A.; Spisni, A.; Marletto, V. The iCOLT Climate Service: Seasonal Predictions of Irrigation for Emilia-Romagna, Italy. *Meteorol. Appl.* **2021**, *28*, e2007. [CrossRef]
35. Laipelt, L.; Rossi, J.B.; de Andrade, B.C.; Scherer-Warren, M.; Ruhoff, A. Assessing Evapotranspiration Changes in Response to Cropland Expansion in Tropical Climates. *Remote Sens.* **2024**, *16*, 3404. [CrossRef]
36. Singh, T.; Kundroo, M.; Kim, T. WSN-Driven Advances in Soil Moisture Estimation: A Machine Learning Approach. *Electronics* **2024**, *13*, 1590. [CrossRef]
37. Salmanpour, A.; Jamshidi, M.; Fatehi, S.; Ghanbarpouri, M.; Mirzavand, J. Assessment of Macronutrients Status Using Digital Soil Mapping Techniques: A Case Study in Maru'ak Area in Lorestan Province, Iran. *Environ. Monit. Assess.* **2023**, *195*, 513. [CrossRef] [PubMed]
38. Budak, M.; Günal, E.; Kılıç, M.; Çelik, İ.; Sırrı, M.; Acir, N. Improvement of Spatial Estimation for Soil Organic Carbon Stocks in Yuksekova Plain Using Sentinel 2 Imagery and Gradient Descent–Boosted Regression Tree. *Environ. Sci. Pollut. Res.* **2023**, *30*, 53253–53274. [CrossRef]

39. Chen, J.; Du, H.; Mao, F.; Huang, Z.; Chen, C.; Hu, M.; Li, X. Improving Forest Age Prediction Performance Using Ensemble Learning Algorithms Base on Satellite Remote Sensing Data. *Ecol. Indic.* **2024**, *166*, 112327. [CrossRef]
40. Ameslek, O.; Zahir, H.; Latifi, H.; Bachaoui, E.M. Combining OBIA, CNN, and UAV Imagery for Automated Detection and Mapping of Individual Olive Trees. *Smart Agric. Technol.* **2024**, *9*, 100546. [CrossRef]
41. Trentin, C.; Ampatzidis, Y.; Lacerda, C.; Shiratsuchi, L. Tree Crop Yield Estimation and Prediction Using Remote Sensing and Machine Learning: A Systematic Review. *Smart Agric. Technol.* **2024**, *9*, 100556. [CrossRef]
42. Vasilakos, C.; Kavroudakis, D.; Georganta, A. Machine Learning Classification Ensemble of Multitemporal Sentinel-2 Images: The Case of a Mixed Mediterranean Ecosystem. *Remote Sens.* **2020**, *12*, 2005. [CrossRef]
43. Li, Z.; Chen, B.; Wu, S.; Su, M.; Chen, J.M.; Xu, B. Deep Learning for Urban Land Use Category Classification: A Review and Experimental Assessment. *Remote Sens. Environ.* **2024**, *311*, 114290. [CrossRef]
44. Wang, G.; Chen, J.; Mo, L.; Wu, P.; Yi, X. Border-Enhanced Triple Attention Mechanism for High-Resolution Remote Sensing Images and Application to Land Cover Classification. *Remote Sens.* **2024**, *16*, 2814. [CrossRef]
45. Multilayer Perceptron—An Overview | ScienceDirect Topics. Available online: https://www.sciencedirect.com/topics/computer-science/multilayer-perceptron (accessed on 9 July 2025).
46. Gevaert, C.M.; Belgiu, M. Assessing the Generalization Capability of Deep Learning Networks for Aerial Image Classification Using Landscape Metrics. *Int. J. Appl. Earth Obs. Geoinf.* **2022**, *114*, 103054. [CrossRef]
47. Vinaykumar, V.N.; Babu, J.A.; Frnda, J. Optimal Guidance Whale Optimization Algorithm and Hybrid Deep Learning Networks for Land Use Land Cover Classification. *EURASIP J. Adv. Signal Process.* **2023**, *2023*, 13. [CrossRef]
48. Albarakati, H.M.; Khan, M.A.; Hamza, A.; Khan, F.; Kraiem, N.; Jamel, L.; Almuqren, L.; Alroobaea, R. A Novel Deep Learning Architecture for Agriculture Land Cover and Land Use Classification from Remote Sensing Images Based on Network-Level Fusion of Self-Attention Architecture. *IEEE J. Sel. Top. Appl. Earth Obs. Remote Sens.* **2024**, *17*, 6338–6353. [CrossRef]
49. Kong, J.; Ryu, Y.; Jeong, S.; Zhong, Z.; Choi, W.; Kim, J.; Lee, K.; Lim, J.; Jang, K.; Chun, J.; et al. Super Resolution of Historic Landsat Imagery Using a Dual Generative Adversarial Network (GAN) Model with CubeSat Constellation Imagery for Spatially Enhanced Long-Term Vegetation Monitoring. *ISPRS J. Photogramm. Remote Sens.* **2023**, *200*, 1–23. [CrossRef]
50. PyTorch. Available online: https://pytorch.org/ (accessed on 9 July 2025).
51. Hamidi, M.; Homayouni, S.; Safari, A.; Hasani, H. Deep Learning Based Crop-Type Mapping Using SAR and Optical Data Fusion. *Int. J. Appl. Earth Obs. Geoinf.* **2024**, *129*, 103860. [CrossRef]
52. Snevajs, H.; Charvat, K.; Onckelet, V.; Kvapil, J.; Zadrazil, F.; Kubickova, H.; Seidlova, J.; Batrlova, I. Crop Detection Using Time Series of Sentinel-2 and Sentinel-1 and Existing Land Parcel Information Systems. *Remote Sens.* **2022**, *14*, 1095. [CrossRef]
53. Gackstetter, D.; Körner, M.; Yu, K. Approaching Holistic Crop Type Mapping in Europe through Winter Vegetation Classification and the Hierarchical Crop and Agriculture Taxonomy. *Int. J. Appl. Earth Obs. Geoinf.* **2024**, *134*, 104159. [CrossRef]
54. Di Tommaso, S.; Wang, S.; Vajipey, V.; Gorelick, N.; Strey, R.; Lobell, D.B. Annual Field-Scale Maps of Tall and Short Crops at the Global Scale Using GEDI and Sentinel-2. *Remote Sens.* **2023**, *15*, 4123. [CrossRef]
55. Zhang, Z.; Wang, S.; Zhang, W. Dilated Spectral–Spatial Gaussian Transformer Net for Hyperspectral Image Classification. *Remote Sens.* **2024**, *16*, 287. [CrossRef]
56. Yue, J.; Tian, Q. Estimating Fractional Cover of Crop, Crop Residue, and Soil in Cropland Using Broadband Remote Sensing Data and Machine Learning. *Int. J. Appl. Earth Obs. Geoinf.* **2020**, *89*, 102089. [CrossRef]
57. Alotaibi, Y.; Rajendran, B.; Rani, K.G.; Rajendran, S. Dipper Throated Optimization with Deep Convolutional Neural Network-Based Crop Classification for Remote Sensing Image Analysis. *PeerJ Comput. Sci.* **2024**, *10*, e1828. [CrossRef]
58. Aljanabi, F.; Dedeoglu, M.; Şeker, C. Environmental Monitoring of Land Use/ Land Cover by Integrating Remote Sensing and Machine Learning Algorithms. *J. Eng. Sustain. Dev.* **2024**, *28*, 455–466. [CrossRef]
59. Sachit, M.; Khazael, S.; Atiyah, H. Evaluating the Performance of Supervised Classification Algorithms in Classifying SENTINEL-2A Images on Land Cover and Land Uses of a Part of Baghdad, Iraq. *Iraqi J. Sci.* **2024**, *65*, 7349–7363. [CrossRef]
60. Atef, I.; Ahmed, W.; Abdel-Maguid, R.H. Modelling of Land Use Land Cover Changes Using Machine Learning and GIS Techniques: A Case Study in El-Fayoum Governorate, Egypt. *Environ. Monit. Assess.* **2023**, *195*, 637. [CrossRef]
61. de Souza, F.E.S.; Rodrigues, J.I.d.J. Evaluation of Machine Learning Algorithms in the Classification of Multispectral Images from the Sentinel-2A/2B Orbital Sensor for Mapping the Environmental Dynamics of Ria Formosa (Algarve, Portugal). *ISPRS Int. J. Geo-Inf.* **2023**, *12*, 361. [CrossRef]
62. Mhanna, S.; Halloran, L.J.S.; Zwahlen, F.; Asaad, A.H.; Brunner, P. Using Machine Learning and Remote Sensing to Track Land Use/Land Cover Changes Due to Armed Conflict. *Sci. Total Environ.* **2023**, *898*, 165600. [CrossRef]
63. Lukas, P.; Melesse, A.M.; Kenea, T.T. Prediction of Future Land Use/Land Cover Changes Using a Coupled CA-ANN Model in the Upper Omo–Gibe River Basin, Ethiopia. *Remote Sens.* **2023**, *15*, 1148. [CrossRef]
64. Kutz, K.; Cook, Z.; Linderman, M. Object Based Classification of a Riparian Environment Using Ultra-High Resolution Imagery, Hierarchical Landcover Structures, and Image Texture. *Sci. Rep.* **2022**, *12*, 11291. [CrossRef]

65. Ali, U.; Esau, T.J.; Farooque, A.A.; Zaman, Q.U.; Abbas, F.; Bilodeau, M.F. Limiting the Collection of Ground Truth Data for Land Use and Land Cover Maps with Machine Learning Algorithms. *ISPRS Int. J. Geo-Inf.* **2022**, *11*, 333. [CrossRef]
66. Lin, M.-H.; Lin, Y.-T.; Tsai, M.-L.; Chen, Y.-Y.; Chen, Y.-C.; Wang, H.-C.; Wang, C.-K. Mapping Land-Use and Land-Cover Changes through the Integration of Satellite and Airborne Remote Sensing Data. *Environ. Monit. Assess.* **2024**, *196*, 246. [CrossRef]
67. Ojwang, G.O.; Ogutu, J.O.; Said, M.Y.; Ojwala, M.A.; Kifugo, S.C.; Verones, F.; Graae, B.J.; Buitenwerf, R.; Olff, H. An Integrated Hierarchical Classification and Machine Learning Approach for Mapping Land Use and Land Cover in Complex Social-Ecological Systems. *Front. Remote Sens.* **2024**, *4*, 1188635. [CrossRef]
68. Barboza, E.; Salazar, W.; Gálvez-Paucar, D.; Valqui Valqui, L.; Valqui Valqui, L.; Zagaceta, L.; Malca, J.; Vásquez, H.; Arbizu, C. Cloud Computing Application for the Analysis of Land Use and Land Cover Changes in Dry Forests of Peru. *Int. J. Environ. Impacts* **2024**, *7*, 505–514. [CrossRef]
69. Ha, T.V.; Tuohy, M.; Irwin, M.; Tuan, P.V. Monitoring and Mapping Rural Urbanization and Land Use Changes Using Landsat Data in the Northeast Subtropical Region of Vietnam. *Egypt. J. Remote Sens. Space Sci.* **2020**, *23*, 11–19. [CrossRef]
70. Dantas, C.F.; Gaetano, R.; Paris, C.; Ienco, D. Reuse Out-of-Year Data to Enhance Land Cover Mapping via Feature Disentanglement and Contrastive Learning. *IEEE J. Sel. Top. Appl. Earth Obs. Remote Sens.* **2025**, *18*, 1681–1694. [CrossRef]
71. Rousset, G.; Despinoy, M.; Schindler, K.; Mangeas, M. Assessment of Deep Learning Techniques for Land Use Land Cover Classification in Southern New Caledonia. *Remote Sens.* **2021**, *13*, 2257. [CrossRef]
72. Ouchra, H.; Belangour, A.; Erraissi, A. Comparison of Machine Learning Methods for Satellite Image Classification: A Case Study of Casablanca Using Landsat Imagery and Google Earth Engine. *J. Environ. Earth Sci.* **2023**, *5*, 118–134. [CrossRef]
73. Rajesh, S.; Nisia, T.G.; Arivazhagan, S.; Abisekaraj, R. Land Cover/Land Use Mapping of LISS IV Imagery Using Object-Based Convolutional Neural Network with Deep Features. *J. Indian Soc. Remote Sens.* **2020**, *48*, 145–154. [CrossRef]
74. Wang, J.; Feng, Y.; Tong, X.; Lei, Z.; Xi, M.; Zhou, Y.; Tang, P. Classification Evaluation and Improvement of Airborne PolSAR Images for Land Use Mapping Using Deep Learning. *Geocarto Int.* **2024**, *39*, 2401937. [CrossRef]
75. Fayaz, M.; Nam, J.; Dang, L.M.; Song, H.-K.; Moon, H. Land-Cover Classification Using Deep Learning with High-Resolution Remote-Sensing Imagery. *Appl. Sci.* **2024**, *14*, 1844. [CrossRef]
76. Hu, K.; Zhang, E.; Dai, X.; Xia, M.; Zhou, F.; Weng, L.; Lin, H. MCSGNet: A Encoder–Decoder Architecture Network for Land Cover Classification. *Remote Sens.* **2023**, *15*, 2810. [CrossRef]
77. Sahu, M.; Dash, R. Cognitive Land Cover Mapping: A Three-Layer Deep Learning Architecture for Remote Sensing Data Classification. *Environ. Chall.* **2024**, *15*, 100876. [CrossRef]
78. Li, X.; Zhao, H.; Wu, D.; Liu, Q.; Tang, R.; Li, L.; Xu, Z.; Lyu, X. SLMFNet: Enhancing Land Cover Classification of Remote Sensing Images through Selective Attentions and Multi-Level Feature Fusion. *PLoS ONE* **2024**, *19*, e0301134. [CrossRef]
79. Xiao, J.; Cheng, T.; Chen, D.; Chen, H.; Li, N.; Lu, Y.; Cheng, L. Robust Land Cover Classification with Local–Global Information Decoupling to Address Remote Sensing Anomalous Data. *IEEE J. Sel. Top. Appl. Earth Obs. Remote Sens.* **2024**, *17*, 5774–5789. [CrossRef]
80. Hao, M.; Dong, X.; Jiang, D.; Yu, X.; Ding, F.; Zhuo, J. Land-Use Classification Based on High-Resolution Remote Sensing Imagery and Deep Learning Models. *PLoS ONE* **2024**, *19*, e0300473. [CrossRef] [PubMed]
81. Masolele, R.; De Sy, V.; Marcos, D.; Verbesselt, J.; Gieseke, F.; Mulatu, K.; Moges, Y.; Sebrala Ahmed, H.; Martius, C.; Herold, M. Using High-Resolution Imagery and Deep Learning to Classify Land-Use Following Deforestation: A Case Study in Ethiopia. *GIScience Remote Sens.* **2022**, *59*, 1446–1472. [CrossRef]
82. Wang, S.; Zou, X.; Li, K.; Xing, J.; Cao, T.; Tao, P. Towards Robust Pansharpening: A Large-Scale High-Resolution Multi-Scene Dataset and Novel Approach. *Remote Sens.* **2024**, *16*, 2899. [CrossRef]
83. Nigar, A.; Li, Y.; Jat Baloch, M.Y.; Alrefaei, A.F.; Almutairi, M.H. Comparison of Machine and Deep Learning Algorithms Using Google Earth Engine and Python for Land Classifications. *Front. Environ. Sci.* **2024**, *12*, 1378443. [CrossRef]
84. Ali, K.; Johnson, B.A. Land-Use and Land-Cover Classification in Semi-Arid Areas from Medium-Resolution Remote-Sensing Imagery: A Deep Learning Approach. *Sensors* **2022**, *22*, 8750. [CrossRef]
85. Aljebreen, M.; Mengash, H.A.; Alamgeer, M.; Alotaibi, S.S.; Salama, A.S.; Hamza, M.A. Land Use and Land Cover Classification Using River Formation Dynamics Algorithm with Deep Learning on Remote Sensing Images. *IEEE Access* **2024**, *12*, 11147–11156. [CrossRef]
86. Zaabar, N.; Niculescu, S.; Kamel, M.M. Application of Convolutional Neural Networks with Object-Based Image Analysis for Land Cover and Land Use Mapping in Coastal Areas: A Case Study in Ain Témouchent, Algeria. *IEEE J. Sel. Top. Appl. Earth Obs. Remote Sens.* **2022**, *15*, 5177–5189. [CrossRef]
87. Mahmoud, R.; Hassanin, M.; Al Feel, H.; Badry, R.M. Machine Learning-Based Land Use and Land Cover Mapping Using Multi-Spectral Satellite Imagery: A Case Study in Egypt. *Sustainability* **2023**, *15*, 9467. [CrossRef]
88. Lemenkova, P. Support Vector Machine Algorithm for Mapping Land Cover Dynamics in Senegal, West Africa, Using Earth Observation Data. *Earth* **2024**, *5*, 420–462. [CrossRef]

89. Zhang, L.; Xu, T.; Zeng, C.; Hao, Q.; Chen, Z.; Liang, X. Semantic-Aware Contrastive Adaptation Bridges Domain Discrepancy for Unsupervised Remote Sensing. *IEEE Access* **2024**, *12*, 140734–140747. [CrossRef]
90. Mienye, I.D.; Swart, T.G.; Obaido, G. Recurrent Neural Networks: A Comprehensive Review of Architectures, Variants, and Applications. *Information* **2024**, *15*, 517. [CrossRef]
91. Ouchra, H.; Belangour, A.; Erraissi, A. Comparing Unsupervised Land Use Classification of Landsat 8 OLI Data Using K-Means and LVQ Algorithms in Google Earth Engine: A Case Study of Casablanca. *Int. J. Geoinform.* **2023**, *19*, 83–92. [CrossRef]
92. Diack, I.; Diene, S.M.; Louise, L.; Aziz, D.A.; Benjamin, H.; Olivier, R.; Philippe, L.; Alain, A.; Idrissa, S.; Moussa, D. Combining UAV and Sentinel-2 Imagery for Estimating Millet FCover in a Heterogeneous Agricultural Landscape of Senegal. *IEEE J. Sel. Top. Appl. Earth Obs. Remote Sens.* **2024**, *17*, 7305–7322. [CrossRef]
93. Kobe, M.; Elias, M.; Merbach, I.; Schädler, M.; Bumberger, J.; Pause, M.; Mollenhauer, H. Automated Workflow for High-Resolution 4D Vegetation Monitoring Using Stereo Vision. *Remote Sens.* **2024**, *16*, 541. [CrossRef]
94. Kalecinski, N.I.; Skakun, S.; Torbick, N.; Huang, X.; Franch, B.; Roger, J.-C.; Vermote, E. Crop Yield Estimation at Different Growing Stages Using a Synergy of SAR and Optical Remote Sensing Data. *Sci. Remote Sens.* **2024**, *10*, 100153. [CrossRef]
95. Sabo, F.; Meroni, M.; Waldner, F.; Rembold, F. Is Deeper Always Better? Evaluating Deep Learning Models for Yield Forecasting with Small Data. *Environ. Monit. Assess.* **2023**, *195*, 1153. [CrossRef]
96. Lv, Z.; Meng, R.; Man, J.; Zeng, L.; Wang, M.; Xu, B.; Gao, R.; Sun, R.; Zhao, F. Modeling of Winter Wheat fAPAR by Integrating Unmanned Aircraft Vehicle-Based Optical, Structural and Thermal Measurement. *Int. J. Appl. Earth Obs. Geoinf.* **2021**, *102*, 102407. [CrossRef]
97. Wu, Z.; Dong, Z.; Yang, K.; Liu, Q.; Wang, W. Floodwater Extraction from UAV Orthoimagery Based on a Transformer Model. *Remote Sens.* **2024**, *16*, 4052. [CrossRef]
98. Pech-May, F.; Aquino-Santos, R.; Delgadillo-Partida, J. Sentinel-1 SAR Images and Deep Learning for Water Body Mapping. *Remote Sens.* **2023**, *15*, 3009. [CrossRef]
99. Xiang, J.; Zang, Z.; Tang, X.; Zhang, M.; Cao, P.; Tang, S.; Wang, X. Rapid Forest Change Detection Using Unmanned Aerial Vehicles and Artificial Intelligence. *Forests* **2024**, *15*, 1676. [CrossRef]
100. Ecke, S.; Stehr, F.; Frey, J.; Tiede, D.; Dempewolf, J.; Klemmt, H.-J.; Endres, E.; Seifert, T. Towards Operational UAV-Based Forest Health Monitoring: Species Identification and Crown Condition Assessment by Means of Deep Learning. *Comput. Electron. Agric.* **2024**, *219*, 108785. [CrossRef]
101. Perbet, P.; Guindon, L.; Côté, J.-F.; Béland, M. Evaluating Deep Learning Methods Applied to Landsat Time Series Subsequences to Detect and Classify Boreal Forest Disturbances Events: The Challenge of Partial and Progressive Disturbances. *Remote Sens. Environ.* **2024**, *306*, 114107. [CrossRef]
102. Lucas, M.; Pukrop, M.; Beckschäfer, P.; Waske, B. Individual tree detection and crown delineation in the Harz National Park from 2009 to 2022 using mask R–CNN and aerial imagery. *ISPRS Open J. Photogramm. Remote Sens.* **2024**, *13*, 100071. [CrossRef]
103. Wang, H.; Hu, C.; Zhang, R.; Qian, W. SegForest: A Segmentation Model for Remote Sensing Images. *Forests* **2023**, *14*, 1509. [CrossRef]
104. Slagter, B.; Reiche, J.; Marcos, D.; Mullissa, A.; Lossou, E.; Peña-Claros, M.; Herold, M. Monitoring Direct Drivers of Small-Scale Tropical Forest Disturbance in near Real-Time with Sentinel-1 and -2 Data. *Remote Sens. Environ.* **2023**, *295*, 113655. [CrossRef]
105. Retallack, A.; Finlayson, G.; Ostendorf, B.; Lewis, M. Using Deep Learning to Detect an Indicator Arid Shrub in Ultra-High-Resolution UAV Imagery. *Ecol. Indic.* **2022**, *145*, 109698. [CrossRef]
106. Guo, Y.; Long, T.; Jiao, W.; Zhang, X.; He, G.; Wang, W.; Peng, Y.; Xiao, H. Siamese Detail Difference and Self-Inverse Network for Forest Cover Change Extraction Based on Landsat 8 OLI Satellite Images. *Remote Sens.* **2022**, *14*, 627. [CrossRef]
107. Mäyrä, J.; Keski-Saari, S.; Kivinen, S.; Tanhuanpää, T.; Hurskainen, P.; Kullberg, P.; Poikolainen, L.; Viinikka, A.; Tuominen, S.; Kumpula, T.; et al. Tree Species Classification from Airborne Hyperspectral and LiDAR Data Using 3D Convolutional Neural Networks. *Remote Sens. Environ.* **2021**, *256*, 112322. [CrossRef]
108. He, S.; Du, H.; Zhou, G.; Li, X.; Mao, F.; Zhu, D.; Xu, Y.; Zhang, M.; Huang, Z.; Liu, H.; et al. Intelligent Mapping of Urban Forests from High-Resolution Remotely Sensed Imagery Using Object-Based U-Net-DenseNet-Coupled Network. *Remote Sens.* **2020**, *12*, 3928. [CrossRef]
109. Li, Y.; Min, S.; Song, B.; Yang, H.; Wang, B.; Wu, Y. Multisource High-Resolution Remote Sensing Image Vegetation Extraction with Comprehensive Multifeature Perception. *Remote Sens.* **2024**, *16*, 712. [CrossRef]
110. Zheng, J.; Chen, D.; Zhang, H.; Zhang, G.; Zhen, Q.; Liu, S.; Zhang, N.; Zhao, H. Remote Sensing Identification of *Picea schrenkiana* Var. *tianschanica* in GF-1 Images Based on a Multiple Mixed Attention U-Net Model. *Forests* **2024**, *15*, 2039. [CrossRef]
111. Nguyen, T.-A.; Rußwurm, M.; Lenczner, G.; Tuia, D. Multi-Temporal Forest Monitoring in the Swiss Alps with Knowledge-Guided Deep Learning. *Remote Sens. Environ.* **2024**, *305*, 114109. [CrossRef]
112. Roßberg, T.; Schmitt, M. A Globally Applicable Method for NDVI Estimation from Sentinel-1 SAR Backscatter Using a Deep Neural Network and the SEN12TP Dataset. *PFG J. Photogramm. Remote Sens. Geoinf. Sci.* **2023**, *91*, 171–188. [CrossRef]

113. Nguyen-Trong, K.; Tran-Xuan, H. Coastal Forest Cover Change Detection Using Satellite Images and Convolutional Neural Networks in Vietnam. *IAES Int. J. Artif. Intell. (IJ-AI)* **2022**, *11*, 930–938. [CrossRef]
114. Torres, D.L.; Turnes, J.N.; Soto Vega, P.J.; Feitosa, R.Q.; Silva, D.E.; Marcato Junior, J.; Almeida, C. Deforestation Detection with Fully Convolutional Networks in the Amazon Forest from Landsat-8 and Sentinel-2 Images. *Remote Sens.* **2021**, *13*, 5084. [CrossRef]
115. de Andrade, R.B.; Mota, G.L.A.; da Costa, G.A.O.P. Deforestation Detection in the Amazon Using DeepLabv3+ Semantic Segmentation Model Variants. *Remote Sens.* **2022**, *14*, 4694. [CrossRef]
116. Rodrigues, J.; Dias, M.A.; Negri, R.; Hussain, S.M.; Casaca, W. A Robust Dual-Mode Machine Learning Framework for Classifying Deforestation Patterns in Amazon Native Lands. *Land* **2024**, *13*, 1427. [CrossRef]
117. Wang, S.; Cui, D.; Wang, L.; Peng, J. Applying Deep-Learning Enhanced Fusion Methods for Improved NDVI Reconstruction and Long-Term Vegetation Cover Study: A Case of the Danjiang River Basin. *Ecol. Indic.* **2023**, *155*, 111088. [CrossRef]
118. Sklyar, E.; Rees, G. Assessing Changes in Boreal Vegetation of Kola Peninsula via Large-Scale Land Cover Classification between 1985 and 2021. *Remote Sens.* **2022**, *14*, 5616. [CrossRef]
119. Marsetič, A.; Kanjir, U. Forecasting Vegetation Behavior Based on PlanetScope Time Series Data Using RNN-Based Models. *IEEE J. Sel. Top. Appl. Earth Obs. Remote Sens.* **2024**, *17*, 5015–5025. [CrossRef]
120. Roßberg, T.; Schmitt, M. Dense NDVI Time Series by Fusion of Optical and SAR-Derived Data. *IEEE J. Sel. Top. Appl. Earth Obs. Remote Sens.* **2024**, *17*, 7748–7758. [CrossRef]
121. Wahelo, T.T.; Mengistu, D.A.; Merawi, T.M. Spatiotemporal Trends and Drivers of Forest Cover Change in Metekel Zone Forest Areas, Northwest Ethiopia. *Environ. Monit. Assess.* **2024**, *196*, 1170. [CrossRef] [PubMed]
122. Isoaho, A.; Elo, M.; Marttila, H.; Rana, P.; Lensu, A.; Räsänen, A. Monitoring Changes in Boreal Peatland Vegetation after Restoration with Optical Satellite Imagery. *Sci. Total Environ.* **2024**, *957*, 177697. [CrossRef]
123. Prodromou, M.; Theocharidis, C.; Gitas, I.Z.; Eliades, F.; Themistocleous, K.; Papasavvas, K.; Dimitrakopoulos, C.; Danezis, C.; Hadjimitsis, D. Forest Habitat Mapping in Natura2000 Regions in Cyprus Using Sentinel-1, Sentinel-2 and Topographical Features. *Remote Sens.* **2024**, *16*, 1373. [CrossRef]
124. Mansouri, J.; Jafari, M.; Taheri Dehkordi, A. Continuous Mapping of Forest Canopy Height Using ICESat-2 Data and a Weighted Kernel Integration of Multi-Temporal Multi-Source Remote Sensing Data Aided by Google Earth Engine. *Environ. Sci. Pollut. Res.* **2024**, *31*, 49757–49779. [CrossRef]
125. Engda, E.M.; Bojer, A.K.; Mekonnen, Z.A.; Tegegn, W.W. Assessment of Forest Cover Dynamics in Dedo District, Oromia Region, Ethiopia, Using Machine Learning Algorithm. *J. Sens.* **2024**, *2024*, 4020990. [CrossRef]
126. Ziegler, A.; Heisig, J.; Ludwig, M.; Reudenbach, C.; Meyer, H.; Nauss, T. Using GEDI as Training Data for an Ongoing Mapping of Landscape-Scale Dynamics of the Plant Area Index. *Environ. Res. Lett.* **2023**, *18*, 075003. [CrossRef]
127. Mouret, F.; Morin, D.; Martin, H.; Planells, M.; Vincent-Barbaroux, C. Toward an Operational Monitoring of Oak Dieback with Multispectral Satellite Time Series: A Case Study in Centre-Val De Loire Region of France. *IEEE J. Sel. Top. Appl. Earth Obs. Remote Sens.* **2024**, *17*, 643–659. [CrossRef]
128. Jiang, H.; Chen, A.; Wu, Y.; Zhang, C.; Chi, Z.; Li, M.; Wang, X. Vegetation Monitoring for Mountainous Regions Using a New Integrated Topographic Correction (ITC) of the SCS + C Correction and the Shadow-Eliminated Vegetation Index. *Remote Sens.* **2022**, *14*, 3073. [CrossRef]
129. Liu, X.; Fatoyinbo, T.E.; Thomas, N.M.; Guan, W.W.; Zhan, Y.; Mondal, P.; Lagomasino, D.; Simard, M.; Trettin, C.C.; Deo, R.; et al. Large-Scale High-Resolution Coastal Mangrove Forests Mapping Across West Africa with Machine Learning Ensemble and Satellite Big Data. *Front. Earth Sci.* **2021**, *8*, 560933. [CrossRef]
130. Guisao-Betancur, A.; Gómez Déniz, L.; Marulanda-Tobón, A. Forest/Nonforest Segmentation Using Sentinel-1 and -2 Data Fusion in the Bajo Cauca Subregion in Colombia. *Remote Sens.* **2024**, *16*, 5. [CrossRef]
131. Zheng, X.; Jia, J.; Chen, J.; Guo, S.; Sun, L.; Zhou, C.; Wang, Y. Hyperspectral Image Classification with Imbalanced Data Based on Semi-Supervised Learning. *Appl. Sci.* **2022**, *12*, 3943. [CrossRef]
132. Rose, M.B.; Mills, M.; Franklin, J.; Larios, L. Mapping Fractional Vegetation Cover Using Unoccupied Aerial Vehicle Imagery to Guide Conservation of a Rare Riparian Shrub Ecosystem in Southern California. *Remote Sens.* **2023**, *15*, 5113. [CrossRef]
133. John, E.; Bunting, P.; Hardy, A.; Silayo, D.S.; Masunga, E. A Forest Monitoring System for Tanzania. *Remote Sens.* **2021**, *13*, 3081. [CrossRef]
134. Holloway-Brown, J.; Helmstedt, K.J.; Mengersen, K.L. Stochastic Spatial Random Forest (SS-RF) for Interpolating Probabilities of Missing Land Cover Data. *J. Big Data* **2020**, *7*, 55. [CrossRef]
135. Liu, Y.; Zhao, Q.; Wang, X.; Sheng, Y.; Tian, W.; Ren, Y. A Tree Species Classification Model Based on Improved YOLOv7 for Shelterbelts. *Front. Plant Sci.* **2024**, *14*, 1265025. [CrossRef]
136. Wang, Z.; Mo, Z.; Liang, Y.; Yang, Z.; Liao, X.; Wang, Z.; Zhang, Q. A Web-Based Prototype System for Deforestation Detection on High-Resolution Remote Sensing Imagery with Deep Learning. *IEEE J. Sel. Top. Appl. Earth Obs. Remote Sens.* **2024**, *17*, 18593–18612. [CrossRef]

137. Alshehri, M.; Ouadou, A.; Scott, G.J. Deep Transformer-Based Network Deforestation Detection in the Brazilian Amazon Using Sentinel-2 Imagery. *IEEE Geosci. Remote Sens. Lett.* **2024**, *21*, 3355104. [CrossRef]
138. Turkulainen, E.; Honkavaara, E.; Näsi, R.; Oliveira, R.A.; Hakala, T.; Junttila, S.; Karila, K.; Koivumäki, N.; Pelto-Arvo, M.; Tuviala, J.; et al. Comparison of Deep Neural Networks in the Classification of Bark Beetle-Induced Spruce Damage Using UAS Images. *Remote Sens.* **2023**, *15*, 4928. [CrossRef]
139. Kislov, D.E.; Korznikov, K.A.; Altman, J.; Vozmishcheva, A.S.; Krestov, P.V. Extending Deep Learning Approaches for Forest Disturbance Segmentation on Very High-Resolution Satellite Images. *Remote Sens. Ecol. Conserv.* **2021**, *7*, 355–368. [CrossRef]
140. Junttila, S.; Näsi, R.; Koivumäki, N.; Imangholiloo, M.; Saarinen, N.; Raisio, J.; Holopainen, M.; Hyyppä, H.; Hyyppä, J.; Lyytikäinen-Saarenmaa, P.; et al. Multispectral Imagery Provides Benefits for Mapping Spruce Tree Decline Due to Bark Beetle Infestation When Acquired Late in the Season. *Remote Sens.* **2022**, *14*, 909. [CrossRef]
141. Iordache, M.-D.; Mantas, V.; Baltazar, E.; Pauly, K.; Lewyckyj, N. A Machine Learning Approach to Detecting Pine Wilt Disease Using Airborne Spectral Imagery. *Remote Sens.* **2020**, *12*, 2280. [CrossRef]
142. Et-Brasil/geeSEBAL 2025. Available online: https://github.com/et-brasil/geeSEBAL (accessed on 9 July 2025).
143. Liu, Q.; Wu, Z.; Cui, N.; Zheng, S.; Zhu, S.; Jiang, S.; Wang, Z.; Gong, D.; Wang, Y.; Zhao, L. Soil Moisture Content Estimation of Drip-Irrigated Citrus Orchard Based on UAV Images and Machine Learning Algorithm in Southwest China. *Agric. Water Manag.* **2024**, *303*, 109069. [CrossRef]
144. dos Santos, E.P.; Moreira, M.C.; Fernandes-Filho, E.I.; Demattê, J.A.M.; Dionizio, E.A.; Silva, D.D.d.; Cruz, R.R.P.; Moura-Bueno, J.M.; dos Santos, U.J.; Costa, M.H. Sentinel-1 Imagery Used for Estimation of Soil Organic Carbon by Dual-Polarization SAR Vegetation Indices. *Remote Sens.* **2023**, *15*, 5464. [CrossRef]
145. Tayebi, M.; Rosas, J.T.F.; Mendes, W.d.S.; Poppiel, R.R.; Ostovari, Y.; Ruiz, L.F.C.; dos Santos, N.V.; Cerri, C.E.P.; Silva, S.H.G.; Curi, N.; et al. Drivers of Organic Carbon Stocks in Different LULC History and along Soil Depth for a 30 Years Image Time Series. *Remote Sens.* **2021**, *13*, 2223. [CrossRef]
146. Jia, X.; Cao, Y.; O'Connor, D.; Zhu, J.; Tsang, D.C.W.; Zou, B.; Hou, D. Mapping Soil Pollution by Using Drone Image Recognition and Machine Learning at an Arsenic-Contaminated Agricultural Field. *Environ. Pollut.* **2021**, *270*, 116281. [CrossRef]
147. Boonupara, T.; Udomkun, P.; Gibson-Poole, S.; Hamilton, A.; Kaewlom, P. Assessing Plant Pigmentation Impacts: A Novel Approach Integrating UAV and Multispectral Data to Analyze Atrazine Metabolite Effects from Soil Contamination. *Smart Agric. Technol.* **2024**, *9*, 100570. [CrossRef]
148. S1 Mission. Available online: https://sentiwiki.copernicus.eu/web/s1-mission (accessed on 9 July 2025).
149. S2 Mission. Available online: https://sentiwiki.copernicus.eu/web/s2-mission (accessed on 9 July 2025).
150. Landsat-8—Earth Online. Available online: https://earth.esa.int/eogateway/missions/landsat-8 (accessed on 9 July 2025).
151. Landsat 4 | Landsat Science. Available online: https://landsat.gsfc.nasa.gov/satellites/landsat-4/ (accessed on 9 July 2025).
152. GF-1 (Gaofen-1)—eoPortal. Available online: https://www.eoportal.org/satellite-missions/gaofen-1 (accessed on 9 July 2025).
153. GF-2 (Gaofen-2)—eoPortal. Available online: https://www.eoportal.org/satellite-missions/gaofen-2 (accessed on 9 July 2025).
154. NASA—NSSDCA—Spacecraft—Details. Available online: https://www.nasa.gov/ (accessed on 9 July 2025).
155. PlanetScope—Earth Online. Available online: https://earth.esa.int/eogateway/missions/planetscope (accessed on 9 July 2025).
156. WorldView-2—Earth Online. Available online: https://earth.esa.int/eogateway/missions/worldview-2 (accessed on 9 July 2025).
157. WorldView-3—Earth Online. Available online: https://earth.esa.int/eogateway/missions/worldview-3 (accessed on 9 July 2025).
158. WorldView-4—Earth Online. Available online: https://earth.esa.int/eogateway/missions/worldview-4 (accessed on 9 July 2025).
159. SPOT—Earth Online. Available online: https://earth.esa.int/eogateway/missions/spot (accessed on 9 July 2025).
160. What Is UAVSAR?—UAVSAR. Available online: https://uavsar.jpl.nasa.gov/education/what-is-uavsar.html (accessed on 9 July 2025).
161. Earth Science Data Systems, N. GEDI Lidar | NASA Earthdata. Available online: https://www.earthdata.nasa.gov/data/instruments/gedi-lidar (accessed on 9 July 2025).
162. DigitalGlobe—30 Cm. Available online: https://microsites.maxar.com/30cm/ (accessed on 9 July 2025).
163. Zenmuse P1—UAV Load Gimbal Camera—DJI Enterprise. Available online: https://enterprise.dji.com/cn/zenmuse-p1 (accessed on 9 July 2025).
164. Yang, W.; Liu, T.; Jiang, P.; Qi, A.; Deng, L.; Liu, Z.; He, Y. A Forest Wildlife Detection Algorithm Based on Improved YOLOv5s. *Animals* **2023**, *13*, 3134. [CrossRef] [PubMed]

165. Ma, Z.; Dong, Y.; Xia, Y.; Xu, D.; Xu, F.; Chen, F. Wildlife Real-Time Detection in Complex Forest Scenes Based on YOLOv5s Deep Learning Network. *Remote Sens.* **2024**, *16*, 1350. [CrossRef]
166. Page, M.J.; McKenzie, J.E.; Bossuyt, P.M.; Boutron, I.; Hoffmann, T.C.; Mulrow, C.D.; Shamseer, L.; Tetzlaff, J.M.; Akl, E.A.; Brennan, S.E.; et al. The PRISMA 2020 statement: An updated guideline for reporting systematic reviews. *BMJ* **2021**, *372*, n71. [CrossRef] [PubMed]

Disclaimer/Publisher's Note: The statements, opinions and data contained in all publications are solely those of the individual author(s) and contributor(s) and not of MDPI and/or the editor(s). MDPI and/or the editor(s) disclaim responsibility for any injury to people or property resulting from any ideas, methods, instructions or products referred to in the content.

sustainability

MDPI

Article

From Benchmark Accuracy to Field Performance: Hybrid Deep Learning-Based Plant Disease Classification with IoT-Enabled Environmental Monitoring

Jalampelli Thirupathi [1,2], Nandagopal Malarvizhi [1] and Potula Sree Brahmanandam [3,*]

[1] Department of Computer Science and Engineering, Vel Tech Rangarajan Dr. Sagunthala R&D Institute of Science and Technology, Chennai 600602, India
[2] Department of Computer Science and Engineering, Institute of Aeronautical Engineering, Hyderabad 500043, India
[3] Department of Physics, Shri Vishnu Engineering College for Women (A), Bhimavaram 534202, India
* Correspondence: dranandpotula@svecw.edu.in

Abstract

Accurate detection of plant leaf diseases is essential for enhancing crop productivity and supporting global food security. In addition to disease classification, understanding how environmental and soil conditions affect model performance is important for developing robust real-world agricultural monitoring systems. Although deep learning (DL) models achieve high accuracy on benchmark datasets, their performance in real-world settings is often limited by variations in illumination, background complexity, and environmental conditions. This study proposes a smart DL framework for detecting and classifying multiple leaf diseases in tomato, potato, and pepper plants. The framework combines U^2-Net-based leaf segmentation with a Convolutional Neural Network–Bidirectional Gated Recurrent Unit (CNN–Bi-GRU) architecture. MobileNetV2 is employed as the feature extraction backbone to capture spatial characteristics, while Bi-GRU layers model sequential feature dependencies, forming a spatio-temporal network whose architectural design prioritizes parameter efficiency through depthwise separable convolutions and reduced gating complexity. The model was trained and validated using the PlantVillage benchmark dataset and achieved a classification accuracy of 99.8% with a macro-averaged F1-score of 94%, outperforming several state-of-the-art architectures. To assess robustness under real-world conditions, the trained model was further tested on leaf images collected from open-field environments near Eluru, South India. The field evaluation revealed a reduction in classification accuracy to 61.97%, indicating the impact of domain shift and environmental variability. To investigate potential contributing factors, soil parameters, including pH, temperature, moisture, and NPK levels, were monitored using an IoT-based Arduino sensing system over ten consecutive days. Rather than serving as direct inputs to the disease classification model, these environmental measurements were analyzed to assess their potential influence on disease symptom expression and the observed reduction in model performance under field conditions. The results suggest that environmental conditions may influence disease symptom expression and model transferability. This study highlights the importance of integrating DL-based disease recognition with environmental monitoring for reliable field-level agricultural applications. Nevertheless, computational complexity metrics, including inference latency and memory footprint, were not evaluated in the present work and are identified as a priority for future edge deployment studies.

Keywords: smart crop monitoring; H-neural network; PlantVillage dataset; field-acquired dataset

1. Introduction

Plant diseases pose a critical challenge to global food security, as early symptoms often manifest as subtle, spatially localized lesions that rapidly intensify. Delays or inaccuracies in diagnosis amplify yield losses, drive pesticide misuse, and create downstream economic risks. Conventional visual inspection remains constrained by human subjectivity, symptom similarity across pathogens, and the sheer scale of monitoring required in commercial cultivation. Consequently, there is an urgent need for automated, accurate, and scalable disease surveillance systems.

Recent advances in deep learning methods have significantly transformed plant disease detection, identification, and classification [1–3]. Convolutional neural networks (CNNs) have been widely adopted for automated classification because of their ability to learn discriminative features directly from raw images without reliance on handcrafted descriptors [4–6]. These approaches mark a paradigm shift toward precision agriculture, where real-time, fine-grained diagnosis enables timely and sustainable interventions. However, single-image CNN classifiers often face limitations in real-world deployments due to small or occluded targets, illumination variations, and an inability to model disease progression. While CNNs are effective for spatial encoding, the inherently dynamic nature of plant disease requires methods that can capture sequential dependencies and contextual transitions [7].

Hybrid architectures address these limitations by combining CNN-based spatial feature extraction with recurrent layers such as Long Short-Term Memory (LSTM) networks or Gated Recurrent Units, which can model sequential relationships among extracted feature representations [8,9]. Bidirectional GRUs further enhance feature learning by processing feature sequences in both forward and backward directions, enabling the network to capture complementary contextual information [10]. When integrated with CNN-based feature extractors, Bi-GRU layers facilitate the learning of both fine-grained lesion characteristics and higher-level feature dependencies, thereby improving disease classification performance in complex agricultural imaging environments.

Hybrid networks that combine convolutional feature extraction with recurrent sequence modeling have increasingly incorporated segmentation and attention modules to improve performance on noisy, real-world data across various domains. For example, previous work proposed an Automatic Segmentation and Hyperparameter Optimization Artificial Rabbits Algorithm (AS-HPOARA) to enhance plant leaf disease classification [11]. A modified U-Net performs segmentation to isolate disease-specific regions, enabling richer feature representation. Classification is then carried out through an Artificial Rabbits Algorithm with hyperparameter optimization, which increases training efficiency, reduces statistical bias, and minimizes model complexity. By combining segmentation, augmentation, and optimized classification, this approach achieves higher accuracy and robustness in disease detection.

While hybrid pipelines improve accuracy on disease progression modeling tasks, they also raise training/inference latency, memory footprint, and engineering complexity (e.g., error propagation across stages, multi-branch losses, and sequence packing). The combination of multiple architectural components creates a highly expressive but computationally expensive network. Such models may be difficult to train and can be unsuitable for real-time applications [12,13]. Particularly, attention modules (e.g., channel and spatial attention mechanisms) have been widely adopted to improve feature representation by emphasizing informative regions and suppressing irrelevant information. However, these modules introduce additional architectural complexity, which may increase computational

https://doi.org/10.3390/su18136867

requirements depending on the model design and deployment environment [12,13]. On the other hand, U^2-Net is designed for explicit pixel-level salient object detection and produces high-resolution masks that preserve both global structure and fine boundary details. When applied as a preprocessing step in plant-disease pipelines, U^2-Net removes background clutter and isolates symptomatic leaf regions, which yields cleaner inputs for feature extractors.

Most importantly, several DL-based studies on disease detection rely on the PlantVillage dataset, a curated benchmark of ≈54,000 single-leaf images across 38 classes captured under controlled conditions [14]. Apart from the PlantVillage dataset [14], other curated repositories such as the PlantDoc dataset [15] and the PlantCLEF [16] dataset are also widely used for disease detection, classification, and precision agriculture research.

While most powerful DL-based studies trained on this dataset often report near-ceiling accuracy, their performance drops significantly when applied to real-world conditions where illumination, canopy clutter, overlapping leaves, and sensor noise are present [6,17]. This "lab-to-field" gap has been repeatedly documented, demonstrating that over-reliance on PlantVillage inflates performance metrics and obscures generalization limits [18]. Beyond curated repositories, researchers are increasingly using field-collected (user-driven) datasets, which capture natural variability such as lighting changes, canopy clutter, overlapping leaves, and mixed symptoms. This data improves the ecological validity of deep learning models, ensuring higher reliability in deployment and better adaptation to region-specific conditions like local cultivars, climates, and pathogen strains [6,19,20]. Additionally, developing original field datasets adds novelty to the research community and contributes new insights to the literature.

In recent years, deep learning and hybrid deep learning models have emerged as powerful tools in crop pest and disease management, becoming standard methodologies for addressing challenges in the detection, identification, and classification of crop pests [1,21,22]. Several review-based studies have further consolidated these advancements, not only outlining effective predetermined steps for predicting plant diseases using DL- and ML-based approaches but also providing critical evaluations of their limitations and challenges [1,17]. Among DL models, CNNs have been particularly successful for image-based classification tasks, primarily due to their ability to extract hierarchical spatial features from visual data. However, CNNs are inherently limited in capturing temporal or sequential dynamics of disease progression, such as the development of spots, lesions, mosaics, mottling, or rings over time. Moreover, CNN-based models often require large volumes of labeled training data and are computationally expensive, which constrains their practical deployment in resource-limited agricultural settings.

To address these limitations and effectively capture both the spatial and temporal aspects of plant disease progression, researchers have increasingly adopted hybrid neural network architectures. Hybrid deep learning frameworks integrating CNN and SVM have been widely investigated for crop disease detection. For instance, a research study presented an automated deep learning framework to improve paddy crop productivity through early disease detection. A hybrid CNN–SVM model was developed to identify brown spot, bacterial leaf blight, and leaf smut, achieving over 98% accuracy [19]. An alternative hybrid architecture integrates a Vision Transformer (ViT) for advanced feature representation with a Support Vector Machine (SVM) for classification, demonstrating high accuracy in bean leaf lesion detection while simultaneously minimizing computational overhead [23].

In another study, the CNN–SVM hybrid model was proposed for automated strawberry leaf disease detection, achieving high accuracy, precision, recall, and F1-score, thereby demonstrating its potential as an effective tool for disease diagnosis and crop health moni-

https://doi.org/10.3390/su18136867

toring [24]. A research study introduced a hybrid framework for automated tomato leaf disease diagnosis by integrating deep learning and machine learning techniques. The model employed a pre-trained CNN, specifically MobileNetV2, for robust feature extraction, which was subsequently coupled with a Support Vector Machine (SVM) classifier for multi-class disease prediction. The hybrid MobileNetV2-SVM model demonstrated superior performance, attaining classification accuracies between 88% and 99%, surpassing several conventional approaches whose accuracies ranged from 70% to 97% [23].

A hybrid CNN-RNN model, such as Xception-GRU, applies the Xception network for deep feature extraction, followed by GRU layers to capture complex sequential dependencies among extracted features. Studies show that these models can reach classification accuracies above 98% on benchmark datasets, significantly outperforming classical CNN-only solutions for plant disease identification [24]. Another approach employed DenseNet-based and Inception-Xception hybrid CNN architectures, sometimes integrated with attention mechanisms, to enhance performance in distinguishing fine-grained disease symptoms, particularly in crops such as rice and wheat [25]. CoAtNet, a hybrid of convolutional and attention-based networks, achieved high precision and F1-scores in the classification of various rice leaf diseases, showing that these architectures are adept at both identifying disease symptoms and ignoring irrelevant background information [26]. Several studies have integrated Grad-CAM and other interpretability frameworks with hybrid models to visualize the features most influential in classification decisions. Such approaches improve model interpretability and enhance trust and transparency in agricultural AI systems [27].

The integration of CNNs with recurrent neural networks (RNNs), such as bidirectional LSTMs or GRUs, has shown great promise. This hybrid CNN–Bi-GRU framework synergistically leverages the feature extraction capabilities of CNNs with the contextual and sequential modeling capabilities of Bi-GRUs. The result is a robust architecture that enhances classification performance by providing spatially rich and temporally informed representations of plant disease symptoms, ultimately leading to more accurate and reliable predictions. Combining CNNs with Bi-GRUs for rice disease identification achieved higher accuracy than standalone models, though the study was limited to four disease types, restricting generalization. The authors emphasized the need for larger, real-field datasets to ensure robustness under complex agricultural conditions.

While CNN-based methods perform well on controlled datasets with consistent imagery, hybrid architectures generally exhibit greater robustness and adaptability under challenging agricultural conditions, including environmental variability and complex disease patterns [21,24]. Extending these developments, Zhang and Wang [10] integrated attention pooling and capsule networks within a BERT-BiGRU-CapsNet framework for crop disease–pest question classification, enabling effective feature extraction from unstructured data and outperforming several conventional machine learning and deep learning approaches.

Across multiple studies, reviews emphasize that hybrid models improve generalization by leveraging complementary strengths of CNNs, sequential models, and advanced pooling mechanisms, making them more resilient to field-level challenges than pure CNNs. Bi-CNNs integrating fine-tuned VGG and pruned ResNet enhance feature extraction while supporting large-scale applications, and integration with edge–cloud systems enables rapid, field-level diagnosis [24].

Recent advancements in deep learning have significantly improved plant disease detection, with hybrid architectures (e.g., CNN–SVM, CNN–BiGRU, MobileNetV2–SVM, and CoAtNet, to name a few) demonstrating superior accuracy and robustness compared to conventional CNN-only models. However, most existing frameworks remain computationally demanding, requiring high memory and processing power, which restricts their deployment in real-world agricultural environments, especially on resource-limited

https://doi.org/10.3390/su18136867

devices. Furthermore, while hybrid models enhance spatial–temporal feature learning and generalization, challenges persist in balancing accuracy with efficiency, adaptability to heterogeneous field data, and scalability for large-scale applications.

Therefore, there is a need to design deep learning frameworks that balance classification accuracy with architectural efficiency for practical agricultural deployment. In response, this study proposes a hybrid U^2-Net–MobileNetV2–Bi-GRU framework for plant disease detection and classification. By leveraging depthwise separable convolutions in MobileNetV2 and sequential feature modeling through Bi-GRU, the proposed architecture seeks to achieve high predictive performance while maintaining a relatively efficient network structure. The framework is further evaluated under both benchmark and field conditions to assess its applicability to real-world agricultural monitoring systems.

The novelty of this work lies in the integration of segmentation-guided spatio-temporal deep learning with real-field environmental sensing to systematically analyze the domain generalization limitations of benchmark-trained plant disease detection models. Most importantly, the present study builds on the research group's expertise in precision agriculture, including IoT-based pesticide spraying [28], soil monitoring with hybrid machine learning [29], and field-based citrus fruit detection and classification using the FIDS-30 datasets [30]. Despite these advances, existing approaches often operate independently, limiting their effectiveness under real-world conditions. Therefore, there is a need for an integrated, soil-aware deep learning framework that combines spatial, temporal, and environmental data. Addressing this gap, the proposed study develops a hybrid model tailored to the agro-ecological conditions of Eluru (India), enabling early stress detection and robust crop monitoring. This integration supports accurate, scalable, and sustainable precision agriculture systems.

Unlike multimodal disease diagnosis frameworks that directly fuse sensor measurements and image features within a unified learning architecture, the present study employs IoT-based soil monitoring as a complementary environmental assessment component. The objective is not to develop a sensor-fusion classifier, but rather to investigate how field-level environmental conditions may influence disease symptom expression and contribute to the performance gap observed between benchmark and real-world datasets.

The present research findings not only establish a benchmark for addressing the lab-to-field gap but also provide a transferable framework for future research in similar agro-climatic regions, particularly for researchers focusing on field-based disease detection with state-of-the-art deep learning approaches.

In view of the above, the present research aims are as follows:

(a) To develop a hybrid deep-learning framework that integrates U^2-Net-based leaf segmentation, MobileNetV2-based feature extraction, and Bidirectional Gated Recurrent Unit (Bi-GRU) networks for automated leaf disease detection.
(b) To quantitatively evaluate the contribution of segmentation-assisted feature extraction and sequential feature modeling by comparing the proposed CNN-Bi-GRU architecture against baseline deep-learning models using accuracy, precision, recall, and F1-score metrics. To assess the effectiveness of the proposed framework for accurate disease recognition across multiple crop species and disease categories. To validate the generalization capability and robustness of the proposed framework using curated PlantVillage datasets and independently collected field datasets, and to assess its suitability for real-time plant disease monitoring applications.
(c) To investigate the influence of field-level soil and environmental conditions on the transferability of deep learning-based disease classification models using an IoT-based soil monitoring system.

https://doi.org/10.3390/su18136867

The paper is organized as follows: Section 2 describes the methodology, including datasets in sub-Section 2.1, pre-processing in sub-Section 2.2, U^2-Net segmentation in sub-Section 2.3, experimental setup in Section 2.4, and a graphical workflow of the study in Section 2.5. Section 3 presents and discusses the experimental results, while Section 4 concludes with key findings and directions for future work. Section 5 presents the limitations and future scope of the present study.

2. Materials and Methods

2.1. Datasets

The present study employed two primary data sources. First, the publicly available PlantVillage dataset was used as a benchmark for training and validation. Secondly, an i*Phone* camera with a 13 mm lens was used to capture high-resolution leaf images in a natural environment. The dataset represents images collected between 9 July and 18 July, 2025, which is a critical period for disease manifestation due to favorable climatic conditions such as high humidity and moderate rainfall. To ensure diversity and model generalizability, images were taken under varying environmental conditions, including different light intensities and disease severities observed in these regions. For preprocessing, the diseased portions of the leaves were manually extracted as patches from the original high-resolution images to focus on the affected areas.

These patches were treated as individual data samples and initially resized to a uniform dimension of 300 $\times$ 300 pixels for U^2-Net-based segmentation. After segmentation and background removal, the resulting leaf regions were resized to 224 $\times$ 224 $\times$ 3, consistent with the input requirements of the MobileNetV2 backbone used for CNN-BiGRU classification.

This comprehensive dataset, with its geographical and seasonal diversity, aims to provide a robust basis for evaluating the model's performance and generalizability across similar agricultural settings [30]. The inclusion of real-field imagery was intended to improve the generalization and robustness of the proposed hybrid deep learning framework under heterogeneous agricultural conditions. Notably, our earlier research utilized citrus fruit data collected from the same fields, where a conventional CNN model was applied for automated fruit detection and classification [30]. Building on this prior work, the present study extends the approach to leaf disease detection, integrating benchmark and field datasets for comprehensive evaluation.

The PlantVillage dataset offers a large-scale, annotated collection of plant leaf images captured under controlled environments [14]. In contrast, the field samples introduce variability in terms of background noise, lighting, and natural disease progression, thereby enhancing the robustness of the proposed model. We considered the leaves of pepper, potato, and tomato plants (both healthy and diseased categories) from the PlantVillage dataset, which comprises 41,276 sample images. Of these, 28,068 images (68%) were allocated for training to optimize model weights, while 4953 images (12%) were used for validation to monitor performance on unseen data, tune hyperparameters, and reduce overfitting. Finally, 8255 images (20%) were reserved as a test set to provide an unbiased evaluation of the trained model's performance. The PlantVillage dataset was partitioned into training (68%), validation (12%), and testing (20%) subsets using stratified sampling to preserve class distributions. This partitioning strategy provides a balance between effective model learning, hyperparameter tuning, and unbiased evaluation while maintaining a sufficiently large independent test set for reliable assessment of model generalization.

Although the 70–15–15 strategy is widely employed in deep learning research [6,31], the slightly larger test set in this study was adopted to ensure robust statistical evaluation across multiple disease categories, particularly in the presence of class imbalance. This allocation is consistent with best practices in CNN-based plant disease recognition, where

https://doi.org/10.3390/su18136867

sufficient validation data is required to optimize loss functions such as class weighting or focal loss [32] and avoid bias toward majority classes. Moreover, for a hybrid CNN-BiGRU model, maintaining relatively larger validation and testing sets is advantageous, as the recurrent component benefits from more diverse unseen examples to fine-tune temporal dependencies and reduce the risk of overfitting to sequential noise during training.

Figure 1 illustrates the geographical location of the study fields near Eluru (16.71° N, 81.10° E), Andhra Pradesh, India. The study area lies within the Krishna–Godavari agro-climatic zone and is characterized by a tropical wet-and-dry climate. The region receives an average annual rainfall of approximately 900–1100 mm, primarily during the southwest monsoon season, and experiences mean temperatures ranging from 20 °C to 40 °C throughout the year. The dominant agricultural soils in the area consist of alluvial and clay loam soils with moderate water-holding capacity and favorable conditions for crop cultivation. These agro-climatic and soil characteristics make the region suitable for evaluating plant disease detection systems under practical field conditions.

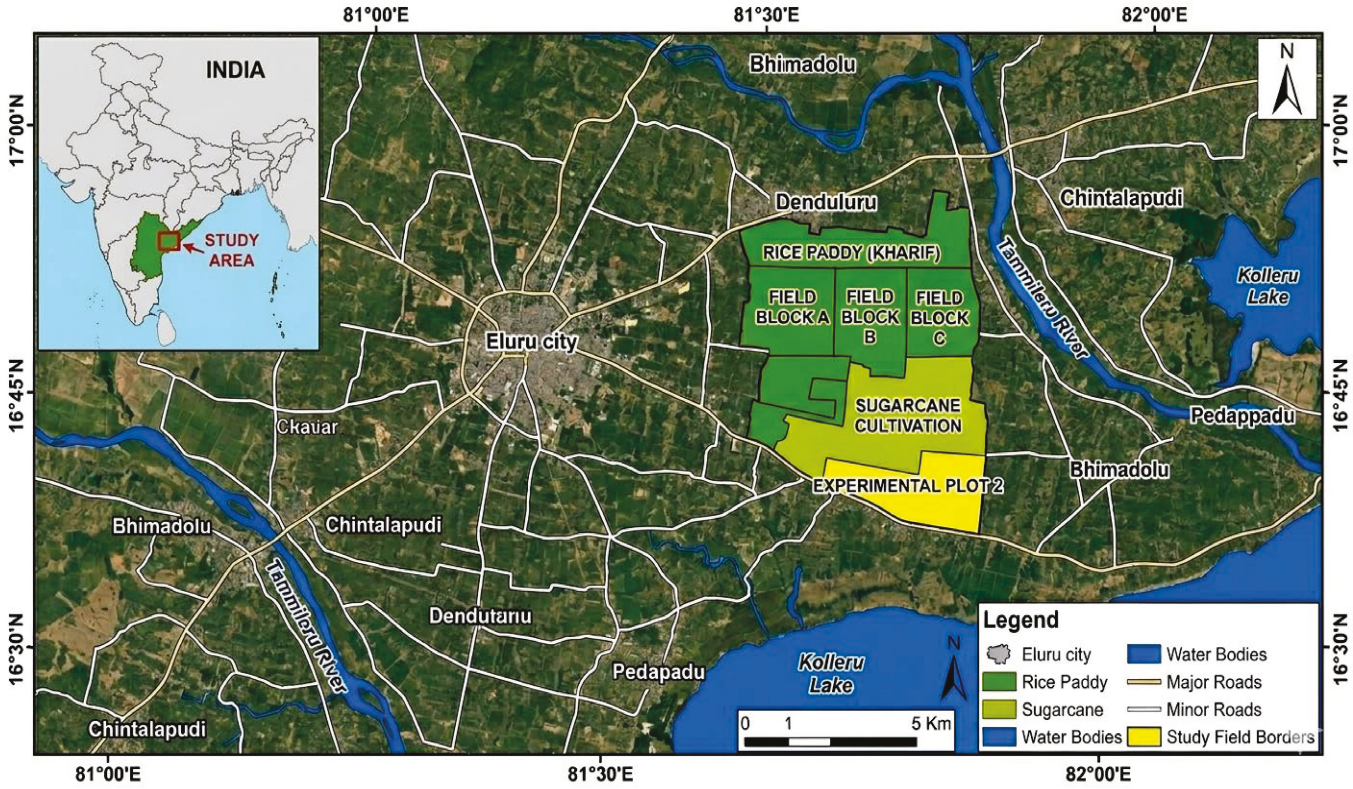

Figure 1. Location of the study area and experimental agricultural fields near Eluru, Andhra Pradesh, India. The inset map shows the study site's location within India, while the main map depicts the field blocks used for crop monitoring, leaf image acquisition, and environmental data collection.

2.2. Pre-Processing Workflow for Leaf Disease Detection

Table 1 shows the representative leaf image dataset comprising field-acquired samples and PlantVillage images. Although the PlantVillage dataset contained Tomato Target Spot and Tomato Mosaic Virus categories, these diseases were not encountered during the field survey period. Consequently, they were not represented in the field-acquired image dataset.

https://doi.org/10.3390/su18136867

Table 1. Healthy and Diseased Leaf Samples from the PlantVillage Database (Bell pepper, Potato, and Tomato crops).

PlantVillage Database		
Bell Pepper	**Potato**	**Tomato**
		
		
Bacterial spot	Early blight	Target spot
		
	Late blight	Mosaic virus
		
		Bacterial spot

PlantVillage samples supplement the dataset with standardized images across diverse pathologies. Diseased categories include Bacterial leaf spot in Mulberry, Bacterial spot in Bell pepper, Early blight and Late blight in Potato, and Target spot, Mosaic virus, and Bacterial spot in Tomato. The diversity across species and pathologies enables robust model training, supporting generalization across different crops. By including both controlled (PlantVillage) and heterogeneous field-acquired samples, the dataset ensures evaluation under conditions approximating practical agricultural deployment. To ensure uniformity and optimize computational efficiency, all images were subjected to a standardized preprocessing pipeline, as illustrated in Figure 2. Each image first underwent resizing to a fixed resolution, ensuring dataset consistency and reducing computational overhead during training [6]. This was followed by normalization, where pixel intensities were scaled to a standard range to accelerate convergence and stabilize the learning process [33].

To enhance data diversity and mitigate overfitting, augmentation techniques such as horizontal flipping, rotation, and scaling were applied, effectively increasing the variability of training samples and improving model robustness to orientation and geometric distortions [34,35]. Finally, an optional segmentation stage was employed using U^2-Net to isolate the leaf from complex backgrounds. This ensured that disease-specific features were emphasized while minimizing the influence of irrelevant background artifacts [12,18]. Through this sequential pipeline—resizing, normalization, augmentation, and segmentation—the dataset was transformed into a balanced, information-rich input set. Such systematic preprocessing not only improved generalization but also enhanced the ability of convolutional

https://doi.org/10.3390/su18136867

neural networks to extract discriminative features, ultimately leading to higher accuracy in leaf disease classification [5,36].

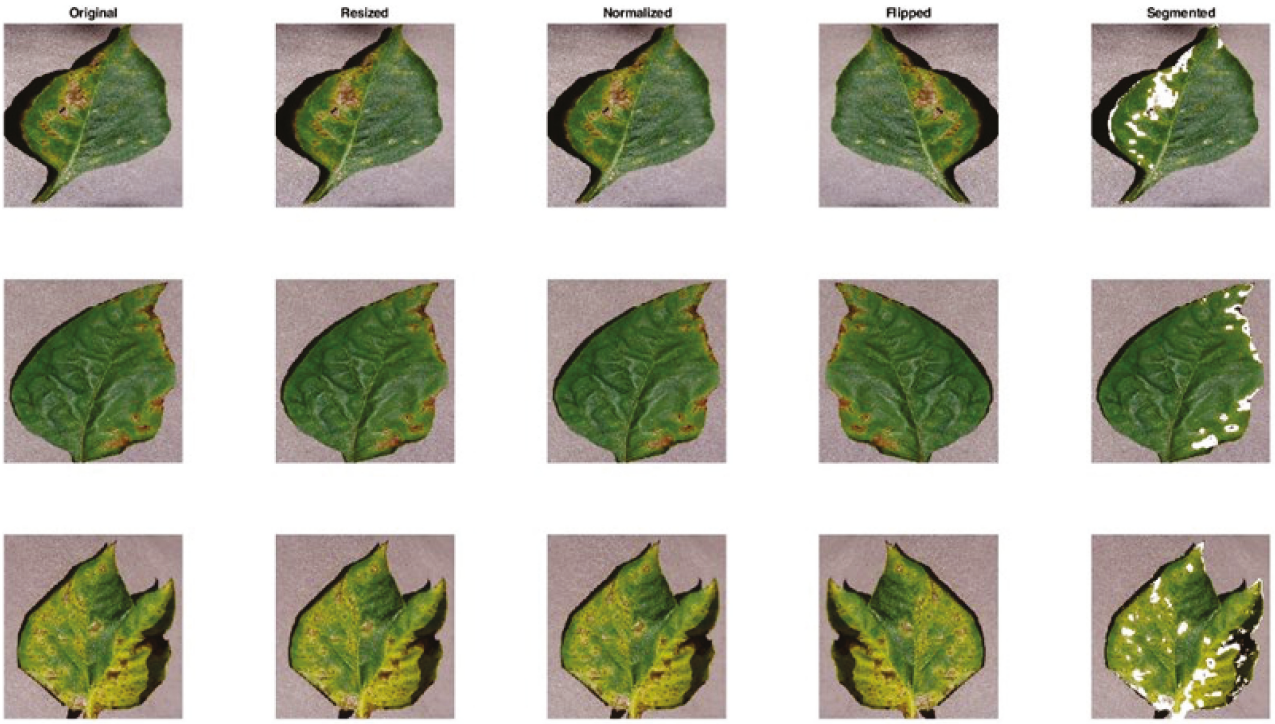

Figure 2. Examples of the pre-processing pipeline applied to representative diseased leaf images from the study dataset. From left to right, the images show the original leaf image, the resized image, the normalized image, and the augmented image generated through flipping. The illustrated samples represent tomato, potato, and pepper leaf diseases used in the classification framework.

To improve generalization and mitigate overfitting, data augmentation techniques, including flipping, rotation, and scaling, were applied to the training images. These transformations increased the diversity of the training samples and enhanced the robustness of the proposed framework to variations in leaf orientation, size, and imaging conditions.

2.3. U^2-Net-Based Segmentation

The segmentation of the pre-processed images is carried out using the U^2-Net model, a two-level and deeply nested U-shaped network specifically designed for salient object detection and fine-grained segmentation tasks [12]. The U-Net architecture's encoder–decoder structure with skip connections efficiently utilizes both local and global information, enabling precise and fine-grained segmentation for tasks such as autonomous driving, scene interpretation, and medical image analysis [36]. The nested residual U-blocks (RSUs) form the core of U^2-Net.

The output of an RSU block is defined as:

$$Y = F(X) + X \quad (1)$$

where X denotes the input feature map, F(X) represents the nested U-shaped feature extraction operation within the RSU block, and Y is the refined output feature map. The residual connection facilitates feature reuse, improves gradient propagation, and enables the network to capture both local details and global contextual information efficiently.

Each RSU embeds a lightweight U-Net structure within a single encoder–decoder stage, enabling effective feature reuse and refinement. In the context of plant disease

https://doi.org/10.3390/su18136867

analysis, U^2-Net significantly enhances the identification of infected regions on leaves by capturing both global contextual features and local fine details.

This design provides several advantages:

(a) The nested architecture bridges the semantic gap between encoder and decoder by preserving multi-scale contextual information.
(b) The residual connections mitigate vanishing gradients and improve training stability.
(c) The saliency-driven mechanism suppresses irrelevant background information while highlighting diseased regions.
(d) Hierarchical multi-level supervision ensures both coarse and fine segmentation maps contribute to the final output.

The nested U-block operation at stage (p, q) can be represented as

$$Y^{(p,\,q)} = R\left\{ f\left(Y^{(p-1,\,q)} \right\},\ q = 0,$$

$$Y^{(p,\,q)} = R\left\{ f\left(\sum_{k=0}^{q-1} C\left(A_g(Y^{(i,\,k)}),\ U\left(Y^{(p+1,\,q-1)}\right) \right) \right) \right\},\ q > 0,$$

where (p) denotes the hierarchical level (depth) of the RSU module and (q) denotes the position of the convolutional layer within that level. $(Y\{^{p,\,q)}\})$ represents the corresponding intermediate feature representation produced during forward propagation.

- $Y^{(p,\,q)}$ denotes the output of the RSU block at depth p and stage q.
- F $(\cdot)$ is a convolutional layer with ReLU activation.
- R $\{\cdot\}$ indicates residual connections.
- A_g $(\cdot)$ is the attention/saliency gating function.
- C $(\cdot)$ denotes the concatenation of feature maps.
- U $(\cdot)$ represents an up-sampling operator.

This recursive formulation enables U^2-Net to simultaneously refine low-level structural details and high-level semantic features (through skip connections), which has been reported to achieve competitive segmentation performance compared with conventional architectures such as U-Net and UNet++ [12,13,36]. The U^2-Net segmentation effectively isolates leaf regions from the background while preserving disease-related visual characteristics. This step is useful before applying classification models like MobileNetV2–BiGRU.

Figure 3 shows representative leaf segmentation results generated using the U^2-Net framework. The model was trained for 50 epochs using the Adam optimizer (learning rate = 1×10^{-4}, batch size = 16) with a hybrid Binary Cross-Entropy (BCE) and Dice loss function. The resulting segmentation masks effectively isolated leaf regions from the background while preserving disease symptoms and lesion characteristics. The extracted leaf images were resized to $224 \times 224 \times 3$ pixels and supplied to the MobileNetV2–BiGRU classifier (Figure 4). This preprocessing step reduced background interference and improved the extraction of disease-relevant features.

The left column of Figure 3 displays representative original leaf images exhibiting varying disease symptoms and severity levels. The middle column presents the corresponding segmentation masks generated by the U^2-Net framework, while the right column shows the extracted leaf regions after background removal. The segmentation process effectively isolates the leaf foreground from complex background elements while preserving disease-relevant visual features, including lesion boundaries, discoloration patterns, and symptomatic regions. By eliminating irrelevant background information, the segmentation stage provides cleaner inputs for subsequent feature extraction and classification. This preprocessing step enhances the ability of the MobileNetV2–BiGRU network to focus on

https://doi.org/10.3390/su18136867

disease-specific characteristics, thereby improving classification robustness and reducing the influence of background variability commonly encountered in field-acquired images.

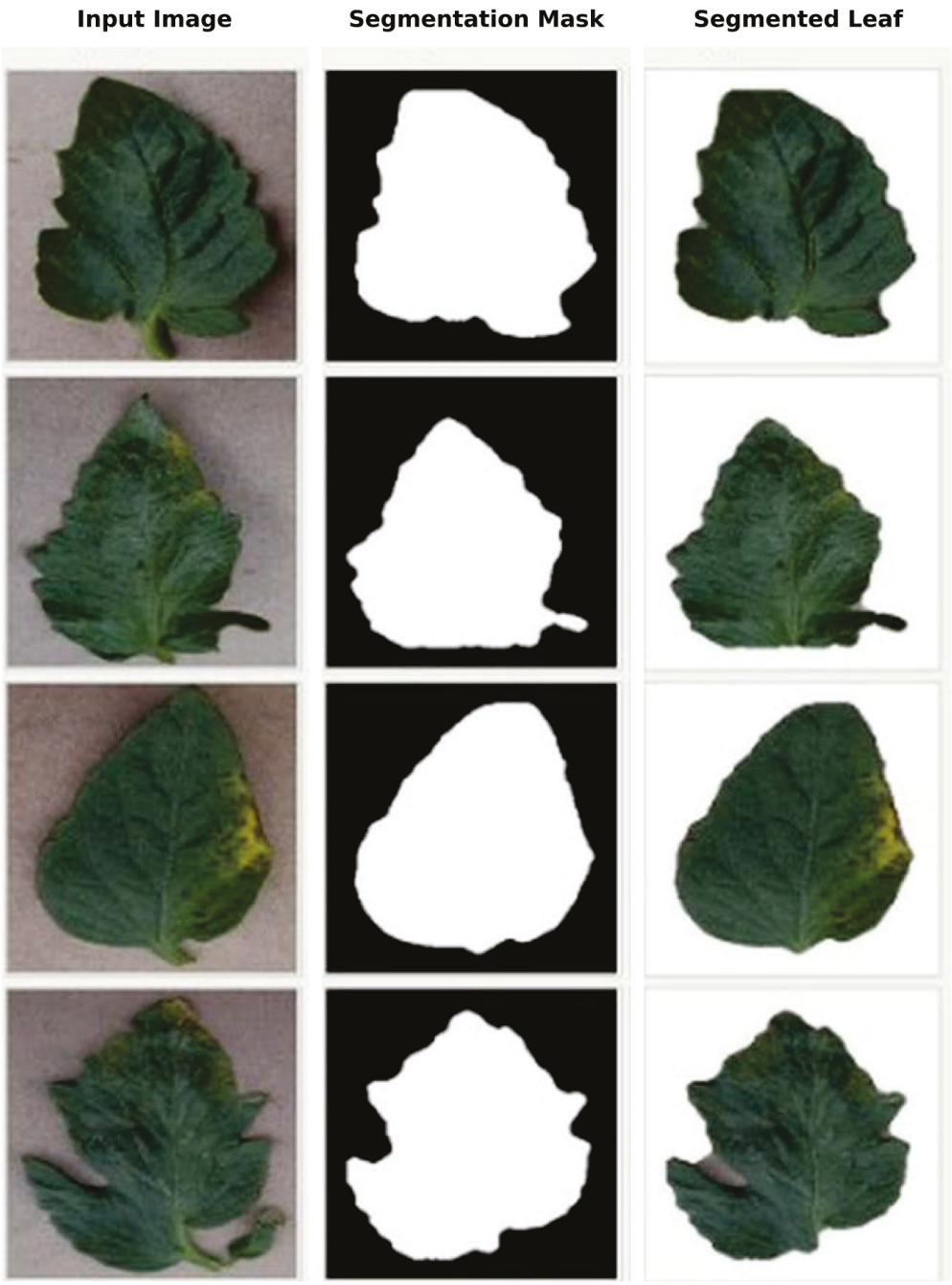

Figure 3. Representative examples of leaf segmentation using the U^2-Net framework: Original leaf images (**left-side panels**), predicted masks (**mid panels**), and extracted leaf regions (**right-side panels**).

The CNN–BiGRU architecture is designed to learn spatial representations via convolutional neural network (CNN) layers and sequential dependencies via Bidirectional Gated Recurrent Unit (BiGRU) layers. In the proposed framework, MobileNetV2 serves as the feature extraction backbone, while the BiGRU component models dependencies among the extracted feature vectors, enabling enhanced representation learning. BiGRU was selected because previous studies have demonstrated its effectiveness in capturing long-range feature dependencies while employing a simpler gating mechanism than conventional Long Short-Term Memory (LSTM) networks [37,38]. The bidirectional structure further improves contextual feature extraction by processing feature sequences in both forward

https://doi.org/10.3390/su18136867

and backward directions. Consequently, the CNN–BiGRU architecture provides a robust framework for plant disease classification and was therefore adopted in the present study.

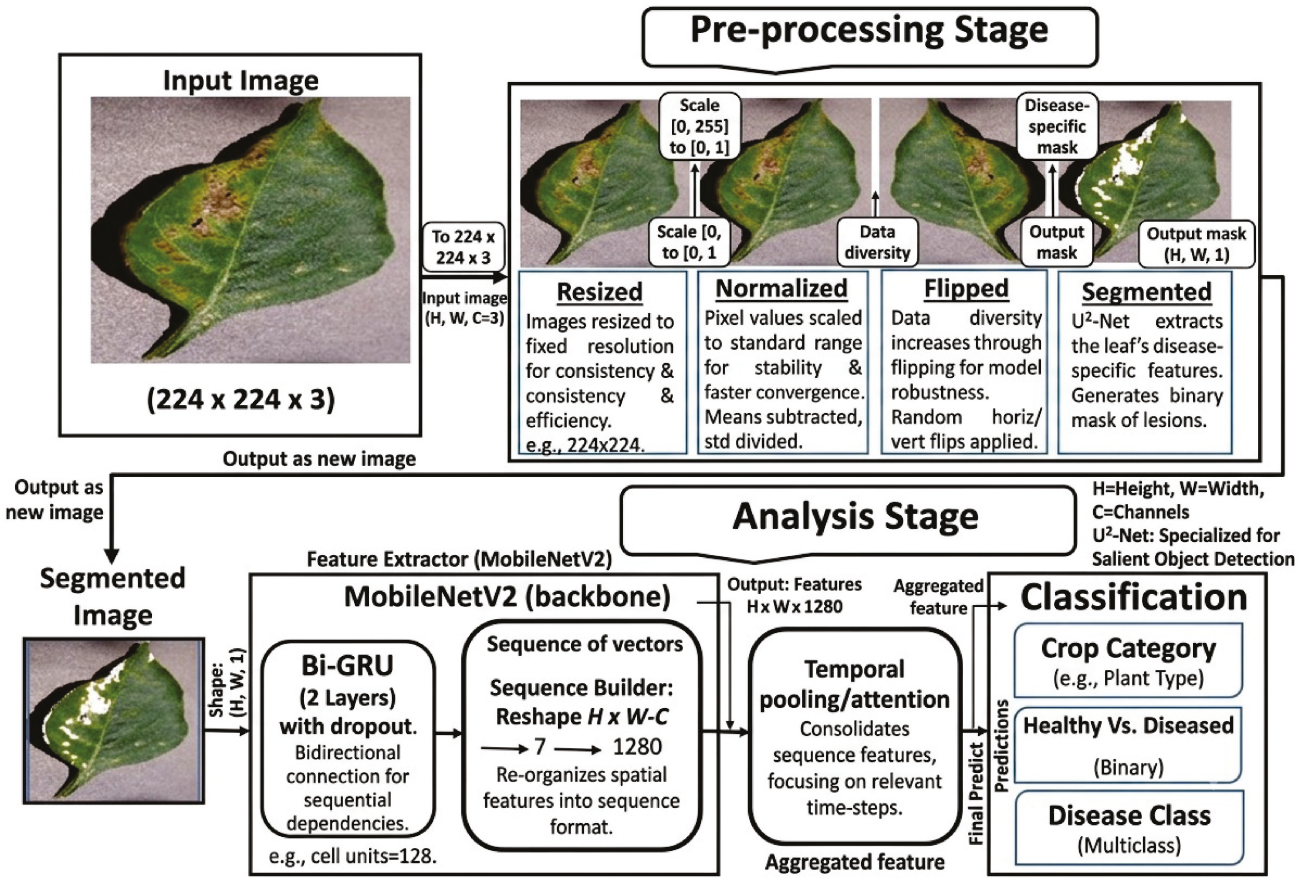

Figure 4. Workflow of the U^2-Net-assisted MobileNetV2-BiGRU framework for Crop Leaf Disease Classification. Proposed image-processing pipeline: 300 × 300 input images are segmented using U^2-Net, and the resulting segmented outputs are resized to 224 × 224 × 3 for MobileNetV2-based classification.

It is worthwhile mentioning that although the input data consist of static leaf images, the Bi-GRU module is employed to process sequentially arranged feature representations generated by the MobileNetV2 backbone rather than temporal image sequences. Specifically, the extracted convolutional feature maps are reshaped into ordered feature vectors and fed into the Bi-GRU layer to capture long-range contextual dependencies among spatial features. Consequently, the Bi-GRU serves as a feature refinement mechanism that enhances discriminative representation learning and classification accuracy, rather than modeling temporal changes in plant disease progression.

To further enhance the discriminative capacity of the model, the pre-processed images were segmented using the U^2-Net model [12], which is specifically designed for salient object detection. By extracting the leaf region and suppressing background artifacts, U^2-Net ensures that the CNN learns only disease-relevant spatial patterns, thereby minimizing overfitting to irrelevant features such as soil, shadows, or imaging conditions. This segmentation not only improves intra-class consistency but also enables the Bi-GRU component to capture sequential dependencies across leaf patches (e.g., tip–midrib–base progression of lesions) in a more meaningful manner. Consequently, the integration of U^2-Net segmentation with CNN-BiGRU is expected to yield superior classification accuracy, better generalization across environments, and enhanced sensitivity to minority disease classes when compared with models trained on unsegmented raw images.

https://doi.org/10.3390/su18136867

2.4. Experimental Setup

The proposed CNN–Bi-GRU framework employed MobileNetV2 as the feature extraction backbone. The extracted feature representations were subsequently processed using Bidirectional Gated Recurrent Unit (Bi-GRU) layers to capture sequential dependencies among spatial features. The model was trained using the Adam optimizer with an initial learning rate of 0.001 and categorical cross-entropy loss. The model was trained for a maximum of 100 epochs using the Adam optimizer and early stopping. Training converged after 43 epochs based on validation loss.

Before classification, leaf images were processed using the U^2-Net segmentation model to isolate symptomatic leaf regions and reduce background interference. The segmentation module generated pixel-level masks that were applied to extract the leaf foreground before feature extraction. This preprocessing step improved disease localization and reduced the influence of complex backgrounds and non-leaf objects.

All experiments were conducted on a Lenovo ThinkCentre M70s Gen 3 desktop computer running Microsoft Windows 11 Pro, equipped with a 12th Generation Intel® Core™ i7-12700 processor (12 cores, 20 logical processors) and 16 GB RAM. Model performance was evaluated using accuracy, precision, recall, and F1-score metrics. Data augmentation techniques, including random rotation, horizontal flipping, zooming, and brightness adjustments, were applied during training to improve model generalization. It is also worthwhile to mention that the field dataset comprised approximately 700 images collected under natural environmental conditions. An examination of the class distribution indicated no severe imbalance among the available categories. Consequently, no additional imbalance-mitigation techniques, such as SMOTE, oversampling, or class-weighted loss functions, were employed.

The present study focused on classification performance and generalization capability. Therefore, detailed measurements of computational complexity, including FLOPs, parameter count, memory footprint, and inference latency, were not included and are identified as an important direction for future investigation.

2.5. Workflow of the Present Research

Figure 4 depicts the workflow of the proposed U^2-Net-assisted CNN (MobileNetV2) + Bi-GRU leaf-diagnostics pipeline. Following U^2-Net segmentation performed on 300 × 300 pixel images, the segmented leaf regions were resized to 224 × 224 × 3 and standardized via normalization and augmentation before being supplied to the MobileNetV2–BiGRU classification framework. In analysis, MobileNetV2 extracts a spatial feature map (e.g., 7 × 7 × 1280), a sequence builder reshapes the map into spatial tokens, and a Bi-GRU models long-range dependencies across tokens. Attention/temporal pooling aggregates the sequence into a global embedding that feeds multi-task heads to predict crop category, healthy vs. diseased, and disease class. This hybrid CNN-BiGRU architecture leverages spatial feature extraction and sequential modeling, making it suitable for complex image analysis tasks like plant disease detection.

3. Results and Discussion

3.1. Classification Performance—PlantVillage Data

The identification and categorization of diverse leaf diseases were systematically performed to ensure accurate recognition of disease types. To establish the robustness of the proposed framework, its classification performance was rigorously benchmarked against state-of-the-art models, including Deep Convolutional Neural Networks (DCNN), DenseNet, Vision Transformer (ViT), and EfficientNet-B3. Comparative evaluation was

https://doi.org/10.3390/su18136867

conducted using a comprehensive set of performance metrics encompassing accuracy, precision, recall, F1-score, specificity, and the area under the ROC curve (AUC-ROC).

The results, illustrated in Figure 5, along with error bars, demonstrate that the proposed approach consistently outperforms existing architectures across multiple evaluation criteria, thereby underscoring its efficacy and reliability for plant disease diagnosis. The performance metrics considered include accuracy, precision, recall, F1-score, and specificity. The results demonstrate that the present research model achieves superior performance across all metrics, reaching an accuracy of 99.8%, thereby significantly outperforming existing approaches in terms of classification efficacy and reliability.

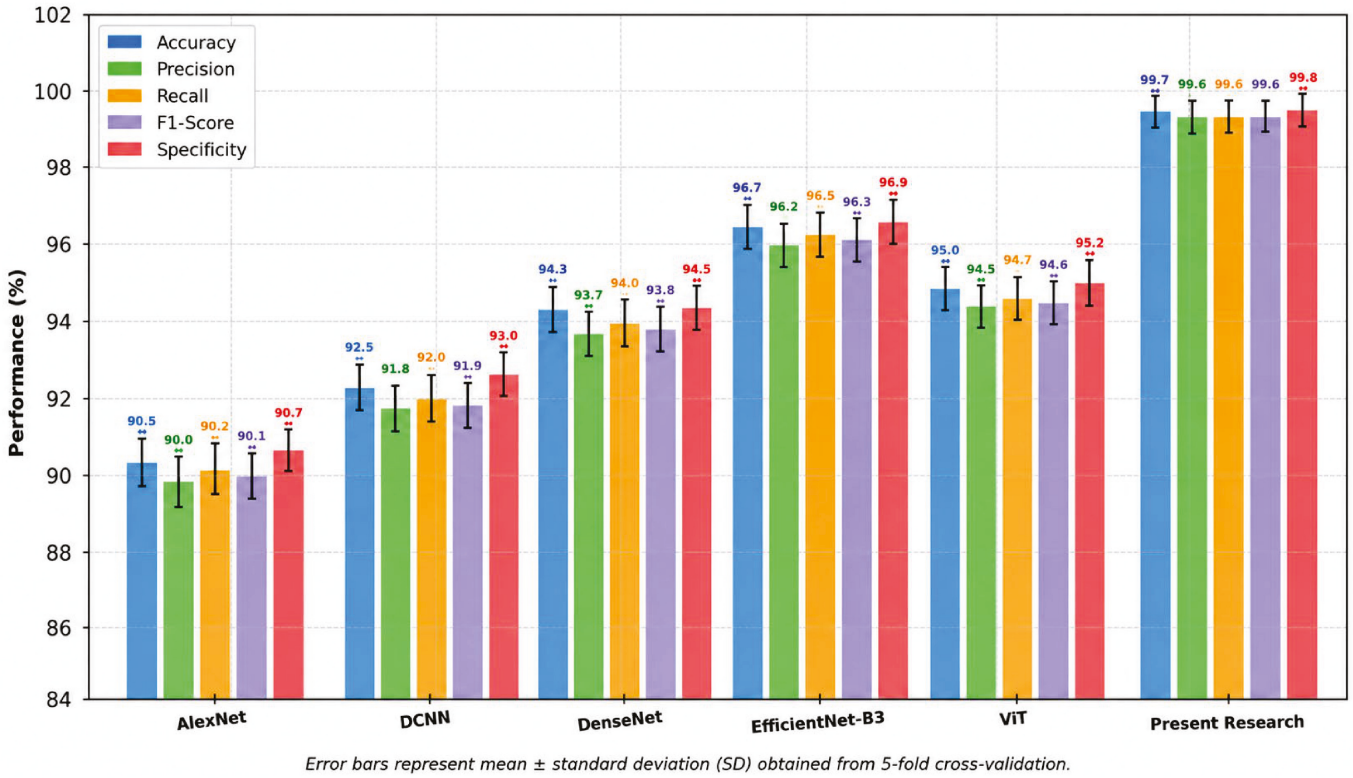

Figure 5. Performance Comparisons of Deep Learning Architectures with Error Bar Analysis. Bars indicate the mean Accuracy, Precision, Recall, F1-Score, and Specificity (%) computed across the validation folds, while error bars denote one standard deviation (±SD). Asterisks indicate statistically significant differences compared with the baseline models (* $p < 0.05$, ** $p < 0.01$). The results demonstrate that the proposed U^2-Net-assisted MobileNetV2–BiGRU model achieves superior predictive performance and lower variability compared with AlexNet, DCNN, DenseNet, EfficientNet-B3, and Vision Transformer (ViT) architectures.

The exceptionally high performance achieved on the PlantVillage dataset should be interpreted with caution because the dataset was acquired under controlled imaging conditions with relatively homogeneous backgrounds and limited environmental variability. Such characteristics reduce intra-class complexity and often facilitate higher classification accuracy than would be expected under real-world conditions. The independent field evaluation conducted near Eluru revealed a substantial decrease in accuracy, demonstrating the presence of domain shift and highlighting the challenges associated with transferring models trained on benchmark datasets to practical agricultural environments. These findings underscore the importance of incorporating field-collected data and environmental sensing information to improve model robustness and generalization.

The inclusion of statistical error bars strengthens the reliability of the comparative analysis by demonstrating the variability of the models under repeated cross-validation

https://doi.org/10.3390/su18136867

experiments. Figure 5 confirms that the proposed framework significantly outperforms the existing deep learning models in terms of predictive accuracy, sensitivity, precision, and specificity, making it highly suitable for reliable and accurate leaf disease classification.

The ROC analysis, as shown in Figure 6, demonstrates the superior classification capability of the proposed deep learning framework compared with the benchmark architectures. The proposed model achieved a near-perfect ROC performance with an average AUC approaching 1.00 (95% CI: 0.99–1.00) across the five-fold cross-validation experiments. Among the comparative models, DCNN exhibited the second-best performance with an AUC of 0.94 ± 0.02, followed by DenseNet with 0.92 ± 0.03. Vision Transformer (ViT) and EfficientNetB3 produced comparable performance levels, each achieving an AUC of approximately 0.91, although with slightly broader confidence intervals, suggesting moderate variability in classification performance. AlexNet recorded the lowest performance with an AUC of 0.89 ± 0.03, indicating comparatively weaker discriminative capability for plant leaf disease classification, particularly for disease classes exhibiting similar visual symptoms.

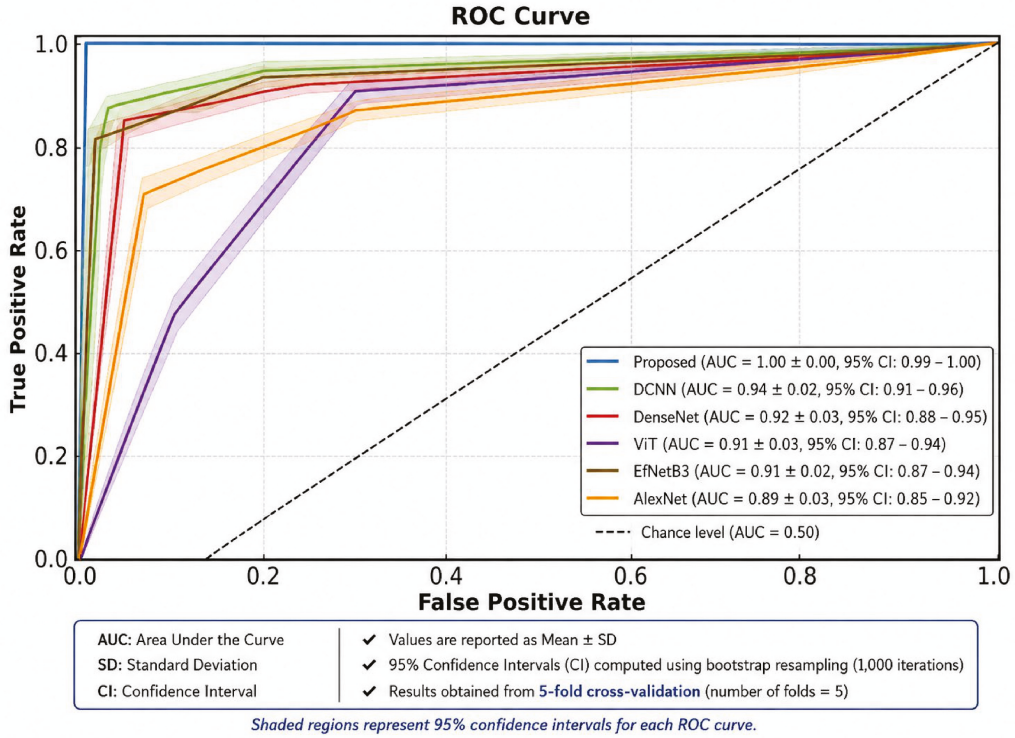

Figure 6. Comparative ROC curve Analysis of Deep Learning Models (AlexNet, DCNN, DenseNet, EfficientNet-B3, ViT, and Present Research) with 95% Confidence Intervals for leaf disease classification.

The shaded confidence bands around each ROC curve represent the 95% confidence intervals obtained through bootstrap resampling, providing an estimate of uncertainty associated with model performance. The relatively narrow confidence intervals observed for the proposed framework indicate stable performance across the cross-validation folds. However, the near-perfect ROC performance achieved on the PlantVillage dataset should be interpreted in the context of the dataset's controlled acquisition conditions and limited environmental variability. The substantial reduction in accuracy observed during independent field validation demonstrates that high benchmark performance does not necessarily translate to equivalent real-world performance. These findings highlight the importance of evaluating plant disease classification models using both benchmark and field-collected datasets to assess robustness and generalization capability under practical agricultural conditions.

https://doi.org/10.3390/su18136867

Further, an ablation study was conducted to evaluate the contribution of the MobileNetV2 backbone, GRU, Bi-GRU, and U^2-Net segmentation modules. The results demonstrated progressive improvements in classification performance from MobileNetV2 (96.4% accuracy) to MobileNetV2+GRU (97.8%), MobileNetV2+Bi-GRU (98.9%), and the complete U^2-Net+MobileNetV2+Bi-GRU framework (99.8%). Detailed results are provided in Supplementary Table S1.

Hybrid architectures combining CNNs with recurrent units like GRU or LSTM consistently exhibit robust performance across diverse domains—including motor imagery classification in EEG [38] and multi-class disease recognition under field conditions [39,40]. Notably, CNN–BiGRU and CNN–BiLSTM structures are repeatedly shown to outperform pure CNNs, particularly with limited training data, due to their ability to capture both spatial features and temporal dependencies [41]. Although some hybrid CNN–RNN models can achieve these gains with relatively lower computational overhead [4], it is also true that more complex hybrids can demand increased computational resources and fine-grained hyperparameter tuning. Nonetheless, their superior generalization—especially in scenarios marked by data scarcity, variability in field setups, and non-local symptom patterns—strongly justifies the architectural complexity for critical agricultural applications.

Several hybrid deep learning models trained on controlled datasets such as PlantVillage and PlantDoc, which are characterized by uniform backgrounds, consistent illumination, and standardized imaging conditions, routinely report accuracies exceeding 99%. However, their performance degrades significantly when applied to authentic in situ field-based imagery. This disparity arises from the profound domain shift between curated datasets and real-world agricultural environments, where variability in lighting, occlusion, background clutter, and symptom expression introduces substantial intra-class variation. Such findings underscore the inherent limitations of current deep learning architectures in generalizing from simplified laboratory settings to complex natural ecosystems. Consequently, field-based evaluation emerges as a more realistic yet inherently challenging benchmark of model robustness, and the present study provides a systematic demonstration of this critical aspect.

3.2. Classification Performance—Field-Based Leaf Images

The performance of the proposed deep learning framework was further evaluated using an independent dataset of 700 leaf images collected from open-field environments near Eluru, India, with 68% used for training, 12% for validation, and 20% for testing (approximately 140 test images). The dataset comprised images of *Epipremnum aureum*, *Mulberry*, *Guava (Psidium guava*), and *Hibiscus (Hibiscus rosasinensis)* leaves, categorized into healthy and diseased classes, including Bacterial leaf spot and Anthracnose. The nearly uniform class distribution was maintained to minimize class imbalance and ensure unbiased model training and evaluation.

All images were manually annotated based on visible disease symptoms and verified using standard plant pathology references and expert consultation. To ensure annotation quality, the labels were reviewed and cross-checked before model training. The dataset was designed to maintain a reasonably balanced distribution among healthy and diseased classes across the selected plant species, thereby reducing potential bias associated with class imbalance. The collected images encompass substantial variability in environmental conditions, disease severity, illumination, and background complexity, making the dataset suitable for evaluating model robustness under real-world agricultural scenarios.

Figure 7 presents the confusion matrix obtained during field validation. The results indicate an overall classification accuracy of approximately 61.97%, with notable misclassification occurring between healthy and diseased categories within the same plant species.

https://doi.org/10.3390/su18136867

Specifically, Epipremnum Healthy, Epipremnum Bacterial spot, Mulberry Healthy, and Mulberry Bacterial spot achieved correct classification rates of 62.86%, 60.00%, 62.86%, and 60.00%, respectively. Similarly, *Guava* Healthy, *Guava* Anthracnose, *Hibiscus* Healthy, and *Hibiscus* Bacterial spot achieved recall values of 55.56%, 66.67%, 61.11%, and 68.42%, respectively. The observed confusion among classes highlights the challenges associated with disease recognition under real-world field conditions, where variations in illumination, background complexity, environmental factors, and symptom severity significantly affect model generalization and transferability.

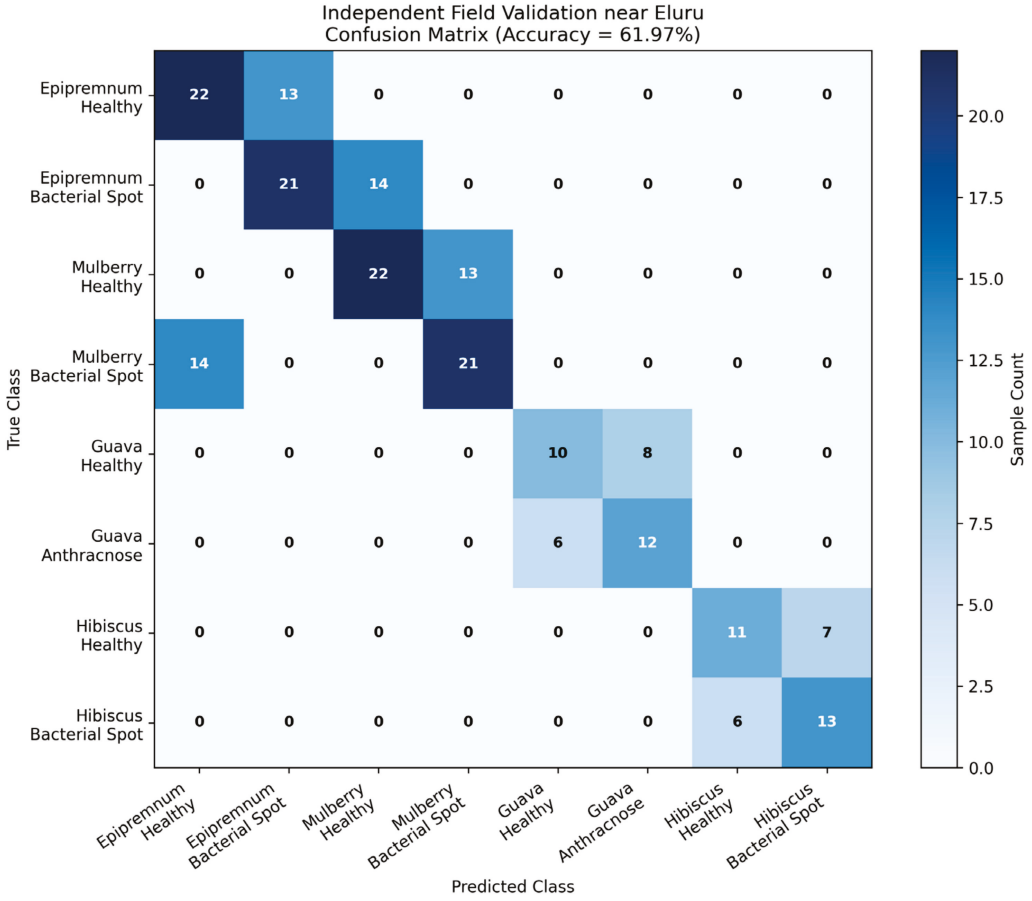

Figure 7. Class-Wise Classification Performance of the Proposed Model Represented as a Confusion Matrix.

Table 2 summarizes the class-wise performance of the proposed framework during independent field validation near Eluru. Recall values ranged from 55.56% to 68.42%, indicating moderate success in correctly identifying healthy and diseased leaf samples under real-world conditions. Specificity values ranged from 92.13% to 96.92%, indicating a strong ability to distinguish target classes from non-target classes despite environmental variability. The highest recall and F1-score were achieved for Hibiscus bacterial spot (68.42% and 66.67%, respectively), while Guava Healthy exhibited the lowest recall (55.56%). Overall, the relatively high specificity combined with moderate recall and F1-scores suggests that the model maintained good discriminative capability but experienced reduced sensitivity under field conditions. These findings are consistent with the effects of domain shift, background complexity, illumination variation, and differences in disease symptom expression between benchmark and real-world agricultural environments.

https://doi.org/10.3390/su18136867

Table 2. Class-wise performance metrics obtained from five-fold cross-validation.

Class	Recall (%)	Specificity (%)	F1-Score (%)
Epipremnum healthy	62.86	92.13	61.97
Epipremnum bacterial spot	60.00	92.70	60.87
Mulberry healthy	62.86	92.13	61.97
Mulberry bacterial spot	60.00	92.70	60.87
Guava healthy	55.56	96.92	58.82
Guava anthracnose	66.67	95.90	63.16
Hibiscus healthy	61.11	96.92	62.86
Hibiscus bacterial spot	68.42	96.39	66.67

The resulting confusion matrix yielded an overall test accuracy of 61.97%, corresponding to 86 correctly classified samples and 54 misclassifications out of 140 field-collected leaf images. A detailed examination of the confusion matrix reveals several notable misclassification patterns. For Epipremnum aureum, 22 healthy leaves were correctly identified, whereas 13 healthy samples were misclassified as bacterial spot-infected leaves. Similarly, 21 bacterial spot-infected leaves were correctly classified, while 14 samples were incorrectly assigned to the Mulberry Healthy category. For Mulberry, 22 healthy leaves were correctly recognized, whereas 13 samples were misclassified as Mulberry bacterial spot. In addition, 21 bacterial spot-infected leaves were correctly classified, while 14 were incorrectly identified as Epipremnum Healthy.

These results highlight the challenges associated with cross-species disease recognition under real-world field conditions. Confusion was particularly evident between healthy and diseased categories, likely due to similarities in visual symptom expression, varying stages of disease progression, heterogeneous backgrounds, illumination changes, and environmental variability present in open-field imagery. Similar observations have been reported in previous studies, where models trained on controlled benchmark datasets such as PlantVillage achieved very high classification accuracies exceeding 99% [6,18] but experienced substantial performance degradation when evaluated on independent field datasets due to domain shift, intra-class variability, and differences in image acquisition conditions. These findings emphasize the importance of incorporating field-specific data and environmental information to improve model robustness and generalization in practical agricultural monitoring systems.

In the following table, we present a few striking examples of healthy and diseased leaves retrieved from an open field and analyzed using our hybrid framework combining deep learning-based disease classification and IoT-enabled environmental monitoring. Table 3 shows various leaves, both healthy and unhealthy, and how the present hybrid approach differentiated crop category, health status, and disease class. The table also includes a remarks column in which possible reasons for correct or incorrect identification are explained.

Table 2 summarizes results for *Epipremnum aureum* and mulberry leaves under open-field conditions. For *E. aureum*, healthy leaves were consistently identified despite natural variegation, confirming the model's ability to distinguish pigmentation from pathological lesions [1,2]. Diseased *E. aureum* with Bacterial Leaf Spot was correctly classified, as CNN-BiGRU effectively captured lesion-specific textures [3]. In mulberry, healthy leaves were correctly classified (Rows 5–6), but diseased samples were misidentified. Likely causes include background bias (desk texture learned instead of leaf features) [4] and loss of disease cues under complete necrosis, reducing inter-class separability [5]. These findings highlight that while CNN-BiGRU performs well on variegated and spot-type lesions, it struggles with advanced necrosis and background interference, emphasizing the need for background-invariant training and progressive disease datasets.

https://doi.org/10.3390/su18136867

Table 3. Evaluation of CNN-BiGRU Model for Classification of Healthy and Diseased Leaf Images from Open Field Crops.

S. No	Classification				
	Leaf Images Retrieved from Open Field	**Crop Category**	**Healthy vs. Diseased**	**Disease Class**	**Remarks**
1.		*Epipremnum aureum*	Healthy	Not Applicable	Correctly identified
2.		*Epipremnum aureum*	Healthy	Not Applicable	Correctly identified.
3.		*Epipremnum aureum*	Healthy	Not Applicable	Correctly identified, though a mix of dark green and light green could appear here and there.
4.		*Epipremnum aureum*	Not Applicable	Unhealthy and the identified disease was bacterial leaf spot.	Identified correctly. The model correctly identified Bacterial Leaf Spot due to distinct lesion patterns and effective CNN-BiGRU feature learning.
5.		*Mulberry*	Healthy	Not Applicable	Correctly identified
6.		*Mulberry*	Healthy	Not Applicable	Correctly identified

https://doi.org/10.3390/su18136867

Table 3. *Cont.*

S. No	Classification				
	Leaf Images Retrieved from Open Field	**Crop Category**	**Healthy vs. Diseased**	**Disease Class**	**Remarks**
7.		*Mulberry*	Not Applicable	Unhealthy	The model did not identify correctly. The probable reasons could be due to the fact that the model may have learned desk color/texture cues instead of leaf cues.
8.		*Mulberry*	Not Applicable	Unhealthy	The model did not identify correctly. The probable reasons could be that disease-specific features are lost in complete necrosis, and class definitions are too narrow, forcing wrong predictions.
9.		*Guava* (*Psidium guajava*)	Healthy	Not Applicable	Correctly identified
10.		*Guava* (*Psidium guajava*)	Not Applicable	Anthracnose	Correctly Identified
11.		*Hibiscus* (*Hibiscus rosa-sinensis*).	Healthy	Not Applicable	Correctly identified.
12.		*Hibiscus* (*Hibiscus rosa-sinensis*).	Not Applicable	Unhealthy, and the identified disease was Bacterial Leaf Spot.	Correctly identified.

The results in Table 3 show that while the CNN–BiGRU framework performs effectively on variegated and spot-type lesions, it struggles with advanced necrosis and background interference, highlighting the need for background-invariant training and progressive disease datasets. A recent engineering-driven study using Retinex, RPN, and

transmission modules reported improved accuracy, though such approaches remain non-organic in scope [42]. Importantly, most current works emphasize detection only after visible symptom onset, whereas transforming leaf images into thermal signatures may enable earlier disease diagnosis through pre-symptomatic temperature variations.

An IoT-based system incorporating an Arduino microcontroller was employed to record soil and environmental parameters at one-minute intervals, including humidity, temperature, pH, nitrogen (N), phosphorus (P), and potassium (K), during the vegetative growth stage [29]. It is worth mentioning that soil and microclimatic measurements are not incorporated as inputs to the CNN–BiGRU classification architecture. Instead, these variables are collected independently and analyzed separately to investigate potential causes of performance variation and reduced model generalization observed during field deployment. A comparison between temperature and humidity measurements obtained from the Arduino sensors and those provided by the India Meteorological Department (IMD, https://mausam.imd.gov.in/) revealed a strong agreement, demonstrating one-to-one similarity.

Figure 8 shows the Pearson correlation matrix with statistical significance, illustrating the relationship between environmental stressors and CNN–BiGRU model accuracy over a 10-day (from 9 July to 18 July 2025) monitoring period in Eluru, India. The Pearson correlation analysis reveals statistically significant relationships between in situ environmental stressors and the classification performance of the CNN–BiGRU model over the 10-day monitoring period in Eluru. A strong negative correlation was observed between soil moisture and model accuracy ($r = -0.89$, $p < 0.001$), indicating that elevated moisture levels substantially degrade classification performance under field conditions. Similarly, soil pH exhibited a significant negative association with accuracy ($r = -0.77$, $p < 0.01$), suggesting that variations in soil chemical properties influence disease manifestation and, consequently, feature discriminability.

The strong negative correlation observed between soil moisture and classification accuracy may be attributed to a combination of biological and imaging-related factors. Increased soil moisture can influence disease development and symptom expression, leading to variations in lesion morphology, color distribution, and tissue characteristics that differ from those represented in the training dataset. Furthermore, high-moisture environments are often associated with increased humidity, leaf wetness, specular reflections, and illumination variability, which may affect image acquisition and feature extraction. Therefore, the observed relationship likely reflects both physiological changes in disease manifestation and environmental factors influencing image quality, rather than a single causal mechanism. The strong negative correlation observed between soil moisture and classification accuracy may be attributed to a combination of biological and imaging-related factors. Increased soil moisture can influence disease development and symptom expression, leading to variations in lesion morphology, color distribution, and tissue characteristics that differ from those represented in the training dataset.

Furthermore, high-moisture environments are often associated with increased humidity, leaf wetness, specular reflections, and illumination variability, which may affect image acquisition and feature extraction. Therefore, the observed relationship likely reflects both physiological changes in disease manifestation and environmental factors influencing image quality, rather than a single causal mechanism. The observed correlations between soil parameters and disease classification performance can be explained by their influence on plant physiology and symptom development. Soil moisture plays a critical role in pathogen proliferation and disease progression, often increasing lesion formation and symptom severity under favorable conditions. Likewise, nutrient availability, particularly nitrogen, phosphorus, and potassium, directly affects chlorophyll synthesis, photosynthetic activity,

https://doi.org/10.3390/su18136867

cell wall strength, and plant defense mechanisms. Deficiencies or imbalances in these nutrients can alter leaf coloration, texture, and lesion expression, thereby affecting the visual features used for disease classification. Soil pH further influences nutrient availability and rhizosphere microbial activity, which indirectly affects plant health and susceptibility to infection. Consequently, variations in soil conditions can modify the visibility and intensity of disease symptoms, explaining their relationship with the classification accuracy observed in this study.

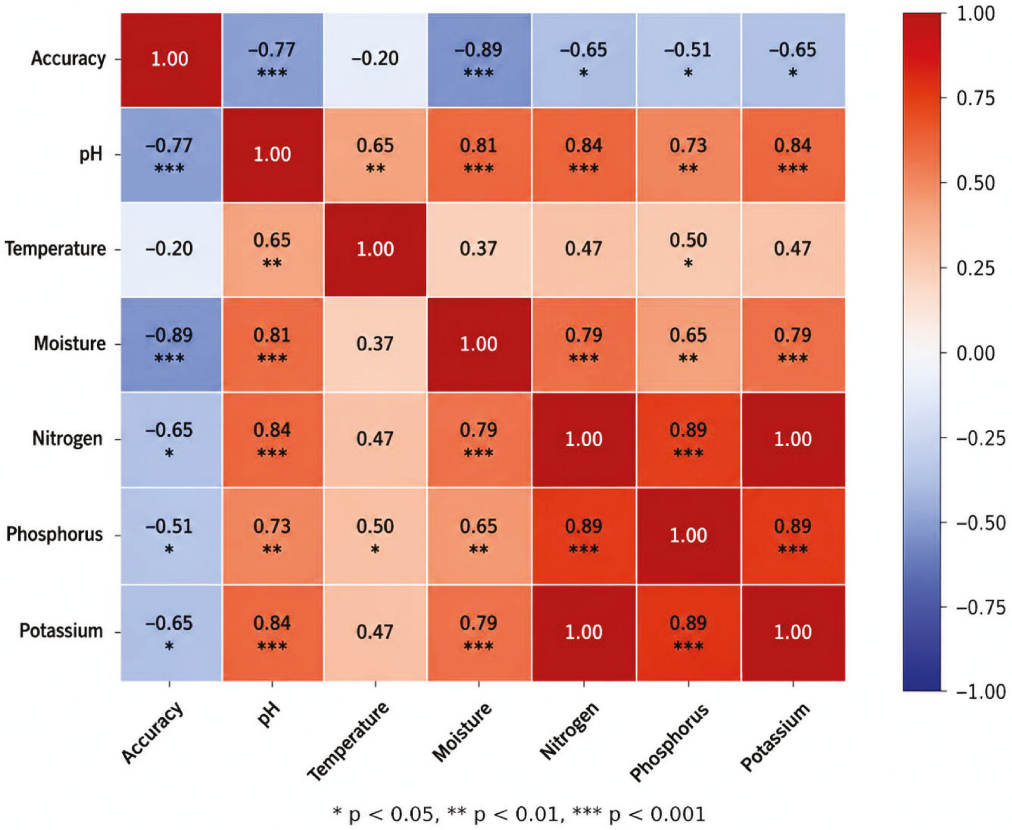

Figure 8. Correlation matrix showing the relationships between classification accuracy and measured soil parameters (pH, temperature, moisture, nitrogen, phosphorus, and potassium). A diverging color scale centered at zero is used, where blue indicates negative correlations, red indicates positive correlations, and white represents weak or negligible correlations. Statistical significance levels are denoted by asterisks (* $p < 0.05$, ** $p < 0.01$, *** $p < 0.001$).

Nutrient parameters, particularly nitrogen and potassium, also demonstrated moderate negative correlations with accuracy ($r \approx -0.65$, $p < 0.05$), highlighting the role of nutrient dynamics in altering plant physiological responses and visual disease characteristics. In contrast, temperature showed a comparatively weaker and statistically non-significant relationship with model performance ($r = -0.20$), indicating a secondary influence relative to soil-driven factors. Furthermore, strong positive intercorrelations among N, P, and K ($r > 0.85$) confirm the coupled nature of soil nutrient dynamics, consistent with established soil chemistry principles. These findings collectively explain the observed decline in model accuracy to approximately 61.97% when evaluated on real-world field images, emphasizing the critical impact of environmental variability on deep learning model generalization in agricultural applications. Similar observations have been reported in recent studies, in which environmental heterogeneity and domain shifts significantly affect the robustness of deep learning-based plant disease detection models [5,6].

To elaborate on this further, the substantial reduction in classification accuracy from 99.8% on the PlantVillage benchmark dataset to 61.97% on field-acquired images indicates

a significant domain shift between controlled laboratory conditions and real-world agricultural environments. PlantVillage images are typically captured under homogeneous backgrounds, controlled illumination, and limited environmental variability, enabling deep learning models to learn highly discriminative disease features. In contrast, field images are characterized by complex backgrounds, non-uniform illumination, shadows, occlusions, variations in camera viewpoints, and heterogeneous environmental conditions, all of which adversely affect model generalization [5,18].

Beyond imaging conditions, disease symptoms observed under natural environments often exhibit considerable variability in lesion morphology, color intensity, severity levels, and progression stages. Similar visual symptoms may arise from multiple biotic and abiotic stressors, including nutrient deficiencies, water stress, temperature fluctuations, and pathogen interactions, making disease discrimination substantially more challenging in field settings [18]. Consequently, models trained predominantly on benchmark datasets may learn dataset-specific visual representations that do not fully capture the diversity of real-world symptom manifestations.

Furthermore, the field evaluation involved plant species such as *Epipremnum aureum* and *Mulberry*, whereas model training was conducted primarily using tomato, potato, and pepper leaf images from the PlantVillage dataset. This introduces a cross-crop domain shift associated with differences in leaf morphology, venation structures, texture patterns, pigmentation, and disease expression characteristics. Previous studies have reported that deep learning models trained on a limited set of crop species frequently experience performance degradation when applied to unseen crops or field environments due to distributional differences between training and deployment data [42].

In addition, environmental variables such as soil moisture, nutrient availability, pH, temperature, and humidity can influence both plant physiology and disease progression, thereby altering the visual appearance of symptoms. The correlation analysis conducted in this study suggests that environmental conditions may contribute to symptom heterogeneity and consequently affect classification performance. These findings emphasize the need for domain adaptation techniques, diverse field-based training datasets, and multimodal learning frameworks that integrate image features with environmental and soil parameters to improve robustness and generalization under real-world agricultural conditions. Table 4 shows a comparative performance analysis of the state-of-the-art methods with the present model.

Table 4. Comparative Performance Analysis of the State-of-the-art Methods.

COMPARISON GROUP	REFERENCE	CROP/ DATASET	MODEL	PERFORMANCE	PROS AND CONS
RICE DISEASE DETECTION	Lu et al. (2023) [41]	Rice	CNN–BiGRU	98.21	Pros: Captures both spatial and sequential features with enhanced attention, yielding very high accuracy. **Cons:** Increased model complexity and computational cost may limit scalability in real-time field applications.
RICE DISEASE DETECTION	Wang et al. (2024) [35]	Rice	DC-GAN+MDF C-ResNet	95.99%	**Pros:** Higher Accuracy, Robust across climates. **Cons**: Model's complexity hinders lightweight deployment; BO adds computational cost.

Table 4. *Cont.*

COMPARISON GROUP	REFERENCE	CROP/ DATASET	MODEL	PERFORMANCE	PROS AND CONS
WHEAT YIELD PREDICTION	Zhang et al., (2024) [43]	Winter wheat	BO-CNN-BiLSTM	R^2 81%	**Pros:** High accuracy, Robust to complex backgrounds, Fewer training parameters. **Cons:** Added sequence module increases model complexity/latency.
TOMATO LEAF DISEASE/ IDENTIFICATION	Ledbin Vini & Rathika (2025) [44]	Tomato	Trio Conv TomatoNet + Bi-LSTM	99.65-99.83%	**Pros:** Strong fine-grained discrimination; better sample quality; training stability. **Cons:** Higher computational cost; GAN training overhead; Reliance on heavy preprocessing
TOMATO LEAF DISEASE/ IDENTIFICATION	Zhou et al. (2021) [45]	Tomato	RDN-based Hybrid DL	95%	**Pros:** High accuracy with efficient parameter usage and better gradient flow. **Cons:** Model re-structuring is complex, and dataset-specific adaptability may be limited.
TOMATO SEED CULTIVAR CLASSIFICATION	Sabanci (2023) [46]	Tomato seed	MobileNetV2 + BiLSTM	96%	**Pros**: Higher accuracy; Robust to subtle inter-class differences. **Cons**: Complex pipeline; Higher compute/memory; Potential overfitting without careful regularization.
POTATO LEAF DISEASE	Arshad et al. (2023) [47]	Potato	PLDPNet	98.66%	**Pros:** High Accuracy, Hybrid Feature Fusion and Vision Transformer Integration. **Cons:** Computationally Intensive, Complex Architecture, Limited Practical Deployment.
POTATO & TOMATO DATASET	Asghar et al. (2025) [48]	Potato and Tomato	HPDC-Net	99%	**Pros:** Lightweight and Compact, High Efficiency. **Cons:** Since the datasets use lab-controlled images, they lack real-world variability and complexity.
COTTON DISEASE DETECTION	Haider et al. (2024) [49]	Cotton	NRB-BiUNet	95.22%	**Pros:** Lightweight model, Robust Architecture. **Cons:** Reduced Prediction Time Limited Scope of diseases, Preprocessing overhead
CUCUMBER CLASSIFICATION	Zhang & Wang (2023) [10]	Cucumber	BBGCAP	F1 92.66%	**Pros:** Improved accuracy, Rich semantic understanding, and Sequential dependency capture. **Cons:** High complexity, Slower training, Limited generalization
PRESENT WORK	Present Research	Pepper/Potato/ Tomato	CNN-BiGRU	99.8%	**Pros:** The CNN–Bi-GRU with U^2-Net achieves 99.8% accuracy on PlantVillage benchmark; employs architecturally parameter-efficient components (MobileNet V2 depthwise separable convolutions, Bi-GRU reduced gating) and robust spatio-contextual feature learning. **Cons:** Significant performance degradation under domain shift (99.8% benchmark vs. 61.97% field accuracy); field evaluation involved cross-species inference beyond the training distribution; computational complexity metrics (FLOPs, parameters, inference latency) not empirically evaluated; IoT soil data analyzed independently rather than integrated into the classification pipeline.

It is important to note that the present study does not claim universal cross-species generalization. Although the proposed framework exhibited promising results on independent field samples, these experiments should be regarded as an initial cross-domain validation rather than definitive evidence of species-independent performance. Further, large-scale studies involving diverse crop species, disease manifestations, environmental conditions, and imaging scenarios are required before broader generalization claims can be established with confidence.

It is worth mentioning here that the model was not retrained on the field species, and the field test was designed to measure the magnitude and correlates of the lab-to-field performance gap rather than to establish species-independent classification efficacy.

3.3. Soil–Disease Mechanism

Soil and environmental conditions play a critical role in disease development by influencing both pathogen activity and host plant responses. Soil moisture is particularly important because elevated moisture levels can enhance pathogen survival, spore germination, dispersal, and infection efficiency, thereby increasing disease severity in many plant-pathogen systems. Likewise, nutrient availability, especially nitrogen, phosphorus, and potassium, affects plant metabolism, immune responses, and susceptibility to disease. Nutrient imbalances may alter symptom expression, resulting in variations in lesion morphology, chlorosis, necrosis, and tissue discoloration. Soil pH further regulates nutrient availability and microbial community composition, indirectly influencing disease incidence and progression. Consequently, environmental conditions can substantially modify the visual manifestation of disease symptoms observed on leaves. Since deep learning models rely primarily on visual features, changes in symptom appearance induced by soil and environmental variability may contribute to reduced classification performance when models trained on controlled benchmark datasets are applied to field conditions. These findings highlight the importance of incorporating environmental context into future multimodal disease prediction frameworks [50].

4. Conclusions

The proposed smart neural network delivers high classification accuracy with acceptable latency and model size for edge deployment. Its structure effectively captured spatial and sequential lesion features. Comparative analysis confirms that transformer-based models (MobileViT, Swin-Tiny) are promising but still slightly outperformed by architectures when dealing with complex real-world leaf disease patterns. The results further show that integrating robust U^2-Net-based segmentation with the classification framework substantially improves disease localization and feature extraction, leading to enhanced predictive reliability. Owing to the use of MobileNetV2 as the feature extraction backbone, the proposed architecture remains relatively compact compared with many conventional deep CNN models.

The proposed CNN–Bi-GRU framework demonstrated strong classification performance on the PlantVillage benchmark dataset and provided valuable insights into the challenges associated with deploying disease detection models under real-world field conditions. The results highlight the effectiveness of combining segmentation and hybrid deep learning architectures for plant disease classification while also revealing the significant impact of environmental variability and dataset domain shift on model generalization. These findings contribute to the ongoing development of intelligent plant disease monitoring systems and provide a foundation for future research aimed at improving robustness, adaptability, and practical deployment in precision agriculture environments.

https://doi.org/10.3390/su18136867

However, there are a number of limitations at the current stage that need to be addressed in future work. First, when tested on a set of images taken under conditions different from the images used for training, the model's accuracy is reduced substantially, to a mere 61.97%. It is important to note that this accuracy is much higher than that based on random selection of 38 classes (2.6%), but a more diverse set of training data is needed to improve the accuracy. Our current results indicate that more (and more variable) data alone will be sufficient to substantially increase the accuracy, and corresponding data collection efforts are underway.

5. Limitations and Future Scope

While the proposed CNN–Bi-GRU framework demonstrated excellent performance on the PlantVillage benchmark dataset, the observed reduction in accuracy under real-field conditions highlights the challenges associated with environmental variability and domain shift. In the present study, soil and environmental parameters, including pH, soil moisture, temperature, and NPK concentrations, were collected using an IoT-based monitoring system and analyzed to investigate their relationship with disease occurrence and model generalization. However, these parameters were not directly incorporated into the disease classification network as predictive inputs. As a result, the current framework should be regarded as an image-based disease classification system supplemented by environmental analysis rather than a true multimodal disease prediction model. Although the correlation analysis provided valuable insights into the influence of soil and microclimatic conditions on disease development and model performance, the direct integration of environmental information with image-derived features was beyond the scope of the present work.

Nevertheless, future research will focus on developing multimodal learning architectures that jointly exploit visual, soil, and environmental data. Feature-level fusion approaches may combine deep image embeddings extracted from convolutional neural networks with IoT-derived soil attributes, while decision-level fusion strategies may integrate predictions from independent image-based and environmental models. Such multimodal frameworks have the potential to provide complementary information for disease diagnosis, improve robustness against variations in illumination, background complexity, and field conditions, and enhance generalization across diverse agricultural environments.

Secondly, the PlantVillage dataset and the field-collected dataset differ substantially in terms of plant species, imaging conditions, disease manifestations, and environmental variability. Therefore, the field evaluation performed in this study should be regarded as a preliminary cross-domain robustness assessment rather than a direct validation of species-independent generalization. While the proposed framework demonstrated encouraging performance on the independent field samples, further validation using larger multi-species and multi-environment datasets is required before broader generalization claims can be established. Future research will focus on domain adaptation strategies and extensive field-scale evaluations to further assess the transferability of the proposed approach.

A limitation of the present study is that image-based disease classification and IoT-derived soil measurements were analyzed independently rather than through a unified multimodal learning framework. Consequently, the environmental data were used to interpret field-level performance variations rather than directly enhancing classification predictions. Nevertheless, the study demonstrates the value of environmental monitoring for understanding model robustness and provides a practical baseline for future sensor-image fusion approaches in smart agriculture.

The field evaluation near Eluru should be interpreted as a cross-domain stress test rather than a species-specific validation experiment, since the CNN–Bi-GRU model was trained on PlantVillage images of tomato, potato, and pepper, while the field dataset

https://doi.org/10.3390/su18136867

comprised entirely different species, including *Epipremnum aureum*, *Mulberry*, *Guava*, and *Hibiscus*. Accordingly, the observed field accuracy of 61.97% reflects the combined effect of cross-species morphological differences, imaging conditions, and background complexity, rather than a direct measure of disease classification robustness within any single target species. Future work will focus on domain adaptation and transfer learning with target-domain fine-tuning, supported by annotated multi-species field datasets spanning diverse crop types, disease severities, and agro-climatic conditions, before broader generalization claims can be established with confidence.

Although the proposed U^2-Net-assisted MobileNetV2–BiGRU framework achieved high classification accuracy on benchmark and field datasets, a detailed computational complexity analysis was not conducted. Metrics such as trainable parameters, FLOPs, memory usage, and inference latency were not evaluated. Future work will quantify these metrics and assess deployment performance on edge devices such as Raspberry Pi, NVIDIA Jetson, and mobile platforms for real-time smart agriculture applications.

Incorporating additional environmental variables, such as humidity, rainfall, solar radiation, and remotely sensed vegetation indices, may facilitate the development of comprehensive disease forecasting systems capable of supporting precision agriculture and real-time crop health management. Therefore, multimodal joint prediction represents a promising extension of the proposed framework and an important direction for future investigation.

Another limitation of the proposed CNN–Bi-GRU framework is that the recurrent module operates on ordered feature representations derived from convolutional feature maps rather than on naturally occurring temporal sequences. Although this design enables the Bi-GRU to capture contextual relationships among extracted features, the resulting sequence is an artificial representation of spatial information and does not correspond to temporal disease progression. Consequently, the recurrent modeling component should be interpreted as a feature refinement mechanism rather than a true temporal learning framework. Future research will investigate attention-based and transformer-based architectures that can model long-range spatial dependencies directly without requiring the construction of sequential feature representations. Although U^2-Net effectively removed background regions and improved classification performance, quantitative segmentation evaluation using metrics such as IoU and Dice Coefficient was not performed due to the absence of manually annotated ground-truth masks. Future work will include the creation of annotated segmentation datasets to facilitate comprehensive evaluation of the segmentation module.

A further limitation of the present study is the relatively modest size of the field dataset used for robustness evaluation. Although the dataset was collected under realistic environmental conditions and included representative healthy and diseased leaf samples, larger datasets encompassing broader variations in crop species, disease severity, environmental conditions, and imaging scenarios would provide a more comprehensive assessment of model generalization.

Supplementary Materials: The following supporting information can be downloaded at: https://www.mdpi.com/article/10.3390/su18136867/s1, Figure S1: Temporal variations in soil and environmental parameters (pH, temperature, moisture, and NPK) recorded over 10 days (from 9 July to 18 July 2025) in Eluru, India. Table S1: Ablation study of the U^2-Net-MobileNetV2-Bi-GRU Framework for Plant Leaf Disease Classification.

Author Contributions: J.T. conducted the main research and collected, analyzed, and interpreted the data. N.M. conceived the idea and developed the theory, supervised the research, and reviewed and edited the manuscript before submission. P.S.B. drafted the manuscript and revised it critically. All authors have read and agreed to the published version of the manuscript.

https://doi.org/10.3390/su18136867

Funding: This research received no external funding.

Institutional Review Board Statement: Not applicable.

Informed Consent Statement: Not applicable.

Data Availability Statement: Data are contained within this present article or as part of the Supplementary Files.

Acknowledgments: The authors acknowledge Vel Tech Rangarajan Sagunthala R&D Institute of Science, Technology, and Shri Vishnu Engineering College for Women (A), Bhimavaram, India, for providing infrastructural facilities that enabled us to carry out this research work.

Conflicts of Interest: The authors declare no conflicts of interest.

References

1. Liu, J.; Wang, X. Plant diseases and pests detection based on deep learning: A review. *Plant Methods* **2021**, *17*, 22. [CrossRef] [PubMed]
2. Lu, J.-Y.; Chang, C.-L.; Kuo, Y.-F. Monitoring Growth Rate of Lettuce Using Deep Convolutional Neural Networks. In Proceedings of the 2019 ASABE Annual International Meeting, Boston, MA, USA, 7–10 July 2019. [CrossRef]
3. Charisis, C.; Argyropoulos, D. Deep Learning-Based Instance Segmentation Architectures in Agriculture: A Review of the Scopes and Challenges. *Smart Agric. Technol.* **2024**, *8*, 100448. [CrossRef]
4. Zhao, S.; Peng, Y.; Liu, J.; Wu, S. Tomato leaf disease diagnosis based on improved convolution neural network by attention module. *Agriculture* **2021**, *11*, 651. [CrossRef]
5. Mohanty, S.P.; Hughes, D.P.; Salathé, M. Using deep learning for image-based plant disease detection. *Front. Plant Sci.* **2016**, *7*, 1419. [CrossRef] [PubMed]
6. Ferentinos, K.P. Deep learning models for plant disease detection and diagnosis. *Comput. Electron. Agric.* **2018**, *145*, 311–318. [CrossRef]
7. Lee, S.H.; Goëau, H.; Bonnet, P.; Joly, A. Attention-based recurrent neural network for plant disease classification. *Front. Plant Sci.* **2020**, *11*, 601250. [CrossRef] [PubMed]
8. Jain, S.; Ramesh, D. AI-based hybrid CNN-LSTM model for crop disease prediction: An ML advent for rice crop. In *Proceedings of the 12th International Conference on Computing Communication and Networking Technologies (ICCCNT), Kharagpur, India, 6–8 July 2021*; IEEE: New York, NY, USA, 2021; pp. 1–7. [CrossRef]
9. Devi, E.; Gopi, S.; Padmavathi, U.; Arumugam, S.R.; Premnath, S.; Muralitharan, D. Plant Disease Classification using CNN-LSTM Techniques. In *Proceedings of the 5th International Conference on Smart Systems and Inventive Technology (ICSSIT), Tirunelveli, India, 23–25 January 2023*; IEEE: New York, NY, USA, 2023; pp. 1225–1229. [CrossRef]
10. Zhang, T.; Wang, D. Classification of crop disease-pest questions based on BERT-BiGRU-CapsNet with attention pooling. *Front. Plant Sci.* **2023**, *14*, 1300580. [CrossRef] [PubMed]
11. Khan, I.R.; Sangari, M.S.; Shukla, P.K.; Aleryani, A.; Alqahtani, O.; Alasiry, A.; Alouane, M.T.-H. An Automatic-Segmentation- and Hyper-Parameter-Optimization-Based Artificial Rabbits Algorithm for Leaf Disease Classification. *Biomimetics* **2023**, *8*, 438. [CrossRef]
12. Qin, X.; Zhang, Z.; Huang, C.; Dehghan, M.; Zaiane, O.R.; Jagersand, M. U^2-Net: Going deeper with nested U-structure for salient object detection. *Pattern Recognit.* **2020**, *106*, 107404. [CrossRef]
13. Ronneberger, O.; Fischer, P.; Brox, T. U-Net: Convolutional Networks for Biomedical Image Segmentation. In *Medical Image Computing and Computer-Assisted Intervention—MICCAI 2015*; Navab, N., Hornegger, J., Wells, W., Frangi, A., Eds.; Lecture Notes in Computer Science; Springer: Cham, Switzerland, 2015. [CrossRef]
14. Hughes, D.P.; Salathé, M. An open access repository of images on plant health to enable the development of mobile disease diagnostics. *arXiv* **2015**, arXiv:1511.08060. [CrossRef]
15. Singh, D.; Jain, N.; Jain, P.; Kayal, P.; Kumawat, S.; Batra, N. Plantdoc: A dataset for visual plant disease detection. In *Proceedings of the 7th ACM IKDD CoDS and 25th COMAD, Hyderabad, India, 5–7 January 2020*; ACM: New York, NY, USA, 2020; pp. 249–253. [CrossRef]
16. Goëau, H.; Martellucci, G.; Bonnet, P.; Vinatier, F.; Joly, A. PlantCLEF2025 @ LifeCLEF & CVPR-FGVC. 2025. Available online: https://kaggle.com/competitions/plantclef-2025 (accessed on 17 March 2026).
17. Das, A.; Pathan, F.; Jim, J.R.; Kabir, M.; Mridha, M. Deep Learning-Based Classification, Detection, and Segmentation of Tomato Leaf Diseases: A State-of-the-Art Review. *Artif. Intell. Agric.* **2025**, *15*, 192–220. [CrossRef]
18. Barbedo, J.G.A. Plant disease identification from individual lesions and spots using deep learning. *Biosyst. Eng.* **2019**, *180*, 96–107. [CrossRef]

19. Padhi, J.; Mishra, K.; Ratha, A.K.; Behera, S.K.; Sethy, P.K.; Nanthaamornphong, A. Enhancing Paddy Leaf Disease Diagnosis -a Hybrid CNN Model Using Simulated Thermal Imaging. *Smart Agric. Technol.* **2025**, *10*, 100814. [CrossRef]
20. Bhaskar, N.; A, P.C.; Tupe-Waghmare, P.; Shetty, P.; Shetty, S.S.; Rai, T. A deep learning hybrid approach for automated leaf disease identification in paddy crops. In *Proceedings of the International Conference on Distributed Computing and Optimization Techniques (ICDCOT), Bengaluru, India, 15–16 March 2024*; IEEE: New York, NY, USA, 2024; pp. 1–5. [CrossRef]
21. Sidana, S. Towards Sustainable Agriculture: A Transformer-based Hybrid Model for Advanced Leaf Disease Classification. In *Proceedings of the 15th International Conference on Computing Communication and Networking Technologies (ICCCNT), Kamand, India, 24–28 June 2024*; IEEE: New York, NY, USA, 2024; pp. 1–6. [CrossRef]
22. Kumar, R.R.; Chauhan, R.; Dhondiyal, S.A.; Singh, A. Deep Learning-Driven Diagnosis: A CNN-SVM Hybrid Approach for Automated Detection of Strawberry Leaf Diseases. In *Proceedings of the IEEE 3rd World Conference on Applied Intelligence and Computing (AIC), Gwalior, India, 27–28 July 2024*; IEEE: New York, NY, USA, 2024; pp. 1467–1470. [CrossRef]
23. Esomonu, N.F.; Eze, U.F.; John-Otumu, A.M.; Ayogu, I.I.; Nwokonkwo, O.C.; Oshoiribhor, E.O.; Okolie, S.A.; Nwokorie, E.C.; Mbamala, C.V.; Dokun, O. A Hybrid Model using MobileNetv2 and SVM for Enhanced Classification and Prediction of Tomato Leaf Diseases. *SSRG Int. J. Electr. Electron. Eng.* **2023**, *10*, 37–50. [CrossRef]
24. Anwar, B.; Hegazy, I.; Mabrouk, M.; Elarif, T.; Taha, Z. Hybrid cnn-rnn architecture for accurate tomato disease diagnosis with xception-gru. *Int. J. Intell. Comput. Inf. Sci.* **2024**, *24*, 60–72. [CrossRef]
25. Shafik, W.; Tufail, A.; Liyanage De Silva, C.; Apong, R.A.A.H.M. A novel hybrid inception-xception convolutional neural network for efficient plant disease classification and detection. *Sci. Rep.* **2025**, *15*, 3936. [CrossRef] [PubMed]
26. Karunanithi, A.; Singh, A.S.; Kannapiran, T. Enhanced hybrid neural networks (Coatnet) for paddy crops disease detection and classification. *Rev. d'Intell. Artif.* **2022**, *36*, 671–679. [CrossRef]
27. Murugesan, S.; Chinnadurai, J.; Srinivasan, S.; Mathivanan, S.K.; Chandan, R.R.; Moorthy, U. Robust multiclass classification of crop leaf diseases using hybrid deep learning and Grad-CAM interpretability. *Sci. Rep.* **2025**, *15*, 29955. [CrossRef] [PubMed]
28. Babu, A.N.; Blossom, M.C.; Praneetha, A.; Shirisha, P.; Kishore, P.M.; Mounika, F.M.; Kumar, G.A.; Brahmanandam, P.S. Internet of Things (IoT) based Pesticide Spraying Robot—A Revolution in Smart Farming. *Indian J. Sci. Technol.* **2023**, *16*, 1676–1681. [CrossRef]
29. Babu, G.R.; Gokuldhev, M.; Brahmanandam, P.S. Integrating IoT for Soil Monitoring and Hybrid Machine Learning in Predicting Tomato Crop Disease in a Typical South India Station. *Sensors* **2024**, *24*, 6177. [CrossRef] [PubMed]
30. Thirupathi, J.; Malarvizhi, N.; Brahmanandam, P.S. Citrus fruit detection and classification: Field-based images and FIDS-30 dataset. *Multidiscip. Sci. J.* **2025**, *7*, 2025582. [CrossRef]
31. Zhang, K.; Wu, Q.; Liu, A.; Meng, X. Can deep learning identify tomato leaf disease? *Adv. Multimed.* **2018**, *2018*, 6710865. [CrossRef]
32. Lin, T.; Goyal, P.; Girshick, R.; He, K.; Dollár, P. Focal loss for dense object detection. In *Proceedings of the IEEE International Conference on Computer Vision (ICCV), Venice, Italy, 22–29 October 2017*; IEEE: New York, NY, USA, 2017; pp. 2980–2988. [CrossRef]
33. Too, E.C.; Yujian, L.; Njuki, S.; Yingchun, L. A comparative study of fine-tuning deep learning models for plant disease identification. *Comput. Electron. Agric.* **2019**, *161*, 272–279. [CrossRef]
34. Shorten, C.; Khoshgoftaar, T.M. A survey on image data augmentation for deep learning. *J. Big Data* **2019**, *6*, 60. [CrossRef]
35. Wang, Y.; Dhamodharan, R.U.S.; Sarwar, N.; Almalki, F.A.; Naith, Q.H. A hybrid approach for rice crop disease detection in agricultural IoT system. *Discov. Sustain.* **2024**, *5*, 99. [CrossRef]
36. Wang, J.; Jia, J.; Zhang, Y.; Wang, H.; Zhu, S. RAAWC-UNet: An apple leaf and disease segmentation method based on residual attention and atrous spatial pyramid pooling improved UNet with weight compression loss. *Front. Plant Sci.* **2024**, *15*, 1305358. [CrossRef] [PubMed]
37. Chung, J.; Gulcehre, C.; Cho, K.; Bengio, Y. Empirical evaluation of gated recurrent neural networks on sequence modeling. *arXiv* **2014**, arXiv:1412.3555v1. [CrossRef]
38. Bouchane, M.; Guo, W.; Yang, S. Hybrid CNN-GRU models for improved EEG motor imagery classification. *Sensors* **2025**, *25*, 1399. [CrossRef] [PubMed]
39. Kanakala, S.; Ningappa, S. Detection and classification of diseases in multi-crop leaves using LSTM and CNN models. *J. Innov. Image Process.* **2025**, *7*, 161–181. [CrossRef]
40. Syed, K.; Asiya Begum, S.S.; Palakayala, A.R.; Vidya Lakshmi, G.V.; Gorikapudi, S. Leaf disease detection and classification in food crops with efficient feature dimensionality reduction. *PLoS ONE* **2025**, *20*, e0328349. [CrossRef] [PubMed]
41. Lu, Y.; Wu, X.; Liu, P.; Li, H.; Liu, W. Rice disease identification method based on improved CNN-BiGRU. *Artif. Intell. Agric.* **2023**, *9*, 100–109. [CrossRef]
42. Sun, J.; Yang, Y.; He, X.; Wu, X. Northern Maize Leaf Blight Detection Under Complex Field Environment Based on Deep Learning. *IEEE Access* **2020**, *8*, 33679–33688. [CrossRef]
43. Zhang, L.; Li, C.; Wu, X.; Xiang, H.; Jiao, Y.; Chai, H. BO-CNN-BiLSTM deep learning model integrating 788 multisource remote sensing data for improving winter wheat yield estimation. *Front. Plant Sci.* **2024**, *15*, 1500499. [CrossRef] [PubMed]

44. Vini, S.L.; Rathika, P. Trioconvtomatonet-bilstm: An efficient framework for the classification of tomato leaf diseases in real-time complex background images. *Int. J. Comput. Intell. Syst.* **2025**, *18*, 79. [CrossRef]
45. Zhou, C.; Zhou, S.; Xing, J.; Song, J. Tomato leaf disease identification by restructured deep residual dense network. *IEEE Access* **2021**, *9*, 28822–28831. [CrossRef]
46. Sabanci, K. Benchmarking of CNN Models and MobileNet-BiLSTM Approach to Classification of Tomato Seed Cultivars. *Sustainability* **2023**, *15*, 4443. [CrossRef]
47. Arshad, F.; Mateen, M.; Hayat, S.; Wardah, M.; Al-Huda, Z.; Gu, Y.H.; Al-Antari, M.A. PLDPNet: End-to-end hybrid deep learning framework for potato leaf disease prediction. *Alex. Eng. J.* **2023**, *78*, 406–418. [CrossRef]
48. Asghar, M.; Khan, Z.F.; Ramzan, M.; Khan, M.A.; Baili, J.; Zhang, Y.; Nam, Y.; Nam, Y.-C. A lightweight hybrid model for scalable and robust plant leaf disease classification. *Sci. Rep.* **2025**, *15*, 32353. [CrossRef] [PubMed]
49. Haider, I.; Nazir, M.; Khan, M.A.; Raza, M. NRB-BiLNET: A Novel Deep Learning Architecture for Crop Leaf Disease Classification. In *Proceedings of the Horizons of Information Technology and Engineering (HITE), Lahore, Pakistan, 15–16 October 2024*; IEEE: New York, NY, USA, 2024; pp. 1–6. [CrossRef]
50. Agrios, G.N. *Plant Pathology*, 5th ed.; Elsevier Science: Burlington, MA, USA, 2005.

Disclaimer/Publisher's Note: The statements, opinions and data contained in all publications are solely those of the individual author(s) and contributor(s) and not of MDPI and/or the editor(s). MDPI and/or the editor(s) disclaim responsibility for any injury to people or property resulting from any ideas, methods, instructions or products referred to in the content.

sustainability

MDPI

Article

Satellite-Guided Delineation of Crop Production Zones from Official Crop Statistics for Spatial Agricultural Decision Support

Ahmed Attia *, Prem Woli, Charles R. Long, Francis M. Rouquette, Jr. and Gerald R. Smith

Texas A&M AgriLife Research and Extension Center, Overton, TX 75684, USA; prem.oli@ag.tamu.edu (P.W.); charles.long@ag.tamu.edu (C.R.L.); monte.rouquette@ag.tamu.edu (F.M.R.J.); gerald.smith@ag.tamu.edu (G.R.S.)
* Correspondence: ahmed.attia@ag.tamu.edu or ahmed.attia3@outlook.com

Abstract

Spatially explicit crop yield information is needed for regional environmental modeling, sustainability assessment, and agricultural decision support, yet official yield statistics are commonly reported only at aggregated administrative scales. This study introduces the NAYD R package, a reproducible geospatial workflow for converting county-level harvested area and yield statistics into spatially explicit production units and zonal clusters while preserving consistency with official records. County-level statistics from the USDA National Agricultural Statistics Service were integrated with USDA Cropland Data Layer crop masks, multi-sensor NDVI products, and satellite-derived evapotranspiration from OpenET SSEBop. An NDVI-based eligibility filter refined crop masks toward reported harvested area, while normalized NDVI and evapotranspiration layers were combined into spatial weighting surfaces and aggregated into contiguous production units and graph-based clusters. Case studies for cotton and winter wheat in Texas showed that the eligibility filter removed approximately 20–40% of CDL-classified pixels while maintaining consistency with reported harvested area and preserving plausible spatial gradients associated with irrigated and dryland systems. Evaluation against independent Texas A&M AgriLife variety trial data indicated that the disaggregated clusters reproduced plausible spatial patterns of yield variability while retaining the county-level NASS constraints. The workflow provides an open-source framework for generating statistically consistent production zones for regional crop modeling, environmental assessment, and sustainable agricultural planning.

Keywords: yield disaggregation; remote sensing; vegetation index; evapotranspiration; crop yield mapping

1. Introduction

Spatial information on crop yields is central for assessing climate risks, evaluating management strategies, and designing policies for water and nutrient management. Yet in most regions, the only consistent, long-term production statistics are reported at administrative units such as counties or districts. In the United States, the USDA National Agricultural Statistics Service (NASS) provides annual county-level planted area, harvested area, and yield for major crops, which underpin a huge body of agronomic and economic work [1]. However, these data say nothing about how production is distributed within counties, or how irrigated "cores" differ from marginal dryland areas scales that matter for both process-based models and on-farm decision support.

Remote sensing has enabled substantial progress in estimating crop yields below administrative reporting units, particularly through vegetation indices, meteorological variables, crop models, and statistical or machine learning approaches. These studies have demonstrated that satellite-derived indicators can capture important spatial and temporal variation in crop growth and productivity, especially when calibrated against plot measurements, combine harvester yield monitors, or well-parameterized crop models [2–7]. For example, the Scalable Satellite-based Crop Yield Mapper (SCYM) framework combines crop model simulations and Landsat-scale vegetation indices to estimate maize and soybean yields across the U.S. Corn Belt [3], while field-scale studies have fused satellite imagery with combine yield observations to generate 10–30 m yield maps for wheat and other cereals [8–10]. These approaches are valuable for yield prediction and precision agriculture applications, but they address a different problem from the one considered here. They generally estimate yield independently from remote sensing or model-derived predictors and then compare predictions with official statistics or field observations. In contrast, many regional modeling and decision support applications require spatial yield layers that remain explicitly consistent with official harvested area and county-level yield statistics, particularly where field-level yield observations are sparse, proprietary, or unavailable.

Beyond purely statistical remote sensing approaches, a large body of work relies on process-based crop growth models, such as WOFOST, APSIM, and DSSAT, sometimes coupled with data assimilation of satellite greenness indices or soil moisture to forecast yields from local to continental scales [11–14]. These models explicitly represent soil–plant–atmosphere processes and management, but their operational use is often limited by the need for detailed input data and careful calibration in each new region. In parallel to process-based models, many studies have pursued purely data-driven routes in which yields are inferred directly from satellite time series and ancillary weather data. Some approaches rely on vegetation indices at a few key phenological stages or on phenology metrics derived from VI curves to forecast county-scale yields weeks to months before harvest [15,16]. Others exploit full-season Landsat or Sentinel-2 trajectories, sometimes combined with gridded climate variables, to calibrate empirical or machine learning models at field scale [17]. Reviews of these machine learning approaches emphasize the flexibility of algorithms such as random forests, gradient boosting, and Gaussian processes to handle multi-sensor inputs and nonlinear responses, while also noting their dependence on large, high-quality yield datasets for training and validation [18,19]. Despite their successes, these model- and ML-based approaches generally require either dense local yield observations or rich management datasets, and they typically use official statistics (e.g., NASS) only as a loose consistency check rather than as a hard constraint on total production.

A parallel stream of work uses remote sensing to construct gridded yield or production surfaces at regional to global scales by downscaling administrative statistics. Classic examples include Spatial Production Allocation Model (SPAM) [20] and M3-Crops [21], which distribute national or subnational crop statistics to grid cells based on cropland maps and suitability layers. More recently, Qin, Wu, Zeng, Zhang, and Tian [5] developed the GGCP10 dataset, a global gridded crop production product at 10 km resolution for 2010–2020 that integrates multiple satellite, climate, and soil datasets with machine learning models and then calibrates grid-level production back to FAO national statistics. Complementing these statistical products, the Global Gridded Crop Model Intercomparison (GGCMI) and related AgMIP studies use ensembles of process-based models (e.g., DSSAT, LPJmL, PRYSBL2) to simulate yields on 0.5° grids under historical and future climates, providing multi-model projections of yield responses to warming and CO_2 [22]. These products demonstrate the feasibility of enforcing consistency with official statistics while ex-

https://doi.org/10.3390/su18146937

ploiting remote sensing signals, but they operate at relatively coarse spatial resolutions and often aggregate management environments (e.g., irrigated vs. rainfed) within a grid cell.

Despite these advances, a methodological gap remains between two dominant types of yield information. On one side, official agricultural statistics such as NASS provide trusted, consistent, long-term estimates of crop area and yield, but only at coarse administrative scales. On the other side, field- or pixel-scale yield mapping approaches can resolve fine spatial variability, but they often require local yield observations, proprietary yield monitor data, detailed management information, or crop model calibration. Existing gridded crop production datasets and downscaling products demonstrate the value of spatializing agricultural statistics, but they typically operate at coarse spatial resolutions or rely on global suitability, climate, or machine learning layers that are not designed to delineate local production zones within individual counties. What is still missing is a transparent, reproducible, and constraint-preserving workflow that uses public satellite data to redistribute official county-level statistics into spatially explicit production units while preserving both harvested area and county mean yield by construction. Furthermore, spatial disaggregation has become an important geospatial modeling problem when detailed spatial processes must be inferred from aggregated administrative statistics, particularly when large spatial domains and fine target resolutions make computation challenging [23].

At the same time, the U.S. now has a mature set of wall-to-wall land use and remote sensing products that, in principle, could support systematic disaggregation of NASS yields. The Cropland Data Layer (CDL) provides annual crop maps at 30 m resolution for the conterminous U.S. and has been widely used to delineate crop-specific masks for yield gap and production analyses. Multi-sensor NDVI products from MODIS, Landsat, and Sentinel-2 offer dense time series of canopy greenness, while satellite-based evapotranspiration (ET) products, such as OpenET SSEBop CONUS GridMET v2.0, quantify spatial patterns in water use. Together with the NASS Quick Stats API, which exposes county statistics programmatically via tools such as the *rnassqs* R package, these datasets create an opportunity: instead of fitting yield models to ground-truth data, we can treat the county mean as fixed and use remote sensing only to decide how that mean should be distributed across space.

This paper develops and demonstrates the NAYD R Package, a NASS-anchored yield disaggregation workflow that converts county-level harvested area and yield statistics into spatially explicit production units and zonal clusters using only publicly available datasets. The goal is not to estimate absolute yield independently of NASS but to spatially redistribute official crop statistics in a way that preserves both harvested area and county mean yield by construction. The workflow (i) refines CDL crop masks using an NDVI-based eligibility filter so that the retained crop area is consistent with NASS harvested area; (ii) combines seasonal NDVI and satellite-derived evapotranspiration into normalized spatial weights representing relative within-county production potential; and (iii) aggregates weighted pixels into realistic harvest units and graph-based production clusters and then allocates county-level yield to these units under explicit area and yield constraints. All steps are implemented in open-source R code and are designed to be adaptable across crops and regions where crop masks, aggregated yield statistics, vegetation index products, and satellite-derived water use indicators are available.

We illustrate the workflow for cotton and winter wheat in two Texas county-year case studies and evaluate its external plausibility using independent Texas A&M AgriLife variety trial data across multiple years and locations. The workflow is not fitted to the trial data; therefore, the comparison is used as an independent check of whether NASS-anchored production clusters reproduce broad spatial yield patterns rather than exact field-level performance.

https://doi.org/10.3390/su18146937

The specific objectives were to: (1) develop and document an open-source, constraint-preserving workflow for converting county-level crop statistics into spatially explicit production units and zonal clusters; (2) evaluate how CDL crop masks, NDVI-based eligibility filtering, and NDVI–ET weighting determine effective harvested area and within-county yield gradients; and (3) assess whether the resulting cluster yields agree with independent cotton and winter wheat variety trial data without using those trials for calibration. The main contribution is a transparent geospatial allocation framework that bridges official agricultural statistics and satellite-derived spatial variability while preserving aggregate statistical consistency.

2. Materials and Methods

2.1. Study Region

This study illustrates cotton and winter wheat NASS yield disaggregation in two counties in the Texas High Plains (THP), a semi-arid agricultural region in northwestern Texas covering approximately 8.9 million ha. The THP is characterized by a relatively flat terrain and a continental climate with hot summers, cold winters, and erratic precipitation of roughly 450–550 mm annually. Major crops include cotton, maize, sorghum (*Sorghum bicolor* L. Moench), and winter wheat, with cotton relying heavily on irrigation and wheat more often grown under rainfed conditions in the northern and central counties [24]. Ongoing Ogalala aquifer depletion has driven a gradual shift toward more water-efficient and rainfed systems, increasing the region's vulnerability to climate variability and water constraints.

Within this broader region, the workflow is illustrated for cotton in Gaines County in 2021 and for winter wheat in Deaf Smith County in 2016. To evaluate the plausibility of the disaggregated yields beyond these examples, we additionally compared cluster mean yields with variety trial data for cotton (2018–2024) and winter wheat (2008–2023) from Texas A&M AgriLife programs at a subset of locations across Texas where trials were available. These sites span multiple counties and environments, including both irrigated and rainfed systems, and thus provide an independent check on whether the NASS-anchored clusters reproduce broad spatial patterns in yield.

2.2. Data Sources

2.2.1. NASS County Statistics

County-level planted area, harvested area, and cotton lint yield and winter wheat grain yield were obtained from the USDA National Agricultural Statistics Service (NASS) for Texas counties in the needed years using the *rnassqs* R package, which provides an interface to the NASS "Quick Stats" web API "https://quickstats.nass.usda.gov/api/ accessed on 12 November 2025" with built-in functions that facilitate building queries based on available parameters. Planted and harvested areas (ha) were used as constraints on the spatial masks (Section 2.3.1), and county average yield (kg ha^{-1}) provided the target for disaggregation to field and cluster scales (Sections 2.3.4 and 2.3.5).

2.2.2. Cropland Data Layer (CDL)

Annual USDA Cropland Data Layer (CDL) maps were used to identify crop-specific pixels for cotton and winter wheat from 2008 onwards "https://www.nass.usda.gov/Research_and_Science/Cropland/Release/index.php accessed on 12 November 2025". CDL rasters were reprojected to an equal-area projection (NAD83/Conus Albers; EPSG:5070) and resampled to a common grid. Pixels mapped as the target crop in the CDL were combined into a binary crop mask with an optional user-defined lower and upper buffer relative to NASS planted area. These buffers are specified as multiplicative factors

https://doi.org/10.3390/su18146937

on area (e.g., 0.6 and 2.3, corresponding to 60% and 230% of the NASS planted area) to accommodate CDL underestimation and overestimation while excluding obvious misclassified patches. When CDL underestimation exceeds a user-defined threshold (e.g., >40%), the workflow expands the mask by taking the union of crop pixels across the three years surrounding the target year; when CDL overestimation exceeds a user-defined threshold (e.g., >70%), it tightens the mask by taking the intersection of crop pixels across the three surrounding years. In our Texas cases, CDL underestimation relative to NASS planted area was uncommon, while overestimation occurred more frequently; nonetheless, setting the upper buffer too low can eliminate genuine crop pixels and should be avoided.

2.2.3. Remote Sensing: NDVI and ET

Multi-sensor vegetation indices and satellite-based evapotranspiration (ET) were used to construct spatial weights for yield disaggregation. For vegetation, we used NDVI derived from MODIS 16-day collections "MODIS/061/MYD13Q1" (250 m, 2023–present) or "MODIS/061/MOD13Q1" (250 m, 2000–2022), or Landsat Tier 1 Collection 2 surface reflectance from Landsat 5 TM, Landsat 7 ETM+, and Landsat 8 OLI (30 m, 1983–present), or Sentinel-2 Level-2A surface reflectance from Sentinel-2A/B MSI (10 m, 2016–present), depending on sensor availability and user preference for each county-year. All products were accessed as atmospherically corrected surface reflectance. Quality control was performed using the accompanying QA bands. (i) For MODIS MO/YD13Q1, we excluded pixels flagged as clouds, cloud shadows, snow/ice, or other low-quality observations in the Summary QA and pixel reliability flags; (ii) for Landsat, we used the pixel_qa band from Collection 2 Tier 1 SR to remove water, clouds, cloud shadows, and snow; (iii) and for Sentinel-2, we masked clouds and cloud shadows using the Scene Classification (SCL) band and/or quality bits, e.g., classes "cloud", "cloud shadow", "cirrus", and "snow/ice". Only cloud-free, snow-free observations over land were retained for NDVI compositing.

NDVI was calculated from red and near-infrared reflectance as:

$$NDVI = \frac{\rho\text{NIR} - \rho\text{RED}}{\rho\text{NIR} + \rho\text{RED}} \quad (1)$$

Within the workflow, the Spatial_Weights module constructs the NDVI–ET weight surface and allows the user to select which NDVI sensor (MODIS, Landsat, or Sentinel-2) to use in a given county-year. This selection is subject to the sensor-specific availability and quality screening (e.g., MODIS from 2000 onward, Sentinel-2 from 2016 onward, and only cloud- and snow-free observations retained). The NDVI composites were generated over crop-specific growing season windows and reprojected to the common 30 m grid in EPSG:5070 using bilinear interpolation when downscaling from coarser products, e.g., MODIS 250 m, or upscaling the original Sentinel-2 scenes. Season start and end dates are user-defined. In this case study, we set the NDVI compositing windows from 1 June to 30 September for cotton and from 1 March to 15 May for winter wheat. These windows ensure that the target crop has emerged and reached canopy development sufficient to cover the soil. In THP, cotton is planted by mid-May and winter wheat resumes spring growth by March.

For ET, we used monthly actual ET from the OpenET (SSEBop CONUS GRIDMET v2.0) Landsat-based 30 m spatial resolution product and aggregated to the seasonal totals over the same crop-specific windows for each crop and year. All satellite products were resampled and reprojected to a common 30 m grid in EPSG:5070, using nearest neighbor resampling for categorical layers and bilinear resampling for continuous layers (NDVI, ET). Within each season, mean NDVI and summed ET were computed for each pixel to represent crop vigor and water use. These two signals were then combined into a single

https://doi.org/10.3390/su18146937

weight layer using user-defined mixture coefficients, e.g., 70% weight on NDVI and 30% weight on ET, as described in the following sections.

2.3. Software Workflow

All components of the NASS-anchored yield disaggregation workflow are implemented in open-source R code and provided in a public GitHub repository as an R library NAYD (Table 1). In what follows, we refer to this implementation simply as "the workflow". Table 2 describes the required libraries and their sources for the NAYD library.

Table 1. General specifics of the NAYD software.

Code Metadata	Details
Name of software	NASS-Anchored Yield Disaggregation Workflow (NAYD)
Date first available	January 2026
Software required	R 4.5.2 and CRAN package releases (see Table 2)
Source code	GitHub repository: https://github.com/attia3/nayd.git, accessed on 14 January 2026
Documentation	README in the GitHub repository
Contact	GitHub repository: (issues/discussions)
Installation requirements	R environment + required CRAN packages; optional Earth Engine access via *rgee*

Table 2. Required libraries and their respective roles for the NAYD package.

Library/ Dependency	Version (CRAN Stable)	Purpose	Reference/Source
R	4.5.2	Programming language/runtime	R Project
sf	1.0-2.4	Vector GIS operations (simple features: counties, field polygons, geometry ops)	CRAN sf
terra	1.8-93	Raster operations (masks, weights, zonal stats; large rasters)	CRAN terra
rgee	1.18	R interface to Google Earth Engine (remote sensing access + processing)	CRAN rgee
reticulate	1.44.1	R↔Python bridge required by rgee	reticulate docs (RStudio) https://rstudio.github.io/reticulate/, accessed on 14 January 2026
Google Earth Engine	Cloud platform	Planetary-scale remote sensing computation platform used by rgee workflows	[25]

County-level NASS statistics are combined with publicly available remote sensing products to generate spatially explicit production units and zonal clusters (Figure 1).

First, CDL crop masks are refined using an NDVI-based eligibility filter so that the retained crop area matches the NASS harvested area within a user-defined tolerance. Second, seasonal NDVI and satellite-derived evapotranspiration (ET) are normalized and combined into spatial weights representing the relative contribution of each pixel to the county mean yield. Third, these weights are aggregated into realistic harvest units and grouped into zonal production clusters using a graph-based connectivity rule with a user-defined distance threshold (10 km in this study). Finally, NASS county mean yield is disaggregated to units and clusters using weighted allocation with a tunable contrast parameter (β), producing spatially explicit yield surfaces suitable for regional modeling and validation. Unlike conventional remote sensing yield estimation approaches, NAYD does not independently predict absolute yield at pixel or field scale. Instead, it uses official NASS county-level harvested area and yield statistics as hard constraints and

applies NDVI and ET only to distribute within-county spatial heterogeneity. Thus, the target output is a set of NASS-consistent production zones rather than an unconstrained satellite-derived yield map. To clarify this methodological positioning, Table S1 compares NAYD conceptually with representative SPAM-type crop production allocation frameworks and SCYM-type satellite-based yield estimation approaches in terms of objective, spatial support, required inputs, treatment of official statistics, and intended output. Because these approaches estimate different quantities and operate under different statistical constraints, Table S1 is intended as a conceptual comparison rather than a direct numerical performance benchmark.

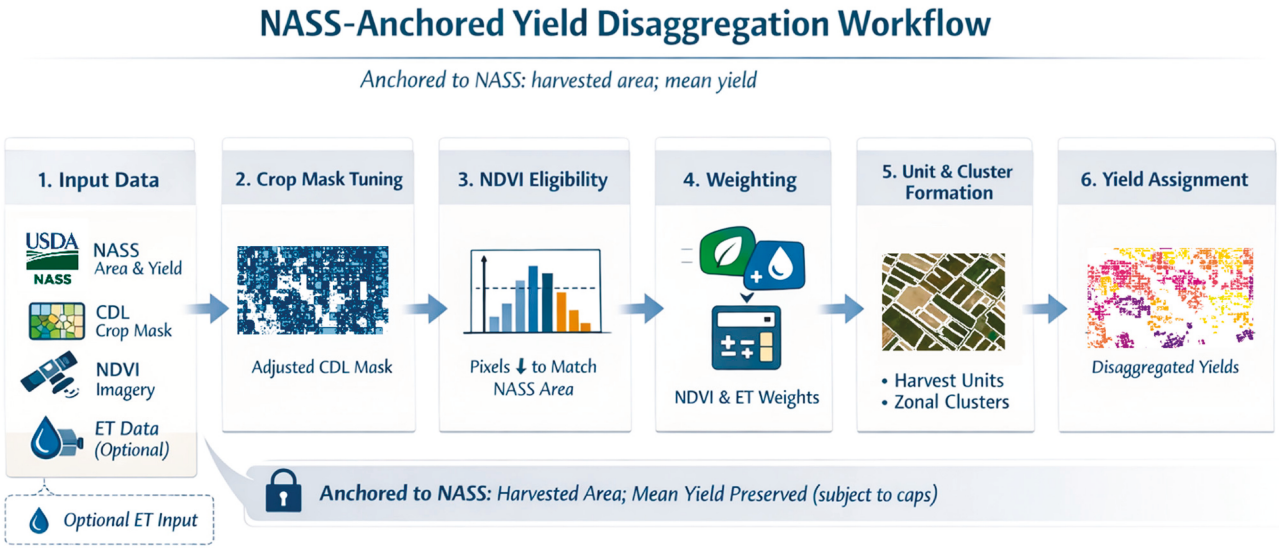

Figure 1. Flowchart of the NASS-anchored workflow for disaggregating county-level yields into spatial production units and zonal clusters using CDL, NDVI, ET, and user-defined constraints.

2.3.1. Crop Masks and NDVI Eligibility

In the workflow, the USDA CDL is used as the initial crop mask for the target crop from 2008 onward. Building on this CDL mask, we implemented an NDVI eligibility function to further restrict the mask to pixels with an actual crop signal (Section 2.2.2). The purpose of this step is to tune the effective crop area so that it is consistent with the NASS harvested area. For each county-year and crop, we applied the NDVI eligibility filter as follows. We first computed a seasonal NDVI composite over pixels classified as the target crop in the CDL. Before quantile-based eligibility screening, non-finite NDVI values were excluded, and the lowest 5% of valid seasonal NDVI values within the CDL crop mask were screened to reduce the influence of very low-signal pixels and residual compositing artifacts. If the seasonal NDVI composite contained no valid pixels after projection to the analysis grid, the workflow retained the CDL-derived crop mask as a fallback rather than applying NDVI-based restriction. We then search over a grid of NDVI quantiles p (from high to low, e.g., 0.90, 0.88, . . ., 0.10). For each candidate quantile p, the function (i) computes an NDVI threshold T_p as the p-th quantile of seasonal NDVI over CDL crop pixels; (ii) retains pixels with NDVI $\geq T_p$; (iii) computes the total area of retained pixels using per-cell areas (via *terra::cellSize* in EPSG:5070); and (iv) compares this area to a target $A_{\text{target}} = A_{\text{harv}} \times (1 + f_{\text{buf}})$, where A_{harv} is the NASS harvested area and f_{buf} is a user-defined fractional buffer (e.g., 0.10–0.20, corresponding to 10–20%). The procedure stops at the first quantile for which the retained area exceeds A_{target}.

The resulting NDVI eligibility mask removes low-signal or misclassified CDL pixels and produces an effective crop area that closely approximates the NASS harvested area

https://doi.org/10.3390/su18146937

(within the chosen buffer). This mask defines the spatial support for all subsequent weighting and disaggregation steps in the workflow.

To assess the structural sensitivity of the eligibility procedure, we conducted a targeted analysis for the representative cotton and winter wheat case study county-years. For Gaines County cotton in 2021 and Deaf Smith County winter wheat in 2016, we varied the NDVI eligibility buffer between 0.10 and 0.20 and shifted the seasonal composite start date by approximately ±15 days around the baseline window while retaining the same seasonal end date. For each configuration, we recorded the selected NDVI threshold, eligible area relative to the NASS harvested area, number and area of selected production units, number of resulting clusters, cluster yield range, and cluster yield coefficient of variation.

2.3.2. Construction of NDVI-ET Weight Layer

For each county-year and crop, a spatial weight surface was constructed combining NDVI and ET information over the eligible pixels. First, NDVI and ET layers were separately min–max scaled to a common weight range. For each pixel i in county c and year y,

$$\boldsymbol{w}_{i,c,y}^{NDVI} = \frac{NDVI_{i,c,y} - \min(NDVI_{c,y})}{\max(NDVI_{c,y}) - \min(NDVI_{c,y})} \times (1 - \in) + \in \quad (2)$$

$$\boldsymbol{w}_{i,c,y}^{ET} = \frac{ET_{i,c,y} - \min(ET_{c,y})}{\max(ET_{c,y}) - \min(ET_{c,y})} \times (1 - \in) + \in \quad (3)$$

where $w_{i,c,y}^{NDVI}$ and $w_{i,c,y}^{ET}$ are the normalized NDVI and ET weights, respectively, and $\in$ is a small positive constant, e.g., 0.01, that prevents 0 weights. The normalized NDVI and ET weight layers were then combined according to user-defined mixture parameters, α_{NDVI} and α_{ET}; therefore, the raw weight equals

$$\boldsymbol{w}_{raw} = \alpha_{NDVI} \times \boldsymbol{w}_{NDVI} + \alpha_{ET} \times \boldsymbol{w}_{ET} \quad (4)$$

where w_{raw} is the raw weight of the NDVI and ET mixed layer, and α_{NDVI} and α_{ET} are user-defined parameters for NDVI and ET, respectively (e.g., 70% for NDVI and 30% for ET). The sum of α_{NDVI} and α_{ET} must equal 1, but if the ET is unavailable, i.e., <1999, $\boldsymbol{w}_{raw}$ is set to $\boldsymbol{w}_{NDVI}$. Finally, $\boldsymbol{w}_{raw}$ was renormalized $\boldsymbol{w}_{norm}$ so that the sum of weights over eligible pixels would be equal to 1. The resulting final normalized weight raster represents a continuous probability surface over the NDVI eligible crop area, with higher values in pixels more likely to contribute to the county's harvested yield.

The physiological rationale for combining NDVI and ET is that they represent complementary aspects of crop functioning. Seasonal NDVI provides an indicator of green canopy development, chlorophyll activity, leaf area, and radiation interception, which are closely associated with biomass accumulation under non-stressed conditions [26,27]. In contrast, actual ET represents integrated crop water use through soil evaporation and plant transpiration and is influenced by root zone water availability, irrigation, atmospheric evaporative demand, and stomatal regulation. Thus, NDVI primarily captures canopy vigor and photosynthetic capacity, whereas ET provides complementary information on the water use conditions that can support or constrain crop growth. These indicators were not treated as direct yield predictors; rather, they were used as relative spatial allocation weights within each county after enforcing the NASS harvested area and yield constraints.

2.3.3. Segmentation into PRODUCTION Units

Within each county-year and crop, the normalized weight $\boldsymbol{w}_{norm}$ was aggregated into spatial production units using a simple segmentation and tiling procedure. First, contiguous patches of NDVI-eligible pixels were delineated using the *patches* function in

https://doi.org/10.3390/su18146937

the *terra* package with 4-neighbor connectivity. Tiny specks (<50 cells) were removed with a sieve operation to ensure that remaining patches represented meaningful contiguous crop areas. For each patch, we computed its total area (ha) using *cellSize* in EPSG:5070 and the sum of normalized weights from w_{norm}.

Patches were then divided into two classes based on a user-defined "giant field" threshold A_{giant} (ha). Patches with area $\leq A_{\text{giant}}$ were treated as standalone production units, whereas patches with area $> A_{\text{giant}}$ were further subdivided into pseudo-fields using a regular fishnet. In this case study, we set $A_{\text{giant}} \approx 800$ ha for both cotton and winter wheat, reflecting the presence of very large, consolidated fields in parts of the THP, but this parameter is fully tunable in the workflow.

For "giant" patches, we generated a square fishnet with a target tile area A_{tile} (default ≈ 200 ha) and clipped the grid to the patch boundary for each resulting tile computed area (ha), total weight, and weight density. Each tile was then treated as a separate pseudo-field nested within the original patch. Finally, standalone patches and tiles were merged into a single set of production units and filtered to retain units within a user-specified size range, e.g., 5–1000 ha in our case study. The remaining units were sorted in descending order of total weight and assigned a cumulative area, which forms the basis for selecting harvest units that match the NASS harvested area.

Small and medium fields and all tiles were then combined into a single set of production units. For each unit u, we computed its area A_u (ha), total weight W_u (the sum of w_{norm} over all pixels in the unit), and weight density W_u/A_u. Units were filtered to retain only those within a plausible size range specified by the user. In this case study, we kept units between 5 and 1000 ha, which removes very small slivers and extremely large polygons. These lower and upper bounds are exposed as arguments in the workflow so that users can adapt them to other crops and regions. The remaining units were sorted in descending order of total weight W_u and assigned a cumulative area:

$$cum_area_k = \sum_{u=1}^{k} A_{\text{u}} \tag{5}$$

which forms the basis for selecting the subset of "harvest units" whose total area matches the NASS harvested area.

Although the present application uses Texas cotton and winter wheat as case studies, the NAYD workflow is intended to be transferable across regions through adjustment of crop-specific inputs and spatial processing parameters. The crop mask source, seasonal compositing window, NDVI eligibility buffer, relative NDVI–ET weighting, production-unit size thresholds, clustering distance, and crop-specific yield bounds should be selected according to the local production system and intended output scale. In landscapes with highly fragmented fields, smaller production units and clustering thresholds may be appropriate to retain fine-scale heterogeneity. In multiple cropping systems, crop masks and seasonal NDVI and ET composites should be constructed separately for each crop cycle. Where the USDA CDL is unavailable, the workflow can use another reliable crop-specific map or a user-supplied crop classification; however, a reasonably accurate crop footprint remains necessary because NAYD redistributes official statistics within an identified crop area rather than independently determining crop identity. Table S2 summarizes the principal inputs and parameters requiring adaptation for applications in different agricultural regions.

2.3.4. Production Units Subset and NASS-Anchored Disaggregation

Within each county-year, a subset of production units (u) was selected such that their cumulative area approximated the A_{harv}, by ranking W_u and calculating the corresponding cum_{area_k} and identifying the index at which the cum_{area_k} first exceeded the A_{harv}. The

https://doi.org/10.3390/su18146937

selected units were rasterized to a mask and used to restrict the $\boldsymbol{w}_{norm}$ layer to $\boldsymbol{A}_{harv}$. The restricted weights were then renormalized so that their sum would be equal to 1, and the pre-unit weight sums over the harvest subset were recomputed:

$$A_u^* = A_u \times \frac{A_{harv}}{\Sigma_u A_u} \tag{6}$$

where A_u^* is the scaled analytical area of unit u. This scaling preserves the spatial geometry of the selected production units while ensuring that the total analytical support is consistent with the official harvested area. Therefore, the disaggregation is constrained by both the NASS harvested area and the NASS county mean yield.

To control the spread of yields around the NASS mean while preserving the NASS anchor, a shape parameter was added $(\beta \geq 0)$. For each unit u in the harvest subset, a transformed weight was computed

$$r_u = W_u^{\beta} \tag{7}$$

where r_u is the beta-transformed relative productivity score for unit u. When $\beta = 1$, the yield pattern follows the original NDVI–ET-derived unit weights. Values of $\beta > 1$ amplify spatial contrasts by increasing the relative influence of high-weight units, whereas values of $\beta < 1$ compress the distribution and produce a flatter yield pattern across units. In the experiments below, several β values were evaluated to quantify how this parameter affects agreement with independent variety trial data. For applications without independent yield validation data, we recommend $\beta = 1$ as the default because it preserves the original relative structure of the NDVI–ET allocation weights without artificially amplifying or compressing spatial contrasts. β should, therefore, be interpreted as a transparent contrast control parameter rather than a universally calibrated optimum.

Importantly, the transformed scores were not treated as direct yield values or simple production shares. Instead, they were interpreted as relative productivity multipliers and normalized by their area-weighted mean:

$$\overline{r_A} = \frac{\Sigma_u r_u A_u^*}{\Sigma_u A_u^*} \tag{8}$$

And unit-level raw yield was then calculated as:

$$\mathrm{Y_u^{raw}} = Y_{NASS}\left(\frac{\mathrm{r_u}}{r_A}\right) \tag{9}$$

where Y_{NASS} is the NASS-reported county mean yield. This formulation guarantees that, before applying yield safeguards, the area-weighted mean of unit-level yields equals the NASS county mean:

$$\frac{\sum_u Y_u^{raw} A_u^*}{\sum_u A_u^*} = Y_{NASS} \tag{10}$$

Thus, the NASS mean yield is preserved by construction while allowing spatial variation among production units according to the NDVI–ET-derived relative productivity scores. To avoid unrealistically low or extreme yield values, crop-specific lower and upper yield bounds were applied to the raw unit-level yields (Table S3):

$$Y_u^{clamped} = \min[\max(Y_u^{raw},\ Y_{floor}),\ Y_{ceiling}] \tag{11}$$

where Y_{floor} and $Y_{ceiling}$ represent crop-specific and, when used, relative yield limits. In the present implementation, these values were specified as fixed general limits for each crop and were applied consistently across counties and years; they were not dynamically derived from historical county-level yield distributions. Where applicable, additional relative limits based on the NASS county mean can also be used to constrain the allowable

https://doi.org/10.3390/su18146937

yield range. Because this clipping step can slightly shift the area-weighted mean away from Y_{NASS}, the clamped yields were re-centered using an adjustment factor:

$$f_{adj} = \frac{Y_{NASS}}{\frac{\sum_u Y_u^{clamped} A_u^*}{\sum_u A_u^*}} \quad (12)$$

And final unit-level yields were calculated as:

$$Y_u^{final} = Y_u^{clamped} \times f_{adj} \quad (13)$$

A final clipping step was applied when necessary to ensure that adjusted yields remained within the specified crop-specific bounds. Unit-level production was then calculated as:

$$P_u = Y_u^{final} A_u^* \quad (14)$$

The resulting production unit yields and production totals, therefore, preserve the NASS harvested area and county-yield constraints as closely as possible while expressing within-county spatial variability derived from NDVI and ET. Any residual deviation from the NASS county mean after clipping and re-centering was reported in the diagnostic summaries.

2.3.5. Construction of Production Clusters

To generate coarser production zones suitable for coupling with crop models or gridded soil datasets, the production units (u) were grouped into production clusters using a spatial connectivity rule. The centroids of harvest units were treated as nodes in a graph. Two units u_i and u_j were connected if the *Euclidean distance* between their centroids, $d(u_i, u_j)$, was $\leq$ a user-defined clustering radius d_{clust}. In this study, the clustering distance threshold was set to 10 km as a practical sub-county production zone scale compatible with the coarser soil, climate, and regional crop model datasets for which the output is intended. This value is a user-adjustable default rather than a universally optimal threshold; users may select smaller or larger distances according to crop type, field configuration, spatial heterogeneity, and intended application. Clusters were then defined as the connected components of this graph, so each production cluster consists of harvest units linked by chains of neighbors separated by at most d_{clust}. Individual cluster areas vary depending on field density. The 10 km was chosen to suit large-scale grid data resolution and is not intended to represent a universal optimum. Nonetheless, end users have the option to either decrease or increase the clustering distance to suit their objectives.

For each cluster c, the areas and weights of its member units were summed as follows:

$$\boldsymbol{A}_c = \sum_{u \in c} \boldsymbol{A}_u \quad (15)$$

$$\boldsymbol{W}_c = \sum\nolimits_{u \in c} \boldsymbol{W}_u \quad (16)$$

Cluster-level yields were obtained by aggregating unit yield $\boldsymbol{Y}_u$ within each cluster, i.e., area-weighted mean, ensuring that the area-weighted mean of cluster yields equals the NASS county-level yield. The resulting cluster yields represent production zones at approximately 10 km spatial scale.

2.4. Evaluation Methodologies

We evaluated the plausibility of disaggregated yields using independent variety trial data for cotton and winter wheat obtained from the Texas A&M AgriLife Variety Testing Programs. For cotton, we used irrigated and dryland Realistic Agronomic Cotton

https://doi.org/10.3390/su18146937

Evaluation (RACE) trials in Texas from 2018 to 2024 (https://varietytesting.tamu.edu/cotton/, accessed on 14 January 2026), extracting the test mean lint yield for each site-year. For winter wheat, we used the Texas Small Grains variety trial reports "https://varietytesting.tamu.edu/smallgrains/ accessed on 14 January 2026" from 2008 to 2023 and extracted the site mean grain yield. Each site was characterized by year, county, and either exact coordinates or the nearest town or experiment station, from which coordinates were approximated. Production environment information, including irrigated or dryland designation, was available for some trial records but was not consistently reported across all sites and years. Field-level soil properties and a spatially balanced sampling design were likewise unavailable. The variety trial dataset was, therefore, used as an independent multi-year external reference for evaluating broad agreement with the derived production zones, rather than as a statistically representative sample of all irrigation, soil, and management conditions across Texas.

Two complementary comparison approaches were used to assess the plausibility of the disaggregated cluster yields. First, a direct point-to-intersecting cluster comparison was conducted by matching each trial location to the production cluster polygon from the same county and year that physically contained the trial point. Where a point intersected more than one cluster because it fell on a shared boundary, the cluster with the largest polygon area was retained. This comparison provides a conservative assessment because it compares the trial yield only with the yield assigned to its intersecting NASS-anchored production zone. Second, a radius-based production zone plausibility comparison was retained to account for the intended spatial support of the workflow and uncertainty in some trial coordinates. For each trial point, clusters from the same county and year with centroids located within 10, 20, or 30 km were identified in EPSG:5070. Among the candidate clusters, the cluster with the smallest absolute difference between cluster yield and observed trial yield was selected. This radius-based comparison does not represent direct polygon-level allocation accuracy; rather, it evaluates whether production zones of comparable yield magnitude occur within the broader landscape surrounding the trial location. Comparisons between variety trial yields and cluster-level disaggregated yields were summarized using standard goodness-of-fit statistics: root mean squared error (RMSE), normalized RMSE (nRMSE), and Willmott's d-index.

3. Results and Discussion

3.1. Multi-Sensor Crop Mask and NDVI Eligibility

Across the Texas High Plains, combining CDL crop masks with the NDVI-based eligibility filter produced consistent, NASS-compatible crop areas for both cotton and winter wheat. Figure 2 illustrates this for one cotton and one wheat example. For Gaines County cotton in 2021 (Landsat NDVI), the initial CDL cotton mask mapped 148,103 ha of cotton pixels (Figure 2A). Applying the NDVI eligibility filter to shrink the CDL mask toward the NASS harvested area removed 30,270 ha (≈20%) of low-signal or misclassified pixels, leaving 117,833 ha of NDVI-active cotton (Figure 2B). In this county-year, the iterative eligibility procedure converged to a seasonal NDVI threshold of 0.310, which defines the NDVI-eligible subset shown in Figure 2B and the ineligible pixels in Figure 2C. The resulting NDVI-eligible area closely matches the NASS harvested area for cotton in that county-year.

For Deaf Smith County winter wheat in 2016 (Sentinel-2 NDVI), the initial CDL wheat mask covered 96,576 ha (Figure 2D). Applying the NDVI eligibility filter to shrink the CDL mask toward the NASS harvested area removed 31,280 ha of low-signal or misclassified pixels, leaving 65,296 ha of NDVI-active wheat (Figure 2E). In this county-year, the iterative eligibility procedure converged to an NDVI threshold of 0.291, which defines

the NDVI-eligible subset in Figure 2E and the excluded pixels in Figure 2F, and brought the trimmed mask into close agreement with the NASS harvested wheat area within the user-defined tolerance.

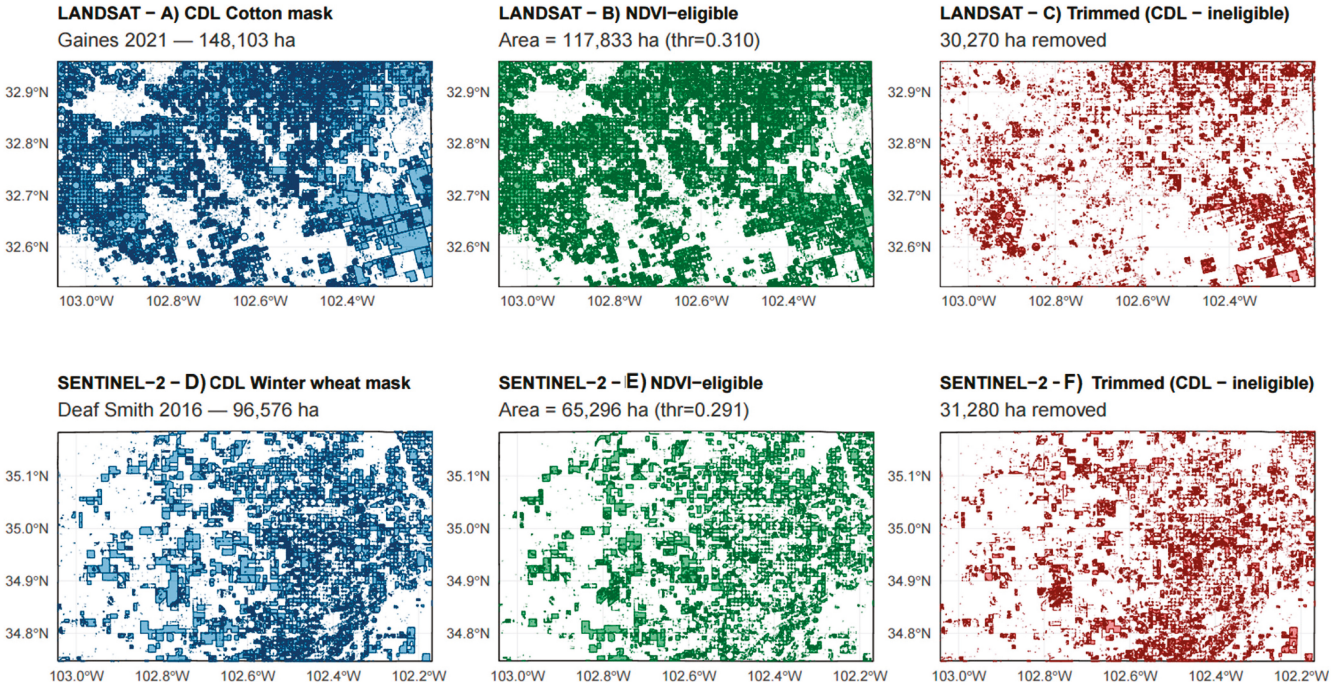

Figure 2. Cropland Data Layer (CDL) crop masks and NDVI-based eligibility for two example county-years in Texas. (**A**–**C**) Gaines County cotton, 2021: (**A**) CDL cotton mask; (**B**) NDVI-eligible cotton pixels after applying the quantile-based NDVI threshold constrained to NASS harvested area; (**C**) CDL cotton pixels removed by the NDVI eligibility filter ("trimmed" CDL area). (**D**–**F**) Deaf Smith County winter wheat, 2016: (**D**) CDL winter wheat mask; (**E**) NDVI-eligible wheat pixels; (**F**) CDL wheat pixels removed by the NDVI eligibility filter.

The targeted sensitivity analysis indicated that the main structural features of the derived production zones were relatively stable across the tested NDVI eligibility buffers and seasonal window start dates (Table S4). For Gaines County cotton, changing the start of the seasonal window altered the selected NDVI threshold and number of production units modestly, whereas the resulting number of clusters and cluster yield variability remained broadly similar within each buffer setting. Increasing the eligibility buffer increased the candidate crop area, as expected, but did not substantially alter the final cluster structure. For Deaf Smith County winter wheat, shifting the seasonal window start date produced only limited changes in selected units, cluster count, and cluster yield range. These results indicate that the production zone delineation was not highly sensitive to the tested operational choices in the representative cotton and winter wheat county-years.

Two points are worth emphasizing: (1) The CDL is not used blindly. Without NDVI eligibility, CDL over- and underestimation relative to NASS can be substantial and spatially structured. The quantile-based NDVI filter removes the noisiest portions of the CDL mask while re-anchoring the total eligible area to NASS harvested area (Section 2.3.1), so the subsequent disaggregation always starts from a NASS-consistent crop footprint rather than raw CDL pixels. In Texas, a significant portion of winter wheat is managed as dual-purpose wheat, where fields are grazed during vegetative stages and may not ultimately be harvested for grain. Approximately 40–50% of planted winter wheat acreage in Texas is either grazed out, terminated early, or abandoned prior to grain harvest, depending on climatic conditions and market incentives "https://varietytesting.tamu.edu/smallgrains/

https://doi.org/10.3390/su18146937

accessed on 14 January 2026. The increasing availability of satellite time series, cloud computing platforms, and AI-based modeling tools has accelerated the development of intelligent agricultural systems [28–31]. The proposed framework complements these predictive approaches by providing statistically consistent spatial yield baselines that can serve as inputs or validation layers for advanced modeling systems.

The present results indicate that this approach is robust across sensors. Figure 2 shows one Landsat-based cotton example and one Sentinel-2-based wheat example, but analogous MODIS-based NDVI masks yielded very similar NDVI-eligible areas in the same county-years. This supports the design choice of allowing sensor flexibility (MODIS, Landsat, Sentinel-2) without materially changing the effective crop area used in the yield disaggregation.

A limitation to acknowledge is that in years or counties with persistent cloud cover, complex mixed pixels, or substantial intercropping, the NDVI filter may remove some genuine crop pixels, particularly for coarser MODIS imagery. The union/intersection rules with neighboring years partly mitigate this, but a formal sensitivity analysis of the NDVI quantile thresholds would be a logical extension of this work.

3.2. NDVI-ET Weight Surfaces

For both crops, the combined NDVI-ET weights reproduced expected within-county gradients in crop vigor and seasonal water use within each county. In the Gaines County cotton example for 2021 (Figure 3), the original NDVI exhibits a heterogeneous mosaic of fields with moderate-to-high greenness (Figure 3A), reflecting variation in crop condition and management, while seasonal ET highlights zones of consistently higher water use, particularly irrigated blocks (Figure 3C). After min–max scaling, the NDVI-based weight field (Figure 3B) enhances contrast among fields with subtle greenness differences, whereas the ET-based weight (Figure 3D) emphasizes fields with persistently higher water use. The raw combined weight (Figure 3E; 0–1 scale) concentrates mass in pixels that are simultaneously green and water-consuming, representing areas with both strong canopy development and sustained transpiration, and the final normalized weight (Figure 3F; $\approx 5 \times 10^{-7}$–2×10^{-6}) further redistributes this mass so that the weights sum to one across the NDVI-eligible cotton area.

A similar pattern is evident for winter wheat in Deaf Smith County in 2016 (Figure S1). Original NDVI and ET again show fine-scale spatial heterogeneity across the eligible wheat area (Figure S1A,C), with NDVI emphasizing canopy density and ET capturing differences in seasonal water use. Their respective weight fields (Figure S1B,D) preserve this heterogeneity while compressing values to [0, 1]. The combined weight (Figure S1E) tends to favor wheat fields that are simultaneously greener and more water-consuming during the critical spring growth period, over the spring season, and the final normalized weights (Figure S1F; $\approx 1 \times 10^{-6}$–3×10^{-6}) identify a subset of fields and partial fields that collectively account for most of the "probability mass" used in subsequent disaggregation.

Because all weights are min–max scaled and then renormalized to sum to one within the NDVI-eligible mask, they can be interpreted probabilistically: a pixel with weight 2×10^{-6} contributes roughly twice as much to the county mean yield as a pixel with weight 1×10^{-6}. The absolute magnitudes are small because the total mass (1) is distributed over tens of thousands of 30 m pixels; spatial allocation depends solely on relative contrasts. This probabilistic interpretation underpins the later β exponent step, where the weight field can be sharpened ($\beta > 1$) or flattened ($\beta < 1$) without changing the county-level NASS constraint.

https://doi.org/10.3390/su18146937

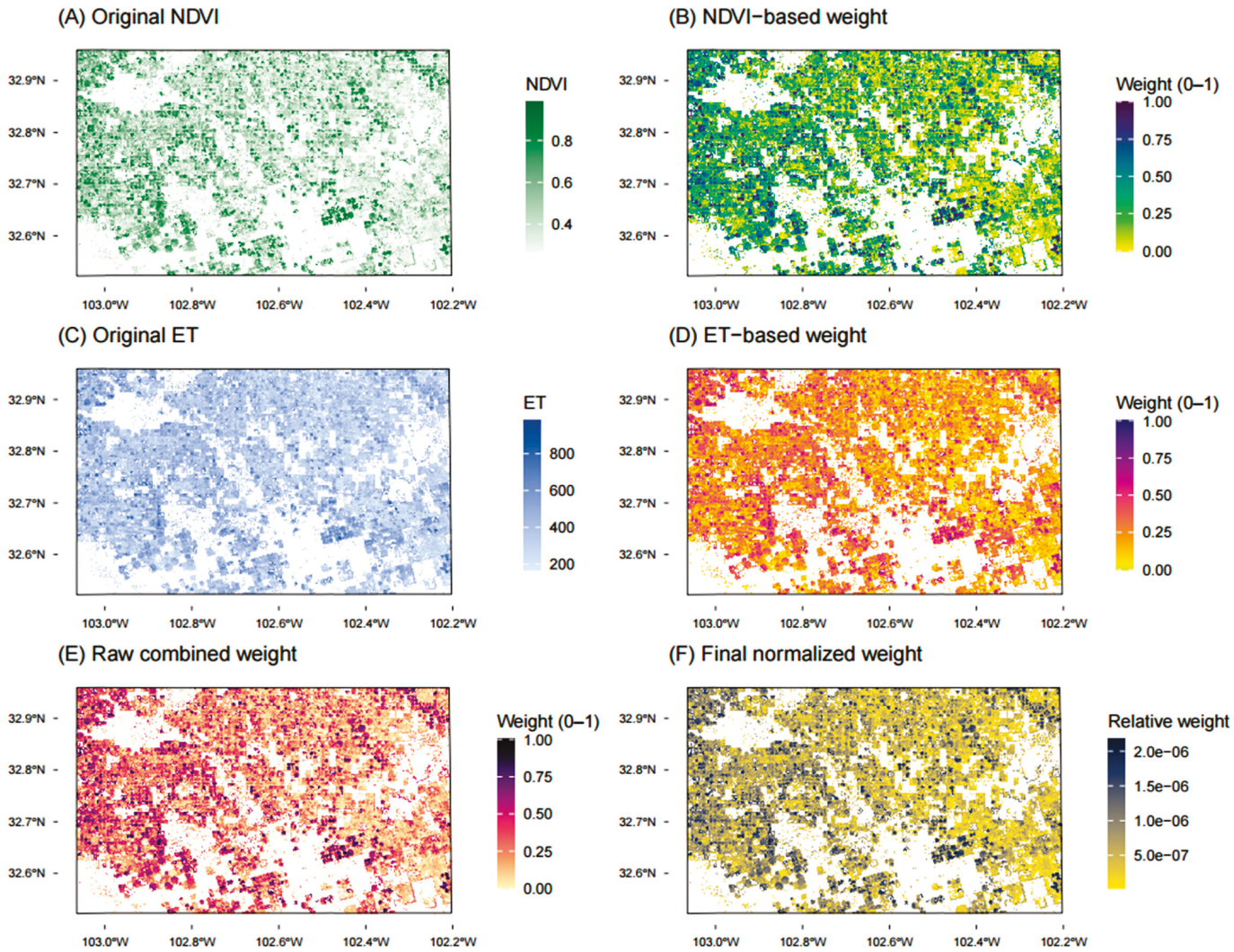

Figure 3. Cotton NDVI and ET weight layers for Gaines County, Texas (2021). (**A**) Seasonal mean (1 June to 30 September) NDVI over the NDVI-eligible cotton area; (**B**) NDVI-based normalized weight layer; (**C**) seasonal summed ET from OpenET SSEBop; (**D**) ET-based normalized weight layer; (**E**) raw combined NDVI–ET weight (before renormalization); and (**F**) final normalized NDVI–ET weight surface used for yield disaggregation.

A limitation that should be acknowledged is that the ET field from OpenET SSEBop is itself model-derived and can smooth or damp local extremes, particularly in heterogeneous irrigated systems. Similar spatial smoothing effects in satellite-based ET products have been noted in previous remote sensing studies, where field-scale irrigation variability or ET estimates can be dampened by model parameterization and spatial averaging [32]. Where irrigation management varies strongly within a county, ET-based weights may under-represent the true yield contrast among fields, which in turn limits how much spatial variability the disaggregation can express even when β is increased.

Although combining NDVI with ET partially mitigates limitations in either individual indicator, uncertainty in ET can propagate through the spatial allocation workflow. An ET error first affects the normalized ET weight assigned to a pixel. Because the ET layer is min–max scaled and then combined with NDVI, the effect is relative rather than a direct one-to-one translation into yield error: local overestimation of ET can increase the relative allocation weight of a pixel or production unit, whereas underestimation can reduce it. The magnitude of this effect depends on the NDVI–ET mixture coefficient, the local range of ET values within the county, and the corresponding NDVI pattern.

https://doi.org/10.3390/su18146937

After weight normalization, ET-related errors can redistribute relative yield allocation among production units. The subsequent β transformation may amplify or compress these differences, while aggregation of pixels into production units and clusters can reduce isolated pixel-scale noise. However, spatially coherent ET biases, such as systematic smoothing of irrigated field contrasts, may persist through aggregation and lead to under- or over-allocation among clusters. Importantly, because the weights are normalized within each county and final yields are constrained by the NASS county mean, ET uncertainty does not alter total county production. Instead, it affects the spatial distribution of the fixed county yield among production units and clusters.

The ablation analysis comparing NDVI-only, ET-only, and alternative NDVI–ET weighting configurations provides an empirical check on the practical contribution of ET to this redistribution. The results show that ET produced a modest improvement for cotton but no consistent validation advantage for winter wheat under the predominantly rainfed conditions represented in this study (Table S5). Thus, ET should be interpreted as an optional complementary allocation indicator rather than as a universally superior source of spatial information. In applications where ET products are expected to be unreliable or where the production environment is relatively homogeneous, users may assign greater weight to NDVI or use an NDVI-only configuration.

3.3. Segmentation and Harvest Unit Selection

The workflow converts the NDVI-ET weight surface into spatially contiguous harvest units through a segmentation procedure designed to approximate realistic harvest units while avoiding pixel-level noise. Adjacent NDVI-eligible pixels are grouped into contiguous patches, very small fragments are removed, and large patches are optionally subdivided into tiles to ensure that all resulting units fall within a plausible range for the crop and region. This ensures that subsequent disaggregation operates at a scale consistent with operational harvest or management units rather than individual pixels. Figure 4 illustrates the resulting segmentation for cotton in Gaines County in 2021. The output consists of spatially explicit harvest units (Figure 4A), each characterized by its area and associated aggregated weight density (Figure 4B). A comparable segmentation for winter wheat in Deaf Smith County in 2016 is shown in Figure S2. Aggregating fine-scale information into coarser modeling units is a standard practice in integrated environmental and agricultural modeling, where the goal is to retain dominant system behavior while reducing dimensionality and noise [33].

In the Gaines County cotton example for 2021 (Figure 5), the cumulative weight curve rises gradually: the top 1096 of 1247 units (87.9%) are sufficient to reach the NASS harvested area, and at this point, the cumulative weight has already reached 99.6% (Figure 5A). The selected subset covers 114,119 ha compared with a NASS harvested area of 114,121 ha, demonstrating close area anchoring (Figure 5B). This relatively flat cumulative weight curve indicates that yield contributions are spatially diffused across many units rather than concentrated in a small core, consistent with a mosaic of irrigated fields interspersed with lower-productivity dryland corners. The log-scale histogram of unit weights spans approximately three orders of magnitude, with many low-weight fringe units and a relatively higher number of high-weight units that carry most of the probability mass (Figure 5C).

https://doi.org/10.3390/su18146937

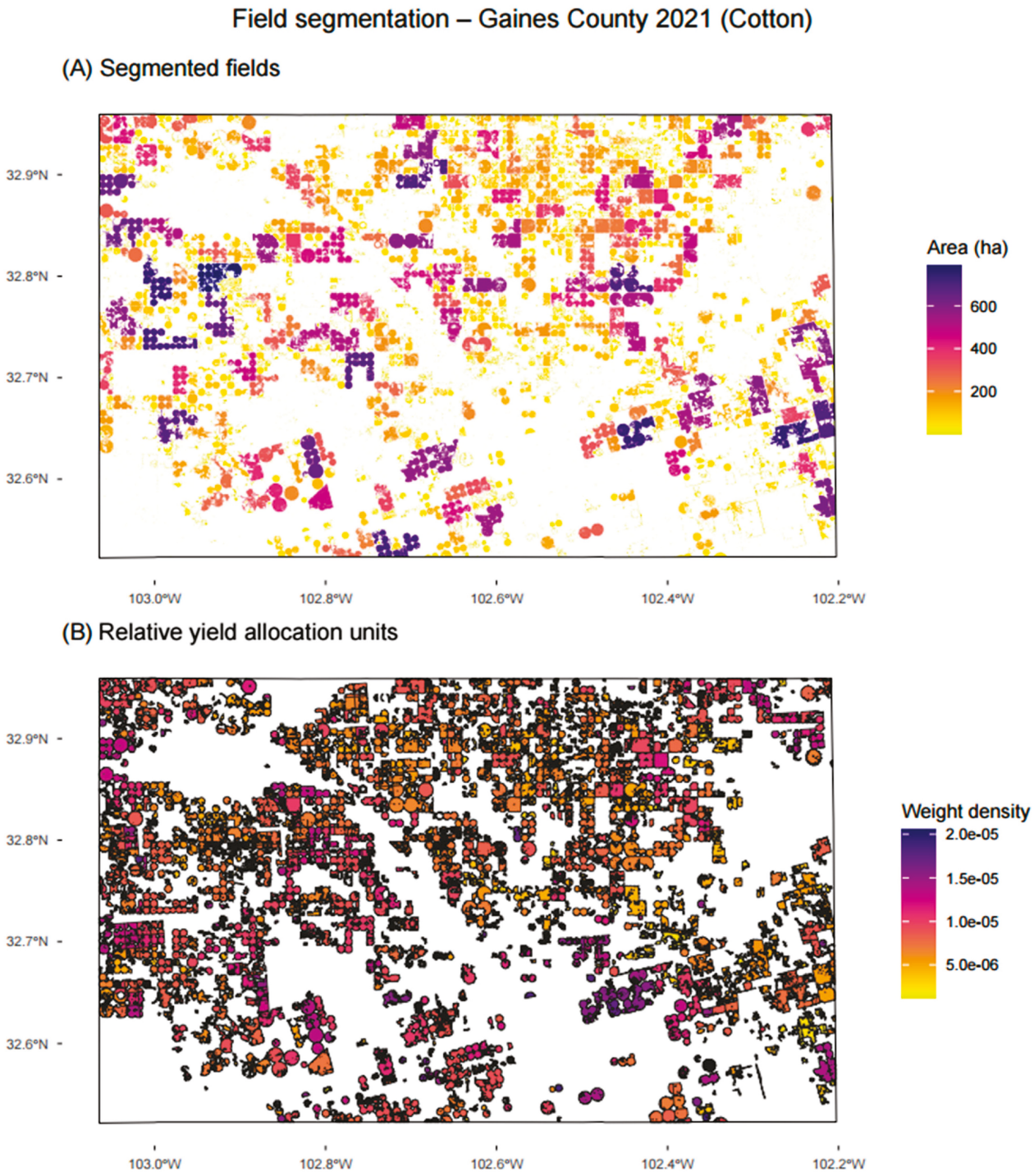

Figure 4. (**A**) Segmentation of NDVI-eligible cotton area and (**B**) relative yield allocation units in Gaines County, Texas, 2021.

In contrast, winter wheat production in Deaf Smith County in 2016 is more concentrated: only 474 of 954 units (49.7%) are required to match the NASS harvested area, yet these units already account for 92.1% of the cumulative weight (Figure S3A,B). This steeper cumulative weight curve indicates that a comparatively small subset of units dominates production, consistent with large, contiguous wheat blocks with broadly similar management and canopy development. The wheat weight histogram is correspondingly broader, with fewer extremely high- or low-weight units (Figure S3C).

https://doi.org/10.3390/su18146937

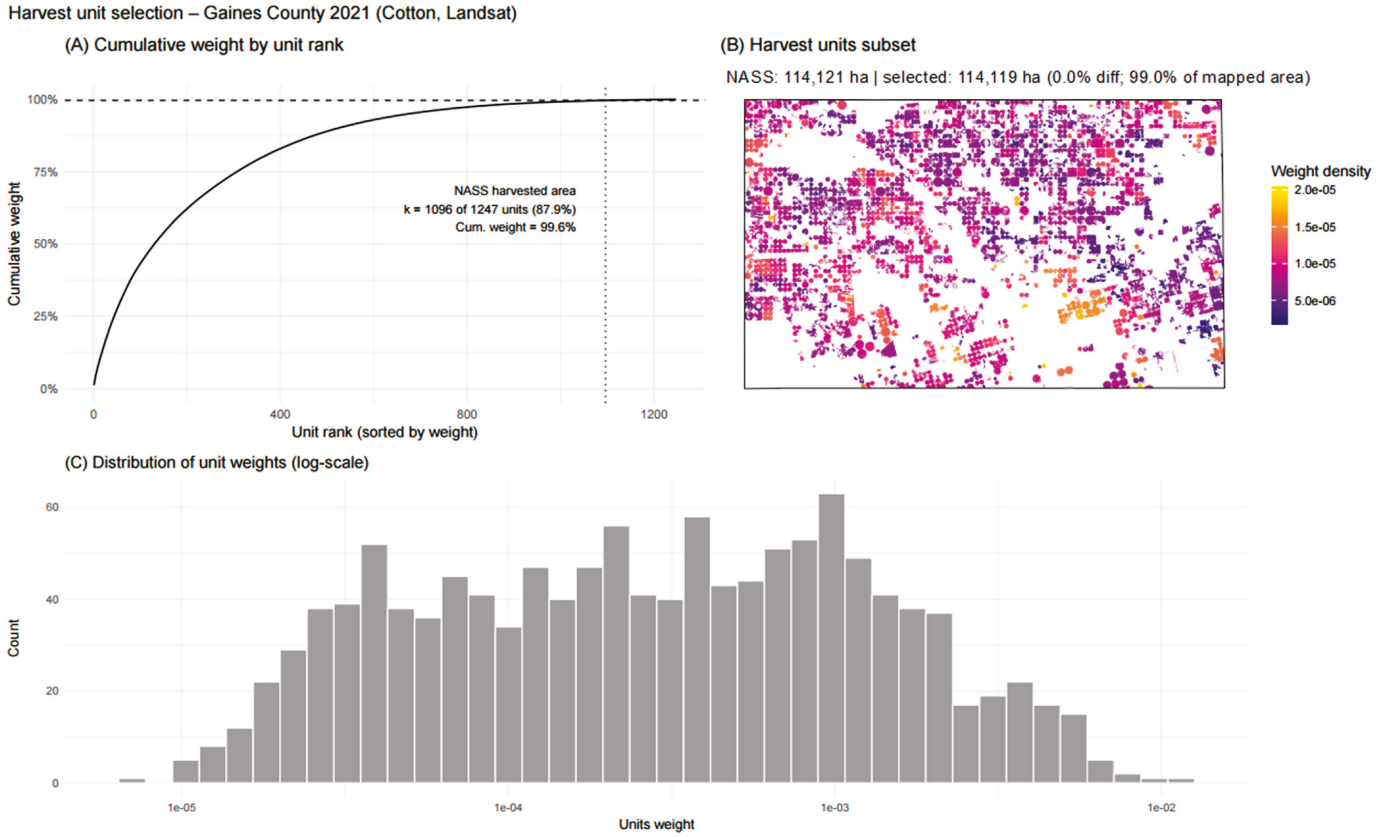

Figure 5. Harvest unit selection for cotton in Gaines County, Texas (2021). (**A**) Cumulative normalized weight as a function of unit rank, showing the point at which the selected harvest subset reaches the NASS-anchored harvested area. (**B**) Spatial distribution of selected harvest units within the NDVI-eligible cotton area. (**C**) Distribution of unit weights for all candidate units, highlighting the higher weights assigned to the harvested subset.

Taken together, these diagnostics demonstrate that the harvest unit selection remains tightly anchored to official harvested area while preserving spatial heterogeneity embedded in the NDVI-ET weight surface. In cotton, production is more spatially diffused, so most units are needed to reach the NASS area, and nearly all units carry non-negligible weight. In winter wheat, a relatively small share of field units accounts for most of the weight and harvested area, consistent with concentrated high-yield, high-ET irrigated blocks surrounded by many low-weight dryland corners. The cumulative weight curves also provide a transparent diagnostic for sensitivity analysis: steeper curves (e.g., under higher β exponents) imply that a smaller fraction of units could, in principle, explain most of the county yield, whereas flatter curves indicate that yield is inherently more spread out and less compressible into a few "core" production zones.

3.4. NASS-Anchored Disaggregation to Production Units and Zonal Clusters

By construction, the disaggregation preserves the NASS county mean: the area-weighted mean of all unit or cluster yields closely matches the reported NASS value (692 vs. 703 kg ha^{-1}) for Gaines County cotton in 2021 (Figure 6C). This area-constrained redistribution approach is conceptually aligned with mass-preserving downscaling methods used in environmental modeling, where fine-scale allocation is required to remain consistent with aggregated statistics [34,35]. The value of the workflow, therefore, lies not in reproducing the county mean itself but in reconstructing the spatial distribution of yield consistent with that constraint. Cluster yields in Gaines span approximately 400–1300 kg ha^{-1}, with a pronounced upper tail (Figure 6B). High-yield clusters are spa-

tially concentrated in contiguous zones in the south-central and western parts of the county, while lower-yield clusters dominate peripheral areas (Figure 6A), consistent with documented contrasts between irrigated cores and marginal dryland lands. Aggregating harvest units into graph-based zonal clusters thus smooths very fine-scale noise but retains dominant spatial gradients, providing production zones that both honor the NASS constraint and preserve within-county heterogeneity.

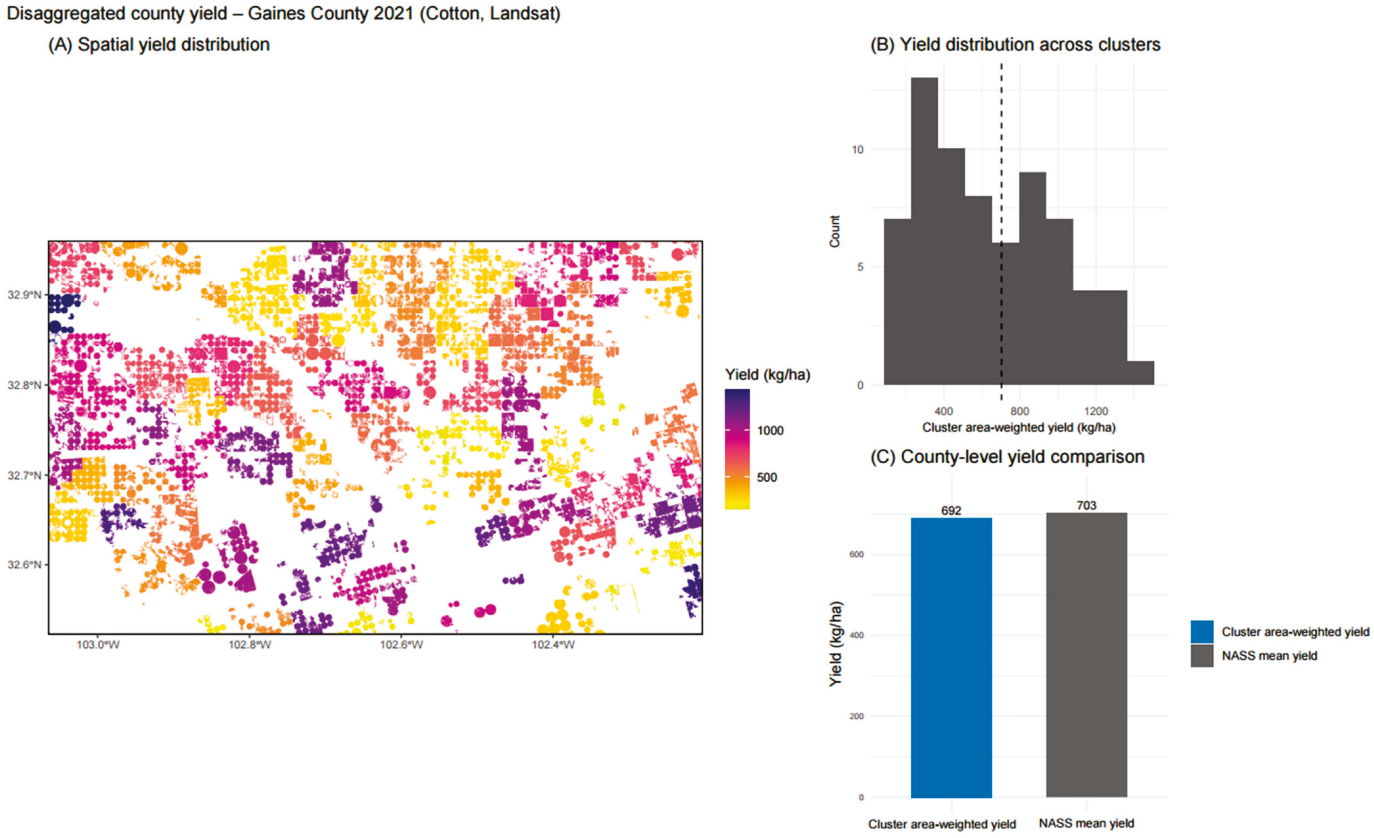

Figure 6. Disaggregated county yield for cotton in Gaines County, Texas (2021). (**A**) Spatial distribution of cluster-level yields within the county. (**B**) Histogram of cluster mean yields; the dashed vertical line indicates the NASS county mean yield. (**C**) Area-weighted cluster yields compared to the NASS mean, illustrating how the disaggregation preserves the county-level constraint while expressing within-county variability.

For Deaf Smith County winter wheat in 2016 (Figure 7), unit-level yields span from low values along the western and southern margins of the county to markedly higher yields in the central and north-eastern blocks (Figure 7A). The resulting histogram is right-skewed, with many clusters around 2–3 Mg ha^{-1} and a smaller number of high-yield zones approaching 6 Mg ha^{-1} (Figure 7B). Aggregating harvest units into connectivity-based production clusters smooths out fragmented small units while preserving these broad contrasts: cluster mean yields still range from <2 to >5 Mg ha^{-1}, and the cluster area-weighted mean remains within ~1% of the NASS county mean (Figure 7C). Importantly, these production clusters operate at spatial scales (~10 km) compatible with coarser gridded soil and climate datasets commonly used in process-based modeling (e.g., SoilGrids, gridded weather forcing). In this sense, clustering provides a scale bridge between pixel-level remote sensing signals and meso-scale crop or environmental models. This is consistent with previous work showing that aggregating sub-field yield signals to meso-scale zones can retain most of the agronomically relevant variability while greatly reducing model complexity [36–38].

https://doi.org/10.3390/su18146937

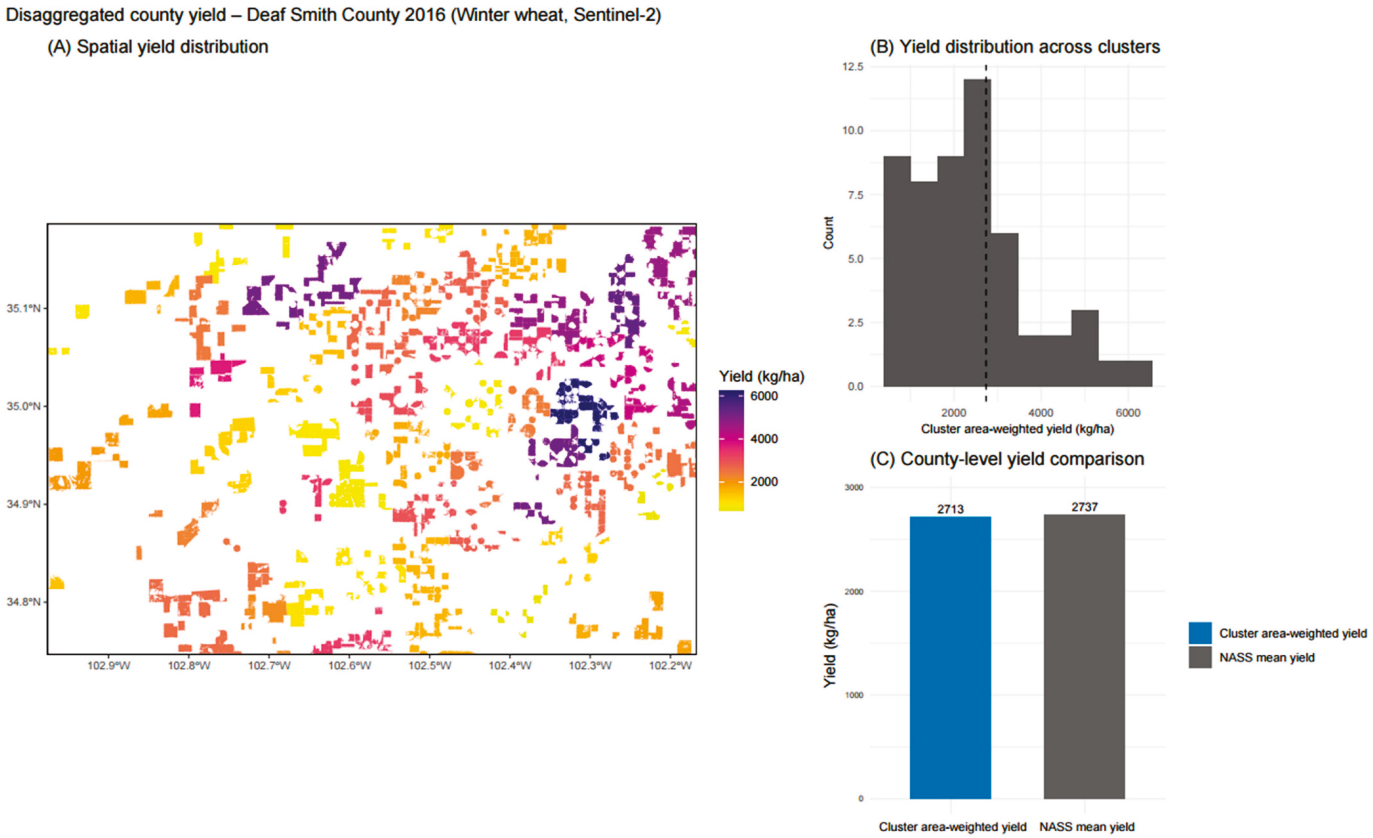

Figure 7. Disaggregated county yield for winter wheat in Deaf Smith County, Texas (2016). (**A**) Spatial distribution of cluster-level yields within the county. (**B**) Histogram of cluster mean yields; the dashed vertical line indicates the NASS county mean yield. (**C**) Area-weighted cluster yields compared to the NASS mean, illustrating how the disaggregation preserves the county-level constraint while expressing within-county variability.

A key control on the contrast of these yield distributions is the β exponent applied to the unit weights. In the baseline configuration shown in Figures 6 and 7, disaggregated yields are proportional to w_u^{β} and then rescaled so that the area-weighted mean matches the NASS yield. When β = 1, yields follow the NDVI-ET weight surface directly; β > 1 amplifies differences and pushes more area toward low and high tails, and β < 1 compresses the distribution toward the county mean. The β parameter provides a transparent mechanism for modifying the contrast of the allocated yield surface while retaining the NASS county-yield constraint. The sensitivity analysis shows that changing β alters the spread and tails of the resulting unit and cluster yields, but no single β value should be interpreted as universally optimal across crops, counties, or production environments. Accordingly, β = 1 was retained as the default configuration because it preserves the original relative NDVI–ET allocation pattern. Higher or lower values should be treated as scenario settings for evaluating the consequences of stronger or weaker spatial contrast, particularly where users have independent knowledge of irrigation, soil, or management heterogeneity.

Taken together, these results show that the workflow can translate a single NASS county mean into a spatially explicit harvest units and zonal clusters that (i) preserve the official statistics by construction, (ii) reflect realistic spatial patterns driven by NDVI and ET, and (iii) expose tunable yield contrasts through β. This approach, therefore, provides a reproducible bridge between county statistics, remote sensing information, and the spatial scales at which process-based models and soil datasets typically operate.

https://doi.org/10.3390/su18146937

3.5. Evaluation Against Variety Trials

Independent variety trial data were used as an external plausibility check of the disaggregated cluster yields. This comparison is demanding because the trial observations represent small experimental sites, whereas the workflow produces NASS-anchored mean yields for larger production clusters. In addition, coordinates for some trial locations were approximated from the nearest town or experiment station. Accordingly, we used two complementary comparison approaches that represent different interpretations of agreement between the trial observations and the disaggregated production zones.

Across all cotton and winter wheat site-years in a radius-based production zone plausibility comparison, performance improved systematically as the search radius increased from 10 to 30 km, but the gains were incremental rather than dramatic. With a 10 km radius, RMSE ranged from 373 to 389 kg ha^{-1} (nRMSE 15.1–15.7%) and Willmott's d-index from 0.86 to 0.87 for cotton (Figure 8) and from 896 to 967 kg ha^{-1} (nRMSE 11.7–12.6%) and Willmott's d-index from 0.87 to 0.85 across β values (0.8–1.8) for winter wheat (Figure S4). At 20 km, errors dropped to RMSE 282–312 and 713–751 kg ha^{-1} (nRMSE 11.4–12.6% and 9.3–9.8%, d 0.90–0.93 and 0.90–0.92) for cotton and winter wheat, respectively. Increasing the radius further to 30 km yielded only modest additional improvement, with an RMSE of 265–302 kg ha^{-1} and nRMSE 10.7–12.2% for cotton, and an RMSE of 629–677 kg ha^{-1} and nRMSE ≈ 8.2–8.8% for winter wheat (d ≈ 0.92). Thus, most of the benefit comes from moving beyond a very tight 10 km search window, while 20–30 km radii give broadly similar levels of agreement.

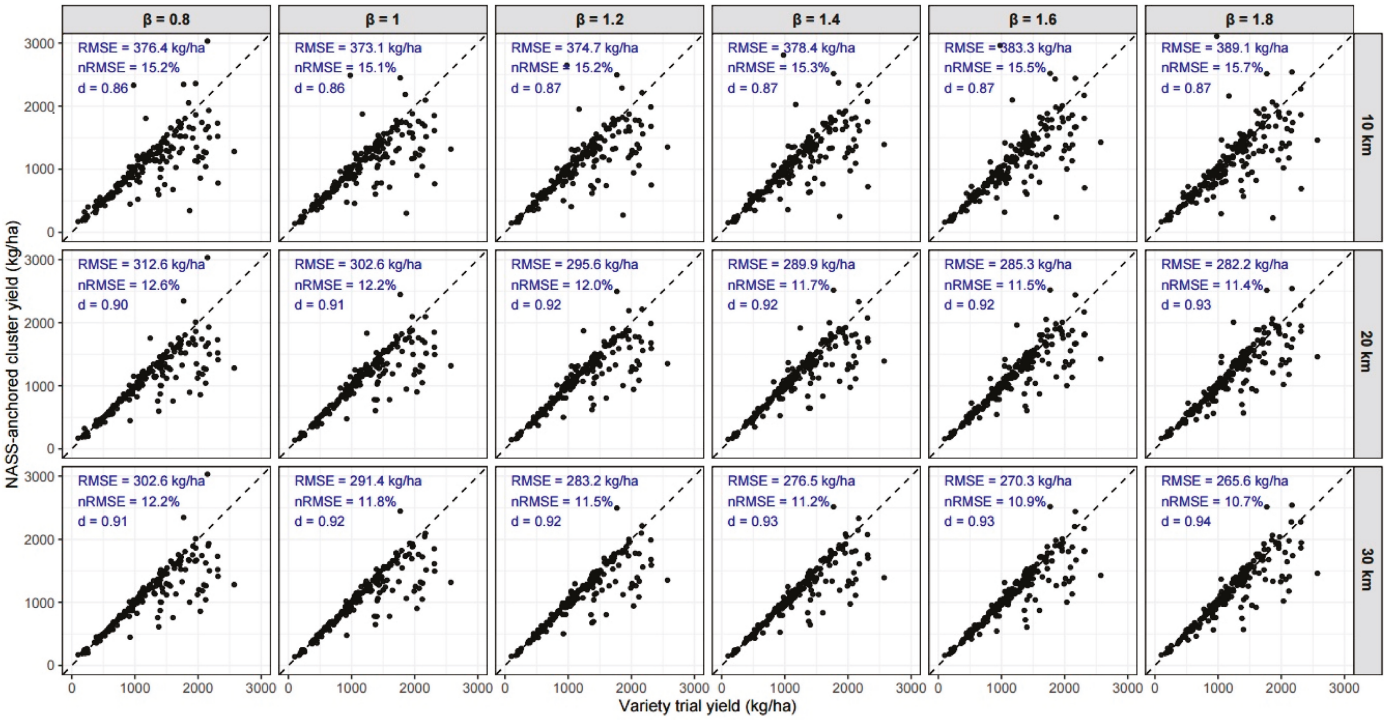

Figure 8. Evaluation of disaggregated cotton yields against Texas A&M AgriLife RACE variety trial means (2018–2024) across combinations of search radius and β exponent. Panels show observed trial yields versus matched cluster mean yields for search radii of 10, 20, and 30 km and β values ranging from 0.8 to 1.8. Each point represents a trial site-year; the solid line is the 1:1 line, and summary statistics (R^2, RMSE, nRMSE, Willmott's d) are reported per radius–β combination.

A direct point-to-intersecting cluster comparison was conducted by matching each variety trial location to the production cluster polygon from the same county and year that physically contained the trial point. This strict comparison does not use a search radius or

select a nearby cluster according to yield similarity. The results are shown in Figure S5. For cotton, the intersecting cluster comparison produced an RMSE of 491.3 kg ha^{-1}, nRMSE of 30.7%, MAE of 395.7 kg ha^{-1}, and Willmott's d-index of 0.647. For winter wheat, the corresponding statistics were RMSE = 2236 kg ha^{-1}, nRMSE = 31.5%, MAE = 1945 kg ha^{-1}, and d-index = 0.48, with lower agreement likely influenced by the prevalence of rainfed, abandoned, and grazed field conditions. The lower agreement under this strict comparison is expected because the cluster yield represents the average of a broader commercial production zone, whereas variety trials may represent relatively well-managed, locally favorable experimental conditions. In particular, the tendency for many high-yield trial observations to exceed the intersecting cluster yield reflects both the support scale mismatch and the county-level NASS constraint, which limits the extent to which local yield extremes can be represented without compensating low-yield areas elsewhere in the county.

The spatial maps in 2018–2019 for cotton and in 2018 and 2021 for winter wheat complement these summary statistics by showing how cluster yields and trial sites co-vary across Texas (Figure 9). In both cotton and winter wheat, NASS-anchored clusters (dots) form coherent production zones that align with known regional patterns: higher yields in the northern and central High Plains and lower yields toward drier western or southern environments. Variety trial sites (plus signs) generally sit within or adjacent to clusters of similar magnitude, rather than appearing as isolated high-yield "spikes" in low-yield surroundings. Years with widespread drought or stress (e.g., 2019 in parts of the Panhandle for cotton and 2018 for winter wheat) show spatially consistent yield reductions in both clusters and trials, whereas better years exhibit broader areas of high-yield clusters with trial means that fall within the local cluster range. For example, winter wheat yield exhibited high values in north and east Texas in 2021 in both clusters and trials (Figure 9). These maps, therefore, demonstrate that the workflow is not only matching trial means in aggregate but is also reproducing plausible spatial gradients across diverse environments.

The radius-based comparison produced lower RMSE and higher d-index values because it identifies a cluster of similar yield magnitude within the surrounding landscape. These metrics should, therefore, be interpreted as evidence of production zone plausibility rather than direct polygon-level allocation accuracy. The stricter point-to-intersecting cluster comparison in Figure S5 produced lower agreement for both crops, as expected, because each trial yield was compared only with the mean yield of the specific NASS-anchored cluster in which the trial occurred. The difference between the two approaches highlights the effect of spatial support: variety trials represent small experimental sites, whereas the intersecting clusters represent broader commercial production zones constrained to preserve the county-level NASS mean.

Across the radius-based comparisons, changes in β altered the range of candidate cluster yields and were not used to define a universally optimal β value. Higher β values increase the contrast among clusters, whereas lower values produce a flatter yield distribution around the county mean. As described in Section 2.3.4, $\beta = 1$ remains the recommended default when independent validation data are unavailable because it preserves the original relative NDVI–ET allocation structure without additional contrast amplification or compression.

The scatterplots from both comparison approaches reveal consistent behavior: the highest trial yields were more difficult to reproduce exactly than yields in the central part of the observed range. This compression is particularly apparent in the point-to-intersecting cluster comparison, where many high-yield trial observations exceeded the yield of their intersecting cluster. This pattern is expected because the disaggregation preserves the county-level NASS mean and cannot assign extreme yields to a small number of locations without introducing compensating low-yield areas elsewhere. In addition, variety trials

https://doi.org/10.3390/su18146937

may represent relatively well-managed experimental conditions, whereas the intersecting cluster includes a broader mixture of commercial fields that may differ in irrigation, soil conditions, management, and yield potential. Overall, the two comparisons indicate that the NASS-anchored clusters provide a plausible representation of production zone-scale yield variability, while very-high-yield experimental sites remain difficult to reproduce under a county-mean constraint.

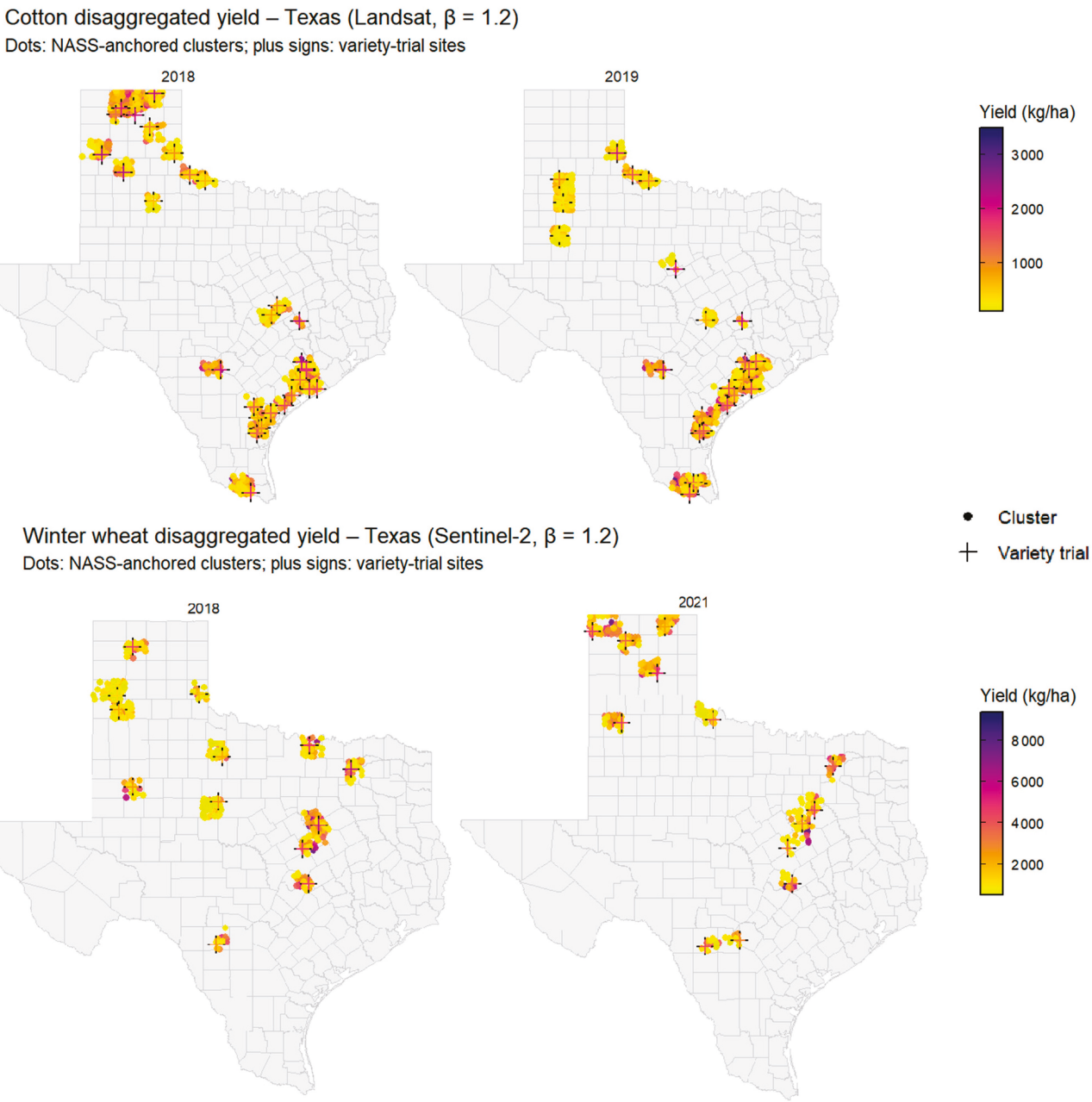

Figure 9. Spatial comparison between disaggregated cotton cluster yields and variety trial means in Texas, 2018 and 2019, and disaggregated winter wheat yields and variety trial means in Texas, 2018 and 2021. Colored polygons show NASS-anchored cluster mean lint or grain yields (kg ha^{-1}) for the matched county-years, while points indicate Texas A&M AgriLife RACE trial sites in cotton or Texas small grain trial sites in winter wheat, symbolized by observed trial mean yield.

3.6. Synthesis and Limitations

Taken together, the results show that the proposed NAYD workflow provides a transparent and reproducible approach for converting aggregated crop statistics into spatially

explicit production units and zonal clusters. Rather than predicting yield independently from many environmental covariates, the workflow uses crop masks, multi-sensor NDVI, satellite-derived evapotranspiration, and official yield statistics within a constrained allocation structure. This design allows within-county yield variability to be reconstructed while preserving consistency with reported harvested area and county mean yield. The NDVI-based eligibility step refines the crop extent toward the harvested area reported by NASS, while the combined NDVI–ET weighting captures dominant spatial gradients in crop vigor and water use.

The main contribution of the workflow is that satellite-derived indicators are embedded directly within a statistically consistent spatial allocation process. The resulting production zones are, therefore, not unconstrained yield predictions but NASS-consistent representations of crop production patterns. This distinction is important for sustainability assessment and regional decision support, where spatially detailed information is needed but field-level yield observations, proprietary yield monitor data, or detailed management records are often unavailable. The present implementation deliberately relies on widely available public datasets to maximize reproducibility and scalability across crops, years, and regions.

The resulting production zones can support several spatial agricultural decision support applications by providing a statistically consistent layer between county-level statistics and gridded environmental information. For example, watershed and hydrological models can use the zones to distribute crop production, harvested area, and crop-specific management scenarios more realistically across sub-county landscapes when assessing nutrient losses, sediment transport, or non-point source pollution. Likewise, regional greenhouse gas, soil carbon, and nutrient balance assessments can use the zones to allocate crop production and associated management inputs across heterogeneous irrigated and rainfed environments while remaining consistent with official county statistics. The zones may also support drought risk mapping, crop insurance risk stratification, and extension prioritization when combined with historical weather, soil, management, and loss information. In these applications, NAYD does not replace field-level observations or actuarial data; rather, it provides a transparent spatial framework for connecting official production statistics with environmental models and decision-relevant spatial covariates.

Validation against independent variety trial data showed that the resulting production zones reproduced broad site-level yield patterns at approximately 10–20 km scales. The β exponent provided a transparent mechanism for controlling spatial contrast while preserving the county-level yield constraint, with values near $\beta \approx 1$ offering a stable default configuration when independent calibration data are unavailable.

Importantly, the framework is not restricted to USDA-NASS or CDL products. The same logic can be applied wherever analogous crop masks, aggregated yield statistics, and satellite-derived vegetation or water use indicators are available. The R-based implementation also allows users to substitute region-specific datasets, adjust growing season windows, modify eligibility thresholds, and tune clustering scales according to the needs of crop modeling, environmental assessment, or sustainable agricultural planning. Overall, the results demonstrate that combining official agricultural statistics with remote sensing indicators can generate reproducible and statistically consistent spatial yield layers for applications that require information beyond coarse administrative units.

4. Conclusions

This study developed NAYD, a reproducible geospatial workflow for converting aggregated county-level crop statistics into spatially explicit production units and zonal clusters using publicly available crop mask, NDVI, and evapotranspiration datasets. Unlike

https://doi.org/10.3390/su18146937

conventional remote sensing yield mapping approaches that estimate yield independently from satellite predictors, NAYD treats official harvested area and county mean yield as fixed statistical constraints. Satellite-derived NDVI and evapotranspiration are used to guide the spatial allocation of those statistics, while NDVI-based crop eligibility, production unit segmentation, graph-based clustering, and β-controlled allocation provide a transparent structure for reconstructing within-county yield variability without breaking consistency with reported aggregate records.

Application to cotton and winter wheat in Texas showed that the framework can refine CDL crop masks toward reported harvested area, preserve realistic spatial gradients associated with irrigated and dryland systems, and generate production zones compatible with regional crop and soil modeling scales. The β parameter provides an interpretable mechanism for controlling spatial contrast without violating the county-level yield constraint, with values near unity offering a stable default configuration when independent calibration data are unavailable. Evaluation against independent variety trial data indicated that the resulting NASS-anchored production zones reproduce broad yield patterns at spatial scales relevant for regional analysis and management, rather than attempting to represent exact field-level performance. Accordingly, the workflow is best suited to representing dominant within-county yield gradients and production zone variation around the county mean, rather than detecting or reproducing isolated anomalous high- or low-yield hotspots.

More broadly, NAYD addresses a practical information gap in agricultural data systems: official statistics provide trusted and temporally consistent yield records but are spatially coarse, whereas satellite observations capture spatial heterogeneity but are not inherently linked to reported production totals. The workflow connects these two information streams in a form that is directly usable for regional crop modeling, environmental assessment, geospatial analysis, and agricultural decision support. It can also be adapted to other crops and regions where analogous datasets are available.

Supplementary Materials: The following supporting information can be downloaded at: https://www.mdpi.com/article/10.3390/su18146937/s1, Table S1. Conceptual comparison of NAYD with representative spatial crop-production allocation and satellite-based yield-estimation frameworks. Figure S1. Winter wheat NDVI and ET weight layers for Deaf Smith County, Texas (2016). (A) Seasonal mean (1 March to 30 May) NDVI over the NDVI-eligible winter wheat area; (B) NDVI-based normalized weight layer; (C) seasonal summed ET from OpenET SSEBop; (D) ET-based normalized weight layer; (E) raw combined NDVI–ET weight (before renormalization); and (F) final normalized NDVI–ET weight surface used for yield disaggregation. Figure S2. (A) Segmentation of NDVI-eligible winter wheat area and (B) relative yield allocation units in Deaf Smith County, Texas, 2016. Figure S3. Harvest-unit selection for winter wheat in Deaf Smith County, Texas (2016). (A) Cumulative normalized weight as a function of unit rank, showing the point at which the selected harvest subset reaches the NASS-anchored harvested area. (B) Spatial distribution of selected harvest units within the NDVI-eligible winter wheat area. (C) Distribution of unit weights for all candidate units, highlighting the higher weights assigned to the harvested subset. Table S2. Core inputs and user-adjustable parameters for transferring NAYD across agricultural regions and cropping systems. Table S3. User-defined crop-specific yield bounds and default allocation parameters used in the NAYD workflow. Table S4. Sensitivity of derived production zones to NDVI eligibility buffer and seasonal-window start date for representative cotton and winter wheat county-years. Table S5. Ablation analysis comparing alternative satellite-weighting schemes for cotton and winter wheat using direct point-to-intersecting-cluster comparison. Figure S4. Evaluation of disaggregated winter wheat yields against Texas A&M AgriLife variety-trial means (2008–2023) across combinations of search radius and β-exponent. Panels show observed trial yields versus matched cluster mean yields for search radii of 10, 20, and 30 km and β values ranging from 0.8 to 1.8. Each point represents a trial site–year; the solid line is the 1:1 line, and summary statistics (R^2, RMSE, nRMSE, Willmott's d) are

reported per radius–β combination. Figure S5. Point-to-intersecting-cluster evaluation for (A) cotton and (B) winter wheat against Texas A&M AgriLife variety-trial means in several locations in Texas, US.

Author Contributions: Conceptualization, A.A.; methodology, A.A.; software, A.A.; validation, A.A. and P.W.; formal analysis, A.A.; investigation, A.A.; resources, C.R.L. and F.M.R.J.; data curation, A.A. and P.W.; writing—original draft preparation, A.A.; writing—review and editing, A.A., P.W., C.R.L., F.M.R.J. and G.R.S.; visualization, A.A.; project administration, C.R.L.; funding acquisition, C.R.L. All authors have read and agreed to the published version of the manuscript.

Funding: This research was funded by the Texas A&M AgriLife Research and Extension Center at Overton.

Institutional Review Board Statement: Not applicable.

Informed Consent Statement: Not applicable.

Data Availability Statement: The data presented in this study were derived from publicly available resources. County-level planted area, harvested area, and yield statistics were obtained from the USDA National Agricultural Statistics Service Quick Stats database and "https://quickstats.nass.usda.gov/api/ accessed on 12 November 2025". Crop masks were derived from the USDA National Agricultural Statistics Service Cropland Data Layer: "https://www.nass.usda.gov/Research_and_Science/Cropland/Release/index.php accessed on 12 November 2025". Satellite vegetation index products, including MODIS, Landsat, and Sentinel-2, were accessed through Google Earth Engine: "https://developers.google.com/earth-engine/datasets accessed on 12 November 2025". Satellite-derived evapotranspiration data were obtained from OpenET SSEBop CONUS GRIDMET monthly products: "https://developers.google.com/earth-engine/datasets/catalog/projects_openet_assets_ssebop_conus_gridmet_monthly_v2_0 accessed on 12 November 2025". Cotton and winter wheat variety trial data were obtained from the Texas A&M AgriLife Variety Testing Program: "https://varietytesting.tamu.edu/ accessed on 14 January 2026. The NAYD R package and workflow documentation are available at: https://github.com/attia3/nayd.git accessed on 14 January 2026.

Acknowledgments: The authors acknowledge Texas A&M AgriLife Research and Extension Center at Overton for institutional support.

Conflicts of Interest: The authors declare no conflicts of interest.

References

1. USDA—NASS (United States Department of Agriculture—National Agricultural Statistics Service). *Quick Stats Database*; USDA—NASS: Washington, DC, USA. Available online: https://www.nass.usda.gov/Quick_Stats/ (accessed on 4 March 2025).
2. Alshihabi, O.; Persson, K.; Söderström, M. Easy yield mapping for precision agriculture. *Acta Agric. Scand. Sect. B—Soil Plant Sci.* **2024**, *74*, 2411950. [CrossRef]
3. Lobell, D.B.; Thau, D.; Seifert, C.; Engle, E.; Little, B. A scalable satellite-based crop yield mapper. *Remote Sens. Environ.* **2015**, *164*, 324–333. [CrossRef]
4. Ma, Y.; Liang, S.-Z.; Myers, D.B.; Swatantran, A.; Lobell, D.B. Subfield-level crop yield mapping without ground truth data: A scale transfer framework. *Remote Sens. Environ.* **2024**, *315*, 114427. [CrossRef]
5. Qin, X.; Wu, B.; Zeng, H.; Zhang, M.; Tian, F. Global gridded crop production dataset at 10 km resolution from 2010 to 2020. *Sci. Data* **2024**, *11*, 1377. [CrossRef] [PubMed]
6. Schulthess, U.; Timsina, J.; Herrera, J.; McDonald, A. Mapping field-scale yield gaps for maize: An example from Bangladesh. *Field Crops Res.* **2013**, *143*, 151–156. [CrossRef]
7. Van Wart, J.; Kersebaum, K.C.; Peng, S.; Milner, M.; Cassman, K.G. Estimating crop yield potential at regional to national scales. *Field Crops Res.* **2013**, *143*, 34–43. [CrossRef]
8. Amin, E.; Belda, S.; Pipia, L.; Szantoi, Z.; El Baroudy, A.; Moreno, J.; Verrelst, J. Multi-season phenology mapping of Nile Delta croplands using time series of Sentinel-2 and Landsat 8 green LAI. *Remote Sens.* **2022**, *14*, 1812. [CrossRef] [PubMed]
9. Amin, E.; Pipia, L.; Belda, S.; Perich, G.; Graf, L.V.; Aasen, H.; Van Wittenberghe, S.; Moreno, J.; Verrelst, J. In-season forecasting of within-field grain yield from Sentinel-2 time series data. *Int. J. Appl. Earth Obs. Geoinf.* **2024**, *126*, 103636. [CrossRef]
10. Bolton, D.K.; Friedl, M.A. Forecasting crop yield using remotely sensed vegetation indices and crop phenology metrics. *Agric. For. Meteorol.* **2013**, *173*, 74–84. [CrossRef]

11. Kivi, M.; Vergopolan, N.; Dokoohaki, H. A comprehensive assessment of in situ and remote sensing soil moisture data assimilation in the APSIM model for improving agricultural forecasting across the US Midwest. *Hydrol. Earth Syst. Sci.* **2022**, *27*, 1173–1199. [CrossRef]
12. Rezaei, E.E.; Ghazaryan, G.; González, J.; Cornish, N.; Dubovyk, O.; Siebert, S. The use of remote sensing to derive maize sowing dates for large-scale crop yield simulations. *Int. J. Biometeorol.* **2021**, *65*, 565–576. [CrossRef] [PubMed]
13. Dhakar, R.; Sehgal, V.K.; Chakraborty, D.; Sahoo, R.N.; Mukherjee, J.; Ines, A.V.; Kumar, S.N.; Shirsath, P.B.; Roy, S.B. Field scale spatial wheat yield forecasting system under limited field data availability by integrating crop simulation model with weather forecast and satellite remote sensing. *Agric. Syst.* **2022**, *195*, 103299. [CrossRef]
14. Attia, A.; Woli, P.; Long, C.R.; Rouquette, F.M., Jr.; Smith, G.R.; Datta, A.; Feike, T.; Rajan, N. Unlocking climate resilience by exploring the mitigation potential of improved rotation with cover cropping. *J. Environ. Manag.* **2025**, *391*, 126352. [CrossRef] [PubMed]
15. Ji, Z.; Pan, Y.; Zhu, X.; Wang, J.; Li, Q. Prediction of crop yield using phenological information extracted from remote sensing vegetation index. *Sensors* **2021**, *21*, 1406. [CrossRef] [PubMed]
16. Franch, B.; Vermote, E.F.; Skakun, S.; Roger, J.-C.; Becker-Reshef, I.; Murphy, E.; Justice, C. Remote sensing based yield monitoring: Application to winter wheat in United States and Ukraine. *Int. J. Appl. Earth Obs. Geoinf.* **2019**, *76*, 112–127. [CrossRef]
17. Skakun, S.; Vermote, E.; Franch, B.; Roger, J.-C.; Kussul, N.; Ju, J.; Masek, J. Winter wheat yield assessment from Landsat 8 and Sentinel-2 data: Incorporating surface reflectance, through phenological fitting, into regression yield models. *Remote Sens.* **2019**, *11*, 1768. [CrossRef]
18. Gautam, V.; Gani, A.; Pathak, S.; Shukla, A.K. Evaluating crop yield prediction models in illinois using aquacrop, semi-physical model and artificial neural networks. *Sci. Rep.* **2025**, *15*, 27494. [CrossRef] [PubMed]
19. Morales, G.; Sheppard, J.W.; Hegedus, P.B.; Maxwell, B.D. Improved yield prediction of winter wheat using a novel two-dimensional deep regression neural network trained via remote sensing. *Sensors* **2023**, *23*, 489. [CrossRef] [PubMed]
20. Yu, Q.; You, L.; Wood-Sichra, U.; Ru, Y.; Joglekar, A.K.; Fritz, S.; Xiong, W.; Lu, M.; Wu, W.; Yang, P. A cultivated planet in 2010: 2. the global gridded agricultural production maps. *Earth Syst. Sci. Data Discuss.* **2020**, *12*, 3545–3572. [CrossRef]
21. Monfreda, C.; Ramankutty, N.; Foley, J.A. Farming the planet: 2. Geographic distribution of crop areas, yields, physiological types, and net primary production in the year 2000. *Glob. Biogeochem. Cycles* **2008**, *22*, GB1022. [CrossRef]
22. Müller, C.; Elliott, J.; Kelly, D.; Arneth, A.; Balkovic, J.; Ciais, P.; Deryng, D.; Folberth, C.; Hoek, S.; Izaurralde, R.C. The global gridded crop model intercomparison phase 1 simulation dataset. *Sci. Data* **2019**, *6*, 50. [CrossRef] [PubMed]
23. Fendrich, A.N.; Neto, E.S.H.; e Moreira, L.E.M.; Neto, D.D. A scalable method for the estimation of spatial disaggregation models. *Comput. Geosci.* **2022**, *166*, 105161. [CrossRef]
24. Attia, A.; Woli, P.; Long, C.R.; Rouquette, F.M., Jr.; Smith, G.R.; Ibrahim, A.M. Mapping spatial zones of climate vulnerability and adaptive potential for major crops in the Texas high plains. *Model. Earth Syst. Environ.* **2025**, *11*, 416. [CrossRef]
25. Gorelick, N.; Hancher, M.; Dixon, M.; Ilyushchenko, S.; Thau, D.; Moore, R. Google Earth Engine: Planetary-scale geospatial analysis for everyone. *Remote Sens. Environ.* **2017**, *202*, 18–27. [CrossRef]
26. Monteith, J.L. Climate and the efficiency of crop production in Britain. *Philos. Trans. R. Soc. Lond. B Biol. Sci.* **1977**, *281*, 277–294. [CrossRef]
27. Tucker, C.J. Red and photographic infrared linear combinations for monitoring vegetation. *Remote Sens. Environ.* **1979**, *8*, 127–150. [CrossRef]
28. Li, Y.; Chen, X.; Miao, Y.; Liu, X.; Tian, Y.; Zhu, Y.; Cao, Q.; Cao, W. Improving wheat nitrogen use efficiency through a management zone-based optimization strategy by integrating crop model and remote sensing. *Field Crops Res.* **2025**, *333*, 110088. [CrossRef]
29. Wang, X.; Miao, Y.; Dong, L.; Mi, G.; Batchelor, W.D.; Kusnierek, K. Precision nitrogen management for maize based on crop modeling, remote sensing and machine learning. *Comput. Electron. Agric.* **2025**, *239*, 111124. [CrossRef]
30. Yang, G.; Jin, N.; Ai, W.; Zheng, Z.; He, Y.; He, Y. Integrating remote sensing data assimilation, deep learning and large language model to interactive yield prediction for wheat breeding. *Comput. Electron. Agric.* **2026**, *244*, 111495. [CrossRef]
31. Zhang, L.; Li, C.; Zhang, G.; Wu, X.; Zhou, L.; Chen, L.; Jiao, Y.; Liu, G.; Hei, W. Winter wheat yield estimation based on multisource remote sensing data: A dual-branch TCN-Transformer model and analysis of growth-stage feature transition mechanisms. *Comput. Electron. Agric.* **2025**, *239*, 111014. [CrossRef]
32. Liu, G.; Liu, Z.; Liu, T.; Wang, L.; Zhu, D. Towards automated crop monitoring: A computer vision solution for maize tassel detection under center-pivot irrigation systems. *Comput. Electron. Agric.* **2026**, *242*, 111304. [CrossRef]
33. Argent, R.M. An overview of model integration for environmental applications—Components, frameworks and semantics. *Environ. Model. Softw.* **2004**, *19*, 219–234. [CrossRef]
34. Maestrini, B.; Basso, B. Drivers of within-field spatial and temporal variability of crop yield across the US Midwest. *Sci. Rep.* **2018**, *8*, 14833. [CrossRef] [PubMed]

35. Metwally, M.S.; Shaddad, S.M.; Liu, M.; Yao, R.-J.; Abdo, A.I.; Li, P.; Jiao, J.; Chen, X. Soil properties spatial variability and delineation of site-specific management zones based on soil fertility using fuzzy clustering in a hilly field in Jianyang, Sichuan, China. *Sustainability* **2019**, *11*, 7084. [CrossRef]
36. Schepers, A.R.; Shanahan, J.F.; Liebig, M.A.; Schepers, J.S.; Johnson, S.H.; Luchiari, A., Jr. Appropriateness of management zones for characterizing spatial variability of soil properties and irrigated corn yields across years. *Agron. J.* **2004**, *96*, 195–203. [CrossRef]
37. Li, X.; Pan, Y.; Zhao, Z.; Wang, J.; Bao, Y.; Wang, J. Delineation and scale effect of precision agriculture management zones using yield monitor data over four years. *Agric. Sci. China* **2007**, *6*, 180–188. [CrossRef]
38. Maestrini, B.; Basso, B. Predicting spatial patterns of within-field crop yield variability. *Field Crops Res.* **2018**, *219*, 106–112. [CrossRef]

Disclaimer/Publisher's Note: The statements, opinions and data contained in all publications are solely those of the individual author(s) and contributor(s) and not of MDPI and/or the editor(s). MDPI and/or the editor(s) disclaim responsibility for any injury to people or property resulting from any ideas, methods, instructions or products referred to in the content.

MDPI AG
Grosspeteranlage 5
4052 Basel
Switzerland
Tel.: +41 61 683 77 34

Sustainability Editorial Office
E-mail: sustainability@mdpi.com
www.mdpi.com/journal/sustainability



Disclaimer/Publisher's Note: The title and front matter of this reprint are at the discretion of the Guest Editors. The publisher is not responsible for their content or any associated concerns. The statements, opinions and data contained in all individual articles are solely those of the individual Editors and contributors and not of MDPI. MDPI disclaims responsibility for any injury to people or property resulting from any ideas, methods, instructions or products referred to in the content.





Academic Open
Access Publishing

mdpi.com

ISBN 978-3-7258-9438-3